ADVANCES IN NANO-SCALE SYSTEMS WITH OPTICS (NANO-CHEMICAL, NANOMATERIAL, AND NANO-BIOMEDICINE)

EDITED BY: Honghui He, Martin Booth, Chao He and Siwei Zhang
PUBLISHED IN: Frontiers in Chemistry

frontiers Research Topics

Frontiers eBook Copyright Statement

The copyright in the text of individual articles in this eBook is the property of their respective authors or their respective institutions or funders. The copyright in graphics and images within each article may be subject to copyright of other parties. In both cases this is subject to a license granted to Frontiers.

The compilation of articles constituting this eBook is the property of Frontiers.

Each article within this eBook, and the eBook itself, are published under the most recent version of the Creative Commons CC-BY licence. The version current at the date of publication of this eBook is CC-BY 4.0. If the CC-BY licence is updated, the licence granted by Frontiers is automatically updated to the new version.

When exercising any right under the CC-BY licence, Frontiers must be attributed as the original publisher of the article or eBook, as applicable.

Authors have the responsibility of ensuring that any graphics or other materials which are the property of others may be included in the CC-BY licence, but this should be checked before relying on the CC-BY licence to reproduce those materials. Any copyright notices relating to those materials must be complied with.

Copyright and source acknowledgement notices may not be removed and must be displayed in any copy, derivative work or partial copy which includes the elements in question.

All copyright, and all rights therein, are protected by national and international copyright laws. The above represents a summary only. For further information please read Frontiers' Conditions for Website Use and Copyright Statement, and the applicable CC-BY licence.

ISSN 1664-8714
ISBN 978-2-83250-035-4
DOI 10.3389/978-2-83250-035-4

About Frontiers

Frontiers is more than just an open-access publisher of scholarly articles: it is a pioneering approach to the world of academia, radically improving the way scholarly research is managed. The grand vision of Frontiers is a world where all people have an equal opportunity to seek, share and generate knowledge. Frontiers provides immediate and permanent online open access to all its publications, but this alone is not enough to realize our grand goals.

Frontiers Journal Series

The Frontiers Journal Series is a multi-tier and interdisciplinary set of open-access, online journals, promising a paradigm shift from the current review, selection and dissemination processes in academic publishing. All Frontiers journals are driven by researchers for researchers; therefore, they constitute a service to the scholarly community. At the same time, the Frontiers Journal Series operates on a revolutionary invention, the tiered publishing system, initially addressing specific communities of scholars, and gradually climbing up to broader public understanding, thus serving the interests of the lay society, too.

Dedication to Quality

Each Frontiers article is a landmark of the highest quality, thanks to genuinely collaborative interactions between authors and review editors, who include some of the world's best academicians. Research must be certified by peers before entering a stream of knowledge that may eventually reach the public - and shape society; therefore, Frontiers only applies the most rigorous and unbiased reviews.
Frontiers revolutionizes research publishing by freely delivering the most outstanding research, evaluated with no bias from both the academic and social point of view. By applying the most advanced information technologies, Frontiers is catapulting scholarly publishing into a new generation.

What are Frontiers Research Topics?

Frontiers Research Topics are very popular trademarks of the Frontiers Journals Series: they are collections of at least ten articles, all centered on a particular subject. With their unique mix of varied contributions from Original Research to Review Articles, Frontiers Research Topics unify the most influential researchers, the latest key findings and historical advances in a hot research area! Find out more on how to host your own Frontiers Research Topic or contribute to one as an author by contacting the Frontiers Editorial Office: frontiersin.org/about/contact

ADVANCES IN NANO-SCALE SYSTEMS WITH OPTICS (NANO-CHEMICAL, NANOMATERIAL, AND NANO-BIOMEDICINE)

Topic Editors:
Honghui He, Tsinghua University, China
Martin Booth, University of Oxford, United Kingdom
Chao He, University of Oxford, United Kingdom
Siwei Zhang, Hong Kong University of Science and Technology, SAR China

Citation: He, H., Booth, M., He, C., Zhang, S., eds. (2022). Advances in Nano-Scale Systems With Optics (Nano-Chemical, Nanomaterial, and Nano-Biomedicine). Lausanne: Frontiers Media SA. doi: 10.3389/978-2-83250-035-4

Table of Contents

frontiers | Frontiers in Chemistry

TYPE Editorial
PUBLISHED 12 August 2022
DOI 10.3389/fchem.2022.989153

Check for updates

OPEN ACCESS

EDITED BY
Shengli Zou,
University of Central Florida,
United States

REVIEWED BY
Yadong Zhou,
China Jiliang University, China

*CORRESPONDENCE
Honghui He,
he.honghui@sz.tsinghua.edu.cn
Chao He,
chao.he@eng.ox.ac.uk
Martin Booth,
martin.booth@eng.ox.ac.uk

SPECIALTY SECTION
This article was submitted to Nanoscience, a section of the journal Frontiers in Chemistry

RECEIVED 08 July 2022
ACCEPTED 19 July 2022
PUBLISHED 12 August 2022

CITATION
Zhang S-W, He H, He C and Booth M (2022), Editorial: Advances in nano-scale systems with optics (nano-chemical, nanomaterial, and nano-biomedicine).
Front. Chem. 10:989153.
doi: 10.3389/fchem.2022.989153

COPYRIGHT
© 2022 Zhang, He, He and Booth. This is an open-access article distributed under the terms of the Creative Commons Attribution License (CC BY). The use, distribution or reproduction in other forums is permitted, provided the original author(s) and the copyright owner(s) are credited and that the original publication in this journal is cited, in accordance with accepted academic practice. No use, distribution or reproduction is permitted which does not comply with these terms.

Editorial: Advances in nano-scale systems with optics (nano-chemical, nanomaterial, and nano-biomedicine)

Si-Wei Zhang[1], Honghui He[2]*, Chao He[3]* and Martin Booth[3]*

[1]Department of Chemistry, Hong Kong Branch of Chinese National Engineering Research Center for Tissue Restoration and Reconstruction, The Hong Kong University of Science and Technology, Kowloon, Hong Kong SAR, China, [2]Shenzhen Key Laboratory for Minimal Invasive Medical Technologies, Guangdong Research Center of Polarization Imaging and Measurement Engineering Technology, Tsinghua Shenzhen International Graduate School, Tsinghua University, Shenzhen, China, [3]Department of Engineering Science, University of Oxford, Oxford, United Kingdom

KEYWORDS

microscopic imaging technology, organic light-emitting devices (OELDs), sensor, raman spectoscopy, weak measurement technology, super-resolution microscopy

Editorial on the Research Topic
Advances in nano-scaled systems with optics (nano-chemical, nano-material, and nano-biomedicine)

Optical properties of materials are important aspects of various recent advances in nanoscience, contributing to plenty of applications from fundamental research to industry. The cross-disciplinary design, synthesis, characterization, and applications the nano-systems are at the heart of various research directions. Novel nano-materials such as nanofibers, quantum dots, and nanoclusters have been adopted in applications such as photoelectric devices, microscopy, and optical communications. By combining organic and inorganic materials, increasingly nanoscale devices have been utilized in various integrated systems such as optical sensors, detectors, and switches, with low-power consumption, high speed, and high stability. Furthermore, optical properties of nanofiber structures inside the tissues also have been harnessed to assist clinical applications.

This special issue collects 14 excellent papers: 10 original research papers and 4 review articles, spanning microscopic imaging technology, super-resolution microscopy, organic light-emitting devices (OLED) and LED, weak measurement technology, Raman spectroscopy, and sensors.

Microscopic imaging technology (MIT) Accelerates the pace of exploring the micro world. Wang et al. reviewed the development of MIT and its application in micro-and nano fields (Wang et al.). Wu et al. developed an imaging technique by circular dichroism second-harmonic generation (CD-SHG) to characterize the 3D distribution of potassium titanyl phosphate (KTP) nanocrystal, which insights into nanoscale morphology of KTP and benefits the experimental configuration optimization of CD-SHG microscopy (Wu

et al.). With machine learning, Zhu et al. designed a U-Net-based neural network to accelerate DNA-PAINT imaging from a widefield fluorescence image and a sparse single-molecule localization image. This approach only requires one-tenth of the original raw data but permits fast imaging and super-resolution reconstruction of microtubules as well as analyzing other SMLM datasets (Zhu et al.). Shao et al. analyzed the influence of imaging resolution on polarization properties of scattering media obtained from a Mueller matrix, which provides a criterion to decide what kind of structural information can be accurately and rapidly obtained using transmission Mueller matrix microscope with low NA objectives to assist pathological diagnosis and other applications (Shao et al.).

Super-resolution microscopy (SRM) has become a powerful tool for visualizing biological activities in both fixed and living cells. Wang et al. reviewed the development of microscope technology, summarized the properties of numerous microscopes, and discussed their applications in micro and nanotechnology (Wang et al.). Jing et al. summarized recent technical advancements in SRM, discussed together with the spectroscopic and chemical demands of the fluorophores, and highlighted some inherent challenges faced in this emerging field (Jing et al.). Sun et al. introduced a novel approach, which combines second-harmonic generation with two-photon excited fluorescence to visualize the dynamics of transdermal collagen absorption *in vivo*, providing a reliable measurement for real-time evaluation of collagen absorption and treatment effects *in vivo* (Sun et al.).

OLEDs and LEDs Liu et al. designed and synthesized a novel 3 + 2+1 coordinated iridium (III) complex for high efficient deep-blue phosphorescent OLED (Liu et al.). Chen et al. reported a promising luminescent phosphor for next-generation illuminant based core/shell CdZnSeS/ZnSeS quantum dots (QDs) (Chen et al.). QDs are promising for next-generation lighting and display. Zhang et al. emphasized the significance of detection of nanoparticles synthesized by a gas-phase method, reviewed the development of detection technology, and prospected its future (Zhang et al.).

Weak measurement technology has great potential in biomolecular detection in the frequency domain field. Xu et al. elucidated the difference between the weak measurement method and the classical measurement process and highlighted the transition conditions of the weak value enhancement. Furthermore, a transition mode of the weak and classical measurements is proposed and an optimized fitting model of the measurement results is found by performing a systematic analysis, suggesting the wide implementation of weak measurement-based detection technology (Xu et al.).

Raman spectroscopy is an essential non-destructive testing method. Li et al. investigated cold cataract cellular mechanisms in young lenses of wild-type C57BL/6J (B6WT) mice treated at different temperatures. Raman spectroscopy fluctuation reveals new mechanistic information about cold cataract formation, which is associated with the uneven distribution of lens proteins and water across lens fiber cells. Raman spectroscopy partly reveals cold temperature-induced redistribution of lens proteins such as intermediate filaments in inner fiber cells (Li et al.).

Sensors are the central part of detection. Zeng et al. developed a high-sensitive surface plasmon resonance imaging (SPRi) biosensor based on the dual-wavelength differential method. The new technique achieved a refractive index resolution of 2.24×10^{-6} RIU and high-throughput real-time detection biomolecular binding, which is expected to promote the development of faster and more accurate SPRi technologies (Zeng et al.). Shen et al. proposed a self-referencing interference sensor based on coherence multiplexing, which can address temperature and non-specific binding. The temperature fluctuations and specific binding experiments of protein A to IgG demonstrate that the proposed sensor can eliminate non-specific binding and temperature disturbances in real-time biomolecule detection, achieving higher detection robustness (Shen et al.).

Author contributions

S-WZ, HH, CH, and MB curated this special issue together.).

Acknowledgments

S-WZ thank the support from the Research Grants Council of Hong Kong (C6014-20W) and the Innovation and Technology Commission (ITC-CNERC14SC01). CH thank the support of the Junior Research Fellowship from St John's College, University of Oxford. The editors are grateful to the authors for submitting their valuable work and to all the reviewers who contributed to this effort by thoroughly evaluating the submitted articles and providing thoughtful advice on how these can be improved.).

Conflict of interest

The authors declare that the research was conducted in the absence of any commercial or financial relationships that could be construed as a potential conflict of interest.).

Publisher's note

All claims expressed in this article are solely those of the authors and do not necessarily represent those of their affiliated organizations, or those of the publisher, the editors and the reviewers. Any product that may be evaluated in this article, or claim that may be made by its manufacturer, is not guaranteed or endorsed by the publisher.

frontiers in Chemistry

REVIEW
published: 14 September 2021
doi: 10.3389/fchem.2021.746900

Super-Resolution Microscopy: Shedding New Light on *In Vivo* Imaging

Yingying Jing, Chenshuang Zhang, Bin Yu, Danying Lin and Junle Qu**

Key Laboratory of Optoelectronic Devices and Systems of Ministry of Education and Guangdong Province, College of Physics and Optoelectronic Engineering, Shenzhen University, Shenzhen, China

Over the past two decades, super-resolution microscopy (SRM), which offered a significant improvement in resolution over conventional light microscopy, has become a powerful tool to visualize biological activities in both fixed and living cells. However, completely understanding biological processes requires studying cells in a physiological context at high spatiotemporal resolution. Recently, SRM has showcased its ability to observe the detailed structures and dynamics in living species. Here we summarized recent technical advancements in SRM that have been successfully applied to *in vivo* imaging. Then, improvements in the labeling strategies are discussed together with the spectroscopic and chemical demands of the fluorophores. Finally, we broadly reviewed the current applications for super-resolution techniques in living species and highlighted some inherent challenges faced in this emerging field. We hope that this review could serve as an ideal reference for researchers as well as beginners in the relevant field of *in vivo* super resolution imaging.

Keywords: super-resolution techniques, *in vivo* imaging, labeling strategies, near-infrared fluorescent probes, *in vivo* applications

OPEN ACCESS

Edited by:
Honghui He,
Tsinghua University, China

Reviewed by:
Changfeng Wu,
Southern University of Science and Technology, China
Jingyu Wang,
University of Oxford, United Kingdom
Martin Booth,
University of Oxford, United Kingdom

****Correspondence:***
Danying Lin
dylin@szu.edu.cn
Junle Qu
jlqu@szu.edu.cn

Specialty section:
This article was submitted to Nanoscience, a section of the journal Frontiers in Chemistry

Received: *25 July 2021*
Accepted: *26 August 2021*
Published: *14 September 2021*

Citation:
Jing Y, Zhang C, Yu B, Lin D and Qu J (2021) Super-Resolution Microscopy: Shedding New Light on In Vivo *Imaging. Front. Chem. 9:746900. doi: 10.3389/fchem.2021.746900*

INTRODUCTION

Cells are the functional units of life and grow in a relative complicated environment. Getting accurate physiological knowledge requires studying cells within their parent organisms, and thus scientific researchers could obtain the biological information in a native state within the organism itself, where all the cues are driven by gene expression (Liu et al., 2018). While many of the structures and organization patterns of biomolecules in *in-vitro* cells have been identified, *in vivo* studies will offer unique insights into the cellular morphology in relation to genetical conditions or pathological modifications (Vacaru et al., 2014; Stone et al., 2017; Zheng et al., 2020). However, at present, it is still a challenge to observe the organelles and macromolecular complexes *in vivo* at high resolution.

So far, fluorescence microscopy has been an unprecedented choice for *in vivo* studies as it offers noninvasive imaging, good specificity and high temporal resolution (Sigrist and Sabatini, 2012). Traditional imaging tools such as confocal microscopy and multiphoton microscopy have been employed to study vital physiological activities in living systems (Heilemann, 2010). Nevertheless, more detailed measurement of morphological changes in living species has been hindered by the diffraction limitation of light, which is about half the wavelength of light (200–300 nm) (Hell et al., 2004; Agrawal et al., 2013). Hence, sub-diffraction imaging techniques are needed urgently for investigating the fine structures *in vivo*.

Over the past 2 decades, advances in super-resolution microscopy (SRM) have revolutionized the field of fluorescent imaging and become valuable tools in biological studies (Coltharp and Xiao, 2012; Baddeley and Bewersdorf, 2018; Schermelleh et al., 2019). These SRM techniques are most

prominently harnessed in two distinct families: one employs patterned illumination to spatially modulate the fluorescence behavior and their related derivatives, such as stimulated emission depletion microscopy (STED) (Hell and Wichmann, 1994; Vicidomini et al., 2018), structured illumination microscopy (SIM) (Gustafsson, 2000; Li et al., 2015; Turcotte et al., 2019) and reversible saturable optically linear fluorescence transitions (RESOLFTs) (Grotjohann et al., 2011); the other obtains super-resolution images based on the localization of individual emitting molecules, such as stochastic optical reconstruction microscopy (STORM) (Rust et al., 2006; Bates et al., 2013) and photoactivated localization microscopy (PALM) (Betzig et al., 2006; Henriques et al., 2011). Now, SRM systems have become central tools in the biomedical research community (Coltharp and Xiao, 2012; Muller and Heilemann, 2013; Stone et al., 2017; Xu J. et al., 2020).

Despite significant progress, the application of present SRM techniques to scattering tissues or living samples are limited due to poor imaging depth. The unnecessary excitation of out-of-focus fluorophores degrades the quality of the in-focus signal, making it difficult to resolve the fine structures. Besides, the imaging rates are still insufficient for many *in vivo* applications, especially those involving signal transportation studies (Galbraith and Galbraith, 2011; Biteen and Willets, 2017). Moreover, even in the absence of aberrations, most SRMs achieve high resolution usually by intense illumination, which can disturb delicate subcellular processes or even introduce permanent phototoxic damages (Hell et al., 2015; Kilian et al., 2018). Consequently, the capabilities of SRM implementations are hampered in the field of *in vivo* imaging.

Even though, to address these challenges, considerable efforts have been extended toward enhancing the imaging depth and developing highly sensitive fluorescent probes to realize real-time imaging *in vivo*. For example, Adaptive Optics (AO) has been introduced in many SRM techniques to enhance the imaging depth by eliminating the sample-induced distortions in the wavefront using a dynamically reconfigurable optical element. Nowadays, the improvements in optical system construction, camera technologies and labeling methods have made SRM possible to visualize physiological activity in living organism. In the following pages, we provide an overview of recent advances in SRM techniques for imaging *in vivo*. The technological modifications in the burgeoning field of "*in vivo* SRM" are first clarified, and the current fluorescent probes for *in vivo* SRM labeling are described. Then, the applications of these techniques in various biological areas are discussed, and the challenges as well as future trends in this emerging field are highlighted.

SUPER-RESOLUTION TECHNIQUES FOR *IN VIVO* IMAGING

Stimulated Emission Depletion (STED) Microscopy

In 1994, the concept of STED microscopy was first proposed and it was subsequently demonstrated experimentally (Hell and Wichmann, 1994). Briefly, STED microscopy is a two-beam technique that applies a STED beam to suppress the emission of the fluorescent molecules located off the core of the excitation region in order to sharpen the effective point spread function (PSF) (**Figure 1A**) (Yang et al., 2016). On that account, the depletion beam needs an illumination pattern shaped like doughnut with non-zero intensity at the periphery and zero intensity at the center of the excitation spot. Scanning the sharpened PSFs across the sample could allow recording a super-resolved image with high resolution. As an extended technique based on confocal microscopy, STED could obtain the images directly, and thus is better suited for *in vivo* imaging (Jahr et al., 2020; Steffens et al., 2020). Moreover, the inherent 3D sectioning capability of STED makes it ideal for whole tissue imaging (Hell and Wichmann, 1994; Spahn et al., 2019).

Because of specimen-induced scattering distortion and aberrations, there is a great challenge for STED microscopy to maintain consistent resolution in deep tissue inside living bodies. In 2011, Stefan W. Hell's group modified STED microscopy equipping with a high-numerical aperture (NA) glycerol immersion objective lens and a correction collar to improve the penetration depth. They could image the actin at a depth of 120 μm below the tissue surface inside living brain slices with a spatial resolution of 60–80 nm (Urban et al., 2011). Afterwards, the real *in vivo* STED microscopy was first demonstrated also by his group in 2012 (Berning et al., 2012). They developed an upright scanning STED microscope with a 1.3 NA objective lens focusing 488 nm wavelength in a mouse brain (**Figure 1B**). The focused excitation pulses were aligned and synchronized with the doughnut-shaped 592 nm STED pulses for silencing the enhanced yellow fluorescent protein (EYFP). This STED technique was successfully applied to image the 10–15 μm molecular layer below the surface with a resolution of about 70 nm. Later, a few groups also modified STED technique to increase the imaging depth through various methods. For example, Kebin Shi's group reported a Gaussian-Bessel STED (GB-STED) microscopy, which achieved an imaging depth of 100 μm in brain tissue by modulating the depletion beam into a hollow Bessel beam and using a conventional Gaussian beam for excitation (Yu et al., 2016).

Two-photon (2P) excitation is important for *in vivo* imaging as it is well suited for deep tissue observation (Helmchen and Denk, 2005). The main strengths of 2P excitation include that typical 2P laser scanning microscopy could increase imaging depth by using near infrared (NIR) excitation laser beam, and the 2P excitation could reduce background by confining excitation to the focal point of the objective (Denk et al., 1990; So et al., 2000). Thus, U Valentin Nagerl et al. combined 2P excitation with STED (2P-STED) microscopy to improve the imaging depth and resolution, exploiting new perspectives for deep tissue imaging both *in vitro* and *in vivo* (Bethge et al., 2013; Ter Veer et al., 2017). In 2013, they constructed 2P-STED microscope incorporating with a pulsed STED laser, a long-working distance water objective and spectral detection for two-color imaging in brain slices (Bethge et al., 2013). The symmetry and central minimum of the STED doughnut were optimized by adjusting a λ/4 wave plate in front of the scanner.

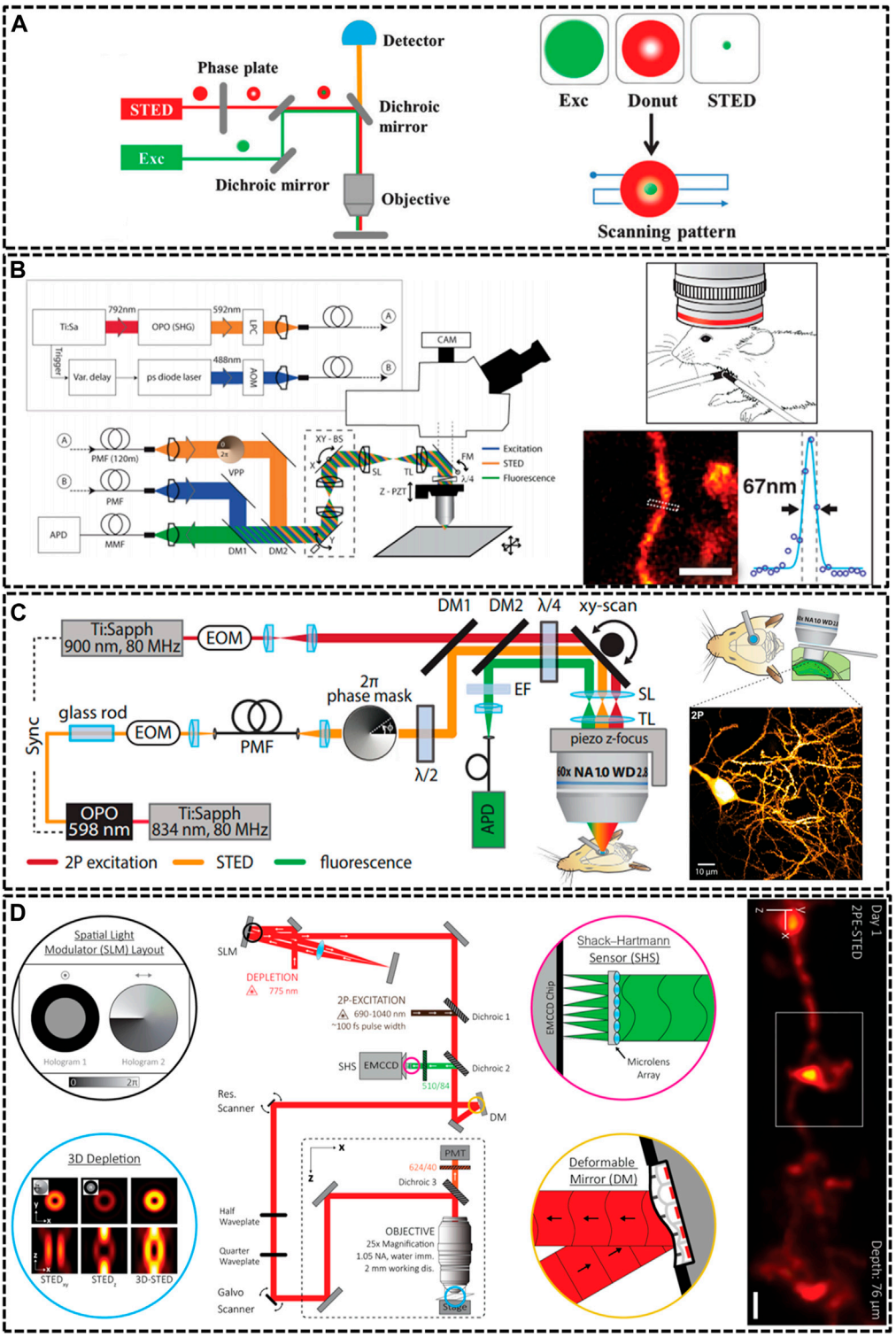

FIGURE 1 | Overview of modified STED microscopy for *in vivo* imaging. **(A)** The principle of STED technique. The combination of excitation laser and donut-shaped STED laser could decrease the size of PSF effectively (Yang et al., 2016). Reprinted from Yang et al. (2016) with permission from Royal Society of Chemistry. **(B)** Schematic drawing of the upright scanning STED for *in vivo* imaging (Berning et al., 2012). Reprinted from Berning et al. (2012) with permission from American Association for the Advancement of Science. The STED image of dendritic and axonal structures was obtained from a living mouse brain under the objective lens (1.3 NA, glycerol immersion). Scale bar, 1 µm. **(C)** Diagram of two photon (2P) STED microscope (Pfeiffer et al., 2018). The 2P image depicted dendrites of pyramidal neuron in hippocampal CA1 region. Scale bar, 10 µm. Reprinted from Pfeiffer et al. (2018) with permission from eLife Sciences. **(D)** Schematic of aberration-corrected 3D-2P-STED instrument (Velasco et al., 2021). The microscopy equipped with a double-pass spatial light modulator (SLM) to impart both the vortex and top-hat phase masks on the depletion beam. Super-resolution image showed a 3D dendrite at 76 µm below the cortical surface. Scale bar: 1 µm. Reprinted from Velasco et al. (2021) with permission from Optical Society of America.

Then, in 2018, they successfully applied the home-built 2P-STED microscope to reach the deeply located hippocampus *in vivo* (**Figure 1C**) (Pfeiffer et al., 2018).

Most life live by means of three-dimensional interplay with millions of components, and thus defining their structural details not only requires subdiffraction resolution in x-y plane, but also along demands high optical resolution in z axis (Lin et al., 2018). Unfortunately, most current depletion effects of PSF remains diffraction limited in the z direction. Several methods have been implemented to improve the axial resolution of STED microscopy, such as 4Pi-STED, isoSTED and the method using the top-hat phase mask (Huang et al., 2010; Galbraith and Galbraith, 2011; Vicidomini et al., 2018). However, these methods still limited the applications of STED in deep-tissue imaging in living specimens. In 2019, Jason R. Swedlow et al. demonstrated a STED microscope that was capable of 3D super-resolution imaging with automated aberration correction (Zdankowski et al., 2020). They introduced an image denoising method based on block-matching and collaborative 3D filtering (BM3D) to numerically enhance fine object details. The technique achieved lateral and axial resolution of 204 and 310 nm in an 80 μm thick layer of tissue. As noted above, AO could enhance imaging depth by adaptively correcting aberration induced from the sample, therefore, it plays a vital role in in vivo imaging. Recent work impressively demonstrated AO-improved STED microscopy of aberrating samples. Joerg Bewersdorf et al. have achieved aberration-corrected 3D STED imaging at 76 μm depth through the combination of 2P excitation, AO correction, organic dye labeling approach, and a long-working-distance water-immersion objective lens (Velasco et al., 2021). As shown in **Figure 1D**, they employed an AO architecture based on wavefront sensing to correct aberrations. Moreover, the 2-mm working distance of objective lens accommodated a wide range of sample dimensions and configurations and allowed long penetration depths into the living species. For 2P excitation, they used light from a femtosecond (fs)-pulsed titanium sapphire laser that was fused with the STED beam via a dichroic mirror. The 3D-2P-STED was successfully applied to the brain of a living mouse with an axial resolution of 321 nm.

Reversible Saturable Optical Fluorescence Transition

The depletion concept has been extended to photoswitchable fluorescent proteins by using the donut-shaped depletion beam to switch fluorophores into the OFF state instead of stimulated emission, which is known as RESOLFT microscopy (Grotjohann et al., 2011; Sharma et al., 2020). The RESOLFT technique employs the genetically encoded markers and minimizes the illumination light intensities, thus it is suitable for discerning molecular structures and individual organelles in the interior of living body. The spatial resolution could be indeed improved through saturating the OFF-switching transition by using a light pattern featuring one or more intensity minima or "zeros" (**Figure 2A**) (Hell et al., 2015). Unlike STED which requires an intense depletion laser, a low saturation intensity was chosen for RESOLFT, permitting much lower phototoxic damage (Grotjohann et al., 2011).

In 2012, Stefan W. Hell's group constructed a RESOLFT setup equipping with dichroic mirrors and filters dedicated for the green fluorescent protein Dronpa-M159T (Testa et al., 2012). The reversibly switchable fluorescent protein (rsFP) Dronpa-M159T was switched on with 405 nm wavelength and switched off by a counterpart of 491 nm wavelength featuring a doughnut shape with central zero intensity, and excited with another light, also of 491 nm illumination. Dendritic spines were recorded for hours inside living organotypic hippocampal brain slices. Moreover, in 2018, Ilaria Testa et al. developed Molecular Nanoscale Live Imaging with Sectioning Ability (MoNaLISA) to image structures in organotypic tissues (Masullo et al., 2018). Principle of MoNaLISA was based on RESOFT but had a little difference. The MoNaLISA imaging employed three light illuminations for ON-switching, OFF-switching, and read-out of the rsFPs, respectively. The ON-switching and read-out pattern contained multiple individual foci which are divided by the same multi-foci periodicity (P_{MF}). The OFF-switching mode, which is responsible for sharpening the PSF with multiple intensity minima, features standing waves at a periodicity of P_{SW}. The independent light patterns could adjust the light doses of the OFF pattern by choosing the smallest P_{SW} and select the optimum P_{MF} to enhance the photon collection and the sectioning. By maximizing the detected photon flux, MoNaLISA enabled long-time and large field-of-view ($50 \times 50\ \mu m^2$) recordings at 15 μm depth with a resolution of 70–100 nm (**Figure 2B**).

Structured Illumination Microscopy

SIM extracts fine structural details from the interference of a structure with predesigned illumination patterns (Gustafsson, 2000; Galbraith and Galbraith, 2011; Huang et al., 2009). This light pattern could rotate into different angles and move along the sample. A super-resolved SIM image with high spatial resolution could be reconstructed from a series of frames with appropriate algorithms (**Figure 3A**) (Sezgin, 2017; Heilemann, 2010). Although the resolution is limited to ~100 nm, SIM has wide applications as it does not need special labelling molecules and can work with common fluorophores unlike other SRM techniques (i.e., fairly photostable probes for STED and photoswitchable probes for PALM/STORM) (Fernandez-Suarez and Ting, 2008; Brunstein et al., 2013; Dan et al., 2014).

In 2012, Hari shroff's group developed a multifocal SIM (MSIM) for super resolution imaging at depths of greater than 45 μm in live transgenic zebrafish embryos (York et al., 2012). They chose a commercially available digital micromirror device (DMD) to generate and switch multifocal patterns. MSIM data acquisition and processing were conceptually divided into multiple steps: 1) exciting the sample with a sparse and multifocal illumination pattern; 2) employing digital pinholes around each fluorescent focus; 3) 2 x scaling; 4) repeating above steps until whole sample has been fully excited; and 5) accumulating all such pinholed and scaled images. Following this outstanding work, they continued to generate an instant SIM technique that permitted acquisition and display of super-resolution images in real time (York et al., 2013). The key

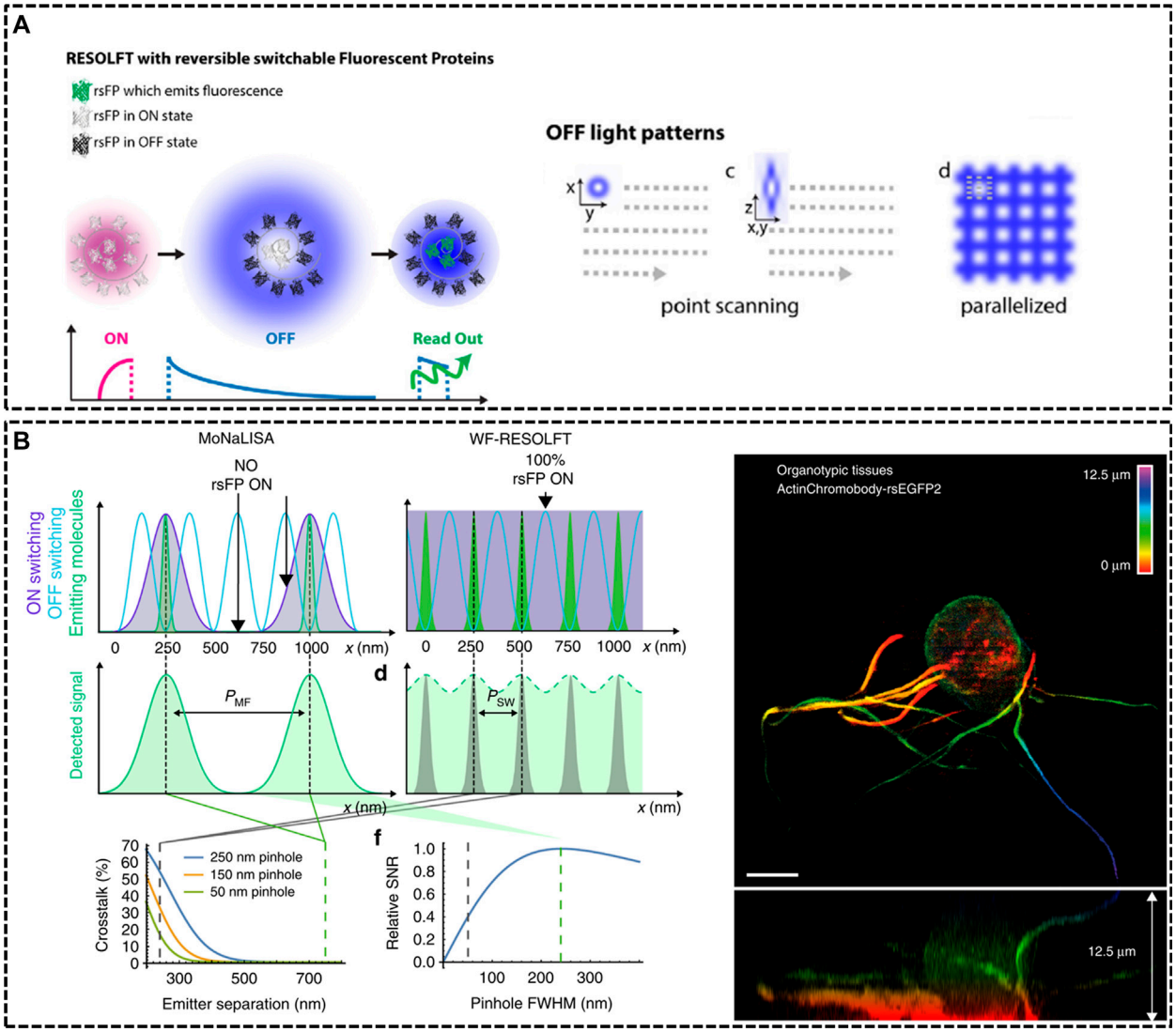

FIGURE 2 | Modified RESOLFT techniques with reversible photoswitchable fluorescent proteins for *in vivo* imaging. **(A)** Left: illustration of the typical pulse mode for RESOLFT. Right: Off light pattern implemented in point scanning and parallelized RESOLFT microscopy (Hell et al., 2015). Reprinted from Hell et al. (2015) with permission from IOP Publishing. **(B)** Schematic representation of Molecular Nanoscale Live Imaging with Sectioning Ability (MoNaLISA) and the actin recorded in a 12.5 µm organotypic hippocampal rodent brain tissue (Masullo et al., 2018). Scale bar, 5 µm. Reprinted from Masullo et al. (2018) with permission from Springer Nature.

concept of realizing instant SIM is that every step of digital combination in MSIM is performed optically. They then applied the instant SIM visualize cytoskeletal detail within flowing blood cells *in vivo* at an unpresented speed. As mentioned above, 2P excitation is an effective way to reduce the effect of optical scattering, causing deeper imaging depth into tissues when compared to single-photon illumination. In 2018, Zhang et al. developed the resonant two-photon Super resolution Patterned Excitation Reconstruction (2P-SuPER) microscopy to realize the observation of the dendrite at depth of up to 120 µm below the brain surface with an imaging rate of 3.5 Hz (Urban et al., 2018).

Afterwards, a few new strategies have been implemented in SIM technique for *in vivo* imaging. In 2019, Na Ji's group developed AO corrected SIM to image the brains of live zebrafish larvae and mice at nanoscale resolution (Turcotte et al., 2019). The optical system for *in vivo* SIM imaging consisted of two modules: one for SIM itself and one for AO to compensating specimen-induced aberrations. With these optimizations, they were able to routinely image sparsely labeled neural structures at a depth of 50 µm (**Figure 3B**). Then, in the next year, they further optimized the optical-sectioning SIM (OS-SIM) technique for imaging *in vivo* through modifying the reconstruction algorithms, correcting

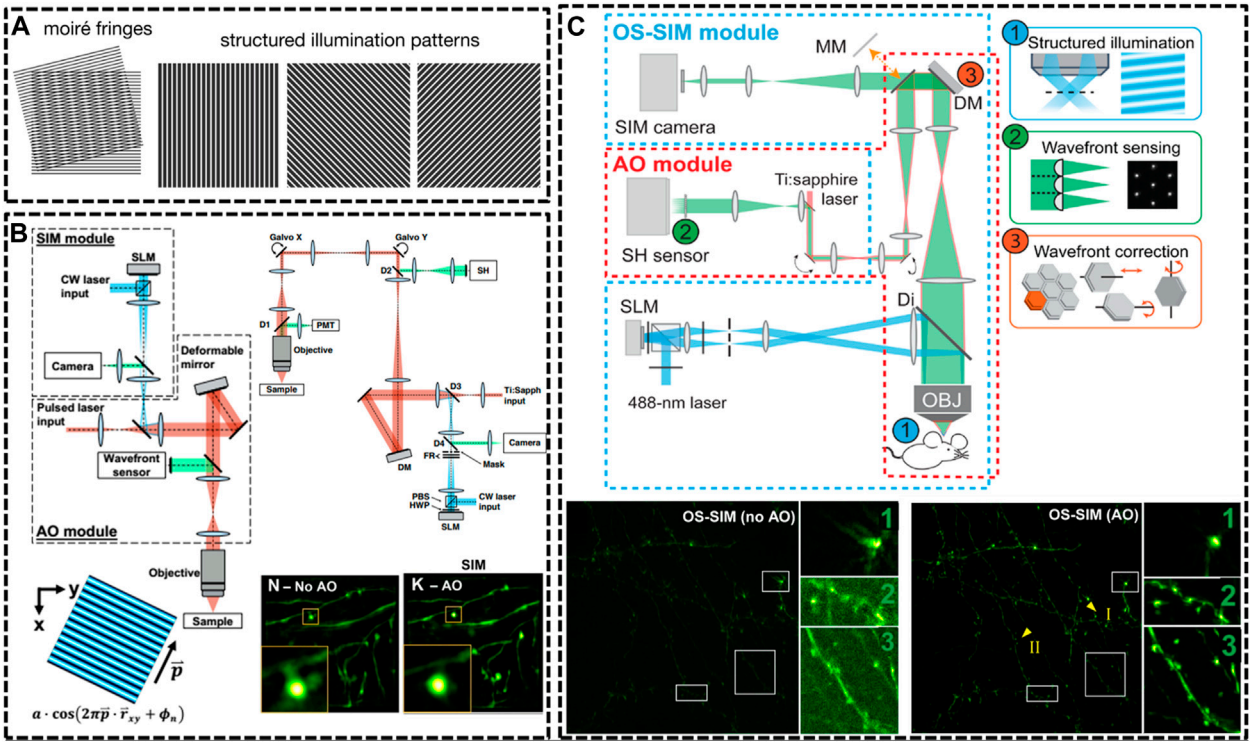

FIGURE 3 | Schematic of improved setups of SIM for *in vivo* imaging. **(A)** Illustration of SIM to resolve an unknown structure with a known periodical pattern (Sezgin, 2017). Reprinted from Sezgin (2017) with permission from IOP Publishing. **(B)** Detailed optical layout of the SIM setup and minimization of aberrations via correction collar and adaptive optics (AO) (Turcotte et al., 2019) Reprinted from Turcotte et al. (2019) with permission from National Academy of Sciences of the United States of America. **(C)** An AO module applied to optical-sectioning structured illumination microscopy (OS-SIM), which enables a marked improvement in resolution, signal, and contrast for imaging spine in mouse brain (Li et al., 2020). Scale bar, 10 μm in original images; 3 μm in magnified box region. Reprinted from Li et al. (2020) with permission from American Association for the Advancement of Science.

motion-induced artifacts and incorporating an AO module (Li et al., 2020). With AO OS-SIM, they demonstrated fast, high-resolution imaging for structural details of mouse cortical neurons *in vivo* (**Figure 3C**).

Lattice Light Sheet Microscopy

Light-Sheet Microscopy (LSM) is a vital technology that is suitable for observing living tissue or whole organism with the advantages of deep penetration depth, high contrast, low phototoxicity, and fast acquisition rate (Adams et al., 2015). LSM realizes high-resolution images by confining a sheet of light within the specimen, which coincides with the focal plane of a high NA objective placed at 90 (**Figure 4A**) (Girkin and Carvalho, 2018; Albert-Smet et al., 2019; Manley et al., 2020). Now, LSM has been successfully applied to record the early stages of fly, mouse embryos and activities in the entire spinal cord of live zebrafish embryos *in vivo* (Chen B.-C. et al., 2014; Liu et al., 2018). More recently, light sheet-based imaging patterns have successfully been coupled with super-resolution imaging paradigms which allow imaging beyond the diffraction limit (Gustavsson et al., 2018; Wang et al., 2021).

The way of generating this light sheet will determine the sensitive degree of the microscopy to scattering (Gao et al., 2019). Conventional light sheets created with Gaussian beams are too thick over cellular scale to enable subcellular observation. In 2014, Eric Betzig's group developed Lattice Light Sheet Microscopy (LLSM) by using 2D optical lattices, which allows for four-dimensional (4D) (x, y, z, and time) imaging with exceptionally high temporal resolution (~100 frames/s, ~1 cell volume/s) and minimal photobleaching (Chen B.-C. et al., 2014). As shown in **Figure 4B**, LLSM utilized an isolated excitation lens which was perpendicular to the widefield detection lens to confine the illumination to the neighboring focal plane. The lattice light sheet intersects the specimen obliquely for the sake of applying such light sheets in *in vivo* imaging. LLSM works in two modes: one is a dithered mode, in which an optical lattice is scanned continuously for high-speed 3D imaging; the other is a super-resolution structured illumination microscopy (SR-SIM) mode, in which an optical lattice is scanned discretely to enhance the spatial resolution. The SR-SIM mode provided a high spatiotemporal resolution for imaging embryogenesis in *Caenorhabditis elegans* at the two-cell stage and the six-cell stage (**Figure 4B**, right). Further, the same group continued to introduce an independent AO module in their LLSM system to decrease the aberrations of light (Liu et al., 2018). The sample-induced aberrations were first measured by creating a reference

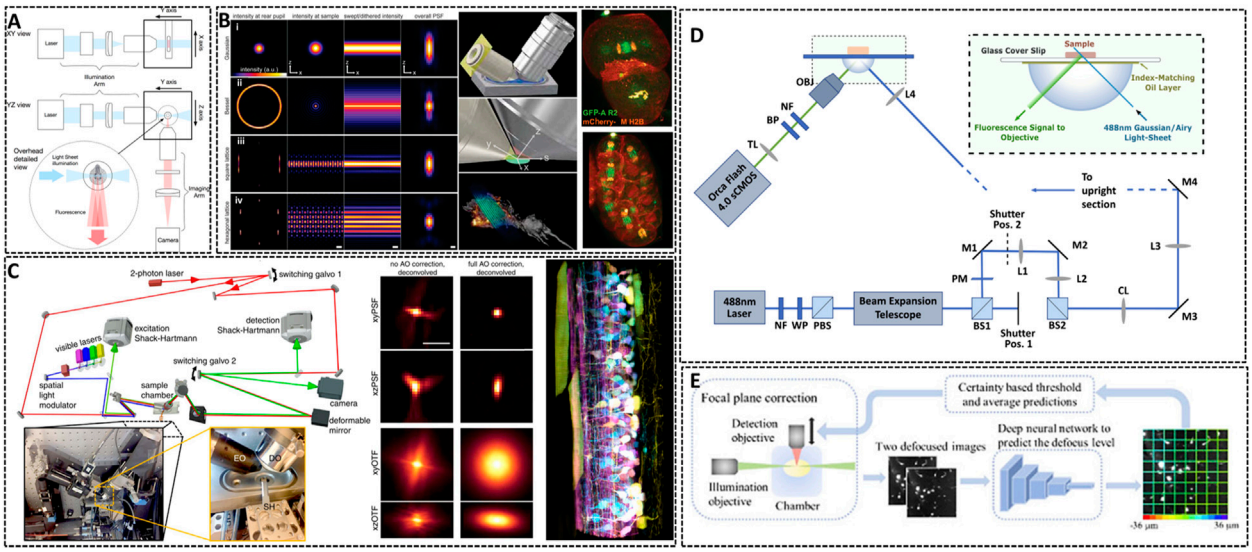

FIGURE 4 | Lattice light-sheet microscopy for *in vivo* imaging. **(A)** Basic working principle for light-sheet microscopy method (Girkin and Carvalho, 2018). The excitation light sheet is generated using a cylindrical lens before the excitation objective and the orthogonal imaging arm. Reprinted from Girkin and Carvalho, (2018) with permission from IOP Publishing. **(B)** Left: methods showing the traditional approach (Gaussian beam, i), Bessel beam (ii), and square (iii) and hexagonal lattice (iv) used for light sheet microscopy (Chen B.-C. et al., 2014). Middle: scheme illustrating the core of light sheet microscopy. Right: distribution of chromosomal passenger protein GFP-AIR-2 (green) relative to plasma membranes and histones (red) in C. elegans embryos at the two-cell stage and the six-cell stage. Reprinted from Chen et al. (2014) with permission from American Association for the Advancement of Science. **(C)** Left: simplified microscope schematic of adaptive optical lattice light-sheet microscopy (AO-LLSM) (Liu et al., 2018). Midddle: maximum intensity projections (MIPs) and corresponding optical transfer function (OTFs) of the uncorrected and fully corrected bead images. Scale bar, 1 μm. Right: image of the spinal cord of a zebrafish embryo 58 hpf. Reprinted from Liu et al. (2018) with permission from American Association for the Advancement of Science. **(D)** Schematic of the setup of LSM using an Airy beam (Corsetti et al., 2020). Reprinted from Corsetti et al. (2020) with permission from Optical Society of America. **(E)** Overview of the integration of the deep learning-based autofocus method with a custom-built LSM (Li et al., 2021). Reprinted from Li et al. (2021) with permission from Optical Society of America.

"guide star" through two-photon excited fluorescence (TPEF), and then corrected with a phase modulation element. Coupling with correction times as short as 70 ms, this AO module is compatible with the speed and noninvasiveness properties of LLSM. One of the main advantages of complete AO correction is that it enables accurate deconvolution (**Figure 4C**), ensuring the most truthful representation of the species within the diffraction limits. With 3D AO-LLSM, they successfully visualize a living zebrafish embryo across 200 μm depth.

Although the unique and orthogonal excitation-detection pattern of LSM makes it fast to record images with a deep imaging depth *in vivo*, there are some limitations for LSM to acquire high-quality images, such as the restrained image resolution, spatial heterogeneity in the refractive index of the specimen and artifact-prone reconstruction process for time-lapse imaging. Remarkable, deep learning approach has become a promising method to resolve above problems and is applied in LSM to enhance the resolution and discover intricate structures (Wagner et al., 2021). Dholakia's group combined the use of a non-diffracting Airy light field and a deep-learning method to demonstrate an open-top light sheet microscopy (**Figure 4D**) (Corsetti et al., 2020). The adoption of deep-learning in their system has demonstrated a near two-fold improvement in resolution whilst maintaining a wide field of view for light sheet imaging. Li et al. introduced a deep learning-based autofocus framework that can estimate the position of the objective-lens focal plane relative to the light-sheet (**Figure 4E**) (Li et al., 2021). They realized a large 3D specimens imaging with high spatial resolution.

Ultrasound Localization Microscopy

In conventional fluorescence microscopes, most illuminated probes emit fluorescence at the same time, resulting an overlay of PSF of several individual fluorophores. Switching on only a random and small subpopulation of fluorescent molecules in each frame could ideally decrease the density of emitting signals, and thus, the neighboring fluorescent emitters do not overlap and each indivi dual PSF can be isolated and determined with subdiffraction accuracy (**Figure 5A**) (Sezgin, 2017). Single molecule localization microscopies (SMLMs), including PALM and STORM, carry out the above principle and employ photoswitchable fluorophores to generate super-resolved images (Sahl and Moerner, 2013; Sauer, 2013). However, SMLMs acquire thousands of frames to reconstruct a single plane, and the associated long acquisition time, as well as the limited photoswitchable probes restrict the general applicability of SMLMs for live-cell or *in vivo* imaging.

Compared with optics, ultrasonic waves could spread deep into tissues maintaining their coherence and are much less influenced by the irrelevant processes *in vivo*. Nevertheless, the resolution of ultrasound imaging technique is impeded by diffraction limitation, which endures a long-standing trade-off between resolution and imaging depth. Ultrasound Super Resolution Microscopy (USRM) has been recently introduced to overcome the diffraction limitation defined by the acoustic

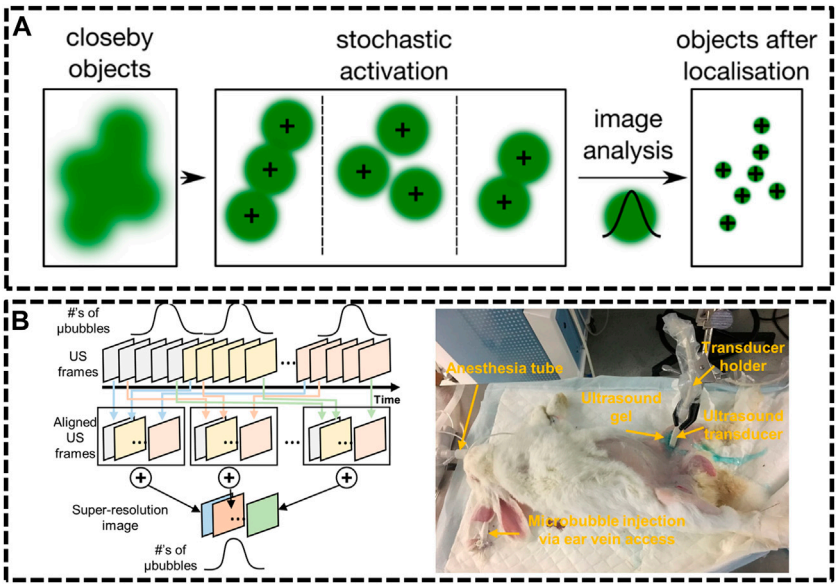

FIGURE 5 | Ultrasound localization microscopy (ULM) systems. **(A)** Principle of single molecule localization microscopies (SMLMs) (Sezgin, 2017). Reprinted from Sezgin (2017) with permission from IOP Publishing. **(B)** Graphical diagram of super-resolution ultrasound data acquisition and experiment setup of rabbit imaging (Yu et al., 2018). Reprinted from Yu et al. (2018) with permission from Springer Nature.

limit (Yoon et al., 2018; Yu et al., 2018). This approach combined the single localization principle with ultrasound technologies. For example, microbubbles were injected to tissue and each microbubble as shown in could be considered as a point source (Errico et al., 2015). The recorded echo signal from individual microbubbles is representation of the PSFs of the points. A super-resolved image can be reconstructed by accumulating the PSF of each separable source over thousands of frames. In 2015, Mickael Tanter et al. demonstrated an ultrafast Ultrasound Localization Microscopy (ULM) to visualize the microvessels *in vivo* by gas microbubbles inserting technology (Errico et al., 2015). The bubbles created separated and rapid-changing localizations within the ultrasound images, which were detected using frame-to-frame differential processing. Each entire ultrasonic frame was generated by using parallel beamforming. As these bubbles are uniquely located, enough positions were recorded to reconstruct a super resolution image through a thinned skull at a coronal section, providing a resolution of 10 μm in depth and 8 μm in lateral direction. Then, in Yu et al. (2018) developed an imaging sequence and signal processing approach to enhance temporal resolution by applying deconvolution and spatio-temporal-interframe-correlation (STIC) based data acquisition (Yu et al., 2018). The STIC method was used to compensate motion over reduced data acquisition time. This technique was demonstrated in the rabbit atherosclerosis model (**Figure 5B**).

Several groups subsequently proposed advanced strategies to improve the frame rate. Xuejun Qian's group developed ultrafast plane wave imaging approach for mapping vasculature using image deconvolution method (Qian et al., 2020). The imaging setup equipped with a high frequency Verasonics Vantage system and a linear array transducer. In order to adjust the distance to imaging targets, the array transducer was mounted on a 3-axis translation motorized linear stage system with a minimum step size of 60 nm. 2D/3D-view images of rabbit eyes *in vivo* were performed to demonstrate the capability of this technique, providing the vasculature network of the posterior pole of the eye, especially for choroidal and retrobulbar vessels.

LABELING APPROACHES

Genetically Encoded Probes

The main bottleneck to apply super-resolution techniques *in vivo* is seeking for appropriate fluorescent probes with deep tissue penetration, high brightness and photostability. Nowadays, many types of fluorophores have been developed for SRM, including fluorescent proteins (FPs), dyes and nanoparticles (Heilemann et al., 2008; Shcherbakova et al., 2014; Wang et al., 2018). However, stringent requirements are needed for their use in SRMs *in vivo*. Much effort has been devoted to the development of advanced labeling protocols, including adeno-associated virus (AAV) vectors, transgenic mice, and inorganic dyes. In the following, we will highlight our discussion to those labeling approaches applicable for *in vivo* SRM.

The transgenic technology has revolutionized the studies inside living systems. Up to date, the majority of *in vivo* SRM experiments have been performed with FPs. For using FPs in *in vivo* imaging, there are two major approaches: one is using transgenic animals or directly transferring FPs in animals for imaging *in vivo*. For example, several experiments for *in vivo* SRM

applied the heterozygous TgN (Thy1-EYFP) mice expressing enhanced yellow fluorescent protein (EYFP) or GFP, EGFP, which is under the control of the regulatory element from the *thy1* gene (**Figure 1A**) (Berning et al., 2012; Bethge et al., 2013). Similarly, zebrafish and *Drosophila melanogaster* are the commonly used animals for *in vivo* studies, such as the *Isl1*: GFP zebrafish larvae, in which *Islet-1* promoter enabled the expression of GFP in all postmitotic motor neurons (**Figure 6A**) (Li et al., 2020), and the rsEGFP2 transfected *Drosophila melanogaster*, expressing rsEGFP2 a-tubulin through a standard phiC31 integrase based germ line transformation procedure (**Figure 6B**) (Schnorrenberg et al., 2016).

The other is to transfer the FPs into animal body to induce the expression of fused FPs or tags through recombinant adeno-associated virus (rAAV, serotype 2) infection method. For example, to label the filamentous actin in neurons, Lifeact, an actin-binding peptide derived from yeast, was usually used as fusion protein by combining diverse FPs (Riedl et al., 2008). The rAAV of serotype 2, facilitated by the neuron specific human synapsin promoter hSYN and Semliki Forest viruses (SFV), could be created to directly express Lifeact-EYFP into the visual cortex of the mouse. A few weeks after infection, the animals could be imaged under SRM systems (**Figure 6C**) (Willig et al., 2014). The improvement of the penetration depth and the compatibility of the light in the tissue could be optimized through the use of far red-shifted fluorescent proteins. Katrin I. Willig and co-workers applied a far-red emitting FP mNeptune2 for STED imaging of F-actin filament in the cortex in layer 5 (L5) and up to L1 of a living mouse (**Figure 6D**) (Wegner et al., 2017).

However, FPs generally have poorer photophysical properties than organic dyes. Thus, it is a promising method to implement the far-red or NIR organic dyes for *in vivo* imaging. Several groups have achieved this goal by the combination of genetical coded method with organic dyes. Prior labeling with dyes, the protein of interest is genetically fused with an engineered enzyme tag such as SNAP-, Halo-, or Clip-tag (Chin, 2014). Then these tags could covalently react with the corresponding fluorescent substrate. For expressing these tags in living body, the use of rAAVs offers flexibility in the labelling scheme. Stefan W. Hell and co-workers introduced the NIR SiR-Halo ligand for specific labeling of PSD95 *in vivo* and obtained super-resolution images with superior signal-to-noise ratio and photostability (**Figure 6E**) (Masch et al., 2018). Similarly, Joerg Bewersdorf et al. utilized the reaction between Halo Tags with Halo reactive ATTO590-chloroalkane (ATTO590-CA) to label neurons as deep as 174 μm below the cortical surface with excellent signal-to-noise ratio by a 3D-2P-STED system (**Figure 6F**) (Velasco et al., 2021). With the improvements in organic dyes, the use of organic dyes for *in vivo* SRMs will become more feasible. However, improving probes for future SRM studies in the living animal is still going on.

Near-Infrared Fluorescent Probes

The ideal probe for live cell imaging should have excellent photophysics and chemical properties, such as high specificity, exquisite photostability and possesses good cell permeability. When used in in vivo, the requirements for florescent probes are even stricter. For the past few decades, super-resolution fluorescence imaging has mainly located in the visible and several used near-infrared I light range (Jin et al., 2018). Compared with the visible, red-shifting fluorophores including NIR I (650–950 nm) and NIR-II (1,000–1700 nm) light, would bear several virtues: 1) far-red light has lower scattering across tissues, enhancing tissue penetration and imaging depth; 2) auto-fluorescence caused by the excitation of molecules, like flavins or haemoglobin, is usually reduced in red-shifted wavelengths; 3) absorption of far-red light is less by the tissue when compared to shorter excitations, causing less phototoxic impact (Lei and Zhang, 2020; Reja et al., 2021). Thus, shifting the excitation and emission wavelength of the probe to the red spectral region is necessary for *in vivo* imaging.

Newly emerging field of *in vivo* supper resolution imaging predicts a significant and large demand for fluorophores in the NIR windows. Current NIR fluorophores are mostly developed based on small organic dyes, inorganic materials, or organic-inorganic hybrid materials. For example, the lanthanide-doped upconversion nanoparticles (UCNPs) have been introduced in super-resolution imaging because of the properties of low excitation power, narrow-band emission, zero auto-fluorescence, large anti-Stokes shifts and high-photostability (Dong et al., 2020; Hu et al., 2020). In 2018, Jin's group developed near-infrared emission saturation (NIRES) nanoscopy applying UCNPs to realize super-resolution imaging in deep tissue. By employing a doughnut beam excitation from a 980 nm diode laser and detecting at 800 nm, they achieved a resolution of sub 50 nm through 93 μm thick liver tissue (**Figure 7A**) (Chen et al., 2018). Following this fascinating work, several NIR-based fluorophores developed for *in vivo* SRM were reported. In 2020, Jin and co-workers developed an upconversion nonlinear SIM (U-NSIM) techniques for fast super-resolution imaging through thick tissues using ytterbium (Yb^{3+}) and thulium (Tm^{3+}) codoped UCNPs as the imaging probe (Liu et al., 2020). They obtained super-resolved image with a resolution below 131 nm and an imaging rate of 1 Hz using this probe (**Figure 7B**). In 2019, Meng's group utilized deep-red fluorescent organic nanoparticles (FONPs) DBTBT-4C8 to *in vivo* imaging of transparent glass catfish by STED nanoscopy (**Figure 7C**) (Xu Y. et al., 2020). In addition, Diao et al. synthesized a near-infrared lysosome-targeted imaging probe HD-Br and applied the probe for 3D lysosomes imaging in live *Caenorhabditis elegans* (**Figure 7D**) (Fang et al., 2019).

Furthermore, longer wavelength of light results in higher photon penetration depth, which will achieve better performance for *in vivo* application. The pioneering bioimaging using NIR-II fluorophore was reported in 2009. Dai's group presented tumor vessels beneath thick skin with high-resolution by using the single-walled carbon nanotubes (SWNTs) as an imaging agent (Welsher et al., 2009). In 2012, they obtained high spatial resolution of about 30 μm and temporal resolution of no more than 200 ms/frame for small vessel imaging at 1~3 mm deep in the tissue with the SWNTs probe (Hong et al., 2012). Besides the SWNTs, the NIR-II quantum dots (QDs) were also reported for *in vivo* imaging

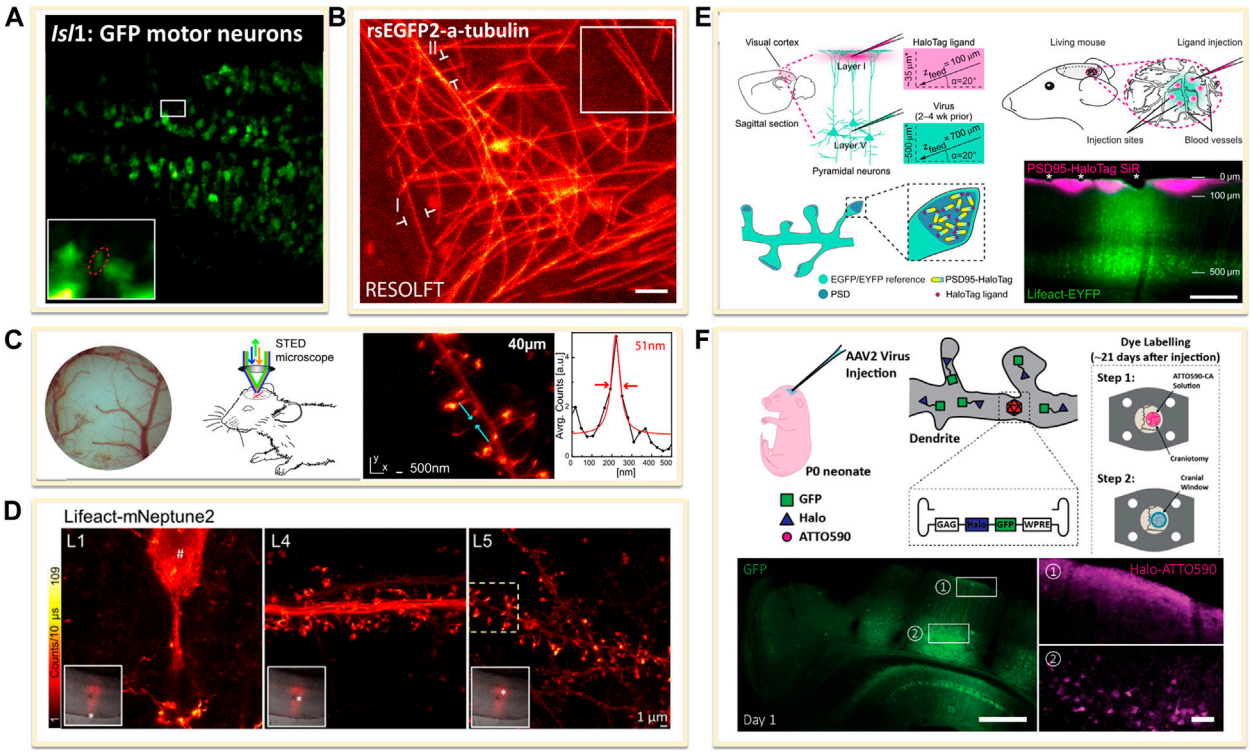

FIGURE 6 | Genetically encoded approaches for *in vivo* labeling. **(A)** Transfected dense Isl1:GFP zebrafish motor neurons (Li et al., 2020). Scale bar, 20 μm. Reprinted from Li et al. (2020) with permission from American Association for the Advancement of Science. **(B)** *Drosophila melanogaster* ubiquitously expressing rsEGFP2-a-tubulin (Schnorrenberg et al., 2016). Scale bar, 1 μm. Reprinted from Schnorrenberg et al. (2016) with permission from eLife Sciences. **(C)** Neurons expressing Lifeact-EYFP by recombinant adeno-associated virus (AAV) infection for STED microscopy (Willig et al., 2014). Reprinted from Willig et al. (2014) with permission from Cell Press. **(D)** A far red-emitting fluorescent protein mNeptune2 to expressed with lifeact to label actin filaments (Wegner et al., 2017). Reprinted from Wegner et al. (2017) with permission from Springer Nature. **(E)** *In vivo* labeling process of endogenous PSD95-HaloTag with organic fluorophores SiR (Masch et al., 2018). SiR-Halo was injected to transgenic PSD95-HaloTag mice for obtaining a final imaging depth of ~35 μm below the cortical surface (magenta). Scale bar: 250 μm. Reprinted from Masch et al. (2018) with permission from National Academy of Sciences of the United States of America. **(F)** Neuron labelling strategy in a living mouse using ATTO590 (Velasco et al., 2021). Scale bars: 500 μm in GFP image and 50 μm in right ATTO590 image. Reprinted from Velasco et al. (2021) with permission from Optical Society of America.

(Chen G. et al., 2014). Wang's group developed a Ag_2Se QDs with emission centered at 1,300 nm, which have been successfully employed in organs and blood vessels imaging with a high signal-to-noise ratio (**Figure 7E**) (Dong et al., 2013). In 2015, an NIR-II small-molecule dye CH1055 was used to observe brain tumors in mice at a depth of ~4 mm (Antaris et al., 2016). Furthermore, Zhang et al. reviewed recent developed NIR-II fluorescent dyes and listed major classes of the probes in **Figure 7F** (Lei and Zhang, 2020). Although these NIR-II probes have a deep imaging depth, when using in conventional microscopy, the resolution was limited to micrometer scale. Therefore, there are many opportunities for these probes to be used in *in vivo* super resolution imaging.

APPLICATIONS OF *IN VIVO* SRMS IN BIOLOGICAL SYSTEMS

Neurosciences

Highly efficient working of the brain mirrors its multiscale complex organization. Altered neuronal morphology and abnormal dynamic actives impair cellular functions, as is observed in various kinds of neurodegenerative disorders such as Parkinson's and Alzheimer's diseases (Badawi and Nishimune, 2020; Minehart and Speer, 2020; Walker and Herskowitz, 2020). Hence, visualizing detailed neuronal morphology could promote understanding of the mechanisms underlying neuronal activities and plasticity as well as the diseased-associated disorders. In particular, neurons are not static but changing during brain activities. To analyse their structure and function physiologically, it is essential to study them in living animals (Carrier et al., 2020; Okabe, 2020). Indeed, neuroscience is one of the first disciplines to which *in vivo* SRM was applied.

The first *in vivo* super resolution imaging was carried out with STED microscopy in the somatosensory cortex of an anaesthetized mouse by Stefan W. Hell's group. They found the morphological changes of the dendritic spines at the head and neck regions in the adult animal brain (**Figure 8A**) (Berning et al., 2012). Following this work, they observed the actin rearrangement in dendritic spines in a mammalian brain *in vivo*. Subsequently, they provided high-quality super resolution images of the key scaffolding protein postsynaptic density 95 (PSD95) at the

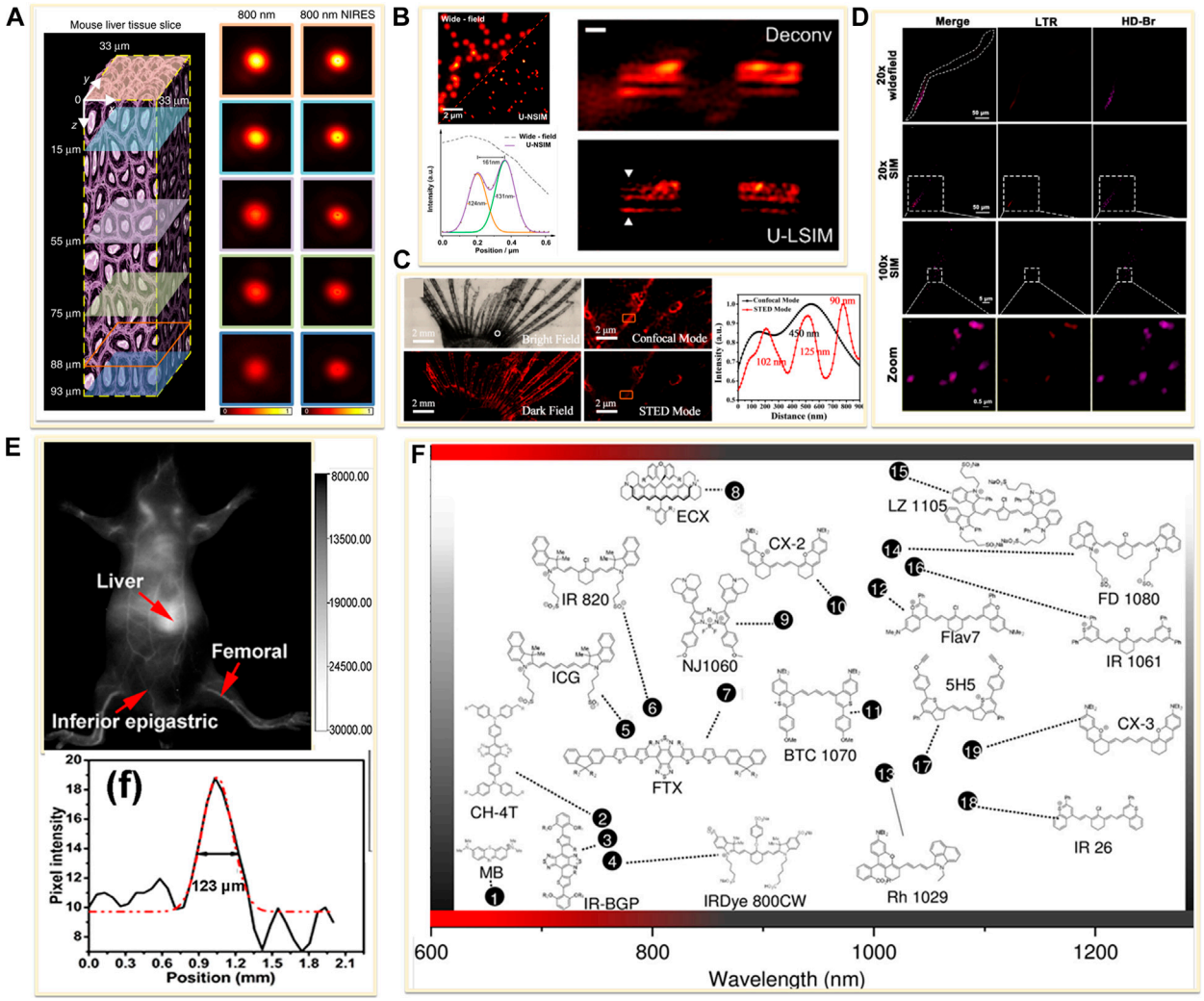

FIGURE 7 | Examples of near-infrared fluorescent probes for *in vivo* imaging. **(A)** Left: diagram of a mouse liver tissue slice with 93 μm thickness (Chen et al., 2018). Right: confocal images and the corresponding near-infrared emission saturation images from 800 nm emission at different depth in liver tissue. Reprinted from Chen et al. (2018) with permission from Springer Nature. **(B)** Left: super-resolution images of the 4% Tm-doped Upconversion nanoparticles (UCNPs) (Liu et al., 2020). Right: comparison of Wiener deconvolution and upconversion nonlinear SIM (U-LSIM) image of the a 51.5 μm liver tissue slice. Scale bar: 1 μm. Reprinted from Liu et al. (2020) with permission from American Chemical Society. **(C)** An enlarged bright view and dark field of glass catfish stained by fluorescent organic nanoparticles (FONPs), and the corresponding confocal and STED images (Xu Y. et al., 2020). Reprinted from Xu Y. et al. (2020) with permission from American Chemical Society. **(D)** SIM imaging of C. elegans labeled with Lyso-Tracker Red (LTR) and developed small molecule dye HD-Br (Fang et al., 2019). Reprinted from Fang et al., 2019 with permission from American Chemical Society. **(E)** Image showing a live mice in supine position after tail injection of C18-PMH-PEG-Ag2Se QDs (Dong et al., 2013). Reprinted from Dong et al. (2013) with permission from American Chemical Society. **(F)** Representative NIR-II dyes used for *in vivo* imaging (Lei and Zhang, 2020). Reprinted from Lei and Zhang (2020) with permission from John Wiley and Sons.

postsynaptic membrane by a combination of STED microscopy and endogenous protein labeling method. They showed the PSD95 scaffolds appeared to be continuous structures *in vivo* (Masch et al., 2018), not a fragmented or clustered distribution revealed in previous studies using dissociated rat hippocampal or cortical neurons *in vitro* (**Figure 8B**) (Hruska et al., 2018; MacGillavry et al., 2013). In 2018, by using 2P-STED microscopy, U Valentin Nagerl et al. showed a twice higher spine density than what was reported in previous works by traditional 2P microscopy, and they disclosed that about 40% of spines turned over within 4 days (**Figure 8C**) (Pfeiffer et al., 2018).

In recent years, advanced SRMs have not only provided sophisticated optical images of neuronal structures but also revealed the rapid dynamic behaviors in neurosciences. Owing to the relative low illumination intensity and fast imaging acquisition, SIM has been widely implemented to monitor various dynamic events at high frame rates. As mentioned above, Na Ji's group developed a series modified SIM systems to realize super resolution imaging *in vivo*. They utilized the OA-SIM technique to visualize the fine structural dynamics across 170 min (**Figure 8D**) (Turcotte et al., 2019). In 2020, they demonstrated a robust quantal

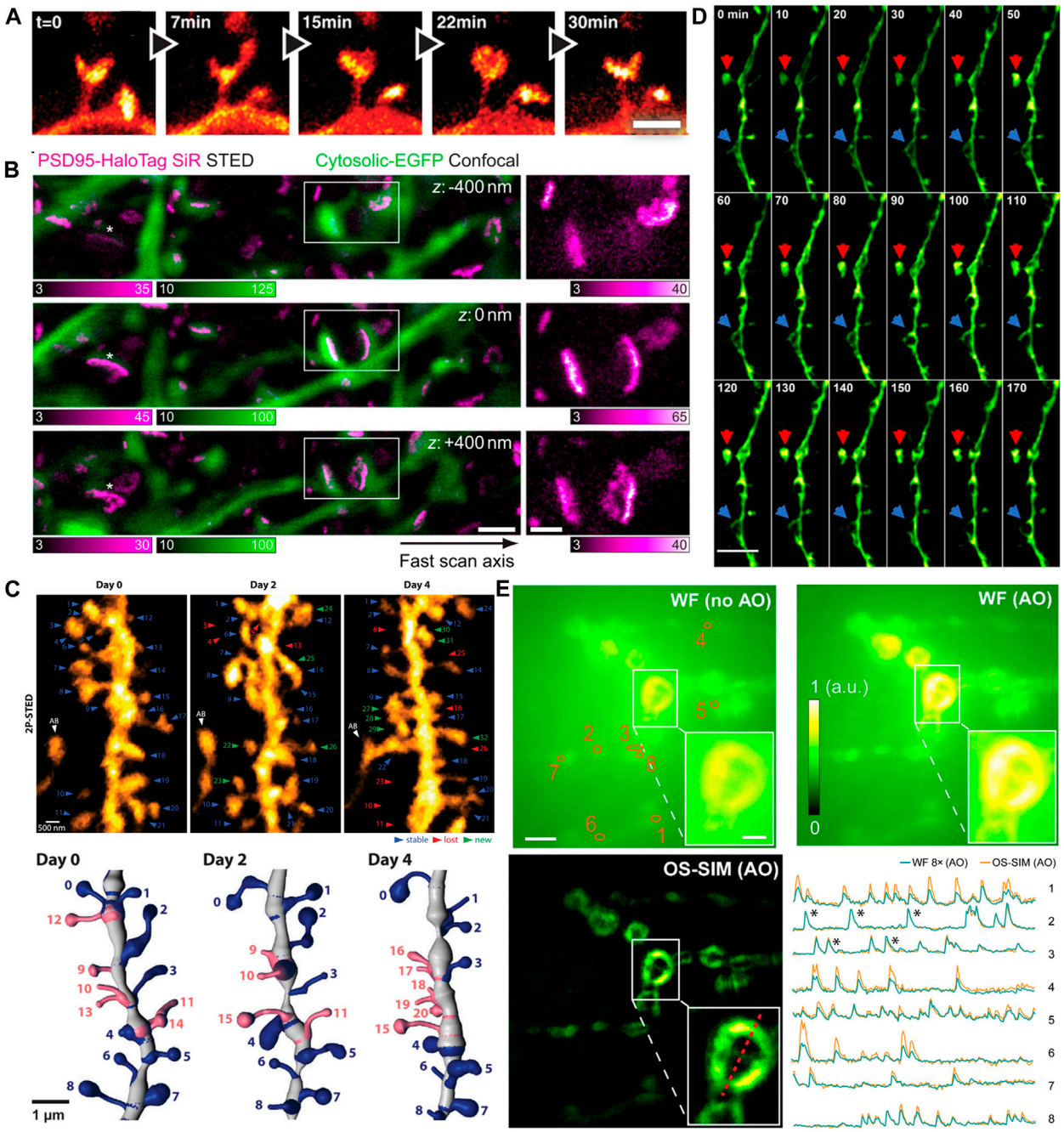

FIGURE 8 | Examples of *in vivo* super-resolution images in the field of neurosciences. **(A)** Dynamics of spines in the molecular layer of the somatosensory cortex with STED microscopy (Berning et al., 2012). Scale bar, 1 µm. Reprinted from Berning et al. (2012) with permission from American Association for the Advancement of Science. **(B)** The 3D images of PSD95 scaffold morphologies in living mouse. Scale bars, 1 µm in original images, 500 nm in magnified views (Masch et al., 2018). Reprinted from Masch et al. (2018) with permission from National Academy of Sciences of the United States of America. **(C)** 2P-STED images of the dendrite over 4 days (Pfeiffer et al., 2018). Reprinted from Pfeiffer et al. (2018) with permission from eLife Sciences. **(D)** Time-lapse *in vivo* SIM images showing structural dynamics of a dendrite in the brain of a Thy1-GFP line M mouse after KCl injection. Arrows point to highly dynamic structures (Turcotte et al., 2019). Scale bar: 4 µm. Reprinted from Turcotte et al. (2019) with permission from National Academy of Sciences of the United States of America. **(E)** *In vivo* functional imaging of quantal releases of a *Drosophila* larva neuromuscular junction with AO OS-SIM (Li et al., 2020). Calcium transients from eight orange regions in wild field view. Scale bars indicated 5 µm in original images and 2 µm in the insets. Reprinted from Li et al. (2020) with permission from American Association for the Advancement of Science.

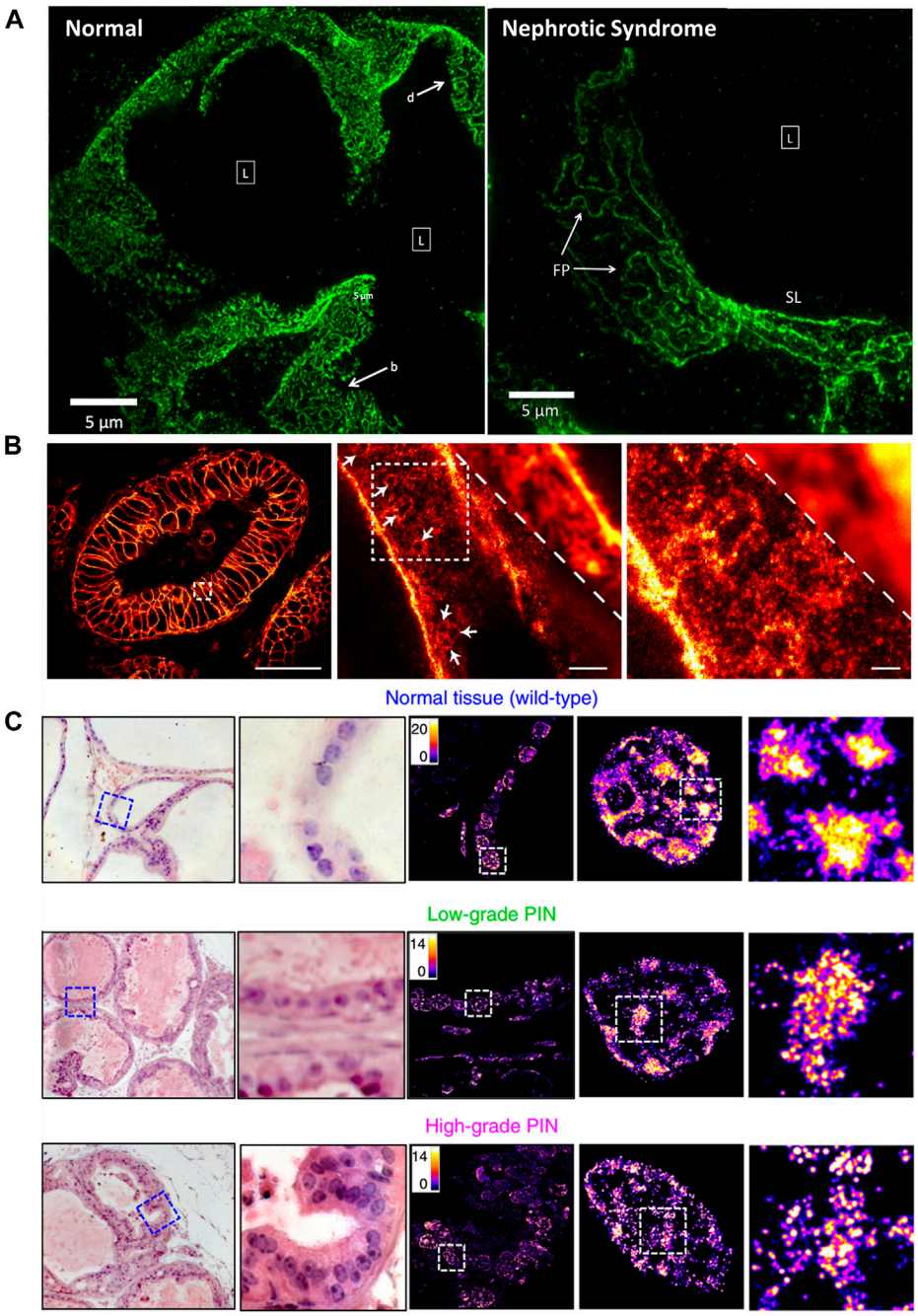

FIGURE 9 | Applications of SRMs in pathobiology. **(A)** Comparison of podocin-stained renal biopsies form normal and nephrotic disease tissue slice by SIM technology (Pullman et al., 2016). Scale bar: 5 μm. Reprinted from Pullman et al. (2016) with permission from the Optical Society of America. **(B)** The diffraction-limited image and STED super-resolution image on sectioned stored tissue of human rectal cancer (Ilgen et al., 2014). Scale bars: 50 μm in original image, 2 μm in magnified images. Reprinted from Ilgen et al. (2014) with permission from Public Library of Science. **(C)** Visualization of disrupted heterochromatin structures in prostate neoplasia by PathSTORM (Xu J. et al., 2020). Reprinted from Xu et al. (2020) with permission from Springer Nature.

synaptic imaging using the *Drosophila* larval neuromuscular junction as a model by genetically encoded calcium indicator (GECI) GCaMP6 (Li et al., 2020). The calcium activity of these terminals was recorded at 25-Hz OS-SIM frame rate (**Figure 8E**). Although resolution of several tens of nanometers is now obtainable *in vivo*, the applications of SRM to map neuronal morphology and connectivity are still under way.

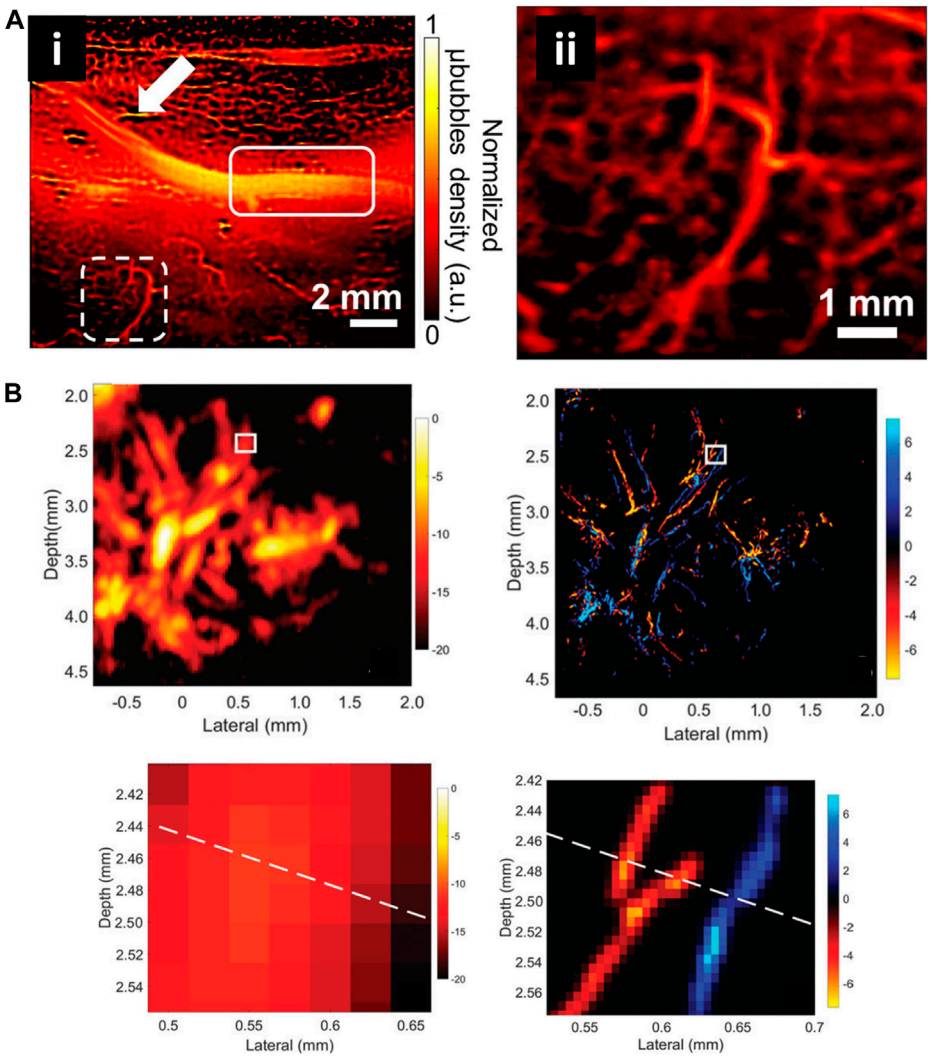

FIGURE 10 | Super-resolved vessel maps by ultrasound localization microscopy. **(A)** The super-resolution ultrasound image of vascular based on Verasonics system (i) and enlarged view of white dashed rectangle (ii) (Yu et al., 2018). Reprinted from Yu et al. (2018) with permission from Springer Nature. **(B)** Acoustic subaperture processing (ASAP)-enhanced power doppler image and ultrasound super-resolution image (Zhu et al., 2019). Magnified views showed the details of boxed region. Reprinted from Zhu et al. (2019) Radiological Society of North America.

Pathology

The conventional morphology-based pathology relies on identifying structural abnormal changes on stained cells and tissues (Si et al., 2020). Clinical imaging techniques such as magnetic resonance and ultrasound imaging enable macroscale detection of the position and morphology of tissues and their obvious changes over time, nevertheless lack cellular- or molecular-scale description of the lesions (Liu and Xu, 2019). At present, optical imaging has been an indispensable tool for preclinical evaluation of diseases. It allows pathologists and biomedical researchers to view 3D volumetric tissue architecture at high resolution and to study pathobiology in both breadth and depth.

In many clinical cases, tissue taken from patients during surgery is stored by formalin- or paraffin-fixed method for disease diagnosis or decision on postoperative treatment plans and subsequent studies. SRMs are introduced to investigate the morphological changes and molecular distribution of some sub-diffraction structures in fixed pathological tissue. Kishan Dholakia et al. performed super-resolution imaging on frozen sections of renal biopsies for podocin protein (**Figure 9A**) (Pullman et al., 2016). The field of view was approximately 50 times larger than Transmission Electron Microscope (TEM) images. They found that podocin distribution in nephrotic disease biopsies were greatly different from that in normal section. As shown in **Figure 9B**, the STED microscopy was introduced to investigate detailed distribution of the human epidermal growth factor receptor 2 (HER2) on archived clinical paraffin-embedded rectal cancer tissues (Ilgen et al., 2014). Recently, in 2020, Liu and coworkers employed STORM technique for studying pathological tissue, which

named as PathSTORM. They discovered a gradual fragmentation of higher-order chromatin assembling during the all stages of carcinogenesis (**Figure 9C**) (Xu J. et al., 2020). Although SRM makes a remarkable impaction on the largely unexplored region of molecular structure in diseases assessment, there are still many challenges for the application of SRMs in future clinical diagnosis, such as the sample preparation and tissue labeling.

Microvessel

The morphological assessment of microvascular network in its natural environment provides a unique perspective for understanding the occurrence and development of infection, hypertension, diabetes, ischemia, cancer and other diseases (Si et al., 2020). As have discussed above, the ultrasound super resolution microscopy (USRM) has been developed for imaging the vasculature *in vivo* beyond the acoustic diffraction limit by the aid of microbubbles (Yoon et al., 2018). This technique can not only obtain the microvasculature in deep tissue, but also provide an accurate blood velocity map.

Currently, several USRM technologies have been successfully applied *in vivo* for imaging microvessels in different organs. Robert J. Eckersley et al. in 2014 realized super resolution imaging of blood velocity by tracking individual microbubbles at depth of more than 1 cm (Christensen-Jeffries et al., 2015). They detected microvasculature of mouse ear with a resolution of 20 μm. Subsequently, Olivier Couture et al. successfully reconstructed the rat brain vasculature network with FWHM as small as 9 μm using a 20 MHz linear array transducer (Errico et al., 2015). Kang Kim et al. enhanced the temporal resolution for imaging vessels over cardiac motion vasa vasorum in the rabbit atherosclerosis model (**Figure 10A**) (Yu et al., 2018). Meng-Xing Tang et al. developed 3D ultrasound super resolution technique to visualize rabbit lymph node microvascular structures and blood flow dynamics with a resolution of 30 μm, which achieve a 15-fold improvement over existing doppler techniques (**Figure 10B**) (Zhu et al., 2019). More recently, in 2020, the micron-level choroidal and retrobulbar vessels around the optic nerve head were successfully reconstructed in rabbit eye by using ultrasound microbubble localization approach (Qian et al., 2020). With the development of USRM techniques, we believed that this method could be of great value for observing pathological changes or therapeutic effect on the microvasculature *in vivo*.

CONCLUSIONS AND FUTURE CHALLENGES

Super-resolution imaging techniques have pushed a vital step forward in how researchers view and study for biological questions, significantly expanding our knowledge of molecular interactions and dynamic processes within cells and tissues. However, more complete understanding of how the biomolecules assemble to create animate lives requires observing the cell in its native state. *In vivo* imaging entails huger challenges of sufficient image resolution and imaging depth. Fortunately, as we indicated in this review, more and better SRM techniques become available for *in vivo* imaging. We have outlined a detailed description of currently improved super-resolution microscopes for *in vivo* imaging, including modified STED, SIM, RESOLFT, LLSM, and ULM and listed the biological applications that benefit from these techniques. Among these advanced techniques, STED method is best suited and widely applied for *in vivo* imaging because of the high resolution, simple data processing, and intrinsic 3D sectioning capability, which is ideal for tissue imaging in living species. Additionally, SIM also gained a lot of interest in *in vivo* applications as minimal amount of photo-damage and commonly used labelling methods. In comparison, the applicability of RESOLFT, LLSM, and ULM in *in vivo* imaging is restricted mainly due to the necessaries for more professional technical modification as well as more rigorous operation.

As we look toward the future of the field, it is clear that there are some key challenges still need to be resolved in the future development of *in vivo* SRM. We would like to conclude this review with some speculative and directional thoughts on the improvements of *in vivo* SRM. First, although the abilities of SRM have expanded in recent years, new strategies and techniques that increase the imaging depth while maintaining a high resolution, especially for 3D imaging, are still required to obtain true information from thicker tissues and whole organs *in vivo*. Correlating diverse imaging methods offer an effective way to realize deep imaging *in vivo*, such as implementing the multiphoton excitation and lattice light sheet illumination pattern for SRMs to enhance imaging depth (Li et al., 2015; Huang et al., 2021), and combining AO with various SRMs to correct sample-induced aberrations (Booth, 2014; Zheng et al., 2017; Johnstone et al., 2019). Second, the labeling probes possessing suitable spectroscopic and chemical properties has become a major bottleneck to unleash the full potential of SRMs. To create super-resolution maps of the local environment, both biologists and chemists could be stimulated to develop new labeling strategies that not only have far red emitting but also minimally disturb the tagged biomolecule (Fernandez-Suarez and Ting, 2008; Wang et al., 2018; Reja et al., 2021). Third, improvements in real-time imaging combining with faster temporal resolution are necessary to resolve time dependent processes *in vivo*. sCMOS cameras have been used as an alternative to the EMCCDs in some super-resolution imaging cases, especially for the dynamic tracking (Schermelleh et al., 2019). With increasing enhancement on the sensitivity and quantum yield of these detectors, faster frame rates and larger pixel arrays will become generally accessible. Last but not the least, the animal preparation is also a vital step for *in vivo* imaging. Any movement caused by vibrations of the microscopy, unavoidable essential functions of the living species including heartbeat, pressure pulse, or thermal drift, will disturb the imaging process (Steffens et al., 2012; Steffens et al., 2020). Advanced imaging strategies employed on the awake or anesthetic animal such as the cranial window technique and optical alignment device should keep pace with the SRM techniques.

We believe that the development of SRMs from *vitro* to *vivo* is in its infancy, and in the coming years, researchers will see continued advances across diverse techniques, enabling new

and multifarious applications to answer more valuable biological questions.

AUTHOR CONTRIBUTIONS

JQ conceived of the presented idea. YJ wrote the article. CZ and BY provided the suggestions. DL revised this paper. All authors contributed to the article and approved the submitted version.

FUNDING

This work has been partially supported by the National Natural Science Foundation of China (61620106016/61835009/61775144/61975131/32101112), the Shenzhen International Cooperation Project (GJHZ20180928161811821, GJHZ20190822095420249), and the Shenzhen Basic Research Project (JCYJ20200109105411133, JCYJ20170412105003520).

REFERENCES

Adams, M. W., Loftus, A. F., Dunn, S. E., Joens, M. S., and Fitzpatrick, J. A. J. (2015). Light Sheet Fluorescence Microscopy (LSFM). *Curr. Protoc. Cytometry* 71, 1–15. doi:10.1002/0471142956.cy1237s71

Agrawal, U., Reilly, D. T., and Schroeder, C. M. (2013). Zooming in on Biological Processes with Fluorescence Nanoscopy. *Curr. Opin. Biotechnol.* 24, 646–653. doi:10.1016/j.copbio.2013.02.016

Albert-Smet, I., Marcos-Vidal, A., Vaquero, J. J., Desco, M., Muñoz-Barrutia, A., and Ripoll, J. (2019). Applications of Light-Sheet Microscopy in Microdevices. *Front. Neuroanat.* 13, 1. doi:10.3389/fnana.2019.00001

Antaris, A. L., Chen, H., Cheng, K., Sun, Y., Hong, G., Qu, C., et al. (2016). A Small-Molecule Dye for NIR-II Imaging. *Nat. Mater* 15, 235–242. doi:10.1038/nmat4476

Badawi, Y., and Nishimune, H. (2020). Super-resolution Microscopy for Analyzing Neuromuscular Junctions and Synapses. *Neurosci. Lett.* 715, 134644. doi:10.1016/j.neulet.2019.134644

Baddeley, D., and Bewersdorf, J. (2018). Biological Insight from Super-resolution Microscopy: What We Can Learn from Localization-Based Images. *Annu. Rev. Biochem.* 87, 965–989. doi:10.1146/annurev-biochem-060815-014801

Bates, M., Jones, S. A., and Zhuang, X. (2013). Stochastic Optical Reconstruction Microscopy (STORM): a Method for Superresolution Fluorescence Imaging. *Cold Spring Harb Protoc.* 2013, 498–520. doi:10.1101/pdb.top075143

Berning, S., Willig, K. I., Steffens, H., Dibaj, P., and Hell, S. W. (2012). Nanoscopy in a Living Mouse Brain. *Science* 335, 551. doi:10.1126/science.1215369

Bethge, P., Chéreau, R., Avignone, E., Marsicano, G., and Nägerl, U. V. (2013). Two-photon Excitation STED Microscopy in Two Colors in Acute Brain Slices. *Biophysical J.* 104, 778–785. doi:10.1016/j.bpj.2012.12.054

Betzig, E., Patterson, G. H., Sougrat, R., Lindwasser, O. W., Olenych, S., Bonifacino, J. S., et al. (2006). Imaging Intracellular Fluorescent Proteins at Nanometer Resolution. *Science* 313, 1642–1645. doi:10.1126/science.1127344

Biteen, J., and Willets, K. A. (2017). Introduction: Super-resolution and Single-Molecule Imaging. *Chem. Rev.* 117, 7241–7243. doi:10.1021/acs.chemrev.7b00242

Booth, M. J. (2014). Adaptive Optical Microscopy: the Ongoing Quest for a Perfect Image. *Light Sci. Appl.* 3, e165. doi:10.1038/lsa.2014.46

Brunstein, M., Wicker, K., Hérault, K., Heintzmann, R., and Oheim, M. (2013). Full-field Dual-Color 100-nm Super-resolution Imaging Reveals Organization and Dynamics of Mitochondrial and ER Networks. *Opt. Express* 21, 26162–26173. doi:10.1364/oe.21.026162

Carrier, M., Robert, M.-È., González Ibáñez, F., Desjardins, M., and Tremblay, M.-È. (2020). Imaging the Neuroimmune Dynamics across Space and Time. *Front. Neurosci.* 14, 903. doi:10.3389/fnins.2020.00903

Chen, B.-C., Legant, W. R., Wang, K., Shao, L., Milkie, D. E., Davidson, M. W., et al. (2014a). Lattice Light-Sheet Microscopy: Imaging Molecules to Embryos at High Spatiotemporal Resolution. *Science* 346, 1257998. doi:10.1126/science.1257998

Chen, C., Wang, F., Wen, S., Su, Q. P., Wu, M. C. L., Liu, Y., et al. (2018). Multi-photon Near-Infrared Emission Saturation Nanoscopy Using Upconversion Nanoparticles. *Nat. Commun.* 9, 3290. doi:10.1038/s41467-018-05842-w

Chen, G., Tian, F., Zhang, Y., Zhang, Y., Li, C., and Wang, Q. (2014b). Tracking of Transplanted Human Mesenchymal Stem Cells in Living Mice Using Near-Infrared Ag2S Quantum Dots. *Adv. Funct. Mater.* 24, 2481–2488. doi:10.1002/adfm.201303263

Chin, J. W. (2014). Expanding and Reprogramming the Genetic Code of Cells and Animals. *Annu. Rev. Biochem.* 83, 379–408. doi:10.1146/annurev-biochem-060713-035737

Christensen-Jeffries, K., Browning, R. J., Tang, M.-X., Dunsby, C., and Eckersley, R. J. (2015). *In Vivo* Acoustic Super-resolution and Super-resolved Velocity Mapping Using Microbubbles. *IEEE Trans. Med. Imaging* 34, 433–440. doi:10.1109/TMI.2014.2359650

Coltharp, C., and Xiao, J. (2012). Superresolution Microscopy for Microbiology. *Cell Microbiol* 14, 1808–1818. doi:10.1111/cmi.12024

Corsetti, S., Wijesinghe, P., Poulton, P. B., Sakata, S., Vyas, K., Simon Herrington, C., et al. (2020). Widefield Light Sheet Microscopy Using an Airy Beam Combined with Deep-Learning Super-resolution. *OSA Continuum* 3, 1068–1083. doi:10.1364/osac.391644Herrington

Dan, D., Yao, B., and Lei, M. (2014). Structured Illumination Microscopy for Super-resolution and Optical Sectioning. *Chin. Sci. Bull.* 59, 1291–1307. doi:10.1007/s11434-014-0181-1

Denk, W., Strickler, J., and Webb, W. (1990). Two-Photon Laser Scanning Fluorescence Microscopy. *Science* 248, 73–76. doi:10.1126/science.2321027

Dong, B., Li, C., Chen, G., Zhang, Y., Zhang, Y., Deng, M., et al. (2013). Facile Synthesis of Highly Photoluminescent Ag2Se Quantum Dots as a New Fluorescent Probe in the Second Near-Infrared Window for *In Vivo* Imaging. *Chem. Mater.* 25, 2503–2509. doi:10.1021/cm400812v

Dong, H., Sun, L.-D., and Yan, C.-H. (2020). Lanthanide-Doped Upconversion Nanoparticles for Super-resolution Microscopy. *Front. Chem.* 8, 619377. doi:10.3389/fchem.2020.619377

Errico, C., Pierre, J., Pezet, S., Desailly, Y., Lenkei, Z., Couture, O., et al. (2015). Ultrafast Ultrasound Localization Microscopy for Deep Super-resolution Vascular Imaging. *Nature* 527, 499–502. doi:10.1038/nature16066

Fang, H., Yao, S., Chen, Q., Liu, C., Cai, Y., Geng, S., et al. (2019). De Novo-designed Near-Infrared Nanoaggregates for Super-resolution Monitoring of Lysosomes in Cells, in Whole Organoids, and *In Vivo*. *ACS Nano* 13, 14426–14436. doi:10.1021/acsnano.9b08011

Fernández-Suárez, M., and Ting, A. Y. (2008). Fluorescent Probes for Super-resolution Imaging in Living Cells. *Nat. Rev. Mol. Cel Biol* 9, 929–943. doi:10.1038/nrm2531

Galbraith, C. G., and Galbraith, J. A. (2011). Super-resolution Microscopy at a Glance. *J. Cel. Sci.* 124, 1607–1611. doi:10.1242/jcs.080085

Gao, L., Tang, W.-C., Tsai, Y.-C., and Chen, B.-C. (2019). Lattice Light Sheet Microscopy Using Tiling Lattice Light Sheets. *Opt. Express* 27, 1497–1506. doi:10.1364/OE.27.001497

Girkin, J. M., and Carvalho, M. T. (2018). The Light-Sheet Microscopy Revolution. *J. Opt.* 20, 053002. doi:10.1088/2040-8986/aab58a

Grotjohann, T., Testa, I., Leutenegger, M., Bock, H., Urban, N. T., Lavoie-Cardinal, F., et al. (2011). Diffraction-unlimited All-Optical Imaging and Writing with a Photochromic GFP. *Nature* 478, 204–208. doi:10.1038/nature10497

Gustafsson, M. G. L. (2000). Surpassing the Lateral Resolution Limit by a Factor of Two Using Structured Illumination Microscopy. SHORT COMMUNICATION. *J. Microsc.* 198, 82–87. doi:10.1046/j.1365-2818.2000.00710.x

Gustavsson, A.-K., Petrov, P. N., Lee, M. Y., Shechtman, Y., and Moerner, W. E. (2018). 3D Single-Molecule Super-resolution Microscopy with a Tilted Light Sheet. *Nat. Commun.* 9, 1–8. doi:10.1038/s41467-017-02563-4

Heilemann, M. (2010). Fluorescence Microscopy beyond the Diffraction Limit. *J. Biotechnol.* 149, 243–251. doi:10.1016/j.jbiotec.2010.03.012

Heilemann, M., van de Linde, S., Schüttpelz, M., Kasper, R., Seefeldt, B., Mukherjee, A., et al. (2008). Subdiffraction-resolution Fluorescence Imaging with Conventional Fluorescent Probes. *Angew. Chem. Int. Ed.* 47, 6172–6176. doi:10.1002/anie.200802376

Hell, S. W., Dyba, M., and Jakobs, S. (2004). Concepts for Nanoscale Resolution in Fluorescence Microscopy. *Curr. Opin. Neurobiol.* 14, 599–609. doi:10.1016/j.conb.2004.08.015

Hell, S. W., Sahl, S. J., Bates, M., Zhuang, X., Heintzmann, R., Booth, M. J., et al. (2015). The 2015 Super-resolution Microscopy Roadmap. *J. Phys. D: Appl. Phys.* 48, 443001. doi:10.1088/0022-3727/48/44/443001

Hell, S. W., and Wichmann, J. (1994). Breaking the Diffraction Resolution Limit by Stimulated Emission: Stimulated-Emission-Depletion Fluorescence Microscopy. *Opt. Lett.* 19, 780–782. doi:10.1364/OL.19.000780

Helmchen, F., and Denk, W. (2005). Deep Tissue Two-Photon Microscopy. *Nat. Methods* 2, 932–940. doi:10.1038/nmeth818

Henriques, R., Griffiths, C., Hesper Rego, E., and Mhlanga, M. M. (2011). PALM and STORM: Unlocking Live-Cell Super-resolution. *Biopolymers* 95, 322–331. doi:10.1002/bip.21586

Hong, G., Lee, J. C., Robinson, J. T., Raaz, U., Xie, L., Huang, N. F., et al. (2012). Multifunctional *In Vivo* Vascular Imaging Using Near-Infrared II Fluorescence. *Nat. Med.* 18, 1841–1846. doi:10.1038/nm.2995

Hruska, M., Henderson, N., Le Marchand, S. J., Jafri, H., and Dalva, M. B. (2018). Synaptic Nanomodules Underlie the Organization and Plasticity of Spine Synapses. *Nat. Neurosci.* 21, 671–682. doi:10.1038/s41593-018-0138-9

Hu, C., Wu, Z., Yang, X., Zhao, W., Ma, C., Chen, M., et al. (2020). MUTE-SIM: Multiphoton Up-Conversion Time-Encoded Structured Illumination Microscopy. *OSA Continuum* 3, 594. doi:10.1364/osac.387129

Huang, B., Babcock, H., and Zhuang, X. (2010). Breaking the Diffraction Barrier: Super-resolution Imaging of Cells. *Cell* 143, 1047–1058. doi:10.1016/j.cell.2010.12.002

Huang, B., Bates, M., and Zhuang, X. (2009). Super-resolution Fluorescence Microscopy. *Annu. Rev. Biochem.* 78, 993–1016. doi:10.1146/annurev.biochem.77.061906.092014

Huang, S.-H., Irawati, N., Chien, Y.-F., Lin, J.-Y., Tsai, Y.-H., Wang, P.-Y., et al. (2021). Optical Volumetric Brain Imaging: Speed, Depth, and Resolution Enhancement. *J. Phys. D: Appl. Phys.* 54, 323002. doi:10.1088/1361-6463/abff7b

Ilgen, P., Stoldt, S., Conradi, L.-C., Wurm, C. A., Rüschoff, J., Ghadimi, B. M., et al. (2014). STED Super-resolution Microscopy of Clinical Paraffin-Embedded Human Rectal Cancer Tissue. *PLoS One* 9, e101563. doi:10.1371/journal.pone.0101563

Jahr, W., Velicky, P., and Danzl, J. G. (2020). Strategies to Maximize Performance in STimulated Emission Depletion (STED) Nanoscopy of Biological Specimens. *Methods* 174, 27–41. doi:10.1016/j.ymeth.2019.07.019

Jin, D., Xi, P., Wang, B., Zhang, L., Enderlein, J., and van Oijen, A. M. (2018). Nanoparticles for Super-resolution Microscopy and Single-Molecule Tracking. *Nat. Methods* 15, 415–423. doi:10.1038/s41592-018-0012-4

Johnstone, G. E., Cairns, G. S., and Patton, B. R. (2019). Nanodiamonds Enable Adaptive-Optics Enhanced, Super-resolution, Two-Photon Excitation Microscopy. *R. Soc. Open Sci.* 6, 190589. doi:10.1098/rsos.190589

Kilian, N., Goryaynov, A., Lessard, M. D., Hooker, G., Toomre, D., Rothman, J. E., et al. (2018). Assessing Photodamage in Live-Cell STED Microscopy. *Nat. Methods* 15, 755–756. doi:10.1038/s41592-018-0145-5

Lei, Z., and Zhang, F. (2021). Molecular Engineering of NIR-II Fluorophores for Improved Biomedical Detection. *Angew. Chem. Int. Ed.* 60, 16294–16308. doi:10.1002/anie.202007040

Li, C., Moatti, A., Zhang, X., Ghashghaei, H., and Greenbaum, A. (2021). Deep Learning-Based Autofocus Method Enhances Image Quality in Light-Sheet Fluorescence Microscopy. *Biomed. Opt. Express* 12, 5214. doi:10.1364/boe.427099

Li, D., Shao, L., Chen, B.-C., Zhang, X., Zhang, M., Moses, B., et al. (2015). Extended-resolution Structured Illumination Imaging of Endocytic and Cytoskeletal Dynamics. *Science* 349, aab3500. doi:10.1126/science.aab3500

Li, Z., Zhang, Q., Chou, S.-W., Newman, Z., Turcotte, R., Natan, R., et al. (2020). Fast Widefield Imaging of Neuronal Structure and Function with Optical Sectioning *In Vivo*. *Sci. Adv.* 6, eaaz3870. doi:10.1126/sciadv.aaz3870

Lin, D., Gagnon, L. A., Howard, M. D., Halpern, A. R., and Vaughan, J. C. (2018). Extended-Depth 3D Super-resolution Imaging Using Probe-Refresh STORM. *Biophysical J.* 114, 1980–1987. doi:10.1016/j.bpj.2018.03.023

Liu, B., Chen, C., Di, X., Liao, J., Wen, S., Su, Q. P., et al. (2020). Upconversion Nonlinear Structured Illumination Microscopy. *Nano Lett.* 20, 4775–4781. doi:10.1021/acs.nanolett.0c00448

Liu, T.-L., Upadhyayula, S., Milkie, D. E., Singh, V., Wang, K., Swinburne, I. A., et al. (2018). Observing the Cell in its Native State: Imaging Subcellular Dynamics in Multicellular Organisms. *Science* 360, eaaq1392. doi:10.1126/science.aaq1392

Liu, Y., and Xu, J. (2019). High-resolution Microscopy for Imaging Cancer Pathobiology. *Curr. Pathobiol Rep.* 7, 85–96. doi:10.1007/s40139-019-00201-w

MacGillavry, H. D., Song, Y., Raghavachari, S., and Blanpied, T. A. (2013). Nanoscale Scaffolding Domains within the Postsynaptic Density Concentrate Synaptic AMPA Receptors. *Neuron* 78, 615–622. doi:10.1016/j.neuron.2013.03.009

Manley, H. R., Potter, D. L., Heddleston, J. M., Chew, T. L., Keightley, M. C., and Lieschke, G. J. (2020). Frontline Science: Dynamic Cellular and Subcellular Features of Migrating Leukocytes Revealed by *In Vivo* Lattice Lightsheet Microscopy. *J. Leukoc. Biol.* 108, 455–468. doi:10.1002/JLB.3HI0120-589R

Masch, J.-M., Steffens, H., Fischer, J., Engelhardt, J., Hubrich, J., Keller-Findeisen, J., et al. (2018). Robust Nanoscopy of a Synaptic Protein in Living Mice by Organic-Fluorophore Labeling. *Proc. Natl. Acad. Sci. USA* 115, E8047–E8056. doi:10.1073/pnas.1807104115

Masullo, L. A., Bodén, A., Pennacchietti, F., Coceano, G., Ratz, M., and Testa, I. (2018). Enhanced Photon Collection Enables Four Dimensional Fluorescence Nanoscopy of Living Systems. *Nat. Commun.* 9, 3281. doi:10.1038/s41467-018-05799-w

Minehart, J. A., and Speer, C. M. (2020). A Picture worth a Thousand Molecules-Integrative Technologies for Mapping Subcellular Molecular Organization and Plasticity in Developing Circuits. *Front. Synaptic Neurosci.* 12, 615059. doi:10.3389/fnsyn.2020.615059

Möckl, L., and Moerner, W. E. (2020). Super-resolution Microscopy with Single Molecules in Biology and Beyond-Essentials, Current Trends, and Future Challenges. *J. Am. Chem. Soc.* 142, 17828–17844. doi:10.1021/jacs.0c08178

Müller, B., and Heilemann, M. (2013). Shedding New Light on Viruses: Super-resolution Microscopy for Studying Human Immunodeficiency Virus. *Trends Microbiology* 21, 522–533. doi:10.1016/j.tim.2013.06.010

Okabe, S. (2020). Recent Advances in Computational Methods for Measurement of Dendritic Spines Imaged by Light Microscopy. *Microscopy (Oxf)* 69, 196–213. doi:10.1093/jmicro/dfaa016

Pampaloni, F., Reynaud, E. G., and Stelzer, E. H. K. (2007). The Third Dimension Bridges the gap between Cell Culture and Live Tissue. *Nat. Rev. Mol. Cel Biol* 8, 839–845. doi:10.1038/nrm2236

Pfeiffer, T., Poll, S., Bancelin, S., Angibaud, J., Inavalli, V. K., Keppler, K., et al. (2018). Chronic 2P-STED Imaging Reveals High Turnover of Dendritic Spines in the hippocampus *In Vivo*. *Elife* 7. doi:10.7554/eLife.34700

Pullman, J. M., Nylk, J., Campbell, E. C., Gunn-Moore, F. J., Prystowsky, M. B., and Dholakia, K. (2016). Visualization of Podocyte Substructure with Structured Illumination Microscopy (SIM): A New Approach to Nephrotic Disease. *Biomed Opt. Express*, 7, 302–311. doi:10.1364/BOE.7.000302

Qian, X., Kang, H., Li, R., Lu, G., Du, Z., Shung, K. K., et al. (2020). *In Vivo* visualization of Eye Vasculature Using Super-resolution Ultrasound Microvessel Imaging. *IEEE Trans. Biomed. Eng.* 67, 2870–2880. doi:10.1109/TBME.2020.2972514

Reja, S. I., Minoshima, M., Hori, Y., and Kikuchi, K. (2021). Near-infrared Fluorescent Probes: a Next-Generation Tool for Protein-Labeling Applications. *Chem. Sci.* 12, 3437–3447. doi:10.1039/d0sc04792a

Riedl, J., Crevenna, A. H., Kessenbrock, K., Yu, J. H., Neukirchen, D., Bista, M., et al. (2008). Lifeact: a Versatile Marker to Visualize F-Actin. *Nat. Methods* 5, 605–607. doi:10.1038/nmeth.1220

Rust, M. J., Bates, M., and Zhuang, X. (2006). Sub-diffraction-limit Imaging by Stochastic Optical Reconstruction Microscopy (STORM). *Nat. Methods* 3, 793–796. doi:10.1038/nmeth929

Sahl, S. J., and Moerner, W. (2013). Super-resolution Fluorescence Imaging with Single Molecules. *Curr. Opin. Struct. Biol.* 23, 778–787. doi:10.1016/j.sbi.2013.07.010

Sauer, M. (2013). Localization Microscopy Coming of Age: from Concepts to Biological Impact. *J. Cel. Sci.* 126, 3505–3513. doi:10.1242/jcs.123612

Schermelleh, L., Ferrand, A., Huser, T., Eggeling, C., Sauer, M., Biehlmaier, O., et al. (2019). Super-resolution Microscopy Demystified. *Nat. Cel Biol.* 21, 72–84. doi:10.1038/s41556-018-0251-8

Schnorrenberg, S., Grotjohann, T., Vorbrüggen, G., Herzig, A., Hell, S. W., and Jakobs, S. (2016). *In Vivo* super-resolution RESOLFT Microscopy of *Drosophila melanogaster*. *eLife* 5. doi:10.7554/eLife.15567

Sezgin, E., et al. (2017). Super-resolution optical microscopy for studying membrane structure and dynamics. *J. Phys.: Condens. Matter* 29, 273001. doi:10.1088/1361-648X/aa7185

Sharma, R., Singh, M., and Sharma, R. (2020). Recent Advances in STED and RESOLFT Super-resolution Imaging Techniques. *Spectrochimica Acta A: Mol. Biomol. Spectrosc.* 231, 117715. doi:10.1016/j.saa.2019.117715

Shcherbakova, D. M., Sengupta, P., Lippincott-Schwartz, J., and Verkhusha, V. V. (2014). Photocontrollable Fluorescent Proteins for Superresolution Imaging. *Annu. Rev. Biophys.* 43, 303–329. doi:10.1146/annurev-biophys-051013-022836

Si, P., Honkala, A., de la Zerda, A., and Smith, B. R. (2020). Optical Microscopy and Coherence Tomography of Cancer in Living Subjects. *Trends Cancer* 6, 205–222. doi:10.1016/j.trecan.2020.01.008

Sigrist, S. J., and Sabatini, B. L. (2012). Optical Super-resolution Microscopy in Neurobiology. *Curr. Opin. Neurobiol.* 22, 86–93. doi:10.1016/j.conb.2011.10.014

So, P. T. C., Dong, C. Y., Masters, B. R., and Berland, K. M. (2000). Two-photon Excitation Fluorescence Microscopy. *Annu. Rev. Biomed. Eng.* 2, 399–429. doi:10.1146/annurev.bioeng.2.1.399

Spahn, C., Grimm, J. B., Lavis, L. D., Lampe, M., and Heilemann, M. (2019). Whole-cell, 3D, and Multicolor STED Imaging with Exchangeable Fluorophores. *Nano Lett.* 19, 500–505. doi:10.1021/acs.nanolett.8b04385

Steffens, H., Nadrigny, F., and Kirchhoff, F. (2012). Preparation of the Mouse Spinal Column for Repetitive Imaging Using Two-Photon Laser-Scanning Microscopy. *Cold Spring Harbor Protoc.* 2012, prot072256–pdb. doi:10.1101/pdb.prot0722562012

Steffens, H., Wegner, W., and Willig, K. I. (2020). *In Vivo* STED Microscopy: A Roadmap to Nanoscale Imaging in the Living Mouse. *Methods* 174, 42–48. doi:10.1016/j.ymeth.2019.05.020

Stone, M. B., Shelby, S. A., and Veatch, S. L. (2017). Super-resolution Microscopy: Shedding Light on the Cellular Plasma Membrane. *Chem. Rev.* 117, 7457–7477. doi:10.1021/acs.chemrev.6b00716

Ter Veer, M. J. T., Pfeiffer, T., and Nägerl, U. V. (2017). Two-photon STED Microscopy for Nanoscale Imaging of Neural Morphology *In Vivo*. *Methods Mol. Biol.* 1663, 45–64. doi:10.1007/978-1-4939-7265-4_5

Testa, I., Urban, N. T., Jakobs, S., Eggeling, C., Willig, K. I., and Hell, S. W. (2012). Nanoscopy of Living Brain Slices with Low Light Levels. *Neuron* 75, 992–1000. doi:10.1016/j.neuron.2012.07.028

Turcotte, R., Liang, Y., Tanimoto, M., Zhang, Q., Li, Z., Koyama, M., et al. (2019). Dynamic Super-resolution Structured Illumination Imaging in the Living Brain. *Proc. Natl. Acad. Sci. USA* 116, 9586–9591. doi:10.1073/pnas.1819965116

Urban, B. E., Xiao, L., Chen, S., Yang, H., Dong, B., Kozorovitskiy, Y., et al. (2018). *In Vivo* Superresolution Imaging of Neuronal Structure in the Mouse Brain. *IEEE Trans. Biomed. Eng.* 65, 232–238. doi:10.1109/TBME.2017.2773540

Urban, N. T., Willig, K. I., Hell, S. W., and Nägerl, U. V. (2011). STED Nanoscopy of Actin Dynamics in Synapses Deep inside Living Brain Slices. *Biophysical J.* 101, 1277–1284. doi:10.1016/j.bpj.2011.07.027

Vacaru, A. M., Unlu, G., Spitzner, M., Mione, M., Knapik, E. W., and Sadler, K. C. (2014). *In Vivo* cell Biology in Zebrafish - Providing Insights into Vertebrate Development and Disease. *J. Cel. Sci.* 127, 485–495. doi:10.1242/jcs.140194

Velasco, M. G. M., Zhang, M., Antonello, J., Yuan, P., Allgeyer, E. S., May, D., et al. (2021). 3D Super-resolution Deep-Tissue Imaging in Living Mice. *Optica* 8, 442. doi:10.1364/optica.416841

Vicidomini, G., Bianchini, P., and Diaspro, A. (2018). STED Super-resolved Microscopy. *Nat. Methods* 15, 173–182. doi:10.1038/nmeth.4593

Wagner, N., Beuttenmueller, F., Norlin, N., Gierten, J., Boffi, J. C., Wittbrodt, J., et al. (2021). Deep Learning-Enhanced Light-Field Imaging with Continuous Validation. *Nat. Methods* 18, 557–563. doi:10.1038/s41592-021-01136-0

Walker, C. K., and Herskowitz, J. H. (2020). Dendritic Spines: Mediators of Cognitive Resilience in Aging and Alzheimer's Disease. *Neuroscientist*, 107385842094596. doi:10.1177/1073858420945964

Wang, F., Ma, Z., Zhong, Y., Salazar, F., Xu, C., Ren, F., et al. (2021). *In Vivo* NIR-II Structured-Illumination Light-Sheet Microscopy. *Proc. Natl. Acad. Sci. USA* 118, e2023888118. doi:10.1073/pnas.2023888118

Wang, L., Frei, M. S., Salim, A., and Johnsson, K. (2018). Small-molecule Fluorescent Probes for Live-Cell Super-resolution Microscopy. *J. Am. Chem. Soc.* 141, 2770–2781. doi:10.1021/jacs.8b11134

Wegner, W., Ilgen, P., Gregor, C., van Dort, J., Mott, A. C., Steffens, H., et al. (2017). *In Vivo* mouse and Live Cell STED Microscopy of Neuronal Actin Plasticity Using Far-Red Emitting Fluorescent Proteins. *Sci. Rep.* 7, 11781. doi:10.1038/s41598-017-11827-4

Welsher, K., Liu, Z., Sherlock, S. P., Robinson, J. T., Chen, Z., Daranciang, D., et al. (2009). A Route to Brightly Fluorescent Carbon Nanotubes for Near-Infrared Imaging in Mice. *Nat. Nanotech* 4, 773–780. doi:10.1038/nnano.2009.294

Willig, K. I., Steffens, H., Gregor, C., Herholt, A., Rossner, M. J., and Hell, S. W. (2014). Nanoscopy of Filamentous Actin in Cortical Dendrites of a Living Mouse. *Biophysical J.* 106, L01–L03. doi:10.1016/j.bpj.2013.11.1119

Xu, J., Ma, H., Ma, H., Jiang, W., Mela, C. A., Duan, M., et al. (2020a). Super-resolution Imaging Reveals the Evolution of Higher-Order Chromatin Folding in Early Carcinogenesis. *Nat. Commun.* 11. doi:10.1038/s41467-020-15718-7

Xu, Y., Zhang, H., Zhang, N., Wang, X., Dang, D., Jing, X., et al. (2020b). Deep-Red Fluorescent Organic Nanoparticles with High Brightness and Photostability for Super-resolution *In Vitro* and *In Vivo* Imaging Using STED Nanoscopy. *ACS Appl. Mater. Inter.* 12, 6814–6826. doi:10.1021/acsami.9b18336

Yang, Z., Sharma, A., Qi, J., Peng, X., Lee, D. Y., Hu, Z., et al. (2016). Super-resolution Fluorescent Materials: an Insight into Design and Bioimaging Applications. *Chem. Soc. Rev.* 45, 4651–4667. doi:10.1039/c5cs00875a

Yoon, H., Hallam, K. A., Yoon, C., and Emelianov, S. Y. (2018). Super-resolution Imaging with Ultrafast Ultrasound Imaging of Optically Triggered Perfluorohexane Nanodroplets. *IEEE Trans. Ultrason. Ferroelect., Freq. Contr.* 65, 2277–2285. doi:10.1109/TUFFC.2018.2829740

York, A. G., Chandris, P., Nogare, D. D., Head, J., Wawrzusin, P., Fischer, R. S., et al. (2013). Instant Super-resolution Imaging in Live Cells and Embryos via Analog Image Processing. *Nat. Methods* 10, 1122–1126. doi:10.1038/nmeth.2687

York, A. G., Parekh, S. H., Nogare, D. D., Fischer, R. S., Temprine, K., Mione, M., et al. (2012). Resolution Doubling in Live, Multicellular Organisms via Multifocal Structured Illumination Microscopy. *Nat. Methods* 9, 749–754. doi:10.1038/nmeth.2025

Yu, J., Lavery, L., and Kim, K. (2018). Super-resolution Ultrasound Imaging Method for Microvasculature *In Vivo* with a High Temporal Accuracy. *Sci. Rep.* 8, 13918. doi:10.1038/s41598-018-32235-2

Yu, W., Ji, Z., Dong, D., Yang, X., Xiao, Y., Gong, Q., et al. (2016). Super-resolution Deep Imaging with Hollow Bessel Beam STED Microscopy. *Laser Photon. Rev.* 10, 147–152. doi:10.1002/lpor.201500151

Zdańkowski, P., Trusiak, M., McGloin, D., and Swedlow, J. R. (2020). Numerically Enhanced Stimulated Emission Depletion Microscopy with Adaptive Optics for Deep-Tissue Super-resolved Imaging. *ACS Nano* 14, 394–405. doi:10.1021/acsnano.9b05891

Zheng, W., Wu, Y., Winter, P., Fischer, R., Nogare, D. D., Hong, A., et al. (2017). Adaptive Optics Improves Multiphoton Super-resolution Imaging. *Nat. Methods* 14, 869–872. doi:10.1038/nmeth.4337

Zheng, X., Duan, R., Li, L., Xing, S., Ji, H., Yan, H., et al. (2020). Live-cell Superresolution Pathology Reveals Different Molecular Mechanisms of Pelizaeus-Merzbacher Disease. *Sci. Bull.* 65, 2061–2064. doi:10.1016/j.scib.2020.08.016

Zhu, J., Rowland, E. M., Harput, S., Riemer, K., Leow, C. H., Clark, B., et al. (2019). 3D Super-resolution US Imaging of Rabbit Lymph Node Vasculature *In Vivo* by Using Microbubbles. *Radiology* 291, 642–650. doi:10.1148/radiol.2019182593

Conflict of Interest: The authors declare that the research was conducted in the absence of any commercial or financial relationships that could be construed as a potential conflict of interest.

Publisher's Note: All claims expressed in this article are solely those of the authors and do not necessarily represent those of their affiliated organizations, or those of the publisher, the editors and the reviewers. Any product that may be evaluated in this article, or claim that may be made by its manufacturer, is not guaranteed or endorsed by the publisher.

Copyright © 2021 Jing, Zhang, Yu, Lin and Qu. This is an open-access article distributed under the terms of the Creative Commons Attribution License (CC BY). The use, distribution or reproduction in other forums is permitted, provided the original author(s) and the copyright owner(s) are credited and that the original publication in this journal is cited, in accordance with accepted academic practice. No use, distribution or reproduction is permitted which does not comply with these terms.

frontiers in Chemistry

ORIGINAL RESEARCH
published: 07 October 2021
doi: 10.3389/fchem.2021.758357

Highly Efficient Phosphorescent Blue-Emitting [3+2+1] Coordinated Iridium (III) Complex for OLED Application

*Zijian Liu[1†], Si-Wei Zhang[1†], Meng Zhang[1], Chengcheng Wu[1], Wansi Li[1], Yuan Wu[2], Chen Yang[2], Feiyu Kang[1,3], Hong Meng[4] and Guodan Wei[1,3]**

[1]Tsinghua-Berkeley Shenzhen Institute (TBSI), Tsinghua University, Shenzhen, China, [2]PURI Materials, Shenzhen, China, [3]Institute of Materials Research, Tsinghua Shenzhen International Graduate School, Tsinghua University, Shenzhen, China, [4]Peking University Shenzhen Graduate School, Peking University, Shenzhen, China

Cyclometalated iridium (III) complexes are indispensable in the field of phosphorescent organic light-emitting diodes (PhOLEDs), while the improvement of blue iridium (III) complexes is as yet limited and challenging. More diversified blue emitters are needed to break through the bottleneck of the industry. Hence, a novel [3+2+1] coordinated iridium (III) complex (noted as **Ir-dfpMepy-CN**) bearing tridentate bis-N-heterocyclic carbene (NHC) chelate (2,6-bisimidazolylidene benzene), bidentate chelates 2-(2,4-difluorophenyl)-4-methylpyridine (dfpMepy), and monodentate ligand (-CN) has been designed and synthesized. The tridentate bis-NHC ligand enhances molecular stability by forming strong bonds with the center iridium atom. The electron-withdrawing groups in the bidentate ligand (dfpMepy) and monodentate ligand (-CN) ameliorate the stability of the HOMO levels. **Ir-dfpMepy-CN** shows photoluminescence peaks of 440 and 466 nm with a high quantum efficiency of 84 ± 5%. Additionally, the HATCN (10 nm)/TAPC (40 nm)/TcTa (10 nm)/10 wt% **Ir-dfpMepy-CN** in DPEPO (10 nm)/TmPyPB (40 nm)/Liq (2.5 nm)/Al (100 nm) OLED device employing the complex shows a CIE coordinate of (0.16, 0.17), reaching a deeper blue emission. The high quantum efficiency is attributed to rapid singlet to triplet charge transfer transition of 0.9–1.2 ps. The successful synthesis of **Ir-dfpMepy-CN** has opened a new window to develop advanced blue emitters and dopant alternatives for future efficient blue PhOLEDs.

Keywords: OLED, Iridium (III) complexes, blue emitters, transient absorption, quantum yield

OPEN ACCESS

Edited by:
Nasir Mahmood,
RMIT University, Australia

Reviewed by:
Tim Connell,
Deakin University, Australia
Lei Lei,
China Jiliang University, China

****Correspondence:***
Guodan Wei
weiguodan@sz.tsinghua.edu.cn

[†]These authors have contributed equally to this work

Specialty section:
This article was submitted to Nanoscience, a section of the journal Frontiers in Chemistry

Received: *13 August 2021*
Accepted: *15 September 2021*
Published: *07 October 2021*

Citation:
Liu Z, Zhang S-W, Zhang M, Wu C, Li W, Wu Y, Yang C, Kang F, Meng H and Wei G (2021) Highly Efficient Phosphorescent Blue-Emitting [3+2+1] Coordinated Iridium (III) Complex for OLED Application. Front. Chem. 9:758357. doi: 10.3389/fchem.2021.758357

INTRODUCTION

Cyclometalated iridium (III) complexes have attracted enormous attention in the field of phosphorescent organic light-emitting diodes (PhOLEDs) due to their relatively short triplet lifetime and high phosphorescence quantum yields (Geffroy et al., 2006). However, the stability of organic luminescence materials at high temperature are worse than inorganic materials, especially the inorganic upconversion materials (Wang et al., 2021a; Wang et al., 2021b). Besides, compared with red and green iridium (III) complexes, the development of blue iridium (III) complexes for PhOLEDs is still limited and challenging (Brown et al., 2004). Several proven strategies benefit the achievement of blue emitters: (Ma et al., 2020). 1), stabilizing the highest occupied molecular orbital

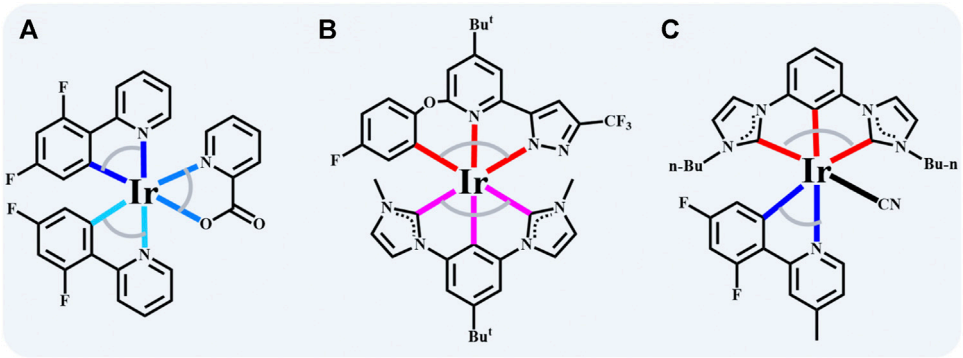

SCHEME 1 | The typic blue emitters of iridium (III) complexes with **(A)** [2+2+2] (**FIrpic**) (Adachi et al., 2001), **(B)** [3+3] (**Ir(minb)(pzpy^{Bu}Oph^{F})**) (Kuo et al., 2017) and **(C)** [3+2+1] (**Ir-dfpMepy-CN** in this work) conformation.

(HOMO) by introducing electron-withdrawing groups on the phenyl ring, like perfluoro carbonyl (Lee et al., 2013), pentafluorophenyl (Tsuzuki et al., 2003), carborane (Furue et al., 2016), sulfonyl (Lim et al., 2017; Lin et al., 2014), dimesitylboron (Lorente et al., 2017), or formyl (Bin Mohd Yusoff et al., 2017). 2), elevating the lowest unoccupied molecular orbital (LUMO) by grafting electron-donating groups onto pyridine moieties, like methoxy group on the pyridyl ring (Yam and Lo, 2006). These two strategies positively influence the energy gap of the iridium (III) emitters, which promote the hypsochromic photoluminescence spectrum. For achieving high phosphorescence quantum yields, a few essential factors should be taken into account, among which the most significant one is to enhance the contribution of the metal to ligand charge transfer (MLCT) in the triplet manifold. The metal d_{π} orbital's involvement increases the coupling of the orbital angular momentum to the electron spin, which enhances the spin-orbit coupling term and drastically decreases the radiative lifetime, and hence realizes the possibility of achieving high quantum yield (Li et al., 2005; Wilkinson et al., 2006).

The blue iridium (III) complexes generally feature an octahedral conformation with three bidentate or two tridentate ligands (labeled as [2+2+2] and [3+3], respectively) due to the d^6 electron configuration of iridium ion (Bin Mohd Yusoff et al., 2017). [2+2+2] Coordinated iridium (III) complexes' inherent superior performance benefits from the diversity of bidentate chelates (Adachi et al., 2001; Holmes et al., 2003), and one of the most typical representatives is greenish-blue bis (4',6'-difluorophenylpyridinato) iridium (III) picolinate (FIrpic) (Adachi et al., 2001). As shown in **Scheme 1A**, incorporating the two strong electron-withdrawing groups (dfppy) facilitates the enlargement of the bandgap of iridium (III) complexes by stabilizing the HOMO levels (Holmes et al., 2003) [3+3]. Coordinated iridium (III) complexes show excellence in rigidity and durability due to the stronger metal-ligand bonding interaction, making the d–d excited states or other unspecified quenching states destabilized to enhance the stability of the complexes (Kuo et al., 2017; Kuo et al., 2018; Gnanasekaran et al., 2019; Hsu et al., 2019). **Scheme 1B** demonstrates a typical [3+3] counterpart, and the interrupted conjugation changes the nature of the frontier orbitals, achieving a blue emission of CIE (0.15, 0.17) (Kuo et al., 2017). Multi-strategies should be utilized together to acquire high-efficiency blue light emitters. Even though some iridium (III) complexes present plausible molecular properties, blue emission severely restricts material selection for PhOLEDs. Consequently, it is imperative to extend the existing iridium (III) complexes system to obtain blue PhOLEDs with high color purity and efficiency.

In this work, a novel [3+2+1] coordinated iridium (III) complex, bearing tridentate bis-N-heterocyclic carbene (NHC) chelate (2,6-bisimidazolylidene benzene), bidentate chelates 2-(2,4-difluorophenyl)-4-methylpyridine (dfpMepy), and monodentate ligand (-CN), has been designed and synthesized. The tridentate ligand improves the molecular stability with the similar function of the [3+3] conformation and sufficient bidentate ligands are available to tune the emission wavelength. Additionally, monodentate ligand (-CN) is a strong electron-withdrawing group, facilitating the stability of the HOMO levels. The designed [3+2+1] iridium (III) complex shows emission peaks of 440 and 466 nm with a high quantum efficiency of 84 ± 5%. Furthermore, the femtosecond transient absorption spectrum further reveals the singlet transition to triplet state with a time constant of 0.9–1.2 ps. This work exhibits a novel cyclometalated iridium (III) complex configuration that will help develop more dopant options for blue PHOLEDs.

MATERIALS AND METHODS

Synthesis of 2-(2,4-Difluorophenyl)-4-Methylpyridine (dfpMepy)

2-bromo-4-methylpyridine (6.84 g, 40 mmol), potassium carbonate (8.29 g, 60 mmol) and tetrakis (triphenylphosphine) palladium (1.49 g, 1.2 mmol) were added into a 250 ml round-bottomed flask. (2,4-Difluorophenyl) boronic acid (4.67 ml, 40 mmol), ethanol (20 ml) and tetrahydrofuran (20 ml) were

slowly added into the flask under stirring conditions. The mixture was then heated to reflux for 20 h under a nitrogen atmosphere. After cooled to room temperature, the resulting solution was firstly washed by water for three times and then filtered, extracted with dichloromethane, and dried with $MgSO_4$, yielding an oily organic layer. The crude product was concentrated and purified by column chromatography (with eluent hexane/DCM, v/v = 5/1) to obtain light yellow powder (6.39 g, 78%). ^{1}H NMR (400 MHz, Chloroform-d): δ = 8.58 (d, J = 5.0 Hz, ^{1}H), 7.98 (td, J = 8.9, 6.7 Hz, ^{1}H), 7.58 (s, ^{1}H), 7.13–7.07 (m, ^{1}H), 7.01 (td, J = 8.3, 2.6 Hz, ^{1}H), 6.93 (ddd, J = 11.3, 8.8, 2.6 Hz, ^{1}H), 2.43 (s, ^{3}H) ppm.

Synthesis of 1,3-Bis(imidazolyl)Benzene (1)

1,3-Dibromobenzene (5 ml, 42 mmol), imidazole (7 g, 104 mmol), potassium carbonate (14.4 g, 104 mmol), cupric oxide (0.83 g, 10.4 mmol) and DMSO (60 ml) were added into a 250 ml flask. The mixture was heated to 150°C for 48 h. After cooling to room temperature, the resulting solution was filtered under reduced pressure and washed by water for three times. DMSO was then removed from the solution by vacuum distillation. The crude product was concentrated and purified by column chromatography to obtain a white powder (5.8 g, 66%). ^{1}H NMR (400 MHz, Chloroform-d): δ = 7.93 (s, ^{2}H), 7.63 (t, J = 8.0 Hz, ^{1}H), 7.45 (s, ^{2}H), 7.42 (d, J = 1.9 Hz, ^{1}H), 7.35 (s, ^{2}H), 7.27 (s, ^{2}H) ppm.

Synthesis of 1,1'-(1,3-Phenylene) bis(3-Butyl-1H-Imidazolium) Bromide (2)

1,3-Bis(imidazolyl)benzene (2.9 g, 13.8 mmol), n-butyl bromide (9.5 g, 69 mmol) and acetonitrile (30 ml) were added to a 100 ml round-bottomed flask. The mixture was heated to 85°C for 3 h. After cooled to room temperature, the solution was concentrated and purified by vacuum distillation to obtain a white powder (9.5 g, 81%). ^{1}H NMR (400 MHz, DMSO-d6): δ = 10.29 (s, ^{2}H), 8.59 (t, J = 1.7 Hz, ^{2}H), 8.53 (*t*, J = 1.9 Hz, ^{1}H), 8.19–8.13 (m, ^{2}H), 8.07 (dd, J = 8.2, 1.7 Hz, ^{2}H), 7.96 (dd, J = 8.9, 7.8 Hz, ^{1}H), 4.33 (*t*, J = 7.2 Hz, ^{4}H), 1.93 (*p*, J = 7.4 Hz, ^{4}H), 1.36 (h, J = 7.8, 7.3 Hz, ^{4}H), 0.95 (*t*, J = 7.4 Hz, ^{6}H) ppm.

Synthesis of Ir-dfpMepy-Br

$[Ir(COD)Cl]_2$ (500 mg, 0.745 mmol) and compound 2 (475 mg, 1.118 mmol) were added into a 25 ml Schlenk tube. Triethylamine (2 ml) and acetonitrile (10 ml) were slowly added into the Schlenk tube under the protection of N_2. The mixture was heated to 90°C for 12 h. After cooled to room temperature, the resulting solution was concentrated by vacuum distillation to get a yellow sticky solid. Then dfpMepy (230 mg, 1.118 mmol) and propionic acid (10 ml) were added for next step reaction with the residual. The mixture was heated to 150°C under N_2 atmosphere for 24 h. After cooled to room temperature, the resulting solution was purified by vacuum distillation, column chromatography to get crude product Ir-dfpMepy-Br (320 mg, 58%). ^{1}H NMR (400 MHz, DMSO-d6): δ = 10.13 (d, J = 5.8 Hz, ^{1}H), 8.16 (s, ^{1}H), 8.04 (d, J = 2.0 Hz, ^{2}H), 7.47 (d, J = 5.9 Hz, ^{1}H), 7.40 (d, J = 7.8 Hz, ^{2}H), 7.23 (d, J = 2.0 Hz, ^{2}H), 7.18 (t, J = 7.7 Hz, ^{1}H), 6.50 (t, J = 11.4 Hz, ^{1}H), 5.27 (dd, J = 9.0, 2.5 Hz, ^{1}H), 2.59 (s, ^{2}H), 1.36–1.27 (m, ^{2}H), 0.95 (s, ^{2}H), 0.81 (td, J = 11.8, 10.5, 6.9 Hz, ^{2}H), 0.65 (d, J = 3.7 Hz, ^{6}H) ppm.

Synthesis of Ir-dfpMepy-CN

Ir-dfpMepy-Br (250 mg, 0.337 mmol) and Silver cyanide (67.68 mg, 0.506 mmol) were dissolved in N. N-dimethylformamide (10 ml) in Schlenk tube. The mixture was then heated to 120°C under N_2 atmosphere. After cooled to room temperature, the resulting solution was further filtered through kieselguhr, evaporated under reduced pressure and purified by silica gel column to get a white powder (206.71 mg, 89%). ^{1}H NMR (400 MHz, Chloroform-d): δ = 9.98 (s, ^{1}H), 8.24 (s, ^{1}H), 7.50 (s, ^{2}H), 7.26 (s, ^{1}H), 7.16 (d, J = 7.5 Hz, ^{3}H), 6.80 (s, ^{2}H), 6.32–6.22 (m, ^{1}H), 5.49 (s, ^{1}H), 3.27 (d, J = 14.5 Hz, ^{4}H), 2.61 (s, ^{3}H), 1.40 (s, ^{2}H), 1.15 (d, J = 3.7 Hz, ^{2}H), 0.94 (s, ^{2}H), 0.80 (s, ^{2}H), 0.77 (s, ^{6}H) ppm.

Materials Characterization

All the reagents were purchased from Leyan, General Reagent and Aldrich and all the reactants and solvents were used without further purification unless otherwise specified. The key reaction products are characterized by a 400 MHz ^{1}H-NMR spectrometer (Bruker AV400) and referenced to tetramethylsilane (TMS) as a standard benchmark at 0.00 ppm. The ultra-violate absorption spectra was performed by Cary 5000 UV-vis-NIR spectrophotometer in degassed dichloromethane at a diluted concentration (2×10^{-5} M) of the iridium (III) complex. The photoluminescence (PL) spectra was obtained by spectrofluorometer of Edinburgh Instruments Ltd FS5. The femtosecond transient absorption (fs-TA) measurements were obtained on a Helios pump-probe system (Ultrafast Systems LLC) with an amplified femtosecond laser system (Coherent 35 fs, 1 kHz, 800 nm). The 320 nm pump pulses were achieved by the optical parametric amplifier (TOPAS-800-fs). The 380–680 nm probe pulses were gained by focusing the tiny portion of the 800 nm laser beams onto a sapphire plate. The fs-TA curves were collected and further analyzed by Surface Xplorer software. Thermogravimetric analysis (TGA) of **Ir-dfpMepy-CN** was recorded by the Mettler TGA2 thermogravimeter. The weight loss of the iridium complex was initially measured from 25 to 100°C at a speed of 10°C/min under a nitrogen atmosphere. Before continuing to heat to 500°C, the sample was kept for 15 min at 100°C. Electrochemical characterization of the iridium complex was measured by PalmSens4 electrochemical workstation, using platinum wire as the counter electrode, platinum-carbon as a working electrode and a saturated calomel electrode (SCE) in a saturated KCl aqueous solution as the reference electrode. The cyclic voltammogram of **Ir-dfpMepy-CN** was referenced to the ferrocene/ferrocenium couple at the scanning rate of 100 mV s^{-1}.

Device Fabrication

The indium-tin-oxide (ITO) coated glass substrates were initially cleaned sequentially by deionized water, ethanol, dichloromethane for 5 min separately and then treated with plasma for 1 min. The dopant material **Ir-dfpMepy-CN** and DPEPO were thermally deposited together at the speed of 0.1 Å s^{-1} and 0.9 Å s^{-1} separately, while the other organic functional layers were evaporated at the same rate of 1.0 Å s^{-1} at a pressure of ca. 3.5×10^{-7} Torr. A 2.5 nm Liq layer was

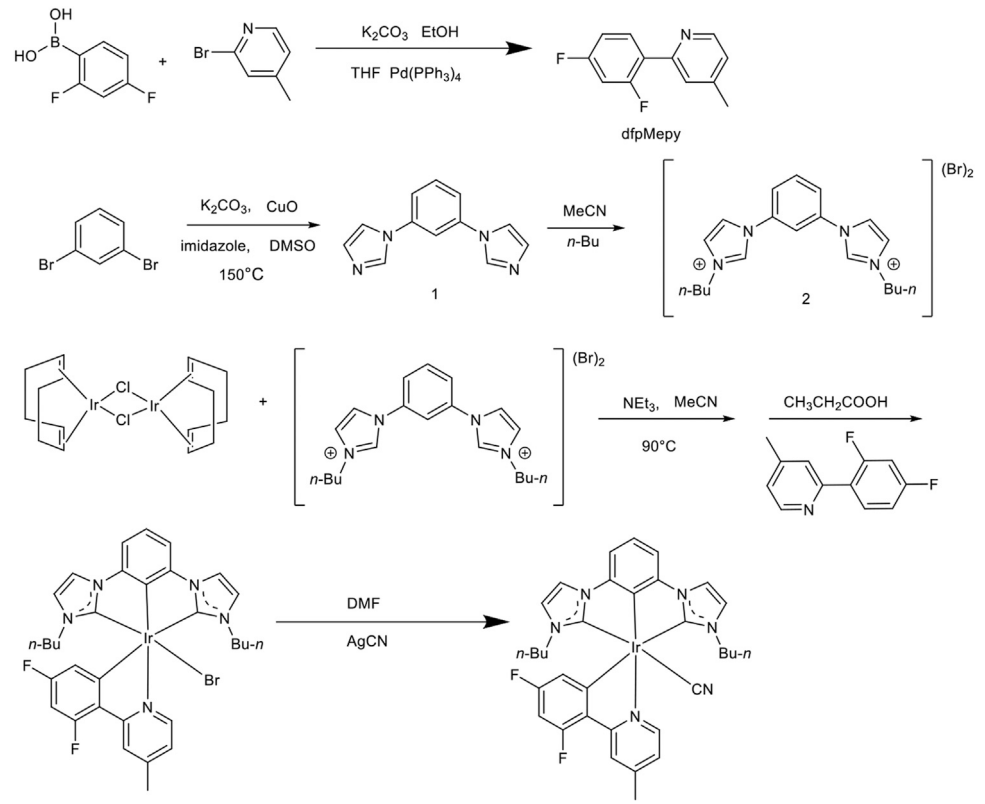

FIGURE 1 | Synthetic route and chemical structure of the **Ir-dfpMepy-CN** with [3+2+1] conformation.

deposited on Al cathode and the two materials are deposited at the rate of 0.1 and 1 Å s^{-1}. The organic diode was assembled on an active area of 3 × 3 mm^2 on the substrates. The device performance, including electroluminescence (EL) spectra, Commission Internationale de L'Eclairage (CIE) and current density-voltage-luminance (J-V-L) curves, were measured by a Keithley 2400 semiconductor characterization system with PR-788 photometer and BM-7A luminance colorimeter.

Theoretical Calculation

The structures were optimized with dispersion density functional theory at the PBE0-D3/def2-SVP level by Gaussian 09. In order to investigate the photophysical properties, the excited electronic structures of these molecules were calculated at the PBE0-D3/def2-TZVP level with the time-dependent density functional theory (TDDFT) method. The electron transition characterization was obtained by electron excitation analysis performed using Multiwfn program from the transition density matrix of TDDFT calculation.

RESULTS AND DISCUSSION

The synthetic route of the **Ir-dfpMepy-CN** with [3+2+1] conformation was depicted in **Figure 1**, and the detailed steps can be obtained in the supporting information (SI). In brief, the tridentate bis-N-heterocyclic carbene (NHC) chelate was synthesized by a two-step reaction of 1,3-dibromobenzene with imidazole and n-butyl bromide, yielding 66 and 81%, respectively. The bidentate ligand dfpMepy was directly synthesized by one step of the Suzuki coupling reaction in an alkaline condition. Controlling the equivalence ratio (1:1) of (2,4-difluorophenyl) boronic acid and 2-bromo-4-methylpyridine, the product was obtained in a relatively high yield of 78%. The -Br was substituted by the stronger electron-withdrawing group of cyanide (-CN), which could significantly influence the metal-centered molecular orbital due to its strong σ-donating p orbital and a low-lying π orbital (Hanusa, 2011). All the compounds were purified by vacuum distillation and column chromatography and subsequently characterized by ^{1}H NMR spectrometry for further study, as shown in **Supplementary Figures S1–S5**. The tridentate bis-NHC chelate serves as electron-donating group in the molecule. Both the bidentate (dfpMepy) and monodentate (-CN) ligand are strong electron-withdrawing groups, expecting to enlarge the complex's bandgap by destabilizing the LUMO and stabilizing the HOMO levels.

The photophysical properties of the [3+2+1] iridium (III) complex were investigated. As shown in **Figures 2A,B**, the absorption and phosphorescent emission (PL) for the **Ir-dfpMepy-CN** were recorded in degassed CH_2Cl_2 (DCM) solution at a concentration of 2 × 10^{-5} M. The strong absorption at 250–280 nm in the ultraviolet region (ε > 2.5 ×

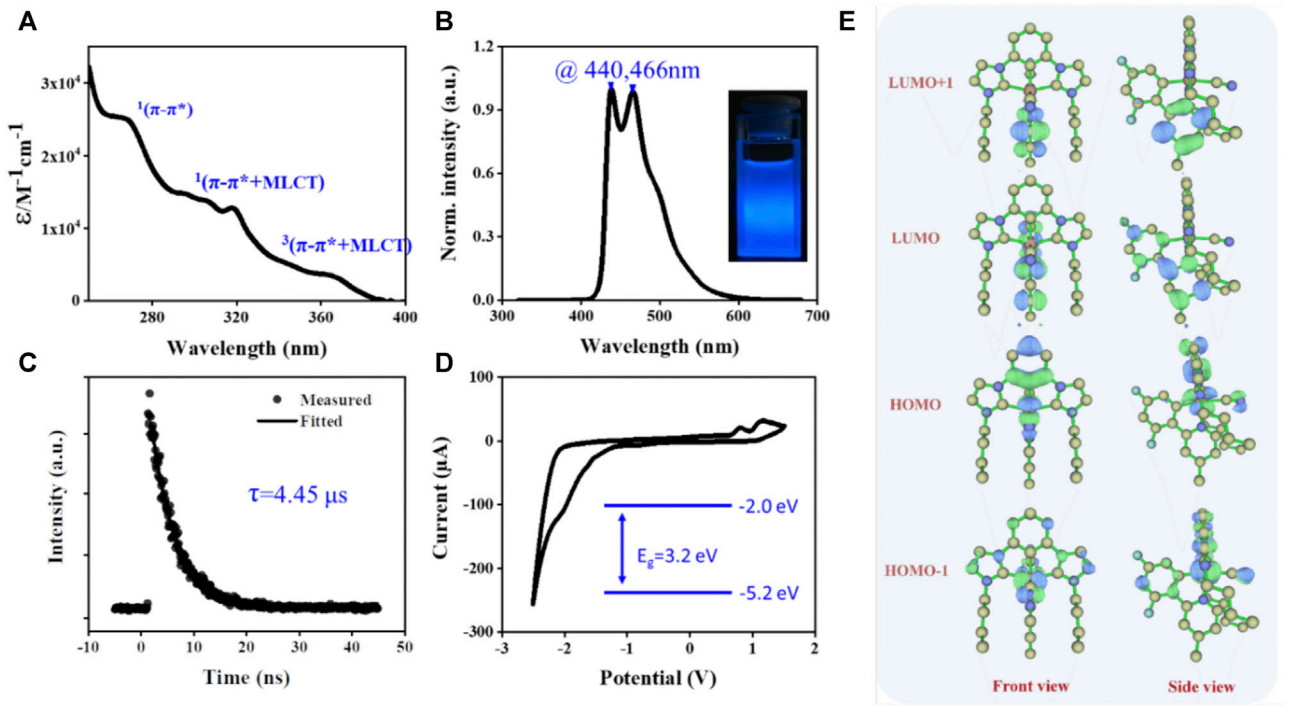

FIGURE 2 | The photophysical properties of the [3+2+1] iridium (III) complex **Ir-dfpMepy-CN**. **(A)** the absorption spectra and **(B)** normalized PL spectra of diluted in CH_2Cl_2 solution. **(C)** Lifetime decay curves at 440 nm and **(D)** cyclic voltammograms (CV) in DCM with $^nBu_4NPF_6$ (0.1 M) as supporting electrolytes. **(E)** The computed frontier molecular orbitals energy surfaces at the ground state (S_0) optimized geometry.

104 M^{-1} cm^{-1}) was assigned to the ligand-centered ($^1\pi\rightarrow\pi^*$) transitions (Ashizawa et al., 2009). The absorption bands with small vibrational shoulders at 300–330 nm were ascribed to spin-allowed intra-ligand ($^1\pi\rightarrow\pi^*$) transition and metal to ligand charge transfer (^{1}MLCT) transitions. The weak absorptions bands ($\varepsilon \approx 0.3 \times 104\ M^{-1}\ cm^{-1}$) lying in the visible light region at 350–400 nm were related to the spin-orbit coupling enhanced $^3\pi\rightarrow\pi^*$ states and spin-forbidden metal to ligand charge transfer (^{3}MLCT) transitions (Chen et al., 2015). The PL spectra of **Ir-dfpMepy-CN** exhibited strong phosphorescent emission at around 430–470 nm with maximum peaks at 440 and 466 nm, which should be attributed to the ^{3}MLCT ^{3}LLCT, ^{3}LC induced by spin-orbit coupling. The PL spectra of the designed **Ir-dfpMepy-CN** with [3+2+1] confirmation is even bluer than that of the classic blue-emitter FIrpic. More gratifyingly, the **Ir-dfpMepy-CN** showed a high absolute quantum efficiency of 84 ± 5%.

The corresponding lifetime decay curve of phosphorescence was presented in **Figure 2C**, revealing a lifetime of 4.6 μs. The electrochemical properties of the [3+2+1] iridium (III) complex in degassed DCM were assessed by cyclic voltammogram (CV). The curve showed positive oxidative peaks (E_{ox}) of 0.80–1.16 V (vs. $Fc^+/0$) due to the electron-deficient property of the pyridine group and reduction peak (E_red) around −2.50 V. The HOMO and LUMO energy of **Ir-dfpMepy-CN** were calculated by **Eqs 1**, **2** below, where the E_ox and E_red were obtained from the onset potential of the first oxidation and reduction peaks and the ferrocene redox value is −4.4 eV (Hack et al., 2005; Leonat et al., 2013). Calculated HOMO and LUMO of **Ir-dfpMepy-CN** is −5.2 and −2.0 eV. Thermogravimetric analysis (TGA) experiments revealed the thermal stability of **Ir-dfpMepy-CN** (**Supplementary Figure S6**). The complex shows good thermal stability, 2 wt% loss >270°C.

$$E_{\mathrm{HOMO}} = -(eE_{ox} + 4.4)\,[\mathbf{eV}] \quad (1)$$

$$E_{\mathrm{LUMO}} = \left(\frac{1240}{\lambda_{UV}} + E_{\mathrm{HOMO}}\right)[\mathbf{eV}] \quad (2)$$

The density functional theory (DFT) and time-dependent density functional theory (TDDFT) calculation were implemented to gain a deeper insight into the ground and excited electronic states of the **Ir-dfpMepy-CN**. The two highest occupied and lowest unoccupied molecular orbitals (HOMO, HOMO-1, LUMO, LUMO+1) surfaces and their corresponding energy levels were given in **Figure 2E**. The LUMO is mainly located on the bidentate ligand (dfpMepy), and the HOMO is a mixed metal-ligand character with contributions from Ir 5d orbitals, tridentate bis- NHC chelate, and monodentate cyanide ligand. Specifically, the participation of Ir 5d orbitals in HOMO and HOMO-1 are 36.6 and 48.2%, and their energy levels are close (−5.70 and −5.78 eV). The large proportion of metals involved is the main reason for the high quantum efficiency of the **Ir-dfpMepy-CN**. The phenyl unit of bis-NHC pincer moiety is suggested to dominate the HOMO, while the difluoro-phenyl unit of dfppy dominates a major contribution in its HOMO-1. The participation of the bis-NHC carbene pincer moiety and monodentate ancillaries in

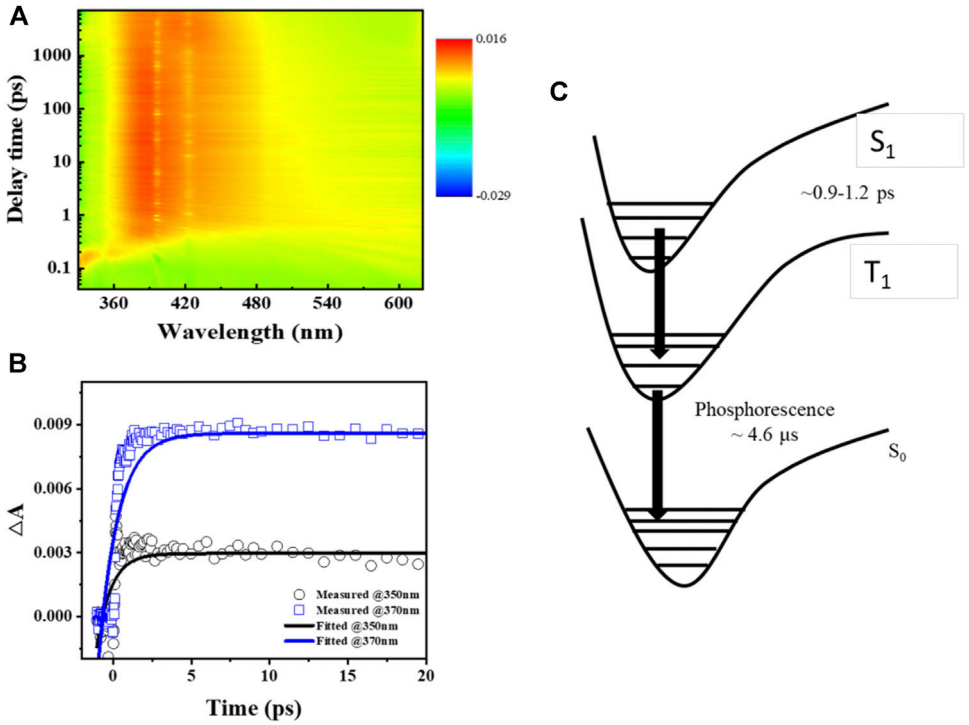

FIGURE 3 | (A) Color plot of femtosecond transient absorption spectra of **Ir-dfpMepy-CN** in DCM at room temperature, **(B)** transient absorption kinetics of 350 and 370 nm, **(C)** schematic illustration of excited-state dynamics occurring in **Ir-dfpMepy-CN**. (The decay data in **Figure 3B** were fitted by a single-term exponential decay model: $y(t) = A_0 * \exp(-\frac{t}{\tau})$, where τ is the decay time and A_0 is a constant).

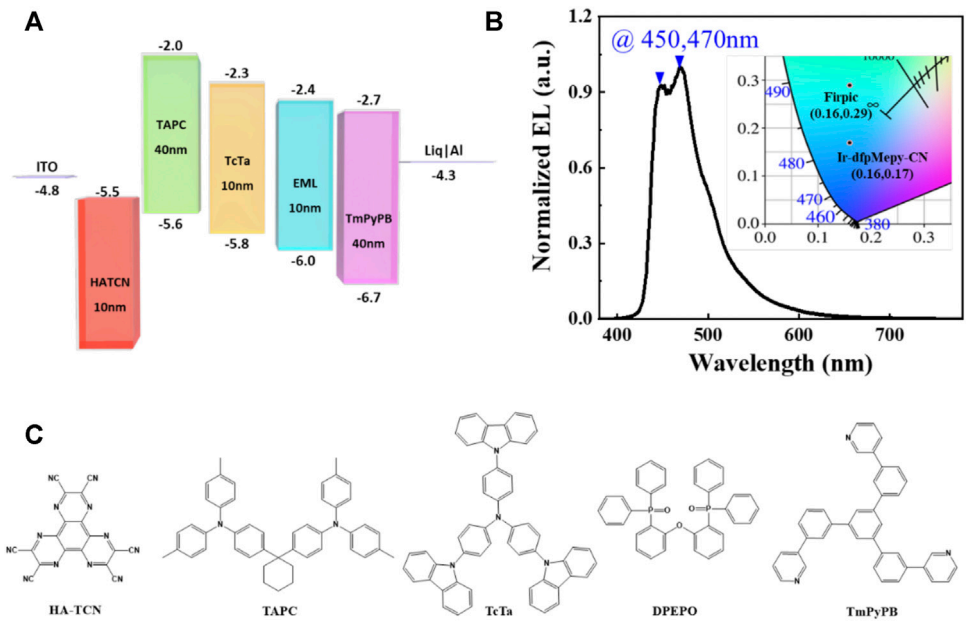

FIGURE 4 | (A) The device structure and **(B)** electroluminescence (EL) spectra at 5 V of OLED fabricated with **Ir-dfpMepy-CN** as dopant (insert: CIE coordinate of **FIrpic** and **Ir-dfpMepy-CN**) **(C)** materials used for device fabrication.

HOMOs keep synergistically. The N-heterocyclic phenyl unit in dfpMepy almost dominates LUMO and LUMO+1. The T_1 optical transition state were calculated by TD-DFT. As shown in **Supplementary Table S1**, the T_1 transition state is contributed by HOMO-3, HOMO-2, HOMO-1 and LUMO. **Supplementary Figure S8** shows the frontier molecular orbitals calculated at T_1

geometries, indicating the T_1 transition state is mixing MLCT, ligand centered (LC) or intra-ligand charge transfer (ILCT) excited state.

The excited-state dynamics of **Ir-dfpMepy-CN** are studied by the femtosecond transient absorption spectroscopy. The iridium complex in DCM solution was pumped by a flash laser at 320 nm, resulting a broad absorption ranging from 340 to 480 nm. Monitoring the kinetics of two absorption peaks at 350 and 370 nm gives two growth lifetimes of 0.9 and 1.2 picoseconds (ps), respectively, and this species has a long lifetime beyond 1,000 ps from fs-TA analysis, revealing the generation of triplet from singlet occurs in 1.2 ps. The non-decaying signal of the absorption spectra indicates the overlap of excited singlet and triplet states of the iridium complex, which adversely influences the relaxation between two energy states and leads to an almost constant transient absorbance (Hedley et al., 2008; Hedley et al., 2010). The schematic illustration of excited-state dynamics occurring in **Ir-dfpMepy-CN** is shown in **Figure 3C**. The relaxation process is proposed as a successive pathway from singlet to triplet and to S_0 state with the relaxation time constant τ_1 and τ_2 (Tang et al., 2004). τ_1 is obtained by transient absorption spectroscopy and τ_2 is the phosphorescent decay time, which can be detected through previous kinetic study of PL measurement. **Ir-dfpMepy-CN**, as a novel [3+2+1] coordinated iridium complex, can achieve the transition lifetime of 0.9–1.2 ps and a phosphorescence lifetime of around 4.6 μs. The comprehensive understanding of the relaxation process of different energy states sheds light on the structural design of high-efficiency blue phosphors in future applications.

The effectiveness of **Ir-dfpMepy-CN** is supported by the OLEDs device made from the novel [3+2+1] iridium complex as the dopant with physical vapor deposition technology. The detailed device structure is schematically shown in **Figure 4A**, including ITO as anode and aluminum as cathode. Matching the HOMO and LUMO energy levels of different functional materials, the active layers combined between the electrodes are HATCN (10 nm)/TAPC (40 nm)/TcTa (10 nm)/10 wt% **Ir-dfpMepy-CN** in DPEPO (10 nm)/TmpypB (40 nm)/Liq (2.5 nm)/Al (100 nm). The electroluminescence spectrum is depicted in **Figure 4B**. The molecular structure of the materials used in the device is shown in **Figure 4C**. Under applied voltage of 5 V, the device shows a stable luminescence with the two maximums at the peak wavelength of 450 and 470 nm separately, slightly different from the PL spectrum in **Figure 2B**. The electroluminescence shows a CIE chromaticity coordinate of (0.16, 0.17), reaching much deeper blue compared with that of the traditional FIrpic (CIE of (0.16, 0.29)). The current density, voltage, and Luminance (J-V-L) curve is depicted in **Supplementary Figure S7**. The device utilizing Ir-dfpMepy-CN as a blue dopant exhibits a turn-on voltage (Von) of 3.3 V and highest EQE of 4.2%, but a quick roll-off as the current density increases. The preliminary OLED device demonstrates that the newly designed and synthesized [3+2+1] conformation compound is amenable to thermally evaporated OLEDs. However, the performance of the device is far from satisfactory which needs further device optimization. Nevertheless, there is a possibility that the [3+2+1] phosphorescent materials may open a new window to explore for deep blue display applications.

CONCLUSION

A novel [3+2+1] coordinated iridium (III) complex was designed and synthesized. The complex shows good stability due to the strong bonds formed by the center iridium atom and tridentate bis-NHC ligand. The designed [3+2+1] iridium (III) complex shows high photoluminescence peaks of 440 and 466 nm as both the bidentate (dfpMepy) and monodentate cyanide (-CN) ligand are strong electron-withdrawing groups, facilitating the stability of the HOMO levels. Notably, the complex shows a high PLQY of 84 ± 5% due to the rapid transition between singlet and triplet state with a time constant of 0.9–1.2 ps. The thermally evaporated device employed the [3+2+1] complex shows a CIE coordinate (0.16, 0.17), reaching deeper blue emission. This work provides a highly efficient blue cyclometalated iridium (III) complex configuration that will help develop more blue emitters and provide more dopant options for blue PhOLEDs.

DATA AVAILABILITY STATEMENT

The original contributions presented in the study are included in the article/**Supplementary Material**, further inquiries can be directed to the corresponding author.

AUTHOR CONTRIBUTIONS

ZL carried out the experimental work and S-WZ carried out the simulation part of the project. MZ, CW, WL, YW, and CY provide experimental help to ZL. ZL finished writing the manuscript and S-WZ, GW, CY, and YW revised it.

FUNDING

We thank the funding support from Shenzhen Municipal Development and Reform Commission, New Energy Technology Engineering Laboratory (Grant Number: SDRC (2016)172), and Shenzhen Science and Technology Innovation Committee (JCYJ20190809172615277). Guangdong Basic and Applied Basic Research Foundation (2020A1515111065).

ACKNOWLEDGMENTS

We would like to thank the rest of the team for the fruitful discussion of this project.

SUPPLEMENTARY MATERIAL

The Supplementary Material for this article can be found online at: https://www.frontiersin.org/articles/10.3389/fchem.2021.758357/full#supplementary-material

REFERENCES

Adachi, C., Kwong, R. C., Djurovich, P., Adamovich, V., Baldo, M. A., Thompson, M. E., et al. (2001). Endothermic Energy Transfer: A Mechanism for Generating Very Efficient High-Energy Phosphorescent Emission in Organic Materials. *Appl. Phys. Lett.* 79, 2082–2084. doi:10.1063/1.1400076

Ashizawa, M., Yang, L., Kobayashi, K., Sato, H., Yamagishi, A., Okuda, F., et al. (2009). Syntheses and Photophysical Properties of Optical-Active Blue-Phosphorescent Iridium Complexes Bearing Asymmetric Tridentate Ligands. *Dalton Trans.* 1700, 1700. doi:10.1039/b820821m

Bin Mohd Yusoff, A. R., Huckaba, A. J., Nazeeruddin, M. K., and Nazeeruddin, M. K. (2017). Phosphorescent Neutral Iridium (III) Complexes for Organic Light-Emitting Diodes. *Top. Curr. Chem.* 375, 39. doi:10.1007/s41061-017-0126-7

Brown, J., Kwong, R., Tung, Y.-J., Adamovich, V., Weaver, M., and Hack, M. (2004). Recent Progress in High-Efficiency Phosphorescent OLED Technology. *J. Soc. Inf. Disp.* 12, 329. doi:10.1889/1.1821306

Chen, D., Han, L., Liu, D., Ye, K., Liu, Y., Zhang, J., et al. (2015). High Performance Blue-Green and Green Phosphorescent OLEDs Based on Iridium Complexes with NCN-coordinated Terdentate Ligands. *RSC Adv.* 5, 18328–18334. doi:10.1039/C4RA17122E

Furue, R., Nishimoto, T., Park, I. S., Lee, J., and Yasuda, T. (2016). Aggregation-Induced Delayed Fluorescence Based on Donor/Acceptor-Tethered Janus Carborane Triads: Unique Photophysical Properties of Nondoped OLEDs. *Angew. Chem. Int. Ed.* 55, 7171–7175. doi:10.1002/anie.201603232

Geffroy, B., le Roy, P., and Prat, C. (2006). Organic Light-Emitting Diode (OLED) Technology: Materials, Devices and Display Technologies. *Polym. Int.* 55, 572–582. doi:10.1002/pi.1974

Gnanasekaran, P., Yuan, Y., Lee, C.-S., Zhou, X., Jen, A. K.-Y., and Chi, Y. (2019). Realization of Highly Efficient Red Phosphorescence from Bis-Tridentate Iridium(III) Phosphors. *Inorg. Chem.* 58, 10944–10954. doi:10.1021/acs.inorgchem.9b01383

Hack, M., Weaver, M. S., Adamovich, V., Kwong, R. C., Lu, M. H., and Brown, J. J. (2005). *Status and Potential for Phosphorescent OLED Technology*. Editors T. P. Pearsall and J. Halls (Cambridge, United Kingdom), 596102. doi:10.1117/12.628991

Hanusa, T. P. (2011). "Cyanide Complexes of the Transition Metals Based in Part on the Article Cyanide Complexes of the Transition Metals by Timothy," in *Encyclopedia of Inorganic and Bioinorganic Chemistry*. Editor R. A. Scott (Chichester, UK: John Wiley & Sons, Ltd), eibc0055. doi:10.1002/9781119951438.eibc0055

Hedley, G. J., Ruseckas, A., and Samuel, I. D. W. (2008). Ultrafast Luminescence in Ir(ppy)3. *Chem. Phys. Lett.* 450, 292–296. doi:10.1016/j.cplett.2007.11.028

Hedley, G. J., Ruseckas, A., and Samuel, I. D. W. (2010). Vibrational Energy Flow Controls Internal Conversion in a Transition Metal Complex. *J. Phys. Chem. A.* 114, 8961–8968. doi:10.1021/jp101087v

Holmes, R. J., Forrest, S. R., Tung, Y.-J., Kwong, R. C., Brown, J. J., Garon, S., et al. (2003). Blue Organic Electrophosphorescence Using Exothermic Host-Guest Energy Transfer. *Appl. Phys. Lett.* 82, 2422–2424. doi:10.1063/1.1568146

Hsu, L. Y., Liang, Q., Wang, Z., Kuo, H. H., Tai, W. S., Su, S. J., et al. (2019). Bis-tridentate Ir III Phosphors Bearing Two Fused Five-Six-Membered Metallacycles: A Strategy to Improved Photostability of Blue Emitters. *Chem. Eur. J.* 25, 15375–15386. doi:10.1002/chem.201903707

Kuo, H.-H., Chen, Y.-T., Devereux, L. R., Wu, C.-C., Fox, M. A., Kuei, C.-Y., et al. (2017). Bis-Tridentate Ir(III) Metal Phosphors for Efficient Deep-Blue Organic Light-Emitting Diodes. *Adv. Mater.* 29, 1702464. doi:10.1002/adma.201702464

Kuo, H.-H., Zhu, Z.-l., Lee, C.-S., Chen, Y.-K., Liu, S.-H., Chou, P.-T., et al. (2018). Bis-Tridentate Iridium(III) Phosphors with Very High Photostability and Fabrication of Blue-Emitting OLEDs. *Adv. Sci.* 5, 1800846. doi:10.1002/advs.201800846

Lee, S., Kim, S.-O., Shin, H., Yun, H.-J., Yang, K., Kwon, S.-K., et al. (2013). Deep-Blue Phosphorescence from Perfluoro Carbonyl-Substituted Iridium Complexes. *J. Am. Chem. Soc.* 135, 14321–14328. doi:10.1021/ja4065188

Leonat, L., Beatrice Gabriela, S., and Brañzoi, I. V. (2013). Cyclic Voltammetry for Energy Levels Estimation of Organic Materials. *UPB Sci. Bull. Ser. B Chem. Mater. Sci.* 75, 111–118.

Li, J., Djurovich, P. I., Alleyne, B. D., Yousufuddin, M., Ho, N. N., Thomas, J. C., et al. (2005). Synthetic Control of Excited-State Properties in Cyclometalated Ir(III) Complexes Using Ancillary Ligands. *Inorg. Chem.* 44, 1713–1727. doi:10.1021/ic048599h

Lim, H., Shin, H., Kim, K.-H., Yoo, S.-J., Huh, J.-S., and Kim, J.-J. (2017). An Exciplex Host for Deep-Blue Phosphorescent Organic Light-Emitting Diodes. *ACS Appl. Mater. Inter.* 9, 37883–37887. doi:10.1021/acsami.7b10914

Lin, N., Qiao, J., Duan, L., Wang, L., and Qiu, Y. (2014). Molecular Understanding of the Chemical Stability of Organic Materials for OLEDs: A Comparative Study on Sulfonyl, Phosphine-Oxide, and Carbonyl-Containing Host Materials. *J. Phys. Chem. C* 118, 7569–7578. doi:10.1021/jp412614k

Lorente, A., Pingel, P., Krüger, H., and Janietz, S. (2017). High Triplet Energy Electron Transport Side-Chain Polystyrenes Containing Dimesitylboron and Tetraphenylsilane for Solution Processed OLEDs. *J. Mater. Chem. C* 5, 10660–10667. doi:10.1039/C7TC03029K

Ma, H., Liu, D., Li, J., Mei, Y., Li, D., Ding, Y., et al. (2020). Sky-blue Iridium Complexes with Pyrimidine Ligands for Highly Efficient Phosphorescent Organic Light-Emitting Diodes. *New J. Chem.* 44, 8743–8750. doi:10.1039/D0NJ01262A

Tang, K.-C., Liu, K. L., and Chen, I.-C. (2004). Rapid Intersystem Crossing in Highly Phosphorescent Iridium Complexes. *Chem. Phys. Lett.* 386, 437–441. doi:10.1016/j.cplett.2004.01.098

Tsuzuki, T., Shirasawa, N., Suzuki, T., and Tokito, S. (2003). Color Tunable Organic Light-Emitting Diodes Using Pentafluorophenyl-Substituted Iridium Complexes. *Adv. Mater.* 15, 1455–1458. doi:10.1002/adma.200305034

Wang, Y., Lei, L., Liu, E., Cheng, Y., and Xu, S. (2021a). Constructing Highly Sensitive Ratiometric Nanothermometers Based on Indirectly Thermally Coupled Levels. *Chem. Commun.* 57, 9092–9095. doi:10.1039/D1CC03407C

Wang, Y., Lei, L., Ye, R., Jia, G., Hua, Y., Deng, D., et al. (2021b). Integrating Positive and Negative Thermal Quenching Effect for Ultrasensitive Ratiometric Temperature Sensing and Anti-counterfeiting. *ACS Appl. Mater. Inter.* 9. doi:10.1021/acsami.1c05611

Wilkinson, A. J., Puschmann, H., Howard, J. A. K., Foster, C. E., and Williams, J. A. G. (2006). Luminescent Complexes of Iridium(III) Containing N^C^N-Coordinating Terdentate Ligands. *Inorg. Chem.* 45, 8685–8699. doi:10.1021/ic061172l

Yam, V. W.-W., and Lo, K. K.-W. (2006). "Luminescence Behavior & Photochemistry of Organotransition Metal Compounds," in *Encyclopedia of Inorganic Chemistry*. Editors R. B. King, R. H. Crabtree, C. M. Lukehart, D. A. Atwood, and R. A. Scott (Chichester, UK: John Wiley & Sons, Ltd), ia271. doi:10.1002/0470862106.ia271

Conflict of Interest: Authors YW and CY were employed by the company Puri Materials Inc.

The remaining authors declare that the research was conducted in the absence of any commercial or financial relationships that could be construed as a potential conflict of interest.

Publisher's Note: All claims expressed in this article are solely those of the authors and do not necessarily represent those of their affiliated organizations, or those of the publisher, the editors and the reviewers. Any product that may be evaluated in this article, or claim that may be made by its manufacturer, is not guaranteed or endorsed by the publisher.

Copyright © 2021 Liu, Zhang, Zhang, Wu, Li, Wu, Yang, Kang, Meng and Wei. This is an open-access article distributed under the terms of the Creative Commons Attribution License (CC BY). The use, distribution or reproduction in other forums is permitted, provided the original author(s) and the copyright owner(s) are credited and that the original publication in this journal is cited, in accordance with accepted academic practice. No use, distribution or reproduction is permitted which does not comply with these terms.

frontiers in Chemistry

ORIGINAL RESEARCH
published: 15 November 2021
doi: 10.3389/fchem.2021.767696

Protein and Water Distribution Across Visual Axis in Mouse Lens: A Confocal Raman MicroSpectroscopic Study for Cold Cataract

Yao Li[1], *Yuxing Li*[1], *Xi Liu*[2], *Yonghong He*[3] *and Tian Guan*[3]*

[1]Tsinghua-Berkeley Shenzhen Institute (TBSI), Shenzhen, China, [2]Department of Ophthalmology, Beijing Children's Hospital, Capital Medical University, National Center for Children's Health, Beijing, China, [3]Department of Life and Health, Tsinghua Shenzhen International Graduate School, Shenzhen, China

Purpose: The aims of the study were to investigate cellular mechanisms of cold cataract in young lenses of wild-type C57BL/6J (B6WT) mice treated at different temperatures and to test a hypothesis that cold cataract formation is associated with the changes in lens protein and water distribution at different regions across lens fiber cells by Raman spectroscopy (RS).

Methods: RS was utilized to scan the mouse lens at different regions with/without cold cataract. Three regions with various opacification along the equatorial axis in the anterior–posterior lens section were scanned. The intensity ratio of Raman bands at 2,935 and 3,390 cm^{-1} (I_p/I_w) were used to evaluate lens protein and water distribution. We further determined water molecular changes through Gaussian profiles of water Raman spectra.

Results: Three specific regions 1, 2, and 3, located at 790–809, 515–534, and 415–434 μm away from the lens center, of postnatal day 14 B6WT lenses, were subjected to RS analysis. At 37°C, all three regions were transparent. At 25°C, only region 3 became opaque, while at 4°C, both regions 2 and 3 showed opacity. The sum of the difference between I_p/I_w and the value of linear fitting line from scattered-line at each scanning point was considered as fluctuation degree (FD) in each region. Among different temperatures, opaque regions showed relatively higher FD values (0.63 and 0.79 for regions 2 and 3, respectively, at 4°C, and 0.53 for region 3 at 25°C), while transparent regions provided lower FD values (less than 0.27). In addition, the decrease in Gaussian peak II and the rising of Gaussian peak III and IV from water Raman spectra indicated the instability of water molecule structure in the regions with cold cataract.

Conclusion: Fluctuation degrees of RS data reveal new mechanistic information about cold cataract formation, which is associated with uneven distribution of lens proteins and water across lens fiber cells. It is possible that RS data partly reveals cold temperature-induced redistribution of lens proteins such as intermediate filaments in inner fiber cells. This lens protein redistribution might be related to unstable structure of water molecules according to Gaussian profiles of water RS.

Keywords: cataract, cold cataract, lens, Raman spectroscopy, protein and water distribution

OPEN ACCESS

Edited by:
Enza Fazio,
University of Messina, Italy

Reviewed by:
Romulo Ando,
University of São Paulo, Brazil
Valentina Venuti,
University of Messina, Italy

***Correspondence:**
Tian Guan
guantian@sz.tsinghua.edu.cn

Specialty section:
This article was submitted to Physical Chemistry and Chemical Physics, a section of the journal Frontiers in Chemistry

Received: *01 September 2021*
Accepted: *07 October 2021*
Published: *15 November 2021*

Citation:
Li Y, Li Y, Liu X, He Y and Guan T (2021) Protein and Water Distribution Across Visual Axis in Mouse Lens: A Confocal Raman MicroSpectroscopic Study for Cold Cataract. Front. Chem. 9:767696. doi: 10.3389/fchem.2021.767696

INTRODUCTION

Cataract is the main cause of blindness among various eye diseases, which has always been a global health issue (Huang and Chen, 2018). Cold cataract is a phenomenon that opacification occurs in young mammalian lenses when cooled, and the whole process is reversible when warmed (Zigman and Lerman, 1964; Zigman and Lerman, 1965; Lo, 1989). By controlling the temperature, cold cataract is a convenient and realizable model for studying cataract and related physicochemical changes in the laboratory (Lo, 1989; Sivak et al., 1992). The formation and components of cold cataract have been studied *via* various methods in the past decades, including laser scanning (Sivak et al., 1992), NMR (Lerman et al., 1982; Lerman et al., 1983), and protein analyses (Broide et al., 1991; Song et al., 2009).

It has been proven that beaded filament is significant to the lens optical transparency (Blankenship et al., 2001; Song et al., 2009). In biochemistry level, α-, β-, and γ-crystallin are related to the formation of cold cataract (Lo, 1989), and aggregation and phase separation of γ-crystallin play the most crucial role (Lerman et al., 1983; Broide et al., 1991). Therefore, γ-crystallin is considered to be the cryoprotein in cold cataract formation (Lerman et al., 1966; Siezen et al., 1985). Both intermediate filaments and crystallins are concerned with the formation of cold cataract. Furthermore, some other researches raised that supermolecular organization accounted for the formation of cold cataract rather than specific lens protein (Loewenstein and Bettelheim, 1979; Lerman et al., 1982). A further study on the mechanisms of cold cataract is still needed.

So far, there are various optical methods involved in interpreting cold cataract based on changes in optical signals. With the laser scanning system, the opacification of the lens can be evaluated for cold cataract by measuring the intensity of scattered light (Benedek et al., 1979; Petta et al., 2008), relative light transmittance (Banh and Sivak, 2004), as well as the equivalent focal length (Sivak et al., 1992). In addition, optical coherence tomography and optical coherence elastography were used to image the cold cataract model, providing structural information and biomechanical properties (Izatt et al., 1994; Zhang et al., 2018).

Raman spectroscopy (RS) is a non-invasive optical technique to determine the existence of certain molecules, which can be used in ophthalmology (Erckens et al., 2001; Lin et al., 2010). In eye lens study, Raman spectra from RS usually provide feature peaks, which are bound to vibrational modes of specific chemical bonds, such as CH_2/CH_3 vibration bond (Smeets et al., 1993) and disulfide bond (Ozaki et al., 1987). Furthermore, amino acid contents along the visual and equatorial axes were scanned in pig lens by Raman spectroscopy (Medina-Gutiérrez et al., 2004). For cold cataract study, Raman spectra for different species were acquired to test the changes in protein and water in lens with cold cataract (Ondruska and Hanson, 1983). Changes in the intensity ratio of tyrosine residues were found in the process of temperature alteration (Mizuno et al., 1984). To further analyze water and protein content in different regions of the lens based on acquired Raman spectra, different studies have used RS to scan lens and lens slices at different positions (Bot et al., 1989; Huizinga et al., 1989). However, among previous researches on cold cataract with RS, the scanning region was usually wide instead of focusing on a small range across lens fiber cells.

The lack of organelles is a feature of lens fiber cells. Lenticular water may play an important role in lens opacification. The state of lens water among different species was studied with NMR (Rácz et al., 1979). Free and bound water mass was evaluated in different lens regions with age-dependent and advanced nuclear cataract (Heys et al., 2008), whereas, molecular level of water distribution was rarely analyzed in the formation of cold cataract. RS is qualified to reveal molecular information of solid and liquid H_2O (Carey and Korenowski, 1998). Raman spectra of water can be analyzed through four of five fitted Gaussian profiles (Crupi et al., 2008; Huang et al., 2009; Baschenko and Marchenko, 2011). These Gaussian peaks are able to provide intra-molecular vibrational distributions of water, and are considered to be various structural types of hydrogen bond in H_2O (Crupi et al., 2008; Huang et al., 2009).

In order to study the cellular mechanisms of cold cataract formation at molecular level, we used RS to scan young mice lens sections across fiber cells in vibratome section *in vitro* for the first time. In this work, we aimed to test the hypothesis that cold cataract formation is associated with the changes in lens protein and water distribution at different regions. With microscopic imaging, the opacity occurred as temperature decreased from 37°C to 4°C. The opacity size varied under the treatment of different temperatures during the cold cataract formation. Raman spectra for three regions along the equatorial axis of anterior–posterior (A/P) lens section were obtained at different temperatures (4°C, 25°C, and 37°C). Protein and water content distribution was evaluated *via* related Raman vibrational band quantification. The distribution showed unevenness in opacification areas due to cold cataract. To further discover molecular changes in water, all the water spectra were analyzed in terms of Gaussian profiles.

MATERIALS AND METHODS

Animals and Lens Image

For cold cataract occurring in young mammalian lenses, female C57bl/6J wild-type mice (B6WT) at the age of postnatal day 14 were used as experiment subjects. All the disposals during experiments with mice were according to the approval of the Animal Ethics Committee of Tsinghua Shenzhen International Graduate School. Mice were euthanized with a suitable amount of 4% chloral hydrate and sacrificed by injecting an overdose of anesthetic after surgery. Lenses were immediately isolated under a dissecting microscope (Leica MZ 95) and were immersed into phosphate-buffered saline (PBS). Three lenses were treated at temperatures 4°C, 25°C, and 37°C, separately. To observe cold cataract, lenses were imaged with the microscope at different temperatures. Lenses developed full cold cataract from transparency in 4°C PBS solution in about 2 min, and they were reversible to transparent in 37°C PBS solution in about 2 min. Images of lens samples were captured according to the

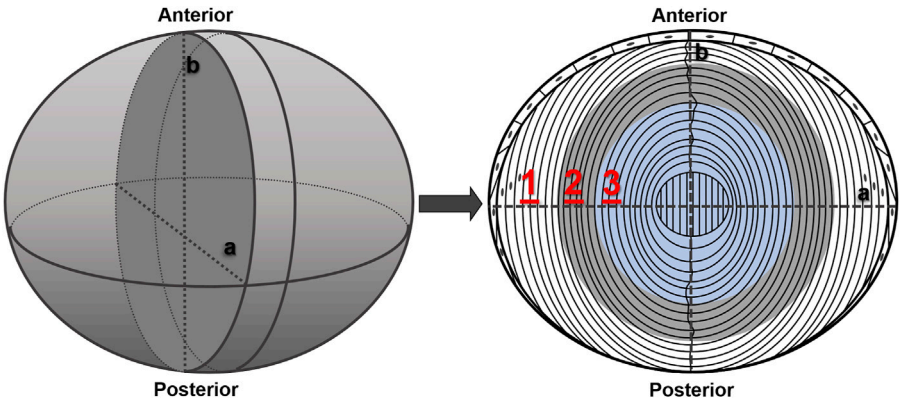

FIGURE 1 | Schematic graph of lens section with different scanning regions. The left plot demonstrates the whole lens after dissection, and the right plot depicts the anterior–posterior (A/P) section of the lens cut as scanning sample. Index lines (a and b) show the orientation of the slice. 1, 2, and 3 in red represents scanning regions 1, 2, and 3 (20 μm in length for each).

software on the computer related to the microscope. The size of lenses and cold cataract regions were recorded.

Lens Vibratome Section

According to previous studies, the fixation procedure shows no impact on water and protein content in the lenses (Bot et al., 1989; Huizinga et al., 1989; Siebinga et al., 1992). Before obtaining B6WT lens slices, fresh lenses should be fixed in 4% paraformaldehyde/PBS (PFA/PBS) solution at different temperatures. To examine 4°C cold cataract, fresh lenses were removed from eyeballs in 4°C PBS and fixed overnight in 4% PFA/PBS solution at 4°C. For lens samples treated at 25°C or 37°C, fresh lenses were dissected in PBS at room temperature, and then transferred to 4% PFA/PBS solution at 25°C or 37°C for 3–5 h. After fixation, lenses were washed with PBS three times and embedded in melting agarose gel on a plane block. The procedures of lens embedding and vibratome section are as follows: about 50 μl of melted agarose gel drop was added on the surface of the plane block. A wedge was cut on the edge of the solid agarose gel to hold the lens with the cutting direction of anterior--posterior (A/P, along the optical axis) plane. Then to glue the lens and agarose gel on the block, about 0.5 μl of superglue drop was added to the wedge *via* pipette without touching the lens. The lens and gel drop were covered with more agarose gel as a whole. After solidification, the block was superglued on the cutting plate of the vibratome microscope (Leica VT 1200S). Then sections with a thickness of 100 μm were cut in a container of PBS. Lens sections around the equator were collected and kept in 4% PFA/PBS solution again for post-fixation for 15 min, then were washed with PBS three times. All the equatorial lens sections were scanned with Raman spectrometer at room temperature.

Raman Spectroscopic Scanning Across Fiber Cells

A confocal Raman microspectrometer (Horiba LabRAM HR800) was used for Raman spectra acquisition. Under the microscope of ×50, the spectrum grating was 600 lines, and the hole was 100 μm. The excitation laser wavelength was 532 nm with the power of 25 mW, and the spectral resolution was 1 cm^{-1}. Through laser focus adjustment, the field of view was approximately 0.8 μm in diameter.

Equatorial lens sections were placed on glass slides and covered with cover glasses of 0.14-mm thickness. A drop of PBS solution was added between sliders and cover glasses to prevent lens sections from drying. To scan the lens section across the fiber cells, we set three scanning regions along the equatorial axis vertical to A/P axis (**Figure 1**) based on the diameter of the lenses and cataract regions under different temperatures. The scanning direction was from cortex to nucleus. For each region, 20 points were collected with the step length of 1 μm, focusing on 50 μm beneath the section surface to avoid uneven interference caused by cutting. In region 1, the lens stays transparent under all temperatures. In region 2, the lens turns opaque at 4°C, while it becomes transparent at 25°C. In region 3, the lens forms cold cataract at both 4°C and 25°C. Raman signal intensity as raw data were acquired for each wavenumber from 2,600 to 3,800 cm^{-1} at each scanning spot. The exposure time was 15 s, with three averaged measurements.

Statistical Analysis

Statistical significance was evaluated with one-way analysis of variance (ANOVA) with Tukey's test, using the software Origin (OriginLab, United States). Values pf p less than or equal to 0.05, 0.01, 0.001, and 0.0001 were considered statistically significant.

RESULTS

Lens Cold Cataract Formation in Microscopic Image

After being immersed in PBS at different temperatures for more than 2 min, lenses were imaged under the dissecting microscope. Three lenses were treated at each different temperature as one control group. As **Figure 2A** shows, from left to right, lenses were at 4°C, 25°C, and 37°C, separately. At 4°C and 25°C, obvious opacity

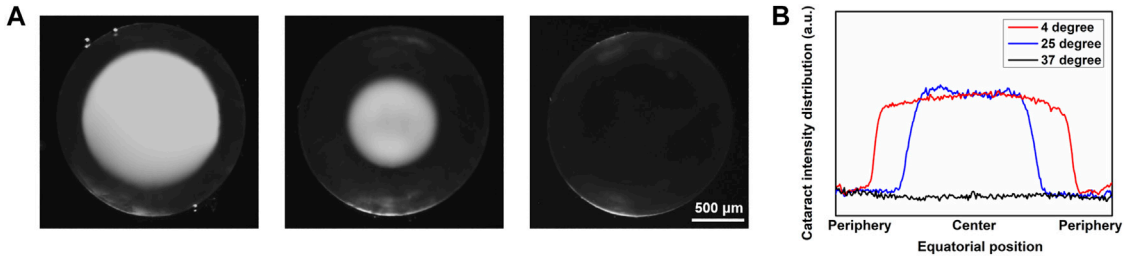

FIGURE 2 | Microscopic image of lens at different temperatures with cold cataract formation. **(A)** Anterior-view images of lens under dissecting microscope. From left to right, lenses were at 4°C, 25°C, and 37°C. Scale bar: 500 μm. **(B)** Plot profile of the equatorial line of the lenses at 4°C, 25°C, and 37°C.

due to cold cataract formation can be seen. However, the diameter of the opacity sphere at 4°C was much bigger than that at 25°C. At 37°C, no opacity was observed. When the temperature was raised from 4°C/25°C to 37°C, the opacity disappeared in about 2 min, which supported that the cold cataract phenomenon was entirely reversible. There was no significant difference in the formation of cold cataract between the different sexes of mice. Also, there was no noticeable difference between the two lenses from a single mouse.

To quantitatively measure the light scattering distribution due to cold cataract, lens images captured by the dissecting microscope were further analyzed *via* software ImageJ. The plot profile of the gray value in the equatorial section of the lens is illustrated in **Figure 2B**. The light scattering distribution of the lens apparently differed from each other at 4°C, 25°C, and 37°C, respectively. The sizes of all lenses of the different mice were similar with a diameter of about 1,780 ± 40 μm (n 9). The diameters of the cold cataracts at 4°C were 1,319 ± 28 μm, about 74% of the whole lens diameter. However, the diameter of the cold cataracts, at 25°C was 962 ± 21.0 μm, about 54% of the whole lens diameter.

Raman Spectra Acquisition and Processing

Based on the different sizes of cold cataract at 4°C, 25°C, and 37°C, regions 1, 2, and 3 were located at about 790–809, 515–534, and 415–434 μm away from the lens center, respectively. To analyze protein distribution at each spot from three regions, three measurements were averaged during signal acquisition. High-wavenumber regions, 2,600–3,800 cm^{-1}, were recorded as raw data in this work. Since the Raman intensities of 2,935 and 3,380 cm^{-1} bands represent C–H vibration mode and O–H vibration mode, lens protein and water content can be evaluated *via* these two bands, respectively.

Raman spectra were smoothed *via* Savitzky–Golay filter. Then background noises caused by fluorescence were subtracted through linear subtraction lines of the intensity of bands 2,600–2,800, 2,800–3,030, 3,030–3,100, and 3,100–3,800 cm^{-1}. The procedure of spectra processing is demonstrated in **Figure 3A**.

Lens Protein and Water Quantitative Analyses

To quantify protein content distribution in different regions under different temperatures, we evaluated the ratio of the intensity of 2,935 cm^{-1} band as protein content and the intensity of 3,380 cm^{-1} band as water content (I_p/I_w) for each scanning point. **Figure 3B** depicts the average values (±S.D.) of I_p/I_w from all scanning points of the three lenses according to the three regions at 4°C, 25°C, and 37°C. For one lens, in regions 1, 2, and 3, the average I_p/I_w values were about 0.31, 1.35, and 1.81, respectively. This accorded with the rising of protein mass and the decreasing of water mass from lens cortex to nucleus. In regions 1 and 2, I_p/I_w values were not significantly different ($p > 0.05$), which revealed that protein total mass was nearly equal in these two regions with or without cold cataract. However, in region 3, I_p/I_w values were significantly different ($p \leq 0.0001$).

In order to visualize the scanning result from different regions, we demonstrated scatter line plots for I_p/I_w values of every scanning point (scanning points 1–20) in three regions from every lens treated with each temperature in **Figures 4A–C**. For the 37°C group, scatter lines in all regions were relatively smooth. For the 25°C group, scatter lines in region 3 fluctuated more than those in regions 1 and 2. For the 4°C group, scatter lines were relatively smooth only in region 1, while scattered lines fluctuated obviously in regions 2 and 3. Generally, cold cataract impacted the protein content distribution in different regions under different temperatures.

To further quantify the fluctuation degree (FD), we processed linear fit to every scatter line. The absolute value of the difference between each scatter point and the linear-fit value line were summed up as FD value. As **Figure 4D** shows, in region 1, FD values were close with an average of 0.22 under different temperatures. However, in region 2, as **Figure 4E** shows, the FD value was much higher at 4°C (0.63 ± 0.17) compared with25°C (0.27 ± 0.05) and37°C (0.27 ± 0.09). The FD values of the 25°C and 37°C groups were still close. In region 3, as **Figure 4F** shows, the FD values of the 4°C (0.79 ± 0.20) and 25°C (0.53 ± 0.16) groups were relatively higher than the 37°C group. This revealed that the opacity from cold cataract formation altered protein content distribution among lens fiber cells. The lower the temperature, the more uneven the protein and water content distribution presented with the formation of cold cataract.

Lens Water Molecular Level Analyses

In order to acquire water molecular information from Raman spectra, the water spectra were analyzed through curve fitting

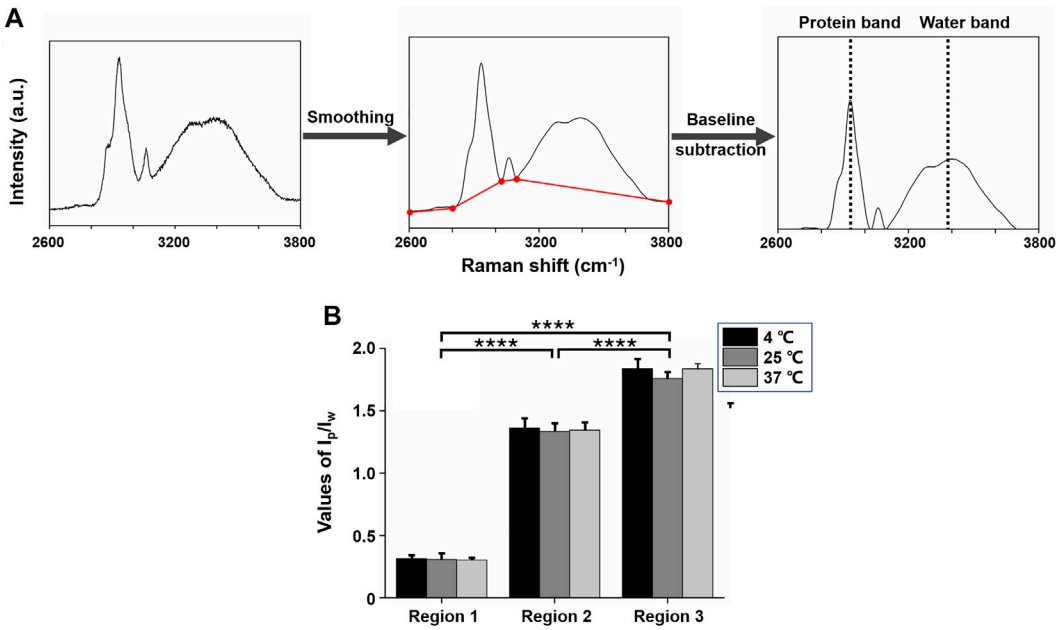

FIGURE 3 | High-wavenumber Raman spectra (2,600–3,800 cm^{-1}) of mice lens. **(A)** Spectra processing procedure. **(B)**: Average ratios of the intensity of protein and water brands (I_p/I_w) for three regions from all three lenses treated with different temperatures. I_p/I_w values increased from regions 1 to 3 and showed statistically significant differences between each region at 4°C, 25°C, and 37°C (****$p \leq 0.0001$).

with the software Origin (OriginLab, United States). The strategy adopted for the curve fitting procedure was to use well-defined shape components of Gaussian functions, whose peaks were located at about (I) 3,230, (II) 3,400, (III) 3,530, and (IV) 3,650 cm^{-1}. All three parameters for each Gaussian function were left to vary upon iteration. The statistical parameters were used as a guide to "best fit" The result of each fitted spectra was characterized by the adjusted R-square of ~0.99 to ensure the stability of the procedure. Typical Gaussian peaks (peak I to peak IV) are demonstrated in **Figure 5A**.

At 37°C, the lenses were kept transparent in all regions. The average values of Gaussian peak amplitudes were evaluated according to all the scanning points (three lenses in total, n = 60). **Figure 5B** depicts the intensity change among the three regions under 37°C. From regions 1 to 3, the intensity of peaks I and II increased, while peaks III and IV decreased.

To reveal temperature dependence in water of normal lens, since there was no opacity in region 1, whether at 4°C, 25°C, or 37°C, Gaussian peak intensities from this region were compared. As **Figure 5C** shows, from 37°C to 4°C, the intensity of peaks I and II increased as temperature decreased, while peaks III and IV presented the opposite evolution with temperature.

Regions 2 and 3 from lenses treated with lower temperature, compared with region 1, presented various patterns of Gaussian components. In region 2, when temperature decreased from 37°C to 25°C, Gaussian peaks were still similar among different scanning points. **Figures 6A,B** show typical Gaussian well-fitted peaks of the lens water Raman spectra under 37°C and 25°C. However, at 4°C, Gaussian peaks were irregularly compared with 37°C and 25°C. The intensity of peaks III and IV was higher, while peak II decreased at some points. The intensity of peak I was higher or lower at some points (**Figure 6C**).

In region 3, Gaussian peaks kept fixed relatively only at 37°C, as **Figure 6D** shows. At 25°C, peaks became fluctuated. The intensity of Peak II decreased, while peaks III and IV increased (**Figure 6E**). At 4°C, the alteration in peaks was obvious and shared the same regulation with that in region 2 (**Figure 6F**).

DISCUSSION

Among previous researches, RS has been utilized to investigate changes in lens with cold cataract. Ondruska et al. studied the formation of dry and cold cataracts from duck, rat, and flounder lenses and found slight changes in Raman spectra (Ondruska and Hanson, 1983). Mizuno et al. investigated the tyrosine doublet in cold cataracts and discovered that some tyrosine residues possessed a change in their hydrogen bonding environment (Mizuno et al., 1984). Other studies basically evaluated protein and water mass in a large range to observe general changing trends (Bot et al., 1989; Huizinga et al., 1989). In this study, we illustrated the various opacity among three regions under different temperatures in P14 B6WT lenses. Region 1 stayed transparent under 4°C, 25°C, and 37°C, while region 2 became opaque only at 4°C. Region 3 became opaque at both 4°C and 25°C. These phenomena and the size of the various opacities with the formation of cold cataract correspond to previous studies from our group (Li et al., 2020). I_p/I_w values represent the protein mass distribution of three regions. Whether at 4°C, 25°C, or 37°C, protein content increases from region 1 to region 3. This result

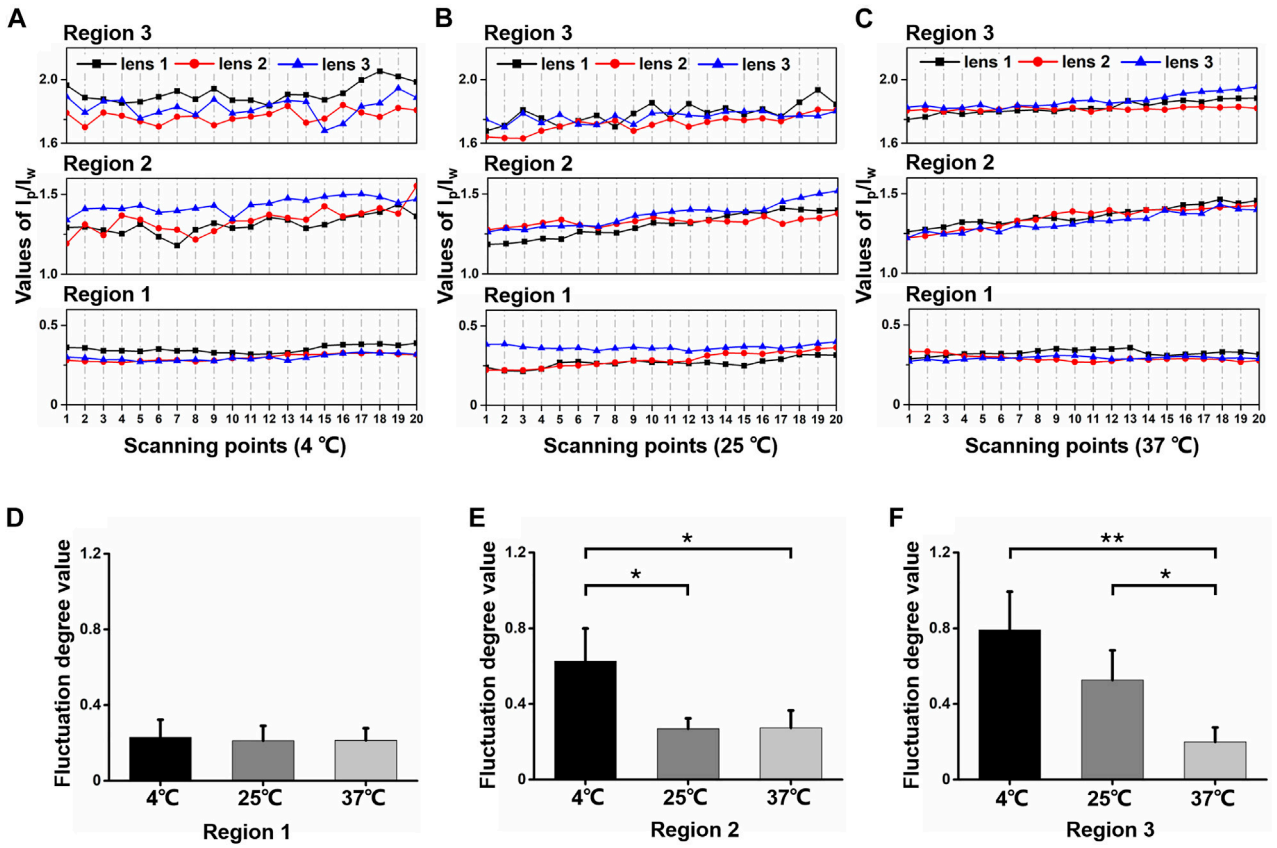

FIGURE 4 | The I_p/I_w values for different regions and different temperatures. **(A–C)** Scattered-line plots of I_p/I_w value for each scanning region at 4°C, 25°C, and 37°C. In each small plot, the display regions of the values were set equal as 0.6. **(D–F)** The value of fluctuation degree for regions 1, 2 and 3 at different temperatures, separately (*$p \leq 0.05$, **$p \leq 0.01$).

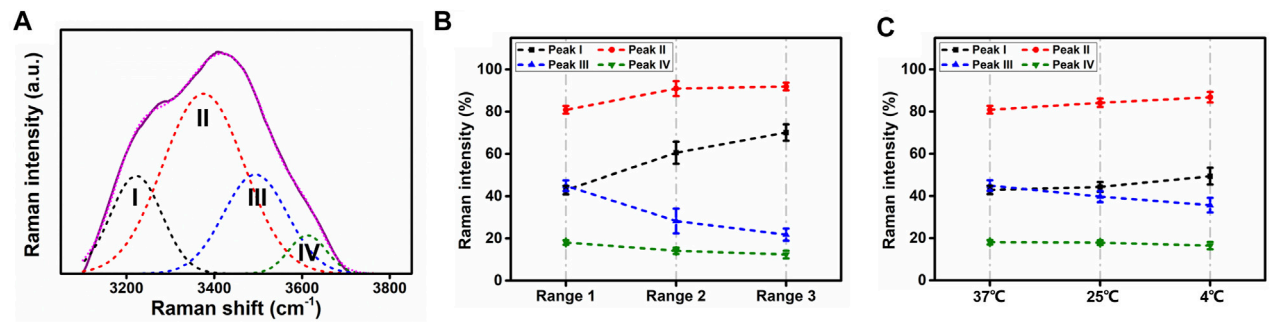

FIGURE 5 | Gaussian peaks and intensity changes without opacity. **(A)** Typical Gaussian fitting components as Gaussian peaks for Raman water spectra, ranging from 3,100 to 3,800 cm^{-1}. I, II, III, and IV stand for Gaussian peaks I, II, III, and IV. **(B)** Raman intensity of four Gaussian peaks from three regions at 37°C. **(C)** Raman intensity of four Gaussian peaks at 37°C, 25°C, and 4°C in region 1.

supported that the relative protein to water content of lenses increases from cortex to nucleus (Bot et al., 1989; Huizinga et al., 1989).

Heys et al. analyzed free and total water in human normal and cataractous lenses with thermogravimetric analysis and differential scanning calorimetry (Heys et al., 2008). Through RS, water spectra may not determine the water state in lens, but the structure information of water can be analyzed. In water spectra analyses with Gaussian profiles, peaks I and II represent fully four-hydrogen bonded water molecules, while peaks III and IV are associated to partly hydrogen-bonded free O-H (Crupi et al., 2008). In particular, peak I refers to the in-phase O-H

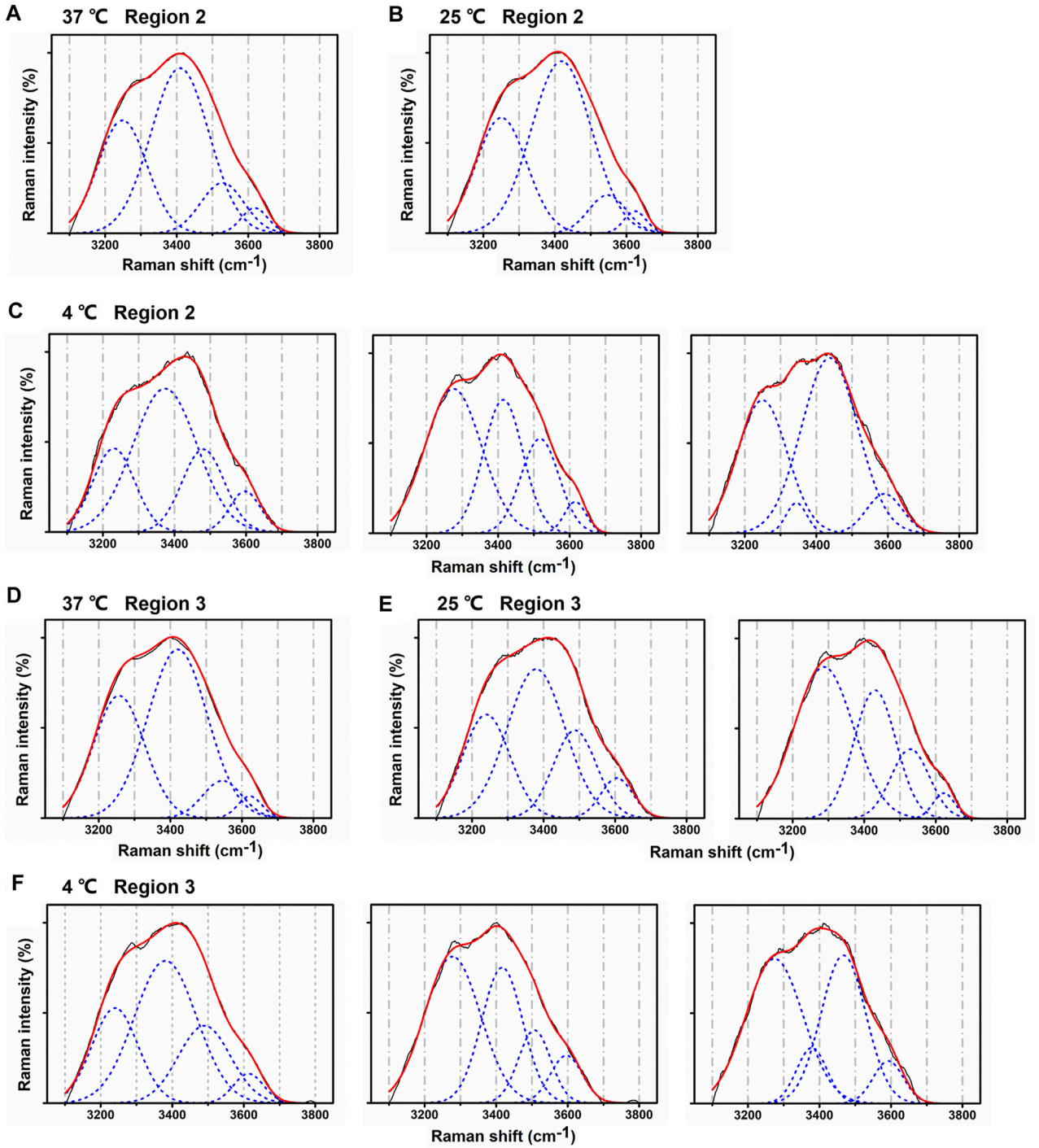

FIGURE 6 | Changes in Gaussian peaks from regions 2 and 3 at different temperatures. **(A–C)** Typical Gaussian peaks from region 2 at 37°C, 25°C, and 4°C. **(D–F)** Typical Gaussian peaks from region 3 at 37°C, 25°C, and 4°C.

stretching vibrations of hydrogen bonds from adjacent water molecules, while peak II is ascribed to out-of-phase O-H stretching vibrations (Walrafen et al., 1986). In region 1, as temperature decreased, although there was no cataract formation, the intensity of peaks I and II increased, while peaks III and IV decreased. This indicated that O-H in water became more stable with more full hydrogen bonded water molecules, which supported the same change in bulk water and confined water (Crupi et al., 2008). However, when opacification occurred (in region 2 at 4°C, in region 3 at 4°C and 25°C), peaks III and IV increased, while peak II was constrained at some scanning points. The changing patterns of

the peaks were irregularly compared with the regions without cataract. These results supported that hydrogen bonds break from water molecules, and out-of-phase O-H stretching vibrations are weakened in lens fiber cells. This corresponded to the evidence that there was lower total water content in the center of advanced nuclear cataractous lenses, and the supported nuclear cataract formation may be associated with lower total hydration of the lens nucleus (Heys et al., 2008).

In this work, we used RS to scan the mice lens in the 20-μm range micron by micron for the first time. By focusing on the protein and water bands of Raman spectra, we discovered that lens opacity due to cold cataract can lead to the fluctuation of protein and water distribution. Compared with regions without cold cataract, in region 3, the I_p/I_w scatter line variance revealed uneven accumulations of proteins at 4°C and 25°C. In region 2, only 4°C of treatment can cause obvious fluctuations in the scatter line. These results showed that low temperature may alter the accumulation or aggregation of filensin proteins in mice lenses, which supported our previous research and the concept of supermolecular organization of protein complexes causing the formation of cold cataract (Ondruska and Hanson, 1983; Li et al., 2020). Furthermore, we used Gaussian peaks of Raman water spectra to investigate cold cataract at the molecular level for the first time. The results supported that hydrogen bonds in water molecules may become unstable and are likely to participate in protein aggregation during cold cataract formation at low temperatures. Mouse cold cataract presents a practical model for understanding the changes in fiber cells during lens development at young ages. Future work is supposed to address the molecular mechanisms on how protein and water distribution become uneven and how water participates in cold cataract formation at low temperatures.

CONCLUSION

We scanned across the fiber cells of the lens along visual axis for the first time with RS. By scanning different regions (20 μm for each) with/without cold cataract at different temperatures, protein and water content distribution was quantified. At 4°C, the protein and water distribution of both regions 2 and 3 were uneven. At 25°C, however, only region 3 showed uneven protein and water distribution. At 37°C, all regions were relatively even as comparison. The discovery testified that RS can be utilized to analyze changes in protein and water distribution across lens fiber cells. This proved that cold cataract formation is associated with the uneven protein and water distribution, revealing supermolecular mechanisms. Furthermore, Gaussian profiles of water Raman spectra demonstrated the activation of hydrogen-bonded free O-H in water molecules. The lens protein and water redistribution might be related to the unstable structure of water molecules so that water may participate in this process during cold cataract formation.

DATA AVAILABILITY STATEMENT

The raw data supporting the conclusions of this article will be made available by the authors, without undue reservation.

ETHICS STATEMENT

The animal study was reviewed and approved by the Animal Ethics Committee of Tsinghua Shenzhen International Graduate School.

AUTHOR CONTRIBUTIONS

YL, YXL, and XL contributed to the conception and design of the study. YL conducted the experiments and performed the statistical analysis. YL wrote the first draft of the manuscript. YH and TG contributed to the manuscript revision. All authors read and approved the submitted version.

FUNDING

The work is supported by the Science and Technology Research Program of Shenzhen City (JCYJ20170412171856582, JCYJ20180508152528735) and Oversea Cooperation Foundation, Graduate School at Shenzhen, Tsinghua University (HW2018007).

ACKNOWLEDGMENTS

The authors thank Xiaohua Gong at the University of California, Berkeley, Berkeley, for the guidance of the research.

REFERENCES

Banh, A., and Sivak, J. G. (2004). Laser Scanning Analysis of Cold Cataract in Young and Old Bovine Lenses. *Mol. Vis.* 10, 144–147.

Baschenko, S., and Marchenko, L. (2011). On Raman Spectra of Water, its Structure and Dependence on Temperature. Semiconductor Physics. *Quantum Electron. Optoelectronics* 14 (1), 77–79. doi:10.15407/spqeo14.01.077

Benedek, G., Clark, J., Serrallach, E., Young, C., Mengel, L., Sauke, T., et al. (1979). Light Scattering and Reversible Cataracts in the Calf and Human Lens. *Phil. Trans. R. Soc. Lond. A.* 293 (1402), 329–340. doi:10.1098/rsta.1979.0100

Blankenship, T. N., Hess, J. F., and FitzGerald, P. G. (2001). Development- and Differentiation-Dependent Reorganization of Intermediate Filaments in Fiber Cells. *Invest. Ophthalmol. Vis. Sci.* 42 (3), 735–742.

Bot, A. C. C., Huizinga, A., de Mul, F. F. M., Vrensen, G. F. J. M., and Greve, J. (1989). Raman Microspectroscopy of Fixed Rabbit and Human Lenses and Lens Slices: New Potentialities. *Exp. Eye Res.* 49 (2), 161–169. doi:10.1016/0014-4835(89)90086-9

Broide, M. L., Berland, C. R., Pande, J., Ogun, O. O., and Benedek, G. B. (1991). Binary-Liquid Phase Separation of Lens Protein Solutions. *Proc. Natl. Acad. Sci.* 88 (13), 5660–5664. doi:10.1073/pnas.88.13.5660

Carey, D. M., and Korenowski, G. M. (1998). Measurement of the Raman Spectrum of Liquid Water. *J. Chem. Phys.* 108 (7), 2669–2675. doi:10.1063/1.475659

Crupi, V., Interdonato, S., Longo, F., Majolino, D., Migliardo, P., and Venuti, V. (2008). A New Insight on the Hydrogen Bonding Structures of Nanoconfined Water: A Raman Study. *J. Raman Spectrosc.* 39 (2), 244–249. doi:10.1002/jrs.1857

Erckens, R. J., Jongsma, F. H. M., Wicksted, J. P., Hendrikse, F., March, W. F., and Motamedi, M. (2001). Raman Spectroscopy in Ophthalmology: From Experimental Tool to Applications *In Vivo*. *Lasers Med. Sci.* 16 (4), 236–252. doi:10.1007/pl00011360

Heys, K. R., Friedrich, M. G., and Truscott, R. J. W. (2008). Free and Bound Water in normal and Cataractous Human Lenses. *Invest. Ophthalmol. Vis. Sci.* 49 (5), 1991–1997. doi:10.1167/iovs.07-1151

Huang, C.-C., and Chen, W. (2018). Raman Spectroscopic Analysis of Cataract Lens: A Compendious Review. *Appl. Spectrosc. Rev.* 53 (9), 689–702. doi:10.1080/05704928.2017.1416476

Huang, X. F., Wang, Q., Liu, X. X., Yang, S. H., Li, C. X., Sun, G., et al. (2009). Vibrational Dynamics of Water within Mesoporous Materials at Different Hydration Levels during Adsorption and Desorption Processes. *J. Phys. Chem. C* 113 (43), 18768–18771. doi:10.1021/jp9051566

Huizinga, A., Bot, A. C. C., de Mul, F. F. M., Vrensen, G. F. J. M., and Greve, J. (1989). Local Variation in Absolute Water Content of Human and Rabbit Eye Lenses Measured by Raman Microspectroscopy. *Exp. Eye Res.* 48 (4), 487–496. doi:10.1016/0014-4835(89)90032-8

Izatt, J. A., Hee, M. R., Swanson, E. A., Lin, C. P., Huang, D., Schuman, J. S., et al. (1994). Micrometer-Scale Resolution Imaging of the Anterior Eye *In Vivo* with Optical Coherence Tomography. *Arch. Ophthalmol.* 112 (12), 1584–1589. doi:10.1001/archopht.1994.01090240090031

Lerman, S., Ashley, D. L., Long, R. C., Goldstein, J. H., Megaw, J. M., and Gardner, K. (1982). Nuclear Magnetic Resonance Analyses of the Cold Cataract: Whole Lens Studies. *Invest. Ophthalmol. Vis. Sci.* 23 (2), 218–226.

Lerman, S., Megaw, J. M., Gardner, K., Ashley, D., Long, R. C., and Goldstein, J. H. (1983). NMR Analyses of the Cold Cataract. II. Studies on Protein Solutions. *Invest. Ophthalmol. Vis. Sci.* 24 (1), 99–105.

Lerman, S., Zigman, S., and Forbes, W. F. (1966). Properties of a Cryoprotein in the Ocular Lens. *Biochem. biophysical Res. Commun.* 22 (1), 57–61. doi:10.1016/0006-291x(66)90602-4

Li, Y., Liu, X., Xia, C. H., FitzGerald, P. G., Li, R., Wang, J., et al. (2020). CP49 and Filensin Intermediate Filaments Are Essential for Formation of Cold Cataract. *Mol. Vis.* 26, 603–612.

Lin, C-C., Kuo, M-T., and Chang, H-C. (2010). Raman Spectroscopy–A Novel Tool for Noninvasive Analysis of Ocular Surface Fluid. *J. Med. Biol. Eng.* 30 (6), 343–354. doi:10.5405/jmbe.846

Lo, W. K. (1989). Visualization of Crystallin Droplets Associated with Cold Cataract Formation in Young Intact Rat Lens. *Proc. Natl. Acad. Sci.* 86 (24), 9926–9930. doi:10.1073/pnas.86.24.9926

Loewenstein, M. A., and Bettelheim, F. A. (1979). Cold Cataract Formation in Fish Lenses. *Exp. Eye Res.* 28 (6), 651–663. doi:10.1016/0014-4835(79)90066-6

Medina-Gutiérrez, C., Frausto-Reyes, C., Quintanar-Stephano, J. L., and Sato-Berrú, R. (2004). Amino Acid Contents along the Visual and Equatorial Axes of a Pig Lens by Raman Spectroscopy. *Spectrochimica Acta A: Mol. Biomol. Spectrosc.* 60 (10), 2269–2274. doi:10.1016/j.saa.2003.11.025

Mizuno, A., Ozaki, Y., Itoh, K., Matsushima, S., and Iriyama, K. (1984). Raman Spectroscopic Evidence for the Microenvironmental Change of Some Tyrosine Residues of Lens Proteins in Cold Cataract. *Biochem. biophysical Res. Commun.* 119 (3), 989–994. doi:10.1016/0006-291x(84)90871-4

Ondruska, O., and Hanson, D. M. (1983). Raman Spectra of Duck, Rat, and Flounder Lenses and the Formation of Dry and Cold Cataracts. *Exp. Eye Res.* 37 (2), 139–143. doi:10.1016/0014-4835(83)90072-6

Ozaki, Y., Mizuno, A., Itoh, K., and Iriyama, K. (1987). Inter- and Intramolecular Disulfide Bond Formation and Related Structural Changes in the Lens Proteins. A Raman Spectroscopic Study *In Vivo* of Lens Aging. *J. Biol. Chem.* 262 (32), 15545–15551. doi:10.1016/s0021-9258(18)47760-5

Petta, V., Pharmakakis, N., Papatheodorou, G. N., and Yannopoulos, S. N. (2008). Dynamic Light Scattering Study on Phase Separation of a Protein-Water Mixture: Application on Cold Cataract Development in the Ocular Lens. *Phys. Rev. E Stat. Nonlin Soft Matter Phys.* 77 (6), 061904. doi:10.1103/PhysRevE.77.061904

Rácz, P., Tompa, K., and Pocsik, I. (1979). The State of Water in normal Human, Bird and Fish Eye Lenses. *Exp. Eye Res.* 29 (6), 601–608. doi:10.1016/0014-4835(79)90015-0

Siebinga, I., Vrensen, G. F. J. M., Otto, K., Puppels, G. J., De Mul, F. F. M., and Greve, J. (1992). Ageing and Changes in Protein Conformation in the Human Lens: A Raman Microspectroscopic Study. *Exp. Eye Res.* 54 (5), 759–767. doi:10.1016/0014-4835(92)90031-m

Siezen, R. J., Fisch, M. R., Slingsby, C., and Benedek, G. B. (1985). Opacification of Gamma-Crystallin Solutions from Calf Lens in Relation to Cold Cataract Formation. *Proc. Natl. Acad. Sci.* 82 (6), 1701–1705. doi:10.1073/pnas.82.6.1701

Sivak, J. G., Stuart, D. D., and Weerheim, J. A. (1992). Optical Performance of the Bovine Lens Before and After Cold Cataract. *Appl. Opt.* 31 (19), 3616–3620. doi:10.1364/ao.31.003616

Smeets, M. H., Vrensen, G. F. J. M., Otto, K., Puppels, G. J., and Greve, J. (1993). Local Variations in Protein Structure in the Human Eye Lens: A Raman Microspectroscopic Study. *Biochim. Biophys. Acta (Bba) - Protein Struct. Mol. Enzymol.* 1164 (3), 236–242. doi:10.1016/0167-4838(93)90254-o

Song, S., Landsbury, A., Dahm, R., Liu, Y., Zhang, Q., and Quinlan, R. A. (2009). Functions of the Intermediate Filament Cytoskeleton in the Eye Lens. *J. Clin. Invest.* 119 (7), 1837–1848. doi:10.1172/jci38277

Walrafen, G. E., Fisher, M. R., Hokmabadi, M. S., and Yang, W. H. (1986). Temperature Dependence of the Low- and High-Frequency Raman Scattering from Liquid Water. *J. Chem. Phys.* 85 (12), 6970–6982. doi:10.1063/1.451384

Zhang, H., Wu, C., Singh, M., and Larin, K. V. (2018). "Quantifying Changes in Lens Biomechanical Properties Due to Cold Cataract with Optical Coherence Elastography," in Ophthalmic Technologies XXVIII, San Francisco, CA, February 19, 2018 (International Society for Optics and Photonics).

Zigman, S., and Lerman, S. (1964). A Cold Precipitable Protein in the Lens. *Nature* 203 (4945), 662–663. doi:10.1038/203662a0

Zigman, S., and Lerman, S. (1965). Properties of a Cold-Precipitable Protein Fraction in the Lens. *Exp. Eye Res.* 4 (1), 24–IN19. doi:10.1016/s0014-4835(65)80005-7

Conflict of Interest: The authors declare that the research was conducted in the absence of any commercial or financial relationships that could be construed as a potential conflict of interest.

Publisher's Note: All claims expressed in this article are solely those of the authors and do not necessarily represent those of their affiliated organizations, or those of the publisher, the editors, and the reviewers. Any product that may be evaluated in this article, or claim that may be made by its manufacturer, is not guaranteed or endorsed by the publisher.

Copyright © 2021 Li, Li, Liu, He and Guan. This is an open-access article distributed under the terms of the Creative Commons Attribution License (CC BY). The use, distribution or reproduction in other forums is permitted, provided the original author(s) and the copyright owner(s) are credited and that the original publication in this journal is cited, in accordance with accepted academic practice. No use, distribution or reproduction is permitted which does not comply with these terms.

frontiers in Chemistry

ORIGINAL RESEARCH
published: 08 December 2021
doi: 10.3389/fchem.2021.801355

High-Sensitive Surface Plasmon Resonance Imaging Biosensor Based on Dual-Wavelength Differential Method

Youjun Zeng[1], Jie Zhou[1], Wei Sang[1], Weifu Kong[1], Junle Qu[1], Ho-Pui Ho[2], Kaiming Zhou[3], Bruce Zhi Gao[4], Jiajie Chen[1] and Yonghong Shao[1]**

[1]Key Laboratory of Optoelectronic Devices and Systems of Ministry of Education and Guangdong Province, College of Physics and Optoelectronics Engineering, Shenzhen University, Shenzhen, China, [2]Department of Biomedical Engineering, The Chinese University of Hong Kong, Shatin, Hong Kong SAR, China, [3]Aston Institute of Photonic Technologies, Aston University, Birmingham, United Kingdom, [4]Department of Bioengineering and COMSET, Clemson University, Clemson, SC, United States

Intensity interrogation surface plasmon resonance (ISPR) sensing has a simple schematic design and is the most widely used surface plasmon resonance technology at present. However, it has relatively low sensitivity, especially for ISPR imaging (ISPRi). In this paper, a new technique for the real-time monitoring of biomolecule binding on sensor surfaces *via* ISPRi detection is described. The technique is based on the interrogation of the differential value of two intensities at two specific wavelengths from the reflected light spectrum. In addition, we also optimized the selection of dual-wavelength parameters under different circumstances to achieve the highest sensitivity. The new technique achieved a refractive index resolution (RIR) of 2.24×10^{-6} RIU, which is far beyond that of traditional ISPRi technique. Moreover, our new ISPRi technique also realized the real-time detection of high-throughput biomolecular binding. This study is expected to promote the development of faster and more accurate SPRi technologies.

Keywords: surface plasmon, biosensing and bioimaging, surface plasmon sensors, biophotonics and plasmonics, biomolecule interaction

OPEN ACCESS

Edited by:
Chao He,
University of Oxford, United Kingdom

Reviewed by:
Le Liu,
Tsinghua University, China
Jianan He,
Shenzhen Academy of Inspection and Quarantine, China

****Correspondence:***
Jiajie Chen
cjj@szu.edu.cn
Yonghong Shao
shaoyh@szu.edu.cn

Specialty section:
This article was submitted to Nanoscience, a section of the journal Frontiers in Chemistry

Received: *25 October 2021*
Accepted: *15 November 2021*
Published: *08 December 2021*

Citation:
Zeng Y, Zhou J, Sang W, Kong W, Qu J, Ho H-P, Zhou K, Gao BZ, Chen J and Shao Y (2021) High-Sensitive Surface Plasmon Resonance Imaging Biosensor Based on Dual-Wavelength Differential Method. Front. Chem. 9:801355. doi: 10.3389/fchem.2021.801355

INTRODUCTION

Surface plasmon resonance (SPR) has become a powerful tool for exploring biomolecular interactions in the last decades (Homola, 2008; Schasfoort et al., 2018; Bockova et al., 2019). Four practical interrogation SPR sensing techniques, namely, intensity, wavelength, angle, and phase interrogation SPR modes, have been widely reported (Homola et al., 1999; Liu et al., 2005; Huang et al., 2012). In the wavelength interrogation SPR mode, the incident angle is fixed, and the SPR spectral profile and resonance wavelength can be obtained by scanning the incidence wavelength or using a spectrometer for analyzing the reflected beam. Angular interrogation SPR usually utilizes monochromatic light as excitation light, and the shift of the SPR dip can be monitored through the continuous scanning of the SPR angular spectrograph. In the phase interrogation SPR mode, the SPR phase shift can be obtained by detecting the phase difference between the signal beam and reference beam.

In intensity interrogation SPR (ISPR) mode, the incidence wavelength and angle are usually fixed, and the reflected light intensity is directly monitored to translate the refractive index variation of the sample. This technology avoids the usage of scanning or modulator devices, such as wavelength scanning devices, angle scanning devices, and phase modulators. Compared with the other three

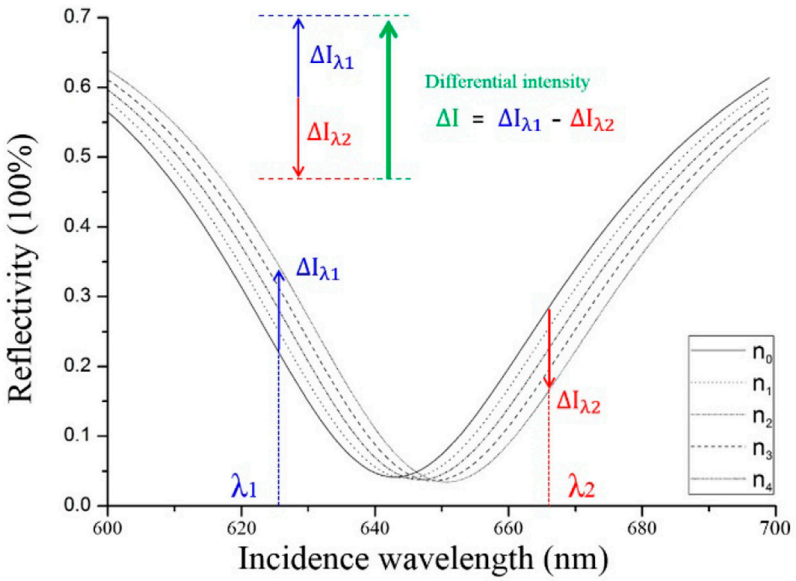

FIGURE 1 | Simulated SPR spectral curves of different sample refractive indexes. n_i is a set of linearly increased refractive indexes, i = 0, 1, 2, 3, 4, 5.

interrogation modes, ISPR mode has a simple structure design, easy operational procedure, and cost-effectiveness (Zeng et al., 2017). Moreover, the detecting speed of the ISPR system solely depends on the speed of the light intensity detector, therefore, it has great application potential in 2D real-time biochemical reaction monitoring. In addition, in terms of producibility, ISPR technology, such as Biacore from GE Healthcare and SPR chips from GWC Technologies, is also the most commonly used method in commercial SPR instruments (Nilvebrant, 2018). These instruments use ISPR for DNA hybridization analysis (Mudgal et al., 2020), protein interaction analysis (Nilvebrant, 2018), and cellular analysis (Zhou X. L. et al., 2020).

In addition, sensitivity is a vital parameter in biochemical detection, Researchers have developed many techniques to increase the sensitivity for detecting biomolecular interactions at lower concentrations with lesser sample consumption. And for a typical SPR sensor, a smaller refractive index resolution (RIR) gives a higher system sensitivity. The RIR of a typical ISPR at present is 10^{-5} RIU (Homola et al., 1999; Yuk et al., 2005; Zeng et al., 2017), which is 1–2 orders lower compared with those of the other three SPR interrogation modes. The low sensitivity has greatly limited the applications of ISPR in biosensing. In addition, detection throughput is another important parameter for biosensors. By combining imaging technology, multichannel SPR and SPR imaging (SPRi) (Wong and Olivo, 2014; Puiu and Bala, 2016; Zeng et al., 2019; Zhou J. et al., 2020) sensors have been developed to achieve the simultaneous detection of multiple samples at high throughput. However, these multipoint detection schemes are more vulnerable to external noise, and their sensitivities are still limited (Zeng et al., 2019). Zybin et al. proposed a double-wavelength SPR interrogation methods to achieve high-throughput monitoring and high sensitivity; in their system, differential measurements are provided by two diode-lasers, and 2D sensor arrays are used as the detector. The system simultaneously monitored four channels and achieved a refractive index resolution of 5×10^{-6} RIU (Zybin et al., 2005). However, the two lasers of their system need to be strictly aligned to a common light path to ensure that they reach the same site on the detector after passing through the sensing module. Moreover, the speckles induced by two coherent light sources also caused much noise, especially for intensity-based SPR sensing. Therefore, in this paper, we present a novel ISPRi biosensor based on the differential of light intensities from two selected wavelengths. The system adopts incoherent light with broadband spectrum for excitation, and the intensity information of two selected wavelengths in the reflected light is recorded by two complementary metal oxide semiconductors (CMOSs). We improved the sensitivity of the traditional ISPRi system by about one order and achieved multichannel high-throughput detection. This technique has great potential to be employed in highly sensitive and real-time SPR imaging benchtop devices for molecular interactions detection.

Principle of the Dual-Wavelength Differential Method

For a Kretschmann-based SPR scheme with gold film (48 nm thickness) on the prism made by SF11, the change in refractive index is from 1.333 RIU to 1.333019 RIU in 10^{-6} RIU by volume, the incidence wavelength is from 600 to 700 nm, and the incidence is 54.2°, which is the optimum for 1.333 RIU. The reflection of incidence light obeys the Fresnel **Eq. 1**, in which $I_0(\lambda)$ is the reflective intensity with incidence wavelength λ; r_{01} and r_{12} are the reflection coefficients of prism–metal and

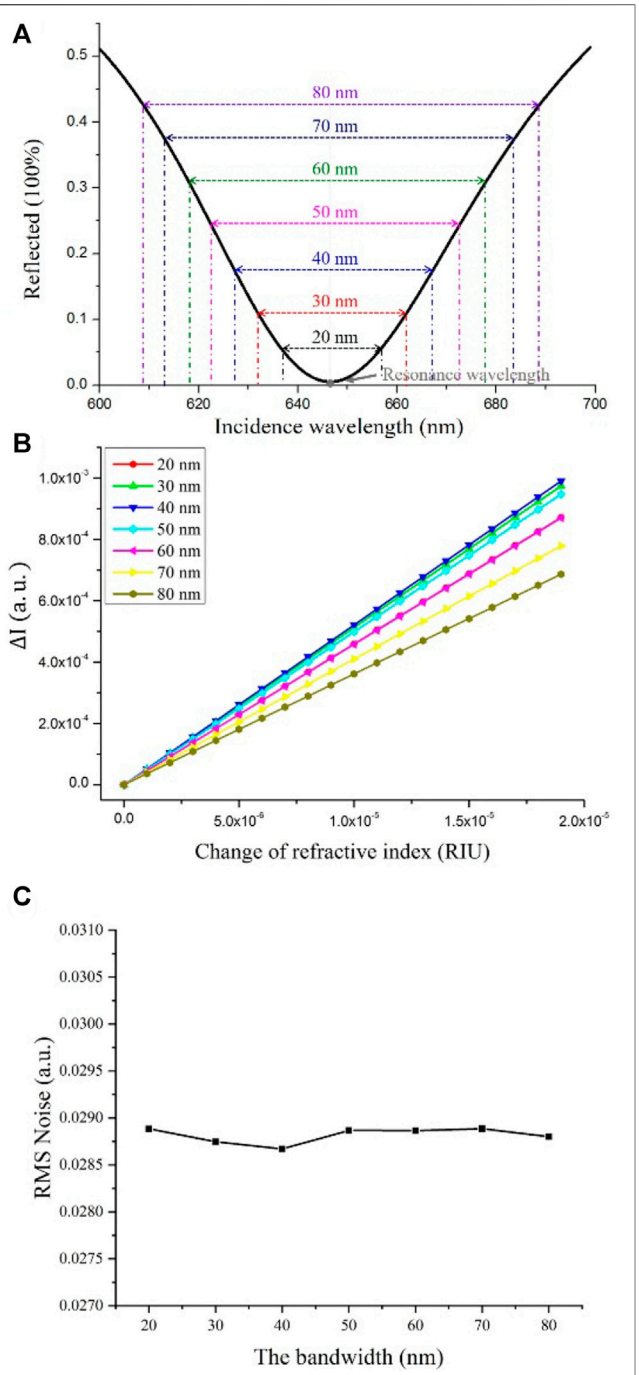

FIGURE 2 | Simulation of intensity amplification optimization and influence of light source noise study. **(A)** Schematic diagram of dual-wavelength selection; **(B)** Dual-wavelength differential value Δ*I* change with sample refractive index variation. **(C)** The RMS noise of Δ*I* in different bandwidths.

metal–sample interfaces, respectively; k_x and ω are the wave vector and angular frequency of the wave of p-polarized light in incident light; ε is the dielectric constant of the sample; d is the metal thickness, and c is the speed of light in vacuum.

$$I_0(\lambda) = \left| \frac{r_{01} + r_{12}\exp\left(\frac{2i\varepsilon d}{\varepsilon\left(\frac{\omega}{c}\right)^2 - k_x^2}\right)}{1 + r_{01}r_{12}\exp\left(\frac{2i\varepsilon d}{\varepsilon\left(\frac{\omega}{c}\right)^2 - k_x^2}\right)} \right|^2 \quad (1)$$

As it's illustrated in **Figure 1**, we simulated the SPR spectral curve under different incident wavelengths. The SPR spectral curve shows two linear regions, in which the reflected light intensity varies linearly with the refractive index. When the refractive index increases, the reflected light intensity increases in one linear region (blue arrow) and decreases in another linear region (red arrow). We can monitor the intensities in the two linear regions at the same time, and make a subtraction ΔI between the two groups of intensity ($I_{\lambda 1} - I_{\lambda 2}$), so the intensity change induced by the sample refractive index variation can be amplified.

In addition, dual-wavelength selection needs to be optimized to obtain the highest sensitivity amplification. Based on the simulation results of intensity difference ΔI at different refractive index change. We studied the influence of the bandwidth between the two selected wavelengths to ΔI. As shown in **Figure 2A**, from the SPR curve, we took the resonance wavelength as the center, symmetrically chose wavelengths of λ_1 and λ_2 with different bandwidths, and detected the corresponding reflected light intensities, $I_{\lambda 1}$ and $I_{\lambda 2}$, respectively. The relationship between ΔI and the refractive index change in different bandwidth is represented in **Figure 2B**. The results show that ΔI gives the largest value at the selected bandwidth of 40 nm (dark blue line). Thus, in our experiments, the bandwidth of the dual wavelengths was set to 40 nm, and they were symmetric with respect to the resonance wavelength. Moreover, we also conducted simulation regarding the influence of light source noise. In the simulation process, we added random generated noise I_{Noise} ranging from 0 to 0.01 (identical to the real experiments) to ΔI, then the SPR signal can be expressed as $\Delta I + I_{Noise}$. After testing of 1000 times, the measured root mean square (RMS) noise obtained under different bandwidth is shown in the Figure 3 (c). It indicates that the RMS noise between different bandwidth is basically identical trivial and the RMS noise variation is within 1%. Therefore, the influence of the noise of the light source can be ignored in our experiments.

Setup

Figure 3 shows the optical path of the system. A 100 W halogen lamp (GCI-060101, Daheng Optics, Beijing, China) was used as the excitation light source. Divergent light from multimode fiber passes through the collimating lens groups of L1 and L2, and diaphragm aperture to produce parallel lights, then enters into the sensing module. And the sensing module includes prism, sensor chip, and flow cell. The parallel light is coupled into the prism to excite the SPR effect on the sensor chip in the gold film.

After the reflected light passes through L3 and P2, it is split by a 635 nm low-pass dichroic mirror (FF635-Di01-25 × 36, Semrock, New York, United States). And two laser line filters of filter 1 (7671, Alluxa, Santa Rosa, United States) and filter 2 (7261, Alluxa, Santa Rosa, United States) are used to filter out the two operating wavelengths. Their center wavelengths are 608 and 650 nm, and their full width at half maximum is 1 nm. The system

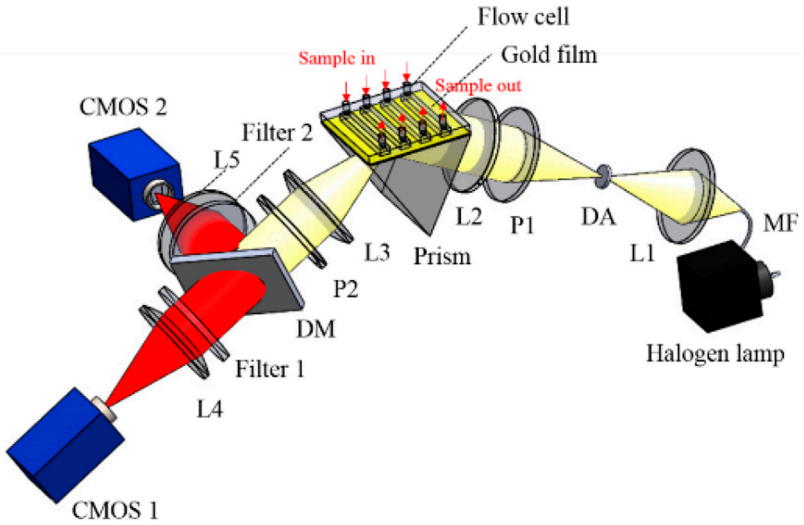

FIGURE 3 | Schematic of ISPRi system based on Kreschmann configuration. L1–L5, lenses; DA, diaphragm aperture; MF, multimode fiber; DM, dichroic mirror; P1 and P2, polarizers.

is controlled by a homemade LabVIEW program. During the test, two CMOSs acquire the images of the sensing surface, simultaneously. The control program differentiates the two intensities at two different wavelengths in real time.

RESULTS AND DISCUSSIONS

We detected the intensity shift induced by small variations in saline water concentration to determine the refractive index resolution of our system. We tested a series of saline water with concentrations of 0–2% in increments of 0.5% by volume, which correspond to the refractive indexes ranging from 1.3330 RIU to 1.3367 RIU. During the test, the incident angle was fixed to 54.9°, which corresponds to the resonance wavelength of 630 nm and sample's refractive index of 1.3330 RIU. Before the test, the system obtained the image of the whole sensor surface, and we evenly divided the entire sensing surface into 3 × 3 array sensor sites. And the nine sites were monitored simultaneously. The results are illustrated in **Figure 4A**. $I_{\lambda 1}$ and $I_{\lambda 2}$ are the changes in intensity that were collected simultaneously by CMOS 1 and CMOS 2, and the black curve is the ΔI obtained after the differential of $I_{\lambda 1}$ and $I_{\lambda 2}$. Note that each data point in the figure is the average value of nine detection sites. The inset is the zoom-in figure at 1% saline water concentration.

We also detected the noise of our ISPRi system. Noise is reduced by averaging multiple acquisitions. The relationship between average times and RMS noise is shown in **Figure 4B**. RMS noise was reduced with the increase in averaging number and tended to be stable and small when the averaging number exceeded 100 times. In our experiments, averaging number was set to 100 to ensure best performance. The frame rates of the two CMOSs were 100 fps, so the imaging time for acquiring one SPR image is 1 s. Therefore, the real-time refractive index monitoring ability of our SPR system is verified.

And the refractive index resolution (RIR) of the system can be calculated from **Eq. 2** (Zeng et al., 2020a; Ng et al., 2013)

$$\sigma_{RI} = \frac{\delta n}{\delta s}\Delta\sigma_{SD} \tag{2}$$

where σ_{RI} is the RIR, δn is the refractive index change, δs is the change in intensity, and $\Delta\sigma_{SD}$ is the RMS noise of our ISPRi system. The samples with concentrations of 0.5–1% caused the maximum intensity change. In this case, the values of δn, δs, and $\Delta\sigma_{SD}$ were 0.000925 RIU, 14.04 a.u., and 0.034 a.u., respectively. From the above calculation, we obtained the RIR of 2.24×10^{-6} RIU.

In addition, we also tested the biosensing capability of our ISPRi sensor in detecting the interactions between two kinds of protein molecules. The biomolecule binding events on the sensing surface is indicated by the change in refractive light intensity (Mudgal et al., 2020). The sensor chip was rinsed with deionized water and dried with nitrogen before being placed on the prism for the biological experiment. The chip was attached to the coupling prism using a small drop of refractive index matching oil. And a four-channel PDMS flow chamber was adopted for sample injection.

For the pretreatment of the sensing surface, the antigen of human IgG was bound to the gold film *via* physical absorption process and real-time monitoring was performed (Zeng et al., 2020b; Miyan et al., 2021; Zhou et al., 2022). First, phosphate-buffered saline (PBS, 0.01 M, pH 7.4) was separately injected into the four channels and flushed for 5 min. Second, human IgG (100 μg/ml) was injected into each channel simultaneously in a flow rate of 10 μL/min until the image intensities were stabilized. Then, PBS was injected and flushing. After the images are stable, bovine serum albumin solution in the concentration of 10 mg/ml was injected into the four channels for 5 min to occupy the possible vacancy sites without the binding of human IgG. Therefore, the nonspecific binding of goat anti-human IgG to

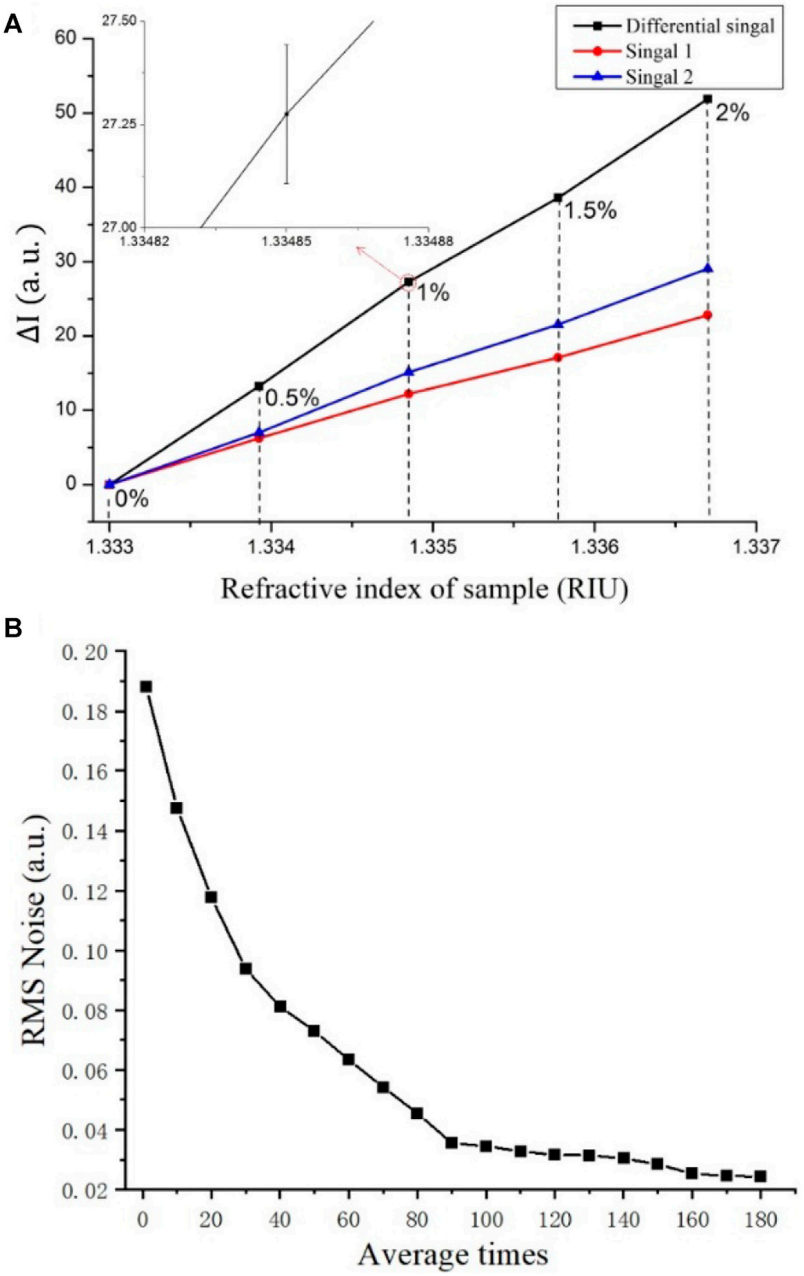

FIGURE 4 | Sensitivity test results. **(A)** Resonance wavelength shift obtained from low-concentration saline water; **(B)** Relation between averaging number and RMS noise.

the surface in the following procedure can be prevented. Then, the PBS solution are injected to each channel for 10 min so as to obtain the baseline for the following bio-experiments.

In the biological binding process. The four channels were injected with PBS buffer and goat anti-human IgG in concentrations of 1, 2, and 5 μg/ml respectively. The channel with PBS was used as the reference channel, and the three other channels were the reaction channels. The differential intensities of all channels were recorded. After the intensity became stationary, PBS was injected to wash the nonspecific binding of goat anti-human IgG to the sensing surface.

The real-time monitoring reflected the light intensities of the four channels as shown in **Figure 5**. The black curve is the reference channel, and the curves with different colors are the reaction channels. The Δ*I*values of the three reaction channels increased linearly with the sample concentration in the biochemical binding process, while the reference channel did not obviously change.

Another unique advantage of our system is its SPR imaging ability. The SPR image of the entire sensing surface can be obtained simultaneously during the detection. As illustrated in

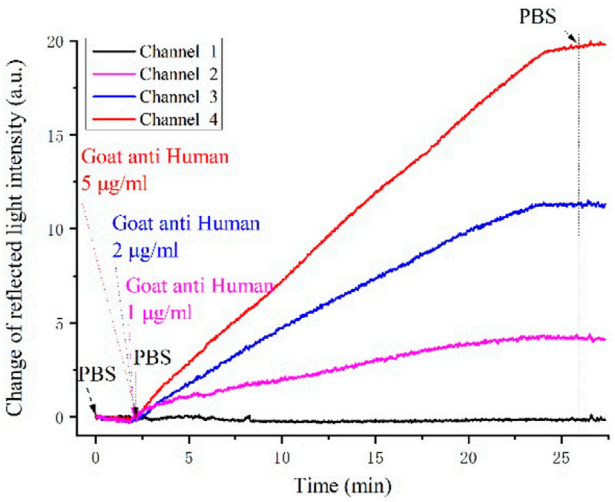

FIGURE 5 | Real-time intensity variation in the antigen-antibody interaction between goat anti-human IgG and human IgG.

intensities from two selected wavelengths. This technique has several advantages compared with traditional ISPR sensors. The proposed technique achieved a higher sensitivity and higher detection throughput in a low-cost optical configuration without using any mechanical moving parts or optical scanning devices compared with other sensors. The results have shown that the SPR refractive index resolution of the scheme is 2.24×10^{-6} RIU, which produces the highest sensitivity in the existing ISPRi system so far. The ability of the developed sensor in the real-time detection of multiple bio-samples was also verified. Nevertheless, the system's sensitivity still has much room for improvement. For example, the differential intensity can be further enlarged by replacing the dual wavelengths from the visible region to the near-infrared region, and the noise can be reduced by employing a high-brightness light source for SPR excitation. Moreover, in terms of SPR imaging, the high-performance 2D detector can be used to suppress dark noise. The imaging resolution and field of view can also be improved if imaging lens groups with high performance are adopted in the future.

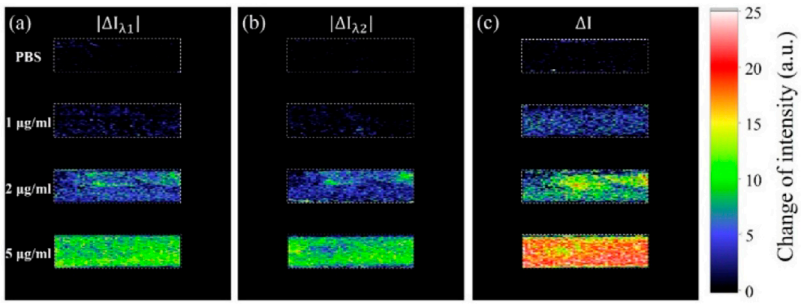

FIGURE 6 | SPR Intensity changes of the four channels treated with PBS and 1, 2, and 5 μg/ml human IgG. **(A,B)** are the images of the intensity based on single wavelength of λ_1 and λ_2. And **(C)** is the image of Δ*I*.

Figure 6, the color of each pixel represents the intensity shift, which indicates the biomolecule binding situation on the corresponding sensing site after the reaction. The light intensity is shown in the false color map. **Figures 6A,B** are the images of the single-wavelength intensity shifts of λ_1 and λ_2, which were directly captured by CMOS 1 and CMOS 2, respectively. **Figure 6C** is total intensity shift induced by the intensity variation of the two wavelengths. Therefore, this high-sensitivity ISPRi scheme gives a higher response compared with single-wavelength SPR sensing. Moreover, the proposed method is also favorable for real-time 2D bio-reaction monitoring, which means that one can monitor the whole 2D sensing sites in real time and select the region of interest anytime during the test.

CONCLUSION

In summary, we developed a versatile real-time ISPRi system, which has improved sensitivity based on the differential light

DATA AVAILABILITY STATEMENT

The raw data supporting the conclusions of this article will be made available by the authors, without undue reservation.

AUTHOR CONTRIBUTIONS

YZ carried out the experimental work and JC carried out the simulation part of the project. JZ, WS, WK, JQ, H-HP, KZ and BG provide experimental help to YZ. YZ and JC finished writing the manuscript, JC and YS revised it.

FUNDING

This work was supported by projects from the National Natural Science Foundation of China (Grant Nos. 61775148 and 61905145), Guangdong Natural Science Foundation and

Province Project (Grant No. 2021A1515011916), and Shenzhen Science and Technology R and D and Innovation Foundation (Grant Nos. JCYJ20200109105608771 and JCYJ20180305124754860).

ACKNOWLEDGMENTS

We would like to thank the rest of the team for the fruitful discussion of this project.

REFERENCES

Bocková, M., Slabý, J., Špringer, T., and Homola, J. (2019). Advances in Surface Plasmon Resonance Imaging and Microscopy and Their Biological Applications. *Annu. Rev. Anal. Chem.* 12, 151–176. doi:10.1146/annurev-anchem-061318-115106

Homola, J., Yee, S. S., and Gauglitz, G. (1999). Surface Plasmon Resonance Sensors Review. *Sens. Actuators B: Chem.* 54 (1-2), 3–15. doi:10.1016/S0925-4005(98)00321-9

Homola, J. (2008). Surface Plasmon Resonance Sensors for Detection of Chemical and Biological Species. *Chem. Rev.* 108, 462–493. doi:10.1021/cr068107d

Huang, Y. H., Ho, H. P., Wu, S. Y., and Kong, S. K. (2012). Detecting Phase Shifts in Surface Plasmon Resonance: A Review. *Adv. Opt. Tech.* 2012, 1–12. doi:10.1155/2012/471957

Liu, X., Song, D., Zhang, Q., Tian, Y., Ding, L., and Zhang, H. (2005). Wavelength-modulation Surface Plasmon Resonance Sensor. *Trends Anal. Chem.* 24, 887–893. doi:10.1016/j.trac.2005.05.010

Miyan, R., Wang, X., Zhou, J., Zeng, Y., Qu, J., Ho, H.-P., et al. (2021). Phase Interrogation Surface Plasmon Resonance Hyperspectral Imaging Sensor for Multi-Channel High-Throughput Detection. *Opt. Express* 29 (20), 31418–31425. doi:10.1364/OE.433052

Mudgal, N., Saharia, A., Choure, K. K., Agarwal, A., and Singh, G. (2020). Sensitivity Enhancement with Anti-reflection Coating of Silicon Nitride (Si3N4) Layer in Silver-Based Surface Plasmon Resonance (SPR) Sensor for Sensing of DNA Hybridization. *Appl. Phys. A.* 126, 126. doi:10.1007/s00339-020-04126-9

Ng, S. P., Loo, F. C., Wu, S. Y., Kong, S. K., Wu, C. M. L., and Ho, H. P. (2013). Common-path Spectral Interferometry with Temporal Carrier for Highly Sensitive Surface Plasmon Resonance Sensing. *Opt. Express* 21 (17), 20268–20273. doi:10.1364/OE.21.020268

Nilvebrant, J. (2018). Kinetic Analysis and Epitope Binning Using Surface Plasmon Resonance. *Meth. Mol. Biol.* 1785, 187–205. doi:10.1007/978-1-4939-7841-0_12

Puiu, M., and Bala, C. (2016). SPR and SPR Imaging: Recent Trends in Developing Nanodevices for Detection and Real-Time Monitoring of Biomolecular Events. *Sensors* 16 (6), 870. doi:10.3390/s16060870

Schasfoort, R., Abali, F., Stojanovic, I., Vidarsson, G., and Terstappen, L. (2018). Trends in SPR Cytometry: Advances in Label-free Detection of Cell Parameters. *Biosensors* 8, 102. doi:10.3390/bios8040102

Wong, C. L., and Olivo, M. (2014). Surface Plasmon Resonance Imaging Sensors: A Review. *Plasmonics* 9, 809–824. doi:10.1007/s11468-013-9662-3

Yuk, J. S., Jung, J.-W., Jung, S.-H., Han, J.-A., Kim, Y.-M., and Ha, K.-S. (2005). Sensitivity of *Ex Situ* and *In Situ* Spectral Surface Plasmon Resonance Sensors in the Analysis of Protein Arrays. *Biosens. Bioelectron.* 20, 2189–2196. doi:10.1016/j.bios.2004.07.034

Zeng, Y., Hu, R., Wang, L., Gu, D., He, J., Wu, S.-Y., et al. (2017). Recent Advances in Surface Plasmon Resonance Imaging: Detection Speed, Sensitivity, and Portability. *Nanophotonics* 6, 1017–1030. doi:10.1515/nanoph-2017-0022

Zeng, Y., Zhou, J., Wang, X., Cai, Z., and Shao, Y. (2019). Wavelength-scanning Surface Plasmon Resonance Microscopy: A Novel Tool for Real Time Sensing of Cell-Substrate Interactions. *Biosens. Bioelectron.* 145, 111717. doi:10.1016/j.bios.2019.111717

Zeng, Y., Wang, X., Zhou, J., Miyan, R., Qu, J., Ho, H.-P., et al. (2020a). Phase Interrogation SPR Sensing Based on white Light Polarized Interference for Wide Dynamic Detection Range. *Opt. Express* 28, 3442–3450. doi:10.1364/OE.382242

Zeng, Y., Wang, X., Zhou, J., Miyan, R., Qu, J., Ho, H.-P., et al. (2020b). High-throughput Imaging Surface Plasmon Resonance Biosensing Based on Ultrafast Two-point Spectral-Dip Tracking Scheme. *Opt. Express* 28 (14), 20624–20633. doi:10.1364/oe.396656

Zhou, J., Zeng, Y., Wang, X., Wu, C., Cai, Z., Gao, B. Z., et al. (2020a). The Capture of Antibodies by Antibody-Binding Proteins for ABO Blood Typing Using SPR Imaging-Based Sensing Technology. *Sensors Actuators B: Chem.* 304, 127391. doi:10.1016/j.snb.2019.127391

Zhou, X. L., Yang, Y., Wang, S., and Liu, X. W. (2020b). Surface Plasmon Resonance Microscopy: From Single-Molecule Sensing to Single-Cell Imaging. *Angew. Chem. Int. Ed.* 59, 1776–1785. doi:10.1002/anie.201908806

Zhou, J., Wang, X., Chen, J. Y., Zeng, Y., Gu, D., Gao, B. Z., et al. (2022). Polymeric Microsphere Enhanced Surface Plasmon Resonance Imaging Immunosensor for Occult Blood Monitoring. *Sensors Actuators B: Chem.* 350, 130858. doi:10.1016/j.snb.2021.130858

Zybin, A., Grunwald., C., Mirsky., V. M., Kuhlmann, J., Wolfbeis, O. S., and Niemax, K. (2005). Double-Wavelength Technique for Surface Plasmon Resonance Measurements: Basic Concept and Applications for Single Sensors and Two-Dimensional Sensor Arrays. *Anal. Chem.* 77 (8), 2393–2399. doi:10.1021/ac048156v

Conflict of Interest: The authors declare that the research was conducted in the absence of any commercial or financial relationships that could be construed as a potential conflict of interest.

Publisher's Note: All claims expressed in this article are solely those of the authors and do not necessarily represent those of their affiliated organizations, or those of the publisher, the editors and the reviewers. Any product that may be evaluated in this article, or claim that may be made by its manufacturer, is not guaranteed or endorsed by the publisher.

Copyright © 2021 Zeng, Zhou, Sang, Kong, Qu, Ho, Zhou, Gao, Chen and Shao. This is an open-access article distributed under the terms of the Creative Commons Attribution License (CC BY). The use, distribution or reproduction in other forums is permitted, provided the original author(s) and the copyright owner(s) are credited and that the original publication in this journal is cited, in accordance with accepted academic practice. No use, distribution or reproduction is permitted which does not comply with these terms.

frontiers in Chemistry

CORRECTION
published: 24 February 2022
doi: 10.3389/fchem.2022.849460

Corrigendum: High-Sensitive Surface Plasmon Resonance Imaging Biosensor Based on Dual-Wavelength Differential Method

Youjun Zeng[1], Jie Zhou[1], Wei Sang[1], Weifu Kong[1], Junle Qu[1], Ho-Pui Ho[2], Kaiming Zhou[3], Bruce Zhi Gao[4], Jiajie Chen[1] and Yonghong Shao[1]**

[1]Key Laboratory of Optoelectronic Devices and Systems of Ministry of Education and Guangdong Province, College of Physics and Optoelectronics Engineering, Shenzhen University, Shenzhen, China, [2]Department of Biomedical Engineering, The Chinese University of Hong Kong, Hong Kong SAR, China, [3]Aston Institute of Photonic Technologies, Aston University, Birmingham, United Kingdom, [4]Department of Bioengineering and COMSET, Clemson University, Clemson, SC, United States

Keywords: surface plasmon, biosensing and bioimaging, surface plasmon sensors, biophotonics and plasmonics, biomolecule interaction

OPEN ACCESS

Approved by:
Frontiers in Editorial Office, Frontiers Media SA, Switzerland

****Correspondence:***
Jiajie Chen
cjj@szu.edu.cn
Yonghong Shao
shaoyh@szu.edu.cn

Specialty section:
This article was submitted to Nanoscience, a section of the journal Frontiers in Chemistry

Received: *06 January 2022*
Accepted: *07 January 2022*
Published: *24 February 2022*

Citation:
Zeng Y, Zhou J, Sang W, Kong W, Qu J, Ho H-P, Zhou K, Gao BZ, Chen J and Shao Y (2022) Corrigendum: High-Sensitive Surface Plasmon Resonance Imaging Biosensor Based on Dual-Wavelength Differential Method. Front. Chem. 10:849460. doi: 10.3389/fchem.2022.849460

A Corrigendum on

High-Sensitive Surface Plasmon Resonance Imaging Biosensor Based on Dual-Wavelength Differential Method

by Zeng, Y., Zhou, J., Sang, W., Kong, W., Qu, J., Ho, H-P., Zhou, K., Gao, BZ., Chen, J. and Shao, Y. (2021). Front. Chem. 9:801355. doi:10.3389/fchem.2021.801355

In the original article there were errors in the Affiliation section. Affiliations 3 and 4 need to be in reversed order. Affiliation 3 should be "Aston Institute of Photonic Technologies, Aston University, Birmingham, United Kingdom". Affiliation 4 should be "Department of Bioengineering and COMSET, Clemson University, Clemson, SC, United States". Affiliation 1 is also corrected to "Key Laboratory of Optoelectronic Devices and Systems of Ministry of Education and Guangdong Province, College of Physics and Optoelectronics Engineering, Shenzhen University, Shenzhen, China".

The authors apologize for this error and state that this does not change the scientific conclusions of the article in any way. The original article has been updated.

Publisher's Note: All claims expressed in this article are solely those of the authors and do not necessarily represent those of their affiliated organizations, or those of the publisher, the editors and the reviewers. Any product that may be evaluated in this article, or claim that may be made by its manufacturer, is not guaranteed or endorsed by the publisher.

Copyright © 2022 Zeng, Zhou, Sang, Kong, Qu, Ho, Zhou, Gao, Chen and Shao. This is an open-access article distributed under the terms of the Creative Commons Attribution License (CC BY). The use, distribution or reproduction in other forums is permitted, provided the original author(s) and the copyright owner(s) are credited and that the original publication in this journal is cited, in accordance with accepted academic practice. No use, distribution or reproduction is permitted which does not comply with these terms.

frontiers in Chemistry

REVIEW
published: 28 February 2022
doi: 10.3389/fchem.2022.845363

Detection Methods of Nanoparticles Synthesized by Gas-Phase Method: A Review

Xiushuo Zhang[1,2], *Xiaolong Zhao*[1,2], *Hongsheng Li*[1,2], *Xiaorui Hao*[1,2], *Jing Xu*[1,2], *Jingjing Tian*[1,2] *and Yong Wang*[1,2]*

[1]*Laboratory of Optical Detection and Imaging, School of Science, Qingdao University of Technology, Qingdao, China,* [2]*Quantum Physics Laboratory, School of Science, Qingdao University of Technology, Qingdao, China*

The detection of nanoparticles is the basis of the study of synthesis mechanism, active regulation of the synthesis process, and the study of nanoparticle properties after synthesis. It is significantly meaningful to the academia and engineering industry. Although there are many relevant detection methods at present, each method has its own advantages and disadvantages, and their measurement quantity and application conditions are also different. There is a lack of unified sorting and generalization. In this paper, the significance of detection of nanoparticles synthesized by a gas-phase method is introduced, the development of detection technology is reviewed, and the future is prospected. It is hoped that this paper will provide a reference for the detection of nanoparticles under various conditions and for the development of new detection methods.

Keywords: gas-phase method, nanoparticles, detection methods, review, expectation

OPEN ACCESS

Edited by:
Chao He,
University of Oxford, United Kingdom

Reviewed by:
Hao Liu,
China University of Geosciences, China
Hao Ni,
China University of Petroleum, China

***Correspondence:**
Yong Wang
wang-yong13@tsinghua.org.cn

Specialty section:
This article was submitted to Nanoscience, a section of the journal Frontiers in Chemistry

Received: *29 December 2021*
Accepted: *11 January 2022*
Published: *28 February 2022*

Citation:
Zhang X, Zhao X, Li H, Hao X, Xu J, Tian J and Wang Y (2022) Detection Methods of Nanoparticles Synthesized by Gas-Phase Method: A Review. Front. Chem. 10:845363. doi: 10.3389/fchem.2022.845363

1 INTRODUCTION

Nanoparticles are those particles whose size is between 1 and 100 nm. In a broad sense, nanoparticles are a category of quasi–zero micro–nano materials, which is between a microsystem and macrosystem; they are neither a typical microsystem nor a typical macrosystem. As a result, nanomaterials made from nanoparticles have some amazing properties compared to ordinary materials, which creates conditions for the production of new materials (Yin and Liu, 2006). At present, the gas-phase method is one of the main preparation methods of nanoparticles. It has the advantages of a simple principle, high purity of preparation, large gas contact surface, and thorough reaction. The methods commonly adopted are evaporative condensation (Cui et al., 2010; Chunrui et al., 2017), gas-state reaction (Yu et al., 2005), chemical vapor deposition (Atchudan et al., 2015), sputtering (Jia, 2004), and gas-phase combustion (Dong et al., 2003). And if you want to get high-performance nanomaterials, the particle size, composition, and other information of nanoparticles must be strictly monitored and regulated during the preparation of nanoparticles. Then the properties of nanoparticles were evaluated after preparation. Therefore, the development of corresponding detection technology is of great significance to evaluate the properties of nanomaterials and improve the preparation efficiency and quality of nanoparticles. At present, the detection technology mainly focuses on the measurement of macroscopic statistical characteristics and microstructure characteristics of nanoparticles (Liu et al., 2005). The commonly used detection methods can be divided into two types according to the detection principle: (1) the optical-based detection method; (2) the electrical-based detection method; and (3) the mechanical-based detection method. In this paper, detection methods for nanoparticles are classified into two categories according to timeliness, namely, online detection and off-line detection.

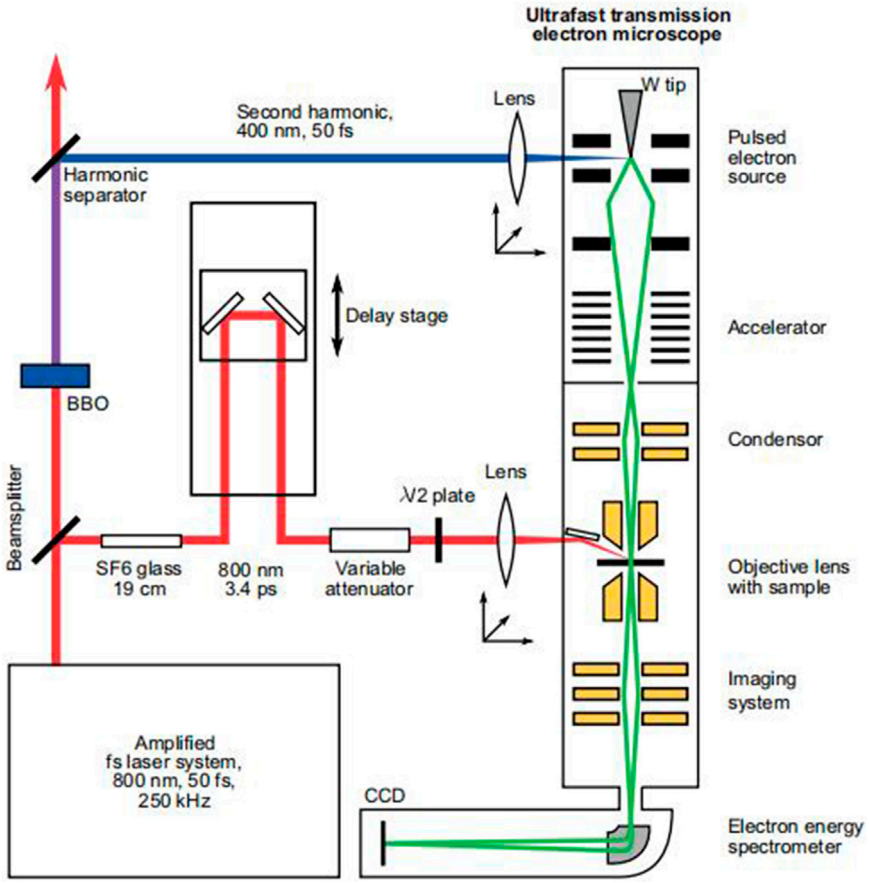

FIGURE 1 | Diagram of the principle of TEM (Feist et al., 2015).

2 OFF-LINE DETECTION OF NANOPARTICLES

2.1 The Electrical-Based Detection Method—Electron Microscopy

Electron microscopy is a method which has high visibility and reliability in measuring the size of nanoparticles. Now, electron microscopy is divided into transmission electron microscopy (TEM) and scanning electron microscopy (SEM) (Zheng, 2018). At the same time, it can also be connected with other technologies. Because of these advantages, electron microscopy has become an important method for measuring the size of nanoparticles. Mäkelä (2002) combined TEM and energy-dispersive X-ray spectroscopy (EDX) technology to detect the iodine content collected by carbon films with the probe and achieved good results. The combination of TEM and EDX is the most widely used semi-quantitative analysis technique in off-line detection, and a detection lower limit of 5 nm can be reached. The following sections discuss these two methods separately.

2.1.1 TEM

2.1.1.1 The Principle of TEM

The principle of TEM is based on the interaction between electrons and solids. When electrons pass through the nanoparticle, they undergo elastic and inelastic scattering, carrying information about the object being measured. TEM can collect scattered electrons and extract their information. A Feist et al. introduced the principle of TEM in a paper published in *Nature* in 2015. The images in the A Feist et al. paper are quoted here (Feist et al., 2015), as shown in **Figure 1**.

2.1.1.2 The Characteristics of TEM

(1) At present, the most advanced TEM has a spatial resolution of less than 0.1 nm and an energy resolution of better than 0.1 eV (Yang et al., 2014).
(2) In addition to the structural information of samples obtained by diffraction and imaging, the chemical composition and electronic structure of samples can be obtained by an energy spectrum (Yang et al., 2014).
(3) TEM is mainly used to observe the surface morphology, dispersion in the matrix, and particle size measurement of nanomaterials.
(4) TEM must operate in a vacuum, as sometimes changing the state of the particle to be measured can affect the measurement.
(5) Compared with other methods, penetrating electron microscopy is a destructive detection.

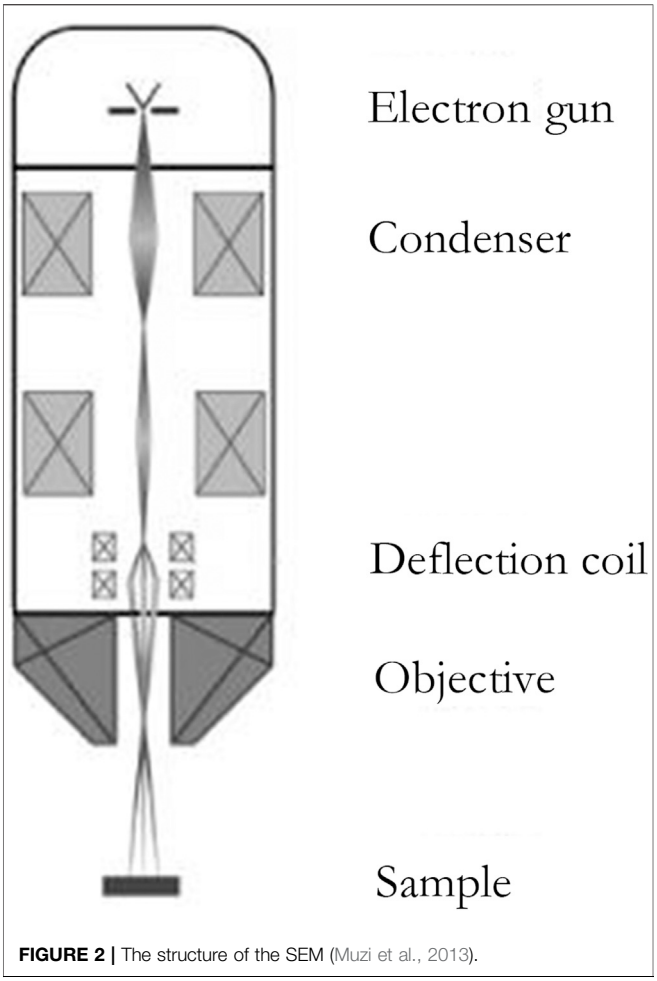

FIGURE 2 | The structure of the SEM (Muzi et al., 2013).

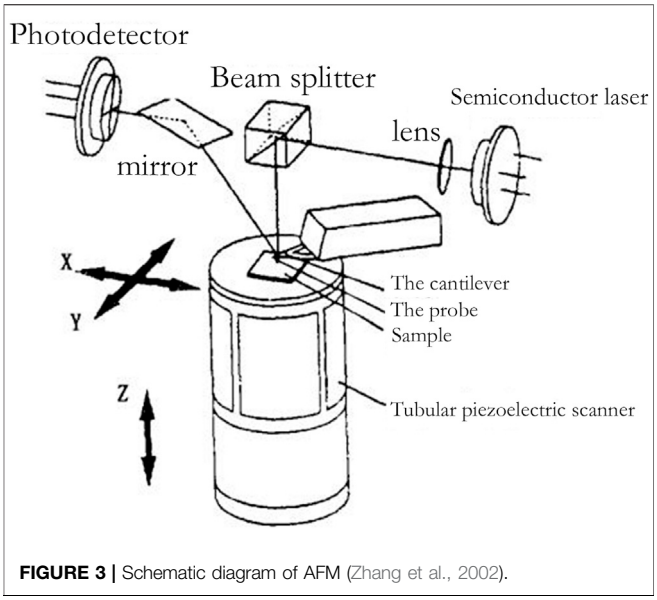

FIGURE 3 | Schematic diagram of AFM (Zhang et al., 2002).

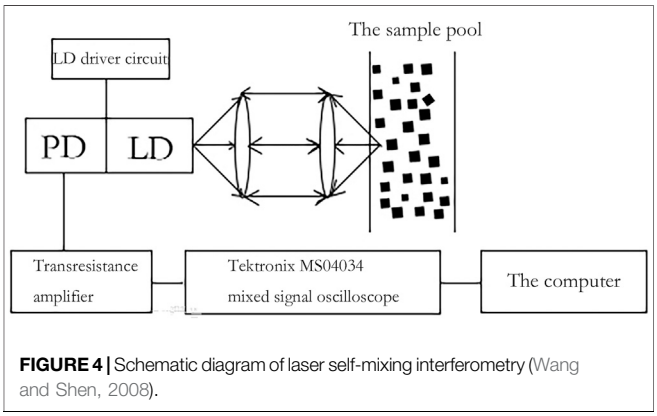

FIGURE 4 | Schematic diagram of laser self-mixing interferometry (Wang and Shen, 2008).

(6) Due to the small sample size used in electron microscopy observation, its measurement results are often statistically lacking, and the observed particle size distribution range may not represent the whole sample size range (Wang, 2018).

2.1.2 SEM

2.1.2.1 The Principle of SEM

In SEM, a sample is scanned by a focused electron beam that will produce secondary or back-scattered electrons when the focused electron beam hits the sample. These electrons are detected by SEM and converted into images of the sample surface. The particle size of nanoparticles can be obtained by observing the images (James et al., 2010).

A secondary electron is a kind of free electron produced by the electron beam bombarding the sample so that the outer electrons of the atom in the sample are separated from the atom. The secondary electron has a lower energy, which is generally below 50 eV. As secondary electrons are generated very close to the surface of the sample (generally 5–10 nm away from the surface), secondary electron imaging (SEI) can characterize the sample surface with a high resolution of up to 1 nm (Ling and Zhong, 2018), as shown in **Figure 2**:

2.1.2.2 The Characteristics of SEM

(1) SEM has an advanced measurement resolution up to 1 nm.
(2) SEM has a wide application range. It not only can measure the particle size of nanoparticles but also can measure the chemical composition of nanoparticles.
(3) SEM has imaging depth of field and good visual field effect, which can provide a clear image for observing the surface topography of the object to be measured.
(4) SEM has a ultra-high resolution that results in a small area or number of nanoparticles being measured at a time, so the measurement results are more accidental and not statistically significant (Yamaguchi et al., 2005).
(5) SEM requires an experimental apparatus that is expensive.

2.2 The Mechanical-Based Detection Method

2.2.1 Centrifugal Sedimentation

2.2.1.1 The Principle of Centrifugal Sedimentation

Centrifugal sedimentation is an indirect method to determine particle size distribution. In the static liquid medium, nanoparticles naturally settle by gravity to overcome the resistance and buoyancy of the medium, which causes a

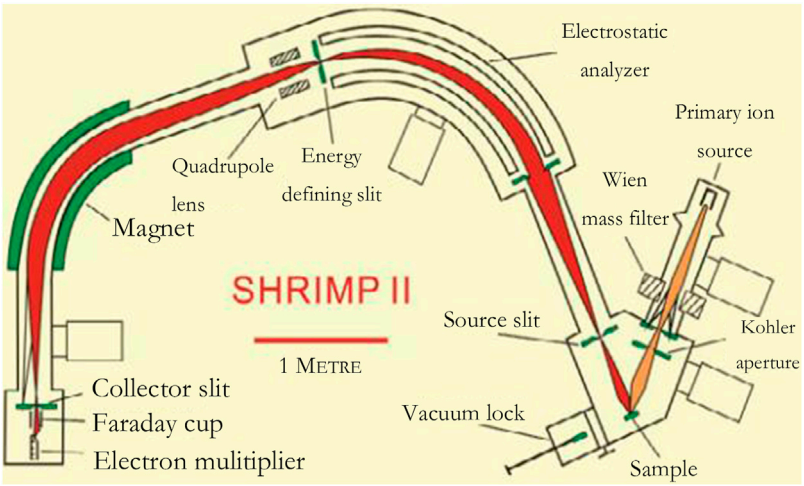

FIGURE 5 | The structure of a secondary ion mass spectrometer (Burgoyne et al., 1997).

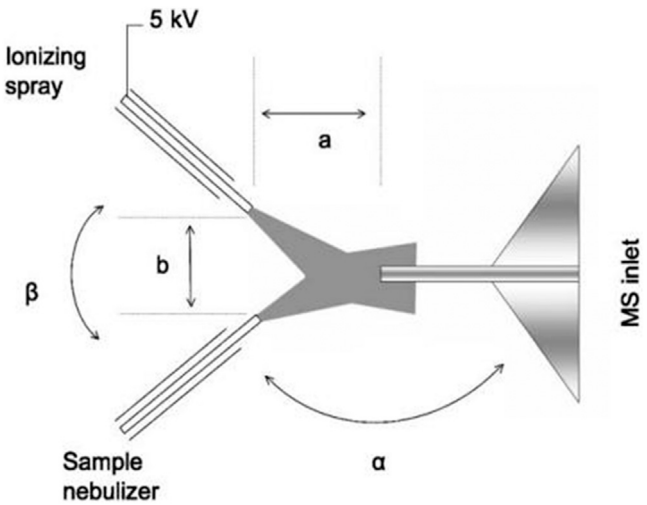

FIGURE 6 | Schematic diagram of extractive ESI (Chen et al., 2006).

change in concentration, pressure, relative density, light transmittance, and settling velocity of the suspension (Chen et al., 2005). These parameters contain information about the particle size and distribution of nanoparticles. According to this, by measuring the variation of these parameters with time, the particle size composition of nanoparticles can be reflected.

2.2.1.2 The Characteristics of Centrifugal Sedimentation

(1) The number of measurements with single measurement is large, so the statistical significance of the measurement results is clear.
(2) With the progress in technology, centrifugal sedimentation was improved to differential centrifugal sedimentation (DCS). The centrifugal sedimentation's measuring range is within 3 nm–80 μm, and it is easier to use. The analysis speed, accuracy, and repeatability were improved greatly, too.
(3) This method is an indirect measurement method and off-line measurement method.
(4) Centrifugal sedimentation is mostly applied to nanoparticles suspended in liquid, so the liquid-phase method is more widely used.

2.2.2 Atomic Force Microscopy (AFM)

Compared with other existing microscopic tools, AFM has attracted much attention for its features of high resolution, simple sample preparation, and easy operation. It has played an important role in life science, material science, and other fields, greatly promoting the development of nanotechnology and encouraging mankind to enter the nano age. International papers on the research and application of AFM have emerged one after another and have made brilliant achievements (Jie and Sun, 2005). **Figure 3** shows the structure of an AFM.

2.2.2.1 The Principle of AFM

The atomic force between atoms is a function of distance, so the surface topography of samples can be obtained by measuring the atomic force of individual atoms. AFM is the measurement of atomic forces on the surface of samples by means of probes. When the atomic force changes, the probe deforms slightly relative to the initial state and is amplified by an optical lever to a position-sensitive detector (PSD). The PSD converts the sample surface topography signal into electrical signal and records the electrical signal. Through continuous measurement, the morphology, particle size, chemical composition, and other characteristics of the samples to be measured are obtained.

2.2.2.2 The Characteristics of AFM (Chunrui et al., 2017)

(1) AFM has a high spatial resolution, and advanced AFM can even reach the sub-angstrom level, which is of great value in

the measurement of particle size and chemical composition of nanoparticles.
(2) Compared with traditional electron microscopy, AFM has no requirement for observing materials, while electron microscopy requires that the observed objects must be conductors or coated objects.
(3) Similar to other probe microscopes, AFM is suitable for measuring a single particle, but it is difficult to measure a large number of particles. Meanwhile, due to the small amount of measurement, the statistical significance of the measurement results is insufficient.
(4) AFM can work in vacuum, atmosphere, room temperature, and other different environments; the sample can even be soaked in water and other solutions without special sample preparation technology; and it causes no damage to the sample during the detection process and can carry out contact and non-contact detection.
(5) The sample can be operated by measuring the interaction force between particles and moving atoms.
(6) AFM can be used in combination with other instruments to achieve greater value. AFM-IR technology combines AFM and infrared spectrum for analysis and observation and significantly improves the spatial resolution of AFM through the chemical analysis and composition imaging capability of the infrared spectrum (Dazzi and Prater, 2017).
(7) Currently, AFM also has problems of having a slow imaging speed and low temporal resolution. But at present, research on high-speed AFM is carried out both at home and abroad, and the current advanced AFM can reach more than 10 fps. Yongho Seo et al. (2008) even improved the time resolution of AFM to 30 fps under certain conditions in their paper. It is reasonable to believe that as its frame rate increases, AFM will play an even greater role in future nanoparticle measurement applications.

2.3 The Optical-Based Detection Method

2.3.1 X-ray Scattering Techniques

The wavelength of X-ray is similar to the particle size of nanoparticles, so diffraction phenomenon is easy to occur. By analyzing the diffraction image, the information of particle size can be obtained. Currently, there are two main types of X-ray diffraction, X-ray powder diffraction (XRD) and small-angle X-ray scattering. These two methods are described in this paper separately.

2.3.1.1 The Principle of X-ray Scattering Techniques

2.3.1.1.1 XRD. The X-ray diffraction peak is related to the crystal structure of the material, and the crystal structure is directly related to the composition of the material. At the same time, the X-ray diffraction image is also related to the particle size of the nanoparticles. Therefore, the average particle size of nanoparticles can be obtained by studying the X-ray diffraction image (Li et al., 2020).

2.3.1.1.2 Small-Angle X-Ray Scattering. When the X-ray passes through the uneven density distribution of nanoparticles, the X-ray will be scattered at a small angle around the X-ray, and the scattering angle is negatively correlated with the particle size of nanoparticles. Therefore, the size and distribution of nanoparticles can be calculated by measuring the angle of scattering the X-ray.

2.3.1.2 The Characteristics of X-ray Scattering Techniques

2.3.1.2.1 XRD.

(1) XRD can measure not only particle size, but also the chemical composition of nanoparticles.
(2) XRD is a non-contact detection method, which does not affect the samples of nanoparticles and belongs to the off-line detection method.
(3) When the particle is a single crystal, the particle size is measured by this method. When grains are polycrystalline, the average grain size of a single grain can be measured by this method. Therefore, the accuracy of the XRD method for particle size measurement is not high, and it cannot identify the aggregation between particles.
(4) XRD is applicable only to the grain size evaluation of crystalline nanoparticles. So the state of the measured nanoparticles has more stringent requirements.

2.3.1.2.2 Small-Angle X-ray Scattering.

(1) Small-angle X-ray scattering deals simply with the particles to be measured and is easy to operate.
(2) Small-angle X-ray scattering has a wide measurement range, which can cover the whole particle size range of nanoparticles.
(3) Small-angle X-ray scattering has a high requirement for the morphology of the particles to be measured, and only for single spherical powder, the small-angle X-ray scattering has a high accuracy.
(4) Due to the weak X-ray on the sample to be tested and the distance between the sample and the negative, the exposure time is long and timely detection is not possible. Therefore, small-angle X-ray scattering is considered an off-line detection method.

2.3.2 Raman Spectroscopy

2.3.2.1 The Principle of Raman Spectroscopy

Raman spectroscopy is based on the principle of light scattering. When light hits an object's surface, different materials produce different Raman scattering or Raman shift. The Raman shift is related to the rotation and vibration of the material, so the Raman shift of the sample to be tested can be measured to identify the size and distribution of the particle size. For the particle size measurement of nanoparticles, it is necessary to measure the peak-to-peak offset between the grain size of nanoparticles and the conventional grain, and the difference can be used to calculate the particle size of nanoparticles.

2.3.2.2 The Characteristics of Raman Spectroscopy

(1) The Raman spectrum is the vibration spectrum of the material itself. Therefore, Raman spectroscopy is specific to the substance, which can measure both particle size and chemical composition of the substance.

(2) Raman spectroscopy is an off-line detection method. This method has high detection sensitivity and is especially suitable for one-dimensional nanomaterial detection. It is easy to operate and does not destroy the sample.

3 ONLINE DETECTION OF NANOPARTICLES

3.1 The Electrical-Based Detection Method

3.1.1 Coulter Counter

3.1.1.1 The Principle of Coulter Counter

The Coulter process works by dissolving nanoparticles in an electrolyte and passing them with the electrolyte through a small tube connected to a constant-current circuit. When it passes through the orifice tube, the internal and external resistance of the orifice tube changes instantaneously, resulting in a pulse voltage. The magnitude and number of pulse voltage are positively correlated with the size and number of nanoparticle sample. By measuring the pulse voltage, the particle size and distribution of the sample can be obtained.

3.1.1.2 The Characteristics of Coulter Counter

(1) The Coulter counter is an online detection method. In other words, nanoparticles can be detected during the preparation process, which is of great significance to adjust the preparation process. Compared with other methods, this method has obvious advantages in timeliness and repeatability with higher resolution and shorter measurement time.
(2) The particle size of nanoparticles measured by the Coulter counter is the particle size of the outer surrounding layer of nanoparticles. Therefore, for spherical solid nanoparticles, the measurement accuracy is high, but for spherical shell nanoparticles, the accuracy will be affected.
(3) The Coulter counter is suitable for nanoparticle samples with narrow particle size distribution. For samples with wide particle size distribution, the detection error is large.
(4) The particle size range measured by the Coulter counter is generally above 0.5 μm. Therefore, the measurement ability of the Coulter counter for nanoparticles with a small particle size is insufficient and needs to be improved.
(5) Usually, the measurement environment of the Coulter counter is liquid, so it is difficult to measure gas-phase nanoparticles.

3.2 The Mechanical-Based Detection Method

3.2.1 BET (Brunauer, Emmett, and Teller)

3.2.1.1 The Principle of BET

The specific surface area is the ratio of area to mass, reflecting the surface area per unit mass. As you can see by definition and by units, in general, because density is constant, the smaller the mass, the larger the specific surface area. Therefore, the measurement and comparison of the mass-specific surface area can reflect the particle size of nanoparticles. By measuring the mass-specific surface area S_ω of nanoparticles, the particle size of nanoparticles can be calculated from **Equation 1**:

$$D = \frac{6}{\rho S_\omega} \tag{1}$$

In the equation, D is the mass-specific surface area diameter; ρ is the density; and the general measurement method of S_ω is the multilayer gas adsorption. And the BET equation is

$$\frac{V}{V_m} = \frac{\kappa P}{(P_0 - P)\left[1 + (\kappa - 1)\frac{P}{P_0}\right]} \tag{2}$$

The entry mode of the sample to be tested by BET is physical adsorption of gas, which could avoid sample contamination caused by chemical adsorption. V is the volume of the adsorbed gas; V_m is the volume of gas adsorbed by the monolayer; P is the gas pressure; P_0 is the saturated gas pressure; P/P_0 is the specific pressure of adsorption; κ is y/x, where $y = (a_1/b_1)P$ and $x = a_1/b_1$; and **i** is the adsorption layer. The V_m obtained is converted to the number of adsorbed gas molecules and multiplied by the cross-sectional area A_m of an adsorbed gas molecule. The product is the specific surface area S_ω. Generally speaking, the BET method is used to measure surface area adsorption-specific pressure P/P_0 in the range of 0.05–0.35. When the adsorption-specific pressure is less than 0.05, the pressure is too small to establish multilayer physical adsorption equilibrium, or monolayer adsorption cannot even be established. However, when the adsorption-specific pressure is greater than 0.35, the capillary condensation benefit will be generated, and the multilayer physical adsorption equilibrium will be destroyed (Li et al., 2020).

3.2.1 2 The Characteristics of BET

(1) BET has become one of the most widely used and most reliable test results in the industry due to its excellent stability and operability.
(2) The measurement range of specific surface area is about 0.1–1,000 $m^2 g^{-1}$. For example, the ZrO_2 powder's particle size can be measured to 1–10 nm.

3.3 The Optical-Based Detection Method

3.3.1 Self-Mixing Interferometry

Foord et al. (1970) first applied PCS (photon correlation spectroscopy) in the study of measuring the diffusion coefficient of hemocyanin at a low concentration. After that, PCS was gradually applied to the detection of nanoparticles and gradually became the mainstream detection method. However, in the detection of high-concentration nanoparticles, due to the complex scattering of particles, the detection error of PCS is large. In order to extend the applicability of PCS, Schtzel (1990) proposed photon cross-correlation spectroscopy (PCCS) to obtain detection data by measuring the fluctuation of the intensity signals of two scattered beams with different angles over time. It could avoid the influence of nanoparticles on the measurement results. And it plays an important role in the detection of nanoparticles. In 2008, Wang and Shen (2008) from the University of Shanghai for Science and Technology

and Xuzhou Normal University improved on the basis of and proposed the self-mixing interferometry (SMI). In this method, the light source and detecting element are integrated and packaged to increase the degree of integration. Compared to traditional PCS and PCCS, this design can significantly reduce the error caused by optical path adjustment, improve the signal-to-noise ratio, and enhance the measurement accuracy.

3.3.1.1 The Principle of Self-Mixing Interferometry

The principle of self-mixing interferometry is that when the laser emits a laser and the incident light hits the Brownian nanoparticles, the light scattered by the particles will have a Doppler shift. This spectrum carries information about the size of the nanoparticles, and some of the light is fed back into the laser resonator. After the self-mixing interferometry of the reflected light and the light in the cavity, the particle size and its distribution can be obtained by measuring the light intensity and power spectrum information. SMI is illustrated in **Figure 4** (Wang and Shen, 2008).

3.3.1.2 The Characteristics of Self-Mixing Interferometry

(1) Self-mixing interferometry is greatly convenient for the calibration of the optical path because the light source and detecting element are integrated into one package and simplifies the experimental equipment.
(2) With Fourier transform, the self-mixing interferometry signal is studied in the frequency domain, which avoids the use of a digital correlator and reduces the cost of the experiment and product.
(3) The improved projection algorithm can reverse calculate more accurate particle sizes than before, and the precision is up to 60 nm in this paper.
(4) Self-mixing interferometry has a high signal-to-noise ratio and belongs to the online measurement method.

3.3.2 Laser Particle Size Analysis

Laser particle size analysis mainly uses a laser particle size analyzer, whose principle is light scattering. When the laser shines on the particle, the spatial density and particle size of the nanoparticles play a decisive role in the characteristic parameters of the scattered light. Therefore, the size and distribution of nanoparticles can be calculated by measuring the scattering light intensity and polarization degree. Static light scattering and dynamic light scattering are widely used in laser particle size analysis. However, static light scattering can only measure particle size range above the submicron level. In view of the particle size range of nanoparticles, this section focuses on dynamic light scattering.

3.3.2.1 The Principle of Dynamic Light Scattering

The theoretical basis of the dynamic light scattering method is PCS theory, which enables the laser particle size analysis to detect the particle size range of submicron. However, this leads to the inability to measure the particle size distribution of nanoparticles at the same time. The principle is as follows.

When the particle size of nanoparticles is smaller than the wavelength of the light wave, the angular distribution of the relative intensity of scattered light is no longer affected by the particle size according to the Rayleigh principle. Therefore, static light scattering cannot be used (Sui et al., 2016). The scattered light, on the other hand, has a Doppler shift due to the Brownian motion of the nanoparticles. And because of the smaller particle size of nanoparticles, Brownian motion is more intense, and the effect on the Doppler shift of the scattered light is also stronger (Guo et al., 2006). By measuring the attenuation of the autocorrelation function of the scattering light over time, the particle size information of the nanoparticles can be obtained.

3.3.2.2 The Characteristics of Dynamic Light Scattering

(1) The sample measured by a laser particle size analyzer is not affected by the state; solid, liquid, and gas states can be measured.
(2) The laser particle size analyzer can be used for online detection, which has an important guiding role in the preparation of nanoparticles.
(3) Laser particle size analysis does not destroy the original system of nanoparticles or does not interfere with the original state of samples, which makes it a nondestructive detection method.
(4) Dynamic light scattering can measure the average particle size, which cannot be measured for a single particle. Therefore, in the sample of nanoparticles with wide particle size distribution, the error is large.
(5) Dynamic light scattering is suitable for measuring submicron particle size in the measurement range of 5 nm–2 μm, while static light scattering is suitable for measuring micron particle size.

3.3.3 Improved Method About Dynamic Light Scattering

At present, dynamic light scattering is one of the few methods that can be used for online detection of gas-phase nanoparticles. However, it can only measure the average particle size of a large number of nanoparticles but cannot measure the particle size or chemical composition of a small number or even a single nanoparticle. Therefore, to obtain more detailed nanoparticle information, additional data dimensions must be introduced, and polarized light is the most feasible scheme among them. Polarized light is sensitive to the size, shape, and composition of tiny particles. At the same time, the polarized light path need not be designed separately, as long as the current dynamic light scattering light path-polarizing element can be added. At present, it has been applied to biomedicine (Xiang-Yu et al., 2019; He et al., 2021; Meng et al., 2021; Shen et al., 2021; Song et al., 2021), marine microbial detection (Wang et al., 2018; Li et al., 2020; Liu et al., 2020; Wang et al., 2020; Li et al., 2021), atmospheric detection (Li et al., 2019; Qizhi et al., 2021), etc. It is believed that with the introduction of polarized light technology, the accuracy, measurable parameters, and applicable range of the dynamic light scattering method will be greatly improved.

3.4 Other Methods With Different Principles

3.4.1 Ultrasonic Attenuation

3.4.1.1 The Principle of Ultrasonic Attenuation

When the ultrasonic wave propagates in a uniform suspension, it will change with the change of the concentration and particle size

of nanoparticles in the tested medium. Ultrasonic transmission is sensitive to the viscosity, temperature, magnetism, and bubbles of the transmission medium, so ultrasonic transmission by the medium will produce scattering loss, viscous inertia dissipation loss, and heat loss, which is called ultrasonic attenuation (Su et al., 2008). The particle size and distribution of nanoparticles can be detected by calculating the ultrasonic attenuation through the theoretical model.

3.4.2 The Characteristics of Ultrasonic Attenuation

(1) Ultrasonic attenuation requires ultrasonic sensors to have full sealing, high permeability, wear resistance, corrosion resistance, and other characteristics.
(2) As an online measurement method, the ultrasonic attenuation spectrum can be measured at the same time as nanoparticles are prepared to ensure the consistency and repeatability of nanoparticles. The current particle size detection range can be up to.
(3) At present, there are many models of ultrasonic attenuation, among which the core–shell model is more suitable for the measurement of the suspension of high-concentration nanoparticles, and the ECAH model is more suitable for the online detection of the particle size of low-concentration nanoparticles.
(4) The ultrasonic attenuation spectrum method needs to dissolve nanoparticles in liquid, so it is suitable for preparing nanoparticles by the liquid method.

3.4.2 Mass Spectrometry

The principle of the method using a mass spectrometer as a means of detection is much the same but can be subdivided depending on the feeding method. In this paper, the principle and characteristics of mass spectrometer detection will be introduced, along with several different feeding methods as a separate detection method. **Figure 5** shows the structure of a secondary ion mass spectrometer:

3.4.2.1 The Principle of Mass Spectrometry

Mass spectrometers are used to measure the particle size of nanoparticles in gases. According to aerodynamics, nanoparticles are sucked into a mass spectrometer by atmospheric pressure. The nanoparticles with a set value of m/z were screened out by speed detection devices such as electric field and laser. Then the particles are decomposed into atoms or molecular ions by collision and other methods. After that, these smaller particles will form ion spectra in the mass spectrometer. The particle size and distribution of the nanoparticles can be obtained by analyzing their physical properties such as mass and shape.

3.4.2.2 The Characteristics of Mass Spectrometry

(1) The particle size range determined by mass spectrometry is generally 1–100 nm. It can measure the particle size of nanoparticles with a small particle size, and it also has the upper limit of measurement.
(2) Mass spectrometry is an online detection method. So it can make up for the timeliness information that cannot be obtained by off-line detection methods such as electron microscopy.
(3) In mass spectrometry, the particles need to be decomposed into atoms or ion particles to be measured, so it has a certain destructive effect on the sample.
(4) Different methods are used to measure the detection speed of nanoparticles with different particle sizes. For example, the larger the particle size is, the heavier the mass will be. When the particle size is bigger than 100 nm, the effect of speed detection using electric field and laser will decrease (Motian, 2012).

3.4.3 Aerodynamic Lens

3.4.3.1 The Principle of Aerodynamic Lens

The aerodynamics lens uses a differential air pressure system as a particle sampling device. The differential air pressure system can make the sample to be tested have a smaller particle beam dispersion angle and higher air inlet efficiency, which can significantly improve the instrument's detection ability. Since the inertia of particles is much greater than that of the surrounding gas molecules, particles tend to converge towards the axis of the lens after multiple lens conversions, while the gas molecules diffuse around during multiple dispersions. For this method, an aerosol mass spectrometer and single particle mass spectrometer are commonly used. When the nanoparticles to be measured into the instrument after the use of a mass spectrometer to achieve the chemical composition of nanoparticle detection.

3.4.3.2 The Characteristics of Aerodynamic Lens

(1) As an online detection method, it can obtain real-time data support and has guiding significance for the preparation of nanoparticles. At the same time, it could serve as a detection method for the preparation of nanoparticles under special conditions.
(2) The method is mainly discussed around the intake process. The traditional aerodynamic lens has a transmission effect for 30–500 nm nanoparticles. However, when the particle size is less than 30 nm, due to the gas expansion and the flow rate not being stable, nanoparticles will also be like air molecules, which cannot gather and diverge around after passing through the lens, and divergence angle and intake efficiency will be greatly affected. Lee et al. (2009) proposed a design scheme of an aerodynamic lens composed of three convergent and divergent holes. Through numerical simulation, his solution can focus the nanoparticles stably under the condition that the airflow is stable and no shock wave is formed. However, in practical application, various conditions are more complex, and the method of Lee et al. should be further improved.
(3) A mass spectrometer is the detection method of an aerodynamics lens. Therefore, it causes certain damage to the samples to be tested and is not suitable for the preparation and detection of nanoparticles for the purpose of use.

3.4.4 Enrichment of Charged Particles

3.4.4.1 The Principle of Enrichment of Charged Particles

According to the principle of electricity, the electric field of specific intensity can screen and enrich charged particles. Therefore, charged nanoparticles can be aggregated in the range below 5 nm, where the aggregation degree of the aerodynamics lens does not work, and they can be detected at the range of 6–20 nm. The method mainly consists of three steps: electrification, enrichment, and detection of nanoparticles. That is, nanoparticles are electrified by an electric charge, and then the particles are concentrated on the wire by means of high voltage. Then the metal wire is moved to the ionization zone, and the enriched particles are thermally volatilized by heating. Finally, these particles will be detected by chemical ionization mass spectrometry.

3.4.4.2 The Characteristics of Enrichment of Charged Particles

(1) The enrichment of charged particles mainly solves the problem of the decrease in the accuracy of the aerodynamics lens in the range below 50 nm and being able to detect at the range of 6–20 nm.
(2) The enrichment of charged particles is mainly used by two kinds of mass spectrometry: one is thermal desorption chemical ionization mass spectroscopy (TD-CIMS) and the other is thermal desorption ion drift chemical ionization mass spectroscopy (TD-ID-CIMS). At present, the main reason that hinders the development of the enrichment of charged particles is that the smaller the particle size is, the more difficult it will be for the charged electric apparatus to charge it, leading to the inability to carry out the next enrichment and measurement. Therefore, Chen et al. (2019) developed a soft X-ray single-stage charger that could replace the charged electric appliance to better charge the nanoparticles to be measured. Meanwhile, Kreisberg et al. (2018) developed a new charged device. By supersaturating the water vapor, the nanoparticles absorb water molecules, increasing their size and thus reducing the difficulty of charging.
(3) The enrichment of charged particles is based on the detection technology of mass spectrometry; it will produce certain damage to the sample. So it is not suitable for chemical composition detection of nanoparticles prepared in small quantities for application purposes.

3.4.5 Electrospray Ionization (ESI)

3.4.5 1 The Principle of ESI

ESI is used to resolve a substance by causing its molecules to form charged ions. The chemical composition of particle was obtained by a mass spectrometer. It is worth mentioning that this method is often used to measure the composition of liquid nanoparticles.

3.4.5.2 The Characteristics of ESI

(1) Since the ESI method can only detect the ionization of liquid substances, Chen et al. (2006) developed a new electrospray ion source (EESI). It has two separate spray ports, one for the particle spray and the other for the charged droplets, which collide with each other to extract their nanoparticles into the charged droplets. Thus, a new method—electrospray extraction ionization—was developed. It can detect solid, liquid, and gas substances in three states without sample pretreatment. It also can detect the chemical composition of nanoparticles as small as 20 nm. The pictures in their paper are shown in **Figure 6**.
(2) ESI is also used as the final determination of chemical composition by mass spectrometry. Therefore, it is not suitable for chemical composition detection of nanoparticles prepared in small quantities for application purposes.

4 CONCLUSION

Since Feynman put forward the concept of a nanometer at the end of the 1950s, nanotechnology has been the forefront and hot spot of human scientific research. The emergence of nanomaterials has changed the human understanding of materials, expanded the application scenarios of materials, and become one of the pillars of modern civilization. At present, gas-phase nanoparticles have become an important branch of nanotechnology. However, due to the differences in nanoparticle preparation of the different detection methods, progress in their development has lagged. For example, some methods cannot detect a single particle, some detection methods have insufficient accuracy, and some methods of chemical composition measurement are destructive to samples. These have slowed down the development of vapor-phase nanoparticle technology and even the whole nanotechnology and affected the nanotechnology development prospect. Therefore, it is important to develop the detection technology of gas-phase nanoparticles. At present, the most widely used method for online particle size measurement is the optical method, which uses the scattering or diffraction of light and other principles for measurement. However, the measurement based on the optical principle has advantages in measuring the average particle size of a large number of particles, but it is powerless to measure the particle size of a small number or even a single particle. In the future, more accurate and comprehensive measurement can be achieved by adding measurement dimensions and comprehensively utilizing optical parameters such as intensity, wavelength, phase, and polarized light. At present, the most widely used detection technology for chemical composition is based on mass spectrometry, but the advantages and disadvantages of mass spectrometry are very obvious. The advantages are that the samples can be decomposed, the detection of chemical composition is more accurate, and the chemical composition of gas-phase nanoparticles can be detected, but the disadvantage is also very serious, such as destruction of the sample, which limits it to the detection of only a small amount of nanoparticles prepared for experimental purposes. So it is of great significance to develop online detection for particle size and chemical composition measurement of nanoparticles at present. This will be the basis for the next step in nanotechnology and is worth the attention of researchers.

AUTHOR CONTRIBUTIONS

XSZ is responsible for literature research and sorting. XLZ is responsible for professional guidance. YW is responsible for overall guidance and thesis revision. HSL, XRH, JX, and JJT are responsible for the revision of the second Manuscript.

FUNDING

This work was supported by the Natural Science Foundation of Shandong Province, China, No. ZR2020QA078, and National Natural Science Foundation of China, No. 12005110.

REFERENCES

Atchudan, R., Perumal, S., Karthikeyan, D., Pandurangan, A., and Lee, Y. R. (2015). Synthesis and Characterization of Graphitic Mesoporous Carbon Using Metal-Metal Oxide by Chemical Vapor Deposition Method. *Microporous Mesoporous Mater.* 215, 123–132. doi:10.1016/j.micromeso.2015.05.032

Burgoyne, T. W., Hieftje, G. M., and Hites, R. A. (1997). Design and Performance of a Plasma-Source Mass Spectrograph. *J. Am. Soc. Mass. Spectrom.* 8 (4), 307–318. doi:10.1016/S1044-0305(96)00290-5

Chen, H., Venter, A., and Cooks, R. G. (2006). Extractive Electrospray Ionization for Direct Analysis of Undiluted Urine, Milk and Other Complex Mixtures without Sample Preparation. *Chem. Commun.* 42 (19), 2042–2044. doi:10.1039/b602614a

Chen, W. P., Dong, X. R., Wang, X. D., and Zhi-Gang, X. U. (2005). Different Methods for Nano-Particle Size Determination. *J. Jinan Uniuersity* 19, 208–209. doi:10.13349/j.cnki.jdxbn.2005.03.006

Chen, X., Jiang, J., and Chen, D.-R. (2019). A Soft X-ray Unipolar Charger for Ultrafine Particles. *J. Aerosol Sci.* 133, 66–71. doi:10.1016/j.jaerosci.2019.04.010

Chunrui, S., Bowen, Y. U., Daitao, K., Bingbing, L., Lizhen, H., Songshan, M. A., et al. (2017). Structure and thermal Stability of Co/c Core/shell Nanoparticles Fabricated by Chemical Vapor Deposition. *Mater. Sci. Eng. Powder Metall.* 22 (2), 270–275. doi:10.3969/j.issn.1673-0224.2017.02.018

Cui, S., Gao, Z., Shen, X., and Lin, B. (2010). Preparation of Ultrafine Mg Powders with Evaporation and Condensation Method. *J. Univ. Sci. Technol. Beijing* 32 (4), 484–487. doi:10.13374/j.issn1001-053x.2010.04.021

Dazzi, A., and Prater, C. B. (2017). AFM-IR: Technology and Applications in Nanoscale Infrared Spectroscopy and Chemical Imaging. *Chem. Rev.* 117 (7), 5146–5173. doi:10.1021/acs.chemrev.6b00448

Dong, J., Yang, H., Chun, L. I., and Jiang, H. (2003). *Study on Process Conditions of Preparation of Sio_2 Nanoparticles by Gas Phase Combustion*. Guizhou, China: Huaxue Shijie (Chemical World).

Feist, A., Echternkamp, K. E., Schauss, J., Yalunin, S. V., Schäfer, S., and Ropers, C. (2015). Quantum Coherent Optical Phase Modulation in an Ultrafast Transmission Electron Microscope. *Nature* 521 (7551), 200–203. doi:10.1038/nature14463

Foord, R., Jakeman, E., Oliver, C. J., Pike, E. R., Blagrove, R. J., Wood, E., et al. (1970). Determination of Diffusion Coefficients of Haemocyanin at Low Concentration by Intensity Fluctuation Spectroscopy of Scattered Laser Light. *Nature* 227 (5255), 242–245. doi:10.1038/227242a0

Guo, Y. C., Wang, Y., Gao, C., and Deng, D. M. (2006). Particle Sizing with Dynamic Light Scattering. *J. Chongqing Univ. (Natural Sci. Edition)* 29 (2), 35–107. doi:10.1088/0253-6102/45/2/018

He, C., He, H., Chang, J., Chen, B., Ma, H., and Booth, M. J. (2021). Polarisation Optics for Biomedical and Clinical Applications: a Review. *Light Sci. Appl.* 10 (1), 1–20. doi:10.1038/s41377-021-00639-x

James, E. M., Yang, Y., Lin, M., Gubbens, A. J., and Petric, P. (2010). Apparatus and Method for Obtaining Topographical Dark-Field Images in a Scanning Electron Microscope. U.S. Patent No. 7,714,287. Washington, DC U.S. Patent and Trademark Office.

Jia, J. (2004). Sputtering Technology of Nano Thin Films. *Semiconductor Technol.* 29 (7), 70–73. doi:10.1088/1009-0630/6/5/011

Jie, Z., and Sun, R. (2005). *Introduction to Atomic Force Microscope and its Manipulation*. Xi'an, China: Life Science Instruments.

Kreisberg, N. M., Spielman, S. R., Eiguren-Fernandez, A., Hering, S. V., Lawler, M. J., Draper, D. C., et al. (2018). Water Condensation-Based Nanoparticle Charging System: Physical and Chemical Characterization. *Aerosol Sci. Technol.* 52 (10), 1167–1177. doi:10.1080/02786826.2018.1503640

Lee, K.-S., Kim, S., and Lee, D. (2009). Aerodynamic Focusing of 5-50nm Nanoparticles in Air. *J. Aerosol Sci.* 40 (12), 1010–1018. doi:10.1016/j.jaerosci.2009.09.004

Li, D., Chen, F., Zeng, N., Qiu, Z., He, H., He, Y., et al. (2019). Study on Polarization Scattering Applied in Aerosol Recognition in the Air. *Opt. Express* 27 (12), A581–A595. doi:10.1364/OE.27.00A581

Li, J., Liao, R., Tao, Y., Zhuo, Z., Liu, Z., Deng, H., et al. (2020). Probing the Cyanobacterial Microcystis Gas Vesicles after Static Pressure Treatment: A Potential *In Situ* Rapid Method. *Sensors* 2015, 4170. doi:10.3390/s20154170

Li, R. Z., Ma, Y. H., and Lu, C. (2020). Study on the Specific Surface Area Determination of Alumina by BET Method. *Light Met.* 9, 13–16. doi:10.13662/j.cnki.qjs.2020.09.003

Li, J., Wang, H., Liao, R., Wang, Y., Liu, Z., Zhuo, Z., et al. (2021). Statistical Mueller Matrix Driven Discrimination of Suspended Particles. *Opt. Lett.* 46 (15), 3645–3648. doi:10.1364/OL.433870

Ling, Y., and Zhong, J. (2018). The Principle and Application of Scanning Electron Microscope. *Shandong Chem. Ind.* 47, 78–79. doi:10.19319/j.cnki.issn.1008-021x.2018.09.033

Liu, T. G., Zhang, F., and Meng, Z. (2005). *Optical Technique*. Tianjin, China.

Liu, Z., Liao, R., Ma, H., Li, J., Leung, P. T. Y., Yan, M., et al. (2020). Classification of marine Microalgae Using Low-Resolution Mueller Matrix Images and Convolutional Neural Network. *Appl. Opt.* 59 (31), 9698–9709. doi:10.1364/AO.405427

Mäkelä, J. M. (2002). Biogenic Iodine Emissions and Identification of End-Products in Coastal Ultrafine Particles durin Nucleation Bursts. *J. Geophys. Res.* 107 (D19), PAR 14-1–PAR 14-14. doi:10.1029/2001JD000580

Meng, R., Shao, C., Li, P., Dong, Y., Hou, A., Li, C., et al. (2021). Transmission Mueller Matrix Imaging with Spatial Filtering. *Opt. Lett.* 46 (16), 4009–4012. doi:10.1364/OL.435166

Motian, Z. (2012). *Recent Technology Progress of Isotope Mass Spectrometer*. Modern Scientific Instruments, 5.

Muzi, C., Weijian, G., Yong, Z., and Shane, F. (2013). Structure and Maintenance of Scanning Electron Microscope. *Anal. Instrumentation* 4, 91–93. doi:10.3969/j.issn.1001-232x.2013.04.021

Qizhi, X., Zeng, N., Wei, G., Guo, J., He, Y., and Ma, H. (2021). Real Time and Online Aerosol Identification Based on Deep Learning of Multi-Angle Synchronous Polarization Scattering Indexes. *Opt. Express* 29 (12), 18540–18564. doi:10.1364/OE.426501

Schtzel, K. (1990). Noise on Photon Correlation Data: I. Auto-Correlation. *Quan. Opt. J. Eur. Opt. Soc. B* 2 (6), 467–468. doi:10.1088/0954-8998/2/6/505

Seo, Y., Choi, C. S., Han, S. H., and Han, S.-J. (2008). Real-time Atomic Force Microscopy Using Mechanical Resonator Type Scanner. *Rev. Scientific Instr.* 79 (10), 103703. doi:10.1063/1.2999579

Shen, Y., Huang, R., He, H., Liu, S., Dong, Y., Wu, J., et al. (2021). Comparative Study of the Influence of Imaging Resolution on Linear Retardance Parameters Derived from the Mueller Matrix. *Biomed. Opt. Express* 12 (1), 211–225. doi:10.1364/BOE.410989

Song, J., Zeng, N., Guo, W., Guo, J., and Ma, H. (2021). Stokes Polarization Imaging Applied for Monitoring Dynamic Tissue Optical Clearing. *Biomed. Opt. Express* 12 (8), 4821–4836. doi:10.1364/BOE.426653

Su, M., Xue, M., Cai, X., Shang, Z., and Xu, F. (2008). Particle Size Characterization by Ultrasonic Attenuation Spectra. *Particuology* 6 (4), 276–281. doi:10.1016/j.partic.2008.02.001

Sui, X., Li, Y., and Hu, X. (2016). Development Progress and Key Technologies of Laser Particle Size Analyzer. *J. Electron. Meas. Instrumentation* 30 (10), 1449–1459. doi:10.13382/j.jemi.2016.10.001

Wang, H., and Shen, J. (2008). Size Measurement of Nano-Particles Using Self-Mixing Effect. *Chin. Opt. Lett.* 6 (11), 871–874. doi:10.3788/col20080611.0871

Wang, R. J. (2018). *Methods and Standardization of Particle Size Testing of Nanomaterials*. Chizhou, China: Anhui Chemical Industry.

Wang, Y., Dai, J., Liao, R., Zhou, J., Meng, F., Yao, Y., et al. (2020). Characterization of Physiological States of the Suspended marine Microalgae Using Polarized Light Scattering. *Appl. Opt.* 59 (5), 1307–1312. doi:10.1364/AO.377332

Wang, Y., Liao, R., Dai, J., Liu, Z., Xiong, Z., Zhang, T., et al. (2018). Differentiation of Suspended Particles by Polarized Light Scattering at 120°. *Opt. Express* 26 (17), 22419–22431. doi:10.1364/OE.26.022419

Xiang-Yu, S., Yong, W., Ran, L., Shu-Qing, S., and Hui, M. (2019). Use Polarization Light Scattering to Detect the Cancer Cell. *Prog. Biochem. Biophys.* 46 (12), 1196–1201. doi:10.16476/j.pibb.2019.0045

Yamaguchi, S., Iizumi, T., Komuro, O., Morokuma, H., Maeda, T., Arima, J., et al. (2005). *Scanning Electron Microscope*. Tokyo, Japan: US The Agent is Blank Rome LLP (Washington, DC, US).

Yang, H., Li, J., Zhang, Y., Ma, C., and Li, J. (2014). Modern Transmission Electron Microscopy and its Application to Multiferroic Materials. *Physics* 43 (2), 105–116. doi:10.7693/wl20140204

Yin, Y. H., and Liu, W. P. (2006). Properties, Preparation and Evaluation of Nanometer Particle. *J. Guangdong Non-Ferrous Met.* 16, 113–114. doi:10.3969/j.issn.1673-9981.2006.02.009

Yu, H. L., Huang, S. Z., Lin, W., and Chen, W. (2005). WO_3 Nanosized Gas Sensitive Powder Synthesized by Gas-State Reaction. *J. Transcluction Technol.* 19, 54–55. doi:10.3969/j.issn.1004-1699.2005.02.029

Zhang, D., He, K., Zhang, S., Yang, Y., Zhou, T., Zhang, X., et al. (2002). *The Development for Atomic Force Microscopy Recently and the Brief Introduction of Application*. Beijing, China: Modern Instruments.

Zheng, Q. G. (2018). *Present Situation and Consideration of the Development of Coal Olefin Industry in china*. Huainan, China: Anhui Chemical Industry.

Conflict of Interest: The authors declare that the research was conducted in the absence of any commercial or financial relationships that could be construed as a potential conflict of interest.

Publisher's Note: All claims expressed in this article are solely those of the authors and do not necessarily represent those of their affiliated organizations, or those of the publisher, the editors, and the reviewers. ***Any product that may be evaluated in this article, or claim that may be made by its manufacturer, is not guaranteed or endorsed by the publisher.

Copyright © 2022 Zhang, Zhao, Li, Hao, Xu, Tian and Wang. This is an open-access article distributed under the terms of the Creative Commons Attribution License (CC BY). The use, distribution or reproduction in other forums is permitted, provided the original author(s) and the copyright owner(s) are credited and that the original publication in this journal is cited, in accordance with accepted academic practice. No use, distribution or reproduction is permitted which does not comply with these terms.

frontiers in Chemistry

ORIGINAL RESEARCH
published: 08 March 2022
doi: 10.3389/fchem.2022.845206

Highly Efficient and Stable CdZnSeS/ZnSeS Quantum Dots for Application in White Light-Emitting Diode

Xi Chen[1,2], Jingzhou Li[3], Yichi Zhong[3], Xin Li[2,3], Mingzhong Pan[3]*, Hongxing Qi[1,2,3]*, Hongxing Dong[3,4] and Long Zhang[3,4]*

[1]Shanghai Institute of Technical Physics, Chinese Academy of Sciences, Shanghai, China, [2]University of Chinese Academy of Sciences, Beijing, China, [3]Hangzhou Institute for Advanced Study, University of Chinese Academy of Science, Hangzhou, China, [4]Shanghai Institute of Optics and Fine Mechanic, Chinese Academy of Sciences, Shanghai, China

Semiconductor quantum dots (QDs) are a promising luminescent phosphor for next-generation lightings and displays. In particular, QD-based white light-emitting diodes (WLEDs) are considered to be the candidate light sources with the most potential for application in displays. In this work, we synthesized quaternary/ternary core/shell alloyed CdZnSeS/ZnSeS QDs with high bright emission intensity. The QDs show good thermal stability by performing high temperature-dependent experiments that range from 295 to 433 K. Finally, the WLED based on the CdZnSeS/ZnSeS QDs exhibits a luminous efficiency (LE) of 28.14 lm/W, an external quantum efficiency (EQE) of 14.86%, and a warm bright sunlight close to the spectrum of daylight (Commission Internationale de l'éclairage (CIE) coordinates 0.305, 0.371). Moreover, the photoluminescence (PL) intensity, LE, EQE, and correlated color temperature (CCT) of as-prepared QD WLED remained relatively stable with only slight changes in the luminescence stability experiment.

Keywords: CdZnSeS/ZnSeS, quantum dots, light-emitting diode, stability, white light-emitting diodes

OPEN ACCESS

Edited by:
Siwei Zhang,
Hong Kong University of Science and Technology, Hong Kong SAR, China

Reviewed by:
Shaocong Hou,
Wuhan University, China
Zheng Zhao,
The Chinese University of Hong Kong, China

****Correspondence:***
Jingzhou Li
lijingzhou@ucas.ac.cn
Mingzhong Pan
mzpan@ucas.ac.cn
Hongxing Qi
qihongxing@ucas.ac.cn

Specialty section:
This article was submitted to Nanoscience, a section of the journal Frontiers in Chemistry

Received: *29 December 2021*
Accepted: *24 January 2022*
Published: *08 March 2022*

Citation:
Chen X, Li J, Zhong Y, Li X, Pan M, Qi H, Dong H and Zhang L (2022) Highly Efficient and Stable CdZnSeS/ZnSeS Quantum Dots for Application in White Light-Emitting Diode. Front. Chem. 10:845206. doi: 10.3389/fchem.2022.845206

INTRODUCTION

Semiconductor quantum dots (QDs) have shown emerging significant promise as solid-state lightings and displays (Li et al., 2020; Zvaigzne et al., 2020), sensors (Koeppel et al., 2007; Liang et al., 2021), biomedicine (Zvaigzne et al., 2016; Pashazadeh-Panahi and Hasanzadeh, 2019), biological labeling (Bai et al., 2020), solar cell (Xu T. et al., 2021; Ostadebrahim and Dehghani, 2021), and laser physics (Nautiyal et al., 2021; Tsuji et al., 2021) owing to their superior optoelectronic properties such as high photoluminescence (PL) quantum yield (QY) (PLQY), narrow emission bandwidth, size-controlled tunable emission wavelength, and high photochemical stability and durability (Zhang et al., 2015; Li Q. et al., 2016; Harris et al., 2016; Leach and Macdonald, 2016; Giansante and Infante, 2017; Owen and Brus, 2017; Ghosh and Manna, 2018). In particular, QDs are considered to be the candidate materials with the most potential for application in the next generation of lightings and displays (Moon and Chae, 2020; Fang et al., 2021; Kıbrıslı et al., 2021; Li et al., 2021; Yuan et al., 2021). As the core materials of light-emitting diode (LED) devices based on the QDs, high luminescence efficiency and stable luminescence properties are one of the crucial factors for large-scale commercialization. However, when QDs are irradiated by strong light for a long time or the temperature of the QD device is high due to the resistance of the electric circuit, the brightness of the QDs often becomes unstable or even dim. Intense efforts have been carried out to solve the stability of the QD device by changing the surface composition, structure, ligand, solvent, etc. (Xie et al., 2018; Li et al., 2019; Zhou et al., 2019; Xu Y. et al., 2021).

Among various QDs, II–VI compounds have attached extensive interest, such as CdSe, CdZn, and CdZnSe. To passivate non-radiative surface states and extend the emission spectral coverage, coating with another semiconductor shell with a relatively wide bandgap is one of the alternative means (Regulacio and Han, 2010; Jia and Tian, 2014). Especially, multicomponent alloy QD materials have attracted more and more attention owing to their excellent stability and optical properties. First, the ternary alloyed QDs, for example, CdZnS (Liu et al., 2013) and CdZnSe (Sheng et al., 2014), can be prepared. But the emission peaks of the ternary CdZnS or CdZnSe QDs are limited from 400 to 620 nm, which restricts them from achieving high color rendering index (CRI) for a white LED (WLED). Several groups (Adegoke et al., 2016; Nasrin et al., 2020) reported water-soluble quaternary/ternary core/shell alloyed CdZnSeS/ZnSeS QDs via tuning and controlling the sulfur molar fraction (ternary shell layer). The QDs exhibited a remarkable PLQY of 36%–98% and good stability. However, systematic studies on the thermal stability of the quaternary alloy QDs have been relatively rare, and the high-quality WLEDs based on the multicomponent alloy QDs still need to be further explored.

Here, the quaternary/ternary alloyed CdZnSeS/ZnSeS QDs with two different emission colors were synthesized by the thermal injection method. In temperature-dependent experiments, the QDs show good thermal stability, with the redshift of only 36.33 meV from 295 to 433 K. The WLED based on the prepared CdZnSeS/ZnSeS QDs exhibits excellent optical performances and high luminous stability. We demonstrate the superior optical properties of quaternary/ternary alloyed CdZnSeS/ZnSeS QDs and show the prospect as WLED luminescent material.

EXPERIMENTAL

Similar to the previously reported synthesis procedure, the quaternary/ternary alloyed CdZnSeS/ZnSeS QDs were fabricated by the hot-injection method (Adegoke et al., 2016). First, a mixture of 1.3 g of CdO, 0.6 g of hexadecylamine (HAD), 50 ml of octadecene (ODE), and 30 ml of oleic acid (OA) was loaded into a 3-neck flask, which was stirred and heated to 280°C under N_2. As the temperature of the solution approached 260°C, trioctylphosphine (TOP) (2.23 ml) and Se/TOP (12 ml) precursors were injected into the Cd-HAD-OA solution to initiate the nucleation and growth of the binary CdSe seeds. Furthermore, the precursors of Se/TOP (12 ml), ZnO/OA (20 ml), and S/trioctylphosphine oxide (TOPO) (50 ml) were added into the complex solution above to initiate the nucleation and growth of the quaternary CdZnSeS QDs in succession. The solutions were taken at different times to record UV–Vis absorption and PL emission spectra of the QDs. After the alloyed core QDs were achieved, a solution of ZnO, S/TOP, and Se/TOP precursors was added swiftly for the overcoating of the ternary ZnSeS shell layer. The obtained QDs in crude solution were separated by centrifuging. After centrifugation, the quaternary/ternary alloyed CdZnSeS/ZnSeS QDs were redispersed in toluene.

The LED chip with the emission peak at 385 nm was used for the fabrication of WLED. The as-prepared green-emitting and red-emitting CdZnSeS/ZnSeS QDs (15 mg/ml) were mixed homogeneously with polymethyl methacrylate (PMMA) (0.1 mg/ml, dissolve into toluene). To avoid self-absorption of green emission light, the PMMA solution containing the red QDs was first coated on the LED chip, and then the mixture with the green QDs was deposited. At the same time, each step was cured at 60°C for 10 min.

Micro-morphologies of the CdZnSeS/ZnSeS QDs were observed via transmission electron microscopy (TEM) (Talos F200X G2, Thermo Fisher Scientific, Waltham, MA, USA). The absorption spectra were recorded at room temperature ranging from 300 to 800 nm using a UV–Vis spectrophotometer (V-770, JASCO, Oklahoma City, OK, USA). The PL spectral and PL delay curves were measured on a steady-state and time-resolved PL spectrometer (FLS1000+FS5). The temperature-dependent PL experiments were performed using a fluorescence spectrometer (FluoroMax-4) with a high-temperature fluorescence controller (TAP-02) at the temperature range from 295 to 433 K. The PLQY, luminous efficiency (LE), external quantum efficiency (EQE), emission spectrum, correlated color temperature (CCT), and Commission Internationale de l'éclairage (CIE) of QD WLED were studied systematically.

RESULT AND DISCUSSION

As shown in **Figures 1A–E**, the quaternary/ternary alloyed CdZnSeS/ZnSeS QDs exhibited good monodispersion and a nearly spherical shape. Nano Measure software was used to estimate the particle size distribution of the sample. The size of the green CdZnSeS/ZnSeS QDs is concentrated at about 7 nm (**Figures 1A,B**). The size of the red CdZnSeS/ZnSeS QDs is about 9 nm (**Figures 1D,E**). **Figures 1C,F** show the absorption spectra and PL emission spectra at room temperature of CdZnSeS/ZnSeS QDs. Here, the band-edge absorption peak of the green QDs was 513 nm (2.41 eV). The PL spectrum showed a full width at half maximum (FWHM) of about 36 nm (160 meV) and was centered at 532 nm (2.33 eV), which corresponded to a non-resonant Stokes shift of 19 nm (80 meV). The band-edge absorption peak of the red QDs was 595 nm (2.08 eV). The PL spectrum showed an FWHM of about 37 nm (123 meV) and was centered at 613 nm (2.02 eV), which corresponded to a non-resonant Stokes shift of 18 nm (60 meV). As shown in the inset of **Figures 1C,F**, the emitting light of the CdZnSeS/ZnSeS QDs exhibits bright light. The PLQY of the QDs is measured to be 63% (green QDs) and 51% (red QDs). **Figure 2** shows representative PL decay curves of the green QDs and red QDs. The results are fitting based on biexponential decay functions, for which the calculated average decay time of the green QDs is 27.98 ns, and the red QDs is 28.02 ns.

To investigate the thermal stability of the CdZnSeS/ZnSeS QDs, we performed variable temperature experiments using a high-temperature fluorescence controller at the range from 295

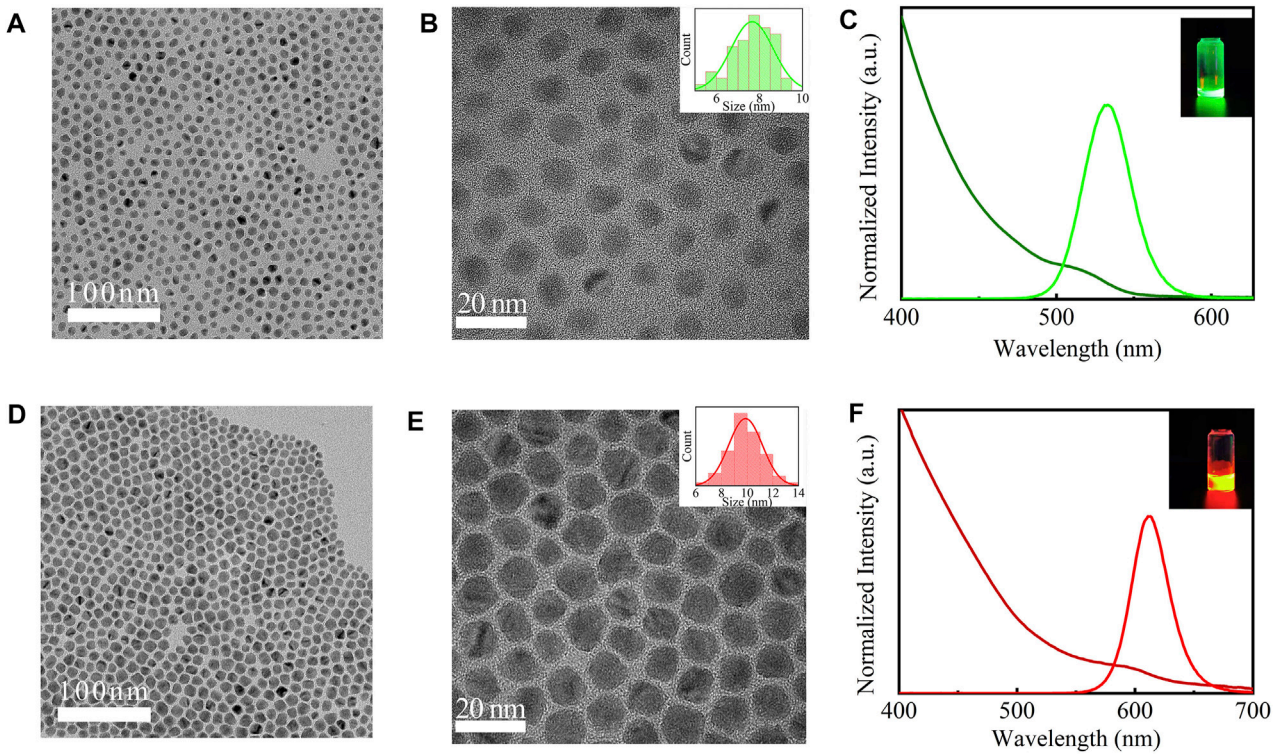

FIGURE 1 | TEM images of the CdZnSeS/ZnSeS QDs. **(A,B)** CdZnSeS/ZnSeS QDs at green emission. **(D,E)** CdZnSeS/ZnSeS QDs at red emission. **(C** and **F)** PL and UV–Vis absorption spectra for the QDs at room temperature. TEM, transmission electron microscopy; QDs, quantum dots; PL, photoluminescence.

to 433 K. The PL spectrum was measured by fluorescence spectrometer with an excitation light source at 361 nm. **Figures 3A,B** show the temperature-dependent PL spectrum of the CdZnSeS/ZnSeS QDs. We can find that the emission peaks have redshift with the increase of temperature. The PL intensities of the two samples decreased significantly with the increase in the temperature. At the same time, the broadening of spectra was observed. As shown in **Figure 3A**, the PL intensity of the green CdZnSeS/ZnSeS QDs at 433 K is 91.1% lower than that at 295 K. The redshift is 32.26 meV from 295 to 433 K. As shown in **Figure 3B**, the PL intensity of the red CdZnSeS/ZnSeS QDs at 433 K is 92.4% lower than that at 295 K. However, the redshift of the red QDs is basically the same as that of green QDs, from 295 to 433 K. According to the PL emission–excitation intensity relationship, the small redshift of the samples with the increase of temperature implies that the quaternary/ternary alloyed CdZnSeS/ZnSeS QDs have a stronger excitonic character with fewer defect states (Chen et al., 2019; Hien et al., 2020), which demonstrated that the synthesized samples have high quality.

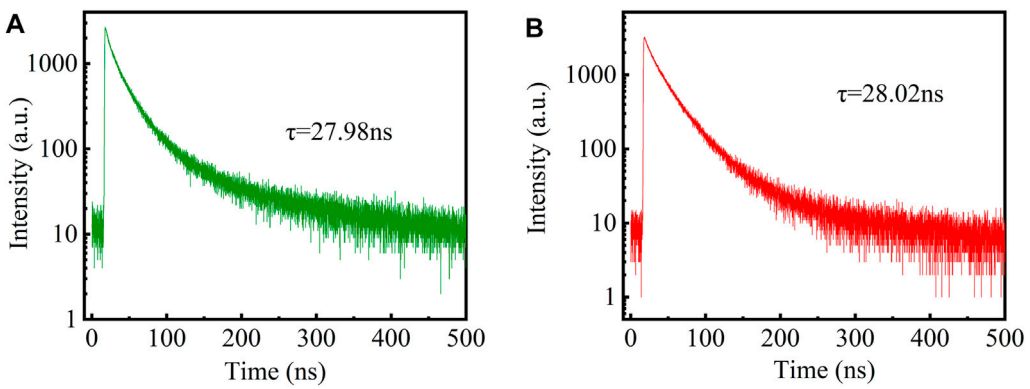

FIGURE 2 | PL decay curves of the CdZnSeS/ZnSeS QDs at room temperature. **(A)** Green QDs. **(B)** Red QDs. PL, photoluminescence; QDs, quantum dots.

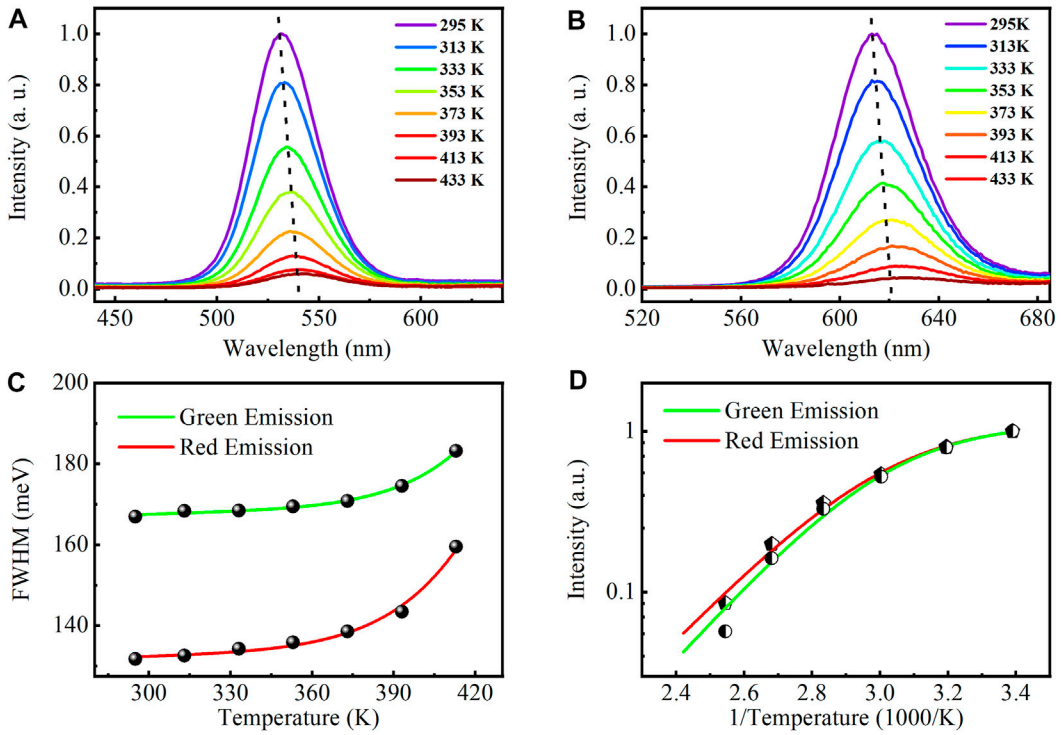

FIGURE 3 | Photoluminescence spectra of the CdZnSeS/ZnSeS QDs at various temperatures (T = 295 K–433 K). **(A)** CdZnSeS/ZnSeS QDs at green emission. **(B)** CdZnSeS/ZnSeS QDs at red emission. Temperature-dependent change of **(C)** FWHM and **(D)** intensity. QDs, quantum dots; FWHM, full width at half maximum.

The exciton–phonon coupling of the quaternary/ternary alloyed CdZnSeS/ZnSeS QDs is studied by analyzing the FWHM energy of emission spectra as a function temperature. **Figure 3C** shows the PL FWHM of the CdZnSeS/ZnSeS QDs at various temperatures. The FWHM of the QD PL spectrum is consistently broadened with the temperature increase from 295 to 433 K, which is close to the inhomogeneity of QD size and the scattering between excitons and optical/acoustic phonons. The experimental data of PL linewidth broadening are well fitted with the following equation (Wright et al., 2016):

$$\Gamma(T) = \Gamma_{inh} + \theta T + \Gamma_{LO}\left(e^{E_{LO}/k_B T} - 1\right)^{-1} \quad (1)$$

where $\boldsymbol{\Gamma_{inh}}$ corresponds to the temperature-independent inhomogeneous broadening, which arises from scattering due to impurities and imperfections; $\boldsymbol{\theta}$ is the acoustic-exciton–phonon interaction coefficient; $\boldsymbol{\Gamma_{LO}}$ is the longitudinal optical (LO)-exciton–phonon coupling coefficient; $\boldsymbol{E_{LO}}$ is the phonon energy; and k_B is the Boltzmann constant. The temperature dependence of the FWHM energy for CdZnSeS/ZnSeS QDs can be fitted well, as shown in **Figure 3C**. The parameters $\boldsymbol{\Gamma_{inh}}$ are calculated to 125 meV (green QDs) and 161 meV (red QDs). The small value of $\boldsymbol{\Gamma_{inh}}$ indicates the uniform size distribution of the particle, which is consistent with the TEM result. The LO-phonon energy ($\boldsymbol{E_{LO}}$) for two of the QDs were calculated to be 575 meV (green) and 643 meV (red), respectively, indicating strong exciton–phonon interactions (He et al., 2019, 3; Hamada et al., 2020). This is significantly higher than the previous binary QD materials (for example, CdSe/ZnS QDs ~24 meV) (Chang et al., 2021).

Furthermore, to analyze PL thermal quenching, the dependence of PL spectral emission intensity with temperature is studied. The Arrhenius equation is used to fit these results (Wu et al., 1996):

$$I(T) = \frac{I(0)}{1 + Ae^{-E_b/k_B T}} \quad (2)$$

where $\boldsymbol{I(T)}$ is the integrated PL intensity at temperature T, $\boldsymbol{I(0)}$ represents the intensity at low temperature, $\boldsymbol{E_b}$ is the effective binding energy, and **A** is a constant. $\boldsymbol{E_b}$ is an intrinsic physical parameter for semiconductors. The parameter $\boldsymbol{E_b}$ was obtained to be 0.364 meV (green) and 0.333 meV (red), which is suggested as originating in the transformation of longitudinal acoustics phonon. This value is significantly lower than the previous binary QD materials (for example, CdSe/ZnS QDs ~50 meV) (Li J. et al., 2016).

The WLED based on the quaternary/ternary alloyed CdZnSeS/ZnSeS QDs is obtained by depositing continuously adjusted quantity ratio of mixture with CdZnSeS/ZnSeS QDs and PMMA. The specific preparation process is shown in **Figure 4**. The detailed preparation process is mentioned above. Typically, we choose the LED chip with a silicone lens for its high light transmission and uniform light emission. The emission spectra of the as-prepared LED used CdZnSeS/ZnSeS

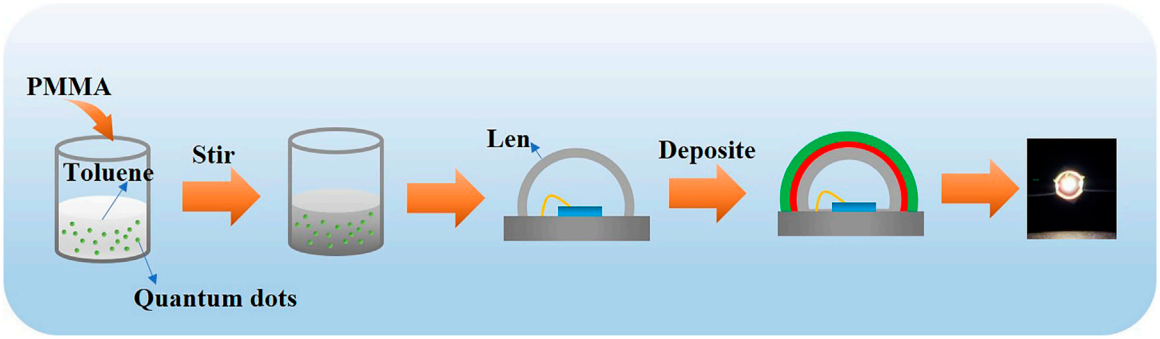

FIGURE 4 | Fabrication process of the CdZnSeS/ZnSeS QD WLED device. QD, quantum dot; WLED, white light-emitting diode.

QDs as green and red phosphors with 120-mA driving current at room temperature as depicted in **Figure 5A**. Three different peaks can be clearly observed for violet GaN-based LED (385 nm), CdZnSeS/ZnSeS green light (531 nm), and CdZnSeS/ZnSeS red light (613 nm).

Figure 5B shows the emission spectra of WLED based on the CdZnSeS/ZnSeS QDs at different forward currents. As the device operating current increases, the emission light intensity of the WLED is gradually enhanced without any visible emission peak shift, indicating that the prepared CdZnSeS/ZnSeS QDs WLED device has good stability under different driving currents and the CdZnSeS/ZnSeS QDs are not saturated. **Figure 5C** shows the performance of the device. As the driving current varies from 10 to 200 mA, the EQE and LE both increase first and then decrease. As a result of the droop effect caused by carrier overflow, among them, EQE reaches a maximum of 14.86% at 110 mA, and LE reaches a maximum of 28.14 lm/W at 70 mA. The LE and EQE of the UV chip used in

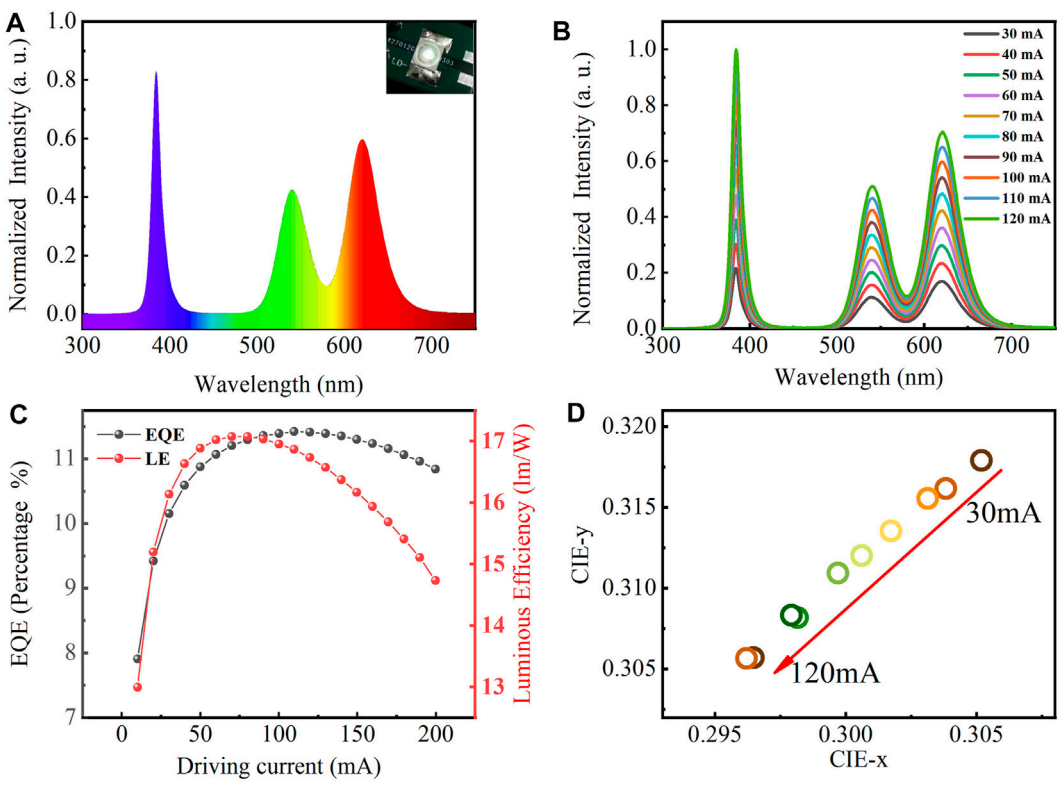

FIGURE 5 | (A) Emission spectra of QD LED device driven at 120 mA. **(B)** Emission spectra of QD WLED under different forward currents and driving current-dependent variations in **(C)** EQE and LE and **(D)** CIE. QD, quantum dot; LED, light-emitting diode; WLED, white light-emitting diode; EQE, external quantum efficiency; LE, luminous efficiency; CIE, Commission Internationale de l'éclairage.

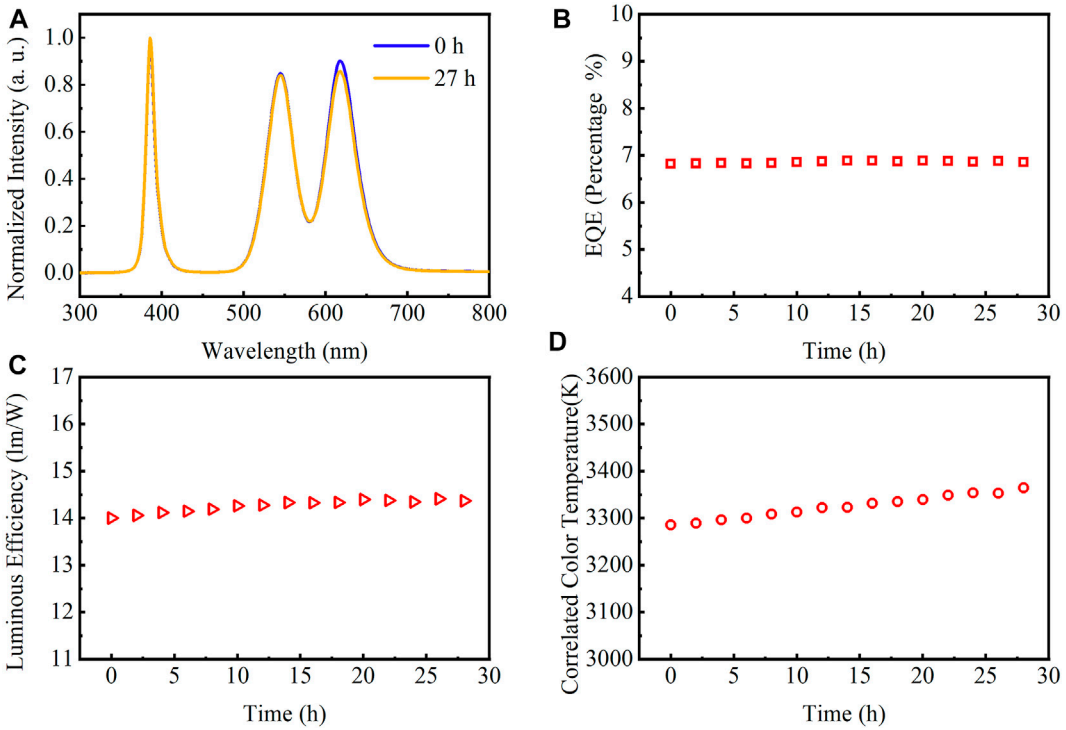

FIGURE 6 | (A) Emission spectra of QD WLED at the start of light emission and after 27 h, **(B)** EQE, **(C)** LE, and **(D)** CCT of QD WLED at different time intervals at 3-V voltage. QD, quantum dot; WLED, white light-emitting diode; EQE, external quantum efficiency; LE, luminous efficiency; CCT, correlated color temperature.

this work are 0.3 lm/W and 20%, respectively, so the light conversion efficiency of the CdZnSeS/ZnSeS QDs in the device can be obtained as more than 70%.

EQE is defined as the ratio of the number of photons emitted from the active region per second and the number of electrons injected into LED per second:

$$EQE = \frac{\frac{P}{(h\nu)}}{I/e} \tag{3}$$

where $\boldsymbol{P}$ is optical power emitted from the free region and $\boldsymbol{I}$ is the injection current.

LE can be calculated by the following equation (Zhu et al., 2010):

$$LE = \frac{\Phi}{P_{in}} = \frac{\Phi}{V_{in} \cdot I_{in}} \tag{4}$$

where Φ is the luminous flux of LED and P_{in} is the input power, which can be calculated by multiplying the input voltage $\boldsymbol{V_{in}}$ and the corresponding current $\boldsymbol{I_{in}}$.

As shown in **Figure 5D**, the device reaches a corresponding color coordinate (0.305, 0.317) at 30 mA, located in the white light-emitting area. Under different forward bias currents, the corresponding color coordinates of the as-prepared LEDs verify from (0.305, 0.317) to (0.296, 0. 305) with slight changes, which shows that WLEDs have good color stability. The slight shift of the color coordinate corresponding to blue light can be attributed to the thermal quenching of the light emission of the QDs as a result of the temperature of the LED chip emerging with the increase of the forward current.

To demonstrate the time stability of the device, we perform a time stability experiment of device performance parameters with a working time of 27 h under a forward voltage of 3 V. **Figure 6A** shows the spectra of the as-papered device before and after 27 h working in that only the red light drops slightly after 27 h, indicating that it has good stability. Since it takes a certain time for the device to reach a stable state, the performance parameters will rise slightly as time increases. Long time operation of the QD WLED at a stable voltage of 3 V reveals that the EQE increased from a maximum of 6.81% to 6.85%, which only increased by 0.5% (**Figure 6B**). The LE of the device increased from a maximum of 13.99 to 14.36 lm/W, which only increased by 0.37 lm/W (**Figure 6C**). The CCT increased from 3,285 to 3,364 after 27 h, i.e., only increased 2.4% to its initial value (**Figure 6D**). These indicate that the thick shell layer CdZnSeS/ZnSeS QDs can maintain good stability during the long-term operation of the device and keep the LE and CCT at an ideal level.

CONCLUSION

In summary, the quaternary/ternary alloyed CdZnSeS/ZnSeS QDs were synthesized with emission wavelengths at 531 and

613 nm, with suitable emission line widths (FWHM ~38 nm). We have demonstrated that the QDs have excellent luminescence performance and thermal stability, fitted well as a luminescent material. The LED integrated with the CdZnSeS/ZnSeS QDs covers the visible spectrum, delivering a LE of 28.14 lm/W, an EQE of 14.86%, and warm bright sunlight close to the spectrum of daylight (CIE coordinates 0.305, 0.317). In particular, as the lighting time increased, the PL intensity, LE, EQE, and CCT of the as-prepared device remained relatively stable with only slight changes. We believe that the device-grade CdZnSeS/ZnSeS QDs with superior optical properties hold great promise for lightings and displays.

DATA AVAILABILITY STATEMENT

The original contributions presented in the study are included in the article/supplementary material, Further inquiries can be directed to the corresponding authors.

AUTHOR CONTRIBUTIONS

JL and HQ planned and programmed all the experiments. YZ fabricated the sample. XC and XL performed the WLED test, and XC wrote the first and final manuscript. MP, HD, and ZL helped with the final manuscript. All authors contributed to the article and approved the submitted version.

FUNDING

This study was supported by the National Natural Science Foundation of China (Grant No. 12104110) and Zhejiang Province Basic Public Welfare Research Project (Grant No. LGN22F050002).

ACKNOWLEDGMENTS

We thank Westlake Center for Micro/Nano Fabrication for the facility support and technical assistance and Instrumentation, Service Center for Molecular Sciences at Westlake University for PL spectral and delay curve measurement, and the support of Huawei Technologies Co., Ltd.

REFERENCES

Adegoke, O., Seo, M.-W., Kato, T., Kawahito, S., and Park, E. Y. (2016). Gradient Band gap Engineered Alloyed Quaternary/ternary CdZnSeS/ZnSeS Quantum Dots: an Ultrasensitive Fluorescence Reporter in a Conjugated Molecular beacon System for the Biosensing of Influenza Virus RNA. *J. Mater. Chem. B* 4, 1489–1498. doi:10.1039/C5TB02449H

Bai, Z., Wei, H., Yang, X., Zhu, Y., Peng, Y., Yang, J., et al. (2020). Rapid Enrichment and Ultrasensitive Detection of Influenza A Virus in Human Specimen Using Magnetic Quantum Dot Nanobeads Based Test Strips. *Sensors Actuators B: Chem.* 325, 128780. doi:10.1016/j.snb.2020.128780

Chang, H., Zhong, Y., Dong, H., Wang, Z., Xie, W., Pan, A., et al. (2021). Ultrastable Low-Cost Colloidal Quantum Dot Microlasers of Operative Temperature up to 450 K. *Light Sci. Appl.* 10, 60. doi:10.1038/s41377-021-00508-7

Chen, X., Wang, Y., Song, J., Li, X., Xu, J., Zeng, H., et al. (2019). Temperature Dependent Reflectance and Ellipsometry Studies on a CsPbBr3 Single Crystal. *J. Phys. Chem. C* 123, 10564–10570. doi:10.1021/acs.jpcc.9b01406

Fang, Z., Wu, K., Wang, L., Xu, D., Wang, W., Lin, Y., et al. (2021). Highly Efficient and Blue-Excitable Mn-Doped PEA2Pb(Br/I)4 Perovskite for Solid Lighting. *J. Lumin.* 237, 118155. doi:10.1016/j.jlumin.2021.118155

Ghosh, S., and Manna, L. (2018). The Many "Facets" of Halide Ions in the Chemistry of Colloidal Inorganic Nanocrystals. *Chem. Rev.* 118, 7804–7864. doi:10.1021/acs.chemrev.8b00158

Giansante, C., and Infante, I. (2017). Surface Traps in Colloidal Quantum Dots: A Combined Experimental and Theoretical Perspective. *J. Phys. Chem. Lett.* 8, 5209–5215. doi:10.1021/acs.jpclett.7b02193

Hamada, M., Rana, S., Jokar, E., Awasthi, K., Diau, E. W.-G., and Ohta, N. (2020). Temperature-Dependent Electroabsorption Spectra and Exciton Binding Energy in a Perovskite CH3NH3PbI3 Nanocrystalline Film. *ACS Appl. Energ. Mater.* 3, 11830–11840. doi:10.1021/acsaem.0c01983

Harris, R. D., Bettis Homan, S., Kodaimati, M., He, C., Nepomnyashchii, A. B., Swenson, N. K., et al. (2016). Electronic Processes within Quantum Dot-Molecule Complexes. *Chem. Rev.* 116, 12865–12919. doi:10.1021/acs.chemrev.6b00102

He, M., Wang, C., Li, J., Wu, J., Zhang, S., Kuo, H.-C., et al. (2019). CsPbBr3-Cs4PbBr6 Composite Nanocrystals for Highly Efficient Pure green Light Emission. *Nanoscale* 11, 22899–22906. doi:10.1039/C9NR07096F

Hien, N. T., Tan, P. M., Van, H. T., Lien, V. T. K., Do, P. V., Loan, P. N., et al. (2020). Photoluminescence Properties of Cu-Doped CdTeSe Alloyed Quantum Dots versus Laser Excitation Power and Temperature. *J. Lumin.* 218, 116838. doi:10.1016/j.jlumin.2019.116838

Jia, J., and Tian, J. (2014). One-pot Synthesis in Liquid Paraffin of Ternary alloy CdSexS1−x Nanocrystals with Fluorescence Emission Covering Entire Visible Region. *J. Nanopart Res.* 16, 2283. doi:10.1007/s11051-014-2283-8

Kıbrıslı, O., Erol, E., Çelikbilek Ersundu, M., and Ersundu, A. E. (2021). Robust CsPbBr3 and CdSe/Dy3++CdSe Quantum Dot Doped Glass Nanocomposite Hybrid Coupling as Color Converter for Solid-State Lighting Applications. *Chem. Eng. J.* 420, 130542. doi:10.1016/j.cej.2021.130542

Koeppel, F., Jaiswal, J. K., and Simon, S. M. (2007). Quantum Dot-Based Sensor for Improved Detection of Apoptotic Cells. *Nanomedicine* 2, 71–78. doi:10.2217/17435889.2.1.71

Leach, A. D. P., and Macdonald, J. E. (2016). Optoelectronic Properties of CuInS2 Nanocrystals and Their Origin. *J. Phys. Chem. Lett.* 7, 572–583. doi:10.1021/acs.jpclett.5b02211

Li, J., Zhang, W., Zhang, Y., Lei, H., and Li, B. (2016a). Temperature-dependent Resonance Energy Transfer from CdSe-ZnS Core-Shell Quantum Dots to Monolayer MoS2. *Nano Res.* 9, 2623–2631. doi:10.1007/s12274-016-1149-z

Li, Q., Luo, T. Y., Zhou, M., Abroshan, H., Huang, J., Kim, H. J., et al. (2016b). Silicon Nanoparticles with Surface Nitrogen: 90% Quantum Yield with Narrow Luminescence Bandwidth and the Ligand Structure Based Energy Law. *ACS Nano* 10, 8385–8393. doi:10.1021/acsnano.6b03113

Li, X., Cai, W., Guan, H., Zhao, S., Cao, S., Chen, C., et al. (2021). Highly Stable CsPbBr3 Quantum Dots by Silica-Coating and Ligand Modification for white Light-Emitting Diodes and Visible Light Communication. *Chem. Eng. J.* 419, 129551. doi:10.1016/j.cej.2021.129551

Li, X., Lin, Q., Song, J., Shen, H., Zhang, H., Li, L. S., et al. (2020). Quantum-Dot Light-Emitting Diodes for Outdoor Displays with High Stability at High Brightness. *Adv. Opt. Mater.* 8, 1901145. doi:10.1002/adom.201901145

Li, Y., Dong, L., Chen, N., Guo, Z., Lv, Y., Zheng, J., et al. (2019). Room-Temperature Synthesis of Two-Dimensional Hexagonal Boron Nitride Nanosheet-Stabilized CsPbBr3 Perovskite Quantum Dots. *ACS Appl. Mater. Inter.* 11, 8242–8249. doi:10.1021/acsami.8b20400

Liang, N., Hu, X., Li, W., Mwakosya, A. W., Guo, Z., Xu, Y., et al. (2021). Fluorescence and Colorimetric Dual-Mode Sensor for Visual Detection of Malathion in Cabbage Based on Carbon Quantum Dots and Gold Nanoparticles. *Food Chem.* 343, 128494. doi:10.1016/j.foodchem.2020.128494

Liu, X., Jiang, Y., Fu, F., Guo, W., Huang, W., and Li, L. (2013). Facile Synthesis of High-Quality ZnS, CdS, CdZnS, and CdZnS/ZnS Core/shell Quantum Dots: Characterization and Diffusion Mechanism. *Mater. Sci. Semiconductor Process.* 16, 1723–1729. doi:10.1016/j.mssp.2013.06.007

Moon, H., and Chae, H. (2020). Efficiency Enhancement of All-Solution-Processed Inverted-Structure Green Quantum Dot Light-Emitting Diodes via Partial Ligand Exchange with Thiophenol Derivatives Having Negative Dipole Moment. *Adv. Opt. Mater.* 8, 1901314. doi:10.1002/adom.201901314

Nasrin, F., Chowdhury, A. D., Takemura, K., Kozaki, I., Honda, H., Adegoke, O., et al. (2020). Fluorometric Virus Detection Platform Using Quantum Dots-Gold Nanocomposites Optimizing the Linker Length Variation. *Analytica Chim. Acta* 1109, 148–157. doi:10.1016/j.aca.2020.02.039

Nautiyal, V., Munjal, D., and P.Silotia, P. (2021). Spin Orbit Effect in a Quantum Dot Confined in a Kratzer Potential. *J. Magnetism Magn. Mater.* 528, 167688. doi:10.1016/j.jmmm.2020.167688

Ostadebrahim, M., and Dehghani, H. (2021). ZnS/CdSe0.2S0.8/ZnSSe Heterostructure as a Novel and Efficient Photosensitizer for Highly Efficient Quantum Dot Sensitized Solar Cells. *Appl. Surf. Sci.* 545, 148958. doi:10.1016/j.apsusc.2021.148958

Owen, J., and Brus, L. (2017). Chemical Synthesis and Luminescence Applications of Colloidal Semiconductor Quantum Dots. *J. Am. Chem. Soc.* 139, 10939–10943. doi:10.1021/jacs.7b05267

Pashazadeh-Panahi, P., and Hasanzadeh, M. (2019). Revolution in Biomedicine Using Emerging of Picomaterials: A Breakthrough on the Future of Medical Diagnosis and Therapy. *Biomed. Pharmacother.* 120, 109484. doi:10.1016/j.biopha.2019.109484

Regulacio, M. D., and Han, M.-Y. (2010). Composition-Tunable Alloyed Semiconductor Nanocrystals. *Acc. Chem. Res.* 43, 621–630. doi:10.1021/ar900242r

Sheng, Y., Wei, J., Liu, B., and Peng, L. (2014). A Facile Route to Synthesize CdZnSe Core-shell-like Alloyed Quantum Dots via Cation Exchange Reaction in Aqueous System. *Mater. Res. Bull.* 57, 67–71. doi:10.1016/j.materresbull.2014.05.033

Tsuji, T., Ozaki, N., Yamauchi, S., Onoue, K., Watanabe, E., Ohsato, H., et al. (2021). 1.1 μm Waveband Tunable Laser Using Emission-Wavelength-Controlled InAs Quantum Dots for Swept-Source Optical Coherence Tomography Applications. *Jpn. J. Appl. Phys.* 60, SBBE02. doi:10.35848/1347-4065/abe5bc

Wright, A. D., Verdi, C., Milot, R. L., Eperon, G. E., Pérez-Osorio, M. A., Snaith, H. J., et al. (2016). Electron-phonon Coupling in Hybrid lead Halide Perovskites. *Nat. Commun.* 7, 11755. doi:10.1038/ncomms11755

Wu, Y.-h., Arai, K., and Yao, T. (1996). Temperature Dependence of the Photoluminescence of ZnSe/ZnS Quantum-Dot Structures. *Phys. Rev. B* 53, R10485–R10488. doi:10.1103/PhysRevB.53.R10485

Xie, B., Liu, H., Hu, R., Wang, C., Hao, J., Wang, K., et al. (2018). Targeting Cooling for Quantum Dots in White QDs-LEDs by Hexagonal Boron Nitride Platelets with Electrostatic Bonding. *Adv. Funct. Mater.* 28, 1801407. doi:10.1002/adfm.201801407

Xu, T., Wan, Z., Tang, H., Zhao, C., Lv, S., Chen, Y., et al. (2021a). Carbon Quantum Dot Additive Engineering for Efficient and Stable Carbon-Based Perovskite Solar Cells. *J. Alloys Comp.* 859, 157784. doi:10.1016/j.jallcom.2020.157784

Xu, Y., Chen, T., Xie, Z., Jiang, W., Wang, L., Jiang, W., et al. (2021b). Highly Efficient Cu-In-Zn-S/ZnS/PVP Composites Based white Light-Emitting Diodes by Surface Modulation. *Chem. Eng. J.* 403, 126372. doi:10.1016/j.cej.2020.126372

Yuan, Q., Wang, T., Yu, P., Zhang, H., Zhang, H., and Ji, W. (2021). A Review on the Electroluminescence Properties of Quantum-Dot Light-Emitting Diodes. *Org. Elect.* 90, 106086. doi:10.1016/j.orgel.2021.106086

Zhang, F., Zhong, H., Chen, C., Wu, X.-g., Hu, X., Huang, H., et al. (2015). Brightly Luminescent and Color-Tunable Colloidal CH3NH3PbX3 (X = Br, I, Cl) Quantum Dots: Potential Alternatives for Display Technology. *ACS Nano* 9, 4533–4542. doi:10.1021/acsnano.5b01154

Zhou, S., Xie, B., Ma, Y., Lan, W., and Luo, X. (2019). Effects of Hexagonal Boron Nitride Sheets on the Optothermal Performances of Quantum Dots-Converted White LEDs. *IEEE Trans. Electron. Devices* 66, 4778–4783. doi:10.1109/TED.2019.2937340

Zhu, Y., Dutta, P., and Narendran, N. (2010), *Post-synthesis Annealing Effects on SrGa 2 Se 4 :Eu $^{2+}$ Phosphors with Peak Emission Wavelength in the green gap*. in, eds. I. Ferguson, M. H. Kane, N. Narendran, and T. Taguchi (San Diego, California, United States). doi:10.1117/12.863065

Zvaigzne, M. A., Martynov, I. L., Samokhvalov, P. S., and Nabiev, I. R. (2016). Fabrication of Composite Materials from Semiconductor Quantum Dots and Organic Polymers for Optoelectronics and Biomedicine: Role of Surface Ligands. *Russ. Chem. Bull.* 65, 2568–2577. doi:10.1007/s11172-016-1620-8

Zvaigzne, M., Domanina, I., Il'gach, D., Yakimansky, A., Nabiev, I., and Samokhvalov, P. (2020). Quantum Dot-Polyfluorene Composites for White-Light-Emitting Quantum Dot-Based LEDs. *Nanomaterials* 10, 2487. doi:10.3390/nano10122487

Conflict of Interest: The authors declare that the research was conducted in the absence of any commercial or financial relationships that could be construed as a potential conflict of interest.

Publisher's Note: All claims expressed in this article are solely those of the authors and do not necessarily represent those of their affiliated organizations, or those of the publisher, the editors, and the reviewers. Any product that may be evaluated in this article, or claim that may be made by its manufacturer, is not guaranteed or endorsed by the publisher.

Copyright © 2022 Chen, Li, Zhong, Li, Pan, Qi, Dong and Zhang. This is an open-access article distributed under the terms of the Creative Commons Attribution License (CC BY). The use, distribution or reproduction in other forums is permitted, provided the original author(s) and the copyright owner(s) are credited and that the original publication in this journal is cited, in accordance with accepted academic practice. No use, distribution or reproduction is permitted which does not comply with these terms.

frontiers in Chemistry

ORIGINAL RESEARCH
published: 23 March 2022
doi: 10.3389/fchem.2022.880081

A Self-Reference Interference Sensor Based on Coherence Multiplexing

*Ying Shen[1], Zeyu Huang[1], Feng Huang[1], Yonghong He[2], Ziling Ye[1], Hongjian Zhang[1] and Cuixia Guo[1]**

[1]School of Mechanical Engineering and Automation, Fuzhou University, Fuzhou, China, [2]Shenzhen Key Laboratory for Minimal Invasive Medical Technologies, Institute of Optical Imaging and Sensing, Tsinghua Shenzhen International Graduate School, Tsinghua University, Shenzhen, China

Interferometry has been widely used in biosensing due to its ability to acquire molecular affinity and kinetics in real-time. However, interferometric-based sensors are susceptible to environmental disturbances, including temperature and non-specific binding of target molecules, which reduces their detection robustness. To address this shortcoming, this paper proposes a self-referencing interference sensor based on coherence multiplexing to resist environmental disturbances. The proposed sensor can address temperature and non-specific binding, but it is not limited only to these types of disturbances. In the proposed sensor design, each sensor signal is encoded using a specific optical path difference determined by the optical thickness of a sensor chip. In addition, two sensor signals for disturbances tracking and biomolecule detection are detected simultaneously without additional cost to the second spectrometer and then differenced to achieve real-time self-reference. The temperature fluctuations experiments and specific binding experiments of protein A to IgG are performed to verify the performance of the proposed sensor. The results demonstrate that the proposed sensor can eliminate non-specific binding and temperature disturbances in real-time during biomolecule detection, achieving higher detection robustness. The proposed sensor is suitable for applications that require large-scale testing of biomolecular interactions, such as drug screening.

Keywords: phase-sensitive interferometry, biosensing, differential measurement, biomolecular interaction, label-free detection

OPEN ACCESS

Edited by:
Honghui He,
Tsinghua University, China

Reviewed by:
Dongmei Li,
Zhejiang University of Technology, China
Shouyu Wang,
Jiangnan University, China

****Correspondence:***
Cuixia Guo
guocx@fzu.edu.cn

Specialty section:
This article was submitted to Nanoscience, a section of the journal Frontiers in Chemistry

Received: *21 February 2022*
Accepted: *08 March 2022*
Published: *23 March 2022*

Citation:
Shen Y, Huang Z, Huang F, He Y, Ye Z, Zhang H and Guo C (2022) A Self-Reference Interference Sensor Based on Coherence Multiplexing. Front. Chem. 10:880081. doi: 10.3389/fchem.2022.880081

INTRODUCTION

The development of simple, sensitive, and rapid molecular detection methods is of great importance to many fields, including medical evaluation, drug screening, and environmental applications. Molecular detection methods can provide accurate and fast drug sensitivity results, providing new tools for better understanding of drug-resistant tuberculosis (Rubin, 2018), and can also identify bacteria (Tardif et al., 2016) and detect specific micro-molecules in areas of water contamination (Dandapat et al., 2016). Hence, the molecular detection and identification methods have high application importance.

The molecular detection and identification methods can be roughly categorized into labeled methods and label-free methods. Due to high sensitivity, labeled methods, e.g., fluorescence (Sun et al., 2018; Burg et al., 2019), chemiluminescence (Jin et al., 2017; Li et al., 2017), enzyme-linked immunosorbent assay (ELISA) (Engvall and Perlmann, 1971), have been used in many sensing

measurements. However, due to the complex structure and reactivity of proteins, an approach of adding additional reagents to improve the accessibility of observation could cause changes in the properties of a target molecule (MacBeath, 2002). In addition, for labeled methods, it is difficult to provide real-time insight into the molecular binding process and allow visualization of the molecular binding kinetics. Due to these disadvantages of the labeled methods, an increasing number of label-free methods have been used in biosensing applications, including optical waveguide lightmode spectroscopy (OWLS) (Orgovan et al., 2014), surface plasmon resonance (SPR) (He et al., 2016; Liu et al., 2017), ellipsometry (Demircioglu et al., 2017), and biolayer interferometry (BLI) (Sztain et al., 2021). However, these methods not only require customized and expensive substrates but also can difficultly achieve *in-situ* detection. For instance, SPR substrates need to be coated with an expensive gold film (Hobbs et al., 2016), whose thickness has to be precisely controlled at the nm level.

Recently, phase-sensitive interferometry (Joo et al., 2009; Chirvi et al., 2012; Ryu et al., 2014; Merryweather et al., 2021) has attracted great attention as a phase image technique. Spectral-domain phase-sensitive interferometry (SD-PSI) has been used as a quantitative phase imaging method in biosensing applications. The SD-PSI can acquire the molecular layer thickness changes caused by binding the target molecules to the probe surface in real-time. A fiber optic molecular sensor based on the SD-PSI can be used to monitor biomolecules *in situ* (Guo et al., 2018). Unlike other label-free detection methods, the SD-PSI does not require custom and expensive sensor substrates, such as gold-plated trigonal prisms, which are used in the SPR (Wu et al., 2010). The previous studies (Joo et al., 2009; Chirvi et al., 2012; Ryu et al., 2014) have demonstrated that laboratory-grade or off-the-shelf glass of a suitable thickness can be used as a sensor chip, and such a design is low-cost and simple to prepare. However, this technique is susceptible to disturbances induced by the temperature response of a sensor chip, non-specific binding of target molecules, and sample background. The previous experiments have required keeping the sensor and buffer solution at a constant temperature as much as possible (Chirvi et al., 2012), which increased experimental complexity and reduced experimental robustness.

The previous solutions are easily affected by different disturbances in biosensing, including temperature response and non-specific binding of target molecules. To overcome this shortcoming, this paper proposes a self-reference interference sensor based on coherence multiplexing, which can provide a differential measurement result with the phase change caused by binding of target molecules. The proposed sensor establishes referential and measuring paths with different optical path differences (OPDs) for disturbance tracking and biomolecule detection, thus realizing a self-reference measurement. The advantage of coherence multiplexing is that it allows simultaneous detection of two OPD-coded sensing signals without adding an expensive additional detection element. In addition, compared to the time-coded sequential measurement self-reference methods, the coherence multiplexing coding methods allow simultaneous biomolecule detection and disturbance dynamics tracking in both paths, thus improving detection robustness. The proposed sensor can be used as a label-free sensor with the advantages of weak temperature sensitivity, low non-specific binding, and picometer-level thickness sensitivity. In addition, the proposed sensor requires using only an ordinary optical glass as a detection substrate, which is low-cost and simple to manufacture.

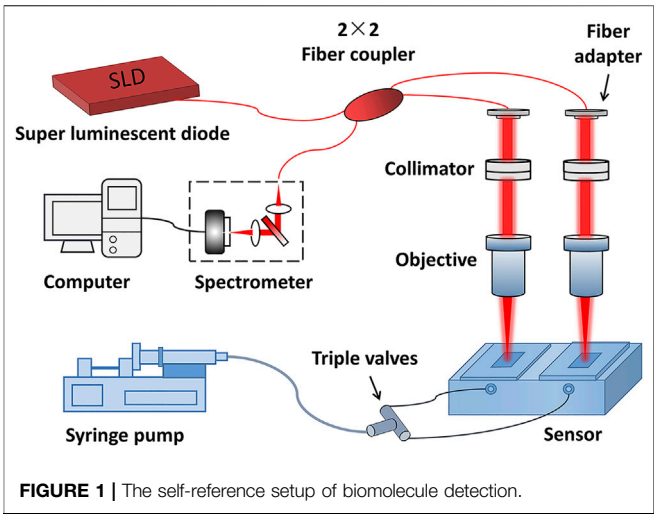

FIGURE 1 | The self-reference setup of biomolecule detection.

PRINCIPLE AND PROPOSED SENSOR DESIGN

The self-reference setup of the biomolecule detection method proposed in this study is presented in **Figure 1**. The setup is based on the SD-PSI. A super-luminescent diode provides the incident light with a central wavelength of 1,310 nm and a bandwidth of 75 nm. The two detection paths are prepared by a single-mode fiber-based 2 × 2 coupler and two sensor chips with different thicknesses. Each path can be considered as a low-coherence interferometer with a common path, where the reference light is reflected from the upper surface of a sensing chip, and the sample light is reflected from the contact surface between the sensor chip and solution. The interference signal of each path is encoded with a specific OPD, which is equal to the optical thickness of the corresponding sensor chip, i.e., the product of refractive index and thickness. The two signals were recorded by a homemade transmission grating structure-based spectrometer with a spectral resolution of 0.07 nm and a spectral measurement range of 1,240–1,380 nm, which was then decomposed from the superimposed interferometric spectra according to the difference in OPD values. The OPD between the two paths needs to be greater than the measuring range of the SD-PSI so that to avoid interference between the two paths' beams. Sample channels are constructed by using epoxy glue to combine two different initial thicknesses of sensing chips (0.17-mm and 0.2-mm glass flakes) with a fluid chip (built-in flow channel and reaction chamber).

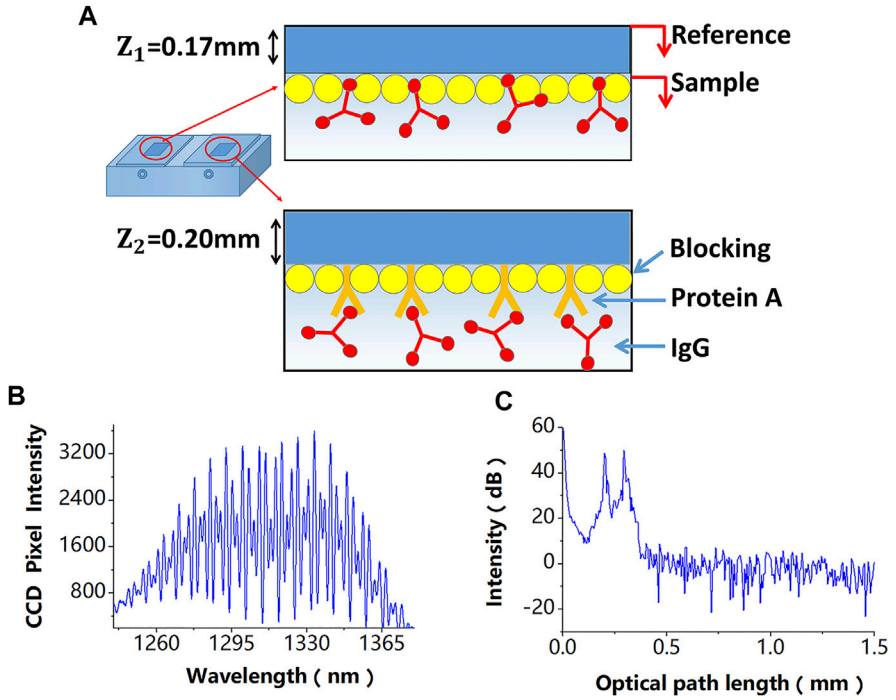

FIGURE 2 | (A) A differential-path modification method of sensing chips, the difference of these modification processes is that the referential path does not modify the probe molecule. **(B)** Superimposed interferometric spectra obtained by the SD-PSI. **(C)** Signal peaks corresponding to different OPDs obtained after performing the fast Fourier transform algorithm on the two superimposed interferometric spectra.

The binding of a molecule to be detected to the probe molecule on the sensing chip surface changes the sensing chip thickness, which causes a phase shift of the interference signal. Disturbances of a sensing chip, including non-specific binding and temperature response, can also induce changes in the interference signal phase. The two detection paths in the self-reference system, denoted as path 1 (P1) and path 2 (P2), are used to detect phase variations induced by the biomolecule detection and disturbances during the biomolecule detection process, respectively. Finally, the self-reference molecule detection is achieved by performing the difference operation between the phases of the two OPD-encoded signals. The basic principle of the self-reference interference sensor based on coherence multiplexing is shown in **Figure 2**.

In the proposed sensor design, a differential-path modification method for sensing chips is shown in **Figure 2A**, which is described in detail in the next section, is used. The two superimposed interferometric spectra signals detected by a spectrometer are shown in **Figure 2B**, which can be expressed as follows:

$$I(k) = 2\beta S(k)\sqrt{R_r R_s}\cos\left(2k(Z_{10} + Z_{20}) + \phi_1^{'}(t) + \phi_2^{'}(t)\right) \quad (1)$$

where k is the wavenumber, β is the beam splitting ratio of the fiber coupler, and $S(k)$ is the spectral density of the Gaussian-type light source; R_r and R_s are the reflectance values of the upper surface of the sensing chip and the sample layer, respectively; Z_{10} and Z_{20} are the initial optical thicknesses of the sensing chips, corresponding to the encoded signals; $\phi_1^{'}(t)$ is the phase induced by the biomolecule detection in molecular detection path P1 due to the true specific molecular binding, as well as temperature and non-specific disturbances; $\phi_2^{'}(t)$ is the phase induced by temperature and non-specific disturbances in disturbances tracking path P2.

Since paths P1 and P2 have different OPDs, their signal peaks can be obtained, as shown in **Figure 2C**, after performing the fast Fourier transform algorithm on the two superimposed interferometric spectra. The phases of the space-domain interference signals at these two peaks, which also include phase variations induced by biomolecule detection and disturbances, can be calculated by:

$$\phi_{c=1,2}(t) = tan^{-1}\left\{\frac{Im\left(I_{c=1,2}(Z)\right)}{Re\left(I_{c=1,2}(Z)\right)}\right\} = \phi_{c=1,2T}(t) + \phi_{Bc=1,2}(t) \quad (2)$$

where $\phi_{c=1,2T}(t)$ is the phase change induced by the temperature response of the sensor chips in paths P1 and P2, and it is in line with the initial optical thickness of the sensing chips and temperature and can be approximately expressed as $\phi_{c=1,2T}(t) \approx TZ_{c=1,20}$.

Thus, the temperature response of the molecular detection path P1 can be calculated by linearly fitting the temperature response of the disturbances tracking path P2, which can be expressed as follows:

$$\phi_{1T}(t) = a\phi_{2T}(t) + b \quad (3)$$

where a denotes the temperature correction factor, and b is the temperature compensation factor.

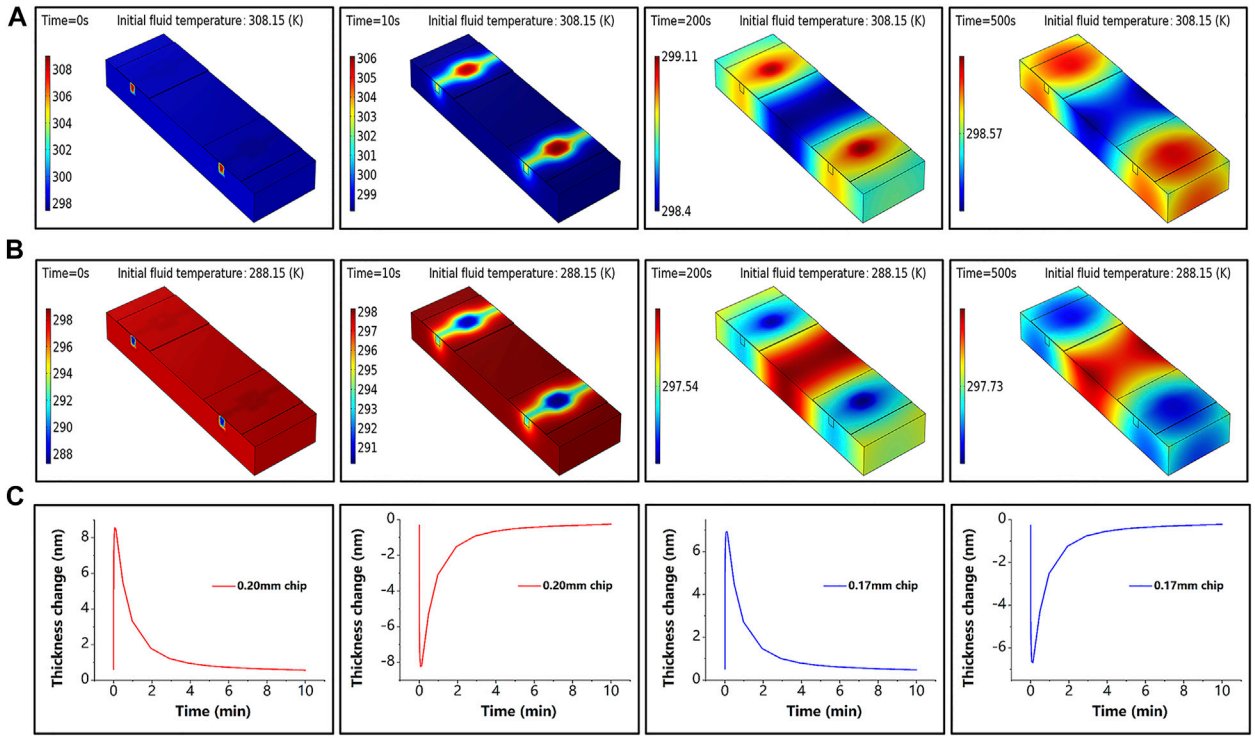

FIGURE 3 | Simulation results. **(A)** Sensor temperature at different moments under the initial temperature of fluid of 308.15 K when the simulated ambient temperature increases. **(B)** Sensor temperature at different moments under the initial temperature of fluid of 288.15 K when the simulated ambient temperature decreases. **(C)** Thickness variation at the center point of the sensing chip for different initial thicknesses during simulated temperature rise and fall; the red line corresponds to a thickness of 0.20 mm and the blue line to a thickness of 0.17 mm.

Different modification processes are used in different thickness chips of the proposed sensor; the difference of these processes is that the referential path does not modify the probe molecule. The proposed design allows tracking the total phase change $\phi_{B1}(t)$ due to specific binding and non-specific disturbance in P1, while the non-specific disturbance $\phi_{B2}(t)$ is simultaneously tracked in P2. Then, $\phi_{Bc=1,2}(t)$ is differenced in real-time to obtain the corrected specific binding by:

$$Z_{corrected} = \frac{\phi_{B1}(t) - \phi_{B2}(t)}{2k_0} = \frac{\phi_1(t) - \phi_2(t) - (a-1)\phi_{2T}(t) - b}{2k_0} \tag{4}$$

where k_0 is the central wavenumber of the light source, and it is given by $k_0 = 2\pi/\lambda_0$, where λ_0 is the central wavelength of the broadband light source.

In the experiment, $\phi_{c=1,2T}(t)$ denotes the average phase change calculated from the stable data before performing molecular detection; $\phi_{c=1,2T}(t)$ is used in **Eq. 3** to obtain a and b.

RESULTS AND DISCUSSION

Weak Temperature Sensitivity

It is well known that using glass as a sensing chip has a low cost and is simple to prepare. The process of glass surface modification has been established and widely used in the preparation of molecular-level sensors (Joo et al., 2009). However, such sensing chips are sensitive to the ambient temperature. Depending on the composition, the thermal expansion coefficient is roughly equal to $[(5.8 \sim 150) \times 10^{-7}]$ per Kelvin temperature (K). For instance, a 0.20-mm laboratory-grade glass sheet used in this study causes a thickness change of about 1 nm/K, which is unfavorable for sub-nanometer thickness measurements.

To confirm that the sensing chip made of glass is sensitive to temperature, the heat transfer process was simulated by COMSOL software. The effect of the ambient temperature change of room temperature (298 ± 10 K) on the glass chip was simulated by changing the fluid's initial temperature. The simulation results are presented in **Figure 3**, where **Figures 3A,B** show the sensor temperature distribution at different moments during the temperature rise and fall, and **Figure 3C** shows the thickness variation of the sensing chip with different initial thicknesses, which is generated by the increase or decrease of the ambient temperature. In the simulation experiment, we measure the temperature variation ΔT at the center point of the sensing chip and set the thermal expansion coefficient δ as $(50 \times 10^{-7})/K$. The thickness variation curve is obtained based on $\Delta Z = \Delta T \times \delta \times Z_0$. Although the thickness converges quickly to the initial value again, it is a challenge to keep the thickness constant. Since this thickness variation is related to temperature variation, reducing the temperature sensitivity in sensing

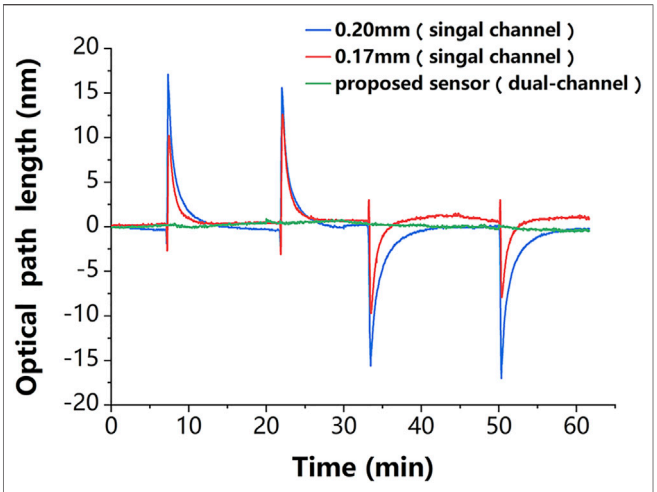

FIGURE 4 | Experimental results. The thickness variation of the chips in the single-channel sensor (red and blue lines) is very consistent with temperature variation in **Figure 3C**, which proves that this sensing chip is sensitive to the temperature disturbance. The phase change of the proposed dual-channel sensor (green line) is about one-tenth of that of the single-channel sensor, which proves that it is less sensitive to temperature disturbance.

measurements at high accuracy levels is a problem that needs to be solved.

In addition, the robustness of the proposed sensor against temperature fluctuations was experimentally evaluated. The experiments followed the control principle and took full advantage of a dual-channel sensor. For a clearer demonstration, the temperature change in the experiment was deliberately magnified. The change in ambient temperature was simulated by simultaneously and repeatedly passing the deionized water at the ambient temperature that was 10 K above (or below) room temperature into the reaction chamber. The thickness variation curves of the sensing chip of the single-chamber sensor and the proposed dual-chamber sensor are presented in **Figure 4**, where it can be seen that compared to the proposed sensor, the sensing chip of the conventional sensor was more sensitive to temperature changes, and its thickness change curve was very consistent with that in **Figure 3C**, indicating that the glass chip was sensitive to temperature; the thickness change curves of the two chips were different due to the difference in their initial thicknesses. It is worth mentioning that the results of the proposed sensor were obtained by linearly fitting the results of single-chambers, which was an improvement of the traditional method. The standard deviation of the phase changes obtained from the experimental results was used to evaluate the temperature sensitivity of the self-reference-type sensor. The experimental results showed that the average value of the conventional sensor was about 2.5×10^{-2} rad, which corresponded to the optical thickness of 2.61 nm, and that of the proposed sensor was 2.9×10^{-3} rad, which corresponded to the optical thickness of 0.30 nm. The results demonstrated good robustness of the proposed sensor to temperature changes.

Track and Suppress Non-Specific Binding

The non-specific binding affects detection results of molecular measurements, and conventional blocking methods cannot completely eliminate non-specific binding. However, the proposed sensor monitors the non-specific binding process using a differential-path detection method and has the ability to correct for specific binding.

To verify the non-specific binding suppression performance of the proposed sensor, first, the stability of phase characterization was examined by injecting only a phosphate-buffered saline (PBS) buffer for 20 min at room temperature. The total phase variation of 4×10^{-4} rad in the first 20 min, which corresponded to the optical thickness variation of 41 p.m., indicated that the phase characterization capability of the proposed sensor was

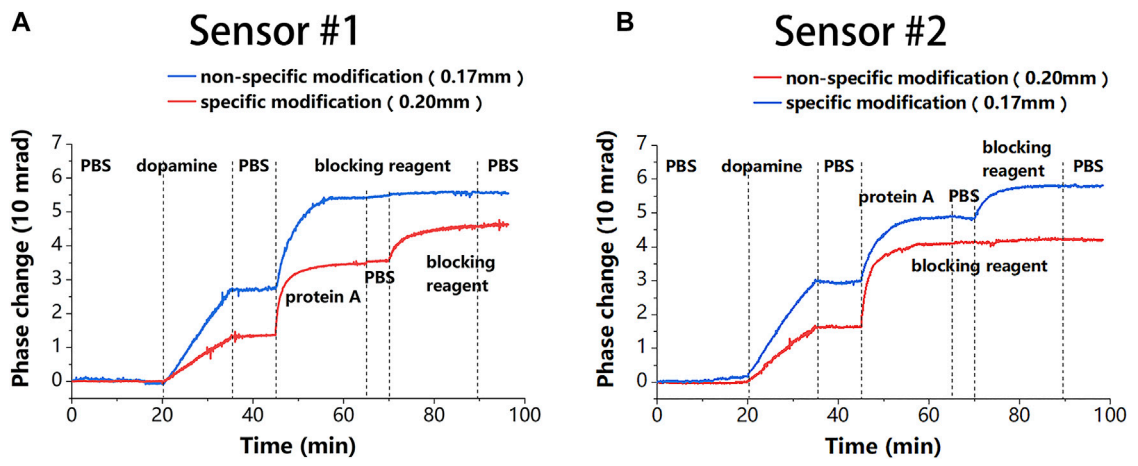

FIGURE 5 | The modification results of the two sensors, where the blue line corresponds to the 0.17-mm chip and the red line corresponds to the 0.20-mm chip. **(A)** The modification result of sensor #1, where a 0.20-mm chip is used for specific binding and a 0.17-mm chip for non-specific binding. **(B)** The modification result of sensor #2, where a 0.17-mm chip is used for specific binding and a 0.20-mm chip for non-specific binding.

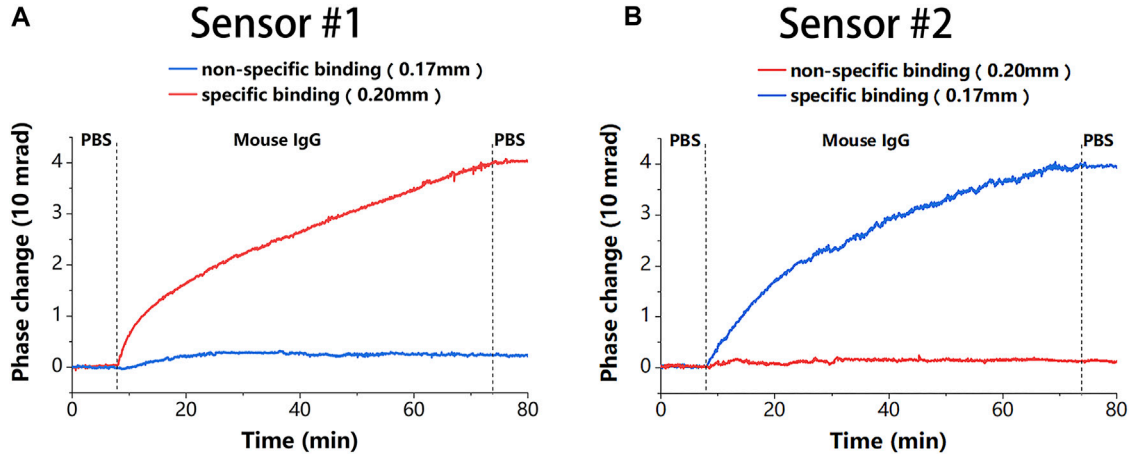

FIGURE 6 | The binding results of the two sensors. **(A)** Binding results corresponding to **Figure 5A** in sensor #1. **(B)** Binding results corresponding to **Figure 5B** in sensor #2.

stable enough. Also, the standard deviation of a phase variation of 6.7×10^{-5} rad, which corresponded to the optical thickness variation of 6.9 p.m., indicated the pico-meter-level thickness sensitivity of the proposed sensor.

Next, one of the glass chips with a 0.20-mm thickness was modified. First, a dopamine-Tris solution of 2 mg/ml was used to form a thin adhesion layer by self-polymerization on the binding surface to improve the biocompatibility of the binding surface. Then, the dopamine layer was non-specifically modified with the protein A (0.5 mg/ml), which acted as probe molecules to capture the target analyte. Finally, the non-specific binding site on the dopamine layer was blocked by passing through the protein-free blocking solution. To reduce the non-specific binding of the target analyte to the dopamine layer, smaller blocking molecules filled the dopamine layer between the protein A molecules. The PBS was introduced to the fluid chip to flush the unbound molecules before passing through a new solution. In addition, an almost identical method was used to modify another glass chip; the only differences were that no protein A solution was passed through, and the dopamine layer directly adhered with the protein-free blocking solution.

The modification processes of the two sensing chips were then exchanged to obtain the second proposed sensor. Due to the modification processes were exchanged, the probe molecules were present on different thickness chips in the two sensors. This difference between the two sensors was used to verify channel uniformity of the proposed sensor, which is a prerequisite for achieving undifferentiated sensor detection. As shown in **Figures 5A,B**, the phase changes of the two sensors under the same reaction were almost identical during specific modifications monitored by different sensing chips (0.17 mm for the blue and 0.20 mm for the red), except for the growth of dopamine. The same results were achieved for non-specific modifications. This shows that the chip thickness does not affect the molecular reaction, thus proving the channel uniformity of the proposed sensor. The results also demonstrated that the total increase in phase caused by blocking molecules under the specific modification was less than that under the non-specific modification. This could be because protein A preoccupied most of the binding sites.

After modification, 20 μg/ml of mouse IgG solution was used to demonstrate the detection capability of the proposed sensor. To reduce the effect of phase noise further, the average phase of 1,000 neighboring measurement points was calculated and used as a phase at that moment in the experiment, and the response time of the system was 27.8 ms, which satisfied the real-time requirement. The results in **Figures 6A,B** show that the binding detected under different initial thicknesses of the sensing chip was almost the same, which further demonstrates good channel uniformity of the proposed sensor. This uniformity makes the proposed sensor more flexible and easier to prepare. The phase change of about 4×10^{-2} rad caused by specific binding was mainly due to the binding of the mouse IgG to protein A. The non-specific binding caused a phase change of about 2×10^{-3} rad, which could be because the dopamine layer was not completely

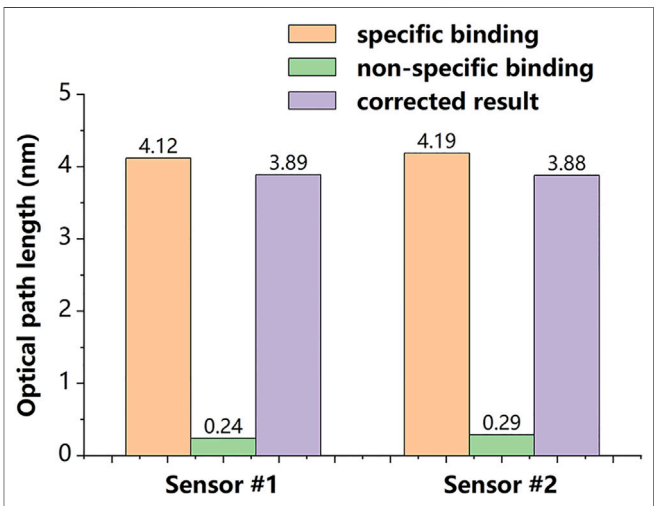

FIGURE 7 | Relationship between the amount of binding and correction.

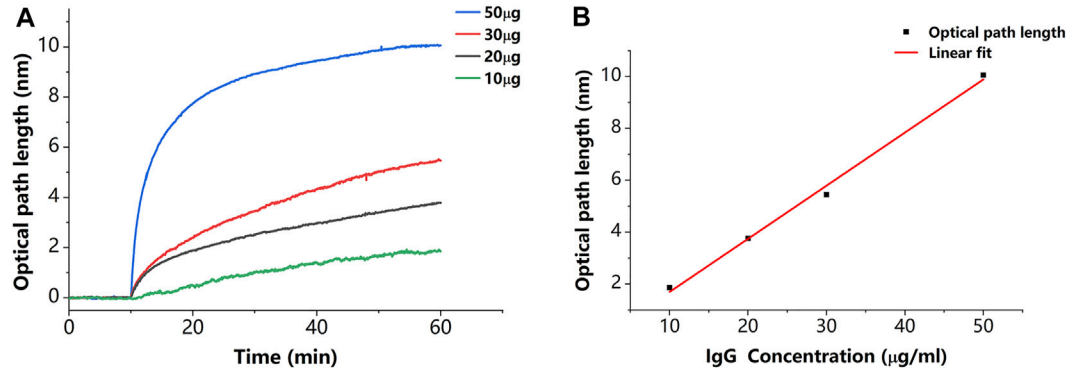

FIGURE 8 | (A) Results of binding of IgG to protein A in different concentrations. **(B)** Relationship between thickness variation and IgG concentration. Each plotted data point in **Figure 8B** is averaged from three measurements.

closed by the blocking reagent molecules, thus allowing IgG to adhere to the dopamine layer. This change was independent of the probe.

We calculated the average value of the peak phase $\Delta\phi$ in **Figure 6** for each reaction after the reaction was completed, and subsequently calculated the growth of optical path length due to specific binding and non-specific binding by $\Delta Z = \Delta\phi/2k_0n$. To eliminate this variation, the stable data were used in the first 5 min to obtain the correction factor a and compensation factor b, which are given by **Eq. 3** and used in **Eq. 4** to correct specific binding. The relationship between the binding and the corrected result is displayed in **Figure 7**. The results demonstrated the proposed sensor has the capability to track and suppress non-specific binding, and this capability offers the potential for more accurate drug screening.

In addition to verifying that the sensor has the described capabilities, we estimated the sensitivity of the described sensor. As shown in **Figure 8A**, we set a concentration gradient to verify that the specific binding of IgG to protein A causes a proportional variation in thickness. The thickness variations caused by 10, 20, 30, and 50 μg/ml concentrations of IgG molecules are 1.86, 3.76, 5.45, and 10.06 nm, respectively. Each plotted data point in **Figure 8B** is averaged from three measurements. The results of the linear fit are shown in **Figure 8B** with a slope of 0.205 nm/(μg/ml). This slope can be used to estimate the minimum detectable concentration, which indicates the sensitivity of the described sensor. The minimum detectable concentration is calculated by $D_{lim} = 3\sigma_s/(\delta h/\delta c)$, where $\delta h/\delta c$ is the slope of linear fit and σ_s is the standard deviation of the thickness after binding is completed. The standard deviation of the thickness from the data of 50 μg/ml is calculated as 0.011 μg/ml. Therefore, the sensitivity of the sensor is calculated as 0.16 μg/ml.

CONCLUSION

This paper presents a sensor based on coherence multiplexing, which can be used to resist different disturbances in biosensing applications, including temperature and non-specific binding disturbances. The proposed sensor has two reaction chambers and sensing chips of different thicknesses, which define two interferometric paths with different OPDs. This allows the proposed sensor to achieve self-reference based on coherent multiplexing. The proposed sensor is suitable for applications that require large-scale testing of biomolecular interactions, such as drug screening. Using fiber optic-based glass as a sensor chip reduces the cost of the proposed sensor. This technology can also be used in other sensing applications, such as multi-channel pressure sensing systems.

DATA AVAILABILITY STATEMENT

The raw data supporting the conclusion of this article will be made available by the authors, without undue reservation.

AUTHOR CONTRIBUTIONS

CG and YS conceived of the presented idea. ZH carried out the experimental work and wrote the article. FH provided the suggestions. YS and CG revised this paper. YH, ZY, and HZ provide experimental help to ZH.

FUNDING

This work was financially supported by the National Science Foundation of China (65105068), Ministry of Education Science and Technology Industry-University Cooperative Education Program (202102153072), Educational Research Project for Young and Middle-aged Teachers of Fujian Provincial Education Department (JAT200009), and Fuzhou University Research Start-up funding (GXRC-21019).

REFERENCES

Burg, S., Cohen, M., Margulis, M., Roth, S., and Danielli, A. (2019). Magnetically Aggregated Biosensors for Sensitive Detection of Biomarkers at Low Concentrations. *Appl. Phys. Lett.* 115 (10), 103702. doi:10.1063/1.5108891

Chirvi, S., Qiang, Z., and Davé, D. P. (2012). Coherence-multiplexed, Label-free Biomolecular Interaction Analysis. *Opt. Lett.* 37 (14), 2952–2954. doi:10.1364/ol.37.002952

Dandapat, K., Tripathi, S. M., Chinifooroshan, Y., Bock, W. J., and Mikulic, P. (2016). Compact and Cost-Effective Temperature-Insensitive Bio-Sensor Based on Long-Period Fiber Gratings for Accurate Detection of E Coli Bacteria in Water. *Opt. Lett.* 41 (18), 4198–4201. doi:10.1364/OL.41.004198

Demircioğlu, Ö., Salas, J. F. L., Rey, G., Weiss, T., Mousel, M., Redinger, A., et al. (2017). Optical Properties of Cu_2ZnSnSe_4 Thin Films and Identification of Secondary Phases by Spectroscopic Ellipsometry. *Opt. Express* 25 (5), 5327–5340. doi:10.1364/OE.25.005327

Engvall, E., and Perlmann, P. (1971). Enzyme-linked Immunosorbent Assay (ELISA) Quantitative Assay of Immunoglobulin G. *Immunochemistry (1965)* 8 (9), 871–874. doi:10.1016/0019-2791(71)90454-x

Guo, C., Yang, X., Shen, Z., Wu, J.-P., Zhong, S., He, Y., et al. (2018). A Fluidic Biosensor Based on a Phase-Sensitive Low-Coherence Spectral-Domain Interferometer. *Sensors* 18 (11), 3757. doi:10.3390/s18113757

He, X., Yi, H., Long, J., Zhou, X., Yang, J., and Yang, T. (2016). Plasmonic crystal Cavity on Single-Mode Optical Fiber End Facet for Label-free Biosensing. *Appl. Phys. Lett.* 108 (23), 231105. doi:10.1063/1.4953413

Hobbs, K., Cathcart, N., and Kitaev, V. (2016). Gold-plated Silver Nanoparticles Engineered for Sensitive Plasmonic Detection Amplified by Morphological Changes. *Chem. Commun.* 52 (63), 9785–9788. doi:10.1039/c6cc05260f

Jin, Y., Song, Y., Qu, X., Li, Z., Ji, Y., and He, A. (2017). Three-dimensional Dynamic Measurements of CH* and C2* Concentrations in Flame Using Simultaneous Chemiluminescence Tomography. *Opt. Express* 25 (5), 4640–4654. doi:10.1364/OE.25.004640

Joo, C., Özkumur, E., Ünlü, M. S., and Boer, J. F. d. (2009). Spectral-domain Optical Coherence Phase Microscopy for Label-free Multiplexed Protein Microarray Assay. *Biosens. Bioelectron.* 25 (2), 275–281. doi:10.1016/j.bios.2009.06.028

Li, S., Liu, C., Yin, G., Zhang, Q., Luo, J., and Wu, N. (2017). Aptamer-molecularly Imprinted Sensor Base on Electrogenerated Chemiluminescence Energy Transfer for Detection of Lincomycin. *Biosens. Bioelectron.* 91, 687–691. doi:10.1016/j.bios.2017.01.038

Liu, Y., Chen, S., Liu, Q., Liu, Z., and Wei, P. (2017). Simple Method for Self-Referenced and Lable-free Biosensing by Using a Capillary Sensing Element. *Opt. Express* 25 (10), 11750–11759. doi:10.1364/OE.25.011750

MacBeath, G. (2002). Protein Microarrays and Proteomics. *Nat. Genet.* 32 (Suppl. l), 526–532. doi:10.1038/ng1037

Merryweather, A. J., Schnedermann, C., Jacquet, Q., Grey, C. P., and Rao, A. (2021). Operando Optical Tracking of Single-Particle Ion Dynamics in Batteries. *Nature* 594 (7864), 522–528. doi:10.1038/s41586-021-03584-2

Orgovan, N., Kovacs, B., Farkas, E., Szabó, B., Zaytseva, N., Fang, Y., et al. (2014). Bulk and Surface Sensitivity of a Resonant Waveguide Grating Imager. *Appl. Phys. Lett.* 104 (8), 083506. doi:10.1063/1.4866460

Rubin, E. J. (2018). TB Diagnosis from the Dark Ages to Fluorescence. *Nat. Microbiol.* 3 (3), 268–269. doi:10.1038/s41564-018-0118-6

Ryu, S., Hyun, K.-A., Heo, J., Jung, H.-I., and Joo, C. (2014). Label-free Cell-Based Assay with Spectral-Domain Optical Coherence Phase Microscopy. *J. Biomed. Opt.* 19 (4), 046003. doi:10.1117/1.jbo.19.4.046003

Sun, F., Zeng, J., Jing, M., Zhou, J., Feng, J., Owen, S. F., et al. (2018). A Genetically Encoded Fluorescent Sensor Enables Rapid and Specific Detection of Dopamine in Flies, Fish, and Mice. *Cell* 174 (2), 481–496. doi:10.1016/j.cell.2018.06.042

Sztain, T., Ahn, S.-H., Bogetti, A. T., Casalino, L., Goldsmith, J. A., Seitz, E., et al. (2021). A Glycan Gate Controls Opening of the SARS-CoV-2 Spike Protein. *Nat. Chem.* 13 (10), 963–968. doi:10.1038/s41557-021-00758-3

Tardif, M., Jager, J.-B., Marcoux, P. R., Uchiyamada, K., Picard, E., Hadji, E., et al. (2016). Single-cell Bacterium Identification with a SOI Optical Microcavity. *Appl. Phys. Lett.* 109 (13), 133510. doi:10.1063/1.4963070

Wu, P.-T., Wu, M.-C., and Wu, C.-M. (2010). Measurement of the Air gap Width between Double-Deck Metal Layers Based on Surface Plasmon Resonance. *J. Appl. Phys.* 107 (8), 083111. doi:10.1063/1.3354011

Conflict of Interest: The authors declare that the research was conducted in the absence of any commercial or financial relationships that could be construed as a potential conflict of interest.

Publisher's Note: All claims expressed in this article are solely those of the authors and do not necessarily represent those of their affiliated organizations, or those of the publisher, the editors and the reviewers. Any product that may be evaluated in this article, or claim that may be made by its manufacturer, is not guaranteed or endorsed by the publisher.

Copyright © 2022 Shen, Huang, Huang, He, Ye, Zhang and Guo. This is an open-access article distributed under the terms of the Creative Commons Attribution License (CC BY). The use, distribution or reproduction in other forums is permitted, provided the original author(s) and the copyright owner(s) are credited and that the original publication in this journal is cited, in accordance with accepted academic practice. No use, distribution or reproduction is permitted which does not comply with these terms.

frontiers | Frontiers in Chemistry

ORIGINAL RESEARCH
published: 08 April 2022
doi: 10.3389/fchem.2022.845311

Circular Dichroism Second-Harmonic Generation Imaging of $KTiOPO_4$ Nanocrystal Through Stratified Media

Biwei Wu[1,2], *Keyi Wu*[1,2], *Xuefeng Sun*[1,2], *Weibo Wang*[1,2]* *and Jiubin Tan*[1,2]

[1]*Institute of Ultra-precision Optoelectronic Instrument Engineering, Harbin Institute of Technology, Harbin, China,* [2]*Key Lab of Ultra-precision Intelligent Instrumentation, Harbin Institute of Technology, Ministry of Industry and Information Technology, Harbin, China*

Potassium titanyl phosphate ($KTiOPO_4$, KTP) particle of nanometric size (nano-KTP) is an attractive material for nonlinear microscopy, and the optimized growth of large-size KTP single crystals has numerous applications for efficient frequency conversion in laser technology. Its three-dimensional orientation and nanoscale morphology are important for growth optimization. In this paper, we introduce an imaging technique based on circular dichroism second-harmonic generation (CD-SHG) to characterize the 3D distribution of KTP nanocrystal. A rigorous theoretical model of CD-SHG imaging for nano-KTP through stratified media is demonstrated. Circular dichroism analysis is used to probe the orientation of 3-axis with respect to the optical observation axis. The research results show that the azimuthal angle of the peak value (SHG) or valley value (CD-SHG) is strongly related to the excitation polarization when the KTP sample is excited by different circular polarizations. Importantly, the refractive index mismatches and the imaging depth also affect the azimuthal angle. Thus, the proposed framework enables a more precise quantitative analysis of the CD-SHG signal of KTP.

Keywords: nanocrystal, nonlinear optics, second-harmonic generation, polarization, imaging

OPEN ACCESS

Edited by:
Chao He,
University of Oxford, United Kingdom

Reviewed by:
Lei Li,
California Institute of Technology, United States
Jianbo Tang,
Southern University of Science and Technology, China

***Correspondence:**
Weibo Wang
wwbhit@hit.edu.cn

Specialty section:
This article was submitted to Nanoscience, a section of the journal Frontiers in Chemistry

Received: *29 December 2021*
Accepted: *08 February 2022*
Published: *08 April 2022*

Citation:
Wu B, Wu K, Sun X, Wang W and Tan J (2022) Circular Dichroism Second-Harmonic Generation Imaging of $KTiOPO_4$ Nanocrystal Through Stratified Media. Front. Chem. 10:845311. doi: 10.3389/fchem.2022.845311

INTRODUCTION

Potassium titanyl phosphate ($KTiOPO_4$; KTP) has been widely used in several nonlinear-optical applications, including parametric generation and amplification, by virtue of its superior performance in nonlinear-optical coefficients, large acceptance angles, high optical damage threshold, and thermally stable phase-matching properties (Bierlein and Vanherzeele, 1989). In particular, the optimized growth of large-size single KTP crystals plays an important role for efficient frequency conversion in laser technology (Driscoll et al., 1986). Recently, second harmonic generation (SHG) in diamond-blade diced KTP ridge waveguides has also been demonstrated (Chen et al., 2016). Furthermore, KTP particle of nanometric size (nano-KTP) is a suitable nonlinear crystal material for SHG microscopy, which can generate a stable blinking-free second-harmonic signal that can be easily detected (Le Xuan et al., 2008). Notably, the three-dimensional orientation and nanoscale morphology of KTP are important for growth optimization.

In a SHG process, two photons of frequency ω absorbed by the ground state combine to form a doubled frequency (2ω) photon. SHG-based techniques have been applied in the investigation of semi-conductor nanowires with different composition and nanoscale morphology detection of nano-objects (Bautista et al., 2015; Ren et al., 2015; Bautista et al., 2012; Bautista et al., 2017). Importantly, polarization-resolved SHG microscopy has proven to be an effective all-optical mode for *in situ*

measurement of underlying crystal structures without sample damages, as SHG is sensitive to the polarization of excitation fields (Gleeson et al., 2020). Moreover, SHG circular dichroism (CD) parameter has been recently developed to explicitly evidence the presence of a chiral response of the nanocrescents induced by the geometry of hybrid plasmonic–photonic nanosurfaces (Belardini et al., 2014). However, the potential of CD-SHG microscopy to probe three-dimensional orientation of KTP with respect to the optical observation axis and the polarity distribution of out-of-plane nanocrystal assemblies has not been explored.

It is worth noting that in polarization-resolved SHG microscopy for crystal material, the specimen is often observed with a high NA objective with immersion medium and a cover glass. Moreover, they usually have different refractive indices. For example, the refractive index of KTP is 1.738 (1,064 nm) (Sutherland, 2003), which is much larger than that of immersion medium or cover glass. When the excitation beams are focused through the stratified media, aberrations are introduced due to the refractive index mismatches. The presence of the aberration will cause a structural and polarization state modification of the focused spot, and then lead to a performance degradation of the polarization-resolved SHG microscopy. However, the currently used theoretical frameworks are inapplicable for the analysis of polarization-resolved SHG imaging, which are based on the assumption that the specimen is situated in a homogeneous medium of propagation or located at a dielectric interface, neglecting the influence of sample refractive index heterogeneity near the focus. As a complementary tool with a different principle, the finite-difference time-domain (FDTD) approach has been adopted in many microscopy technique simulations, such as wide-field, confocal, and SHG microscopy (Török et al., 2008; Choi et al., 2007; van der Kolk et al., 2018). More recently, the ubiquitous geometry of a vertical interface between index-mismatched media and the case of polarized THG contrasts are analyzed based on FDTD methods (Morizet et al., 2021). The effects of the refractive index mismatches and the imaging depth on CD-SHG microscopy have not yet been studied.

Here, we present a rigorous theoretical framework of CD-SHG microscopy through stratified media for KTP crystal. The SHG intensity patterns for left-handed and right-handed circular polarized excitations and the corresponding CD-SHG signal obtained in a mismatch free medium and in a mismatched stratified media will be compared from several aspects. The quantitative analysis of azimuthal angle of SHG signal and the SHG response to a specific point object as a function of the effective NA in different depths will be demonstrated. In addition, circular-polarization-excited SHG imaging in index-mismatched media in the case of a vertical interface between water and a KTP material are investigated based on FDTD methods. As a complementary polarization-resolved scheme, CD-SHG imaging not only provides intrinsic 3D imaging capabilities with sub-micrometer spatial resolution, but also paves the way for determining the local 3D orientation of KTP molecules information with a new structural contrast mechanism. We also expect that the study can contribute towards new insights into optimization of CD-SHG microscopy instrumentation.

MODELING OF CIRCULAR DICHROISM SECOND-HARMONIC GENERATION THROUGH STRATIFIED MEDIA

Figure 1 shows the most common geometry of a polarization-resolved SHG microscope, including the configuration for excitation by left-handed and right-handed circular polarized beams through a high NA objective and a three-layer medium. The specimen is observed through an immersion medium and a coverslip. The first interface, perpendicular to the optical axis, is at $z = -h_1$, and the second at $z = -h_2$. The wave numbers of the light beam in the immersion medium, cover glass and specimen are k_1, k_2, and k_3, respectively. $k_1 = 2\pi n_1/\lambda_0$, $k_2 = 2\pi n_2/\lambda_0$, and $k_3 = 2\pi n_3/\lambda_0$. n_1, n_2, and n_3 are the refractive index of the immersion medium, cover glass, and specimen respectively.

Based on the Richards–Wolf vectorial diffraction integral (Richards and Wolf, 1959; Török and Varga, 1997; Haeberlé et al., 2003), the generalized formulae for the vectorial electric field in the focal region illuminated by left-handed and right-handed circular polarized beams through an N-layer medium are derived. Under the idiomatic polar coordinate system notation, the Cartesian components of the electric field in the focal region can be expressed as:

$$E_{Nx} = A\left[I_{cir-0}^{(N)} + I_{cir-2}^{(N)} \exp\left(\pm 2i\phi_P\right)\right], \tag{1}$$

$$E_{Ny} = iA\left[I_{cir-0}^{(N)} - I_{cir-2}^{(N)} \exp\left(\pm 2i\phi_P\right)\right], \tag{2}$$

$$E_{Nz} = -2iAI_{cir-1}^{(N)} \exp\left(\pm i\phi_P\right), \tag{3}$$

and the integrals $I_{cir-0}^{(N)}$, $I_{cir-1}^{(N)}$, and $I_{cir-2}^{(N)}$ are given by

$$I_{cir-0}^{(N)} = \int_0^{\alpha_1} \cos^{1/2}\theta_1 \sin\theta_1 \exp\left(ik_0\psi_i\right)\left(T_s^{(N-1)} + T_p^{(N-1)} \cos\theta_N\right) \times J_0\left(k_1 r_P \sin\theta_1 \sin\theta_P\right) \exp\left(ik_N r_P \cos\theta_N \cos\theta_P\right) d\theta_1, \tag{4}$$

$$I_{cir-1}^{(N)} = \int_0^{\alpha_1} \cos^{1/2}\theta_1 \sin\theta_1 \exp\left(ik_0\psi_i\right) T_p^{(N-1)} \sin\theta_N \times J_1\left(k_1 r_P \sin\theta_1 \sin\theta_P\right) \exp\left(ik_N r_P \cos\theta_N \cos\theta_P\right) d\theta_1, \tag{5}$$

$$I_{cir-2}^{(N)} = \int_0^{\alpha_1} \cos^{1/2}\theta_1 \sin\theta_1 \exp\left(ik_0\psi_i\right)\left(T_s^{(N-1)} - T_p^{(N-1)} \cos\theta_N\right) \times J_2\left(k_1 r_P \sin\theta_1 \sin\theta_P\right) \exp\left(ik_N r_P \cos\theta_N \cos\theta_P\right) d\theta_1, \tag{6}$$

$$\psi_i = h_{N-1} n_N s_{Nz} - h_1 n_1 \cos\theta_1 s_{1z}, \tag{7}$$

where (r_P, θ_P, ϕ_P) are the spherical polar coordinates of an observation point P near the focal region, respectively. α_1 is the convergence semi-angle of the illumination, and is given as $\alpha_1 = \arcsin(\mathrm{NA}/n1)$. l_0 (θ_1) is the amplitude function in terms of θ_1 and $J_n(x)$ denotes a Bessel function of the first kind, of order n. $T_p^{(N-1)}$ and $T_s^{(N-1)}$ are the transmission coefficient of the stratified medium describing the p- and s-polarized light traversing N–1 media respectively and calculated as in Török

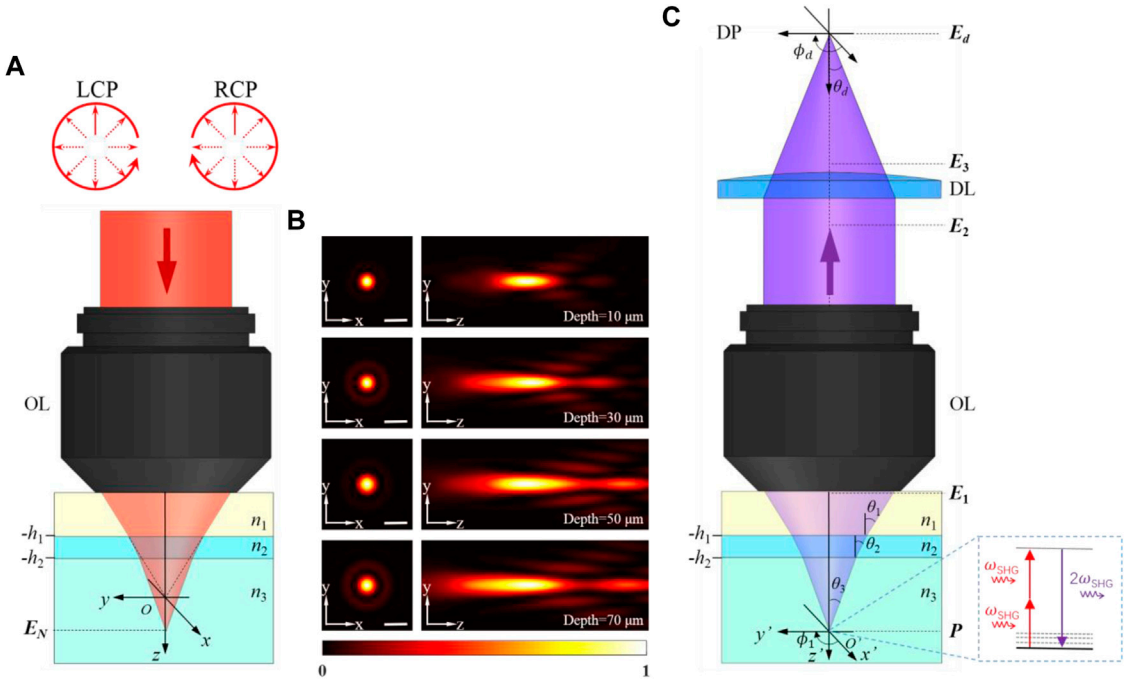

FIGURE 1 | (A) Schematic of focusing through a three-layer stratified medium for left-handed and right-handed circular polarized beams. The origin *O* of the (*x*, *y*, *z*) reference frame locates at the nominal focal point position. **(B)** Near-focus excitation intensity distributions at different depths. **(C)** SHG radiation imaged through the same medium. The specimen is placed at the origin *O'* of the (*x'*, *y'*, *z'*) reference frame. LCP: left-handed circular polarization, RCP: right-handed circular polarization, OL: objective lens, DP: detector plane, DL: detector lens. Scale bar, 1 μm.

and Varga (1997). ψ_i denotes the initial aberration function. **Figure 1B** shows the near-focus excitation intensity distributions at different depths.

As the focal electric field distribution is determined, the interaction with the material can be calculated. SHG intensity has a quadratic relationship with the optical field intensity of the excitation beam at the focus region, which is also dependent on the nonlinear susceptibility tensor of the sample. When the frequency of the laser light source is far away from the resonant frequency of the specimen, the number of non-zero elements in this third-order tensor with 27 separate elements reduces according to Kleinmann's symmetry (Kleinman, 1962; Yew and Sheppard, 2006). SHG polarization is related to the focused laser excitation field by:

$$\begin{bmatrix} P_x \\ P_y \\ P_z \end{bmatrix} = \begin{bmatrix} d_{xxx} & d_{xyy} & d_{xzz} & d_{xyz} & d_{xxz} & d_{xxy} \\ d_{yxx} & d_{yyy} & d_{yzz} & d_{yyz} & d_{yxz} & d_{yxy} \\ d_{zxx} & d_{zyy} & d_{zzz} & d_{zyz} & d_{zxz} & d_{zxy} \end{bmatrix} \begin{bmatrix} E_{Nx}E_{Nx} \\ E_{Ny}E_{Ny} \\ E_{Nz}E_{Nz} \\ 2E_{Ny}E_{Nz} \\ 2E_{Nx}E_{Nz} \\ 2E_{Nx}E_{Ny} \end{bmatrix}. \tag{8}$$

The SHG polarization emits corresponding radiation, and the harmonic field $\boldsymbol{E_1}$ traverses back the stratified medium (**Figure 1C**). The distribution before the objective lens (in medium 1) can be expressed as (Török, 2000):

$$E_{1x'} = \frac{1}{2}\Big[P_x^*\left(T_s' + T_p' \cos\theta_N \cos\theta_1\right) - 2P_z^* T_p' \sin\theta_N \cos\theta_1 \cos\phi_1 - \left(T_s' - T_p' \cos\theta_N \cos\theta\right)_1 \left(P_x^* \cos 2\phi_1 + P_y^* \sin 2\phi_1\right)\Big], \tag{9}$$

$$E_{1y'} = \frac{1}{2}\Big[P_y^*\left(T_s' + T_p' \cos\theta_N \cos\theta_1\right) - 2P_z^* T_p' \sin\theta_N \cos\theta_1 \sin\phi_1 - \left(T_s' - T_p' \cos\theta_N \cos\theta_1\right)\left(P_x^* \sin 2\phi_1 - P_y^* \cos 2\phi_1\right)\Big], \tag{10}$$

$$E_{1z'} = \left[P_z^* T_p' \sin\theta_N \sin\theta_1 - T_p' \cos\theta_N \sin\theta_1 \left(P_x^* \cos\phi_1 + P_y^* \sin\phi_1\right)\right]. \tag{11}$$

(P_x^*, P_y^*, P_z^*) denotes the Cartesian components of the complex conjugate of $\boldsymbol{P}$. The transmission coefficients T_s' and T_p' for the stratified medium can be calculated as in Haeberlé et al. (2003) and Török and Varga (1997), but with propagation direction from medium *N* to medium 1.

After being collimated by the objective lens, the Cartesian components of the harmonic field vector $\boldsymbol{E_2}$ in the intermediate plane is given by (Wang et al., 2019):

$$E_{2x'} = (\cos\theta_1)^{-1/2}\Big\{P_x^*\left(T_p' \cos^2\phi_1 \cos\theta_N + T_s' \sin^2\phi_1\right) + P_y^*\left(T_p' \cos\theta_N - T_s'\right)\sin\phi_1 \cos\phi_1 - P_z^* T_p' \sin\theta_N \cos\phi_1\Big\}, \tag{12}$$

$$E_{2y'} = (\cos\theta_1)^{-1/2}\Big\{P_x^* \cos\phi_1\left(T_p' \cos\theta_N - T_s'\right)\sin\phi_1 + P_y^*\left(T_s' \cos^2\phi_1 + T_p' \sin^2\phi_1 \cos\theta_N\right) - P_z^* T_p' \sin\phi_1 \sin\theta_N\Big\}, \tag{13}$$

Next, the field vector $\boldsymbol{E_3}$, behind the detector lens can be described by

$$E_{3x} = (\cos\theta_d)^{1/2}(\cos\theta_1)^{-1/2}\Big\{P_x^*\Big[\frac{1}{2}T_s^{'}(1-\cos 2\phi_1) + \frac{1}{2}T_p^{'}\cos\theta_d\cos\theta_N(1+\cos 2\phi_1)\Big] + P_y^*\Big[\frac{1}{2}T_p^{'}\cos\theta_d\cos\theta_N - \frac{1}{2}T_s^{'}\Big]\sin 2\phi_1 - P_z^*T_p^{'}\cos\theta_d\sin\theta_N\cos\phi_1\Big\}, \tag{14}$$

$$E_{3y} = (\cos\theta_d)^{1/2}(\cos\theta_1)^{-1/2}\Big\{P_x^*\Big[\frac{1}{2}\Big(-T_s^{'} + T_p^{'}\cos\theta_d\cos\theta_N\Big)\sin 2\phi_1\Big] + P_y^*\Big[\frac{1}{2}T_s^{'}(1+\cos 2\phi_1) + \frac{1}{2}T_p^{'}\cos\theta_d\cos\theta_N(1-\cos 2\,\phi)\Big] - P_z^*T_p^{'}\cos\theta_d\sin\theta_N\sin\phi_1\Big\}, \tag{15}$$

$$E_{3z} = (\cos\theta_d)^{1/2}(\cos\theta_1)^{-1/2}\Big\{P_x^*\Big(-T_p^{'}\sin\theta_d\cos\theta_N\cos\phi_1\Big) + P_y^*\Big(-T_p^{'}\sin\theta_d\cos\theta_N\sin\phi_1\Big) + P_z^*T_p^{'}\sin\theta_d\sin\theta_N\Big\}. \tag{16}$$

Hence, the expression for the SHG field components at the detector plane can be obtained by using the integral formula of Richards and Wolf (Richards and Wolf, 1959; Török et al., 1998), as:

$$E_{dx} = -iA_dP_x^*I_{d01} + iA_dP_x^*I_{d21}\cos 2\phi_d + iA_dP_y^*I_{d21}\sin 2\phi_d - 2A_dP_z^*I_{d11}\cos\phi_d, \tag{17}$$

$$E_{dy} = iA_dP_x^*I_{d21}\sin 2\phi_d - iA_dP_y^*I_{d01} - iA_dP_y^*I_{d21}\cos 2\phi_d - 2A_dP_z^*I_{d11}\sin\phi_d, \tag{18}$$

$$E_{dz} = -2A_dP_x^*I_{d12}\cos\phi_d - 2A_dP_y^*I_{d12}\sin\phi_d - 2iA_dP_z^*I_{d02}, \tag{19}$$

with the quantities I_{d01}, I_{d02}, I_{d11}, I_{d12}, and I_{d21} defined as:

$$I_{d01} = \int_0^{\alpha_d}(\cos\theta_d)^{1/2}(\cos\theta_1)^{-1/2}\Big(T_s^{'}\sin\theta_d + T_p^{'}\sin\theta_d\cos\theta_d\cos\theta_N\Big)J_0(k_d\rho_d\sin\theta_d)\times\exp\big(-ik_{d0}\psi_{\mathrm{det}}\big)\exp\big(-ik_dz_d\cos\theta_d\big)d\theta_d, \tag{20}$$

$$I_{d02} = \int_0^{\alpha_d}(\cos\theta_d)^{1/2}(\cos\theta_1)^{-1/2}\Big(T_p^{'}\sin^2\theta_d\sin\theta_N\Big)J_0(k_d\rho_d\sin\theta_d)\times\exp\big(-ik_{d0}\psi_{\mathrm{det}}\big)\exp\big(-ik_dz_d\cos\theta_d\big)d\theta_d, \tag{21}$$

$$I_{d11} = \int_0^{\alpha_d}(\cos\theta_d)^{1/2}(\cos\theta_1)^{-1/2}\Big(T_p^{'}\cos\theta_d\sin\theta_d\sin\theta_N\Big)J_1(k_d\rho_d\sin\theta_d)\times\exp\big(-ik_{d0}\psi_{\mathrm{det}}\big)\exp\big(-ik_dz_d\cos\theta_d\big)d\theta_d, \tag{22}$$

$$I_{d12} = \int_0^{\alpha_d}(\cos\theta_d)^{1/2}(\cos\theta_1)^{-1/2}\Big(T_p^{'}\sin^2\theta_d\cos\theta_N\Big)J_1(k_d\rho_d\sin\theta_d)\times\exp\big(-ik_{d0}\psi_{\mathrm{det}}\big)\exp\big(-ik_dz_d\cos\theta_d\big)d\theta_d, \tag{23}$$

$$I_{d21} = \int_0^{\alpha_d}(\cos\theta_d)^{1/2}(\cos\theta_1)^{-1/2}\Big(-T_s^{'}\sin\theta_d + T_p^{'}\sin\theta_d\cos\theta_d\cos\theta_N\Big)\times J_2(k_d\rho_d\sin\theta_d)\cdot\exp\big(-ik_{d0}\psi_{\mathrm{det}}\big)\exp\big(-ik_dz_d\cos\theta_d\big)d\theta_d, \tag{24}$$

α_d is the angular aperture of the detector lens. ρ_d, ϕ_d, and z_d are the cylindrical coordinates of an observation point near the detection region and the azimuthal angle θ_d is related to the azimuthal angle θ_1 by the relationship:

$$\frac{k_{d1}\sin\alpha_1}{k_d\sin\alpha_d} = \frac{k_{d1}\sin\theta_1}{k_d\sin\theta_d} = M, \tag{25}$$

where M is the magnification of the imaging system. k_{d0}, k_{d1}, and k_d are the wave numbers for the second-harmonic field in vacuum, medium 1 (immersion medium), and the image space, respectively, expressed as $k_{d0} = 2\pi/\lambda_{\mathrm{SHG}}$, $k_{d1} = 2\pi n_1/\lambda_{\mathrm{SHG}}$, and $k_d = 2\pi n_d/\lambda_{\mathrm{SHG}}$. λ_{SHG} denotes the wavelength of SHG. n_d is the refractive index of the image space. The aberration function in the detection path ψ_{det} can be expressed by

$$\Psi_{\mathrm{det}} = n_1h_1\cos\theta_1 - n_Nh_{N-1}\cos\theta_N. \tag{26}$$

As a result, the detected SHG intensity excited by left-handed and right-handed circular polarized beams through stratified media can be obtained according to:

$$I_{SHG} = |E_{dx}|^2 + \big|E_{dy}\big|^2 + |E_{dz}|^2. \tag{27}$$

In the end, CD-SHG is measured as the normalized difference between SHG signals I_{SHG}^L and I_{SHG}^R excited with a left-handed circular and a right-handed circular polarization (Schmeltz et al., 2020):

$$\mathrm{CD-SHG} = \frac{I_{SHG}^L - I_{SHG}^R}{\big(I_{SHG}^L + I_{SHG}^R\big)/2}. \tag{28}$$

RESULTS AND DISCUSSION

KTP is a non-centrosymmetric orthorhombic crystal with large nonlinear-optical coefficients. The accurate magnitude of the nonlinear optical coefficients d (in pm/V) of KTP has been measured (Vanherzeele and Bierlein, 1992), and with the values $d_{xxz} = 1.91$, $d_{yyz} = 3.64$, $d_{zxx} = 2.54$, $d_{zyy} = 4.35$, $d_{zzz} = 16.9$ when excited in the wavelength of 1,064 nm. It is noteworthy that d_{zzz} is the dominant nonlinear optical coefficient. The induced SHG polarization can be expressed as:

$$\begin{aligned} P_x &= 2d_{xxz}E_{Nx}E_{Nz},\\ P_y &= 2d_{yyz}E_{Ny}E_{Nz},\\ P_z &= d_{zxx}E_{Nx}E_{Nx} + d_{zyy}E_{Ny}E_{Ny} + d_{zzz}E_{Nz}E_{Nz}, \end{aligned} \tag{29}$$

The SHG intensity patterns for a refractive index perfectly matched, aberration-free medium ($n_1 = n_2 = n_3$) and mismatched stratified media, excited by left-handed and right-handed circular

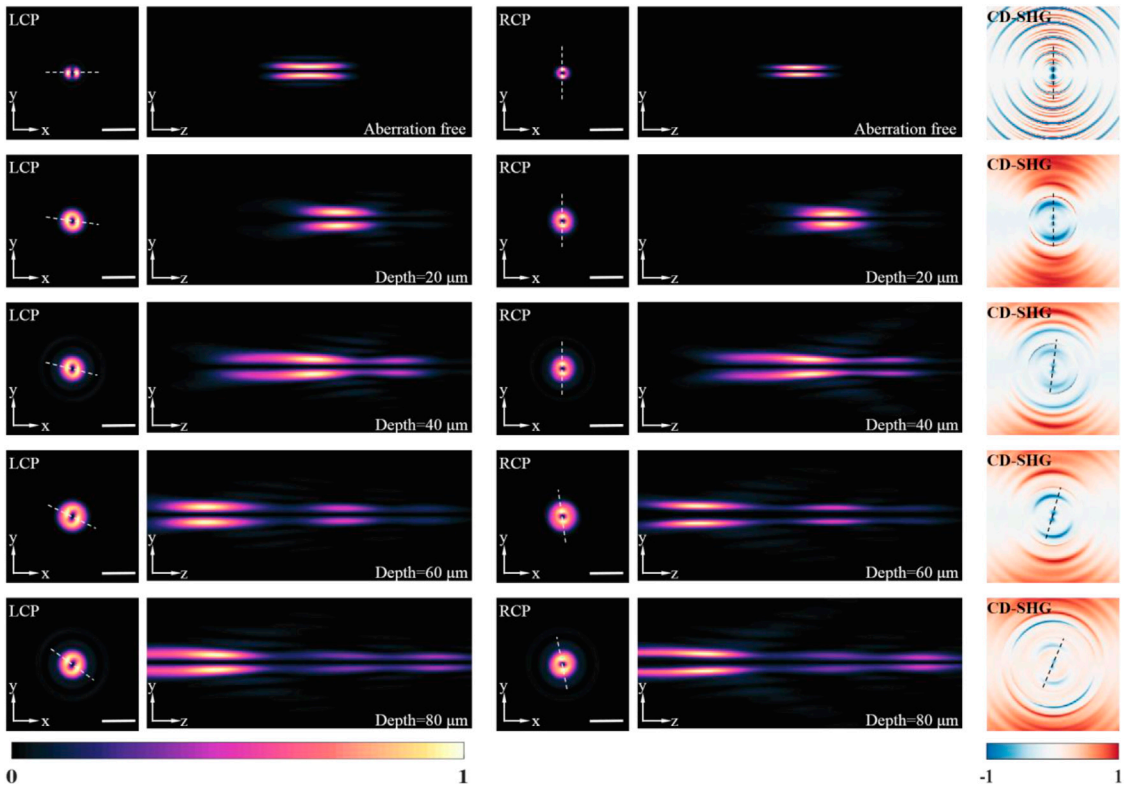

FIGURE 2 | The detected SHG intensity distributions excited by left-handed, right-handed circular polarized beams at different imaging depths, and corresponding CD-SHG signal. All the intensity distributions are normalized by the respective maximum value. Scale bar, 1 μm.

polarized beams at different imaging depths, are shown in **Figure 2**. For a fair comparison, the calculations are performed at λ = 1,064 nm and an oil immersion (n_1 = 1.518) objective of NA = 1.2 is considered. The nominal magnification of the imaging system M is set to 100. For the mismatched stratified media, the KTP specimen (n_3 = 1.738) is mounted below a 170-μm cover glass (n_2 = 1.525). The imaging depth (h_2) is set to 20, 40, 60, and 80 μm, respectively. It is easy to observe a variation for the SHG intensity pattern when the KTP sample is excited by different circular polarizations. The azimuthal angle of the peak value (SHG) or valley value (CD-SHG) were calculated, as listed in **Table 1**. The azimuthal angle of the peak value (SHG) or valley value (CD-SHG) is strongly related to the excitation polarization. Besides, for the same excitation, the refractive index mismatches and the imaging depth also affect the azimuthal angle of the peak value (SHG) or valley value (CD-SHG). On the other hand, the SHG intensity distribution of aberration-free medium is symmetric along the z-axis and has no side lobes. The location of the peak intensity is at the nominal focus. In contrast, for the mismatched layered media, there is an aberrational focus shift. As the imaging depth increases, the displacement increases and the stretching of the intensity distribution in the z-direction becomes more pronounced. In this context, the three-dimensional orientation of KTP can be probed *via* the sign, azimuthal angle, and CD-SHG amplitude distribution. At the same time, the nanoscale morphology can be revealed by the scanned CD-SHG images.

The effects of varying effective NA when focusing to a certain depth in the specimens is essential for the optimization of the experimental polarization-resolved SHG configuration. The variation of effective NA is controlled by changing the pupil size with the iris. The other configuration parameters of the polarization-resolved SHG imaging system are identical to the system described above. **Figure 3** shows how the SHG response to a specific point object, excited with a left-handed circular polarization, is affected by altering the pupil size. The point object is located at the coordinate (x = 0.14 μm, y = 0 μm), which corresponds to the SHG signal peak location of aberration-free medium excited by left-handed circular polarized beams. The distribution along each vertical section shows the axial distribution for a given NA. Each distribution is normalized to the respective maximum intensity. The results for focusing into a perfectly matched, aberration-free medium are shown in **Figure 3A**. There is a regular shape of the SHG distribution for this case. **Figures 3B–D** reveal the distributions when focusing to depths of 20, 40, and 60 μm with refractive index mismatch, respectively. As the focusing depth gets to 20 μm, the distribution along the vertical section is broader than that in the aberration-free case, with no significant side lobes. It should also be pointed out that the NA corresponding to the peak intensity changes to 1.19. The shape of the axial

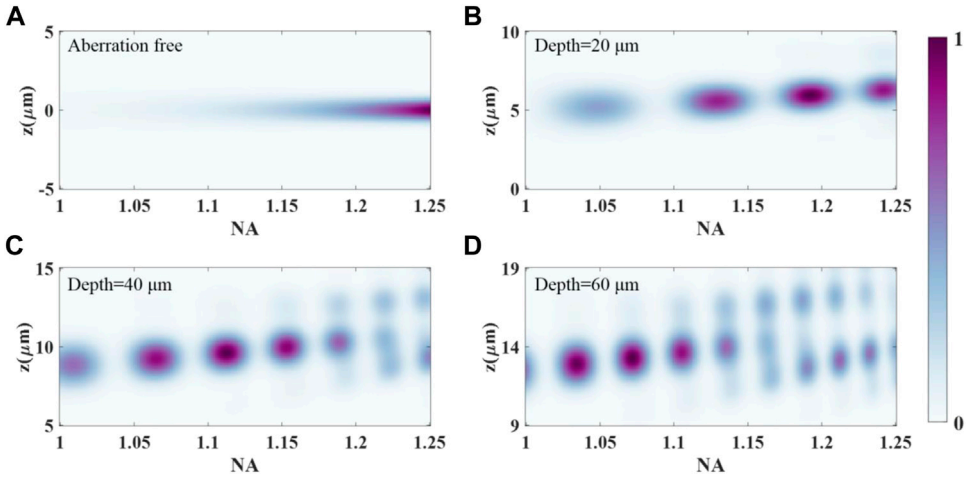

FIGURE 3 | SHG response to a point object located at the coordinate (x = 0.14 μm, y = 0 μm), excited with a left-handed circular polarization, as a function of the effective NA for an oil immersion objective of maximum NA = 1.25. **(A)** Refractive index mismatch free, **(B)** depth = 20 μm, **(C)** depth = 40 μm, **(D)** depth = 60 μm.

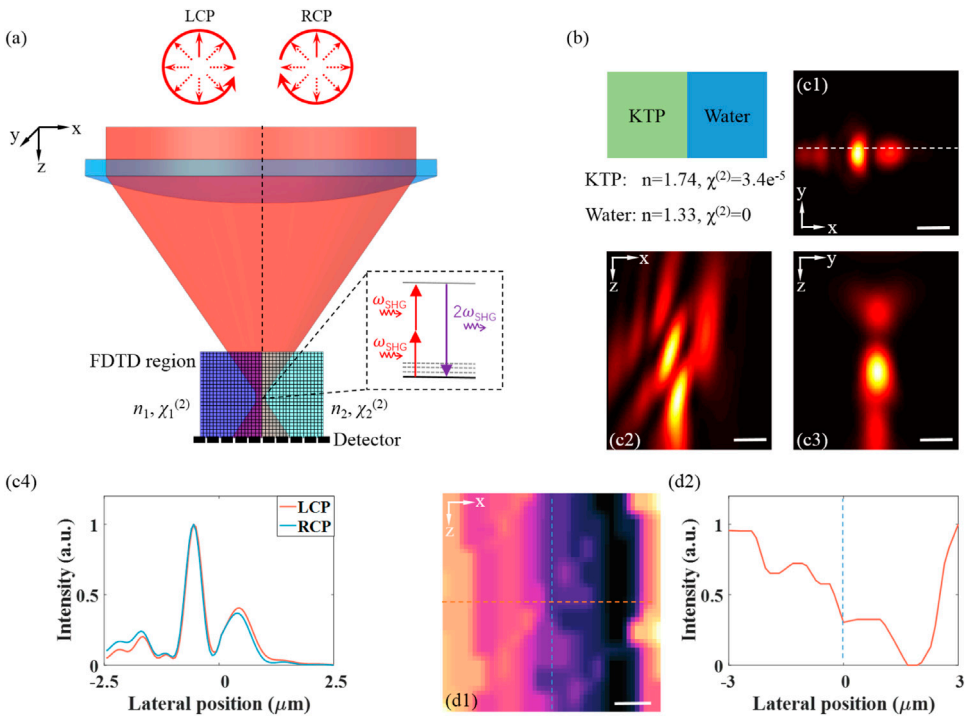

FIGURE 4 | (A) Schematic of an FDTD simulation for nonlinear microscopy for under circular polarized excitations to a vertical interface. **(B)** Simplified simulation geometry and properties of the simulation materials. **(C1–C3)** Near-focus excitation intensity distributions along a vertical interface located near the focus for left-handed circular polarized beams. **(C4)** The intensity line profiles along the horizontal lines in **(C1)**. **(D1,D2)** The SHG signal response distribution to a vertical KTP–water interface and corresponding intensity line profile. Scale bar, 1 μm.

distribution degenerates at higher NAs when focusing to a depth of 40 μm. These effects are further exaggerated at an imaging depth of 60 μm, and the axial distribution is severely distorted due to the specimen-induced spherical aberration. There are also significant side lobes along the vertical profile as the effective NA increases. These results are in accordance with the fact that high NA imaging systems are more sensitive to the aberration. In addition, it has been found that right-handed circular polarization has almost the same analysis result with left-handed circular polarization.

For a vertical interface between materials with refractive index mismatches, it has been found that commonly used diffraction-

TABLE 1 | The azimuthal angle (degree) of the peak value (SHG) or valley value (CD-SHG) in **Figure 2**.

Depth (μm)	LCP	RCP	CD-SHG
Aberration free	0	90.0	90.0
20	172.9	90.0	90.0
40	166.0	90.0	82.9
60	153.4	97.1	73.3
80	143.1	100.6	66.8

integral-based simulation strategies fail to generate accurate SHG distribution. In contrast, the FDTD family of methods calculate the electric fields at every point of a 3D grid in successive times by solving discretized Maxwell equations for specified materials. The implementation details and the validity of FDTD strategies in the context of nonlinear microscopy have been demonstrated (Morizet et al., 2021). **Figure 4A** shows the schematic of an FDTD simulation for SHG microscopy under circular polarized excitation to a vertical interface. Here, FDTD calculations are performed firstly to evaluate the field distribution when focused on a vertical KTP–water interface for circular polarized beams. An incoming Gaussian beam with a central wavelength of 1,045 nm and 10-nm bandwidth is tightly focused by an objective lens (NA = 1.0) in the simulation. The calculations are carried out over a focal region spanning 15 μm^3 × 15 μm^3 × 8 μm^3 discretized over 50-nm steps. The simulation time resolution is set to 160 fs. The intensity distribution is calculated as the beam was focused 5 μm below the sample surface. FDTD simulations were performed with Lumerical version 2020a in the Microsoft Windows 10 operating system. The calculation was implemented on a PC equipped with Intel Core i7-11800H CPU and one NVIDIA GeForce RTX 3050Ti Laptop graphical processing unit (GPU) with a typical computing mesh accuracy of 3. As shown in **Figures 4C1–C3**, the dramatic distortions of the focal field distribution caused by the mismatched vertical interface can be revealed by FDTD calculations. An asymmetric double-peaked distribution close to the interface is generated due to the vertical refractive index mismatches. Traditional propagation models could not take full account of sample heterogeneity near focus, which are usually neglected in polarization-resolved SHG microscopy studies. **Figure 4C4** shows the intensity line profiles along the horizontal lines in **Figure 4C1** at the position of y = 250 nm. It is particularly interesting to find that there is a slight difference between the focus field distributions of left-handed and right-handed circular polarized beams.

Next, the capability of FDTD methods to model circular-polarization-excited SHG imaging in index-mismatched media in the case of a vertical interface between water and a KTP material are investigated. For the KTP material, a non-zero diagonal second-order susceptibility was considered. We speculate that index mismatch of the vertical interface results in significant profile distortions. **Figure 4D1** illustrates the SHG intensity distribution when the focused beam is 2D scanned across the interface in a region of x ∈ (−3 μm, 3 μm), z ∈ (−5 μm, 3 μm). As shown in the extracted profile (**Figure 4D2**), for refractive index mismatch, the position of the peak or valley signals is not located at the interface, which is inconsistent with intuitive perception. The right-handed circular polarization has almost the same distribution with left-handed circular polarization. These results are important for the quantitative interpretation of SHG images of KTP growth.

CONCLUSION

In summary, we have demonstrated a previously unidentified rigorous model to demonstrate circular dichroism SHG microscopy through stratified media for KTP crystal. In our proposed model, the refractive index mismatches and the imaging depth are taken into account for quantitative analysis of the CD-SHG signal. It has been demonstrated that the azimuthal angle of the peak value (SHG) or valley value (CD-SHG) is strongly related to the excitation polarization when the KTP sample is excited by different circular polarizations. Importantly, for the same excitation, the refractive index mismatches and the imaging depth also affect the azimuthal angle. Besides, the numerical framework based on FDTD can be an applicable simulation strategy to investigate CD-SHG microscopy with sample refractive index heterogeneity. It is expected that the proposed model can contribute towards new insights into nanoscale morphology of KTP and the experimental configuration optimization of CD-SHG microscopy.

DATA AVAILABILITY STATEMENT

The raw data supporting the conclusion of this article will be made available by the authors, without undue reservation.

AUTHOR CONTRIBUTIONS

BW and WW conceived the project. WW and JT supervised the research. BW and KW performed all simulations. BW and XS performed data analyses. BW and WW wrote the manuscript with assistance from all authors.

FUNDING

This work was funded by the National Natural Science Foundation of China (Nos. 51775148 and 51975161).

ACKNOWLEDGMENTS

We would like to thank the rest of the team for the fruitful discussion of this project.

REFERENCES

Bautista, G., Huttunen, M. J., Mäkitalo, J., Kontio, J. M., Simonen, J., and Kauranen, M. (2012). Second-harmonic Generation Imaging of Metal Nano-Objects with Cylindrical Vector Beams. *Nano Lett.* 12 (6), 3207–3212. doi:10.1021/nl301190x

Bautista, G., Kakko, J.-P., Dhaka, V., Zang, X., Karvonen, L., Jiang, H., et al. (2017). Nonlinear Microscopy Using Cylindrical Vector Beams: Applications to Three-Dimensional Imaging of Nanostructures. *Opt. Express* 25 (11), 12463–12468. doi:10.1364/oe.25.012463

Belardini, A., Benedetti, A., Centini, M., Leahu, G., Mura, F., Sennato, S., et al. (2014). Second Harmonic Generation Circular Dichroism from Self-Ordered Hybrid Plasmonic-Photonic Nanosurfaces. *Adv. Opt. Mater.* 2 (3), 208–213. doi:10.1002/adom.201300385

Bierlein, J. D., and Vanherzeele, H. (1989). Potassium Titanyl Phosphate: Properties and New Applications. *J. Opt. Soc. Am. B* 6 (4), 622–633. doi:10.1364/josab.6.000622

Chen, C., Rüter, C. E., Volk, M. F., Chen, C., Shang, Z., Lu, Q., et al. (2016). Second Harmonic Generation of diamond-blade Diced KTiOPO_4 ridge Waveguides. *Opt. Express* 24 (15), 16434–16439. doi:10.1364/oe.24.016434

Choi, K., Chon, J. W. M., Gu, M., and Lee, B. (2007). Characterization of a Subwavelength-Scale 3D Void Structure Using the FDTD-Based Confocal Laser Scanning Microscopic Image Mapping Technique. *Opt. Express* 15 (17), 10767–10781. doi:10.1364/oe.15.010767

Driscoll, T. A., Perkins, P. E., Hoffman, H. J., and Stone, R. E. (1986). Efficient Second-Harmonic Generation in KTP Crystals. *J. Opt. Soc. Am. B* 3 (5), 683–686. doi:10.1364/josab.3.000683

Gleeson, M., O'Dwyer, K., Guerin, S., Rice, D., Thompson, D., Tofail, S. A. M., et al. (2020). Quantitative Polarization-Resolved Second-Harmonic-Generation Microscopy of Glycine Microneedles. *Adv. Mater.* 32 (46), 2002873. doi:10.1002/adma.202002873

Haeberlé, O., Ammar, M., Furukawa, H., Tenjimbayashi, K., and Török, P. (2003). The point Spread Function of Optical Microscopes Imaging through Stratified media. *Opt. Express* 11 (22), 2964–2969. doi:10.1364/oe.11.002964

Kleinman, D. A. (1962). Nonlinear Dielectric Polarization in Optical media. *Phys. Rev.* 126 (6), 1977–1979. doi:10.1103/physrev.126.1977

Le Xuan, L., Zhou, C., Slablab, A., Chauvat, D., Tard, C., Perruchas, S., et al. (2008). Photostable Second-Harmonic Generation from a Single KTiOPO4Nanocrystal for Nonlinear Microscopy. *Small* 4 (9), 1332–1336. doi:10.1002/smll.200701093

Morizet, J., Sartorello, G., Dray, N., Stringari, C., Beaurepaire, E., and Olivier, N. (2021). Modeling Nonlinear Microscopy Near index-mismatched Interfaces. *Optica* 8 (7), 944–951. doi:10.1364/optica.421257

Ren, M.-L., Agarwal, R., Liu, W., and Agarwal, R. (2015). Crystallographic Characterization of II-VI Semiconducting Nanostructures via Optical Second Harmonic Generation. *Nano Lett.* 15 (11), 7341–7346. doi:10.1021/acs.nanolett.5b02690

Richards, B., and Wolf, E. (1959). Electromagnetic Diffraction in Optical Systems, II. Structure of the Image Field in an Aplanatic System. *Proc. Roy. Soc. Lond. Ser. A.* 253 (1274), 358–379.

Schmeltz, M., Teulon, C., Pinsard, M., Hansen, U., Alnawaiseh, M., Ghoubay, D., et al. (2020). Circular Dichroism Second-Harmonic Generation Microscopy Probes the Polarity Distribution of Collagen Fibrils. *Optica* 7 (11), 1469–1476. doi:10.1364/optica.399246

Sutherland, R. L. (2003). *Handbook of Nonlinear Optics*. New York: CRC Press.

Török, P., Higdon, P. D., and Wilson, T. (1998). Theory for Confocal and Conventional Microscopes Imaging Small Dielectric Scatterers. *J. Mod. Optic.* 45 (8), 1681–1698.

Török, P., Munro, P. R. T., and Kriezis, E. E. (2008). High Numerical Aperture Vectorial Imaging in Coherent Optical Microscopes. *Opt. Express* 16 (2), 507–523.

Török, P. (2000). Propagation of Electromagnetic Dipole Waves through Dielectric Interfaces. *Opt. Lett.* 25 (19), 1463–1465.

Török, P., and Varga, P. (1997). Electromagnetic Diffraction of Light Focused through a Stratified Medium. *Appli. Opt.* 36 (11), 2305–2312.

van der Kolk, J. N., Bancelin, S., Kioulos, C., Lesina, A. C., Légaré, F., and Ramunno, L. (2018). Effect of Refractive index Mismatch on Forward-To-Backward Ratios in SHG Imaging. *Opt. Lett.* 43 (20), 5082–5085. doi:10.1364/ol.43.005082

Vanherzeele, H., and Bierlein, J. D. (1992). Magnitude of the Nonlinear-Optical Coefficients of KTiOPO_4. *Opt. Lett.* 17 (14), 982–984. doi:10.1364/ol.17.000982

Wang, W., Wu, B., Lin, S., Li, X., Liu, J., and Tan, J. (2019). Rigorous Modelling of Second Harmonic Generation Imaging through Stratified media Focused by Radially Polarized Beams. *Opt. Express* 27 (14), 19737–19748. doi:10.1364/oe.27.019737

Yew, E. Y. S., and Sheppard, C. J. R. (2006). Vectorial Approach to Studying Second Harmonic Generation in Collagen Using Linearly and Radially Polarized Beams Proc. *SPIE* 6163, 61630L.

Conflict of Interest: The authors declare that the research was conducted in the absence of any commercial or financial relationships that could be construed as a potential conflict of interest.

Publisher's Note: All claims expressed in this article are solely those of the authors and do not necessarily represent those of their affiliated organizations, or those of the publisher, the editors and the reviewers. Any product that may be evaluated in this article, or claim that may be made by its manufacturer, is not guaranteed or endorsed by the publisher.

Copyright © 2022 Wu, Wu, Sun, Wang and Tan. This is an open-access article distributed under the terms of the Creative Commons Attribution License (CC BY). The use, distribution or reproduction in other forums is permitted, provided the original author(s) and the copyright owner(s) are credited and that the original publication in this journal is cited, in accordance with accepted academic practice. No use, distribution or reproduction is permitted which does not comply with these terms.

frontiers | Frontiers in Chemistry

ORIGINAL RESEARCH
published: 10 May 2022
doi: 10.3389/fchem.2022.864701

DNA-PAINT Imaging Accelerated by Machine Learning

Min Zhu[1†], *Luhao Zhang*[1†], *Luhong Jin*[1,2], *Jincheng Chen*[1], *Yongdeng Zhang*[3] *and Yingke Xu*[1,2,4,5]*

[1]Key Laboratory of Biomedical Engineering of Ministry of Education, State Key Laboratory of Modern Optical Instrumentation, Zhejiang Provincial Key Laboratory of Cardio-Cerebral Vascular Detection Technology and Medicinal Effectiveness Appraisal, Department of Biomedical Engineering, Zhejiang University, Hangzhou, China, [2]Alibaba-Zhejiang University Joint Research Center of Future Digital Healthcare, Hangzhou, China, [3]School of Life Sciences, Westlake University, Hangzhou, China, [4]Binjiang Institute of Zhejiang University, Hangzhou, China, [5]Department of Endocrinology, The Affiliated Sir Run Run Shaw Hospital, Zhejiang University School of Medicine, Hangzhou, China

DNA point accumulation in nanoscale topography (DNA-PAINT) is an easy-to-implement approach for localization-based super-resolution imaging. Conventional DNA-PAINT imaging typically requires tens of thousands of frames of raw data to reconstruct one super-resolution image, which prevents its potential application for live imaging. Here, we introduce a new DNA-PAINT labeling method that allows for imaging of microtubules with both DNA-PAINT and widefield illumination. We develop a U-Net-based neural network, namely, U-PAINT to accelerate DNA-PAINT imaging from a widefield fluorescent image and a sparse single-molecule localization image. Compared with the conventional method, U-PAINT only requires one-tenth of the original raw data, which permits fast imaging and reconstruction of super-resolution microtubules and can be adopted to analyze other SMLM datasets. We anticipate that this machine learning method enables faster and even live-cell DNA-PAINT imaging in the future.

Keywords: DNA-PAINT, machine learning, super-resolution imaging, U-Net, single-molecule localization microscopy

OPEN ACCESS

Edited by:
Chao He,
University of Oxford, United Kingdom

Reviewed by:
Shouyu Wang,
Jiangnan University, China
Jingyu Wang,
University of Oxford, United Kingdom

***Correspondence:**
Yingke Xu
yingkexu@zju.edu.cn

†These authors have contributed equally to this work

Specialty section:
This article was submitted to Nanoscience, a section of the journal Frontiers in Chemistry

Received: *28 January 2022*
Accepted: *08 April 2022*
Published: *10 May 2022*

Citation:
Zhu M, Zhang L, Jin L, Chen J, Zhang Y and Xu Y (2022) DNA-PAINT Imaging Accelerated by Machine Learning. Front. Chem. 10:864701. doi: 10.3389/fchem.2022.864701

INTRODUCTION

Super-resolution microscopy allows for optical imaging beyond Abbe's diffraction limit, enabling the visualization of subcellular structures up to the molecular scale. Super-resolution approaches can be roughly divided into two types, illumination pattern-based microscopy and single-molecule localization microscopy (SMLM) (Schnitzbauer et al., 2017). DNA point accumulation in nanoscale topography (DNA-PAINT) is a promising SMLM method. It requires transient binding of short dye-labeled oligonucleotides to their complementary target strands, which creates the necessary "blinking" to enable stochastic super-resolution imaging of nanoscale structures (Guo et al., 2019; Huang et al., 2020). Different from other SMLM (e.g. PALM and STORM) techniques, the pool of fluorophores for DNA-PAINT could be continuously replenished from the imaging buffer, thus eliminating the concerns over photo-budget. Previous work has shown that DNA-PAINT could achieve a 5 nm localization accuracy with bright fluorescence and longer imaging time (Liu et al., 2019). Therefore, conventional DNA-PAINT requires a large scale of raw data, typically more than 10,000 images, to reconstruct one super-resolution image (Clowsley et al., 2020), which prevents it from being applied to subcellular structure imaging in live cells (Schlichthaerle et al., 2017; Brockman et al., 2020).

Machine learning is a data-oriented method, which can perform complicated tasks by employing artificial neural networks. Machine learning has been applied to increase magnification and resolution in fluorescence microscopy (Wang et al., 2019). A method called ANNA-PALM was demonstrated to only use 1% of raw data to reconstruct one super-resolution image by applying machine learning methods (Ouyang et al., 2018). Localization tasks can be accelerated, and the accuracy can be improved by convolutional neural network (CNN) (Nehme et al., 2018; Cardoen et al., 2020), which is the most commonly used artificial neural network. Machine learning is a potential approach to accelerate DNA-PAINT imaging.

To accelerate DNA-PAINT imaging, we developed U-Net-assisted DNA-PAINT (U-PAINT) based on CNN. We have achieved fast super-resolution imaging of microtubule by applying U-PAINT. This strategy uses one-tenth of frames and independent localizations to reconstruct a super-resolution image without trading off spatial resolution.

MATERIALS AND METHODS

Sample Preparation

COS-7 cells and HeLa cells were cultured in high glucose Dulbecco's modified Eagle's medium (DMEM) (Cytiva, SH30243.01B), supplemented with 10% fetal bovine serum (HyClone, SV30087) and 1% penicillin–streptomycin (Beyotime, C0222) at 37°C in a humidified 5% CO_2 incubator. Cells were grown on a 35-mm glass-bottom dish (Cellvis, D35-20-1-N) for immunostaining experiments.

The detailed procedures for immunofluorescence cell staining were as follows. The cells were first incubated in a pre-fixation buffer (0.4% glutaraldehyde and 0.25% Triton X-100 in PBS) for 90 s at 37°C and then fixed with a fixation buffer (3% glutaraldehyde and 0.25% Triton X-100 in PBS) at room temperature. Fixatives were quenched with newly dissolved 1 mg/ml $NaBH_4$ in PBS for 30 min. After washing three times with PBS, the cells were incubated in a blocking buffer (5% BSA and 0.25% Triton X-100 in PBS) for 2 h, rinsed three times, and then incubated with a mouse monoclonal antibody to beta-tubulin (Abcam, ab231082) at a concentration of 1:500 overnight at 4°C. The cells were then incubated with a biotin-labeled goat anti-mouse IgG secondary antibody (Abcam, ab6788) at a concentration of 1:500 for 2 h at room temperature and subsequently incubated with Alexa Fluor 488 conjugated streptavidin (Invitrogen, S32354) at a concentration of 1:1,000 for 15 min at room temperature. After washing three times with PBS, the cells were incubated with biotin-conjugated docking strands (biotin-TTATACATCTATACATCTA) at a concentration of 1 μM for 15 min at room temperature protected from light. Finally, the cells were preserved for imaging in PBS at 4°C.

DNA-PAINT Imaging

The imaging buffer consists of 0.5 nM Cy3B-conjugated imager strands (TAGATGTAT-Cy3B), 50 mM $MgCl_2$, and 50 mM NaCl. An Olympus IX83 microscope was used and set to a TIRF mode with a penetration depth of 200 nm. For widefield imaging, 488-nm laser (5 mW) was used for illumination. Widefield images were acquired under the control of Cellsense software with an exposure time of 100 ms. For DNA-PAINT imaging of the same region, 561-nm laser (100 mW) was used for illumination. A total of 30,000 TIRFM images were acquired with an exposure time of 100 ms.

DNA-PAINT Image Reconstruction

DNA-PAINT images were reconstructed with Picasso software developed by the Jungmann Lab (Schnitzbauer et al., 2017). Minimal net gradient was set manually to avoid background fluorescence from being localized. After localization, the maximum likelihood estimation was applied for fitting and then fitted localizations with an ellipticity greater than 0.6 were removed. The rest data were rendered into 16 time-scaled 8-bit png files whose pixel size was 8 × 8 nm after a redundant cross-correlation drift correction (RCC). To obtain 16-bit images as the output of reconstruction, R package EBImage (Pau et al., 2010) was used. Reconstructions with 1,000 and 3,000 raw images were performed using R. The R script can be found in the GitHub repository (https://github.com/ccchin999/PAINT-learning).

Real Microtubule Dataset Preparation

Reconstructed DNA-PAINT images from 30,000 raw frames (ground truth), 1,000 frames, or 3,000 frames (input) were cut by 256 × 256 pixel grids. The cropped images were filtered according to a comparison of mean intensity values of themselves and the whole image. Those with low mean values were excluded to guarantee image quality. And then, widefield images were cut and selected accordingly. We obtained about 1,300 sets of cropped images for data training and an additional 36 ones as the testing dataset. Each set consists of widefield images, reconstructed DNA-PAINT images from 1,000, 3,000, and 30,000 raw images. Reconstructed DNA-PAINT images from 30,000 raw images were treated as the ground truth. Those images were normalized to the maximum intensity of the corresponding uncut images.

PALM image data were downloaded from the ANNA-PALM GitHub repository (Ouyang et al., 2018). PALM data of 60,000 frames was rendered to an image with the same resolution of DNA-PAINT images. The image was then cut by 256 × 256 pixel grids. PALM data of randomly selected 6,000 frames was processed as stated above. The corresponding widefield image was scaled to the same size and cut by 256 × 256 pixel grids. The images with a low mean intensity were removed. We chose 90 pairs of PALM images as testing datasets.

Simulated Microtubule Datasets

The microtubular structures were stimulated using the random-walk simulation as previously published (Weigert et al., 2018). In the first frame, approximately 10 starting points of trajectories were selected randomly on the boundary of the image. In each frame, microtubules moved a fixed length (about a half-pixel to make trajectories continuous and smooth) toward the center, with the displacement between the nearby positions according to the normal distribution. We simulated 500 frames for one set of images to make sure most microtubule trajectories were across the entire image, which resembles the real data. For ground truth, all these frames were overlaid to one image, which was rescaled, blurred with a Gaussian kernel with a standard deviation of 1.25 pixels, and then cropped into 256-pixel-width squares. For widefield images, 256-

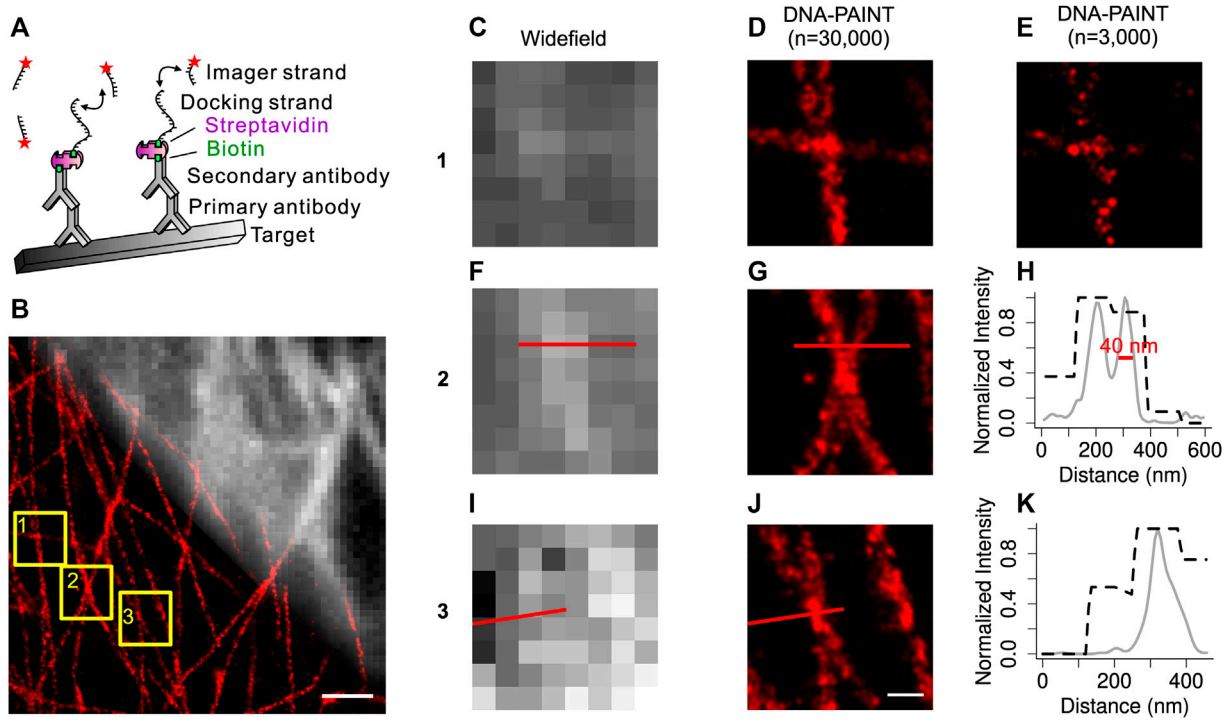

FIGURE 1 | Development of the improved DNA-PAINT labeling method. **(A)** Overview of the improved DNA-PAINT system. Labeling strategy for DNA-PAINT using antibodies, fluorescent dye-conjugated streptavidin, docking strands, and complementary imager strands. **(B)** Overlay of a widefield microtubule image (top right) with its DNA-PAINT reconstruction image (bottom left). **(C) (F) (I)** Widefield images of the boxed regions 1, 2, 3 from **(B) (D) (G) (J)** DNA-PAINT reconstructions (n = 30,000) of the same boxed regions 1, 2, 3 from **(B) (E)** Sparse localization image (n = 3,000) of **(D) (H)** Normalized intensity plot of regions from F, **(G) (K)** Normalized intensity plot of regions from I, **(J)**. Black dashed curves from widefield images; gray solid curves from DNA-PAINT reconstructions (n = 30,000). Scale bar: 1,000 nm **(B)**, 200 nm **(J)**. Machine learning approach for the DNA-PAINT image reconstruction.

pixel-width ground-truth images were blurred with a Gaussian kernel with a standard deviation of 20 pixels, resized to 32-pixel-length squares, and scaled to the same size as original ground-truth images. For sparse localization images, 10% frames were randomly selected and overlaid to one image, rescaled, Gaussian-blurred, and cropped, as stated above. The R script for microtubule simulation can be found at the GitHub repository (https://github.com/ccchin999/PAINT-learning).

Model Training

We adopted the *Python* package U-Net as previously reported (Jin et al., 2020) and with similar computation platform (Intel Core i9-10900KF CPU and NVIDIA GeForce RTX 3080 GPU). We trained three different models, U-PAINT (3,000), U-PAINT (WF), and U-PAINT (WF+3,000). They share similar network architectures, with the only difference being input channel numbers. The U-PAINT (3,000) model was trained from reconstructed DNA-PAINT images with sparse localization (3,000 raw images). The U-PAINT (WF) model was trained with widefield images, whereas the U-PAINT (WF+3,000) was trained with both sparse localization images and the corresponding widefield image. The reconstructed DNA-PAINT images with 30,000 raw images were used as the ground truth. Each model was trained for 2,000 epochs, which cost approximately 10–15 h. Additionally, we trained U-PAINT (3,000) and U-PAINT (WF+3,000) for 2,000 more epochs with simulated microtubule data and 500 epochs using real data. The additional training spent about 40 h.

Model Performance Quantification

The peak signal-to-noise ratio (PSNR), root-mean-square error (RMSE), and structural similarity image measurement (SSIM) were used to evaluate the performance of trained models. All values come from the differences between the output (OP) and ground truth (GT) of the testing datasets. The intensity of images was mapped to the interval [0, 255]. PSNR, RMSE, and SSIM were calculated using the following functions, where $cov(GT, OP)$ is referred to as the covariance of GT and OP, sd function is the represented standard deviation, and c_1, c_2 are the small positive constants.

$$RMSE = \sqrt{mean\left((\mathrm{GT} - OP)^2\right)}$$

$$PSNR = \begin{cases} 100 & , when\ RMSE = 0 \\ 20lg\left(\dfrac{255}{RMSE}\right) & , when\ RMSE > 0 \end{cases}$$

$$SSIM = \frac{[2mean(\mathrm{GT})mean(OP) + c_1][cov(\mathrm{GT}, OP) + c_2]}{[mean(\mathrm{GT})^2 + mean(OP)^2 + c_1][sd(\mathrm{GT})^2 + sd(OP)^2 + c_2]}$$

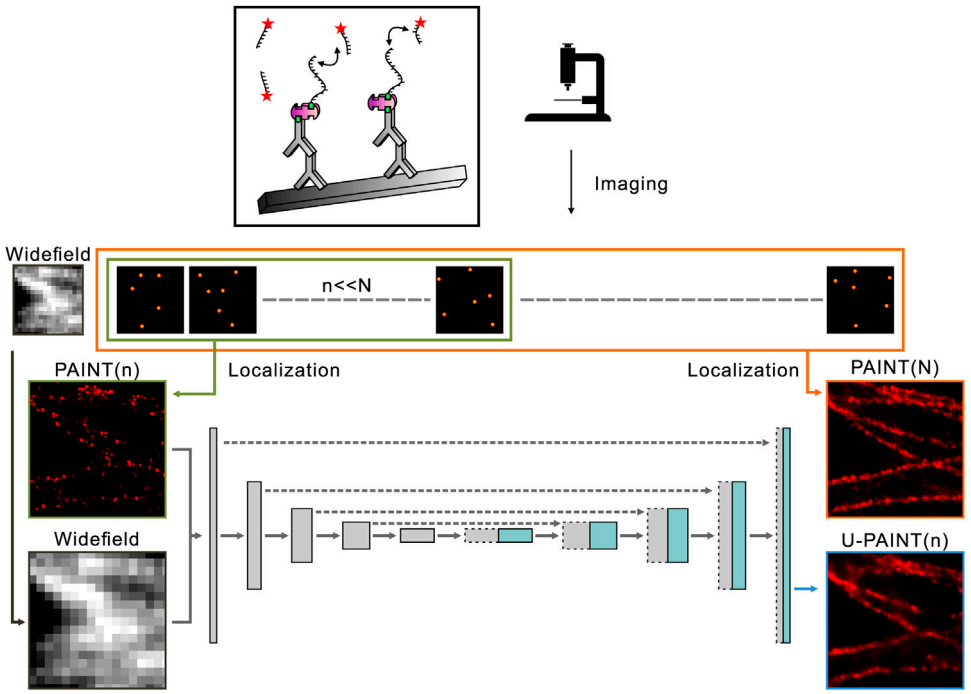

FIGURE 2 | Overview of U-PAINT. Training images are localized and rendered from long sequences of single-molecule image frames or widefield images. Sparse localization images from the first n frames and widefield images are set as inputs of U-PAINT, while dense localization images of N frames (N >> *n*) are outputs. Simulated microtubule data enhance U-PAINT training.

RESULTS AND DISCUSSION

Improved DNA-PAINT Labeling Method

To acquire super-resolution DNA-PAINT images together with widefield images of the same endogenous structures, we developed an improved DNA-PAINT labeling method. This DNA-PAINT system, as illustrated in **Figure 1A**, uses immunostaining approaches with an Alexa Fluor 488 conjugated streptavidin- and biotin-modified docking strand to target a subcellular structure of interest. The imager strand conjugated to the Cy3B dye can diffuse freely in the imaging buffer. Owing to their complementary sequence, blinking occurs during the transient binding events of imager strands and docking strands. All materials mentioned above have been optimized by commercial companies, and immunostaining is easy to achieve.

With this improved DNA-PAINT system, we carried out widefield and DNA-PAINT imaging of the endogenous microtubules in COS-7 cells (**Figure 1B**). Comparison of the widefield images and DNA-PAINT images revealed that DNA-PAINT images were consistent with widefield images but with much better spatial resolution. Zoom-in views (**Figures 1C,D,F,G,I,J**) of three areas confirmed the high resolution of DNA-PAINT images. Quantification of the reconstructed DNA-PAINT image demonstrated that a spatial resolution of 40 nm could be achieved on microtubules (**Figures 1H,K**). Thus, by using this improved DNA-PAINT system, we could simultaneously obtain the diffraction-limited widefield images and super-resolution DNA-PAINT images of the endogenous microtubules in cells.

Originally designed for biomedical segmentation, U-Net has proven to be a useful machine learning network architecture and is widely applied to image restoration, classification, and quantification (Ronneberger et al., 2015; Falk et al., 2019; Byra et al., 2020; Clowsley et al., 2020; Yan et al., 2022). To reconstruct a super-resolution image with the resolution similar to a standard DNA-PAINT image but with a much smaller number of blinking points (less raw data), the machine learning method U-PAINT derived from U-Net is developed. U-PAINT contains a total of 10 layers, including four downsampling convolutional layers, four upsampling convolutional layers, an input layer, and an output layer. A slightly more than 31 million parameters are modified through backpropagation algorithms and stochastic gradient descent. As shown in **Figure 2**, super-resolution images of microtubules (N frames) are obtained by the conventional DNA-PAINT imaging and are processed with Picasso software (**Figures 1D,G,J**). The widefield images of the same structure can be acquired through imaging the dye Alexa Fluor 488 labeled on streptavidin. Sparse DNA-PAINT images are yielded by using a much smaller number of DNA-PAINT frames (n frames, $n \ll N$) from the same localization (**Figure 1E**). Once trained, U-PAINT can be applied to new sparse DNA-PAINT images obtained from image sequences of another microtubule sample with only a few frames in a much shorter time, which can contribute to the reconstruction of high-quality super-resolution images, with or without widefield images.

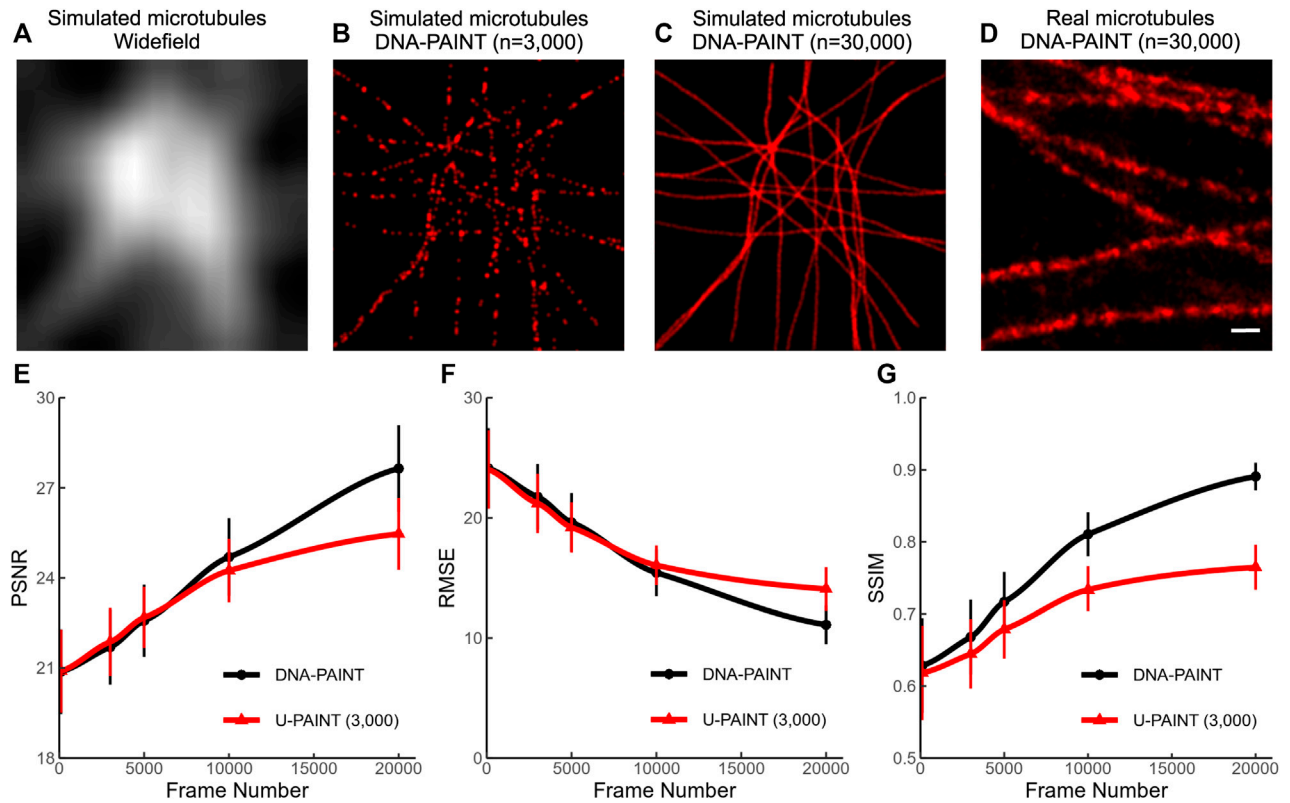

FIGURE 3 | Simulation of microtubules and their reconstruction quality. **(A)** Widefield image of simulated microtubules. **(B)** Sparse localized DNA-PAINT image (n = 3,000) of simulated microtubules. **(C)** Dense localized DNA-PAINT image (n = 30,000) of simulated microtubules. **(D)** Dense localized DNA-PAINT image (n = 30,000) of real microtubules. **(E)** PSNR of U-PAINT (3,000) reconstruction results and DNA-PAINT results with different frame numbers. **(F)** RMSE of U-PAINT (3,000) reconstruction results and DNA-PAINT results with different frame numbers. **(G)** SSIM of U-PAINT (3,000) reconstruction results and DNA-PAINT results with different frame numbers. PSNR, RMSE, and SSIM are measured compared with results and ground truth. Red lines with triangle points: performance of U-PAINT (3,000); black lines with circle points: performance of conventional DNA-PAINT. Dots are averages from 36 simulations; error bars show s.d. Scale bar: 200 nm. U-PAINT reconstruction of endogenous microtubules.

We simulated more than 3,000 artificial microtubule images to satisfy U-PAINT's demand of a larger training dataset. A random walk-based simulation example is listed in **Figure 3C**. The widefield image (**Figure 3A**) was rendered by blurring with a Gaussian kernel of a 20-pixel standard deviation. The sparse localization image (**Figure 3B**) was generated with only 1 in 10 of the randomly chosen simulation localizations. Those artificial microtubules are more controllable in both continuity and density. However, microtubules are hollow cylinders with ~26 nm diameter, which is not considered in our simulation. As a result, our simulated microtubules are thinner than real microtubules (**Figure 3D**). This noticeable difference actually affects our U-PAINT models. After training with artificial microtubule datasets, our models could not restore real microtubules correctly. Thus, we retrained the model for 500 epochs with real microtubule training datasets.

We tested our U-PAINT (3,000) model on simulation data with different frame numbers from 100 to 20,000 (**Figures 3E–G**). The parameters PSNR, RMSE, and SSIM are quantitatively measured. Higher PSNR implies stronger signals and lesser noise being identified as part of the microtubules. Lower RMSE suggests more precise reconstruction. SSIM lies between 0 and 1 and reaches 1 when reconstruction images are the same as ground truth. The performance of U-PAINT is greatly enhanced with an increased frame number. However, when the frame number is larger than 5,000, U-PAINT (3,000) becomes unable to increase image quality for DNA-PAINT.

We tested U-PAINT on immunostained microtubules. DNA-PAINT images with the corresponding widefield images were obtained during a 50-min-long imaging (N = 30,000; Δt = 100-ms exposure time) (**Figures 4A,D**). The sparse DNA-PAINT images were obtained from only 5- or 2-min imaging (n = 3,000 or 1,000) (**Figures 4B,C**). Although microtubule filaments can already be seen in sparse DNA-PAINT images, structural details below the diffraction limit are hard to discern, making it difficult to identify features such as filament crossings (**Figures 4B,C**). We first tried to reconstruct super-resolution images from widefield images. Our results show that a few structures are restored (**Figure 4H**; UPW-R refers to U-PAINT (WF) trained with only real data), which means that precise restoration requires super-resolution localization images. Then, we attempted to restore images from sparsely localized images. After training with ~1,300 sparse-and-dense image pairs of real microtubules, U-PAINT

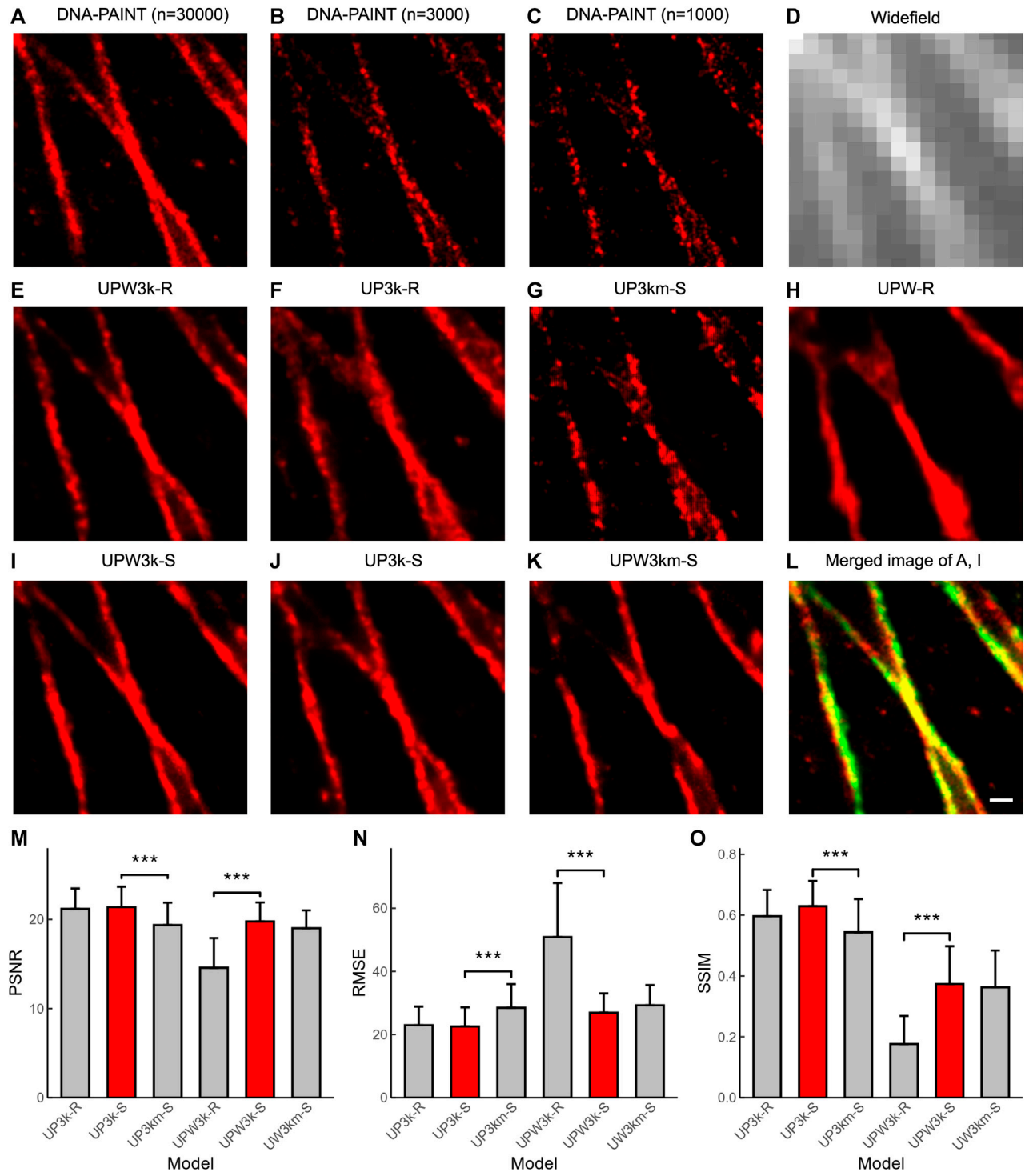

FIGURE 4 | U-PAINT reconstruction of microtubules. **(A)** DNA-PAINT reconstruction images with n = 30,000 raw data. **(B)** DNA-PAINT reconstruction image with n = 3,000 raw data. **(C)** DNA-PAINT reconstruction image with n = 1,000 raw data. **(D)** Widefield image. **(E)** Real data-based U-PAINT (WF+3,000) reconstruction image with B and D as inputs. **(F)** Real data-based U-PAINT (3,000) reconstruction image with B as input. **(G)** Real data-based U-PAINT (1,000) reconstruction image with C as input. **(H)** Real data-based U-PAINT reconstruction image with **(D) (I)** Simulated and real data-based U-PAINT (WF+3,000) reconstruction image with B and D as inputs. **(J)** Simulated and real data-based U-PAINT (3,000) reconstruction image with B as input. **(K)** Simulated and real data-based U-PAINT (WF+3,000) reconstruction image with C and D as inputs. **(L)** Merged image of A (red) and I (green). **(M)** PSNR of U-PAINT models. **(N)** RMSE of U-PAINT models. **(O)** SSIM of U-PAINT models. Red bars refer to better U-PAINT models; bars are average values from testing dataset; error bars show s.d.; UP3k-R: U-PAINT (3,000) model trained with only real data; UP3k-S: U-PAINT (3,000) model trained with real and simulated data; UP3km-S: U-PAINT (3,000) model trained with real and simulated data, and the input was a sparse DNA-PAINT image localized from 1,000 frames of raw data; UPW3k-R:

(*Continued*)

FIGURE 4 | U-PAINT (WF+3,000) model trained with only real data; UPW3k-S: U-PAINT (WF+3,000) model trained with real and simulated data; UPW3km-S: U-PAINT (WF+3,000) model trained with real and simulated data, and the inputs are a widefield image and a sparse DNA-PAINT image localized from 1,000 frames of raw data. *** represents $p < 0.001$ as tested by two independent sample t-test; scale bar: 200 nm. Comparison between ANNA-PALM and U-PAINTs.

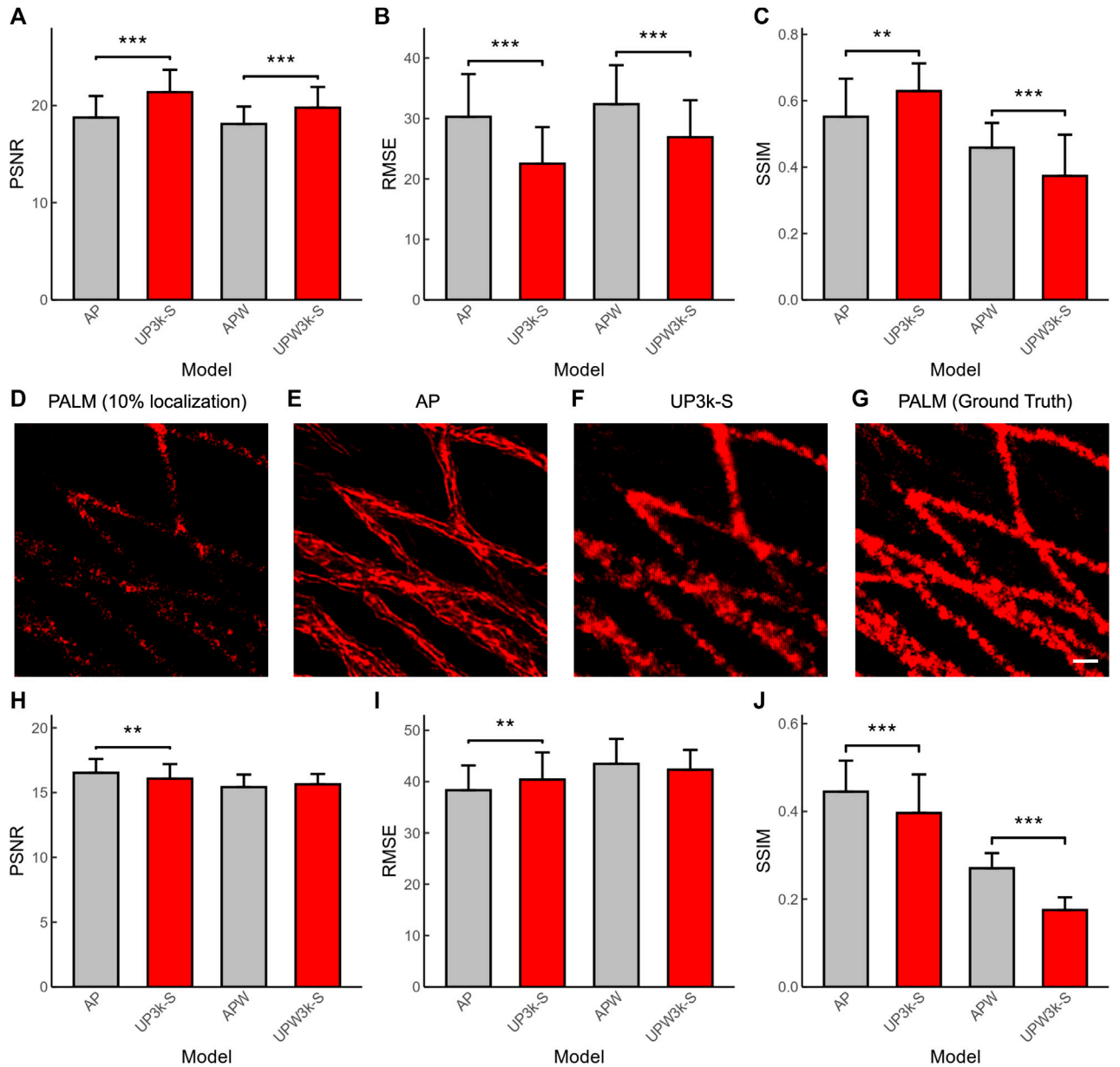

FIGURE 5 | Quantification of the performance of U-PAINT models and ANNA-PALM (AP). The performance of U-PAINT models and AP in DNA-PAINT reconstruction as analyzed by PSNR **(A)**, RMSE **(B)**, and SSIM **(C)**. **(D)** A representative image of sparse-localized PALM as reconstructed by the traditional method. The accelerated reconstruction images by ANNA-PALM **(E)** and U-PAINT **(F)** and the ground-truth image **(G)**. The performance of U-PAINT models and AP in PALM reconstruction as analyzed by PSNR **(H)**, RMSE **(I),** and SSIM **(J)**. Red bars refer to U-PAINT models; bars are average values; error bars show s.d.; ** represents $p < 0.01$ and *** represents $p < 0.001$, as tested by two independent sample t-test. AP: ANNA-PALM pre-trained model with a sparse localization image as input; UP3k-S: U-PAINT (3,000) model trained with real and simulated data; APW: ANNA-PALM pre-trained model with a sparse localization image and a widefield image as inputs; UPW3k-S: U-PAINT (WF+3,000) model trained with real and simulated data. Scale bar: 200 nm.

completed the detailed structures of input sparse DNA-PAINT images (**Figure 4F**; UP3k-R represents U-PAINT (3,000) model trained with only real data). However, the result is not perfect enough as artifacts cover signals to some extent and reconstructed microtubules are fragmented.

We further tested whether adding matched widefield images with DNA-PAINT images could promote reconstruction quality. Our results show that adding widefield images brings more continuity and instability. In some cases, widefield images make restored structures more precise and continuous (**Figure 4E**; UPW3k-R represents U-PAINT (WF+3,000) model trained with only real data), while more severe artifacts were induced otherwise. We continued testing whether the addition of simulated data in the training period could improve reconstruction quality. For U-PAINT (WF+3,000), instability from widefield images is inhibited and progress of continuity can be noticed (UPW3k-R and UPW3k-S in **Figures 4M–O**; UPW3k-R refers to the U-PAINT (WF+3,000) model trained with only real data and UPW3k-S refers to the U-PAINT (WF+3,000) model trained with real and simulated data). Most structures are restored by U-PAINT (WF+3,000) trained with both real and artificial microtubule data (**Figures 4I,L**). In addition, we also noticed a slight enhancement for the performance of U-PAINT (3,000) when trained with both real and simulated data (**Figures 4F,J**; UP3k-S refers to U-PAINT (3,000) trained with real and simulated data).

Then, we tested whether the reconstruction quality could remain for U-PAINT after decreasing the number of input sparse-localized DNA-PAINT frames (n) to 1,000, where the image acquisition time was cut down to only 100 s. Although microtubule filaments appear completely discrete, most structural details below the optical diffraction limit are restored (**Figures 4G,K**; UP3km-S represents the U-PAINT (3,000) model trained with simulated data and real data and inputs are a sparse DNA-PAINT image localized from 1,000 frames of raw data; UPW3km-S represents the U-PAINT (WF+3,000) model trained with simulated data and real data and inputs are a widefield image and a sparse DNA-PAINT image localized from 1,000 frames of raw data). For U-PAINT (WF+3,000), only a slight decrease in performance is noticed (UPW3k-S and UPW3km-S of **Figures 4M–O**). However, the performance of U-PAINT (3,000) is reduced significantly (UP3k-S and UP3km-S of **Figures 4M–O**).

Using testing datasets as input, we obtained 36 output images. The quantitative values of PSNR, RMSE, and SSIM between output and ground truth were calculated and plotted (**Figures 4M–O**). By the addition of the simulated microtubule data, the U-PAINT (WF+3,000) model is improved, while the U-PAINT (3,000) model has no significant enhancement. When we reduce the input frame number to 1,000, the output quality of U-PAINT (WF+3,000) remains at a relatively high level, while the quality of U-PAINT (3,000) decreases remarkably. Collectively, these results demonstrate the advantage of using both widefield and super-resolution DNA-PAINT images and the importance of including both real data and simulated data in model training.

PALM is another SMLM that shares the same reconstruction algorithm with DNA-PAINT. Here, we applied the deep-learning based ANNA-PALM models (AP) (Ouyang et al., 2018) and compared its performance with our established U-PAINT models. The results show that U-PAINT has higher restoration quality (AP and UP3k-S in **Figures 5A,B**; AP represents ANNA-PALM). Although ANNA-PALM brings better precision of output image quality when both widefield images and sparsely localized images are used as inputs (APW and UPW3k-S in **Figure 5C**; APW refers to ANNA-PALM with an extra widefield image as input), it restores fewer signals (APW and UPW3k-S in **Figure 5A**). Thus, we conclude that U-PAINT is more suitable for DNA-PAINT imaging acceleration.

Similarly, we also tested whether our developed U-PAINT models can be used to accelerate PALM imaging (**Figures 5D–G**). The original PALM images were from the ANNA-PALM GitHub repository (Ouyang et al., 2018). Our result shows that U-PAINT without inputting widefield images is able to accelerate PALM imaging, although its performance quantification indicators are not as excellent as ANNA-PALM (**Figures 5H,I,J**). However, the restored image of ANNA-PALM shows abnormal artifacts (**Figure 5E**), which makes the ANNA-PALM reconstruction output unauthentic. Taken together, our U-PAINT model is practical to accelerate SMLM other than DNA-PAINT.

CONCLUSION

We introduced a new DNA-PAINT labeling method that allows for imaging of cellular structures with both DNA-PAINT and widefield illumination. We proposed machine learning-based U-PAINT model that manages to reduce the demanded number of raw images for the DNA-PAINT reconstruction of microtubules to less than 10% of the conventional method but still achieving comparable spatial resolution. By co-training with simulated microtubule datasets, we showed that the performance of the U-PAINT model can be further elevated. In addition, our method can be easily transferred to process other types of SMLM, such as PALM, and enables the acceleration of SMLM imaging. Therefore, we anticipate that live-cell DNA-PAINT imaging can be potentially realized for some specific subcellular structures in the future.

DATA AVAILABILITY STATEMENT

The raw data supporting the conclusion of this article will be made available by the authors without undue reservation.

AUTHOR CONTRIBUTIONS

MZ and LZ are the co-first authors. YX, MZ, and LZ conceived and designed research. MZ and LZ performed research. LJ and JC contributed to machine learning. YZ contributed to DNA-PAINT reconstruction. YX, MZ, and LZ wrote the manuscript with inputs from all authors. Correspondence should be addressed to YX.

FUNDING

This work was supported by the National Key Research and Development Program of China (2021YFF0700305 and

2018YFE0119000), the National Natural Science Foundation of China (22104129 and 62105288), the Fundamental Research Funds for the Central Universities (2021XZZX022), the Zhejiang Provincial Natural Science Foundation (LR18H180001 and LQ22F050018), Zhejiang Province Science and Technology Research Plan (2022C03014), and Alibaba Cloud. The funder was not involved in the study design, collection, analysis, interpretation of data, the writing of this article or the decision to submit it for publication.

REFERENCES

Byra, M., Jarosik, P., Szubert, A., Galperin, M., Ojeda-Fournier, H., Olson, L., et al. (2020). Breast Mass Segmentation in Ultrasound with Selective Kernel U-Net Convolutional Neural Network. *Biomed. Signal Process. Control.* 61, 102027. doi:10.1016/j.bspc.2020.102027

Cardoen, B., Yedder, H. B., Sharma, A., Chou, K. C., Nabi, I. R., and Hamarneh, G. (2020). ERGO: Efficient Recurrent Graph Optimized Emitter Density Estimation in Single Molecule Localization Microscopy. *IEEE Trans. Med. Imaging* 39, 1942–1956. doi:10.1109/TMI.2019.2962361

Clowsley, A. H., Kaufhold, W. T., Lutz, T., Meletiou, A., Di Michele, L., and Soeller, C. (2020). Detecting Nanoscale Distribution of Protein Pairs by Proximity-dependent Super-resolution Microscopy. *J. Am. Chem. Soc.* 142, 12069–12078. doi:10.1021/jacs.9b03418

Falk, T., Mai, D., Bensch, R., Çiçek, Ö., Abdulkadir, A., Marrakchi, Y., et al. (2019). U-net: Deep Learning for Cell Counting, Detection, and Morphometry. *Nat. Methods* 16, 67–70. doi:10.1038/s41592-018-0261-2

Guo, S.-M., Veneziano, R., Gordonov, S., Li, L., Danielson, E., Perez de Arce, K., et al. (2019). Multiplexed and High-Throughput Neuronal Fluorescence Imaging with Diffusible Probes. *Nat. Commun.* 10, 4377. doi:10.1038/s41467-019-12372-6

Huang, K., Demirci, F., Batish, M., Treible, W., Meyers, B. C., and Caplan, J. L. (2020). Quantitative, Super-resolution Localization of Small RNAs with sRNA-PAINT. *Nucleic Acids Res.* 48, e96. doi:10.1093/nar/gkaa623

Jin, L., Liu, B., Zhao, F., Hahn, S., Dong, B., Song, R., et al. (20201934). Link to External Site, This Link Will Open in a New Window. *Nat. Commun.* 11. Deep learning enables structured illumination microscopy with low light levels and enhanced speed. doi:10.1038/s41467-020-15784-x

Liu, N., Dai, M., Saka, S. K., and Yin, P. (2019). Super-resolution Labelling with Action-PAINT. *Nat. Chem.* 11, 1001–1008. doi:10.1038/s41557-019-0325-7

Nehme, E., Weiss, L. E., Michaeli, T., and Shechtman, Y. (2018). Deep-STORM: Super-resolution Single-Molecule Microscopy by Deep Learning. *Optica* 5, 458–464. doi:10.1364/OPTICA.5.000458

Ouyang, W., Aristov, A., Lelek, M., Hao, X., and Zimmer, C. (2018). Deep Learning Massively Accelerates Super-resolution Localization Microscopy. *Nat. Biotechnol.* 36, 460–468. doi:10.1038/nbt.4106

Pau, G., Fuchs, F., Sklyar, O., Boutros, M., and Huber, W. (2010). EBImage--an R Package for Image Processing with Applications to Cellular Phenotypes. *Bioinformatics* 26, 979–981. doi:10.1093/bioinformatics/btq046

Ronneberger, O., Fischer, P., and Brox, T. (2015). "U-net: Convolutional Networks for Biomedical Image Segmentation," in *Medical Image Computing and Computer-Assisted Intervention*. Editors N. Navab, J. Hornegger, W. M. Wells, and A. F. Frangi (Springer International Publishing), 234–241. doi:10.1007/978-3-319-24574-4_28

Schnitzbauer, J., Strauss, M. T., Schlichthaerle, T., Schueder, F., and Jungmann, R. (2017). Super-resolution Microscopy with DNA-PAINT. *Nat. Protoc.* 12, 1198–1228. doi:10.1038/nprot.2017.024

Wang, H., Rivenson, Y., Jin, Y., Wei, Z., Gao, R., Günaydın, H., et al. (2019). Deep Learning Enables Cross-Modality Super-resolution in Fluorescence Microscopy. *Nat. Methods* 16, 103–110. doi:10.1038/s41592-018-0239-0

Weigert, M., Schmidt, U., Boothe, T., Müller, A., Dibrov, A., Jain, A., et al. (2018). Content-aware Image Restoration: Pushing the Limits of Fluorescence Microscopy. *Nat. Methods* 15, 1090–1097. doi:10.1038/s41592-018-0216-7

Yan, Y., Liu, Y., Wu, Y., Zhang, H., Zhang, Y., and Meng, L. (2022). Accurate Segmentation of Breast Tumors Using AE U-Net with HDC Model in Ultrasound Images. *Biomed. Signal Process. Control.* 72, 103299. doi:10.1016/j.bspc.2021.103299

Conflict of Interest: The authors declare that the research was conducted in the absence of any commercial or financial relationships that could be construed as a potential conflict of interest.

Publisher's Note: All claims expressed in this article are solely those of the authors and do not necessarily represent those of their affiliated organizations, or those of the publisher, the editors, and the reviewers. Any product that may be evaluated in this article, or claim that may be made by its manufacturer, is not guaranteed or endorsed by the publisher.

Copyright © 2022 Zhu, Zhang, Jin, Chen, Zhang and Xu. This is an open-access article distributed under the terms of the Creative Commons Attribution License (CC BY). The use, distribution or reproduction in other forums is permitted, provided the original author(s) and the copyright owner(s) are credited and that the original publication in this journal is cited, in accordance with accepted academic practice. No use, distribution or reproduction is permitted which does not comply with these terms.

frontiers | Frontiers in Chemistry

ORIGINAL RESEARCH
published: 30 May 2022
doi: 10.3389/fchem.2022.913035

Demonstration of a New Characterization Method for Weak Measurement

Yang Xu[1,2], Lixuan Shi[1,3], Chongqi Zhou[1,3], Zhangyan Li[1,3], Tian Guan[1,4], Xinhui Xing[2], Le Liu[5] and Yonghong He[1,2]**

[1]Shenzhen Key Laboratory for Minimal Invasive Medical Technologies, Tsinghua Shenzhen International Graduate School, Institute of Optical Imaging and Sensing, Tsinghua University, Shenzhen, China, [2]Institute of Biopharmaceutical and Health Engineering, Tsinghua Shenzhen International Graduate School, Tsinghua University, Shenzhen, China, [3]Department of Physics, Tsinghua University, Beijing, China, [4]School of Medicine, Tsinghua University, Beijing, China, [5]Shenzhen International Graduate School, Institute of Materials Research, Tsinghua University, Shenzhen, China

In this work, the difference between the weak measurement method and the weak value amplification process and the classical measurement process is thoroughly discussed, and the transition conditions of the weak value enhancement are obtained. A transition mode of the weak measurement and the classical measurement is proposed for the first time, and a better fitting model of the measurement results is found by performing a systematic analysis. On top of that, the importance of the new fitting method for the application of the weak measurement system is verified during the industrial production of organic molecular -nucleic acid, protein, polysaccharide-hydrolysis or synthesis. At the same time, a variety of spectral characterization methods are proposed and the advantages and disadvantages of the different characterization methods are analyzed through carrying out experiments. Consequently, the wide implementation of weak measurement-based detection technology is attained.

Keywords: weak measurement, molecular hydrolyzed, characterization methods, transition conditions, measuring range

OPEN ACCESS

Edited by:
Honghui He,
Tsinghua University, China

Reviewed by:
Guiqiang Wang,
Hefei University of Technology, China
Qinghua He,
University of Washington, United States

****Correspondence:***
Le Liu
liu.le@sz.tsinghua.edu.cn
Yonghong He
heyh@sz.tsinghua.edu.cn

Specialty section:
This article was submitted to Nanoscience, a section of the journal Frontiers in Chemistry

Received: *05 April 2022*
Accepted: *29 April 2022*
Published: *30 May 2022*

Citation:
Xu Y, Shi L, Zhou C, Li Z, Guan T, Xing X, Liu L and He Y (2022) Demonstration of a New Characterization Method for Weak Measurement. Front. Chem. 10:913035. doi: 10.3389/fchem.2022.913035

1 INTRODUCTION

The concept of the weak measurement was proposed in 1988 by Aharonov, Albert and Vaidman (AAV) on the basis of "two-state vector representation of quantum mechanics" (Aharonov et al., 1988; Ritchie et al., 1991). In 2005 and 2007, the teams of Pryde and Jozsa realized and measured complex weak values in polarization detection based on the weak measurement theory and explained in detail the physical significance of the weak values in both the real and imaginary parts of the actual measurement (Pryde et al., 2005; Jozsa, 2007). With this approach, it was possible to achieve high precision measurement with weak measurement technology (Xu et al., 2013; Vella et al., 2019; Xu et al., 2020; Yin et al., 2021). Since 2010, relevant theories have shown that the weak measurement technology exhibits more obvious detection advantages in the frequency domain than the other fields (Brunner and Simon, 2010; Xu et al., 2013). In 2015, our group first proposed a novel optical frequency domain weak measurement system with universal value, which has shown amazing potential in the field of biomolecular detection (Zhang et al., 2016; Li et al., 2017; Li et al., 2018; Xu et al., 2018; Xu et al., 2019a; Xu et al., 2019b; Xu et al., 2021).

Since it was put forward, the weak measurement method has been considered a theoretical scheme of indirect measurement by means of pointer coupling with pre-selected system states. However, the

amplification effect of the weak measurement relies on the theory of quantum measurement and has been widely discussed in many aspects for a long time. Even some fundamental properties of the quantum measurement itself have been debated and unsolved since its birth. Along these lines, Von Neumann's mathematical description is considered the theoretical basis of quantum measurement (Von Neumann, 2018). It was assumed that the measurement process could be regarded as the measurement of the probability of the quantum operator A in each state, which is the measurement, where. Compared with the classical measurement approach, the weak measurement method proposes the utilization of a weak measurement quantum system with a weak value amplification effect, which is induced by introducing a post-selection process. More specifically, when the weak value decreases, the probability of the post-selection is very low, but the amplification effect of the measurement system is greatly improved (Hosoya and Shikano, 2010; Pusey, 2014; Avella et al., 2017). The proposed theory has been verified in many experiments since then (Hosten and Kwiat, 2008; Dixon et al., 2009; Jordan et al., 2014), and has been also successfully implemented in a variety of fields (Aharonov et al., 2003; Kocsis et al., 2011). The difference between the weak measurement and the strong measurement method is theoretically considered to be the strength of the interaction between the measurement system and the measurement object. On the other hand, the use of weak values is often considered to be the fundamental difference between the weak and strong measurements, especially in the experimental-related work since the weak and expected values are different both in concept and in the extracted measurement results (Duck et al., 1989; Dziewior et al., 2019).

Therefore, the quantitative description of the difference between the weak and strong measurements, and even the realization of the transition between the weak and strong measurements in the experiment, becomes particularly important. PAN, Y successfully realized the continuous transition scheme from weak to the strong measurement of a bound 40Ca + single atom, while it was assumed that the transition process can be expressed by the characteristic index (Pan et al., 2020). This transformation of the continuous connection between the weak and strong measurements opens up new experimental possibilities for testing the basis of quantum measurement, and also renders the improvement of the measurement scheme of the related quantum technology of vital importance.

Under this direction, in this work, the premise of the weak value amplification is systematically examined. In addition, the significance of the weak measurement procedure itself is explored, as well as the fundamental difference between the weak and classical measurement approaches. By discussing the approximate range of weak values, a unified equation to the description of both of them is provided, whereas the principle of the weak value enhancement effect and the significance of weak value for the weak value amplification process is examined providing a possible way of the enhancement. The reliability of the proposed theory is also proved in the frequency domain, space domain and electronic case, and the acquired experimental results are proved in the frequency and space domains. A new fitting method is established by using the new descriptive equation, which can smoothly provide the transition to the classical measurement state.

2 THEORY

$$H = -g(t)PA \tag{1}$$

The discussion of this work still considers the coupling Hamiltonian as the starting point, and the eigenvalues of 1 and -1 as the measurement results of the orthogonal photon polarization operator A are used. The coupled Hamiltonian satisfies the following equation:where g(t) represents the time-dependent coupling strength, satisfying the following condition: $g(t)dt = k$. k stands for the coupling strength of the system state and the readout pointer state; P is the intrinsic state of the photon (which can represent the transverse distribution of the photon or the photon momentum distribution). In the case of post-selection, the eigenstate can be expressed as follows:

$$\begin{aligned}
&\langle\psi_f\left|e^{-i\int Hdt}\right|\psi_i\rangle \exp\left(-\frac{P^2}{4(\Delta P)^2}\right) = \langle\psi_f|\psi_i\rangle\sum_{n=0}^{\infty}\frac{(iP)^n}{n!}(A^n)_\omega \exp\left(-\frac{P^2}{4(\Delta P)^2}\right)\\
&= \langle\psi_f|\psi_i\rangle \exp\left(iP\frac{\langle\psi_f|\hat{A}|\psi_i\rangle}{\langle\psi_f|\psi_i\rangle}\right)\exp\left(-\frac{P^2}{4(\Delta P)^2}\right)\\
&= +\langle\psi_f|\psi_i\rangle\sum_{n=0}^{\infty}\frac{(iP)^n}{n!}\left[(A^n)_\omega - (A_\omega)^n\right]\exp\left(-\frac{P^2}{4(\Delta P)^2}\right)
\end{aligned} \tag{2}$$

In the weak measurement-related discussions, the second term of the above equation is usually omitted to ensure the validity of the weak value description of the optical path system (Aharonov and Vaidman, 1990). It is generally believed that this approximation needs to meet the following precondition:

$$(2\Delta P)^n\frac{\Gamma(n/2)}{(n-2)!}\left|(A^n)_\omega - (A_\omega)^n\right| \ll 1 \tag{3}$$

The approximate condition is accepted by most of the weak measurement-related theories (Aharonov et al., 1988; Ritchie et al., 1991; Brunner and Simon, 2010; Xu et al., 2013; Zhang et al., 2016), but the constraint is not natural. A photon dimorphic system is considered as follows: only two states exist in the input light, and the pre- and post-selective states of the photon can be expressed as follows:

$$\begin{aligned}
|\psi_i\rangle &= \sin\alpha|H\rangle + \cos\alpha|V\rangle\\
|\psi_f\rangle &= e^{-i\delta}\cos\beta|H\rangle - e^{i\delta}\sin\beta|V\rangle
\end{aligned} \tag{4}$$

The above equations represent the polarization angle of the selected states before and after, respectively, and denote the phase difference to be measured. At this point, since the system pointer is selected as the photon wavelength, the system Hamiltonian can be expressed by the following expression:

$$H = -k\left(\hat{\lambda} - \lambda_0\right)\hat{A} \tag{5}$$

$|VV|$ asthe observation operator of the system. When the incident light is $e^{\frac{(\lambda-\lambda_0)^2}{\sigma_\lambda^2}}$, λ_0 is the central wavelength of the incident light spectrum, and σ_λ is the standard deviation of a Gaussian wave, and in calculations, we use the half-peak width for approximation. At this point, the pointer state after passing the weak measurement system can be represented as follows:

$$\begin{aligned}\left|\varphi_o\right\rangle &= \left\langle\psi_f\right|e^{-ikA(\lambda-\lambda_0)}\left|\psi_i\right\rangle\left|\varphi_i\right\rangle \\ &= \left[\sin(\alpha-\beta)\cos\delta - i\sin(\alpha+\beta)\sin\delta\right]e^{-\frac{(\lambda-\lambda_0)^2}{\sigma_\lambda^2}}\left|\lambda\right\rangle\end{aligned} \tag{6}$$

The weak value is defined as (Li et al., 2018; Xu et al., 2021):

$$\begin{aligned}A_\omega = &\frac{\sin(\alpha+\beta)\sin(\alpha-\beta)}{\sin^2(\alpha+\beta)\sin^2\delta + \sin^2(\alpha-\beta)\cos^2\delta} \\ &+ i\frac{\left[\sin^2(\alpha+\beta) - \sin^2(\alpha-\beta)\right]\cos\delta\sin\delta}{\sin^2(\alpha+\beta)\sin^2\delta + \sin^2(\alpha-\beta)\cos^2\delta}\end{aligned} \tag{7}$$

Because the constraints need to be satisfied, the value of $(A^n)_\omega$ has to be calculated.

$$\begin{aligned}(A^n)_\omega &= \frac{\left\langle\psi_f\right|\hat{A}\left|\psi_i\right\rangle}{\left\langle\psi_f\right|\left.\psi_i\right\rangle} = \frac{\sin\alpha\cos\beta e^{-i\delta} - (-1)^n\cos\alpha\sin\beta e^{i\delta}}{\sin\alpha\cos\beta e^{-i\delta} - \cos\alpha\sin\beta e^{i\delta}} \\ &= \begin{cases} 1, n = 2m, m = 1, 2, 3, \ldots \\ A_\omega, n = 2m+1, m = 1, 2, 3, \ldots \end{cases}\end{aligned} \tag{8}$$

When $(A^n)_\omega$ does not converge with n it is implied that the constraints of **Eq. 3** should be changed to $|A_\omega| \ll 1$ and $\Delta q \ll 1$. In general, the initial state of the optical path satisfies the following condition: $\alpha, \beta \ll 1$, which does not always make the constraint hold. The constraints for the fore and the aft polarization states need to be modified to $\alpha \neq \beta$ and $b \ll 1$. If the condition of $\alpha \neq \beta$ is not satisfied, the spectral form of the double peaks will appear (although it does not meet the phenomenon of Gaussian center "offset" that was mentioned in AAV theory, it can still calculate the center of the double peaks to measure the "offset"). If the condition of $b \ll 1$ is not satisfied, the phase change only affects the light intensity, but the shift of the central wavelength is not affected. Thus, the law of the weak measurement system is consistent with that of the classical measurement. Therefore, the premise of the approximation condition of the weak value description is that the pre-and post-selection states are not orthogonal and the readout spectrum has a direct flow. In fact, the form is closer to the motion of the spectral wave packet. At the same time, because A_ω cannot be infinitely enlarged, the impact of the weak value amplification cannot be infinitely enlarged.

The change of the spectrum when the phase difference of the optical path is adjusted is basically consistent with the change of the experimental measurement, but there are still some special cases. In one case, the fitting effect is not good when the initial optical path difference is very large. At this point $ReA_\omega \gg 1$, and the system can be considered as a classical measurement form. In the other case, the offset cannot increase infinitely, which corresponds to $ImA_\omega \gg 1$. Consequently, the fitting condition of the weak value amplification is not met at this time, but the description method of the weak value is still applicable. Hence, the weak measurement establishment condition in AAV theory can only fit a certain part of the corresponding curve well.

When the post-selection state of the system is set to a specific state, the displacement of the pointer far exceeds the eigenvalue of the system in the interaction Hamiltonian of the weakly coupled pointer measurement. In addition, under the first-order approximation, the displacement of the center of the pointer state is proportional to both the coupling parameter and the weak value. **Figure 1** shows the spectral migration modes of the pre- and post-selection states under the application of the non-orthogonal and near-orthogonal conditions respectively. The theoretical curve described in AAV theory is shown in **Figure 1A**, which represents the offset of the Gaussian distribution spectrum. **Figure 1B** illustrates a more common result when the system's pre- and post-selection states are in a nearly orthogonal combination. The spectrum is found in the form of two peaks, and when the post-selection state changes, the two peaks decrease in the opposite direction. This law has been well studied in-depth in past work (Zhang et al., 2016; Li et al., 2018; Xu et al., 2018), while the latter mode is generally selected in the experiments to obtain both better measurement range and resolution.

For the sake of discussion, let $x = \lambda - \lambda_0$ represent the narrow band width of the spectrum and let $y = I_{rec}(x)$ be the distribution function of the spectrum. On the premise of $\delta \ll 1$ and $\alpha \approx \beta$, we can obtain the following form:

$$y = [1 - cos(kx + \delta)]e^{-x^2/\sigma_\lambda^2} \tag{9}$$

We now need to estimate the phase difference information from the measured spectral y(x) relation plot. The theoretical spectrum given by **Eq. 9** can be obtained from the maximum likelihood estimate (Strubi and Bruder, 2013).

$$\begin{aligned}&\sum_i (1 - cos(kx_i + \delta))sin(kx_i + \delta)e^{-2x_i^2/\sigma_\lambda^2} \\ &\quad = \sum_i y_i\, sin(kx_i + \delta)e^{-x_i^2/\sigma_\lambda^2}\end{aligned} \tag{10}$$

In the above formula, x_i and y_i represent the normalized wavelength and the corresponding normalized light intensity distribution respectively. At this point, another constraint needs to be considered: $kx \ll 1$, which implies that the product of the coupling constant and the measurement bandwidth is relatively small. Therefore, δ can be divided into the following two forms:

1) If $\delta \gg kx$, then $kx_i + \delta \approx \delta$, and **Eq. 10** can be simplified as follows:

$$1 - \cos\delta = \frac{\sum e^{-x_i^2} y_i}{\sum e^{-2x_i^2}} \tag{11}$$

2) If $\delta, kx \ll 1$, then kx_i cannot be ignored, but $kx_i + \delta \ll 1$ still exists. In this case, **Eq. 10** can be simplified as follows:

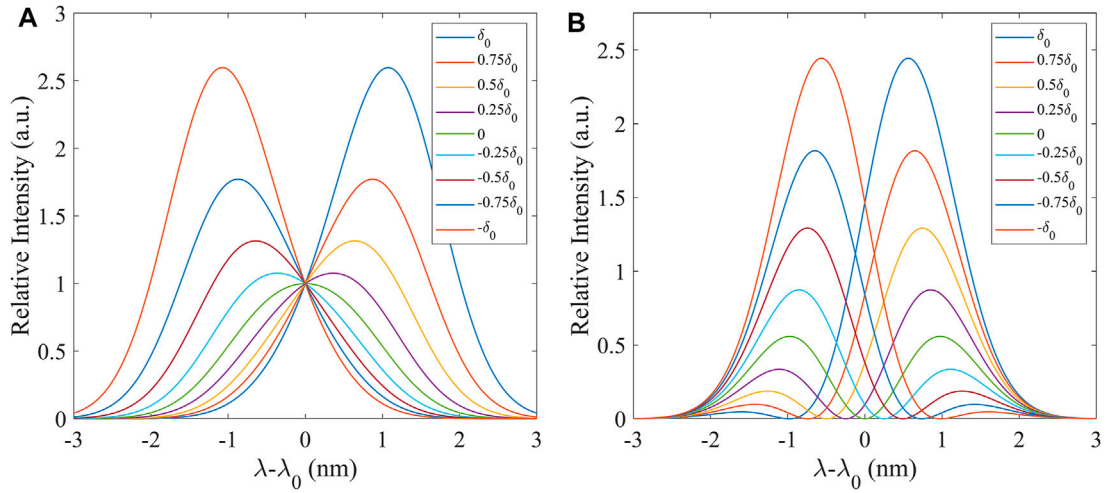

FIGURE 1 | Theoretical spectra of the different phase differences under the enforcement of weak measurement conditions. The spectrum with different colors represents the various phase differences in the light path. **(A)** The $\alpha \neq \beta$ ideal case is described in AAV theory. **(B)** $\alpha = \beta$ or α is often close to β.

$$\tan\delta == \frac{k\sum e^{-x_i^2}x_i y_i}{\sum e^{-x_i^2}y_i} \tag{12}$$

In the first case, the phase difference that has to be measured is relatively large. Therefore, the right-hand side of the equation represents the ratio of the received light intensity to the initial light intensity $\sum y_i$ and the ratio of the outgoing light intensity $\sum e^{-2x_i^2}$. In the second case, the right side of the equation represents the shift of the central wavelength $\sum x_i y_i / \sum y_i$ after multiplying the weight of the light intensity $\sum e^{-x_i^2}$, whereas the coupling intensity K needs to be considered as the coupling amplification factor. This situation is generally consistent with the previously reported weak measurement theory, but the initial spectral intensity should be considered as the weight of the central wavelength shift. When $\delta = 0$, the measurement sensitivity is proportional to 1/K in case 2 and to 0 in case 1. Because the value of K is relatively small, the measurement sensitivity of case 2 is far higher than that of case 1 at this time, and the amplification effect of the weak value can be reflected at this time. A similar conclusion can be obtained for the non-Gaussian incident light, but the initial light intensity distribution term in **Eqs 11**, **12** needs to be modified.

The transition from weak to classical measurements can be now further obtained. If the above equation is expanded with respect to kx_i and δ, the following equation is derived:

$$\begin{aligned}&\sum_i (1-\cos(kx_i+\delta))tan\ \ k\ x_i e^{-2x_i^2/\sigma_\lambda^2}\\ &+\sum_i (1-\cos(kx_i+\delta))tan\ \ \delta\ e^{-2x_i^2/\sigma_\lambda^2}\\ &=\sum_i y_i\, tan\, kx_i e^{-x_i^2/\sigma_\lambda^2}+\sum_i y_i \tan\delta e^{-2x_i^2/\sigma_\lambda^2}\end{aligned} \tag{13}$$

We note that due to the first-order approximation, in case 1 the first term on both sides of **Eq. 13** is ignored, and in case 2 the left side of the equation is completely ignored. Therefore, in order to obtain an equation that can satisfy the transition process, the first term on the left side of the equation can be ignored, and the remaining three terms of the equation, under the constraint condition $kx_i \ll 1$, can be obtained as follows:

$$\frac{2z^2}{1+z^2}\sum_i e^{-2x_i^2/\sigma_\lambda^2} - \sum_i e^{-x_i^2/\sigma_\lambda^2} y_i = \frac{2z}{1-z^2}\sum_i e^{-x_i^2/\sigma_\lambda^2} y_i kx_i \tag{14}$$

where $z = \tan\delta/2$. At this point, an implicit function can be used for the transition from the weak measurement state to the classical measurement state, where the phase difference can be predicted from the spectrogram.

So far, a calculation function independent of the weak value has been obtained, but the influence of the weak value amplification can be still achieved. Since the weak measurement method has an amplification effect, the source of the amplification is weak to the coupling mode k, and the weak value is only a representation form of the amplification effect. For example, $b \ll 1$ and $ImA_\omega \approx \frac{(sin^2(\alpha+\beta)-sin^2(\alpha-\beta))ranb}{sin^2(\alpha-\beta)} \propto \tan b \propto b$, the central wavelength can be represented by the following expression: $\mathrm{Im}A_\omega$, by considering the second-order Taylor approximation:

$$\tan b = \frac{\sum e^{-x_i^2}\tan(kx_i)y_i}{\sum e^{-x_i^2}y_i} \propto \mathrm{Im}A_\omega \tag{15}$$

At this point, we can argue that $\mathrm{Im}A_\omega$ is a better approximation under this premise. Therefore, the following expression is still valid and can be used: $d\lambda \propto \mathrm{Im}A_\omega$. According to the AAV theory, weak values occur during the interaction coupling process as can be ascertained from the following equation:

$$\begin{aligned}|\varphi_o\rangle &= \langle\psi_f|e^{-gAx}|\psi_i\rangle|\varphi_i\rangle\\ &= [\sin(\alpha-\beta)\cos b - i\sin(\alpha+\beta)\sin b]e^{-x^2}e^{-gA_\omega x}\end{aligned} \tag{16}$$

Obviously, the theory of AAV is a general framework, which represents the strength of the mutual coupling between the measurement operator and the coordinate space. However, if the

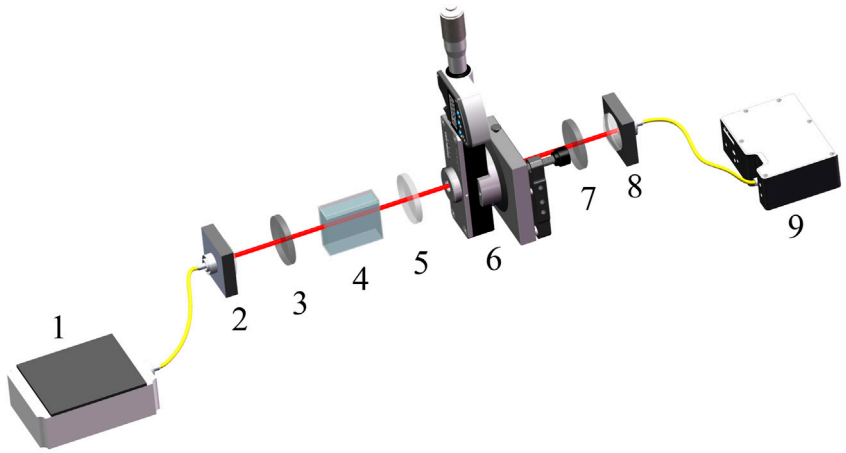

FIGURE 2 | Schematic installation of the weak measurement sensor. 1, Superluminescent laser diode (SLD, IPSDD0804, 5 mW, Center wavelength: 840 nm, bandwidth: 40 nm, Inphenix). 2 and 8, Collimating and coupling lenses. 3 and 7, Pre- and post-selection polarizer (Thorlabs Inc., 180 LPVIS050-MP, extinction ratio of 100,000:1). 4, Sample Cell. 5, Achromatic Quarter Wave Plate (Thorlabs Inc., AQWP05M-980). 6, Soleil-Babinet Compensators (SBC, Thorlabs Inc., SBC-IR). 9, Spectrometer (Ocean Optics, HR4000).

measurement operator A is acting on mutually orthogonal eigenstates, it can be directly calculated without using the AVV. In this case, since $ImA_\omega \propto \tan b$ can be used as the description of the phase under the second-order Taylor approximation, and $\mathrm{Im}A_\omega$ can measure the constraint of $\sin^2(\alpha-\beta) \ll 1$. Besides, it can also measure the weak value amplification effect of the system. However, the sensitivity enhancement of the weak values is relatively limited (Aharonov et al., 1988; Ritchie et al., 1991; Xu et al., 2013), because the approximation conditions of AAV are not satisfied at $ImA_\omega \gg 1$. Therefore, the theory of the weak value amplification is not valid beyond a certain measurement range. In addition, the employed Gaussian light may not be completely normal in the experiment, so the waveform of the incident light needs to be considered for the weight calculation during the fitting procedure.

3 EXPERIMENT

3.1 A Comparison of Multiple Characterisation Methods for Weak Measurements

The experiments in this work were carried out by using an optical rotation weak measurement system (Li et al., 2018). As is shown in **Figure 2**, an SLD was selected as the light source. After collimation is performed through the coupling lens, the light beam entered the weak measurement system that was coupled to the spectrometer to read the spectral signal. Additionally, the weak measurement system consists of a front selective polarizer, a wave plate and Soleil-Babinet Compensators (which provide the initial phase difference), a sample cell and a rear selective polarizer. In the experiment, only distilled water was injected into the sample cell to simulate the actual measurement scene, and the Soleil-Babinet Compensators were adjusted to simulate the phase difference of the circularly polarized light generated in the system.

Since **Eq. 13** requires that the phase difference estimation should be performed by using weighted central wavelength offset, this approach is inconsistent with the requirements of the AAV theory. At the same time, since the outgoing spectrum of the SLD light source does not completely conform to the Gaussian distribution, and the transmittance of components may be affected in the transmission process, resulting in the manifestation of spectral morphology changes, the influence of the non-Gaussian spectrum distribution on measurement should also be considered. In order to compare the advantages and disadvantages of these methods, five different wavelength-processing methods were selected for the phase difference estimation, while their measurement range and resolution are analyzed. The five treatment methods are as follows:

A. Based on our previous work (Zhang et al., 2016; Li et al., 2017; Li et al., 2018), $\delta \propto I_m A_m$; B. This can be approximated to $\delta \propto \frac{\Sigma e^{-\lambda^2}\lambda\varphi(\lambda)}{\Sigma e^{-\lambda^2}\varphi(\lambda)}$ according to **Eq. 12**. here we assume a Gaussian distribution for $\varphi(\lambda)$. $\varphi(\lambda) = e^{-\frac{(\lambda-\lambda_0)^2}{\sigma_\lambda^2}}$, where λ_0 is the central wavelength and σ_λ is the standard deviation of the wavelength (here we use the spectral half-peak width approximation). When the central wavelength is calculated, the theoretical intensity of 840 and 40 nm half peak width is weighted;

C. According to **Eq. 12**, $\delta \propto \frac{\Sigma e^{-\lambda^2}\lambda\varphi(\lambda)}{\Sigma e^{-\lambda^2}\varphi(\lambda)}$, considering that the spectral shape of the original spectrum is a skewed Gaussian distribution, we assume $\varphi(\lambda) = \begin{cases} e^{-\frac{(\lambda-\lambda_0)^2}{\sigma_{\lambda_1}^2}} & \lambda < \lambda_0 \\ e^{-\frac{(\lambda-\lambda_0)^2}{\sigma_{\lambda_2}^2}} & \lambda > \lambda_0 \end{cases}$ and use Newton's method to approximate σ_{λ_1}, σ_{λ_2}.

D. According to **Eq. 12**, $\delta \propto \frac{\Sigma e^{-\lambda^2}\lambda\varphi(\lambda)}{\Sigma e^{-\lambda^2}\varphi(\lambda)}$, $\varphi(\lambda)$ is given directly from the original spectrum.

E. According to **Eq. 14**, we solve directly for δ

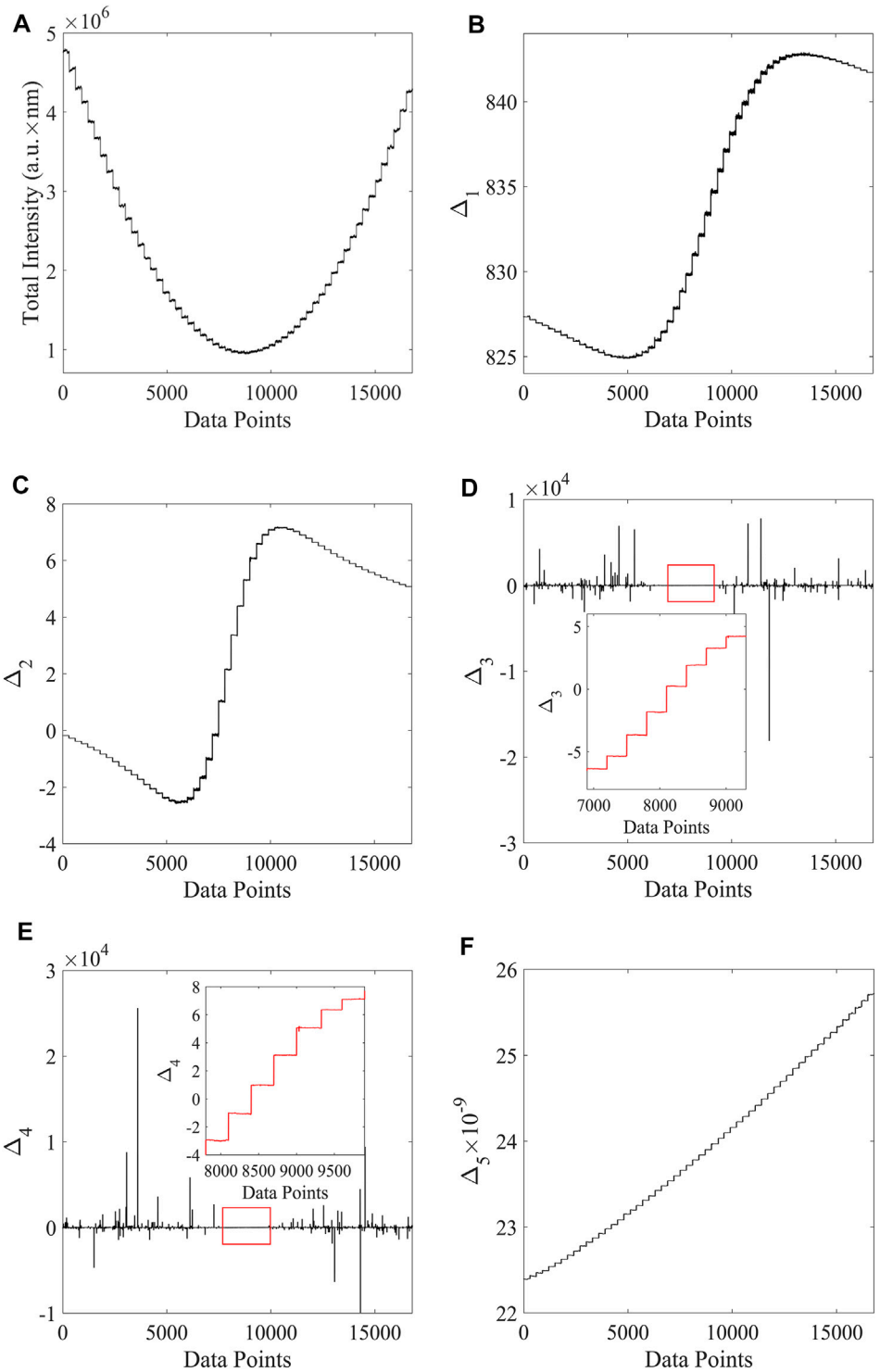

FIGURE 3 | (A) Distribution of the spectral relative light intensity corresponding to different phases. **(B–F)** Offsets and phase diagrams corresponding to the five different characterization methods A, B, C, D, **(E)**

In A, B, C, D, and E, δ indicates the phase difference to be measured.

The measurement results are shown in **Figure 3**, and the measurement range and resolution are summarized in **Table 1**.

The system was firstly adjusted to the vicinity of the bimodal working area (Zhang et al., 2016; Xu et al., 2018). As is shown in **Figure 3**, the spectra of the system were obtained at different optical rotation angles through the SBC. For every 300 data points

TABLE 1 | Comparison of the measurement effects of various characterization schemes.

Characterization Methods	Resolution (rad)	Measurement Range (rad)
Method A	5.6×10^{-6}	0.042
Method B	1.6×10^{-6}	0.024
Method C	0.9×10^{-6}	0.018
Method D	1.2×10^{-6}	0.015
Method E	7.2×10^{-6}	0.168

recorded during the measurement, the rotation angle in the optical path was changed by 0.003 rad by SBC. **Figure 3A**: Relative light intensity corresponding to the different optical rotation angles. **Figures 3B–** Method A: No weighting. **Figures 3C–** method B: weighted with a central wavelength of 840 nm and half peak width of 40 nm. **Figures 3D–** Method C: Perform skewness fitting merge weighting calculation. **Figures 3E–** Method D: Weighted calculation by original spectrum. **Figures 3F–** Method E: In order to achieve a wider measurement range and transition from the weak to strong measurements, this problem was solved by using the transition **Eq. 16**.

Under this perspective, the measurement range of the above fitting methods was firstly compared. According to the conclusion of the existing work, the weak value amplification range near the spectrum appears as a bimodal state. Furthermore, there is a sensitive range by adjusting the polaroid and the wave plate group before and after the weak value enlarged working range is derived. By working in the same range, and selecting a continuous adjustment of 0.003 rad as the step for the phase difference, the spectrum data changes over time were recorded. The measurement range of the fitting method is the linear relationship between the spectral characterization results and the optical rotation Angle. Then, the resolution of the system under different fitting methods was calculated by employing the following formula: $\delta\lambda/\delta\alpha\sigma_\alpha = 3\sigma_s/(\delta\lambda/\delta\alpha)$. As is shown in **Table 1**, the resolution obtained by the central wavelength shift-A scheme is 5.6×10^{-6} rad, and the linear measurement range is 0.036 rad. The resolution was 1.6×10^{-6} rad with the weighted central wavelength shift-B scheme, and the measurement range was reduced to 0.024 rad. The resolution of skewness Gaussian fitting-C scheme was 0.9×10^{-6} rad and the measurement range was 0.018 rad, while the resolution of the original spectral fitting-D scheme was 1.2×10^{-6} rad and the measurement range was 0.015 rad. The extracted results show that the weighted center wavelength has a higher resolution and a narrower linear measurement range. In addition, if a non-Gaussian initial spectrum is considered for the fitting process, the resolution will be improved. The resolution can also be improved to some extent by using the original spectral weight during the fitting process. However, this method means that the measurement range will be narrower than the original scheme proposed by the AAV. However, compared with the classical measurement method, the method of solving the equation-E scheme has a wider linear region, while the measurement range is greatly increased to 0.168 rad, but the detection accuracy is reduced to 7.2×10^{-6} rad.

3.2 Sucrose Hydrolysis Was Monitored by a Weak Measurement System, and Characterised by Different Methods

Fructose is the sweetest monosaccharide in nature. It is interesting to notice that its sweetness is about 1.8 times that of sucrose and 3 times that of glucose. Fructose will not only cover up the flavor of food, but also has the effect of enhancing the flavor of food. On top of that, it possesses greater solubility and faster dissolution than sucrose and glucose, so it is widely used in the beverage and food industry. At present, monosaccharides are mainly produced by hydrolysis of starch or sucrose in industrial production. Since it is very important to monitor the sugar production process, and because the raw materials and products of the sugar production have optical rotation, the product transformation procedure can be monitored by controlling the optical rotation change in the reaction tank during the implementation of the hydrolysis sugar production process.

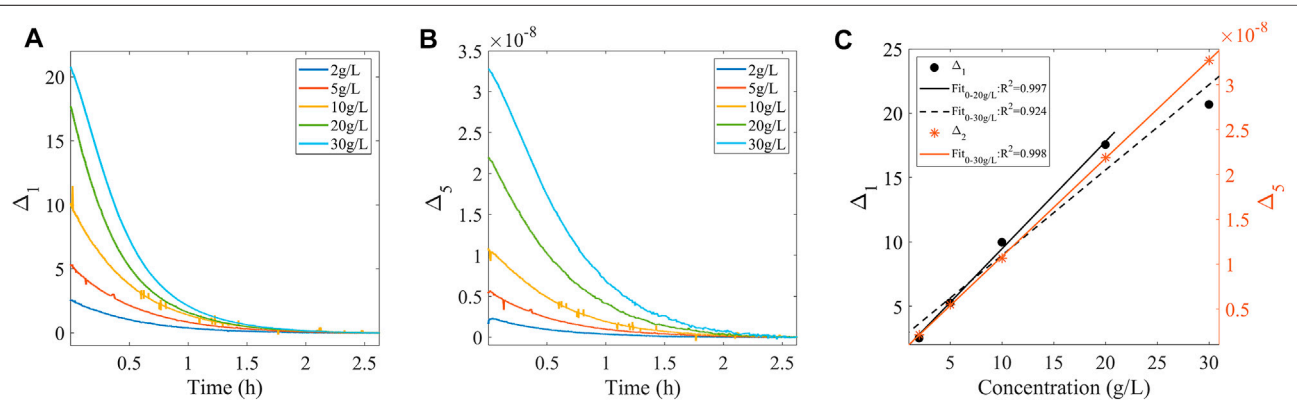

FIGURE 4 | (A,B) Characterization results of the hydrolysis process of sucrose for Methods A and E, respectively. **(C)** Linear fit of the two characterization methods corresponding to the amount of change in the hydrolysis process for different concentrations of the sucrose solutions.

$$C_{12}H_{22}O11 + H_2O \xrightarrow{H^+} C_6H_{12}O_6 + C_6H_{12}O_6 \quad (17)$$

The weak measurement system in **Figure 2** was used for the sucrose hydrolysis experiment, and the reaction equation is shown in **(17)**. More specifically, sucrose solutions with concentrations of 2, 5, 10, 20, and 30 g/L were placed in the sample tank in **Figure 2**, and an appropriate amount of hydrochloric acid was added for the hydrolysis process. Meanwhile, the spectral changes during hydrolysis were monitored. As is shown in **Figures 4A,B**, methods A and E were used to characterize the hydrolysis process, respectively (methods B, C, and D were not considered here due to their small measurement range). As is shown in **Figure 4C**, when method A was used to characterize the sucrose hydrolysis process, good linearity in the range of sucrose concentration 0–20 g/L was demonstrated, but it was decreased in the range of sucrose concentration 0–30 g/L. However, when represented by method E, good linearity was always acquired. Many industrial processes, such as hydrolyzed starch, sucrose to sugar, hydrolyzed protein to the polypeptide, are carried out under the manifestation of high concentration conditions, accompanied by a wide range of rotation of the reactants. Therefore, for practical scenarios such as industrial production, method E is considered more suitable.

4 CONCLUSION

In this work, the premise of weak value amplification was discussed, and the improvement scheme of the weak measurement method was proposed, as well as the difference between the weak value amplification and the classical measurement processes and the transition conditions. The premise of the weak value amplification is that the form of pre- and post-selection states is close to or completely orthogonal, and the weak coupling condition of pre- and post-selection states is required, which is consistent with the conclusion of other works (Leggett, 1989; Peres, 1989). In addition, aiming at the narrow measurement range of the weak measurement in the frequency domain, a transition scheme between the weak measurement and the classical measurement is proposed for the first time, and a better fitting model of the measurement results was found. In addition, insights from the sucrose hydrolysis experiments confirmed that this model has more advantages than the other characterization schemes in a large range of detection scenarios. Under the application of the classical conditions, the measurement effect of this transition measurement method is no different from that of the polarimeter. Under the premise of the weak value amplification, the measurement results obtained by the new transition equation can extend the application range of the weak measurement and realize the transition with the classical measurement method. Interestingly, the fittingmethod is not affected by the experimental device, and can be applied to many measurement fields of weak measurement in the frequency domain, such as biomolecular measurement, chiral molecular measurement, chiral material detection, and temperature detection, etc.

DATA AVAILABILITY STATEMENT

The original contributions presented in the study are included in the article/Supplementary Material, further inquiries can be directed to the corresponding authors.

AUTHOR CONTRIBUTIONS

YX, CZ, LL, and YH put forward the main conceptualization and methodology. YX performed the walking experiments and wrote the paper.LS was helping to refine the theory of the paper. TG, XX, LS, ZL, revised the paper.

FUNDING

This research was made possible with the financial support from National Science Foundation of China (NSFC) (61975089, 61875102), Science and Technology Research Program of Shenzhen City (JCYJ20200109110606054), Chunfeng foundation, Tsinghua University (2020Z99CFZ023), Natural Science Foundation of Guangdong Province (2019A1515012105).

REFERENCES

Aharonov, Y., Albert, D. Z., and Vaidman, L. (1988). How the Result of a Measurement of a Component of the Spin of a Spin-1/2particle Can Turn Out to Be 100. *Phys. Rev. Lett.* 60 (14), 1351–1354. doi:10.1103/PhysRevLett.60.1351

Aharonov, Y., Rohrlich, D., and Paradoxes, Q. (2003). *Quantum Theory for the Perplexed*. Wiley VCH, 299.

Aharonov, Y., and Vaidman, L. (1990). Properties of a Quantum System during the Time Interval between Two Measurements. *Phys. Rev. A* 41 (1), 11–20. doi:10.1103/PhysRevA.41.11

Avella, A., Piacentini, F., Borsarelli, M., Barbieri, M., Gramegna, M., Lussana, R., et al. (2017). Anomalous Weak Values and the Violation of a Multiple-Measurement Leggett-Garg Inequality. *Phys. Rev. A* 96 (5), 5. doi:10.1103/PhysRevA.96.052123

Brunner, N., and Simon, C. (2010). Measuring Small Longitudinal Phase Shifts: Weak Measurements or Standard Interferometry? *Phys. Rev. Lett.* 105 (1), 010405. doi:10.1103/PhysRevLett.105.010405

Dixon, P. B., Starling, D. J., Jordan, A. N., and Howell, J. C. (2009). Ultrasensitive Beam Deflection Measurement via Interferometric Weak Value Amplification. *Phys. Rev. Lett.* 102 (17), 4. doi:10.1103/PhysRevLett.102.173601

Duck, I. M., Stevenson, P. M., and Sudarshan, E. C. G. (1989). The Sense in Which a "Weak Measurement" of a Spin-½ Particle's Spin Component Yields a Value 100. *Phys. Rev. D.* 40 (6), 2112–2117. doi:10.1103/PhysRevD.40.2112

Dziewior, J., Knips, L., Farfurnik, D., Senkalla, K., Benshalom, N., Efroni, J., et al. (2019). Universality of Local Weak Interactions and its Application for Interferometric Alignment. *Proc. Natl. Acad. Sci. U.S.A.* 116 (8), 2881–2890. doi:10.1073/pnas.1812970116

Hosoya, A., and Shikano, Y. (2010). Strange Weak Values. *J. Phys. A Math. Theor.* 43 (38), 385307. doi:10.1088/1751-8113/43/38/385307

Hosten, O., and Kwiat, P. (2008). Observation of the Spin Hall Effect of Light via Weak Measurements. *Science* 319 (5864), 787–790. doi:10.1126/science.1152697

Jordan, A. N., Martínez-Rincón, J., and Howell, J. C. (2014). Technical Advantages for Weak-Value Amplification: When Less Is More. *Phys. Rev. X* 4 (1), 11. doi:10.1103/PhysRevX.4.011031

Jozsa, R. (2007). Complex Weak Values in Quantum Measurement. *Phys. Rev. A* 76 (4), 044103. doi:10.1103/PhysRevA.76.044103

Kocsis, S., Braverman, B., Ravets, S., Stevens, M. J., Mirin, R. P., Shalm, L. K., et al. (2011). Observing the Average Trajectories of Single Photons in a Two-Slit Interferometer. *Science* 332 (6034), 1170–1173. doi:10.1126/science.1202218

Leggett, A. J. (1989). Comment on "How the Result of a Measurement of a Component of the Spin of a Spin-(1/2 Particle Can Turn Out to Be 100". *Phys. Rev. Lett.* 62 (19), 2325. doi:10.1103/PhysRevLett.62.2325

Li, D., Guan, T., He, Y., Liu, F., Yang, A., He, Q., et al. (2018). A Chiral Sensor Based on Weak Measurement for the Determination of Proline Enantiomers in Diverse Measuring Circumstances. *Biosens. Bioelectron.* 110, 103–109. doi:10.1016/j.bios.2018.03.033

Li, D., He, Q., He, Y., Xin, M., Zhang, Y., and Shen, Z. (2017). Molecular Imprinting Sensor Based on Quantum Weak Measurement. *Biosens. Bioelectron.* 94, 328–334. doi:10.1016/j.bios.2017.03.021

Pan, Y., Zhang, J., Cohen, E., Wu, C.-w., Chen, P.-X., and Davidson, N. (2020). Weak-to-Strong Transition of Quantum Measurement in a Trapped-Ion System. *Nat. Phys.* 16 (12), 1206–1210. doi:10.1038/s41567-020-0973-y

Peres, A. (1989). Quantum Measurements With Postselection. *Phys. Rev. Lett.* 62 (19), 2326. doi:10.1103/PhysRevLett.62.2326

Pryde, G. J., O'Brien, J. L., White, A. G., Ralph, T. C., and Wiseman, H. M. (2005). Measurement of Quantum Weak Values of Photon Polarization. *Phys. Rev. Lett.* 94 (22), 220405. doi:10.1103/PhysRevLett.94.220405

Pusey, M. F. (2014). Anomalous Weak Values Are Proofs of Contextuality. *Phys. Rev. Lett.* 113 (20), 5. doi:10.1103/PhysRevLett.113.200401

Ritchie, N. W. M., Story, J. G., and Hulet, R. G. (1991). Realization of a Measurement of a "Weak Value". *Phys. Rev. Lett.* 66 (9), 1107–1110. doi:10.1103/PhysRevLett.66.1107

Strübi, G., and Bruder, C. (2013). Measuring Ultrasmall Time Delays of Light by Joint Weak Measurements. *Phys. Rev. Lett.* 110 (8), 5. doi:10.1103/PhysRevLett.110.083605

Vella, A., Head, S. T., Brown, T. G., and Alonso, M. A. (2019). Simultaneous Measurement of Multiple Parameters of a Subwavelength Structure Based on the Weak Value Formalism. *Phys. Rev. Lett.* 122 (12), 123603. doi:10.1103/PhysRevLett.122.123603

Von Neumann, J. (2018). *Mathematical Foundations of Quantum Mechanics*. New Edition. Princeton university press. doi:10.1515/9781400889921

Xu, L., Liu, Z., Datta, A., Knee, G. C., Lundeen, J. S., Lu, Y.-q., et al. (2020). Approaching Quantum-Limited Metrology with Imperfect Detectors by Using Weak-Value Amplification. *Phys. Rev. Lett.* 125 (8), 080501. doi:10.1103/PhysRevLett.125.080501

Xu, X.-Y., Kedem, Y., Sun, K., Vaidman, L., Li, C.-F., and Guo, G.-C. (2013). Phase Estimation with Weak Measurement Using a White Light Source. *Phys. Rev. Lett.* 111 (3), 033604. doi:10.1103/PhysRevLett.111.033604

Xu, Y., Shi, L., Guan, T., Guo, C., Li, D., Yang, Y., et al. (2018). Optimization of a Quantum Weak Measurement System with its Working Areas. *Opt. Express* 26 (16), 21119–21131. doi:10.1364/OE.26.021119

Xu, Y., Shi, L., Guan, T., Zhong, S., Zhou, X., Li, D., et al. (2019a). Multifunctional Weak Measurement System that Can Measure the Refractive Index and Optical Rotation of a Solution. *Appl. Phys. Lett.* 114 (18), 181901. doi:10.1063/1.5091468

Xu, Y., Shi, L., Li, S., Guan, T., Zhong, S., Zhou, X., et al. (2019b). Detection of Macromolecular Content in a Mixed Solution of Protein Macromolecules and Small Molecules Using a Weak Measurement Linear Differential System. *Anal. Chem.* 91 (18), 11576–11581. doi:10.1021/acs.analchem.9b01657

Xu, Y., Zhou, C., Shi, L., Zhang, X., Guan, T., Guo, C., et al. (2021). Imaging Sensor for the Detection of the Flow Battery via Weak Value Amplification. *Anal. Chem.* 93 (38), 12914–12920. doi:10.1021/acs.analchem.1c02189

Yin, P., Zhang, W.-H., Xu, L., Liu, Z.-G., Zhuang, W.-F., Chen, L., et al. (2021). Improving the Precision of Optical Metrology by Detecting Fewer Photons with Biased Weak Measurement. *Light Sci. Appl.* 10 (1), 103. doi:10.1038/s41377-021-00543-4

Zhang, Y., Li, D., He, Y., Shen, Z., and He, Q. (2016). Optical Weak Measurement System with Common Path Implementation for Label-Free Biomolecule Sensing. *Opt. Lett.* 41 (22), 5409–5412. doi:10.1364/OL.41.005409

Conflict of Interest: The authors declare that the research was conducted in the absence of any commercial or financial relationships that could be construed as a potential conflict of interest.

The handling editor HH declared a shared affiliation with the authors at the time of review.

Publisher's Note: All claims expressed in this article are solely those of the authors and do not necessarily represent those of their affiliated organizations, or those of the publisher, the editors and the reviewers. Any product that may be evaluated in this article, or claim that may be made by its manufacturer, is not guaranteed or endorsed by the publisher.

Copyright © 2022 Xu, Shi, Zhou, Li, Guan, Xing, Liu and He. This is an open-access article distributed under the terms of the Creative Commons Attribution License (CC BY). The use, distribution or reproduction in other forums is permitted, provided the original author(s) and the copyright owner(s) are credited and that the original publication in this journal is cited, in accordance with accepted academic practice. No use, distribution or reproduction is permitted which does not comply with these terms.

frontiers | Frontiers in Chemistry

ORIGINAL RESEARCH
published: 03 June 2022
doi: 10.3389/fchem.2022.925931

In vivo Visualization of Collagen Transdermal Absorption by Second-Harmonic Generation and Two-Photon Excited Fluorescence Microscopy

Yanan Sun[1,2†], *Lishuang Li*[1,2†], *Shuhua Ma*[1,2], *Gaiying He*[1,2], *Weifeng Yang*[1,2] *and Yi Wang*[1,2*]

[1]*Experimental Research Center, China Academy of Chinese Medical Sciences, Beijing, China,* [2]*Beijing Key Laboratory of Research of Chinese Medicine on Prevention and Treatment for Major Disease, China Academy of Chinese Medical Sciences, Beijing, China*

The transdermal administration of collagen is an important method used for wound healing and skin regeneration. However, due to the limitations of previous approaches, the process and degree of collagen transdermal absorption could only be quantitatively and qualitatively evaluated *in vitro*. In the present study, we introduced a novel approach that combines second-harmonic generation with two-photon excited fluorescence to visualize the dynamics of collagen transdermal absorption *in vivo*. High-resolution images showed that exogenous recombinant human collagen permeated the epidermis through hair follicles and sebaceous glands reached the dermis, and formed reticular structures in real time. We also validated these findings through traditional *in vitro* skin scanning and histological examination. Thus, our approach provides a reliable measurement for real-time evaluation of collagen absorption and treatment effects *in vivo*.

Keywords: transdermal absorption, second-harmonic generation, two-photon excited fluorescence, recombinant human collagen, live tracking

OPEN ACCESS

Edited by:
Honghui He,
Tsinghua University, China

Reviewed by:
Lingqian Chang,
Beihang University, China
Yu Cao,
China Academy of Chinese Medical Sciences, China

***Correspondence:**
Yi Wang
prof.wangyi@foxmail.com

[†]These authors have contributed equally to this work and share first authorship

Specialty section:
This article was submitted to Nanoscience, a section of the journal Frontiers in Chemistry

Received: *22 April 2022*
Accepted: *09 May 2022*
Published: *03 June 2022*

Citation:
Sun Y, Li L, Ma S, He G, Yang W and Wang Y (2022) In vivo Visualization of Collagen Transdermal Absorption by Second-Harmonic Generation and Two-Photon Excited Fluorescence Microscopy. Front. Chem. 10:925931. doi: 10.3389/fchem.2022.925931

1 INTRODUCTION

The skin is the largest organ in the human body and plays a key role in protecting our body from the diverse external environment (Bouwstra et al., 2003). It is mainly composed of three layers that span from superficial to deep, including the epidermis, dermis, and hypodermis (Menon, 2015). The dermal skin contains components of the extracellular matrix, such as collagen fibers, that contribute to the strength and toughness of the skin (Ngan et al., 2015). As the main component of connective tissue, collagen is the most abundant protein in the skin, comprising 25–35% of the protein content in the whole body (Di Lullo et al., 2002). Collagen is also widely used in cosmetics and biomedical products (Toki et al., 2013; Sun et al., 2015). After exogenous collagen is smeared on the skin, it permeates through the cuticle to the dermis and forms a reticular structure to support the structure of the dermis and supply more extracellular matrix to keep the skin elastic (Chai et al., 2010). Thus, we need to dynamically visualize the process of transdermal absorption of exogenous collagen and measure the extent of collagen absorption with qualitative and quantitative approaches.

To date, various technologies have been applied to measure the biomedical administration of collagen to skin, including chemical assays (Fediuk et al., 2012), tissue inspection (Schulz et al., 2002),

isotope tracing (Cross et al., 2007) and circulating diffusion chamber (Gamer et al., 2006), which can only be used to quantitatively examine the transdermal absorption of exogenous collagen *in vitro*. However, these approaches could not dynamically track the process of transdermal absorption *in vivo* and evaluate the real-time effects of biomedical administration. These limitations could be overcome by nonlinear optical microscopy, such as two-photon excitation fluorescence (TPEF) (Denk et al., 1990; König et al., 2007), and second harmonic generation (SHG) (Campagnola and Loew, 2003; Pittet et al., 2014). Among such technologies, SHG is a well-established method to directly visualize anisotropic biological tissues that possess large hyperpolarizabilities, such as collagen (Thrasivoulou et al., 2011). Moreover, SHG imaging has many advantages, such as a higher signal-to-noise ratio than autofluorescence imaging, detection of intrinsic signals without extrinsic dyes, and the utilization of nonlinear excitation from molecular fluorescence (Kiyomatsu et al., 2015). Nonetheless, few studies have examined the effects of drug administration on the skin using SHG because of the challenges in using it to distinguish endogenous from exogenous collagen. Recently, two-photon excited fluorescence (TPEF) imaging has been widely applied to visualize the dynamics of intrinsic molecules and cells in living specimens through conventional labeling via staining or fluorescent proteins (Miller et al., 2017). Due to the divergent mechanisms of SHG and TPEF, we speculate that they could be combined to provide complementary information for the dynamic observation of biological processes. However, few studies have reported the *in vivo* imaging of the transdermal absorption of collagen with a combination of SHG and TPEF (SHG-TPEF). Therefore, there is an urgent need to obtain *in vivo* high-resolution images of fibrillar collagen during the process of transdermal absorption using SHG-TPEF imaging, which could provide a novel approach for estimating the extent of drug absorption and further assessing the treatment effects of dermal drugs.

To address these issues, we first constructed a mouse model of transdermal absorption through administrating exogenous recombinant human collagen (R-hc), which was proved to be effective in skin absorption in our previous studies (Ma et al., 2018). Second, we set up the platform of *in vivo* SHG-TPEF skin imaging. Third, we tracked the dynamic process of collagen absorption of short-term administration by *in vivo* SHG-TPEF imaging and observed the transdermal absorption pathway. Finally, we applied Franz-type diffusion method to evaluate the collagen absorption at different time points as validation.

2 METHODS

2.1 Animals

Healthy BALB/c mice were purchased from Vital River Laboratories (China). All animals used in this study were male adults (6–8 weeks, 20 ± 2 g body weight). Mice were kept in a specific pathogen-free environment with freely available food and water and a 12 h light-dark cycle. In this study, five mice were used at each time point, each of which received a topical dose of 1 mg/ml of R-hc on a shaved back on the left side of the thoracic spine and a saline control area on the right. The animal experiments were supervised and approved by the Research Ethics Committee of the China Academy of Chinese Medical Sciences (ERCCACMS21-2106-12). All experiments compliance with the Regulations for the administration of affairs concerning experimental animals of the People's Republic of China.

2.2 Quality Control of R-hc

2.2.1.R-hc

R-hc is expressed by eukaryotic cells and integrates the human-like collagen gene, which is a heterozygous type I and type III collagen gene, into the yeast chromosome. The hydroxyproline in R-hc was replaced by proline. In our previous study, we analyzed the effect of R-hc on the repair of laser skin damage in mice. The results showed that R-hc can significantly accelerate wound healing, shorten wound healing time, and promote collagen production in wounds (Ma et al., 2018), which suggests that R-hc could be transdermally absorbed.

Fluorescent Label

For fluorescent labeling, a protein stock solution was prepared by mixing 100 mg R-hc freeze-dried powder (TianJin Irheaya Biological Technology Co., Ltd., Tianjin) with 10 ml 1 M phosphate buffer (pH 8.5–9.0) to produce the 1 ml protein labeling stock solution. To prepare the dye stock solution, anhydrous DMSO was added into a vial of iFluor™ 750 SE (AAT Bioquest, Ex/Em = 749/775 nm) to produce a 10–20 mM stock solution, which was mixed by vortexing. Then, 1 ml of the dye stock solution was added to the vial of protein solution (10 ml) and shaken thoroughly. The concentration of the protein was 10 mg/ml. The reaction mixture was rotated at 4°C for 12 h. The reaction mixture was loaded into a dialysis bag (<1 kd) and placed in a large beaker containing ultrapure water in the dark. The water was changed every 4 h until no fluorescence was detected in the ultrapure water. The fluorescent protein was freeze-dried into a powder for future use.

2.3 SHG-TPEF Skin Imaging

2.3.1 In vivo

The back hair was shaved from the mice, which were treated with iFluor-R-hc (1 mg/ml) for 0, 1, 2, 3, 4 and 5 h at room temperature while avoiding light. At the end of the experiment, all mice were anesthetized with isoflurane and fixed on a mouse plate while the back skin was fixed on holder. The full-thickness skin tissue was scanned by a two-photon scanning confocal microscope (FV1000-MPE, Olympus, Japan).

A two-photon excited fluorescence microscopy system was used for image acquisition based on the reverse detection of SHG and two-photon excited fluorescence signals from the skin. The two-photon excited fluorescence microscopy system was equipped with a water-immersion objective lens (PLAN 25X OB. W IMM, NA 1.05, Olympus) and a Ti:sapphire laser oscillator (wavelength: 690–1040 nm; repetition rate: 80 MHz, pulse width: 100 fs; MaiTai HP DS-OL, Spectra-Physics, Inc. CA).

The SHG image acquisition was performed at an excitation wavelength of 950 nm with a 690 nm dichroic mirror and a 475/20 nm emission filter (center wavelength/bandwidth). For the observation of iFluor-R-hc, an excitation wavelength of 790 nm and a 605–680 nm emission filter were used to isolate the SHG signal. The autofluorescence image was acquired with an excitation wavelength of 750 nm and a 495–540 nm emission filter.

The images were obtained from the epidermis and dermis and stored as a z-stack image sequence (step size of 1 μm in the z-axis). The image size was 512 × 512 pixels, and the scanning speed was 2 μm/pixel. The merging of the color channels was performed using FV1000 Viewer 3.1 software (Olympus). The three-dimensional image was performed using Imaris (Imaris ver. 8.4.2, Bitplane AG, Switzerland). To examine the collagen staining intensity, we calculated the SHG signal intensity, which has been considered a good predictor of collagen structure (Dunn et al., 2000; Theer et al., 2011). Thus, we calculated the signal intensity of SHG in the dermis at different time points after iFluor-R-hc administration and determined the collagen thickness based on the z-stack depth of the SHG signal.

2.3.2 In vitro

Whole skin tissue (1 × 0.5 cm^2) was removed at 0, 1, 2, 3, 4, and 5 h after the imaging of the mice. The tissues were examined as frozen sections (10 μm). The lateral plane of the skin was exposed under the objective lens of a two-photon excited fluorescence microscopy system. The above-mentioned scanning process was repeated to observe the iFluor-R-hc transdermal absorption. The laser condition settings were consistent with those used for the above-mentioned *in vivo* SHG-TPEF skin imaging.

2.4 HE, Immunofluorescence and Immunochemistry Staining

All frozen sections were subjected to hematoxylin and eosin (HE) staining for the histological study. Differential interference contrast images of the sections were captured using an Olympus BX51 microscope (PlanApo 20x/NA: 0.45).

The localization of collagen III and collagen I proteins was assessed by immunofluorescence. The skin tissue was taken from the left side of the thoracic spine after treated with R-hc for 24 h. The frozen sections were obtained in an ultralow temperature freezer after 30 min at room temperature. The slides were washed in 0.02 M PBS 3 times and then blocked with QuickBlock™ Blocking Buffer for Immunological Staining (Beyotime, China) for 1 h. A 1:500 dilution of anti-collagen III mouse monoclonal antibody and anti-collagen I rabbit polyclonal antibody (ab6310, ab34710; Abcam, United States) was added and incubated overnight at 4°C. After washing with PBS, the sections were incubated for 1 h at room temperature in the dark with a secondary antibody (Dylight 488-goat anti-mouse and Dylight 594-goat anti-rabbit; EARTHox, China). After immunostaining, the specimens were examined with a wide-field fluorescence microscope (BX51, Olympus, Tokyo, Japan) fitted with a digital camera (DP71; Olympus). The relative intensity of the staining was analyzed by Image Pro Plus 6.0 software (Media Cybernetics, Inc., United States).

The localization of R-hc was assessed by immunochemisty staining. The back of the rat was taken after treated with R-hc for 5 h. The protocol to follow was as follows: Endogenous peroxidase in the skin sections was blocked by hydrogen peroxide followed by a trypsin solution. After the protein block was used to eliminate background absorption, the samples were incubated with R-hc antibody (Biogot technology, co, Ltd., China), followed by treatment with Rabbit streptavidin-biotin assay system (SP9001, Beijing Zhongshan Golden Bridge Biotechnology Co., Ltd., China). DAB staining solution was added to the sections. Hematoxylin was used for the nuclear counterstain. The slides were observed by Olympus microscope BX51.

2.5 SDS-PAGE and Western Blotting

The amount of total protein in the receptor solution was separated by sodium dodecyl sulfate-polyacrylamide gel electrophoresis (SDS-PAGE). The samples were stained with Coomassie Brilliant Blue R-250 stain (P0017F, Beyotime Biotechnology, China), and then scanned with ChemiDoc™ Touch Imaging System (Bio-Rad Laboratories, Inc., United States).

Protein samples were quantified using the Beyotime Protein Assay Kit (P0013, Nanjing, China). SDS/PAGE was used to separate molecules of different molecular weights. The proteins were transferred to PVDF membranes (Millipore, PVH00010) and then incubated with the R-hc antibody. Then an HRP-conjugated secondary antibody was added and the sample was incubated with an enhanced chemiluminescent reagent. GAPDH was used as an internal control, and scanning densitometry was applied to obtain protein signals.

2.6 The Franz-Type Diffusion

Mouse skin was mounted in the receptor compartment of a Franz-type diffusion cell (TP-6, HT, Jintao Instrument Technology Co., Ltd., Tianjin, China). Ten milligrams of iFluor-R-hc dissolved in normal saline or normal saline alone was added to the tight interface facing the mouse skin. The donor cap was covered with tin foil. A 0.9% sodium chloride buffer solution (pH 7.4) was used as the receptor solution. The receptor solution was stirred by a magnetic stirrer rotating at 300 rpm at 37°C. The samples were examined at 1, 2, 3, 4, and 6 h. The amount of total protein in the receptor solution was measured by a BCA protein assay kit (Beyotime, China), and the fluorescence intensity was measured with a fluorescence microplate reader (Synergy H1Hybrid Multi-Mode Reader, BioTek Instruments, Inc., United States) at Ex/Em = 640/670 nm.

2.7 Statistical Analysis

The results were statistically analyzed by one-way ANOVA and differences between groups were identified using Tukey's post hoc test using GraphPad Prism v.6.0 (GraphPad software, Inc., La Jolla, Calif.). The difference was considered statistically significant

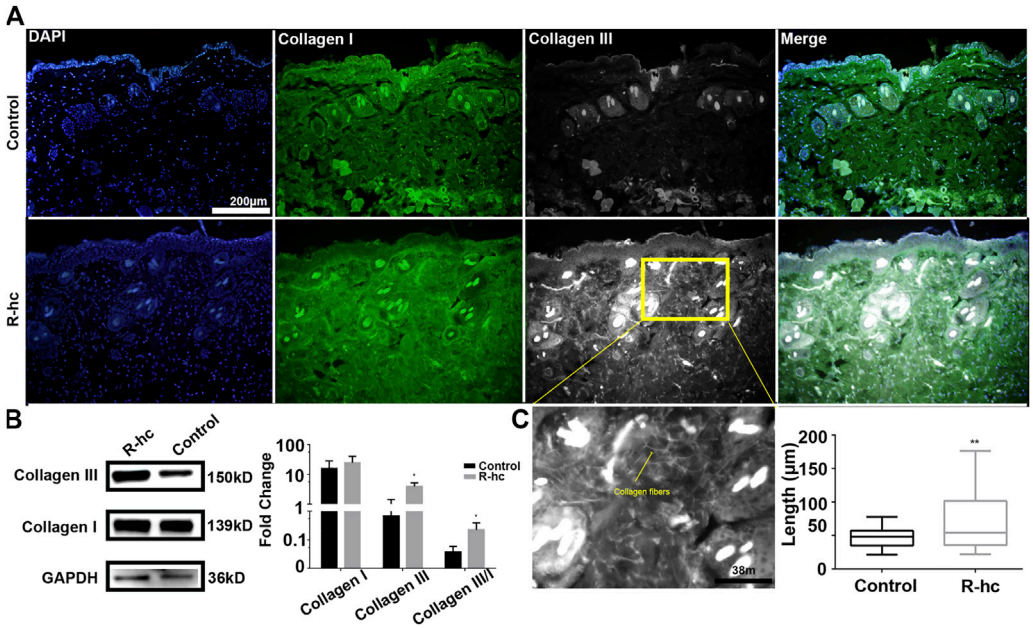

FIGURE 1 | R-hc could be transdermally absorbed by the skin and increase the collagen content of the dermis. **(A)**. IF imaging of type I collagen (green), type III collagen (white), and DAPI (blue); scale bar: 200 μm. **(B)**. Western blotting and quantitative results of collagen type I and III ($n = 3$). Data are presented as means ± SD. $^{*}p < 0.05$. **(C)**. Magnification image of the R-hc and quantitative results of collagen fibers, length, $n = 10$; scale bar: 38 μm. Data are presented as means ± SD. $^{*}p < 0.05$, $^{**}p < 0.01$ *vs*. Control.

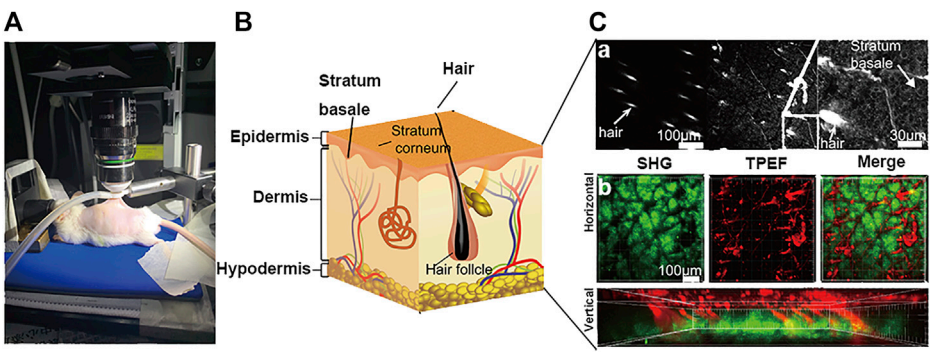

FIGURE 2 | Schematic illustration of skin imaging. **(A)** *In vivo* SHG-TPEF skin imaging platform. **(B)**. Schematic diagram of the skin structure. **(C)**. Scanning images of different layers of the skin, including epidermis skin (a), dermis skin in 2D (horizontal plane) and 3D images (vertical plane) (b); scale bar: 100 μm.

at $p < 0.05$. Post-hoc analysis was performed with $p < 0.05$ as the threshold for statistical significance.

3 RESULTS

3.1 R-hc Supplements Collagen in the Dermis by Transdermal Absorption

24 h after R-hc administration, we observed an increase in the fluorescence intensity of collagen types I and III in the dermis relative to that observed in the control group (**Figure 1A**). Type III collagen was significantly increased by Western blotting (**Figure 1B**). At the same time, we calculated the ratio of type III and type I collagen (**Figure 1B**), and compared with the control group, the increase rate of type III collagen was more notable. We also observed that type III collagen was interwoven in the reticular structures in the superficial dermis (**Figure 1C**). Compared with the control group, the long fiber content of type III collagen increased significantly in the R-hc-treated group (**Figure 1D**). These findings suggest that R-hc could be transdermally absorbed and supplement type III collagen in the dermis.

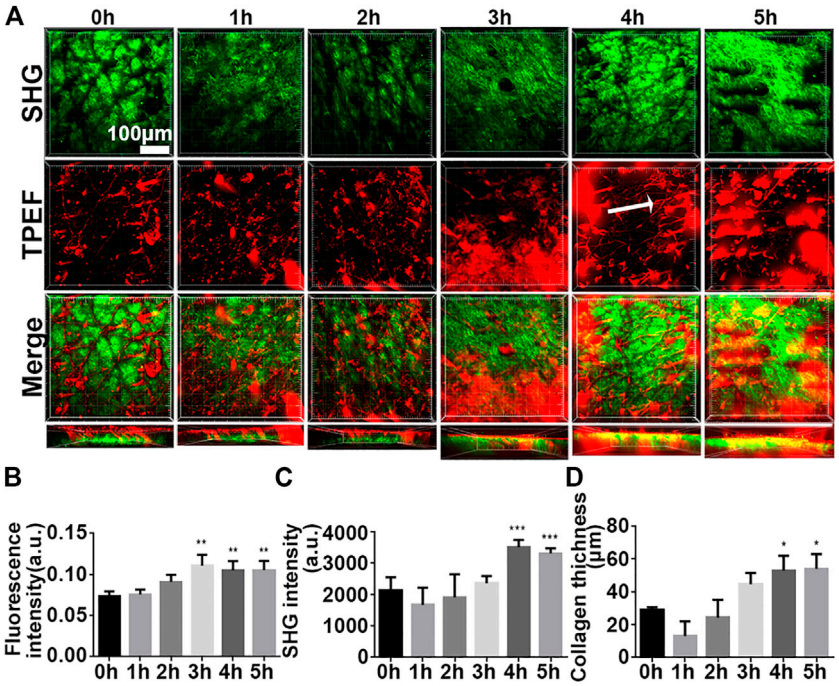

FIGURE 3 | High-resolution images illustrated the process of iFluor-R-hc absorption by *in vivo* SHG-TPEF imaging. **(A)**. SHG image and TPEF image of iFluor-R-hc. White arrow represents reticular structure; scale bar: 100 μm. **(B)**. Statistical analysis of iFluor 750 nm intensity ($n = 5$). **(C)**. Statistical analysis of SHG intensity ($n = 5$). **(D)**. Statistical analysis of collagen layer thickness (n = 5). Data are presented as means ± SD. $^{*}p < 0.05$, $^{**}p < 0.01$, $^{***}p < 0.001$ *vs*. 0 h.

3.2 Schematic Diagram of SHG-TPEF Skin Imaging

We characterized the structure of the distribution of skin and iFluor-R-hc from the epidermis to the dermis. Specifically, in the epidermis, we used TPEF imaging at an excitation wavelength of 750 nm to observe the stratum spinosum and the stratum basale (**Figure 2A**). Then, in the dermis, we separately used SHG and TPEF imaging at excitation wavelengths of 950 and 790 nm, respectively, to visualize the dynamic process of iFluor-R-hc absorption (**Figure 2B**). Here, we used two-dimensional (2D) images and three-dimensional (3D) images to illustrate the scanning results. In the 2D images, we scanned the histological structures of the skin by utilizing the SHG signal (λ = 950 nm) and iFluor-R-hc by utilizing the TPEF signal (λ = 790 nm) (**Figure 2B**). Furthermore, as shown in **Figure 2B**, we revealed intrinsic collagen, and exogenous iFluor-R-hc was mutually linked to reticular structures in the dermis.

3.3 Tracking the Transdermal Absorption of iFluor-R-hc Using SHG-TPEF Imaging *in vivo*

In this paper, the infrared fluorescent probe is used to label the to be detected, which can avoid autofluorescence of the skin, reducing background noise (Cross et al., 2007). We first analyzed mouse skin at the time point 0 h and showed a small amount of noise in the epidermis and autofluorescence of the dermis and TPE in the hair shaft (**Figure 3A**), which was considered to represent the baseline. Over time, we observed that the TPEF signal gradually increased (**Figure 3A**), suggesting that iFluor-R-hc permeated the cuticle and reached the dermis. Then, it formed reticular structures at the dermis-epidermal junction after 4 h (**Figure 3A**). Statistically, the iFluor intensity significantly increased after 3 h administration of iFluor-R-hc (**Figure 3B**), indicating that R-hc was gradually absorbed after 3 h of application. Furthermore, both the intensity of the SHG and the thickness of the collagen increased significantly after 4 and 5 h of iFluor-R-hc compared to baseline (**Figures 3C,D**, 4 h time point: $t = 5.43$, $p < 0.001$; 5 h time point: $t = 4.68$, $p < 0.001$), which indicated increased collagen density in the dermis.

To test whether our findings were the result of false positive signals in the *in vivo* SHG-TPEF imaging, we performed vertical plane observations. The results revealed that both iFluor and SHG intensity of iFluor-R-hc were significantly increased after 4 and 5 h iFluor-R-hc administration (**Figures 4**), which was consistent with the findings obtained from the *in vivo* SHG-TPEF imaging. The hair follicles were localized by histological examination; in the magnified TPEF image, the yellow arrows indicated the autofluorescence of the hair, while the white arrows in the circled follicles indicated the iFluor-R-hc absorbed by the hair follicles and sebaceous glands. This result indicated that R-HC may be absorbed into the dermis through the hair follicles and sebaceous glands.

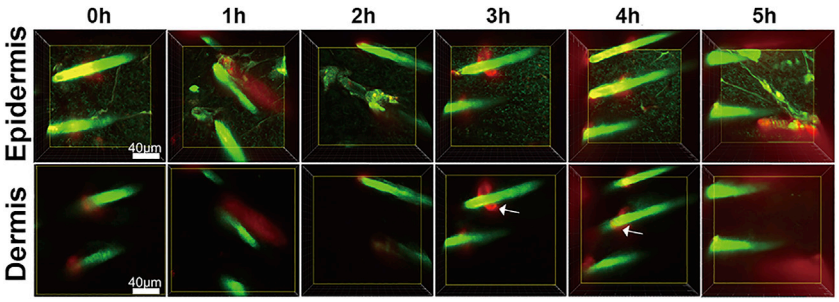

FIGURE 4 | SHG-TPEF imaging of iFluor-R-hc around hair follicles. Green: hair shaft and stratum spinosum/stratum basale (λ = 750 nm); Red: iFluor-R-hc (λ = 790 nm); White arrow: iFluor-R-hc in hair follicle.

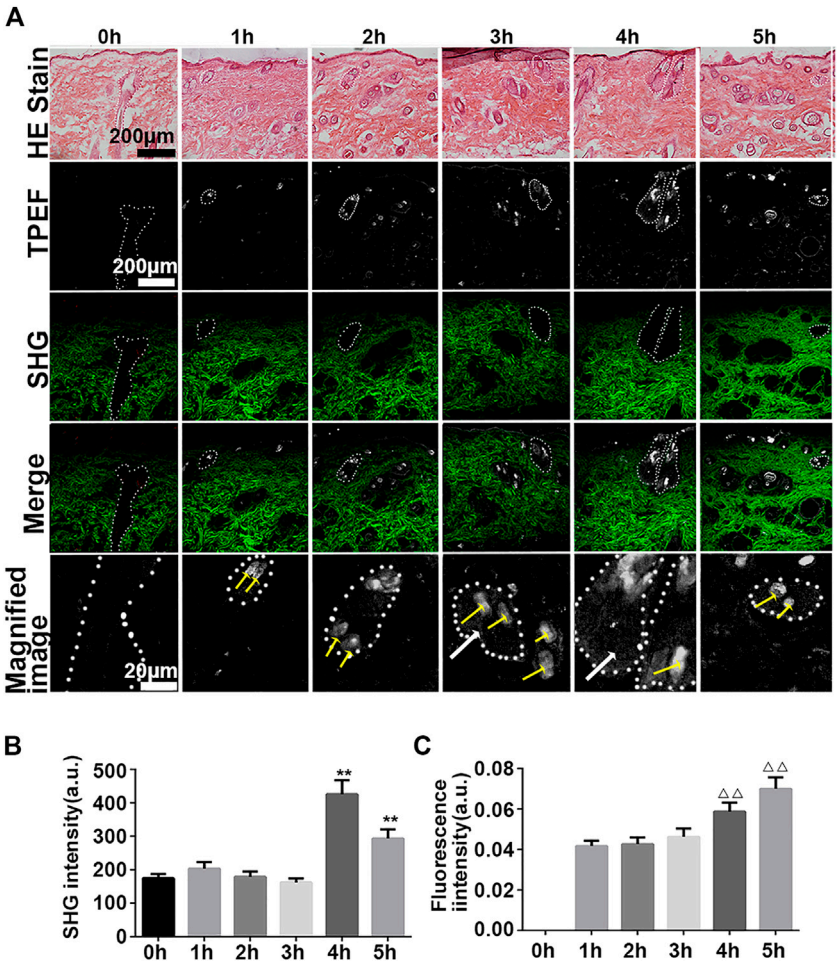

FIGURE 5 | Vertical plane view of the skin after administration of iFluor-R-hc. **(A)**. HE imaging, SHG-TPEF imaging, and Magnified image of TPEF after iFluor-R-hc administration; scale bar: 100 μm, 20 μm (yellow arrows indicated hairs, white arrows indicated iFluor-R-hc, and white circles indicated hair follicles and sebaceous glands) **(B)** Statistical analysis of SHG intensity (n = 5). **(C)**. Statistical analysis of fluorescence intensity (n = 5). Data are presented as means ± SD. $^{**}p < 0.01$ *vs*. 0h, $^{\triangle\triangle}p < 0.01$ *vs*. 1 h.

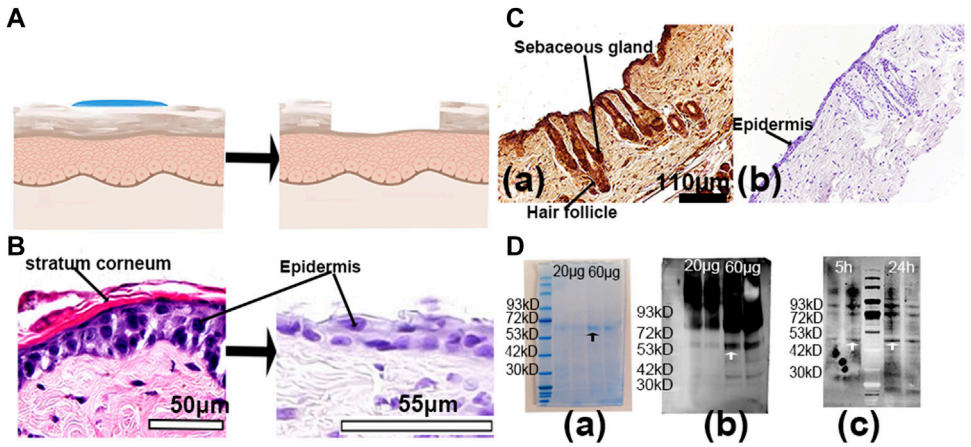

FIGURE 6 | *In vitro* experiments of R-hc absorbed into the dermis through hair follicles. **(A)**. Schematic diagram of the tape stripping method. **(B)**. Skin tissue before and after tape stripping observed by histological staining; scale bar: 50 and 55 μm. **(C)**. Immunochemical staining of skin tissue with R-hc after 5 h of transdermal absorption, scale bar: 110um (a. with R-hc antibody, b. without R-hc antibody). **(D)**. Western blot of skin tissue (a. SDS-PAGE of R-hc, b. Western blot of R-hc, c. Western blot of administration of R-hc after 5 and 24 h.

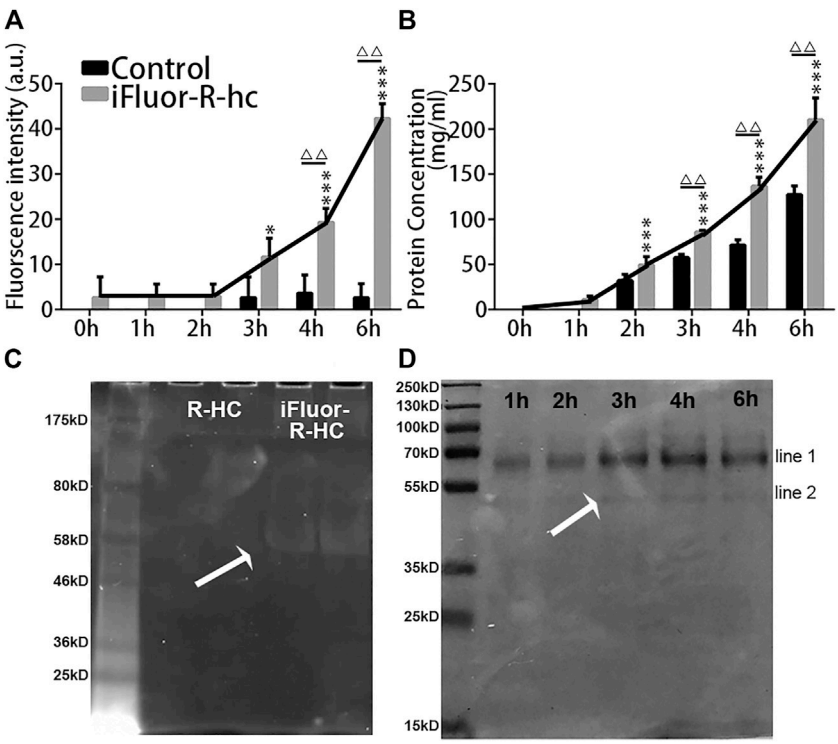

FIGURE 7 | *In vitro* examination of iFluor-R-hc Transdermal absorption. **(A)**. iFluor-R-hc fluorescence intensity detected by fluorescence microplate reader ($n = 5$). **(B)**. Determination of iFluor-R-hc concentration by BCA method ($n = 5$). **(C)**. R-hc was labeled with iFluor™ 750 SE, Ex = 700 nm. The molecular weight of R-hc is between 46 kd and 58 kd. **(D)**. Coomassie blue staining of iFluor-R-hc. The protein band shown in line1 was between 55 kd and 70 kd, which may be a water-soluble protein degraded in skin tissue during transdermal absorption. The protein band shown in line2 was close to the molecular weight at around 55 kd. Data are presented as means ± SD.$^{*}p < 0.05$, $^{***}p < 0.01$ *vs.* 1h; $^{\triangle\triangle}p < 0.01$ *vs.* Control.

3.4 Transdermal Absorption of R-HC Through Hair Follicles

We found that iFluor-R-hc could permeate and disperse around hair follicles after 3 h of administration (**Figures 5B,C**). This result is consistent with the results of our previous *in vitro* experiments that the protein first accumulated in the hair follicle and then absorbed into the dermis (Sun et al., 2017), which suggests that R-hc may be absorbed into the dermis through the hair follicle.

To verify whether R-hc was absorbed into the dermis through the hair follicle, we removed the stratum corneum and part of the dermis by tape stripping (**Figure 6A**). After 20 times, the stratum corneum was removed and the epidermis was incomplete (**Figure 6B**). Immunohistochemical staining indicated that R-hc was localized in the epidermis, hair follicles, and sebaceous glands (**Figures 6A–C**), while no positive expression of R-hc was observed in images without the R-hc antibody (**Figures 6B,C**). The molecular weight of R-hc was around 55kD (**Figures 6A–D**). The results of the Western blot showed that the R-hc antibody could specifically immunoreact with R-hc (**Figures 6B–D**). The skin tissue was taken out of R-hc after 5 and 24 h of transdermal absorption, the stratum corneum and part of the epidermis were removed, and the R-hc in the skin was detected by Western blotting. A clear band near 55kd was observed.

3.5 In vitro Tracking of the Transdermal Absorption of iFluor-R-hc

Next, we used traditional *in vitro* Franz diffusion cells to test whether *in vivo* SHG-TPEF imaging could sensitively and accurately track transdermal absorption, which could confirm the generality of our novel approach. Specifically, compared with the baseline (0 h), we first observed the significantly increased fluorescence intensity of iFluor-R-hc after 3 h of administration (**Figure 7A**). Moreover, the iFluor-R-hc group showed significantly increased protein concentrations after 2 h of administration of iFluor-R-hc (**Figure 7B**). Compared with the control group, the iFluor-R-hc group showed both significantly increased iFluor intensity and iFluor-R-hc concentration after 4 h of administration of iFluor-R-hc (**Figures 7A,B**). These findings were consistent with the observations of *in vivo* SHG-TPEF imaging, which suggests that our novel approach could sensitively and dynamically visualize collagen transdermal absorption *in vivo*. In addition, in the collected liquid, we found no change in the molecular weight of R-hc after iFluor™ 750 SE labeling, and there was a clear target protein band about 55 kD after 4 h of administration in the iFluor-R-hc group (**Figures 7C,D**).

4 DISCUSSION

In this study, we used a novel noninvasive approach to dynamically capture the process of collagen transdermal absorption *in vivo* by combining SHG with TPEF. Both two-photon fluorescence imaging and second harmonic imaging are second-order nonlinear processes. In addition to the needs of different filter addition, TPEF and SHG are almost identical in the optical detection system, the obtained information for both complement and confirm each other, so it has received much attention in recent years. In this paper, the infrared fluorescent probe was used to label the collagen, which can avoid the autofluorescence of the skin and reducing background noise (Li et al., 2019). Over time, we observed that collagen permeated through the hair follicle, reached the dermis, and formed reticular structures in the dermis after 4 h of administration of exogenous iFluor-R-hc, which was also confirmed by *in vitro* examinations. To the best of our knowledge, this approach is the first to be used for the *in vivo* visualization of the transdermal absorption of biochemically administered collagen, and these findings provide a technological method for the clinical assessment of transdermal drugs in the future.

A previous study showed that compounds with a molecular weight greater than 50 kDa penetrate the dermis was difficulty because of blockage by the stratum corneum (Ogiso et al., 2000). Therefore, various transdermal drug delivery systems have been developed (Chang et al., 2019; Lin et al., 2021), but whether macromolecules can penetrate the skin is still not clear. In our study, we used *in vivo* SHG-TPEF skin imaging to track the process of transdermal absorption of exogenous collagen, which is approximately 55 kDa in size. The iFluor fluorescence signal was first detected in the hair follicle 3 h after coating R-hc on the skin, which confirms that macromolecules could be absorbed by the skin. The above experimental results were confirmed by immunohistochemical staining and western blotting. Moreover, this combined technology has many advantages, such as noninvasiveness, the absence of conventional dyes, and good penetration of biological tissues (Kiyomatsu et al., 2015). Thus, it allows the long-term observation of dynamic changes at the same skin site, which can be extended to the development of an *in vivo* real-time assessment method for cosmetics and biomedical administration.

The results of the examination of R-hc transdermal absorption provided a quantitative approach for the *in vivo* assessment of the transdermal absorption of protein drugs through the combined measurement of collagen density and absorption. Specifically, we first demonstrated that a typical application of R-hc increased type III collagen and collagen fiber growth, which suggests that R-hc could increase skin elasticity. Second, we used TPEF combined with SHG imaging to study the manner and depth of R-hc absorption *in vivo*. Since the stratum corneum acts as a physical barrier to skin on the surface of the epidermis (Elias and Choi, 2005), it has an impact on the penetration efficiency of R-hc. However, the results of the *in vivo* transdermal absorption model showed that the fluorescence intensity of type III collagen was significantly increased after 24 h of R-hc administration, which suggesed that iFluor-R-hc could still effectively permeate the epidermal skin. Potts and colleagues found that an increased molecular weight increased lipophilicity and

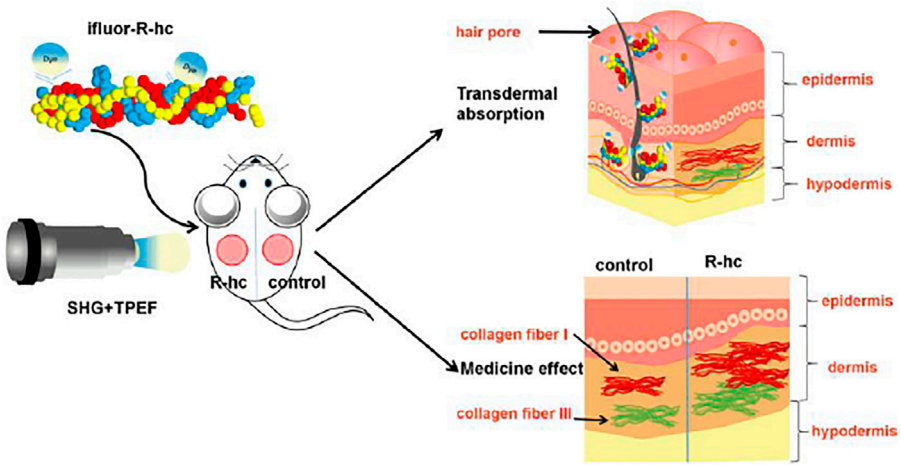

FIGURE 8 | Schematic representation of the transdermal absorption of R-hc. The R-hc was fluorescently labeled and smeared on the back of the mice. The dynamic process of R-hc transdermal absorption was observed by SHG-TPEF imaging *in vivo*. R-hc can be absorbed into the dermis through hair follicles and sebaceous glands, and increases the content of type III collagen in the dermis.

permeability, which suggests that the penetration of drugs into the skin is tightly associated with the molecular characteristics of the drug (Potts and Guy, 1992). Lin and colleagues also considered that the effect of lipophilicity is a more dominant factor than the molecular weight in the passive diffusion permeability (Lin et al., 1996). We observed the fluorescence signal of iFluor in the hair follicle after 3 h of R-hc application by *in vivo* SHG-TPEF imaging, and the dermis was interlaced into a reticular network after 4 h. Therefore, we assume that the osmotic effect of R-hc in the dermis could be attributed to higher permeability.

HE staining is a classic method to detect the pathophysiological changes of skin, but it can only observe the skin's thickness changes in various layers, inflammatory cell invasion, and other indicators, but the absorption and distribution route and collagen content, which are directly related to wound healing or drug efficacy assessment, can not be observed. In our study, we examined SHG intensity to measure the content of collagen in the dermal skin. SHG imaging provides increased resolution and contrast when examining collagen than typical histological staining analysis (Tanaka et al., 2013). Moreover, it is also a feasible and fast method that could be applied to the imaging of thicker tissue without fixing, slicing and staining (Sun et al., 2003). SHG intensity could accurately reflect the *in vivo* changes in collagen. Specifically, in the examination of HE staining of R-hc, we found that the amount of R-hc gradually increased after iFluor-R-hc administration and reached a peak at the 4 h time point. Similar results were also observed in the analysis of Franz-type diffusion, which was consistent with the findings of *in vivo* SHG-TPEF skin imaging. These findings indicate that SHG imaging could provide reliable measurements for the real-time evaluation of collagen absorption.

Collagen is one of the core constituents that maintains the elasticity of the skin; thus, reducing collagen in the skin would result in wrinkled and flabby skin (Lee et al., 2001). In our study, we observed that R-hc gradually permeated the dermal skin and formed the reticular structure after 3 h of administration. This suggests that exogenous collagen could not only supplement skin collagen to meet the needs of anti-aging cosmetics but also form granulation tissue together with intrinsic collagen to fill wounds in tissue.

SHG-TPEF imaging allows us to observe the manner of transdermal absorption and aggregation sites of R-hc *in vivo*, but some limitations still exist for this technology. For example, individual differences in cortical thickness might cause variation in the scanning results, which could have an impact on examining SHG intensity. Alternatively, the autofluorescence of tissue might affect the detection of exogenous collagen labeled with fluorescent probes. A previous study showed that the excitation wavelength of tissue autofluorescence was between 720 and 880 nm, and the overall signal sensitivity (420–490 nm) was affected by the convolution of the spectral transmittance and the detector efficiency (Breunig et al., 2010). Therefore, the use of infrared dyes could be useful for the fluorescent labeling of exogenous proteins, and bandpass filters could be adjusted to reduce the effects of autofluorescence on skin scanning.

In this study, we used *in vivo* SHG-TPEF skin imaging to track the dynamic process of the transdermal absorption of exogenous collagen in a mouse model. We observed that exogenous collagen gradually permeated the dermal skin via hair follicles and sebaceous glands and formed a reticular structure (**Figure 8**), which was also confirmed by traditional *in vitro* skin imaging. This is the first study to use a noninvasive approach to visualize the absorption of exogenous collagen in skin *in vivo*, which could extend our understanding of the process of skin absorption and provide the feasible technology for the clinical assessment of drugs for external use.

DATA AVAILABILITY STATEMENT

The original contributions presented in the study are included in the article/Supplementary Material; further inquiries can be directed to the corresponding author.

ETHICS STATEMENT

The animal study was reviewed and approved by Research Ethics Committee of the China Academy of Chinese Medical Sciences (ERCCACMS21-2106-12).

AUTHOR CONTRIBUTIONS

Conception and design:YW. Drafting the manuscript: YS. Operating the two-photon fluorescence microscope: YS. Model investigation: LL. 3D image analysis: SM; Franz-type diffusion: GH; Immunofluorescence&HE staining: WY.

FUNDING

This work was supported by the Fundamental Research Funds of the Central Public Welfare Research Institutes (JBGS2021007, ZZ13-YQ-077, XTCX2021002), National Natural Science Foundation of Beijing, China (7192141).

ACKNOWLEDGMENTS

The authors would like to thank TianJin Irheaya Biological Technology Co., Ltd. for providing R-hc.

REFERENCES

Bouwstra, J., Honeywell-Nguyen, P. L., Gooris, G. S., and Ponec, M. (2003). Structure of the Skin Barrier and its Modulation by Vesicular Formulations. *Prog. lipid Res.* 42, 1–36. doi:10.1016/s0163-7827(02)00028-0

Breunig, H. G., Studier, H., and König, K. (2010). Multiphoton Excitation Characteristics of Cellular Fluorophores of Human Skin *In Vivo*. *Opt. Express* 18, 7857–7871. doi:10.1364/oe.18.007857

Campagnola, P. J., and Loew, L. M. (2003). Second-harmonic Imaging Microscopy for Visualizing Biomolecular Arrays in Cells, Tissues and Organisms. *Nat. Biotechnol.* 21, 1356–1360. doi:10.1038/nbt894

Chai, H.-J., Li, J.-H., Huang, H.-N., Li, T.-L., Chan, Y.-L., Shiau, C.-Y., et al. (2010). Effects of Sizes and Conformations of Fish-Scale Collagen Peptides on Facial Skin Qualities and Transdermal Penetration Efficiency. *J. BioMed Res.* 2010, 757301, doi:10.1155/2010/757301

Chang, L., Wang, Y.-C., Ershad, F., Yang, R., Yu, C., and Fan, Y. (2019). Wearable Devices for Single-Cell Sensing and Transfection. *Trends Biotechnol.* 37, 1175–1188. doi:10.1016/j.tibtech.2019.04.001

Cross, S. E., Innes, B., Roberts, M. S., Tsuzuki, T., Robertson, T. A., and Mccormick, P. (2007). Human Skin Penetration of Sunscreen Nanoparticles: In-Vitro Assessment of a Novel Micronized Zinc Oxide Formulation. *Skin. Pharmacol. Physiol.* 20, 148–154. doi:10.1159/000098701

Denk, W., Strickler, J. H., and Webb, W. W. (1990). Two-photon Laser Scanning Fluorescence Microscopy. *Science* 248, 73–76. doi:10.1126/science.2321027

Di Lullo, G. A., Sweeney, S. M., Körkkö, J., Ala-Kokko, L., and San Antonio, J. D. (2002). Mapping the Ligand-Binding Sites and Disease-Associated Mutations on the Most Abundant Protein in the Human, Type I Collagen. *J. Biol. Chem.* 277, 4223–4231. doi:10.1074/jbc.m110709200

Dunn, A. K., Wallace, V. P., Coleno, M., Berns, M. W., and Tromberg, B. J. (2000). Influence of Optical Properties on Two-Photon Fluorescence Imaging in Turbid Samples. *Appl. Opt.* 39, 1194–1201. doi:10.1364/ao.39.001194

Elias, P. M., and Choi, E. H. (2005). Interactions Among Stratum Corneum Defensive Functions. *Exp. Dermatol* 14, 719–726. doi:10.1111/j.1600-0625.2005.00363.x

Fediuk, D. J., Wang, T., Chen, Y., Parkinson, F. E., Namaka, M. P., Simons, K. J., et al. (2012). Metabolic Disposition of the Insect Repellent DEET and the Sunscreen Oxybenzone Following Intravenous and Skin Administration in Rats. *Int. J. Toxicol.* 31, 467–476. doi:10.1177/1091581812459893

Gamer, A. O., Leibold, E., and van Ravenzwaay, B. (2006). The *In Vitro* Absorption of Microfine Zinc Oxide and Titanium Dioxide through Porcine Skin. *Toxicol. vitro* 20, 301–307. doi:10.1016/j.tiv.2005.08.008

Kiyomatsu, H., Oshima, Y., Saitou, T., Miyazaki, T., Hikita, A., Miura, H., et al. (2015). Quantitative SHG Imaging in Osteoarthritis Model Mice, Implying a Diagnostic Application. *Biomed. Opt. Express* 6, 405–420. doi:10.1364/boe.6.000405

König, K., Ehlers, A., Riemann, I., Schenkl, S., Bückle, R., and Kaatz, M. (2007). Clinical Two-Photon Microendoscopy. *Microsc. Res. Tech.* 70, 398–402. doi:10.1002/jemt.20445

Lee, C. H., Singla, A., and Lee, Y. (2001). Biomedical Applications of Collagen. *Int. J. Pharm.* 221, 1–22. doi:10.1016/s0378-5173(01)00691-3

Li, C., Wang, J., Sun, Y., and Wang, Y. (2019). Comparison of the Stability and Biological Activity of Two Fluorescent Labeling Pilose Antler Extracts. *Acta laser Biol. sin.* 28, 46. doi:10.3969/j.issn.1007-7145.2019.01.007

Lin, L., Wang, Y., Cai, M., Jiang, X., Hu, Y., Dong, Z., et al. (2021). Multimicrochannel Microneedle Microporation Platform for Enhanced Intracellular Drug Delivery. *Adv. Funct. Mater.*, 2109187. online ahead of print. doi:10.1002/adfm.202109187

Lin, R.-Y., Hsu, C.-W., and Chen, W.-Y. (1996). A Method to Predict the Transdermal Permeability of Amino Acids and Dipeptides through Porcine Skin. *J. Control. Release* 38, 229–234. doi:10.1016/0168-3659(95)00124-7

Ma, S., Sun, Y., Yang, W., Sun, G., Li, S., Jiang, Y., et al. (2018). Repair Effect and Mechanism of Recombinant Human Collagen on Laser Induced Damage of Mice Skin. *Acta laser Biol. sin.* 27, 399. doi:10.3969/j.issn.1007-7146.2018.05.003

Menon, G. K. (2015).Skin Basics; Structure and Function, *Lipids Skin Health*. 25, 9–23. doi:10.1007/978-3-319-09943-9_2

Miller, D. R., Jarrett, J. W., Hassan, A. M., and Dunn, A. K. (2017). Deep Tissue Imaging with Multiphoton Fluorescence Microscopy. *Curr. Opin. Biomed. Eng.* 4, 32–39. doi:10.1016/j.cobme.2017.09.004

Ngan, C. L., Basri, M., Tripathy, M., Abedi Karjiban, R., and Abdul-Malek, E. (2015). Skin Intervention of Fullerene-Integrated Nanoemulsion in Structural and Collagen Regeneration against Skin Aging. *Eur. J. Pharm. Sci.* 70, 22–28. doi:10.1016/j.ejps.2015.01.006

Ogiso, T., Iwaki, M., Tanino, T., Yono, A., and Ito, A. (2000). *In Vitro* skin Penetration and Degradation of Peptides and Their Analysis Using a Kinetic Model. *Biol. Pharm. Bull.* 23, 1346–1351. doi:10.1248/bpb.23.1346

Pittet, J.-C., Freis, O., Vazquez-Duchêne, M.-D., Périé, G., and Pauly, G. (2014). Evaluation of Elastin/Collagen Content in Human Dermis *In-Vivo* by Multiphoton Tomography-Variation with Depth and Correlation with Aging. *Cosmetics* 1, 211–221. doi:10.3390/cosmetics1030211

Potts, R. O., and Guy, R. H. (1992). Predicting Skin Permeability. *Pharm. Res.* 09, 663–669. doi:10.1023/a:1015810312465

Schulz, J., Hohenberg, H., Pflücker, F., Gärtner, E., Will, T., Pfeiffer, S., et al. (2002). Distribution of Sunscreens on Skin. *Adv. drug Deliv. Rev.* 54, S157–S163. doi:10.1016/s0169-409x(02)00120-5

Sun, C.-K., Chen, C.-C., Chu, S.-W., Tsai, T.-H., Chen, Y.-C., and Lin, B.-L. (2003). Multiharmonic-generation Biopsy of Skin. *Opt. Lett.* 28, 2488–2490. doi:10.1364/ol.28.002488

Sun, W., Inayathullah, M., Manoukian, M. A. C., Malkovskiy, A. V., Manickam, S., Marinkovich, M. P., et al. (2015). Transdermal Delivery of Functional Collagen via Polyvinylpyrrolidone Microneedles. *Ann. Biomed. Eng.* 43, 2978–2990. doi:10.1007/s10439-015-1353-0

Sun, Y., Zhao, J., Li, C., Liu, J., Li, S., Chen, H., et al. (2017). Application of Second Harmonic Generation and Two-Photon Fluorescence in the Distribution Tracing of Fluorescence Labelled Collagen. *Acta laser Biol. sin.* 26, 24. doi:10.3969/j.issn.1007-7146.2017.01.004

Tanaka, R., Fukushima, S., Sasaki, K., Tanaka, Y., Murota, H., Matsumoto, T., et al. (2013). *In Vivo* visualization of Dermal Collagen Fiber in Skin Burn by Collagen-Sensitive Second-Harmonic-Generation Microscopy. *J. Biomed. Opt.* 18, 61231. doi:10.1117/1.JBO.18.6.061231

Theer, P., Denk, W., Sheves, M., Lewis, A., and Detwiler, P. B. (2011). Second-harmonic Generation Imaging of Membrane Potential with Retinal Analogues. *Biophysical J.* 100, 232–242. doi:10.1016/j.bpj.2010.11.021

Thrasivoulou, C., Virich, G., Krenacs, T., Korom, I., and Becker, D. L. (2011). Optical Delineation of Human Malignant Melanoma Using Second Harmonic Imaging of Collagen. *Biomed. Opt. Express* 2, 1282–1295. doi:10.1364/boe.2.001282

Toki, F., Honkura, N., Shirakata, Y., Imamura, T., Higashiyama, S., and Nanba, D. (2013). Second Harmonic Generation Reveals Collagen Fibril Remodeling in Fibroblast-Populated Collagen Gels. *Cell. Struct. Funct.* 38, 227–236. doi:10.1247/csf.13017

Conflict of Interest: The authors declare that the research was conducted in the absence of any commercial or financial relationships that could be construed as a potential conflict of interest.

The handling editor HH declared a past collaboration with the authors YW, YS.

Publisher's Note: All claims expressed in this article are solely those of the authors and do not necessarily represent those of their affiliated organizations, or those of the publisher, the editors and the reviewers. Any product that may be evaluated in this article, or claim that may be made by its manufacturer, is not guaranteed or endorsed by the publisher.

Copyright © 2022 Sun, Li, Ma, He, Yang and Wang. This is an open-access article distributed under the terms of the Creative Commons Attribution License (CC BY). The use, distribution or reproduction in other forums is permitted, provided the original author(s) and the copyright owner(s) are credited and that the original publication in this journal is cited, in accordance with accepted academic practice. No use, distribution or reproduction is permitted which does not comply with these terms.

frontiers | Frontiers in Chemistry

REVIEW
published: 20 June 2022
doi: 10.3389/fchem.2022.916553

The Development and Progression of Micro-Nano Optics

Yong Wang[1,2,3*†], *Jie Yang*[1,2,3†], *Zhiwei Wang*[1,2,3†], *Xiaofei Kong*[1,2,3†], *Xiangyu Sun*[4], *Jingjing Tian*[1,2], *Xiushuo Zhang*[1,2,3], *Xiaolong Zhao*[1,2], *Yanping Liu*[1,2,3], *Hongsheng Li*[1,2,3], *Yuqing Su*[1,2,3], *Xiaorui Hao*[1,2] *and Jing Xu*[1,2]

[1]*Laboratory of Optical Detection and Imaging, School of Science, Qingdao University of Technology, Qingdao, China,* [2]*Quantum Physics Laboratory, School of Science, Qingdao University of Technology, Qingdao, China,* [3]*Qingdao Technology Innovation Center of Remote Sensing and Precise Measurement, Qingdao, China,* [4]*Torch High Technology Industry Development Center, Ministry of Science and Technology, Beijing, China*

Micro-Nano optics is one of the most active frontiers in the current development of optics. It combines the cutting-edge achievements of photonics and nanotechnology, which can realize many brand-new functions on the basis of local electromagnetic interactions and become an indispensable key science and technology of the 21st century. Micro-Nano optics is also an important development direction of the new optoelectronics industry at present. It plays an irreplaceable role in optical communication, optical interconnection, optical storage, sensing imaging, sensing measurement, display, solid-state lighting, biomedicine, security, green energy, and other fields. In this paper, we will summarize the research status of micro-nano optics, and analyze it from four aspects: micro-nano luminescent materials and devices, micro-nano optical waveguide materials and devices, micro-nano photoelectric detection materials and devices, and micro-nano optical structures and devices. Finally, the future development of micro-nano optics will be prospected.

Keywords: micro-nano optics, luminescent materials, optical waveguides, photoelectric detection, structures, review

OPEN ACCESS

Edited by:
Honghui He,
Tsinghua University, China

Reviewed by:
Limin Jin,
Harbin Institute of Technology, Shenzhen, China
Menglong Zhang,
South China Normal University, China

****Correspondence:***
Yong Wang
wang-yong13@tsinghua.org.cn

[†]These authors have contributed equally to this work and share first authorship

Specialty section:
This article was submitted to Nanoscience, a section of the journal Frontiers in Chemistry

Received: *09 April 2022*
Accepted: *24 May 2022*
Published: *20 June 2022*

Citation:
Wang Y, Yang J, Wang Z, Kong X, Sun X, Tian J, Zhang X, Zhao X, Liu Y, Li H, Su Y, Hao X and Xu J (2022) The Development and Progression of Micro-Nano Optics. Front. Chem. 10:916553. doi: 10.3389/fchem.2022.916553

INTRODUCTION

Micro-nano optics, also known as micro-optics, is an emerging research direction resulting from the organic combination of optics and nanotechnology, which carries the scientific extension of traditional optics at sub-wavelength scales and promotes the development of substantive innovations in nanotechnology with the help of optical platforms. It is an optical theory for the study of micro-nano optical structures and the study of micro-optical components, systems, and devices on the micro-nano scale. Micro-nano optics is not only one of the important development directions of the optoelectronics industry, but also a frontier research direction in the field of optics, which has a wide range of application prospects in many fields such as optical communication, optical storage, laser nuclear fusion engineering, laser weapons, solar energy utilization, semiconductor laser, and optical anti-counterfeiting technology, etc. It is the frontier of current optical research and an important branch. In 1852, Faraday first reported on the experimentally detected optical properties of metal nanoparticles (Faraday, 1857). As early as 1880, before the concept of "integrated optics" was proposed, Wheeler first mentioned a similar concept of optical waveguides in a patent, calling it an "optical pipe" (Wheeler, 1881). The structure is similar to the well-known optical fiber structure, which can realize point-to-point light wave transmission. The study of dielectric optical waveguides began in 1910 when Hondros and Debye (1910) proposed the theory of dielectric waveguides based on the study of

cylindrical dielectric optical waveguides. In 1936, Carson et al. (1936) theoretically refined the dielectric guided-mode transmission, and in the same year, Southworth (1936) started a related experimental study. In 1964, Osterberg and Smith (1964) completed the first experiments on beam coupling in planar waveguides using prisms and thin slides to make a theoretical analysis of optical field coupling. In the same year, Schlosser (1964) conducted a theoretical study on rectangular waveguides. In 1965, Anderson (1965) developed a thin-film planar optical waveguide that could be used for transmission in the infrared band. Based on the above-mentioned extensive research work, the requirements for optical waveguides have gradually increased, and are not only limited to the field of low-loss and long-range transmission of optical fiber, but also multi-functional integrated optical waveguide devices have attracted extensive attention from scientists since the beginning of the 1969. In 1960, the world's first ruby solid-state laser was introduced (Maiman, 2018). Compared to electrical signals such as radio and microwave, this monochromatic coherent light generation provides a stable high frequency signal carrier and solves the problem of information transmission bandwidth. In order to avoid the influence of atmospheric or climatic conditions when the light signal propagates in the air medium, people began to try to use various optical materials as the transmission medium of light to reduce transmission loss. In 1966, the scientist Gao set up the idea that light signals could be transmitted in pure glass-based optical fibers with low loss, ushering in a new era of optical fiber communication (Kao and Hockham, 1966). In 1969, Miller of Bell Labs first introduced the concept of "integrated optics," which is similar to "integrated circuits" (Hunsperger, 2009). By reducing the size of traditional optical components, optical devices with different functions, such as light sources, optical waveguides and optical detectors, are integrated into photonic chips to achieve a variety of functions such as information processing and information transmission. Compared with integrated circuits, the transmission speed and frequency of light waves are high, and the linear transmission of light waves of different wavelengths in optical media does not interfere with each other, so integrated optical systems based on optical "carrier" signals have greater information capacity, wider transmission bandwidth, faster transmission speed, lower transmission loss, and more stable transmission performance (Tamir, 1975; Ginés, 2003; Kokubun and Iga, 2005; Okamoto, 2006; Bohren and Huffman, 2008; Olson et al., 2014). Compared to conventional optical systems, integrated optical systems are not only smaller and lighter, but also more efficient and stable, which is why they are favored by scientists.

In 1987, Yabnolovitch (1987a) and John (1987) extended the concept of electron energy bands to light waves when discussing how to suppress spontaneous radiation from atoms and photonic localization, introducing the concept of photonic crystals. In 1998, Ebbesen et al. (1998) discovered the existence of super-intense light transmission peaks in thick metallic films punched with periodic subwavelength nanopores, a discovery that sparked a wave of research into surface equipartition excitations in metallic periodic structures. Since 1987, the research of micro-nano optical structure has been developing vigorously in various fields.

CURRENT STATUS OF RESEARCH IN MICRO-NANO OPTICS

This paper will summarize the development of micro-nano optics in four directions: micro-nano emitting materials and devices, micro-nano optical waveguide materials and devices, micro-nano optical detection materials and devices, and micro-nano optical structures and devices.

Micro-Nano Luminescent Materials and Devices

Luminescence is the direct conversion of energy absorbed in some way within an object into non-equilibrium radiation without going through a thermal phase. Luminous materials generally consist of a matrix (the material's subject compound) and an activator (a small amount of dopant ions that act as a luminous centre). For rare-earth ions co-doped luminescent materials, a sensitizer is usually incorporated into the matrix to absorb the excitation radiation and transfer the energy to the activator. Micro-nano luminescent materials mainly use micro-nano particles as a luminescent matrix, including pure and doped micro-nano semiconductor luminescent materials, rare earth ions and excessive metal ions doped nano-oxides, sulfides, composite oxides, and a variety of micro-nano inorganic salt luminescent materials. For activator materials, there are usually two types of ions: a class of transition metal ions, such as Mn^{4+}/Mn^{2+} (Huang et al., 2016a), Ti^{4+} (Page et al., 2010), Cr^{3+} (Chen et al., 2014), Cd^{2+} (Mall and Kumar, 2010), etc.; the second group is rare earth metal ions Eu^{3+}/Eu^{2+}, and Tb^{3+}, Pr^{3+}, etc. Fluoride is an ideal matrix material for various fluorescent materials, and the doping of rare earth ions etc. into fluoride matrix can lead to luminescent materials with good optical properties (Kasturi et al., 2016; Keevend et al., 2017). Patra et al. (Ghosh et al., 2010) prepared Na (Y1.5Na0.5) F_6:Ce:Tb nanomaterials by microemulsion method, and studied their morphological, structure and luminescent properties (see **Figure 1**). They found that Na (Y1.5Na0.5) F_6:Ce:Tb nanorods or nanowires could be prepared by using cationic surfactant cetyltrimethylammonium bromide to mediate reverse micelle technology. The morphology of nanorods or nanowires can be changed by coating TbF_3 on the surface. The morphology of Na (Y1.5Na0.5) F6:Ce:Tb nanomaterials is shown in **Figure 2**. The obtained Na (Y1.5Na0.5) F6:Ce:Tb nanomaterials can obtain green light emission with the main emission peak at 544 nm under the excitation of ultraviolet light with an excitation wavelength of 256 nm, which is mainly attributed to the $^5D_4 \rightarrow {}^7F_5$ magnetic dipole transition of Tb^{3+} ions. The sample obtained by the co-doping method of Ce^{3+} and Tb^{3+} causes the energy of Ce^{3+} to transfer to Tb^{3+} due to the energy level matching of Ce^{3+} and Tb^{3+}, thereby emitting green light, and the light intensity of the surface coated with TbF_3 is much stronger than that of the uncoated sample. Gulina et al. (2017) used a gas-liquid interface technique to prepare LaF_3:Eu^{3+} nanomaterials. The orange-red light with the main emission peaks at 590 and 615 nm was obtained under UV excitation at 394 nm (see **Figure 3**). The luminescence intensity of the sample

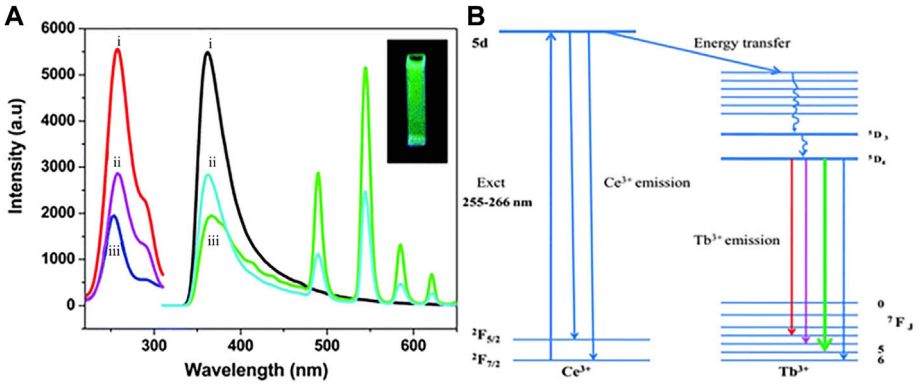

FIGURE 1 | (A) Excitation and emission spectra. 1) 1 mol% Ce^{3+} doped, 2) 1 mol% Ce^{3+} and 0.5 mol% Tb^{3+} doped, 3) 1 mol% Ce^{3+} doped and 0.5 mol% Tb^{3+} coated Na(Y1.5Na0.5)F6 nanocrystals. **(B)** Energy level diagram for electronic transitions and energy transfer process of Na(Y1.5Na0.5)F6:Ce:Tb (Ghosh et al., 2010).

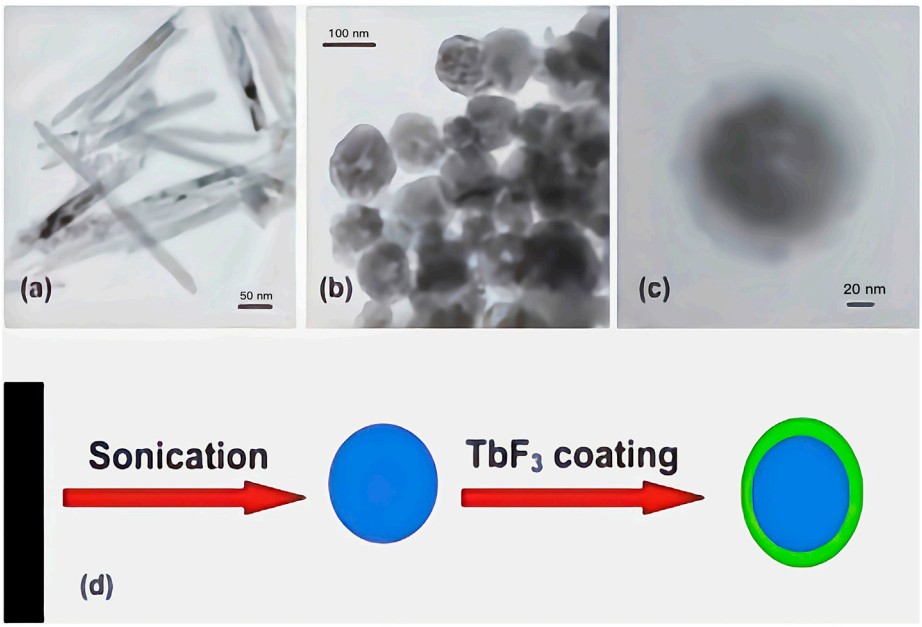

FIGURE 2 | Morphology of Na(Y1.5Na0.5)F6:Ce. **(A)** Low magnification TEM images of 75 C dried Na(Y1.5Na0.5)F6:Ce (1) doped nanorods, **(B)** 75 C dried sonicated Na(Y1.5Na0.5)F6:Ce (1) doped nanoparticles, **(C)** core-shell NaYF4:Ce (1)/Tb nanoparticles. **(D)** Schematic diagram of morphology change (Ghosh et al., 2010).

increases and then decreases with increasing Eu^{3+} doping concentration, which is a typical behavior of rare earth doped samples: concentration quenching phenomenon. β-$NaLaF_4$:Eu^{3+}, Gd^{3+} red light nanomaterials were synthesized by the solvothermal method by Xie et al. (Nie et al., 2017) (see **Figure 4**). The addition of Gd^{3+} improves the red light emission intensity, which they believe is due to the Gd^{3+} entry of β-$NaLaF_4$:Eu^{3+} nanocrystals in the lattice gap, which affects the symmetry of the local crystal field. Zeolites have gradually attracted attention because of their microporous nature and their properties in terms of adsorption and ion exchange. In 1948, Barrer et al. (1948) synthesized artificial zeolites for the first time, providing a solid basis for the later diversification of molecular screening species and their widespread use in science and industry (Barrer and Hinds, 1950; Weitkamp, 2000). The phenomenon that the luminescence intensity of the luminescent material decreases as the temperature increases is called temperature quenching. Xiangfu Wang et al. (2015a). found that the luminescence of Er^{3+}, Tm^{3+}, Ho^{3+}, Nd^{3+}, Dy^{3+}, and Eu^{3+} doped phosphors is very weak at temperatures great than 773 K, due to intense thermal quenching. It is difficult to measure temperature change in the range of more than 500°C through the conventional optical temperature sensing technology. New phosphors with low thermal quenching rates and high luminescence efficiency should be synthesized cheaply. Instead of rare-earth ions, new luminescence centers with high

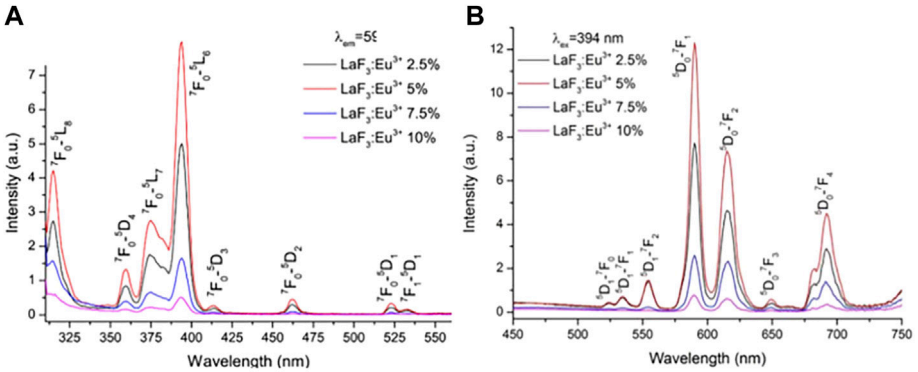

FIGURE 3 | Excitation spectra **(A)** and emission spectra **(B)** of LaF3:Eu^{3+} with different Eu^{3+}-doping concentration (Gulina et al., 2017).

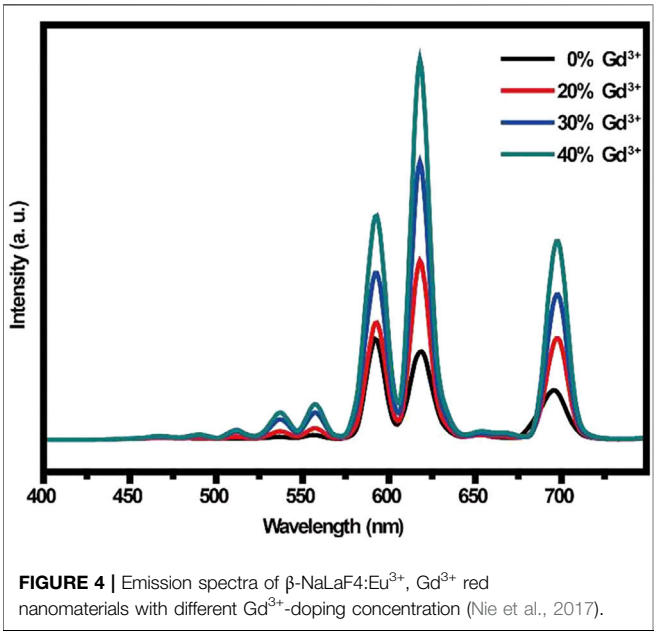

FIGURE 4 | Emission spectra of β-NaLaF4:Eu^{3+}, Gd^{3+} red nanomaterials with different Gd^{3+}-doping concentration (Nie et al., 2017).

luminescence intensity at high temperature (>773 K) may be excellent candidate activated ions in novel fluorescence sensors. Yu et al. (Wu et al., 2009) of Shanghai Normal University exchanged Eu^{3+} with 13X zeolite using a water bath ion exchange method to prepare red phosphor. The emission wavelength of this red phosphor is 612 nm, and the optimal excitation wavelength is 397 nm. These works lay a foundation for the subsequent application of UV-excited LEDs devices.

Micro-nano emitting materials are mainly used in the design and preparation of various micro-nano emitting devices such as micro-nano emitting diodes or micro-nano lasers, which can achieve light-emitting properties not available in macroscopic bulk materials, and also have a wide range of applications in bio-imaging and food safety detection. Light Emitting Diodes (LEDs) are electroluminescent semiconductor devices that are sealed by encapsulants to convert electrical energy into light energy, and they are the focus of research in the fields of materials science, physics and chemistry, and will become the next generation of Solid State Lighting (SSL) devices (Li et al., 2015). Jone's group (Jang et al., 2008) prepared TOP/TOPO/HAD-coated CdSe red-emitting quantum dots by coating CdSe quantum dots with trioctylphosphine (TOP), trioctylphosphine oxide (TOPO) and cetylamine (HDA). They also prepared $Sr3SiO_3$:Ce^{3+}, Li+ green light-emitting materials, and then mixed the two light-emitting materials to assemble white LED devices which were excited by blue chips, with a color rendering index higher than 85. They also assembled red LED devices excited by blue light chips based on TOP/TOPO/HAD-coated CdSe red quantum dots. The spectrograms and luminescence photographs are shown in **Figure 5**. In 2015, Zeng Haibo's team (Song et al., 2015) reported for the first time the preparation of yellow, green and blue LEDs based on all-inorganic Chalcogenide quantum dots ($CsPbX_3$) (X = Cl, Br, and I), proving that all-inorganic chalcogenide quantum dots as a new optoelectronic material has great application prospects in the field of optoelectronics, and the quantum efficiency (EQE) of all-inorganic chalcogenide nano crystal light-emitting diodes rapidly developed from less than 1%–21.3%. In 2019, the team of Gao Feng and his co-workers (Xu et al., 2019) reported the results of molecular passivation for the preparation of high-efficiency chalcogenide light-emitting diodes, which were optimized to achieve an EQE of up to 21.6% for red chalcogenide diodes, the highest external quantum efficiency reported for red chalcogenide light-emitting diodes. In 2020, Edward H. Sargent's team and his co-workers (Dong et al., 2020) used a surface repair treatment of chalcogenide quantum dots to achieve a bipolar shell consisting of an inner anionic shell and an outer cationic and polar solvent molecular shell. The outer shell is electrostatically adsorbed onto the negatively charged inner shell. This method produces high domain limiting chalcogenide quantum dot solids with improved carrier mobility and reduced defect density, resulting in photoluminescence quantum yields in excess of 90% for blue quantum dot films. By exploiting the improved mobility, highly efficient blue and green light diodes based on $CsPbBr_3$ quantum dots were fabricated. After optimisation, the blue chalcogenide light-emitting diodes have an EQE of up to 12.3%. This is the highest exo-quantum efficiency reported for blue chalcogenide light-emitting diodes. On 23 February 2021, Yang Xuyong's team at Shanghai University and his collaborating team Andrey L. Rogach's team at

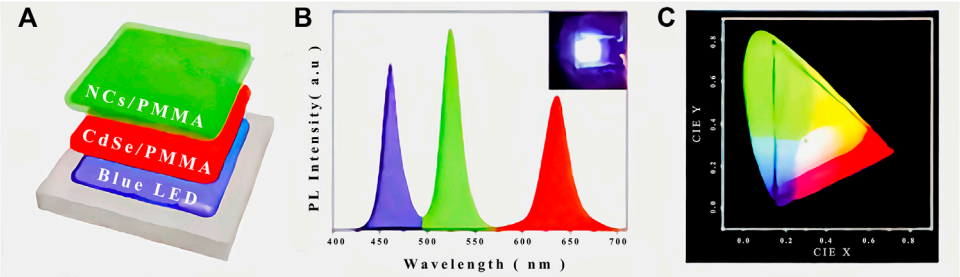

FIGURE 5 | (A) Schematic illustration of the configuration, **(B)** PL spectra (Inset shows a photograph of the device) and **(C)** CIE color coordinate of the CsPbBr3/SiO_2 based WLED (Li et al., 2015).

City University of Hong Kong (Kong et al., 2021) published in Nature Communications their research on the use of methane sulfonate to smooth energy transfer pathways in quasi-2D chalcogenide films for the preparation of highly efficient LEDs. Reconstruction of quasi-2D chalcogenide structures using strong hydrogen bonding between methane sulfonate (MeS) and BA to increase the energy acceptor to donor ratio and enhance energy transfer in chalcogenide films, resulting in improved luminescence efficiency. The MeS additive also reduces the defect density in RP chalcogenides due to the elimination of unliganded Pb^{2+} by the electron-rich Lewis base MeS and the weakening of the adsorbate blocking effect. As a result, green LEDs prepared using these quasi-2D RP chalcogenide films achieved a current efficiency of 63 cd/A and 20.5% EQE, which is the best performance to date for quasi-2D chalcogenide-based devices and the highest exo-quantum efficiency reported for green chalcogenide light-emitting diodes. In 2021, the team of Ziming Chen and Xuanli Ye (Chen et al., 2021) reported the results of realizing white light-emitting diodes of chalcogenide with an external quantum efficiency of more than 12% through near-field optical coupling. The blue chalcogenide LEDs were optically coupled to red chalcogenide nanocrystals in the near field by means of rationally designed multilayer translucent electrodes to construct high-performance white chalcogenide LEDs with high light extraction efficiency. The red chalcogenide nano-crystal layer allows the extraction of waveguide modes and surface equipartition exciton polarization modes captured in the blue chalcogenide diode and their conversion to red light emission, thereby increasing the light extraction efficiency by 50%. At the same time, the complementary emission spectra of blue photons and down-converted red photons contribute to the formation of white light-emitting diodes. Finally, the device has an external quantum efficiency of over 12% and a brightness of over 2000 cd/m^2, both of which are the highest in the field of chalcogenide white light emitting diodes.

According to statistics from the US Department of Energy in 2012, LEDs are the most important green and energy-saving light sources in the 21st century. It will save at least 20% of the total US national electricity consumption each year form 2010 to 2030 (George et al., 2013), which shows that LEDs have great potential for future development. For bioimaging, Tan et al. (2018) from Harbin Institute of Technology prepared $NaYF_4$:Yb^{3+}, Nb^{3+}@CaF_2 core-shell structured luminescent nanoparticles and investigated their luminescence mechanism, and the resulting samples were applied to live imaging in the second infrared window (e.g., **Figure 6**) with better performance than commercial AgS_2 nanoparticles. They injected the resulting core-shell structured luminescent material into six rats at the same time and used the laser-pulsed material to emit light and observe intracellular conditions. For food safety detection, Li et al. (Hu et al., 2015) synthesised a highly efficient strong blue light metal organic framework luminescent material (LMOF-241) and used it to detect aflatoxin in food, showing that it was responsive to aflatoxin B1 at one part per billion (**Figure 7**).

Micro-Nano Optical Waveguide Materials and Devices

Micro-Nano optical waveguides are the most fundamental units for studying the mechanism of micro-nano photonics and designing micro-nano photonic devices, which have become a hot research topic today and have received great attention in related fields (van Eijkelenborg et al., 2003; Noginov et al., 2009; Khatua et al., 2011; Knight et al., 2011; Sivis et al., 2013). Common micro-nano optical waveguides mainly include micro-nano optical fibers (Miura et al., 1997; Brambilla et al., 2009; Brambilla, 2010), silicon-based planar waveguides (Jalali et al., 1998; Lee et al., 2001; Celler and Cristoloveanu, 2003; Xia et al., 2007), semiconductor nanowires (Sirbuly et al., 2005), and metal surface equipartition excitonic waveguides (Ozbay, 2006). Micro-Nano fibers have sub-wavelength sized fibers diameter and their optical properties present a great difference from conventional fibers. This sub-wavelength scale micro-nano fiber is not only easy to prepare, but also has a series of advantages, such as extremely low optical transmission loss (Brambilla et al., 2004; Brambilla et al., 2006), large waveguide dispersion (Holmes et al., 2000; Mingo, 2003), strong optical field confinement (Polynkin et al., 2005; Villatoro and Monzón-Hernández, 2005), strong abrupt field propagation properties (Brambilla et al., 2007), and easy integration with existing systems (Liu et al., 2011), so it has a very broad application prospect and good potential in optical communication, optical sensing, optical filtering and super continuous spectrum generation.

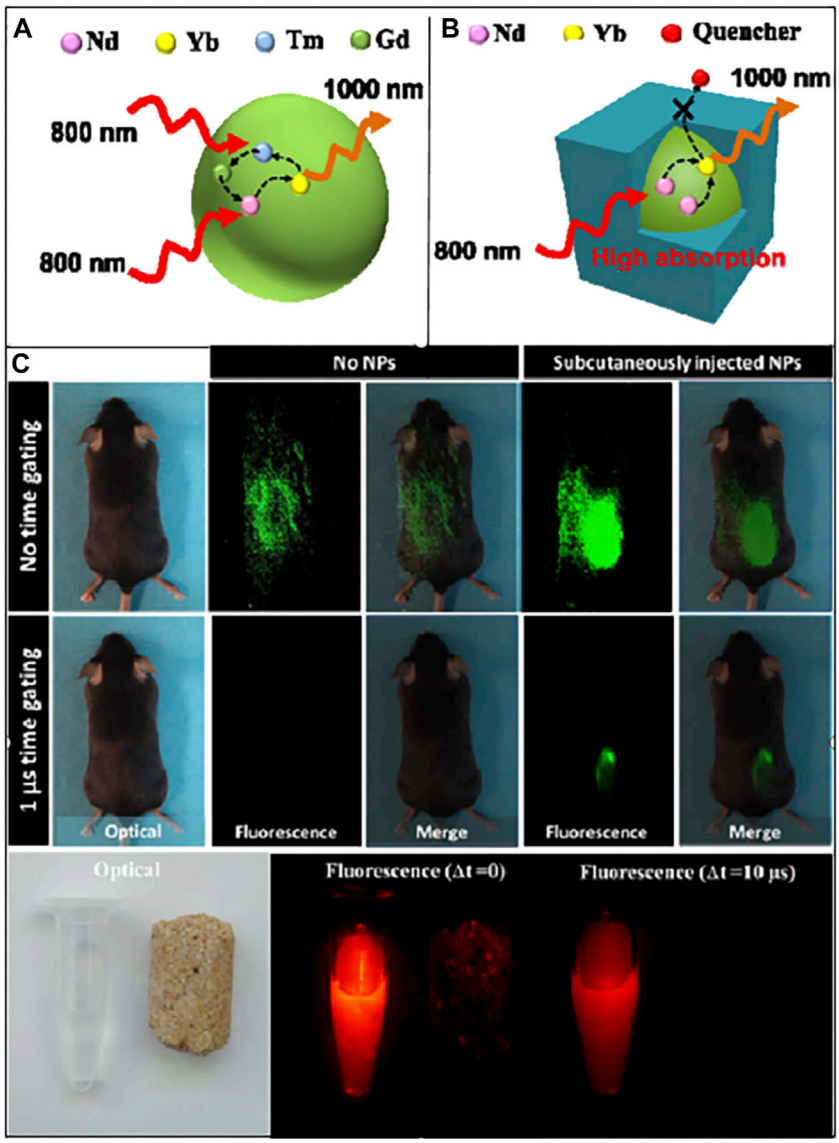

FIGURE 6 | (A) Schematic diagram of energy transfer in NaYF4:Yb^{3+}, Nb^{3+}, and Tm^{3+}NPs, **(B)** the core/shell structure of NaYF4:Yb^{3+}, Nb^{3+}@CaF_2NPs, **(C)** optical and NIR images of C57BL/6 mice and NaYF4:Yb^{3+}, Nb^{3+}@CaF_2 (George et al., 2013).

Micro-Nano fibers can be divided into solid-core fibers and hollow-core fibers according to their structure. Solid-core optical fibers are mainly glass optical fibers and crystal optical fibers. In the 1980s, British scientists such as Boys (1887), in order to analyze the mechanical properties of glass filaments, heated the ore to a molten state and drew it into 100 um filaments, which was the earliest preparation of optical fibers in the world. In 1959, American scientist N.S. Kapany prepared glass filaments with an average diameter of 2.5 nm in the laboratory, which was the first report of the use of micro-nano optical fibers for the transmission of light and images. Constrained by factors such as fiber transmission loss, this glass fiber was difficult to get practical (Kapany, 1959), and for many years after this, no substantial progress was made in the field of micro-nano fiber research. It wasn't until1966 that Dr. Gao pointed out that optical fibers could be used in optical communications when their transmission loss was reduced by 20 dB/km, and that the theoretical value of attenuation loss could be as low as a limit of 0.1 dB/km, and that it was extremely possible to pull ultra-low loss fibers for optical communications by improving manufacturing equipment and processes (Kao and Hockham, 1996). In 1970, Corning produced the first practical optical fiber with a loss of only 20 dB/km, which allowed people to see the dawn of using optical fibers for communication (Kapron et al., 1970). After the 1970s, scientists began to experiment with the use of flame or laser heating to stretch high-quality glass fibers, resulting in micro-nano waveguides with smooth surfaces and homogeneous structures (Burns et al., 1986; Love and Henry,

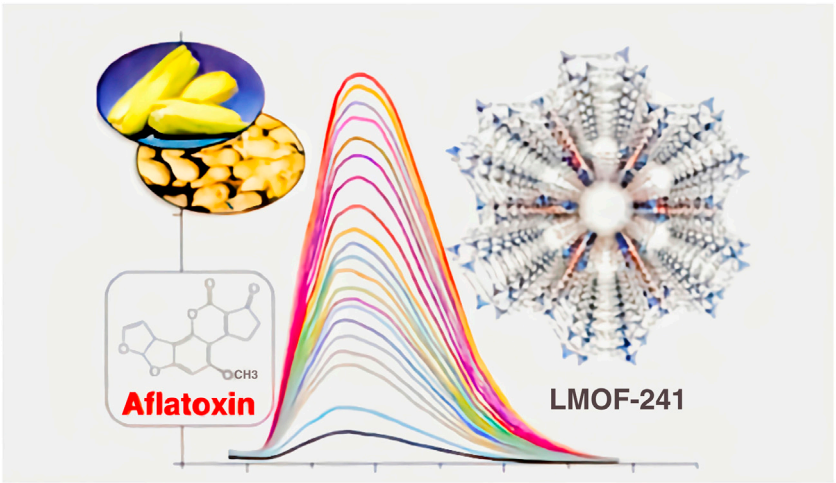

FIGURE 7 | Emission spectra of LMOF-241 with the incremental addition of aflatoxin (Tan et al., 2018).

1986; Black et al., 1988). In 2003, Professor Tong Limin of Zhejiang University proposed the famous "two-step stretching method," using sapphire rods as an aid to produce glass fibers with uniform and uniform diameters down to 50 nm, with a loss of only 0.1 dB/mm in this micro-nano fiber (Tong et al., 2003). By improving the experimental setup, Tong et al. (2005) proposed a self-modulated two-step method and succeeded in obtaining a micro-nano fiber with an even lower transmission loss of only 20 nm. In order to solve the disadvantages of the self-modulated two-step process, such as the difficulty of reproducibility, high manual dependence and difficulty in controlling the accuracy, Brambilla et al (2004) used a stepper motor to control the moving speed and used oxygen and isobutane flames to heat the cone region of the fiber to draw ultra-low loss nanowires with a diameter of 320 nm and a loss of about 0.01 dB/mm. In 2004, Leon-Saval et al. (2004) succeeded in drawing a 950 nm diameter micro-nano fiber with a loss of only 0.0014 dB/mm at a wavelength of 1,550 nm. After research, Brambilla et al. (2006) again reduced the diameter of the fiber to 60 nm, reducing the loss to 0.001 dB/mm. In 2006, Tong et al. (2005) successfully prepared glass fibers doped with rare-earth ion disks, silicates, tellurates and fluorides by focal melting, making the fabrication of micro-nano optical fibers no longer limited by raw materials and achieving a leap from passive to active micro-nano photonic devices. First proposed in the 1850s (Christopher, 1998), hollow-core fibers are a new type of waveguide structure with an air core. The main tool for fabricating hollow-core fibers is two different inner diameters of capillaries, which can be well used for making sub-wavelength diameter fibers due to their small inner diameter, which is almost the same as the inner and outer diameters of ordinary fibers. The first successful hollow-core energy transfer fibers were manufactured in the 1960s, mainly from vulcanized glass and metals, but the hollow-core fibers produced at that time had obvious defects in both structure and material selection, and had significant transmission losses that prevented their use in practice (Kubo and Hashishin, 1987; Miyagi and Karasawa, 1990). Mareatillli and Sehmeltzer were the first to develop a systematic theory and analysis of the transmission of hollow-core fibers, summarizing the factors affecting the transmission loss of light in hollow-core fibers and forming the original theory of hollow-core waveguide transmission, the famous M-S theory. In the late seventies and early eighties, according to the classical microwave waveguide structure theory system, Professor Marhic from Northwestern University in the United States conducted a study on the bending loss and mode coupling of optical fibers. Immediately afterwards, Professor Mitagi from Tohoku University in Japan further refined the M-S theory and improved the Miyagi formula with even greater precision. The concept of infrared hollow-core fibers, first introduced by Hidaka et al. (1981) in 1981, has sparked a wave of interest among scientists in the investigation of hollow-core fibers in high-power laser transmission applications. A group led by J.A. Harrington, at Rutgers University, United States, developed a glass hollow-core fiber that could reach 6 m in length (Nubling and Harrington, 1996; Nubling and Harrington, 1997). In 2002, Yushan Yan's research group at the University of California used natural spider silk as a fabrication tool and a specific process to achieve a hollow fiber structure with a hollow core diameter of only 2 nm in silicon oxide micro-nano hollow core fiber (Wang et al., 2002). In 2015, Habib et al. (2015) from the Technical University of Denmark reduced the loss at mid-infrared 2.85 μm wavelength to 0.002 dB/km through a rational design. In 2016, Habib et al. (2016) designed an elliptical structure of hollow-core anti-resonant micro structured fibers, which can have an extinction ratio greater than 1,000 in broadband 1.0–1.65 μm range, while the leakage loss of the fundamental mode is less than 15 dB/km in the same range. In 2016, Professor Fan Zhongwei's team from the Institute of Optoelectronics, the Chinese Academy of Sciences (Liu et al., 2016) theoretically demonstrated that circular double-core hollow-core antiresonant micro structured fibers have low

limiting loss and elliptical double-core hollow-core antiresonant micro structured fibers have a wide transmission band. In 2017, Habib et al. (2017) designed a low-loss hollow-core antiresonant micro structured fiber with a loss as low as 0.0015 dB/km at wavelength 1.06 μm and 0.006 dB/km when the bending radius was 5 cm, while achieving a high extinction ratio in the 1–1.1 μm wavelength range with a 1,500 extinction ratio of. In 2017, Hayes et al. (2017) from the University of Southampton achieved short-range data transmission with a bandwidth greater than 1,000 nm and a low loss of 25 dB/km at wavelengths 1,065, 1,565, and 1963 nm using a hollow-core anti-resonant micro structured fiber. In 2018, Adaum et al. (2018) from the Technical University of Denmark used argon gas-filled hollow-core anti-resonant micro structured fibers to achieve 200–4,000 nm multi-octave super continuum spectrum through mid-infrared ultrashort pulse pumping. The current hollow-core anti resonant micro structured deflection-preserving fibers are mainly designed theoretically. In 2018, Tu et al. (2018) of Hokkaido University, Japan theoretically proposed two types of As_2S_3 glass hollow-core anti resonant micro structured fibers for high-power CO_2 laser transmission with a loss of 2.6 dB/km at wavelength 10.6 μm, achieving both low loss of less than 1 dB/km and high birefringence of greater than 1×10^{-4} in the broadband range. Wei et al. (2018) designed a polarized low-loss negative curvature hollow-core fiber with a loss of 0.020 dB/m and a birefringence of 10^{-4} and an extinction ratio of 850. The team led by Professor Shuqin Lou from Beijing Jiaotong University (Yan et al., 2018) designed a single-polarization single-mode double-ring hollow-core anti-resonant micro-structure fiber, which can achieve single polarization in two wavelength bands of 1,545–1,553 nm and 1,591–1,596 nm. At the wavelength of 1,550 nm, the fundamental mode loss of the *x*-axis is only 0.04 dB/m, the extinction ratio is 17,662, and the minimum extinction ratio of the high-order mode is 393.

Compared to solid core fibers, hollow core fibers exhibit superior performance and are mainly used for energy transmission. It has a longer service life, greater transmission power, less loss at the input end, and more stable output optical field characteristics. It can be well used to transmit high-power optical radiation fields, which will bring new opportunities for future optical communication systems, medical equipment, military, sensing and even military fields.

Micro-Nano Photoelectric Detection Materials and Devices

Photodetectors are like the "eyes" of mankind and play a very important role in the development of human civilization. A photodetector is a photoelectric device that receives light signals from a target or from its own radiation and, through transformation, processing and control, obtains the required information. Its basic function is to convert the received light signal into an electrical signal and achieve some application purposes, such as photoelectric imaging, weather observation, night vision, remote sensing, etc. By the material theory limit of materials and other factors, the traditional detection materials cannot meet the current stage of photodetector device development needs. Therefore, continuously deepening and optimizing the existing material system research, expanding the application direction, while continuing to carry out research and development of new materials, looking for better performance of the detection materials, are the inevitable requirements of the development of photodetector technology. With the rapid development of nanoscience and materials science, hundreds or thousands of new nanomaterials have emerged in the past decade, such as quantum dot (Hwang et al., 2005; Krishna, 2005; Kufer et al., 2015), nanowire (Liu et al., 2010; Zhang et al., 2010; Miao et al., 2014a; Miao et al., 2014b), two-dimensional material (Li et al., 2008; Liu et al., 2012; Furchi et al., 2014; Sun and Chang, 2014; Zhang et al., 2014), nanosheets (Amini et al., 2012; Tian et al., 2017), and dye molecule materials etc. These new nanomaterials have different characteristics from conventional thin film materials, such as nanoscale geometry and large specific surface area in a certain dimension, making them exhibit novel physical and chemical properties and excellent optoelectronic performance. In recent years, two-dimensional van der Waals layered materials have become a strong contender for photo detectable materials for artificial micro-nano structures due to their novel physicochemical properties and excellent optoelectronic performance. Two-dimensional materials are a new class of materials with similar atomic arrangements, scales, and bond strengths in two dimensions, but significantly stronger than in the third dimension. When nanomaterials and device structures are comparable to Fermi wavelengths in one spatial dimension, electrons moving in restricted directions are scattered by boundaries and cannot be seen as classical particles moving in an external field, and the density of electron energy levels near the Fermi plane changes from quasi-continuous to discrete quantized energy levels. The quantum size effect in this low-dimensional material system makes the electron density of states exhibit significantly different low-dimensional characteristics from those of conventional bulk materials, and the physical behavior of carrier transport and optical leap has quantum confinement, resulting in many novel physical properties and effects that are highly promising for new electron transport devices and optoelectronic devices.

In 2010, Muller et al. (2010) prepared an MGM photodetector that responds to NIR using heterogeneous metals (titanium and palladium) fork-finger electrodes, as shown in **Figure 8A**. The heterogeneous metal configuration in the fork-finger electrode increases the junction area while breaking the mirror-image energy band bending of the original two adjacent metal/graphene contact surfaces to achieve efficient collection of optoelectronic signals. Under 1.55 μm NIR laser irradiation, the superimposed electron-hole pairs within each junction zone of the device are directionally separated by means of an applied source-drain bias Vds, contributing to the overall current, with a final photo response of 6.1 mA/W. In 2016, Guo et al. (2016) prepared a mid-infrared photo detector using forked-finger electrodes on a 12 nm thick two-dimensional layered BP, as shown in **Figure 8B**. The staggered short channel of the device is formed by the forked finger electrode and the BP accelerates the

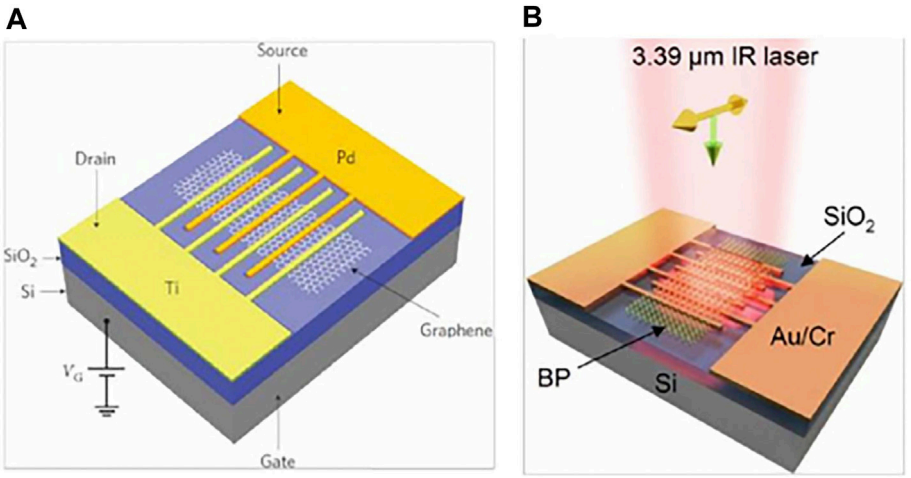

FIGURE 8 | (A) MGM photodector with heterogeneous metal interdigital electrode (Mueller et al., 2010); **(B)** BP mid infrared detector integrated interdigital electrode (Guo et al., 2016). (Neto et al., 2007)

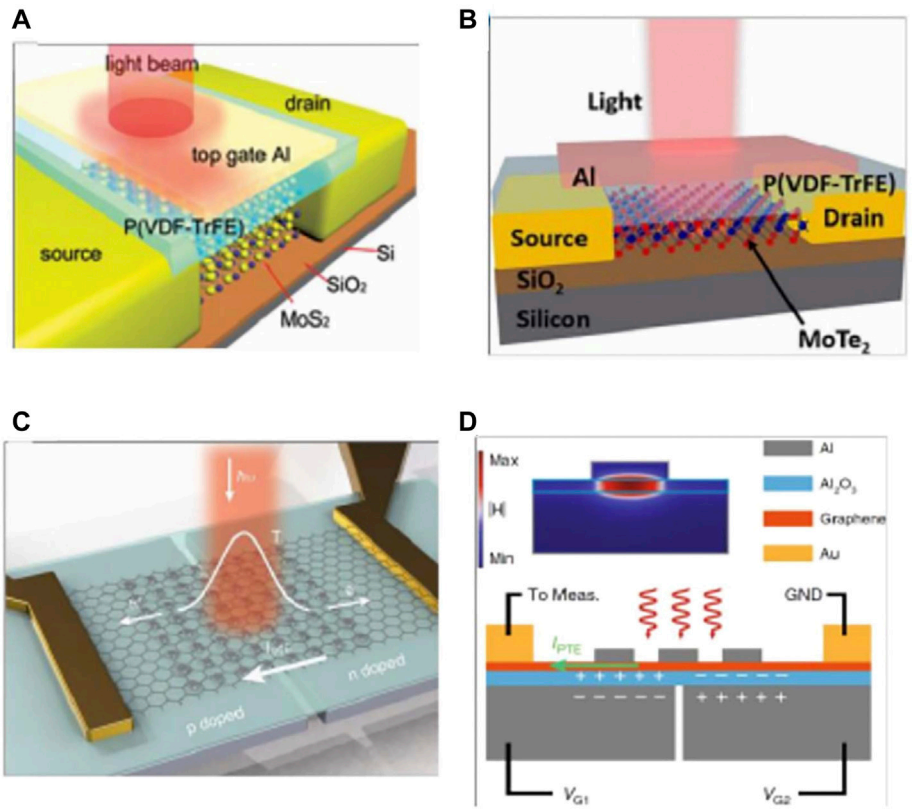

FIGURE 9 | (A) Photodetector based on ferroelectric polymer and MoS_2 (Wang et al., 2015b). **(B)** Photodetector based on ferroelectric polymer and $MoTe_2$ (Huang et al., 2016b). **(C)** Plasmonic microcavity integrated graphene photodetector (Wang et al., 2020). **(D)** Cross-sectional schematic of the graphene photodetector with split gates and a nano disk (Wang et al., 2020).

carrier's movement under the action of the applied electric field, reducing the crossing time of the photogenerated carriers and significantly enhancing the photoelectric gain. Due to the presence of a forbidden band in the BP, dark currents can be suppressed to a certain extent and weak light detection is achieved, with the final device achieving a photoresponse of 82 A/W in the mid-infrared band at 3.39 m. In 2016, Wang et al. (2015a) of Shanghai Institute of Technology combined ferroelectric polymer P (VDF-TrFE) with MoS_2 to prepare a high performance FET photodetector, and the device schematic is shown in **Figure 9A**, with the ferroelectric polymer acting as a floating gate to modulate MoS_2. Since the ferroelectric polymer can generate an ultra-high local electrostatic field on the semiconductor material through polarization, this property enabled the first extension of the light detection capability of the MoS_2 from the visible to the near-infrared (0.85–1.55 μm). In 2016, Huang et al. (2016b) prepared a $MoTe_2$ transistor detector with a ferroelectric polymer as the top gate, as shown in **Figure 9B**, where the residual polarization of the ferroelectric body can be used to deplete $MoTe_2$ without gate voltage Vg, significantly improving the device's performance. Under the effect of ferroelectric polymer polarization, $MoTe_2$-based FET devices can achieve broad spectrum detection (600–1,650 nm) from the visible to the near infrared, with an optical responsivity of 16.4 mA/W and a detection rate of 1.94×10^8 Jones at a wavelength of 1,060 nm. In 2020, Wang et al. (2020) elaborated a graphene-bound plasmonic microcavity photodetector. As shown in **Figure 9C**, the bottom metal is a double-gate structure, and graphene p-n junctions can be artificially constructed by applying different gate pressures. In this composite structure, the bottom metal Al, the middle dielectric layer Al_2O_3, the monolayer graphene and the top gold nano-disc together form a plasmonic microcavity (**Figure 9D**), which excites the graphene plasmonic resonance and heats up the carriers by modulating the local state of the optical field. The result is a composite detector with a photo thermal effect (PTE) of 51.99 A/W (incident wavelength 638 nm). With this photo-electric coupling mode, the photocurrent response is enhanced by a factor of 25 one compared to a normal device. In 2018, Wang et al. (2018) proposed an ultra-thin class II superlattice detector structure. The thickness of the detector IR absorbing material is 1/50th of the wavelength, and by introducing heavily doped InAs and a surface nano-antenna structure, the incident light at the resonant wavelength is localised in the ultra-thin absorber layer, achieving nearly 50% of the detector absorption. Feng et al. (2019) from Fudan University proposed an improved all-Si thermo electronic photodetector structure using electron-beam lithography self-alignment to integrate a specially designed super-surface as an antenna into an array of silicon nanowires on an insulator. The responsivity and detectivity of the detector at 1.15 μm and 480 nm bandwidths are as high as 94.5 mA/W and 4.38×10^{11} cm $Hz^{1/2}$/W, respectively. In 2020, Nordin et al. (2020) proposed and fabricated a class II superlattice LWIR detector structure with an integrated heavily doped semiconductor, exploiting the metal plasma properties of the heavily doped semiconductor (1×10^{19} cm^{-3} doping concentration) to form a resonant cavity to enhance the absorption of long-wave infrared radiation at resonance. The structure is designed to enhance the absorption of long-wave infrared light at resonance. Two detectors were designed with a target absorption wavelength of 8 and 10 μm, with a total absorber layer thickness of only 1.42 and 1.80 μm, respectively. 45 and 27% peak external quantum efficiencies were achieved for the two devices, respectively. In 2021, Kamboj et al. (2021) in the D. Wasserman's group also reported a fully epitaxially guided mode resonant mid-wave IR type II superlattice nBn photodetector consisting of a high refractive index absorber/waveguide layer, a low refractive index semiconductor absorber layer and a heavily doped reflector layer. The experimental results show that the absorption is strongly enhanced at the wavelengths coupled to the guided mode resonance. For TE polarised light with an absorber layer thickness of only 250 nm, the detector achieves an external quantum efficiency of more than 50% and a detection rate D^* of 4×10^{10} cm $Hz^{1/2}$ W^{-1} at a high operating temperature (T = 200 K).

Micro-Nano Optical Structures and Devices

Micro-nano optical structure technology refers to the realization of new optical functional devices by introducing micro-nano optical structures into materials. Photonic crystal is a regular three-dimensional microstructure, which refers to an ordered structure material formed by two or more dielectric materials with different dielectric constants (refractive indices) arranged in a certain periodic order in space. The scale of repeating building blocks is on the order of wavelengths of light. The so-called "crystal" is not a crystal formed by the periodic distribution of molecules, atoms or ions in the usual sense, but refers to the "periodicity" of the microstructure. The spatial period scale of photonic crystals is comparable to the wavelength of visible light, and the Bragg diffraction caused by the structural periodicity can generate a "photonic band gap," also called a photonic band gap, within a certain frequency range. Electromagnetic waves with frequencies in the photonic energy band can propagate almost losslessly in photonic crystals, but electromagnetic waves in the photonic forbidden band cannot propagate in photonic crystals. Therefore, the main optical feature of photonic crystal materials is the photonic band gap. By rationally designing the material composition, effective refractive index, lattice parameters, etc. of the photonic crystal, photonic crystals with photonic band gaps in specific wavelength bands can be artificially prepared. Compared with electrons, light can carry more information, have a wider band gap, and reduce energy loss. As a new type of optical material, the existence of photonic band gaps endows photonic crystals with very important application value, which can be used to fabricate high-performance optical devices that were impossible to fabricate before, such as straight (acute) angle optical waveguides, photonic crystal fibers, low-closure optical devices Value laser oscillators, integrated optical circuits, thermoelectric systems and biochemical sensors, etc.

Photonic crystals are periodic arrangements of different dielectrics in one, two or three dimensions, and Bragg diffraction occurs when light propagates in this periodic medium. Referring to the method of crystal research, the space

period of photonic crystal is divided into a family of parallel and equally spaced plane lattices (hkl), then the Bragg equation can be expressed as: $m\lambda = 2ndhklsin\theta$. Among them, m is the Bragg diffraction order and the diffraction wavelength, n is the average refractive index of the photonic crystal material, d_{hkl} is the coordinate (hkl) interplanar spacing, and θ is the Bragg diffraction angle. The properties of Bragg diffraction of photonic crystals are similar to the forbidden band theory of photonic crystals: Bragg diffraction is the reason for the optical forbidden band of photonic crystals. In photonic crystals, light waves in the forbidden band cannot propagate in any direction due to Bragg diffraction in all directions. If the periodicity of the dielectric arrangement at a certain position in the photonic crystal is broken, the light waves can be emitted from this defect, which is the principle for the application of photonic crystals for signal transmission.

In 1987, John (1987) and Yablonovitch (1987b) first proposed the theory of photonic crystals. According to the periodic structure characteristics of different directions in space, photonic crystals are divided into one-dimensional, two-dimensional, and three-dimensional photonic crystals. One-dimensional photonic crystals are the simplest photonic crystals. It only requires the distribution of periodic components of the same refractive index material in one direction, and the other two directions have a periodic qualitative multilayer structure, and the photonic band gap can only exist in one direction. In 2013, Yan et al. (2013) studied the influence of micro-nano fiber diameter and incident wavelength on electric field and energy distribution through theoretical calculation and simulation. The results show that as the incident wavelength decreases, the electric field mode and the time-averaged energy density in the fiber increase at the same core diameter. At the same incident wavelength, with the increase in the diameter of the fiber, the time average value of the electric field mode and the energy density also increases, and when the diameter increases to be equivalent to the incident wavelength, the maximum value is reached, and then as the diameter continues to increase, the average value of the electric field mode and energy density of the fiber is reduced again. In addition, when the diameter of the micro-nano fiber is constant, the energy confined in the core is inversely proportional to the incident wavelength. The shorter the incident wavelength, the more energy is confined in the core. When the incident wavelength is constant, the energy density in the fiber core is proportional to the fiber diameter, that is, as the fiber diameter increases, the energy confined in the fiber core gradually increases. In 2019, Xiang (2019) conducted research on III-V nanowire lasers based on photonic crystal microcavities, designed an In0.53Ga0.47As nanowire laser based on photonic crystal microcavities, and compared mode field distribution and threshold gain of microcavity nanowire lasers. The results show that in the absence of a photonic crystal microcavity, as the diameter of the nanowire decreases, the confinement ability of the light field is weakened and the threshold gain is increased, and it is impossible to excite when the radius is less than 140 nm. Due to the strong mode confinement effect of the photonic crystal microcavity, the lasing cut-off radius of the In0.53Ga0.47As nanowire laser based on the photonic crystal microcavity is reduced to 70 nm. A two-dimensional optical crystal refers to a material whose dielectric constant is distributed periodically in one plane, while its structure is uniform in the third dimension, and there are photonic band gaps in two directions. A three-dimensional photonic crystal refers to a dielectric material whose dielectric constant changes periodically in three directions. If the structural parameters are selected properly, it is possible to have an omnidirectional photonic band gap, and after entering the photonic crystal, some specific frequencies of light are prohibited from propagating in all directions. Although this structure has many advantages, it is not easy to manufacture, especially it is difficult to achieve below the order of millimeters.

Currently, three-dimensional photonic crystals are favored by researchers because of their ability to produce omnidirectional photonic forbidden bands, so their preparation and applications are also more mature, and their applications cover communication propagation, intelligent sensing and other fields. For example, Chen et al. (2010) immobilised photonic crystal arrays in a polyvinyl alcohol (PVA) hydrogel matrix by physical cross-linking to effectively modulate the diffraction wavelength in the visible region, and based on this, developed a series of sensing materials that rapidly respond to a variety of environmental stimuli such as solvents, pH, glucose, etc. The resulting color changes can be easily discerned by the naked eye (Chen et al., 2015; Chen et al., 2017a; Ruan et al., 2017); Xiao et al. (2017) developed a smart photonic crystal hydrogel material that can be used for the real-time monitoring and removal of uranium ions (UO_2^{2+}). The introduction of defects in photonic crystals can form special materials for applications in waveguides (introduction of line defects), lasers (introduction of point defects), etc. However, the precise introduction of defects in three-dimensional photonic crystals is difficult with the current state of the art, and the preparation of three-dimensional photonic crystals is more complex. As semiconductor planar technology has been developed more maturely, two-dimensional photonic crystals have the advantage of being easier to prepare and easier to introduce defects than one- and three-dimensional photonic crystals, and therefore, two-dimensional photonic crystals are gradually entering the vision of researchers. Using the characteristics of 2D photonic crystal point defects, Zhao (2015) modelled a 2D photonic crystal point defect thick plate structure, which can change the transmission spectrum of the thick plate by changing the pressure, as shown in **Figure 10**, and theoretically demonstrated the feasibility of 2D photonic crystal as a pressure sensing material. Unlike traditional photoelectric sensors, photonic crystal sensors do not require complex circuitry and large structural equipment, and are simple in structure and can discern changes in physical quantities by naked-eye observation. Zlatanovic et al. (2009) used the principle of photonic crystal microcavity structure to prepare a photonic crystal microcavity sensor for quantitative detection of trace proteins. The sensor operates with energy concentrated in the photonic crystal microcavity structure, and changes in the microcavity structure can have a significant effect on the output spectrum. When the carboxyl group of the functionalised group

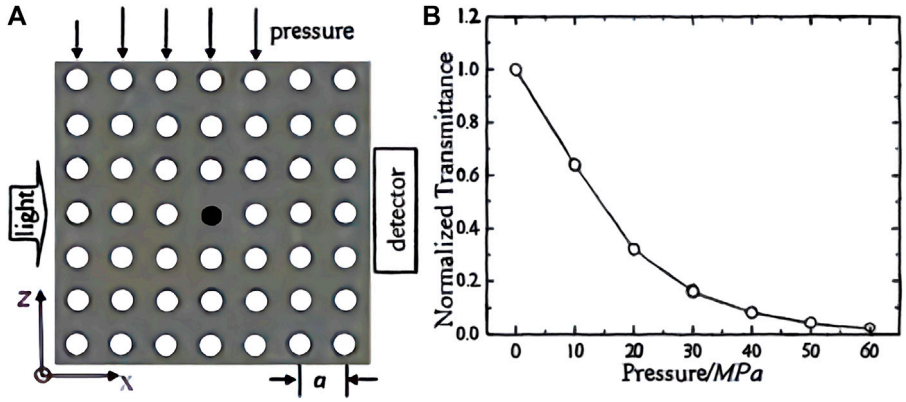

FIGURE 10 | (A) 2D-PC thin film point defect structure; **(B)** Relationship between transmittance and pressure (Zhao, 2015).

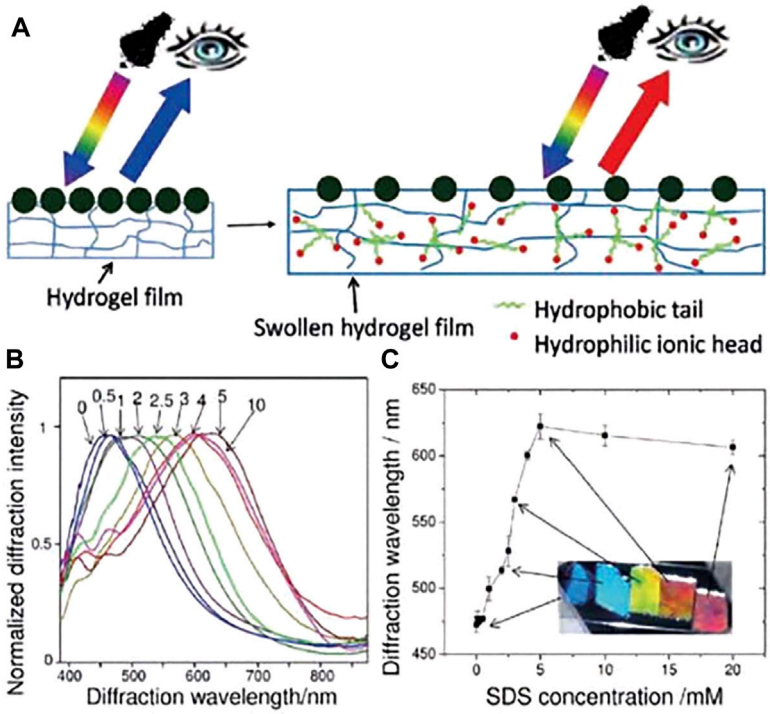

FIGURE 11 | (A) Schematic of a 2D-PC sensor formed by polymerizing a PNIPAAm hydrogel onto a single-layer microsphere array. The PNIPAAm hydrogel swells after binding to the surfactant molecule, and the ball spacing increases, resulting in diffraction red-shift; **(B)** The normalized diffraction spectrum of the 2D-PC PNIPAAm sensor in aqueous solution of sodium dodecylsulfonate (SDS) at different concentrations; **(C)** The diffraction wavelength to the SDS concentration response and corresponding color change (Zhang et al., 2012).

in the microcavity is combined with the biotin bovine serum albumin molecule (b-BSA), the resonance wavelength in the microcavity changes, and when the concentration of b-BSA changes, the concentration can be detected by measuring the standard curve of the change in the wavelength position of the resonance peak. Zhang et al. (2012) developed a two-dimensional photonic crystal sensing material for visual detection of anionic and cationic surfactant concentrations in water, which is a hydrogel film based on a two-dimensional microsphere array of poly (N-isopropylacrylamide) (PNIPAAm) that can detect surfactant concentrations down to 0.1 mM in aqueous solutions (**Figure 11**). Men et al. (2016) attached Au nanosphere arrays to poly (acrylic acid) (PAA) hydrogel membranes to prepare stand-alone two-dimensional Au

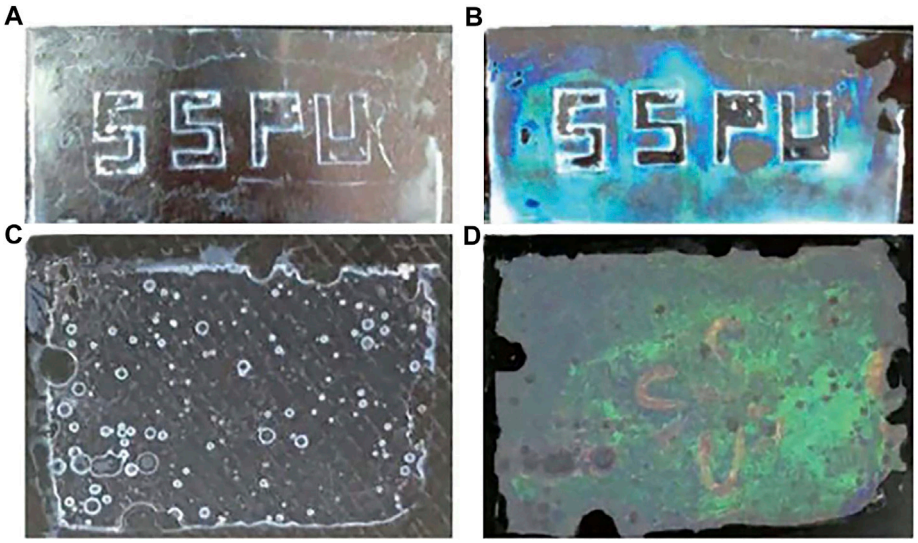

FIGURE 12 | 2D-PC material with invisible markings: **(A)** colorless and transparent when dehydrated; **(B)** PC film with blue and green when rehydrated; **(C)** colorless and transparent when dehydrated; **(D)** The PC film turned green while the printed part showed red (Chen et al., 2017b).

nanosphere array/hydrogel composite sensing membranes. The Au nanosphere array/hydrogel composite membranes showed visual diffraction colors and enhanced diffraction intensity due to the periodic structure and the large scattering cross-section of Au nanospheres, and the proposed strategy can be extended to various functional hydrogel membranes to develop different visualization sensors. Similarly, a range of optical devices can be designed and developed using the material's response to environmental stimuli to produce volume changes that alter the crystal plane spacing of 2D photonic crystals. Chen et al. (2017b) prepared a two-dimensional photonic crystal film material for invisible markers, as shown in **Figure 12**, which can be used for controlled color development or anti-counterfeit printing by not only going from transparent to visible, but also revealing pre-printed patterns when wetted with water. Dalstein et al. (2016) developed a soft lithography method for fabricating two-dimensional photonic structures of submicron metal-organic backbones (MOF). ZIF-8 (zinc) is a suitable MOF material due to its good chemical stability and vapour-selective adsorption properties. Combining these photonic MOF heterostructures with smartphone technology allows for the development of very low-cost sensing and monitoring platforms. The method can detect changes in the diffraction efficiency of photonic MOF patterns due to changes in the MOF refractive index by a charge-coupled device (CCD) camera, which is integrated into the smartphone and does not require complex optical instrumentation to transmit the data. In 2016, Jiaming Shi et al. of the School of Electronic Countermeasures proposed a one-dimensional Si-doped film of ZnSe/Te photonic crystal (Miao et al., 2016) to achieve an infrared camouflaged selective radiator for laser and double detectable windows by doping Si films. In 2017, his team introduced a Si film inside a Ge/ZnS photonic crystal (Zhang et al., 2017) to propose a one-dimensional doped structured photonic crystal to achieve IR-laser-radar compatible stealth. In 2019, his team optimized the visible-IR compatible camouflage design for the ZnSe/Ge system (Zhang et al., 2019), and the thickness of the proposed dual-band IR camouflage selective radiator was further optimized to 7.8 μm. In 2021, Gong Rongzhou's team at Huazhong University of Science and Technology prepared a one-dimensional photonic crystal and covered it with a thin film of phase change material GST, and such photonic crystal has an adaptive effect of infrared camouflage (Su et al., 2021).

Two-dimensional photonic crystal sensors have the advantage of compact structure compared to traditional sensors, which is more conducive to the miniaturization and portability of sensors. Two-dimensional photonic crystal sensors will become a research hotspot in the field of sensor technology in the coming period, and will then have a wide range of applications in fields such as the Internet of Things and biomedicine, especially in the area of flexible wearable sensing and display devices. This also places higher demands on the reusability, sensitivity and fast response to environmental parameters of photonic crystal materials.

CONCLUSION

Optical devices with feature sizes up to the micro-nano scale give rise to many new phenomena that are not available under macroscopic conditions. The optical properties of micro-nano structures allow the design of new optical devices and systems, but the technology for the preparation of micro-nano optical materials and structures has become a technical bottleneck in the development of micro-nano optics. Research on optical micro-nano structures has been carried out for more than

20 years, many problems have been overcome, and many preparation methods and applications have been developed. However, the preparation of optical micro-nano structures has been costly and time consuming, and for optical structures responding to visible wavelengths or even shorter wavelengths, microfabrication means are even more limited and expensive. These reasons inevitably prevent the excellent properties of optical micro-nano structures from being used on a large scale in industry. In addition, the size or structural parameters of almost all current optical micro-nano structures cannot be changed once they are set during the preparation process and therefore have a fixed optical effect. In practical production applications, there is a desire to obtain devices that can be self-executing and adjusted in real time to achieve more functions. The question of how to achieve a large degree of tuning output in the history of optical micro-nano structures is still an issue worth investigating. Finally, the properties of optical micro-nano structures should not only be limited to the control of light transport processes, but also how to effectively apply their advantages to industries related to people's livelihood, such as LED lighting and solar energy generation, etc.

The downstream applications of micro-nano optics are extensive, with public security anti-counterfeiting, laser packaging materials, and display and lighting being the three most representative industry applications. Meanwhile, the electronic device industry has entered the next generation of nanotechnology, in which optical super-resolution techniques, fabricated micro-nano structures, manipulation of surface equipartition excitations, and other micro-nano optical technologies and fast phase change materials have received extensive attention and research. In the field of photoelectric detection, artificial micro-nano structured photodetectors have surpassed traditional material detection performance in certain performance indicators. In particular, the artificial micro-nano structure-based photodetector shows excellent photoconversion performance at room temperature and will be one of the most competitive detector technologies for the next generation of high-performance, uncooled photodetection. For the bright application prospect, micro nano optics deserves more attention from researchers.

AUTHOR CONTRIBUTIONS

JY and ZW are responsible for literature research and sorting. XK is responsible for the embellishment and revision of the manuscript. XS, XLZ, YL, and HL are responsible for professional guidance. JT, XSZ, YS, XH, and JX are responsible for the revision of the manuscript. YW is responsible for overall guidance and thesis revision.

FUNDING

Natural Science Foundation of Shandong Province, China, No. ZR2020QA078; National Natural Science Foundation of China, No. 12005110; Institute of Scientific and Technical Information of China, No. QN2022-03.

REFERENCES

Adamu, A. I., Habib, M. S., Petersen, C. R., Zhou, B., Schulzgen, A., Lopez, J. E. A., et al. (2018). Supercontinuum Generation from Deep-UV to Mid-IR in a Noble Gas-Filled Fiber Pumped with Ultrashort Mid-IR Pulses. *Opt. Sensors* 2, 5. doi:10.1364/bgppm.2018.jtu6e.2

Amini, E., Dolatyari, M., Rostami, A., Shekari, H., Baghban, H., Rasooli, H., et al. (2012). Solution-Processed Photoconductive UV Detectors Based on ZnO Nanosheets. *IEEE Phot. Technol. Lett.* 24 (22), 1995–1997. doi:10.1109/LPT.2012.2217375

Anderson, W. (1965). Mode Confinement and Gain in Junction Lasers. *IEEE J. Quantum Electron.* 1 (6), 228–236. doi:10.1109/JQE.1965.1072228

Barrer, R. M. (1948). 33. Synthesis of a Zeolitic Mineral with Chabazite-like Sorptive Properties. *J. Chem. Soc.* 127, 127–132. doi:10.1039/JR9480000127

Barrer, R. M., and Hinds, L. (1950). Hydrothermal Synthesis of Potash Feldspar in the Range 195-200° C. *Nature* 166, 562. doi:10.1038/166562a0

Black, R. J., Gonthier, E., Lacroix, S., Lapierre, J., and Bures, J. (1988). Tapered Fibers:an Overview. *Components Fiber Opt. Photonics* 839, 2–20. doi:10.1117/12.942540

Bohren, C. F., and Huffman, D. R. (2008). *Absorption and Scattering of Light by Small Particles*. Chichester, UK: John Wiley & Sons.

Boys, C. V. (1887). On the Production, Properties, and Some Suggested Uses of the Finest Threads. *Proc. Phys. Soc. Lond.* 9, 8–19. doi:10.1088/1478-7814/9/1/303

Brambilla, G., Finazzi, V., and Richardson, D. J. (2004). Ultra-low-loss Optical Fiber Nanotapers. *Opt. Express* 12 (10), 2258–2263. doi:10.1364/OPEX.12.002258

Brambilla, G., Murugan, G. S., Wilkinson, J. S., and Richardson, D. J. (2007). Optical Manipulation of Microspheres along a Subwavelength Optical Wire. *Opt. Lett.* 32 (20), 3041–3043. doi:10.1364/ol.32.003041

Brambilla, G. (2010). Optical Fibre Nanowires and Microwires: a Review. *J. Opt.* 12 (4), 043001. doi:10.1088/2040-8978/12/4/043001

Brambilla, G., Xu, F., and Feng, X. (2006). Fabrication of Optical Fibre Nanowires and Their Optical and Mechanical Characterisation. *Electron. Lett.* 42 (9), 517–519. doi:10.1049/el:20060611

Brambilla, G., Xu, F., Horak, P., Jung, Y., Koizumi, F., Sessions, N. P., et al. (2009). Optical Fiber Nanowires and Microwires: Fabrication and Applications. *Adv. Opt. Phot.* 1 (1), 107–161. doi:10.1364/aop.1.000107

Burns, W., Abebe, M., Villarruel, C., and Moeller, R. (1986). Loss Mechanisms in Single-Mode Fiber Tapers. *J. Light. Technol.* 4 (6), 608–613. doi:10.1109/JLT.1986.1074764

Carson, J. R., Mead, S. P., and Schelkunoff, S. A. (1936). Hyper-Frequency Wave Guides-Mathematical Theory. *Bell Syst. Tech. J.* 15 (2), 310–333. doi:10.1002/j.1538-7305.1936.tb00734.x

Celler, G. K., and Cristoloveanu, S. (2003). Frontiers of Silicon-On-Insulator. *J. Appl. Phys.* 93 (9), 4955–4978. doi:10.1063/1.1558223

Chen, C., Zhao, X. L., Li, Z. H., Zhu, Z. G., Qian, S. H., and Flewitt, A. J. (2017). Current and Emerging Technology for Continuous Glucose Monitoring. *Sensors (Basel)* 17 (1), 182. doi:10.17863/CAM.834110.3390/s17010182

Chen, C., Dong, Z. Q., Chen, Y., Hu, X. B., Zhu, X. R., Zhu, Z. G., et al. (2017). Revealing Invisible Photonic Printing: Colorful Pattern Shown by Water. *IOP Conf. Ser. Mat. Sci. Eng.* 167, 012073. doi:10.1088/1757-899X/167/1/012073

Chen, C., Zhu, Y., Bao, H., Yang, X., and Li, C. (2010). Physically Controlled Cross-Linking in Gelated Crystalline Colloidal Array Photonic Crystals. *ACS Appl. Mat. Interfaces* 2 (5), 1499–1504. doi:10.1021/am100130n

Chen, C., Zhu, Z., Zhu, X., Yu, W., Liu, M., Ge, Q., et al. (2015). A Composite Hydrogels-Based Photonic Crystal Multi-Sensor. *Mat. Res. Express* 2 (4), 046201. doi:10.1088/2053-1591/2/4/046201

Chen, D., Chen, Y., Lu, H., and Ji, Z. (2014). A Bifunctional Cr/Yb/Tm: Ca3Ga2Ge3O12 Phosphor with Near-Infrared Long-Lasting

Phosphorescence and Upconversion Luminescence. *Inorg. Chem.* 53 (16), 8638–8645. doi:10.1021/ic501238u

Chen, Z., Li, Z., Chen, Z., Xia, R., Zou, G., Chu, L., et al. (2021). Utilization of Trapped Optical Modes for White Perovskite Light-Emitting Diodes with Efficiency over 12%. *Joule* 5 (2), 456–466. doi:10.1016/j.joule.2020.12.008

Christopher, D. R. (1998). *Gregory Hollow Waveguides*. New York: CRC Press LLC.

Dalstein, O., Ceratti, D. R., Boissière, C., Grosso, D., Cattoni, A., and Faustini, M. (2016). Nanoimprinted, Submicrometric, MOF-Based 2D Photonic Structures: Toward Easy Selective Vapors Sensing by a Smartphone Camera. *Adv. Funct. Mat.* 26 (1), 81–90. doi:10.1002/adfm.201503016

Dong, Y., Wang, Y.-K., Yuan, F., Johnston, A., Liu, Y., Ma, D., et al. (2020). Bipolar-shell Resurfacing for Blue LEDs Based on Strongly Confined Perovskite Quantum Dots. *Nat. Nanotechnol.* 15, 668–674. doi:10.1038/s41565-020-0714-5

Ebbesen, T. W., Lezec, H. J., Ghaemi, H. F., ThioWolff, T. P. A., and Wolff, P. A. (1998). Extraordinary Optical Transmission through Sub-wavelength Hole Arrays. *Nature* 391, 667–669. doi:10.1038/35570

Faraday, M. (1857). The Bakerian Lecture: Experimental Relations of Gold (And Other Metals) to Light. *Phil. Trans. R. Soc.* 147, 145–181. doi:10.1098/rstl.1825.0022

Feng, B., Zhu, J., Lu, B., Liu, F., Zhou, L., and Chen, Y. (2019). Achieving Infrared Detection by All-Si Plasmonic Hot-Electron Detectors with High Detectivity. *ACS Nano* 13 (7), 8433–8441. doi:10.1021/acsnano.9b04236

Furchi, M. M., Pospischil, A., Libisch, F., Burgdörfer, J., and Mueller, T. (2014). Photovoltaic Effect in an Electrically Tunable van der Waals Heterojunction. *Nano Lett.* 14 (8), 4785–4791. doi:10.1021/nl501962c

George, N. C., Denault, K. A., and Seshadri, R. (2013). Phosphors for Solid-State White Lighting. *Annu. Rev. Mat. Res.* 43, 481–501. doi:10.1146/annurev-matsci-073012-125702

Ghosh, P., KarPatra, A. A., and Patra, A. (2010). Energy Transfer Study between Ce3+ and Tb3+ Ions in Doped and Core-Shell Sodium Yttrium Fluoride Nanocrystals. *Nanoscale* 2, 1196–1202. doi:10.1039/C0NR00019A

Ginés, L. (2003). *Integrated Photonics: Fundamentals*. Chichester, UK: John Wiley & Sons. doi:10.1002/0470861401.fmatter

Gulina, L. B., Tolstoy, V. P., Kasatkin, I. A., Kolesnikov, I. E., and Danilov, D. V. (2017). Formation of Oriented LaF 3 and LaF 3 :Eu 3+ Nanocrystals at the Gas Solution Interface. *J. Fluor. Chem.* 200, 18–23. doi:10.1016/j.jfluchem.2017.05.006

Guo, Q., Pospischil, A., Bhuiyan, M., Jiang, H., Tian, H., Farmer, D., et al. (2016). Black Phosphorus Mid-infrared Photodetectors with High Gain. *Nano Lett.* 16 (7), 4648–4655. doi:10.1021/acs.nanolett.6b01977

Habib, M. S., Bang, O., and Bache, M. (2015). Low-loss Hollow-Core Silica Fibers with Adjacent Nested Anti-resonant Tubes. *Opt. Express* 23 (13), 17394–17406. doi:10.1364/OE.23.017394

Habib, M. S., Bang, O., and Bache, M. (2016). Low-loss Single-Mode Hollow-Core Fiber with Anisotropic Anti-resonant Elements. *Opt. Express* 24 (8), 8429–8436. doi:10.1364/OE.24.008429

Habib, M. S., Markos, C., Bang, O., and Bache, M. (2017). "Curvatureand Position of Nested Tubes in Hollow-Core Anti-resonant fibers//Conference on Lasers and Electro-Optics Europe&amp," in European QuantumElectronics Conference (CLEO/Europe-EQEC), 25-29 June 2017 (New York: IEEE), 17350440.

Hayes, J. R., Fokoua, E. N., Petrovich, M. N., Richardson, D. J., Poletti, F., Sandoghchi, S. R., et al. (2017). Antiresonant Hollow Core Fiber with an Octave Spanning Bandwidth for Short Haul Data Communications. *J. Light. Technol.* 35 (3), 437–442. doi:10.1109/JLT.2016.2638205

Hidaka, T., Morikawa, T., and Shimada, J. (1981). Hollow-core Oxide-glass Cladding Optical Fibers for Middle-infrared Region. *J. Appl. Phys.* 52 (7), 4467–4471. doi:10.1063/1.329373

Holmes, J. D., Johnston, K. P., Doty, R. C., and Korgel, B. A. (2000). Control of Thickness and Orientation of Solution-Grown Silicon Nanowires. *Science* 287 (5457), 1471–1473. doi:10.1126/science.287.5457.1471

Hondros, D., and Debye, P. (1910). Elektromagnetische Wellen an Dielektrischen Drähten. *Ann. Phys.* 337 (8), 465–476. doi:10.1002/andp.19103370802

Hu, Z., Lustig, W. P., Zhang, J., Zheng, C., Wang, H., Teat, S. J., et al. (2015). Effective Detection of Mycotoxins by a Highly Luminescent Metal-Organic Framework. *J. Am. Chem. Soc.* 137 (51), 16209–16215. doi:10.1021/jacs.5b10308

Huang, H., Wang, X., Wang, P., Wu, G., Chen, Y., Meng, C., et al. (2016). Ferroelectric Polymer Tuned Two Dimensional Layered MoTe2 Photodetector. *RSC Adv.* 6 (90), 87416–87421. doi:10.1039/C6RA18238K

Huang, L., Zhu, Y., Zhang, X., Zou, R., Pan, F., Wang, J., et al. (2016). HF-free Hydrothermal Route for Synthesis of Highly Efficient Narrow-Band Red Emitting Phosphor K2Si1-xF6:xMn4+ for Warm White Light-Emitting Diodes. *Chem. Mat.* 28 (5), 1495–1502. doi:10.1021/acs.chemmater.5b04989

Hunsperger, R. G. (2009). *Integrated Optics: Theory and Technology*. Berlin, Heidelberg: Springer.

Hwang, S. H., Shin, J. C., Song, J. D., Choi, W. J., Lee, J. I., and Han, H. (2005). Detection Wavelength Tuning of InGaAs/GaAs Quantum Dot Infrared Photodetector with Thermal Treatment. *Microelectron. J.* 36 (3-6), 203–206. doi:10.1016/j.mejo.2005.02.006

Jalali, B., Yegnanarayanan, S., Yoon, T., Yoshimoto, T., Rendina, I., and Coppinger, F. (1998). Advances in Silicon-On-Insulator Optoelectronics. *IEEE J. Sel. Top. Quantum Electron.* 4 (6), 938–947. doi:10.1109/2944.736081

Jang, H. S., Yang, H., Kim, S. W., Han, J. Y., Lee, S.-G., and Jeon, D. Y. (2008). White Light-Emitting Diodes with Excellent Color Rendering Based on Organically Capped CdSe Quantum Dots and Sr3SiO5:Ce3+,Li+Phosphors. *Adv. Mat.* 20 (14), 2696–2702. doi:10.1002/adma.200702846

John, S. (1987). Strong Localization of Photons in Certain Disordered Dielectric Superlattices. *Phys. Rev. Lett.* 58 (23), 2486–2489. doi:10.1103/physrevlett.58.2486

Kamboj, A., Nordin, L., Petluru, P., Muhowski, A. J., Woolf, D. N., and Wasserman, D. (2021). All-epitaxial Guided-Mode Resonance Mid-wave Infrared Detectors. *Appl. Phys. Lett.* 118 (20), 201102. doi:10.1063/5.0047534

Kao, K. C., and Hockham, G. A. (1966). Dielectric-fibre Surface Waveguides for Optical Frequencies. *Proc. Institution Electr. Eng.* 113 (7), 1151–1158. doi:10.1049/piee.1966.0189

Kapany, N. S. (1959). High-Resolution Fibre Optics Using Sub-micron Multiple Fibres. *Nature* 184 (4690), 881–883. doi:10.1038/184881a0

Kapron, F. P., Keck, D. B., and Maurer, R. D. (1970). Radiation Losses in Glass Optical Waveguides. *Appl. Phys. Lett.* 17 (10), 423–425. doi:10.1063/1.1653255

Kasturi, S., Sivakumar, V., and Jeon, D. Y. (2016). Europium-activated Rare Earth Fluoride (LnF3:Eu3+-Ln = La, Gd) Nanocrystals Prepared by Using Ionic liquid/NH4F as a Fluorine Source via Hydrothermal Synthesis. *Luminescence* 31 (5), 1138–1145. doi:10.1002/bio.3083

Keevend, K., Stiefel, M., Neuer, A. L., Matter, M. T., Neels, A., Bertazzo, S., et al. (2017). Tb3+-doped LaF3nanocrystals for Correlative Cathodoluminescence Electron Microscopy Imaging with Nanometric Resolution in Focused Ion Beam-Sectioned Biological Samples. *Nanoscale* 9 (13), 4383–4387. doi:10.1039/c6nr09187c

Khatua, S., Chang, W.-S., Swanglap, P., Olson, J., and Link, S. (2011). Active Modulation of Nanorod Plasmons. *Nano Lett.* 11 (9), 3797–3802. doi:10.1021/nl201876r

Knight, M. W., Sobhani, H., Nordlander, P., and Halas, N. J. (2011). Photodetection with Active Optical Antennas. *Science* 332 (6030), 702–704. doi:10.1126/science.1203056

Kokubun, Y., and Iga, K. (2005). *Encyclopedic Handbook of Integrated Optics*. Washington, DC: J. Opt. Soc. Am.

Kong, L., Zhang, X., Li, Y., Wang, H., Jiang, Y., Wang, S., et al. (2021). Smoothing the Energy Transfer Pathway in quasi-2D Perovskite Films Using Methanesulfonate Leads to Highly Efficient Light-Emitting Devices. *Nat. Commun.* 12, 1246. doi:10.1038/s41467-021-21522-8

Krishna, S. (2005). Quantum Dots-In-A-Well Infrared Photodetectors. *Infrared Phys. Technol.* 47 (1-2), 153–163. doi:10.1016/j.infrared.2005.02.020

Kubo, U., and Hashishin, Y. (1987). Hollow Light Guide Tube for CO2 Laser Beam. Optical Fibers in Medicine II. *Int. Soc. Opt. Photonics* 713, 17–22. doi:10.1117/12.937362

Kufer, D., Nikitskiy, I., Lasanta, T., Navickaite, G., Koppens, F. H. L., and Konstantatos, G. (2015). Hybrid 2D-0D MoS2-PbS Quantum Dot Photodetectors. *Adv. Mat.* 27 (1), 176–180. doi:10.1002/adma.201402471

Lee, K. K., Lim, D. R., Kimerling, L. C., Shin, J., and Cerrina, F. (2001). Fabrication of Ultralow-Loss Si/SiO_2 Waveguides by Roughness Reduction. *Opt. Lett.* 26 (23), 1888–1890. doi:10.1364/OL.26.001888

Leon-Saval, S. G., Birks, T. A., Wadsworth, W. J., Russell, P. S. J., and Mason, M. W. (2004). Supercontinuum Generation in Submicron Fibre Waveguides. *Opt. Express* 12 (13), 2864–2869. doi:10.1364/OPEX.12.002864

Li, G., Tian, Y., Zhao, Y., and Lin, J. (2015). Recent Progress in Luminescence Tuning of Ce3+and Eu2+-Activated Phosphors for Pc-WLEDs. *Chem. Soc. Rev.* 44 (23), 8688–8713. doi:10.1039/c4cs00446a

Li, X., Wang, X., Zhang, L., Lee, S., and Dai, H. (2008). Chemically Derived, Ultrasmooth Graphene Nanoribbon Semiconductors. *Science* 319 (5867), 1229–1232. doi:10.1126/science.1150878

Liu, H., Neal, A. T., and Ye, P. D. (2012). Channel Length Scaling of MoS2MOSFETs. *ACS Nano* 6 (10), 8563–8569. doi:10.1021/nn303513c

Liu, K., Sakurai, M., Liao, M., and Aono, M. (2010). Giant Improvement of the Performance of ZnO Nanowire Photodetectors by Au Nanoparticles. *J. Phys. Chem. C* 114 (46), 19835–19839. doi:10.1021/jp108320j

Liu, X., Fan, Z., Shi, Z., Ma, Y., Yu, J., and Zhang, J. (2016). Dual-core Antiresonant Hollow Core Fibers. *Opt. Express* 24 (15), 17453–17458. doi:10.1364/oe.24.017453

Liu, Y., Meng, C., Zhang, A. P., Xiao, Y., Yu, H., and Tong, L. (2011). Compact Microfiber Bragg Gratings with High-Index Contrast. *Opt. Lett.* 36 (16), 3115–3117. doi:10.1364/OL.36.003115

Love, J. D., and Henry, W. M. (1986). Quantifying Loss Minimisation in Single-Mode Fibre Tapers. *Electron. Lett.* 22 (17), 912–914. doi:10.1049/el:19860622

Maiman, T. H. (2018). Addendum 10: Reprint of T.H. Maiman, "Stimulated Optical Radiation in Ruby. *Nature* 187, 299–301. doi:10.1007/978-3-319-61940-8_35

Mall, M., and Kumar, L. (2010). Optical Studies of Cd2+ and Mn2+ Co-doped ZnS Nanocrystals. *J. Luminescence* 130 (4), 660–665. doi:10.1016/j.jlumin.2009.11.012

Men, D., Zhou, F., Hang, L., Li, X., Duan, G., Cai, W., et al. (2016). A Functional Hydrogel Film Attached with a 2D Au Nanosphere Array and its Ultrahigh Optical Diffraction Intensity as a Visualized Sensor. *J. Mat. Chem. C* 4 (4), 2117–2122. doi:10.1039/C5TC04281J

Miao, J., Hu, W., Guo, N., Lu, Z., Liu, X., Liao, L., et al. (2014). High-Responsivity Graphene/InAs Nanowire Heterojunction Near-Infrared Photodetectors with Distinct Photocurrent On/Off Ratios. *Small* 11, 936–942. doi:10.1002/smll.201402312

Miao, J., Hu, W., Guo, N., Lu, Z., Zou, X., Liao, L., et al. (2014). Single InAs Nanowire Room-Temperature Near-Infrared Photodetectors. *ACS Nano* 8 (4), 3628–3635. doi:10.1021/nn500201g

Miao, L., Shi, J., Wang, J., Zhao, D., Chen, Z., and Wang, Q. (2016). Heterogeneous Doped One-Dimensional Photonic Crystal with Low Emissivity in Infrared Atmospheric Window. *Opt. Eng.* 55, 057101. doi:10.1117/1.OE.55.5.057101

Mingo, N. (2003). Calculation of Si Nanowire Thermal Conductivity Using Complete Phonon Dispersion Relations. *Phys. Rev. B* 68 (11), 845–846. doi:10.1103/PhysRevB.68.113308

Miura, K., Qiu, J., Inouye, H., Mitsuyu, T., and Hirao, K. (1997). Photowritten Optical Waveguides in Various Glasses with Ultrashort Pulse Laser. *Appl. Phys. Lett.* 71 (23), 3329–3331. doi:10.1063/1.120327

Miyagi, M., and Karasawa, S. (1990). Waveguide Losses in Sharply Bent Circular Hollow Waveguides. *Appl. Opt.* 29 (3), 367–370. doi:10.1364/ao.29.000367

Mueller, T., Xia, F., and Avouris, P. (2010). Graphene Photodetectors for High-Speed Optical Communications. *Nat. Phot.* 4 (5), 297–301. doi:10.1038/nphoton.2010.40

Neto, A., Guinea, F., Peres, N., Novoselov, K. S., and Geim, A. K. (2007). The Electronic Properties of Graphene. *Rev. Mod. Phys.* 81, 109. doi:10.48550/arXiv.0709.1163

Nie, L., Shen, Y., Zhang, X., Wang, X., Liu, B., Wang, Y., et al. (2017). Selective Synthesis of LaF3 and NaLaF4 Nanocrystals via Lanthanide Ion Doping. *J. Mat. Chem. C* 5 (35), 9188–9193. doi:10.1039/C7TC02362F

Noginov, M. A., Zhu, G., Belgrave, A. M., Bakker, R., Shalaev, V. M., Narimanov, E. E., et al. (2009). Demonstration of a Spaser-Based Nanolaser. *Nature* 460 (7295), 1110–1112. doi:10.1038/nature08318

Nordin, L., Kamboj, A., Petluru, P., Shaner, E., and Wasserman, D. (2020). All-Epitaxial Integration of Long-Wavelength Infrared Plasmonic Materials and Detectors for Enhanced Responsivity. *ACS Photonics* 7 (8), 1950–1956. doi:10.1021/acsphotonics.0c00659

Nubling, R. K., and Harrington, J. A. (1996). Hollow-waveguide Delivery Systems for High-Power, Industrial CO_2 Lasers. *Appl. Opt.* 35 (3), 372–380. doi:10.1364/AO.35.000372

Nubling, R. K., and Harrington, J. A. (1997). Optical Properties of Single-Crystal Sapphire Fibers. *Appl. Opt.* 36 (24), 5934–5940. doi:10.1364/AO.36.005934

Okamoto, K. (2006). Fiber Optics. *Opt. fibers* 97 (5), 56–63. doi:10.1016/B978-012525096-2/50004-0

Olson, J., Dominguez-Medina, S., Hoggard, A., Wang, L.-Y., Chang, W.-S., and Link, S. (2014). Optical Characterization of Single Plasmonic Nanoparticles. *Chem. Soc. Rev.* 44 (1), 40–57. doi:10.1039/c4cs00131a

Osterberg, H., and Smith, L. W. (1964). Transmission of Optical Energy along Surfaces: Part II, Inhomogeneous Media. *J. Opt. Soc. Am.* 54, 1078. doi:10.1364/josa.54.001078

Ozbay, E. (2006). Plasmonics: Merging Photonics and Electronics at Nanoscale Dimensions. *Science* 311 (5758), 189–193. doi:10.1126/science.1114849

Page, P. S., Dhabekar, B. S., Bhatt, B. C., Dhoble, A. R., and Godbole, S. V. (2010). Role of Ti4+ in the Luminescence Process of Al2O3:Si,Ti. *J. Luminescence* 130 (5), 882–887. doi:10.1016/j.jlumin.2009.12.029

Polynkin, P., Polynkin, A., Peyghambarian, N., and Mansuripur, M. (2005). Evanescent Field-Based Optical Fiber Sensing Device for Measuring the Refractive Index of Liquids in Microfluidic Channels. *Opt. Lett.* 30 (11), 1273–1275. doi:10.1364/ol.30.001273

Ruan, J.-L., Chen, C., Shen, J.-H., Zhao, X.-L., Qian, S.-H., and Zhu, Z.-G. (2017). A Gelated Colloidal Crystal Attached Lens for Noninvasive Continuous Monitoring of Tear Glucose. *Polymers* 9 (12), 125. doi:10.3390/polym9040125

Schlosser, W. (1964). Der rechteckige dielektrische Draht. Archi. Elekt. *Übertz* 7, 403–410.

Sirbuly, D. J., Law, M., Yan, H., and Yang, P. (2005). Semiconductor Nanowires for Subwavelength Photonics Integration. *ChemInform* 36, 15190–15213. doi:10.1002/chin.200543243

Sivis, M., Duwe, M., Abel, B., and Ropers, C. (2013). Extreme-ultraviolet Light Generation in Plasmonic Nanostructures. *Nat. Phys.* 9 (5), 304–309. doi:10.1038/NPHYS2590

Song, J., Li, J., Li, X., Xu, L., Dong, Y., and Zeng, H. (2015). Quantum Dot Light-Emitting Diodes Based on Inorganic Perovskite Cesium Lead Halides (CsPbX3). *Adv. Mat.* 27 (44), 7162–7167. doi:10.1002/adma.201502567

Southworth, G. C. (1936). Hyper-Frequency Wave Guides-General Considerations and Experimental Results*. *Bell Syst. Tech. J.* 15 (2), 284–309. doi:10.1002/j.1538-7305.1936.tb00733.x

Su, Y., Deng, Z., Qin, W., Wang, X., and Gong, R. (2021). Adaptive Infrared Camouflage Based on Quasi-Photonic Crystal with Ge2Sb2Te5. *Opt. Commun.* 497, 127203. doi:10.1016/j.optcom.2021.127203

Sun, Z., and Chang, H. (2014). Graphene and Graphene-like Two-Dimensional Materials in Photodetection: Mechanisms and Methodology. *ACS Nano* 8 (5), 4133–4156. doi:10.1021/nn500508c

Tamir, T. (1975). Integrated Optics. *Top. Appl. Phys.* 5, 639–656. doi:10.1007/978-3-662-43208-2

Tan, M., DelRosal, B., Zhang, Y., Martín Rodríguez, E., Hu, J., Zhou, Z., et al. (2018). Rare-earth-doped Fluoride Nanoparticles with Engineered Long Luminescence Lifetime for Time-Gated *In Vivo* Optical Imaging in the Second Biological Window. *Nanoscale* 10 (37), 17771–17780. doi:10.1039/C8NR02382D

Tian, H., Wang, X., Zhu, Y., Liao, L., Wang, X., Wang, J., et al. (2017). High Performance Top-Gated Ferroelectric Field Effect Transistors Based on Two-Dimensional ZnO Nanosheets. *Appl. Phys. Lett.* 110 (4), 043505. doi:10.1063/1.4975061

Tong, L., Gattass, R. R., Ashcom, J. B., He, S., Lou, J., Shen, M., et al. (2003). Subwavelength-Diameter Silica Wires for Low-Loss Optical Wave Guiding. *Nature* 426 (6968), 816–819. doi:10.1038/nature02193

Tong, L., Lou, J., Ye, Z., Svacha, G. T., and Mazur, E. (2005). Self-modulated Taper Drawing of Silica Nanowires. *Nanotechnology* 16 (9), 1445–1448. doi:10.1088/0957-4484/16/9/004

Tu, J., Zhang, B., Liu, Z., Zhou, X., Long, K., Li, Z., et al. (2018). Chalcogenide-Glass Nested Anti-resonant Nodeless Fibers in Mid-infrared Region. *J. Light. Technol.* 36 (22), 5244–5253. doi:10.1109/JLT.2018.2870434

van Eijkelenborg, M. A., Argyros, A., Barton, G., Bassett, I. M., Fellew, M., Henry, G., et al. (2003). Recent Progress in Microstructured Polymer Optical Fibre Fabrication and Characterisation. *Opt. Fiber Technol.* 9 (4), 199–209. doi:10.1016/S1068-5200(03)00045-2

Villatoro, J., and Monzón-Hernández, D. (2005). Fast Detection of Hydrogen with Nano Fiber Tapers Coated with Ultra Thin Palladium Layers. *Opt. Express* 13 (13), 5087–5092. doi:10.1364/opex.13.005087

Wang, D., Allcca, A. E. L., Chung, T.-F., Kildishev, A. V., Chen, Y. P., Boltasseva, A., et al. (2020). Enhancing the Graphene Photocurrent Using Surface

Plasmons and a P-N Junction. *Light Sci. Appl.* 9 (1), 126. doi:10.1038/s41377-020-00344-1

Wang, H., Holmberg, B. A., and Yan, Y. (2002). Homogeneous Polymer-Zeolite Nanocomposite Membranes by Incorporating Dispersible Template-Removed Zeolite Nanocrystals. *J. Mat. Chem.* 12 (12), 3640–3643. doi:10.1039/B207394C

Wang, S., Yoon, N., Kamboj, A., Petluru, P., Zheng, W., and Wasserman, D. (2018). Ultra-thin Enhanced-Absorption Long-Wave Infrared Detectors. *Appl. Phys. Lett.* 112 (9), 091104. doi:10.1063/1.5017704

Wang, X., Liu, Q., Bu, Y., Liu, C.-S., Liu, T., and Yan, X. (2015). Optical Temperature Sensing of Rare-Earth Ion Doped Phosphors. *RSC Adv.* 5, 86219–86236. doi:10.1039/c5ra16986k

Wang, X., Wang, P., Wang, J., Hu, W., Zhou, X., Guo, N., et al. (2015). Ultrasensitive and Broadband MoS2Photodetector Driven by Ferroelectrics. *Adv. Mat.* 27 (42), 6575–6581. doi:10.1002/adma.201503340

Wei, C., Menyuk, C. R., and Hu, J. (2018). Polarization-filtering and Polarization-Maintaining Low-Loss Negative Curvature Fibers. *Opt. Express* 26 (8), 9528–9540. doi:10.1364/OE.26.009528

Weitkamp, J. (2000). Zeolites and Catalysis. *Solid State Ionics* 131, 175–188. doi:10.1016/S0167-2738(00)00632-9

Wheeler, W. (1881). *Apparatus for Lighting Dwellings or Other Structures*. Morton, Pennsylvania: US Patent Office.

Wu, H., Yang, X., Yu, X., Liu, J., Yang, H., Lv, H., et al. (2009). Preparation and Optical Properties of Eu3+/Eu2+ in Phosphors Based on Exchanging Eu3+-Zeolite 13X. *J. Alloys Compd.* 480 (2), 867–869. doi:10.1016/j.jallcom.2009.02.050

Xia, F., Sekaric, L., and Vlasov, Y. (2007). Ultracompact Optical Buffers on a Silicon Chip. *Nat. Phot.* 1 (1), 65–71. doi:10.1038/nphoton.2006.42

Xiang, G. (2019). Research on Deep Sub-wavelength Nanowire Laser Based on Photonic Crystal Microcavity. Beijing: Engineering Technology. Doctoral dissertation.

Xiao, F., Sun, Y., Du, W., Shi, W., Wu, Y., Liao, S., et al. (2017). Smart Photonic Crystal Hydrogel Material for Uranyl Ion Monitoring and Removal in Water. *Adv. Funct. Mat.* 27 (42), 1702147. doi:10.1002/adfm.201702147

Xu, W., Hu, Q., Bai, S., Bao, C., Miao, Y., Yuan, Z., et al. (2019). Rational Molecular Passivation for High-Performance Perovskite Light-Emitting Diodes. *Nat. Photonics* 13, 418–424. doi:10.1038/s41566-019-0390-x

Yablonovitch, E. (1987). Inhibited Spontaneous Emission in Solid-State Physics and Electronics. *Phys. Rev. Lett.* 58 (20), 2059–2062. doi:10.1103/PhysRevLett.58.2059

Yablonovitch, E. (1987). Inhibited Spontaneous Emission in Solid-State Physics and Electronics. *Phys. Rev. Lett.* 58 (20), 2059–2062. doi:10.1103/physrevlett.58.2059

Yan, S., Lou, S., Zhang, W., and Lian, Z. (2018). Single-polarization Single-Mode Double-Ring Hollow-Core Anti-resonant Fiber. *Opt. Express* 26 (24), 31160–31171. doi:10.1364/OE.26.031160

Yan, Z., Ling, Z., Ai, Z., Li, W., and Guo, C. (2013). Electricfield and Energy Distributionsdepend on Diameterand Incident Opticalfibers, Wavelength of Micro Nano Opticalfibers. *J. Nat. Sci. Heilongjiang Univ.* 30 (5), 685–690. doi:10.13482/j.issn1001-7011.2013.05.013

Zhang, A., Kim, H., Cheng, J., and Lo, Y.-H. (2010). Ultrahigh Responsivity Visible and Infrared Detection Using Silicon Nanowire Phototransistors. *Nano Lett.* 10 (6), 2117–2120. doi:10.1021/nl1006432

Zhang, J.-K., Shi, J.-M., Zhao, D.-P., Wang, Q.-C., and Wang, C.-M. (2017). Realization of Compatible Stealth Material for Infrared, Laser and Radar Based on One-Dimensional Doping-Structure Photonic Crystals. *Infrared Phys. Technol.* 85, 62–65. doi:10.1016/j.infrared.2017.05.018

Zhang, J.-T., Smith, N., and Asher, S. A. (2012). Two-Dimensional Photonic Crystal Surfactant Detection. *Anal. Chem.* 84 (15), 6416–6420. doi:10.1021/ac300174m

Zhang, J. K., Liu, R. H., Zhao, D. P., Wang, H., Zhang, Y. Q., Wang, C. M., et al. (2019). Design, Fabrication and Characterization of a Thin Infrared-Visible Bi-stealth Film Based on One-Dimensional Photonic Crystal. *Opt. Mat. Express* 9, 195–202. doi:10.1364/OME.9.000195

Zhang, W., Chiu, M.-H., Chen, C.-H., Chen, W., Li, L.-J., and Wee, A. T. S. (2014). Role of Metal Contacts in High-Performance Phototransistors Based on WSe2 Monolayers. *ACS Nano* 8 (8), 8653–8661. doi:10.1021/nn503521c

Zhao, N. S. (2015). Net-zero Emissions Energy Systems. *Sci. Technol. Visio* 33, 142. doi:10.1126/science.aas9793

Zlatanovic, S., Mirkarimi, L. W., Sigalas, M. M., Bynum, M. A., Chow, E., Robotti, K. M., et al. (2009). Photonic Crystal Microcavity Sensor for Ultracompact Monitoring of Reaction Kinetics and Protein Concentration. *Sensors Actuators. B Chem.* 141 (1), 13–19. doi:10.1016/j.snb.2009.06.007

Conflict of Interest: The authors declare that the research was conducted in the absence of any commercial or financial relationships that could be construed as a potential conflict of interest.

Publisher's Note: All claims expressed in this article are solely those of the authors and do not necessarily represent those of their affiliated organizations, or those of the publisher, the editors and the reviewers. Any product that may be evaluated in this article, or claim that may be made by its manufacturer, is not guaranteed or endorsed by the publisher.

Copyright © 2022 Wang, Yang, Wang, Kong, Sun, Tian, Zhang, Zhao, Liu, Li, Su, Hao and Xu. This is an open-access article distributed under the terms of the Creative Commons Attribution License (CC BY). The use, distribution or reproduction in other forums is permitted, provided the original author(s) and the copyright owner(s) are credited and that the original publication in this journal is cited, in accordance with accepted academic practice. No use, distribution or reproduction is permitted which does not comply with these terms.

frontiers | Frontiers in Chemistry

REVIEW
published: 05 July 2022
doi: 10.3389/fchem.2022.931169

The Development of Microscopic Imaging Technology and its Application in Micro- and Nanotechnology

Yong Wang[1,2,3]†, Xiushuo Zhang[1,2,3]†, Jing Xu[1,2]†, Xiangyu Sun[4]†, Xiaolong Zhao[1,2], Hongsheng Li[1,2,3], Yanping Liu[1,2,3], Jingjing Tian[1,2], Xiaorui Hao[1,2], Xiaofei Kong[1,2], Zhiwei Wang[1,2], Jie Yang[1,2] and Yuqing Su[1,2]*

[1]Laboratory of Optical Detection and Imaging, School of Science, Qingdao University of Technology, Qingdao, China, [2]Quantum Physics Laboratory, School of Science, Qingdao University of Technology, Qingdao, China, [3]Qingdao Technology Innovation Center of Remote Sensing and Precise Measurement, Qingdao, China, [4]Torch High Technology Industry Development Center, Ministry of Science and Technology, Beijing, China

OPEN ACCESS

Edited by:
Siwei Zhang,
Hong Kong University of Science and Technology, Hong Kong SAR, China

Reviewed by:
Dongmei Li,
Zhejiang University of Technology, China
Honglei Zhan,
China University of Petroleum, Beijing, China

***Correspondence:**
Yong Wang
wang-yong13@tsinghua.org.cn

†These authors have contributed equally to this work and share first authorship

Specialty section:
This article was submitted to Nanoscience, a section of the journal Frontiers in Chemistry

Received: 28 April 2022
Accepted: 16 May 2022
Published: 05 July 2022

Citation:
Wang Y, Zhang X, Xu J, Sun X, Zhao X, Li H, Liu Y, Tian J, Hao X, Kong X, Wang Z, Yang J and Su Y (2022) The Development of Microscopic Imaging Technology and its Application in Micro- and Nanotechnology. Front. Chem. 10:931169. doi: 10.3389/fchem.2022.931169

As a typical microscopic imaging technology, the emergence of the microscope has accelerated the pace of human exploration of the micro world. With the development of science and technology, microscopes have developed from the optical microscopes at the time of their invention to electron microscopes and even atomic force microscopes. The resolution has steadily improved, allowing humans to expand the field of research from the initial animal and plant tissues to microorganisms such as bacteria, and even down to the nanolevel. The microscope is now widely used in life science, material science, geological research, and other fields. It can be said that the development of microscopes also promotes the development of micro- and nanotechnology. It is foreseeable that microscopes will play a significant part in the exploration of the microworld for a long time to come. The development of microscope technology is the focus of this study, which summarized the properties of numerous microscopes and discussed their applications in micro and nanotechnology. At the same time, the application of microscopic imaging technology in micro- and nanofields was investigated based on the properties of various microscopes.

Keywords: microscopic, imaging, micro-nano, review, expectation

1 INTRODUCTION

A microscope is an instrument that magnifies the image of an observed object. It has a history of 400 years since its invention at the end of the 16th century. Because of its ability to magnify images, the microscope has played a vital part in the investigation of the microscopic world. Microscopic imaging technology evolves in tandem with human awareness of the microcosmic world. For the time being, the microscope includes the following three types according to the principles: optical microscope, electron microscope, and scanning probe microscope. The different principles make the use and contribution significantly different. In this study, we will discuss the evolution of the microscope and its applications in micro- and nanotechnology.

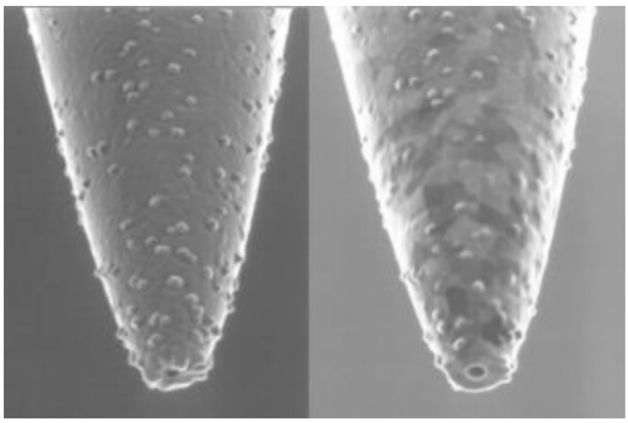

FIGURE 1 | Near-field scanning optical microscope probe (Dunn et al., 2009).

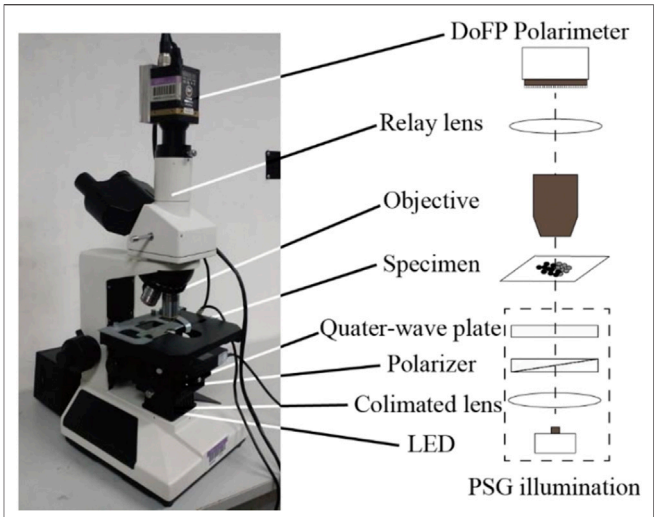

FIGURE 2 | Polarization microscope based on division-of-focal plane (DoFP) polarimeter (Chang et al., 2016).

2 THE OPTICAL MICROSCOPE

2.1 Introduction to Optical Microscope

The optical microscope is the first human-made microscope. It has played an extremely important role in the initial stage of human understanding of the micro world. For the past 400 years, the basic construction of the optical microscope remained stable without major changes, including objective lens, eyepiece, light source, condenser, and the mechanical structure. The resolution of traditional optical microscopes meets the Abbe formula: $\delta = \frac{0.61\lambda}{n \sin \alpha}$,

where δ is the optical microscope resolution, λ is the wavelength of light, n is the refractive index, and α is the aperture angle. The resolution limit of an optical microscope calculated is about 0.2 microns, so an optical microscope is widely used at a micron level, especially for the study of cells in biology and medicine. However, further observations of smaller objects are limited.

With the development of science and technology, near-field optical microscopy (NSOM) has been developed in recent years. Compared to the traditional optical microscope, its resolution has substantially enhanced. The structure includes the local light source, laser, fiber probe sample station, and optical amplification system. The characteristic of the near-field microscope is that at least one illumination and imaging must work in the near field, while both traditional optical microscopes work in the far field. The resolution of traditional far-field optical microscopes has been limited to wavelength λ or aperture $n \sin \alpha$. The working mode of the near-field optical microscope is to obtain information on fine structure and fluctuation smaller than the super-resolution limit of wavelength from the electromagnetic field (evanescent field) in the near field, and then transform the evanescent field containing this information into a propagation field that can transmit energy, allowing the detector and imaging device placed in the distance to receive the information in the evanescent field. It works by the reversibility of light, which means that when the direction of light is reversed in diffraction, the light will go backward along the incident route.

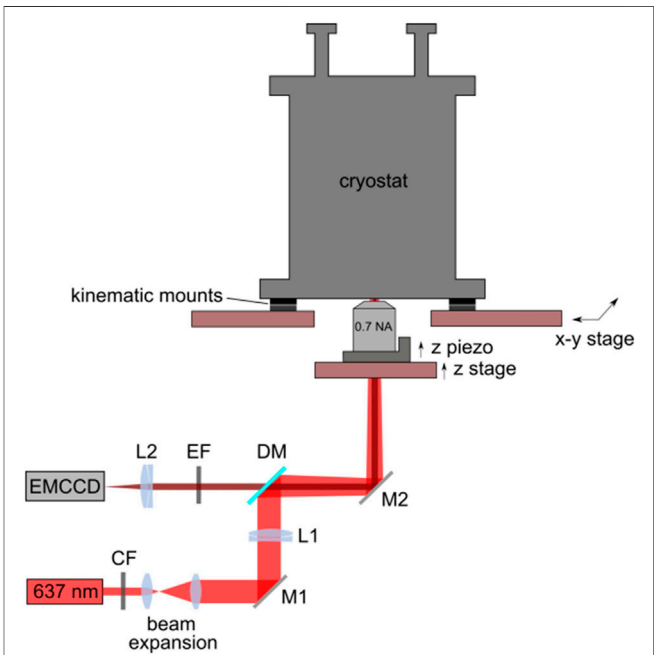

FIGURE 3 | Structure diagram of low temperature fluorescence microscope (Li et al., 2015).

Therefore, when the evanescent wave containing super-resolution information is used to irradiate objects with fine structure or spatial fluctuation smaller than the wavelength, such as gratings and small holes, these gratings or small holes can convert the evanescent wave into a propagation wave containing super-resolution information, which can be accepted by distant detectors. Currently, the near-field scanning optical microscope is used extensively in biomedical research. The probe section of a near-field scanning optical

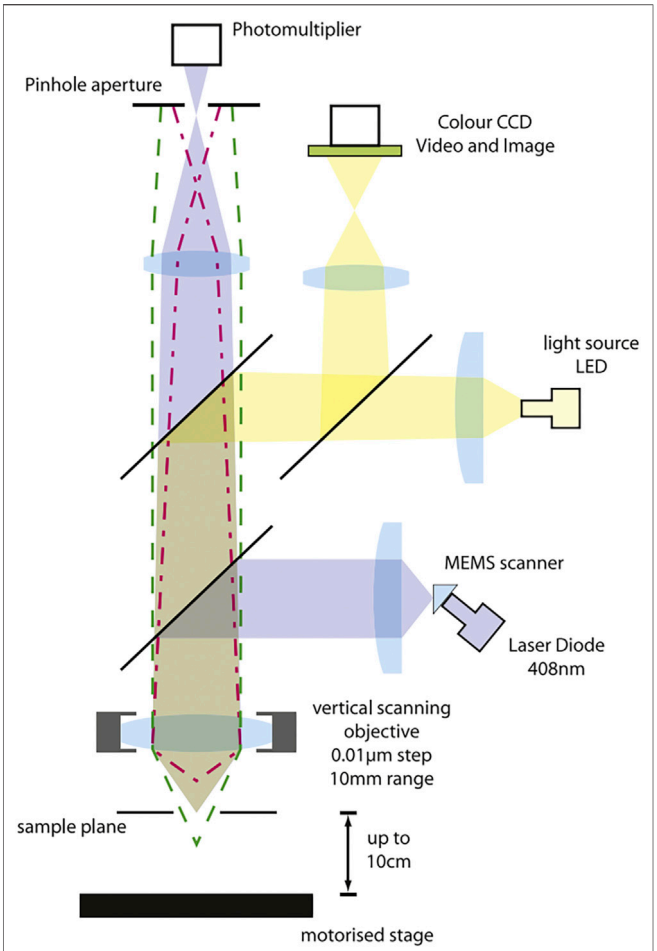

FIGURE 4 | Principle diagram of laser confocal scanning microscope (Evans and Donahue, 2008).

microscope is shown in **Figure 1** cited from JP Dunn's article in 2014.

Increasing the information dimension is one of the important directions to improving the traditional optical microscope. Polarization is an inherent property of light, which is more sensitive to microstructure. Through polarization measurement, we can obtain more sample information including light intensity (Wang et al., 2018; Wang et al., 2020). Therefore, realizing polarization measurement in a traditional microscope has unique advantages in detecting samples. This is the polarization microscope. The main structure of a polarization microscope is similar to that of a traditional optical microscope, but polarizers and analyzers are added into its optical path system to realize polarization measurement. The picture from J Chang's research article in 2016 is quoted in **Figure 2** to show the polarization microscope.

At the same time, it should be noted that a fluorescence microscope is another traditional optical principle-based microscope. Many materials fluoresce when exposed to a specifically engineered excitation light source, which is often ultraviolet, blue violet, or green light. Other non-fluorescent materials can be stained, and associated materials can then be monitored using UV light. Weixing Li et al. (2015) are cited in this study to demonstrate the structural properties of a low-temperature fluorescence microscope as shown in **Figure 3**.

It is worth noting that in recent years, with the advent of super-resolution fluorescence microscopy, fluorescence microscopy can get rid of the resolution of traditional optical microscopy. Photoactivated localization microscopy (PALM), stochastic optical reconstruction microscopy (STORM), and stimulated emission depletion (STED) are currently used to improve microscopic imaging in the direction perpendicular to light propagation, while STED-4 3D imaging and 3D SSIM imaging saturated structure illumination (SSIM) are used to improve microscopic imaging in the direction of light propagation. The resolution is at the nanoscale. It is widely used in the field of life science to observe the expression and embodiment of biological macromolecules and cellular functions in living cells at the molecular level.

It must be mentioned that laser scanning confocal microscopy has become one of the important microscopy tools nowadays. A laser scanning confocal microscope is a set of observation, analysis, and output systems. The key technology is conjugate focusing based on a traditional optical microscope. It consists primarily of a laser light source, an automatic microscope, a scanning module (which contains a confocal optical route channel and pinhole, a scanning mirror, and a detector), a digital signal processor, a computer, and also an image output device, among others. In **Figure 4**, there is an image from a research published by AA Evans in 2008 to show the structure and principle of laser scanning confocal microscopy.

2.2 Application of Optical Microscope in Micro- and Nanotechnology

2.2.1 Application of Traditional Optical Microscope

The imaging process in optical microscopy is nondestructive to the material. It is a reasonably simple observation technique, which can realize real-time imaging. The contemporary conventional optical microscope, however, has fewer applications at the nanoscale scale than other microscopes because its resolution is limited by light diffraction, and its applications are mostly centered on the micron size. Traditional optical microscopy is still one of the most important detection tools in the field of life sciences and clinical medicine because of the advantages of non-destructive observation of samples, real-time imaging, and a relatively simple observation process. In a study published in 2015, Fu Rong et al. used urine routine combined with optical microscopy for morphological examination of urine erythrocytes and thus for early diagnosis of Alport syndrome (Rong et al., 2015). R Hauser et al. investigated the effect of optical and tracking features on the accuracy of an optical microscope guidance system used in sinus surgery in 1999 (Hauser and Westermann, 1999). In addition, Kamimura, Shinji et al., in their study in 1987, proposed a method of using a prism to divide the pinhole magnified image of optical microscope into two parts and directly measuring the nano displacement by measuring the light intensity difference

(Kamimura, 1987). At the same time, as one of the branches of optical microscope, metallographic microscope also plays an important role in the detection of metal and rock structure. The findings of a study conducted by B Szala et al. (2013) using metallographic microscopy for the observation of corroded cross-sectional layers revealed that in addition to reacting to the color and thickness of the corroded layer, metallographic microscopy can also try to determine the crystal structure generated, while the location of inclusions, cracks, and blisters in the sample will help to determine the history of the sample (Szala et al., 2013).

2.2.2 Application of Near-Field Scanning Optical Microscope

The NSOM successfully breaks the resolution limit of traditional optical microscope by detecting evanescent waves containing object details. Near-field scanning optical microscope has made significant advances in theory and practice, and is now being used in micron and nanotechnology. In a study published in 2002, RS Decca, Lee, and others proposed a system for tracking single molecules using a near-field scanning optical microscope (Decca et al., 2002). Meanwhile, AL Campillo's group reported in 2001 plotting light intensity distribution in photonic crystals using a near-field scanning optical microscope (Campillo et al., 2001). In addition, progress has been achieved in the application of near-field scanning optical microscopes in biomedicine. CI Smith et al. (2018) used a quantum cascade laser in combination with an infrared aperture near-field scanning optical microscope to dramatically improve the capacity to identify esophageal cancer cells (Smith et al., 2018). It is believed that with the development of near-field optics, near-field optical microscopy will play a greater role in the micro- and nanotechnology.

2.2.3 Application of Polarization Microscope

At present, polarized light microscope is playing a unique role in life science and material science. The polarization microscope is useful in biological studies because different biological tissues and even distinct proteins have variable polarization characteristics (He et al., 2021). In a 2016 study, J Chang et al. used a polarization microscope based on the DoFP polarimeter to examine living tissue samples (Chang et al., 2016). The results demonstrated that the DoFP polarimeter-based polarization microscope could monitor the dynamic process of biological samples in real time. It is reasonable to believe that this study will play an important role in the exploration of disease pathology in the future. At the same time, the polarization microscope also plays a unique role in material science. In 2019, Y Saito employed polarization Raman microscopy to assess the longitudinal strain of an epitaxial graphene monolayer on a Sic substrate, and the results revealed that polarization Raman microscopy could accurately assess the local stress of two-dimensional atomic materials (Saito et al., 2019).

2.2.4 Application of Fluorescence Microscope

The fluorescent microscope is now employed in a variety of fields. Fluorescence microscopes are employed in biological molecular identification and genetic engineering in life science. Takao et al. examined the interior structure of a single DNA molecule employing optics under a fluorescent microscope in 2016. This research will be used to inform future DNA microstructure design (Takao et al., 2016). Fluorescence microscopy has also been used in material science at the same time. CAJ Putman et al. observed and imaged films LB using AFM and fluorescence microscopy in 2017 (Takao et al., 2016). The atomic force microscope and fluorescence microscopy are combined to consider the fluorescence microscope's target localization and selection function as well as the atomic force microscope's high-resolution imaging function. In the future, this combination will be used to create a new high-resolution imaging tool. For the examination of cell submicroscopic structure, super-resolution fluorescence microscopy is commonly used. In 2017, Matthew et al. employed super-resolution fluorescence microscopy to investigate the kinds and content of proteins during yeast division (Matthew et al., 2017).

2.2.5 Application of Laser Confocal Scanning Microscope

Laser confocal scanning microscopes are now widely employed in sectors such as life sciences and materials science. Especially for life sciences, it has become an important research tool in the frontier research of life sciences. In a previous study, PJ Verschure applied laser confocal scanning microscopy to cartilage research in 1997. Their findings suggest that in the future, the application of laser confocal scanning microscopy will be important for studying the *in situ* immunolocalization of factors associated with joint pathology in intact cartilage (Verschure et al., 1997). In 2017, S Mursalimov's team applies laser confocal scanning microscopy to analyze cell fusion studies in tobacco microspore cells. This study has provided the first 3D analysis of the cytological pattern of cell fusion in uncompressed cells. The results not only support the accuracy of results provided by other prior microscopy methods, but they also provide additional evidence that cell fusion is not caused by cell mechanics. This research will be useful for future cell fusion research (Mursalimov et al., 2019).

3 ELECTRON MICROSCOPE

3.1 Transmission Electron Microscope

3.1.1 Introduction to Transmission Electron Microscope

According to the calculation results of Abbe's formula, the limit of the resolution of traditional optical microscopes is about 0.2 microns, which limits further exploration of the microscopic world by human beings. People began to recognize that electron microscope resolution might theoretically reach the atomic level as their understanding of electron characteristics improved, especially after the publication of de Broglie's theory of matter waves in 1927. The interaction of electrons with solids is the fundamental premise of TEM. The TEM emits a beam of electrons to the sample under test while it operates in vacuum. Electrons scatter elastic and inelastic information as they move

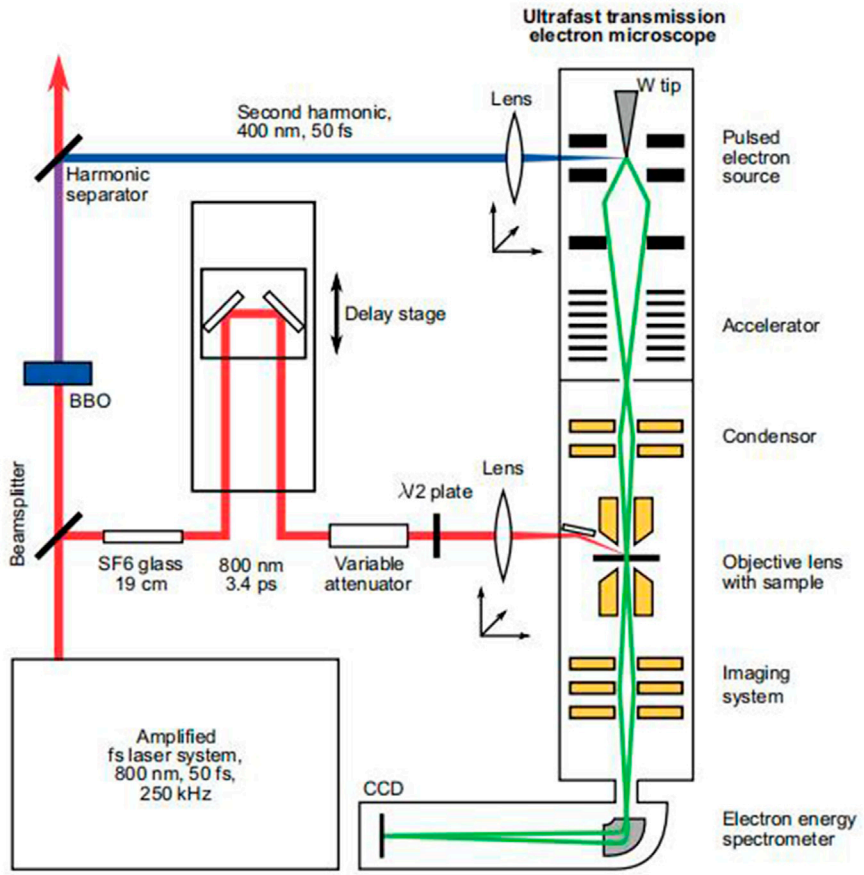

FIGURE 5 | TEM principle diagram (Feist et al., 2015).

through the material. TEM can capture and extract information from dispersed electrons. In 2015, a Feist team published a work that included the TEM concept. The following illustration is taken from this study (Feist et al., 2015) to illustrate the TEM principle (**Figure 5**).

3.1.2 Application of Transmission Electron Microscope

The most modern transmission electron microscopes now available have a spatial resolution of sub-angstroms, or less than 0.1 nm, with an energy resolution of more than 0.1 eV (Feist et al., 2015). The chemical composition and electronic structure of samples can also be determined using the energy spectrum, in addition to diffraction and imaging (Yang et al., 2014). Therefore, transmission electron microscopy is widely used in nanotechnology to observe the surface morphology, as well as to measure particle size and dispersion in the matrix. In a study, Christian et al. (2016) used a transmission electron microscope to tomography of cellulose nanocrystals aerogel, revealing the nanocrystalline aerogel of CNC′s detailed arrangement. This study will contribute to the further study of the properties of nanocrystal aerogel and its future applications (Buesch et al., 2016). Penetrating electron microscopy has been utilized to measure the physical properties of materials at the same time. In a study, P. Schattschneider et al. (2006) used transmission electron microscopy to identify magnetic circular dichroism. The combination of EMCD and TEM has been proposed as a critical microscopic approach for spintronics and nanomagnetism (Schattschneider et al., 2006). The TEM has been widely used in life science, particularly in the study of cell submicroscopic structures and biological macromolecules, as well as in the observation of life processes. In 2009, GB Chapman used transmission electron microscope TEM to observe the retina of zebrafish, and the results strongly support zebrafish as a vertebrate visual model, which is a useful tool for the study of vertebrates (Chapman et al., 2009). In 2018, J Abbas observed the antimalarial activity of bicolor calcification and heme crystal *in vitro* using TEM, which will contribute to the research and development of new antimalarial drugs (Abbas et al., 2018).

3.2 Scanning Electron Microscope

3.2.1 Introduction to Scanning Electron Microscope

With its ultrahigh resolution, the TEM, as the first invented electron microscope, has been widely employed. However, because scattering electrons are utilized to see things in TEM, there is some damage to the sample during observation, limiting its usage. The scanning electron microscope was created as the theory of electron microscopy progressed. A sample is scanned by

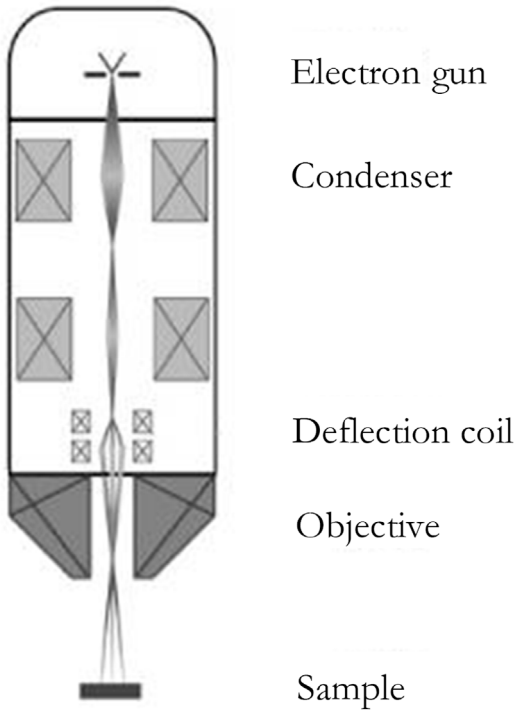

FIGURE 6 | structure of the SEM (Chen et al., 2013).

a focused electron beam in scanning electron microscopy, which produces secondary or backscattered electrons as it contacts the material. SEM detects these electrons and converts them into pictures on the sample surface, which can be used to determine the particle size of nanoparticles (James et al., 2010). A secondary electron is a type of free electron created when an electron beam is used to bombard a sample, separating the atom's outer electrons from the atom. The energy of the secondary electron is typically less than 50 eV. Secondary electron imaging (SEI) can analyze the sample surface with a high resolution of 1 nm since secondary electrons are created extremely close to the sample surface (usually 5–10 nm away from the surface) (Yan et al., 2018), as seen in **Figure 6** (Chen et al., 2013) and **Figure 7**.

3.2.2 Application of Scanning Electron Microscope

Advanced SEM measurement resolution can currently exceed 1 nm. In the realm of nanotechnology, SEM is used to assess the particle size of nanoparticles as well as their chemical composition. Simultaneously, scanning electron microscopy has been used in geological research to investigate the microstructure of rocks and soil, as well as the morphology and formation mechanism of crust. A work by Y Chen et al. (1980) used SEM to examine a soil sample. The findings demonstrate that observing crust morphology and development mechanisms using SEM on soil is beneficial. It has a significant impact on geology (Chen et al., 1980). JL Pilote studied the relative enrichment time of gold in volcanic massive sulfide deposits using scanning electron microscope mineral liberation analysis (SEM-MLA) in 2016, contributing

FIGURE 7 | High-resolution scanning electron microscope (Amirthapandian, 2010).

to the research of deposit formation (Pilote et al., 2016). In the biomedical field, in addition to the traditional structure observation research direction, SEM has been applied in some research directions, which is emerging. In the biomedical field, RM Jarvis with Raman spectroscopy in a 2004 study interface of the scanning electron microscope (SEM) of bacterial surface-enhanced Raman spectra, which can identify the bacteria identification and characterization of a breakthrough in the study, laid the foundation for future single-cell level research (Jarvis et al., 2004). In a study, Zavialova et al. (2017) used scanning electron microscopy to reconstruct the ultrastructure of spore filaments, which will contribute to the structural analysis of fossilized macrospores (Zavialova and Karasev, 2017) and the combination of scanning electron microscopy and transmission electron microscope. Because SEM captures secondary electrons for image rendering, the imaging depth of field and visual field effect are good, allowing for clear images of the item to be measured using surface topography.

3.3 Scanning Transmission Electron Microscopy

3.3.1 Introduction to Scanning Transmission Electron Microscopy

Crewe et al. (1968) pioneered field emission scanning transmission electron microscopy research, combining the advantages of the scanning electron microscope and transmission electron microscope, and using a field emission electron cannon as an electron source, considerably improving microscopic performance. In materials science and life science, scanning transmission electron microscopy has become a useful instrument.

3.3.2 Application of Scanning Transmission Electron Microscopy

Because scanning transmission electron microscopy has a higher resolution, it has become an important experimental apparatus in the field of nanotechnology for information such as the structure of

FIGURE 8 | Scanning tunneling microscope (Snv et al., 2020)

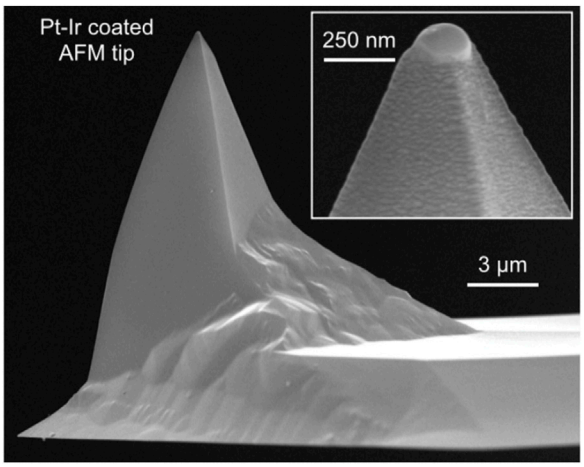

FIGURE 10 | SEM image of AFM platinum-iridium layer probe (Kim et al., 2015).

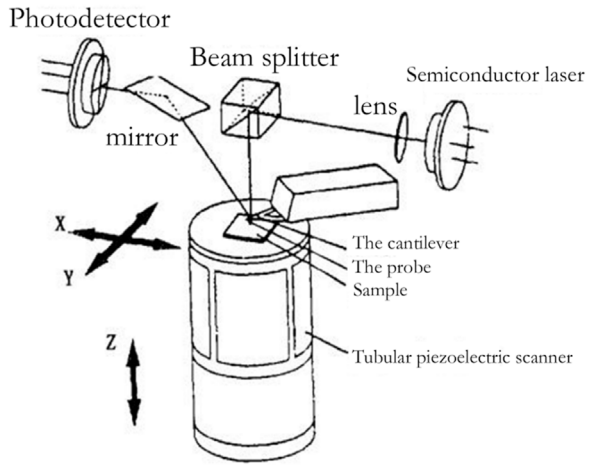

FIGURE 9 | Schematic diagram of atomic force microscopy (Zhang, 2002).

nanoparticles and the structural design of auxiliary nanomaterials. At the same time, scanning transmission electron microscopy is an important experiment instrument for the growth of nanocrystalline processes. In 2015, AV Levlev et al. used *in situ* liquid scanning transmission electron microscopy to study the growth process of platinum nanocrystals, which is important for optimizing nanocrystal preparation conditions and nanostructure synthesis (Ievlev et al., 2015). Masahiro Kawasaki et al. used scanning transmission electron microscopy to view graphite carbon nitride nanocomposite powder for a study in 2015, which will aid in the development of anode materials for high-energy lithium batteries (Kawasaki et al., 2015). On the other hand, scanning transmission electron microscopy is critical for microbial identification and observation of cell submicroscopic life activities. The microstructure of ferritin was studied using scanning transmission electron microscopy by N Jian et al. (2016). This research will aid in a better understanding of the iron nanoparticle formation mechanism in ferritin. Simultaneously, a medicine delivery system based on ferritin, as well as tailored treatment strategies for the disease (Jian et al., 2016).

4 SCANNING PROBE MICROSCOPE

4.1 Scanning Tunneling Microscope

4.1.1 Introduction to Scanning Tunneling Microscope

With the continuous maturity and improvement of the theory of probe-principle microscopy, the scanning tunneling microscope was invented in 1980s. The probe is used by the STM to approach the surface of the item to be examined. At this time, due to its quantum mechanical properties, the electron will have the probability of quantum tunneling at the tip of the needle and the atomic surface constituting the object to be measured, and then produce electric current. The surface topography of the object can be examined by detecting the current. The invention of the scanning tunneling microscope is a milestone, giving humans the first opportunity to observe the arrangement of individual atoms on the surface of an object in real time. When the temperature falls below 4°C, the scanning tunneling microscope can be utilized as a processing tool to move individual atoms. Scanning tunneling microscopes are now widely employed in domains such as surface science, material science, and biological science. A laboratory scanning tunneling microscope image from SNV A research (Snv et al., 2020) is quoted here as a demonstration (**Figure 8**).

4.1.2 Application of Scanning Tunneling Microscope

Because it can directly detect the arrangement of atoms in the sample, the scanning tunneling microscope (STM) is currently widely employed in material research. At the same time, because the resolution of scanning tunneling microscopy reaches a single atom, it is employed as a detection method in nanotechnology to determine the particle size of nanoparticles. SNV A used a scanning

TABLE 1 | Summary of the characteristics of all the microscopes mentioned in the study.

	Resolution	Work environment	Principle
Traditional optical microscope	0.2 μm	Atmospheric	Optical principle
Near-field scanning optical microscope	60–100 nm	Atmospheric	Near-field optics
Polarization microscope	0.2 μm	Atmospheric	Polarization optics
Fluorescence microscope	0.2 μm	Atmospheric	Fluorescence of the sample to be measured using UV excitation
Laser confocal scanning microscope	0.12 μm	Atmospheric	Laser scanning
Transmission electron microscope	0.2 nm	Vacuum	Collecting transmission electrons for imaging
Scanning electron microscope	1 nm	Vacuum	Collecting secondary electrons for imaging
Scanning transmission electron microscopy	1 nm	Vacuum	Collecting scattered electrons for imaging
Scanning tunneling microscope	0.2 nm	Vacuum	Exploiting the tunneling effect in quantum theory
Atomic force microscope	0.1 nm	Vacuum	Detecting changes in atomic forces on the surface of the object to be measured using a probe

tunneling microscope to observe gold nanoparticles made by the sputtering approach in 2020 and went on to conduct nanotechnology research (Snv et al., 2020). STM can also be utilized as a processing tool, which is particularly useful in nanotechnology. S Tjung et al. (2017) used scanning tunneling microscopy to carry out crystallization hydrogenation of graphene and studied the nanocrystalline structure produced by crystallization hydrogenation (Tjung et al., 2017), which will contribute to the processing and operation of scanning tunneling microscopy to process nanocrystals in the future. We have reason to anticipate that as scanning tunneling microscope (STM) applications continue to be researched, STM will become a key detection and processing tool for current promising emerging technologies such as nanotechnology (**Figure 9**).

4.2 Atomic Force Microscope

4.2.1 Introduction to Atomic Force Microscope

With the invention of the scanning tunneling microscope, the probe microscope has become a new type of high-precision microscope. In 1986, G. Binning invented AFM using the STM probe measurement method. AFM currently has a bright future (Jie and Sun, 2005). The basic concept of AFM and the microstructure of an AFM probe under SEM observation are depicted in **Figure 10**.

Because the atomic force between atoms is a function of distance, measuring the atomic force of individual atoms can be used to determine the surface topography of samples. The atomic force microscope measures the atomic force on the sample surface through the probe. When the atomic force changes, the probe produces a small deformation relative to the initial state, which is amplified and transmitted to the position sensitive detector (PSD) through the optical lever, so as to convert the surface morphology signal of the sample into an electrical signal. Through continuous measurement, the morphology, particle size, chemical composition, and other characteristics of the sample to be tested are finally obtained.

4.2.2 Application of Atomic Force Microscope

As one of the few tools that directly utilize atomic force, AFM has a resolution up to the atomic level, while the scanning tunneling microscope can arrange and process atoms at low temperatures. The atomic force microscope is now widely used in life science, material science, and other disciplines. The atomic force microscope (AFM) is an important tool in nanotechnology for detecting the particle size and chemical composition of nanoparticles as well as processing them. M Kim used an atomic force microscope to manipulate and assemble super-spherical AuNPs in 2015, resulting in supramolecules with uniform structure. Hyperspherical AuNPs' dependable and deterministic operation will increase the accessibility of supramolecular bases and improve spatial positioning precision (Tjung et al., 2017). H Jin et al. (2016) used atomic force microscopy to detect the ultrastructure of erythrocytes of patients with type 2 diabetes and erythrocytes affected by aging in their research on type 2 diabetes, and found the difference in ultrastructure. This research will help us better understand the pathogenesis of type 2 diabetes from the ultrastructural level of red blood cells (Jin et al., 2016), and combined with this technology, it may be possible for forensics to use atomic force microscopy to judge the age of the deceased in the future.

5 CONCLUSION

From the perspective of development, this study systematically summarizes the development of microscopic imaging technology, and the principles, characteristics, and applications of various technologies in the field of micro-nanoscience as shown in the following table. The development of micro-imaging technology has greatly promoted the development of micro-nanoscience, and the human exploration demand in the field of micro-nanoscience also drives the development of micro-imaging technology. At present, the lower resolution limit of the traditional optical microscope is not enough to support the needs of micro-nanotechnology. The polarization microscope, fluorescence imaging microscope, and super-resolution microscope developed on the basis of the traditional optical microscope have brought new possibilities for further tapping the

application potential of the optical microscope in micro-nanoscience. Although the resolution of an electron microscope is higher than that of a traditional optical microscope, its application environment must be vacuum. The resolution of the probe microscope reaches the atomic level, but the imaging speed is relatively slow. With the deepening of human understanding of the micro field, the requirements for micro-imaging technology will be higher and higher. Higher resolution, fewer environmental restrictions, and faster imaging speed will be the development direction of the new generation of the micro-imaging technology, which will be the breakthrough for the further development of micro-nanotechnology, and worth more energy from scientists, **Table 1**.

AUTHOR CONTRIBUTIONS

YW is responsible for overall guidance and thesis revision. XZ and JX are responsible for literature research and sorting. XZ, HL, and YL are responsible for professional guidance. XS, JT, XH, XK, ZW, JY, and YS are responsible for the revision of the manuscript.

FUNDING

Natural Science Foundation of Shandong Province, China, No. ZR2020QA078; National Natural Science Foundation of China, No. 12005110; Institute of Scientific and Technical Information of China, No. QN2022-03.

REFERENCES

Abbas, J., Ma'Mun, S., Tamura, H., and Purnomo, M. (2018). *In Vitro* antimalarial Activity of calophyllum Bicolor and Hemozoin Crystals Observed by Transmission Electron Microscope (Tem). *MATEC Web Conf.* 154, 04004. doi:10.1051/matecconf/201815404004

Amirthapandian, S., Schuchart, F., and Bolse, W. (2010). A High Resolution Scanning Electron Microscope for *In Situ* Investigation of Swift Heavy Ion Induced Modification of Solid Surfaces. *Rev. Sci. Instrum.* 81 (3), 3645. doi:10.1063/1.3316803

Buesch, C., Smith, S. W., Eschbach, P., Conley, J. F., and Simonsen, J. (2016). The Microstructure of Cellulose Nanocrystal Aerogels as Revealed by Transmission Electron Microscope Tomography. *Biomacromolecules* 17 (9), 2956–2962. doi:10.1021/acs.biomac.6b00764

Campillo, A. L., Hsu, J. W. P., White, C. A., and Rosenberg, A. (2001). Mapping the Optical Intensity Distribution in Photonic Crystals Using a Near-Field Scanning Optical Microscope. *J. Appl. Phys.* 89 (5), 2801–2807. doi:10.1063/1.1343898

Chang, J., He, H., He, C., and Ma, H. (2016). DoFP Polarimeter Based Polarization Microscope for Biomedical Applications. *SPIE BiOS* 2016, 10896. doi:10.1117/12.2210896

Chapman, G. B., Tarboush, R., Eagles, D. A., and Connaughton, V. P. (2009). A Light and Transmission Electron Microscope Study of the Distribution and Ultrastructural Features of Peripheral Nerve Processes in the Extra-retinal Layers of the Zebrafish Eye. *Tissue Cell* 41 (4), 286–298. doi:10.1016/j.tice.2008.12.003

Chen, M., Gao, W., Yong, Z., and Feng, S. (2013). Structure and Maintenance of Scanning Electron Microscope. *Anal. Instrum.* 2013, 5018. doi:10.11779/CJGE202105018

Chen, Y., Tarchitzky, J., Brouwer, J., Morin, J., and Banin, A. (1980). Scanning Electron Microscope Observations on Soil Crusts and Their Formation. *Soil Sci.* 130 (1), 49–55. doi:10.1097/00010694-198007000-00008

Decca, R. S., Lee, C.-W., Lall, S., and Wassall, S. R. (2002). Single Molecule Tracking Scheme Using a Near-Field Scanning Optical Microscope. *Rev. Sci. Instrum.* 73 (7), 2675–2679. doi:10.1063/1.1482153

Dunn, J. P. (2009). A Near-Field Scanning Optical Microscope: Construction and Operation. Master's Thesis. Austin, TX: The University of Texas at Austin. *Near-field Scanning Opt. Microsc.* 2014.

Evans, A. A., and Donahue, R. E. (2008). Laser Scanning Confocal Microscopy: A Potential Technique for the Study of Lithic Microwear. *J. Archaeol. Sci.* 35 (8), 2223–2230. doi:10.1016/j.jas.2008.02.006

Feist, A., Echternkamp, K. E., Schauss, J., Yalunin, S. V., Schäfer, S., and Ropers, C. (2015). Quantum Coherent Optical Phase Modulation in an Ultrafast Transmission Electron Microscope. *Nature* 521 (7551), 200–203. doi:10.1038/nature14463

Hauser, R., and Westermann, B. (1999). Optical Tracking of a Microscope for Image-Guided Intranasal Sinus Surgery. *Ann. Otol. Rhinol. Laryngol.* 108 (1), 54–62. doi:10.1177/000348949910800108

He, C., He, H., Chang, J., Chen, B., Ma, H., and Booth, M. J. (2021). Polarisation Optics for Biomedical and Clinical Applications: a Review. *Light Sci. Appl.* 10 (11), 20. doi:10.1038/s41377-021-00639-x

Ievlev, A. V., Jesse, S., Cochell, T. J., Unocic, R. R., Protopopescu, V. A., and Kalinin, S. V. (2015). Quantitative Description of Crystal Nucleation and Growth from *In Situ* Liquid Scanning Transmission Electron Microscopy. *Acs Nano, acsnano* 2015, 5b03720. doi:10.1021/acsnano.5b03720

James, E. M., Yang, Y., Lin, M., Gubbens, A. J., and Petric, P. (2010). Apparatus and Method for Obtaining Topographical Dark-Field Images in a Scanning Electron Microscope. *US* 2010, 14287.

Jarvis, R. M., Brooker, A., and Goodacre, R. (2004). Surface-enhanced Raman Spectroscopy for Bacterial Discrimination Utilizing a Scanning Electron Microscope with a Raman Spectroscopy Interface. *Anal. Chem.* 76 (17), 5198–5202. doi:10.1021/ac049663f

Jian, N., Dowle, M., Horniblow, R. D., Tselepis, C., and Palmer, R. E. (2016). Morphology of the Ferritin Iron Core by Aberration Corrected Scanning Transmission Electron Microscopy. *Nanotechnology* 27 (46), 46LT02. doi:10.1088/0957-4484/27/46/46LT02

Jie, Z., and Sun, R. (2005). Introduction to Atomic Force Microscope and its Manipulation. *Life Sci. Instrum.* 38, 76. doi:10.3969/j.issn.1671-7929.2005.01.006

Jin, H., Xing, X., Zhao, H., Yong, C., and Cai, J. (2016). Detection of Erythrocytes Influenced by Aging and Type 2 Diabetes Using Atomic Force Microscope. *Biochem. Biophys. Res. Commun.* 391 (4), 1698–1702. doi:10.1016/j.bbrc.2009.12.133

Kamimura, S. (1987). Direct Measurement of Nanometric Displacement under an Optical Microscope. *Appl. Opt.* 26 (16), 3425–3427. doi:10.1364/ao.26.003425

Kawasaki, M., Sompetch, K., Sarakonsri, T., and Shiojiri, M. (2015). Scanning Transmission Electron Microscopy Analysis of Ge(o)/(graphitic Carbon Nitride) Nanocomposite Powder. *US* 110, 60–67. doi:10.1016/j.matchar.2015.10.015

Kim, M., Lee, S., Lee, J., Kim, D. K., Hwang, Y. J., Lee, G., et al. (2015). Deterministic Assembly of Metamolecules by Atomic Force Microscope-Enabled Manipulation of Ultra-smooth, Super-spherical Gold Nanoparticles. *Opt. Express* 23 (10), 12766–12776. doi:10.1364/OE.23.012766

Li, W., Stein, S. C., Gregor, I., and Enderlein, J. (2015). Ultra-stable and Versatile Widefield Cryo-Fluorescence Microscope for Single-Molecule Localization with Sub-nanometer Accuracy. *Opt. Express* 23 (3), 3770–3783. doi:10.1364/oe.23.003770

Matthew, A., Lin, Y., Joerg, B., Bewersdorf, A., et al. (2017). Analysis of Interphase Node Proteins in Fission Yeast by Quantitative and Superresolution Fluorescence Microscopy. *Mol. Biol. Cell* 28 (23), 3203–3214. doi:10.1091/mbc.E16-07-0522

Mursalimov, S., Sidorchuk, Y., and Deineko, E. (2017). Analysis of Cytomixis in Tobacco Microsporocytes With Confocal Laser Scanning Microscopy. *Protoplasma* 254 (1), 539–545. doi:10.1007/s00709-016-0973-z

Pilote, J. L., Piercey, S. J., Brueckner, S. M., and Grant, D. (2016). Resolving the relative timing of au enrichment in volcanogenic massive sulfide deposits using scanning electron microscopy-mineral liberation analyzer: empirical evidence

from the ming deposit, newfoundland, canada. *Econ. Geol.* 111 (6), 1495–1508. doi:10.2113/econgeo.111.6.1495

Rong, F. U., Qing-Yan, W. U., Liu, J., Gou, M. F., Tong, S. F., Jun-Jie, H. E., et al. (2015). Evaluation of Routine Urine Check with Optical Microscopy Measuring Urinary Erythrocyte Morphology in Early Diagnosis of Alport Syndrome in Seven Families. *J. Xinxiang Med. Univ.* 2015. doi:10.7683/xxyxyxb.2015.09.022

Saito, Y., Tokiwa, K., Kondo, T., Bao, J., Terasawa, T.-o., Norimatsu, W., et al. (2019). Longitudinal Strain of Epitaxial Graphene Monolayers on SiC Substrates Evaluated by Z-Polarization Raman Microscopy. *AIP Adv.* 9 (6), 065314. doi:10.1063/1.5099430

Schattschneider, P., Rubino, S., Hébert, C., Rusz, J., Kuneš, J., Novák, P., et al. (2006). Detection of Magnetic Circular Dichroism Using a Transmission Electron Microscope. *Nature* 441 (7092), 486–488. doi:10.1038/nature04778

Smith, C. I., Siggel-King, M. R. F., Ingham, J., Harrison, P., MartinMartinVarro, D. S., Varro, A., et al. (2018). Application of a Quantum Cascade Laser Aperture Scanning Near-Field Optical Microscope to the Study of a Cancer Cell. *Analyst* 143 (24), 5912–5917. doi:10.1039/C8AN01183D

Snv, A., Tnr, A., and Pv, B. (2020). Investigation on Nanoscale Imaging of Gold Sputtered Sample by Scanning Tunneling Microscope. *Mater. Today Proc.* 22 (1), 2439–2445. doi:10.1016/j.matpr.2020.03.370

Szala, B., Greiner-Wronowa, E., and Kwaśniak-Kominek, M. (2013). Analysis of Cross-Sectional Layers of Corrosion Using Metallographic Microscope. *Geol* 39 (2), 125–132. doi:10.7494/geol.2013.39.2.125

Takao, H., Suzuki, T., Oana, H., Washizu, M., and Masuda, C. (2016). Characterisation of Optically Driven Microstructures for Manipulating Single Dna Molecules under a Fluorescence Microscope. *Iet Nanobiotechnology* 10 (3), 124. doi:10.1049/iet-nbt.2015.0036

Tjung, S., Hollen, S., Gambrel, G., Santagata, N., Johnstonhalperin, E., and Gupta, J. (2017). Crystalline Hydrogenation of Graphene by Scanning Tunneling Microscope Tip-Induced Field Dissociation of H2. *Carbon* 124. doi:10.1016/j.carbon.2017.07.044

Verschure, P. J., Marle, J. V., Noorden, C., and Berg, W. (1997). The Contribution of Quantitative Confocal Laser Scanning Microscopy in Cartilage Research: Chondrocyte Insulin-Like Growth Factorreceptors in Health and Pathology. *Microsc. Res. Tech.* 37 (4), 285–298. doi:10.3969/j.issn.1672-7916.2002.03.002

Wang, Y., Liao, R., Dai, J., Liu, Z., Xiong, Z., Zhang, T., et al. (2018). Differentiation of Suspended Particles by Polarized Light Scattering at 120°. *Opt. express* 26 (17), 22419–22431. doi:10.1364/OE.26.022419

Wang, Y., Dai, J., Liao, R., Zhou, J., Meng, F., Yao, Y., et al. (2020). Characterization of Physiological States of the Suspended Marine Microalgae using Polarized Light Scattering. *Appl. Opt.* 59 (5), 1307–1312. doi:10.1364/AO.377332

Yan, L., Zhong, J., Tang, X., and Li, D. Y. (2018). The Principle and Application of Scanning Electron Microscope. *Shandong Chem. Ind.* 2018, 113–145. doi:10.19319/j.cnki.issn.1008-021x.2018.09.033

Yang, H. X., Jun, L. I., Zhang, Y., Chao, M. A., and Jian-Qi, L. I. (2014). Modern Transmission Electron Microscopy and its Application to Multiferroic Materials. *Physics* 42 (2), 105–116. doi:10.7693/wl20140204

Zavialova, N., and Karasev, E. (2017). The Use of the Scanning Electron Microscope (Sem) to Reconstruct the Ultrastructure of Sporoderm. *Palynology* 41 (1-2), 89–100. doi:10.1080/01916122.2015.1093560

Zhang, D. (2002). The Development for Atomic Force Microscopy Recently and the Brief Introduction of Application. *Mod. Instrum.* 102, 6–9. doi:10.3969/j.issn.1672-7916.2002.03.002

Conflict of Interest: The authors declare that the research was conducted in the absence of any commercial or financial relationships that could be construed as a potential conflict of interest.

Publisher's Note: All claims expressed in this article are solely those of the authors and do not necessarily represent those of their affiliated organizations, or those of the publisher, the editors, and the reviewers. Any product that may be evaluated in this article, or claim that may be made by its manufacturer, is not guaranteed or endorsed by the publisher.

Copyright © 2022 Wang, Zhang, Xu, Sun, Zhao, Li, Liu, Tian, Hao, Kong, Wang, Yang and Su. This is an open-access article distributed under the terms of the Creative Commons Attribution License (CC BY). The use, distribution or reproduction in other forums is permitted, provided the original author(s) and the copyright owner(s) are credited and that the original publication in this journal is cited, in accordance with accepted academic practice. No use, distribution or reproduction is permitted which does not comply with these terms.

frontiers | Frontiers in Chemistry

ORIGINAL RESEARCH
published: 12 July 2022
doi: 10.3389/fchem.2022.936255

Analyzing the Influence of Imaging Resolution on Polarization Properties of Scattering Media Obtained From Mueller Matrix

Conghui Shao[1,2], *Binguo Chen*[2,3,4], *Honghui He*[2,3]*, *Chao He*[5]*, *Yuanxing Shen*[2,3,4], *Haoyu Zhai*[2,3,4] *and Hui Ma*[1,2,3]

[1]Department of Physics, Tsinghua University, Beijing, China, [2]Guangdong Research Center of Polarization Imaging and Measurement Engineering Technology, Shenzhen Key Laboratory for Minimal Invasive Medical Technologies, Institute of Optical Imaging and Sensing, Shenzhen International Graduate School, Tsinghua University, Shenzhen, China, [3]Institute of Biopharmaceutical and Health Engineering, Tsinghua Shenzhen International Graduate School, Tsinghua University, Shenzhen, China, [4]Department of Biomedical Engineering, Tsinghua University, Beijing, China, [5]Department of Engineering Science, University of Oxford, Oxford, United Kingdom

OPEN ACCESS

Edited by:
Yu Chen,
the University of Strathclyde,
United Kingdom

Reviewed by:
Arturo Mendoza-Galvan,
Cinvestav, Unidad Querétaro, Mexico
Baolei Liu,
Beihang University, China

***Correspondence:**
Honghui He
he.honghui@sz.tsinghua.edu.cn
Chao He
chao.he@eng.ox.ac.uk

Specialty section:
This article was submitted to Nanoscience, a section of the journal Frontiers in Chemistry

Received: 05 May 2022
Accepted: 09 June 2022
Published: 12 July 2022

Citation:
Shao C, Chen B, He H, He C, Shen Y, Zhai H and Ma H (2022) Analyzing the Influence of Imaging Resolution on Polarization Properties of Scattering Media Obtained From Mueller Matrix. Front. Chem. 10:936255. doi: 10.3389/fchem.2022.936255

The Mueller matrix contains abundant micro- and even nanostructural information of media. Especially, it can be used as a powerful tool to characterize anisotropic structures quantitatively, such as the particle size, density, and orientation information of fibers in the sample. Compared with unpolarized microscopic imaging techniques, Mueller matrix microscopy can also obtain some essential structural information about the sample from the derived parameters images at low resolution. Here, to analyze the comprehensive effects of imaging resolution on polarization properties obtained from the Mueller matrix, we, first, measure the microscopic Mueller matrices of unstained rat dorsal skin tissue slices rich in collagen fibers using a series of magnifications or numerical aperture (NA) values of objectives. Then, the first-order moments and image texture parameters are quantified and analyzed in conjunction with the polarization parameter images. The results show that the Mueller matrix polar decomposition parameters diattenuation D, linear retardance δ, and depolarization Δ images obtained using low NA objective retain most of the structural information of the sample and can provide fast imaging speed. In addition, the scattering phase function analysis and Monte Carlo simulation based on the cylindrical scatterers reveal that the diattenuation parameter D images with different imaging resolutions are expected to be used to distinguish among the fibrous scatterers in the medium with different particle sizes. This study provides a criterion to decide which structural information can be accurately and rapidly obtained using a transmission Mueller matrix microscope with low NA objectives to assist pathological diagnosis and other applications.

Keywords: Mueller matrix microscope, Monte Carlo simulation, fibrous structure, imaging resolution, polarization

INTRODUCTION

The polarization imaging approach has shown broad application potential in biomedical studies in recent years for its advantages of being noninvasive, label free, and sensitive to subwavelength structures (Alali and Vitkin, 2015; Qi and Elson, 2017; He C et al., 2019; He et al., 2021). The Mueller matrix, which characterizes the change of polarization state of light after light–matter interaction, contains rich microstructural information about the medium (Chen et al., 2020; Hu et al., 2020). However, it is often difficult to obtain specific microstructural information through individual Mueller matrix elements (He et al., 2022; Li et al., 2022). To further disentangle the information encoded in the Mueller matrix, the Mueller matrix polar decomposition (MMPD) method (Lu and Chipman, 1996; Ghosh et al., 2008) was proposed and prevalently used in the biomedical studies (Morio and Goudail, 2004) to derive a group of polarization parameters with clear physical meanings. These parameters can be applied on characterizing structure features of various abnormal tissue samples, such as liver fibrosis (Wang et al., 2016; Meng et al., 2021; Yao et al., 2022), breast ductal carcinoma (Dong and Qi, 2017; He H et al., 2019; Dong et al., 2021a), skin cancer (Steven et al., 2002; Jacques et al., 2002; Wood et al., 2009; Du et al., 2014), colon cancer and inflammatory bowel disease, cervical cancer (Sun et al., 2014; Dong et al., 2021b), and oral cancer (Chung et al., 2007). In addition, polarization imaging methods are particularly sensitive to fibrous structures in tissues, such as the location, density, and orientation arrangement of fibers at different stages of pathological tissue development (Dong and Qi, 2017; He H et al., 2019). Thus, the Mueller matrix-derived parameters can be used for differential diagnosis of Crohn's disease and intestinal luminal tuberculosis by various features in the distribution of fibers around the granuloma (Liu et al., 2019). Moreover, Mueller matrix polarimetry has also shown potential to quantitatively distinguish among different types of fibrous tissues, such as collagen fibers, connective tissues, and muscle fibers (Zhai et al., 2022).

For optical methods, higher resolution images provided by a high numerical aperture (NA) objective often give us more detailed microstructural information about the sample. However, the field of view (FOV) of the image provided by a high NA objective is smaller compared to that provided by a low NA objective, which means that the acquisition speed is slow for high-resolution images. When applied to clinical detection, the imaging speed should be considered in addition to the impact of imaging resolution. Some recent researches have shown that the polarization imaging method can better preserve the microstructural information of the sample when imaging resolution decreased compared to unpolarized optical imaging methods (Shen et al., 2020; Liu et al., 2021; Chen et al., 2022; Yao et al., 2022). It indicates that adopting the polarization imaging method can well balance the requirements of imaging resolution and FOV, to acquire the micro- and even nanostructural (Dong et al., 2020; Chen et al., 2021a; Wang et al., 2021; Fang et al., 2022) properties of the scattering medium quickly using a relatively low NA objective. In addition, to further obtain more quantitative information, many studies combined polarization parameters and image texture methods together to better distinguish characteristic tissue structures (Liu et al., 2019; Zhai et al., 2022). However, recent studies mainly investigated the influence of imaging resolution on linear retardance parameters reflecting orientation and density information of the fibrous structures, with less analysis of the influence on other Mueller matrix derived parameters revealing such as particle size information that may exist at nanoscale. Here, to further analyze the comprehensive effects of imaging resolution on polarization properties obtained from the Mueller matrix, namely diattenuation, linear retardance, and depolarization, we, first, measure the Mueller matrices of unstained rat dorsal skin tissue slices rich in collagen fiber using a transmission Mueller matrix microscope. The MMPD parameters D, δ, and Δ images of the sections are calculated at a series of magnifications of objectives with 4×/NA 0.10, 10×/NA 0.25, 20×/NA 0.40, 40×/NA 0.65, and 60×/NA 0.80. Then, the first-order moments and image texture parameters are quantified and analyzed in conjunction with the polarization parameter images. The results show that the MMPD parameters D, δ, and Δ images obtained using a low NA objective, such as 10×/NA 0.25, retain most of the structural information of the sample, and can provide fast imaging speed. In addition, the analysis based on the scattering phase function calculation of cylinders and the Monte Carlo simulation based on the cylindrical scatterers reveal that diattenuation parameter D images with different imaging resolutions are expected to be used to distinguish among the fibrous scatterers in a medium with different particle sizes. This study provides a criterion to decide which structural information can be accurately and rapidly obtained using a transmission Mueller matrix microscope with low NA objectives to assist pathological diagnosis and other applications.

MATERIALS AND METHODS

Setup and Samples

Figure 1 shows the schematic of this study. The transmission Mueller matrix microscope used in this study is based on the dual-rotating quarter-wave plate method (Goldstein, 1992). As shown in **Figure 1B**, the illuminating light from the light-emitting diode (Cree, 3W, 633 nm, $\Delta\lambda$ = 20 nm) is collimated by a lens, and then passes through the polarization states generator (PSG). Light carrying different polarization states transmits the sample and is collected by the objective lens at different magnifications. It is then analyzed by the polarization states analyzer (PSA) and focused on the CMOS camera (MV-CA016-10UM, 1,440 × 1,080 pixels, 12-bit, 3.45 μm × 3.45 μm pixel size, Hikvision, China) through an imaging lens. PSG and PSA have similar structures, both consisting of a linear polarizer fixed in the horizontal direction (extinction ratio 1000:1, Daheng Optics, China) and a rotatable quarter-wave plate (Daheng Optics, China) as shown in **Figure 1B**. In this setup, both PSG and PSA are driven to rotate thirty times by the servo motor drivers (PRM1Z8E, Thorlabs, United States) with the fixed

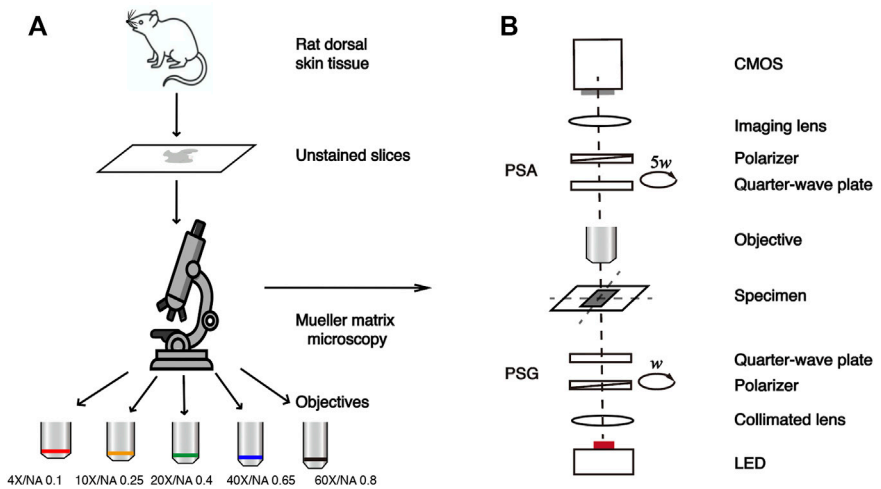

FIGURE 1 | Schematic of the study. **(A)** Flow chart of the experiment. **(B)** Schematic of the transmission Mueller matrix microscope.

rates ω and 5ω, respectively. Then the Mueller matrix elements can be calculated by using the Fourier coefficients (Azzam, 1978; Chenault et al., 1992). The Fourier series intensities are given as

$$I = \alpha_0 + \sum_{n=1}^{12} (\alpha_n \cos n\omega t + \beta_n \cos n\omega t), \quad (1)$$

where α_n and β_n are the Fourier coefficients. Before the measurement, the Mueller matrix microscope was calibrated using some standard samples such as air, polarizers, and retarders in different directions. The error is within 1% and the detailed calibration procedure can be found in (Zhou et al., 2018).

In this study, the samples are 6-μm-thick dewaxed, unstained slices of rat dorsal skin tissues, provided by the Experimental Research Center, China Academy of Chinese Medical Sciences. The rat dorsal skin tissue contains skeletal muscle fibers, connective tissues, and collagen fibers (Sun et al., 2018; Chen et al., 2021b; Zhai et al., 2022). Here we selected a total of 27 tissue regions rich in collagen fibers, which have prominent optical anisotropy as the experimental samples for the Mueller matrix measurement. The flow chart of this study is illustrated in **Figure 1A**.

Mueller Matrix Polar Decomposition

The polarization state of light can be changed after the scattering process, and the micro- and nanostructural information of the scattering sample can be reflected by measuring the Mueller matrix, which is a comprehensive description of polarization-related optical properties of the medium. However, the physical meanings of individual Mueller matrix elements are not clear. To develop associations between structural features and the elements, the MMPD method decomposes a Mueller matrix into three submatrices of major polarization properties: diattenuation matrix M_D, retardance matrix M_R, and depolarization matrix M_Δ as shown in **Eq. 2**. It is noted that M_{ij} (i,j = 1,2,3,4) in **Eq. 3** represents the corresponding Mueller matrix elements before decomposition, while M_R(i,j) (i,j = 2,3) and M_Δ in **Eqs (4)** and **(5)** represent the matrix elements in the 4 × 4 retardance matrix and the depolarization matrix, respectively. Here, the retardance can be further decomposed into circular retardance and linear retardance (Ghosh, Wood, and Vitkin, 2008), where δ is the magnitude of linear retardance. In this study, we adopt the MMPD-derived parameters D, δ, and Δ, which reflect diattenuation, the value of linear retardance, and the depolarization of tissue samples, respectively.

$$M = M_\Delta M_R M_D, \quad (2)$$

$$D = \sqrt{M_{12}^2 + M_{13}^2 + M_{14}^2}, \quad (3)$$

$$\delta = \cos^{-1}\left\{ \left[(M_R(2,2) + M_R(3,3))^2 + (M_R(3,2) + M_R(2,3))^2 \right]^{\frac{1}{2}} - 1 \right\}, \quad (4)$$

$$\Delta = 1 - \frac{|tr(M_\Delta) - 1|}{3}. \quad (5)$$

Image Analysis Method

During the Mueller matrix measurement of tissue sections, to ensure that the same area is detected by different magnification objectives, we only rotate the objective without changing the position of tissue slices. The field of view difference is calibrated by measuring the coordinate positions of the standard sample (calibration plate) in the same area under different magnification objectives.

To quantitatively investigate the effect of different magnifications on polarization microscopic imaging, we first compare MMPD D, δ, and Δ parameters images at the

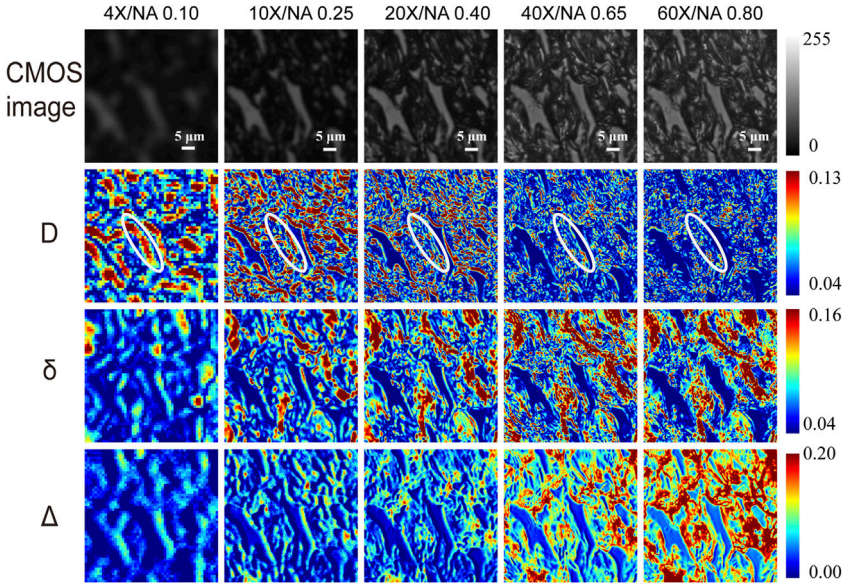

FIGURE 2 | The first row shows the unpolarized light intensity images of the unstained tissue slice under different magnification objectives (4×/NA 0.10, 10×/NA 0.25, 20×/NA 0.40, 40×/NA 0.65, and 60×/NA 0.80). The second to fourth rows show MMPD parameters *D*, *δ*, and *Δ* images of the same region under different magnification objectives. Where the area marked by the white elliptical line in the D images is an example of a coarse fibrous structure that is not clear under high NA but obvious under low NA. The unit for *δ* is radian angle. The white scale bar is 5 μm.

magnification objectives of 4×/NA 0.10, 10×/NA 0.25, 20×/NA 0.40, 40×/NA 0.65, and 60×/NA 0.80, as shown in **Figure 2**. Then, to further quantify the changes of the MMPD parameters at different magnification objectives, we use two first-order statistical moment parameters, the Mean and Entropy shown in **Eqs (6)** and **(7)** for evaluations, where $p(z_i)$ represents the ratio of the number of pixels with the value of z_i to the total number of the pixels.

$$\boldsymbol{Mean} = \sum_i \boldsymbol{z_i p(z_i)}, \tag{6}$$

$$\boldsymbol{Entropy} = -\sum_i \boldsymbol{p(z_i) log_2 p(z_i)}. \tag{7}$$

Additionally, we also choose the gray scale co-occurrence matrix (GLCM) method (Haralick et al., 1973), which has been demonstrated as a powerful tool for the Mueller matrix imaging results analysis in recent studies (Shen et al., 2020; Liu et al., 2021; Zhai et al., 2022), for the MMPD parameters comparisons. Here, the GLCM parameters Contrast, Correlation, Energy, and Homogeneity are adopted as shown in **Eqs 8–12**. For the analysis, the ranges of gray value for the parameters *D*, *δ*, and *Δ* images are normalized to [0,255], the gray levels N_g was set as 64, the inter-pixel displacement *d* was set to 1, 3, 5, 11, and 15 under 4×/NA 0.10, 10×/NA 0.25, 20×/NA 0.40, 40×/NA 0.65, and 60×/NA 0.80 objectives, respectively, to compensate the differences induced by the different FOV. $p(i, j)$ is the relative frequency of two adjacent pixels (gray level *i* and *j*, respectively) separated by an inter-pixel displacement (*d*) occurring in a specific direction on the image. μ_x, μ_y, σ_x, and σ_y are the mean and standard deviations of p_x and p_y, respectively. Contrast characterizes the local variation in GLCM, the higher the Contrast value, the better the ability to distinguish the various components of the image. Correlation is a measure of the correlation of a pixel with its neighboring pixels in the whole image. Energy characterizes the joint probability of the occurrence of a given pixel pair, reflecting the order in the image, a higher Energy value means a more uniform texture of the image. Homogeneity returns a value that measures the closeness of the distribution of elements in the co-occurrence matrix, reflecting the order of the local image.

$$\boldsymbol{p_x(i)} = \sum_{j=1}^{N_g} \boldsymbol{p(i,j)}\ \boldsymbol{p_y(j)} = \sum_{j=1}^{N_g} \boldsymbol{p(i,j)}, \tag{8}$$

$$\boldsymbol{Contrast} = \sum_{n=0}^{N_g-1} \boldsymbol{n^2} \left\{ \sum_{i=1}^{N_g} \sum_{j=1}^{N_g} \boldsymbol{p(i,j)} \middle| \boldsymbol{|i-j| = n} \right\}, \tag{9}$$

$$\boldsymbol{Correlation} = \frac{\sum_i \sum_j \boldsymbol{(ij)p(i,j) - \mu_x \mu_y}}{\boldsymbol{\sigma_x \sigma_y}}, \tag{10}$$

$$\boldsymbol{Energy} = \sum_i \sum_j \boldsymbol{p(i,j)^2}, \tag{11}$$

$$\boldsymbol{Homogeneity} = \sum_i \sum_j \frac{\boldsymbol{1}}{\boldsymbol{1 + (i-j)^2}} \boldsymbol{p(i,j)}. \tag{12}$$

Monte Carlo (MC) Simulation

To better understand the relationship between the micro- and nanostructural features observed at different magnifications and the Mueller matrix derived parameters, we use the MC simulation program based on the cylinder scattering model (CSM) developed in our previous studies (Yun et al., 2009; Guo et al., 2013; Li et al., 2016) to track the trajectories and polarization states of scattered photons as they propagate in the skin tissues (Chen et al., 2017;

Dong and He, 2017). The detailed parameters used in MC simulations will be introduced in the following sections.

RESULTS

To further analyze the influence of different magnifications, or the imaging resolutions on the polarization information acquired by Mueller matrix derived parameters, in this section the first-order statistical moments Mean and Entropy as well as the GLCM parameters Contrast, Correlation, Energy, and Homogeneous are used to quantify the MMPD D, δ, and Δ parameters.

Also, to compare the structural evaluation ability under different magnifications, the correlation of the Mean values between each of the two objectives is analyzed to characterize the similarity of the structure contained in the MMPD parameters. A higher R-value (the Pearson correlation coefficient) indicates a stronger correlation between the two sets of data, or in other words the more similar information contained in Mueller matrix images obtained by the two objectives. In addition, for a deeper understanding of the experimental results, we use the MC simulation, in which the fibers are simplified to infinitely long cylindrical scatters with different particle sizes and phase functions, to analyze the influence of collecting angle on Mueller matrix derived parameters.

Figure 2 shows the microscopic imaging results of a normal rat dorsal skin region that is abundant in collagen fibers at different magnifications. The first row from left to right shows the unpolarized light intensity images of unstained tissue sections under 4×/NA 0.10, 10×/NA 0.25, 20×/NA 0.40, 40×/NA 0.65, and 60×/NA 0.80 objective cases, respectively. The second, third, and fourth rows show the D, δ, and Δ images of 4×, 10×, 20×, 40×, and 60× for the same region, respectively. We can observe from the first row of **Figure 2** that unpolarized images obtained at high magnifications are significantly sharper and richer in microstructural information than those obtained at low magnifications. It is confirmed that a better imaging resolution can provide more structural details when using unpolarized light microscopy. However, for Mueller matrix microscopic imaging, our previous studies indicated that some structural information contained in the linear retardance δ parameter image is preserved well with the decline of imaging resolution or objective magnifications (Shen et al., 2020). We can also see from **Figure 2** that when the magnification decreases from 60× to 4×, the changes in MMPD parameters are different. For instance, for δ and Δ images, with the decreasing resolution, tiny fibrous structures become less obvious and lack some detailed information. On contrary, the regions containing coarse fibrous structures can be observed at low magnification, and we can see that they are composed of tiny fiber bundles at high magnification. However, this does not prevent us from being able to roughly obtain structural information such as fiber density and location from the low-resolution polarization images. It can also be noticed that the fibrous structures are not obvious in high magnification parameter D images, and detailed information on the fibers can be observed in low-resolution D images. For D images, the coarse fibrous structures marked with white elliptical lines in **Figure 2**, as an example, have lower values at high magnification, which are not obvious at high NA. The coarser fibrous structures are more visible at low magnification, and only some tiny fibrous structures can be observed at high NA. The results shown in **Figure 2** indicate that when tissue samples with certain polarization properties are analyzed, a criterion for choosing an appropriate objective magnification or NA value to achieve a balance between FOV and enough feature information extraction is crucial.

Analysis of Diattenuation

First, we analyze the MMPD diattenuation parameter D as shown in the second row of **Figure 2**. In previous studies, it was shown that D can also be used for describing the changes in the fibrous microstructures in tissues (Swami et al., 2006; Fan and Yao, 2013; Menzel et al., 2019). Meanwhile, it is shown in **Figure 2** that the changing trend of D is different from parameters δ and Δ. Hence, in this section, we first analyze the variation of parameter D with the objective magnification. As we can see in **Figure 3**, both the Mean (**Figure 3A**) and Entropy (**Figure 3B**) values of D initially increase and then gradually decrease as the objective magnification becomes larger, reaching their peak values at 10×. For GLCM parameters, the variation trend of Contrast (**Figure 3C**) is similar to that of Mean and Entropy. It means that the fibrous structure information contained in the D image first increases and then gradually decreases. However, the values of the remaining three parameters: Correlation (**Figure 3D**), Homogeneous (**Figure 3E**), and Energy (**Figure 3F**) decreased significantly from 4× to 10×, and then increase slowly with the increasing objective magnification. It indicates that from 10× to 60× the image texture of the obtained D parameter becomes more uniform, similar, and ordered. The possible reason is that there may be the loss of image details for large magnifications, which can result in smooth and blurry image textures. It can also be demonstrated in **Figure 2** that in parameter D images some fibers with small particle sizes are gradually unobservable with the increasing magnification, especially when the 60× objective was used. It may be induced by a significant decrease in D of the tiny cylinder at high magnification, where the fiber structures are no longer apparently leading to a decrease in imaging contrast at high magnification and the image texture becomes smooth and blurred. To testify, we obtain the phase functions of the infinitely long cylindrical scatterers (Kienle et al., 2003; Yun et al., 2009) with different particle sizes as shown in **Figures 3G,H**, in which the zenith angle is 90°. Here, the cylinders with a radius of 100 nm (blue solid lines) and 200 nm (red dashed lines) represent the small fibers, while the cylinders with a radius of 1 μm (yellow dashed lines) and 1.5 μm (purple dashed lines) represent the coarse fibers in the tissue samples. Obviously, the phase functions confirm that the distribution of light scattered by the coarse cylinders (yellow and purple lines) is mainly concentrated in the range of small angles (15° corresponds to the scattering angle of 10×), or in other words, more photons are forward scattered by large fibers. For the objective lens, a large magnification means a large NA and an increased angle of reception for the scattered light. It can be clearly seen from **Figure 3H** that the diattenuation

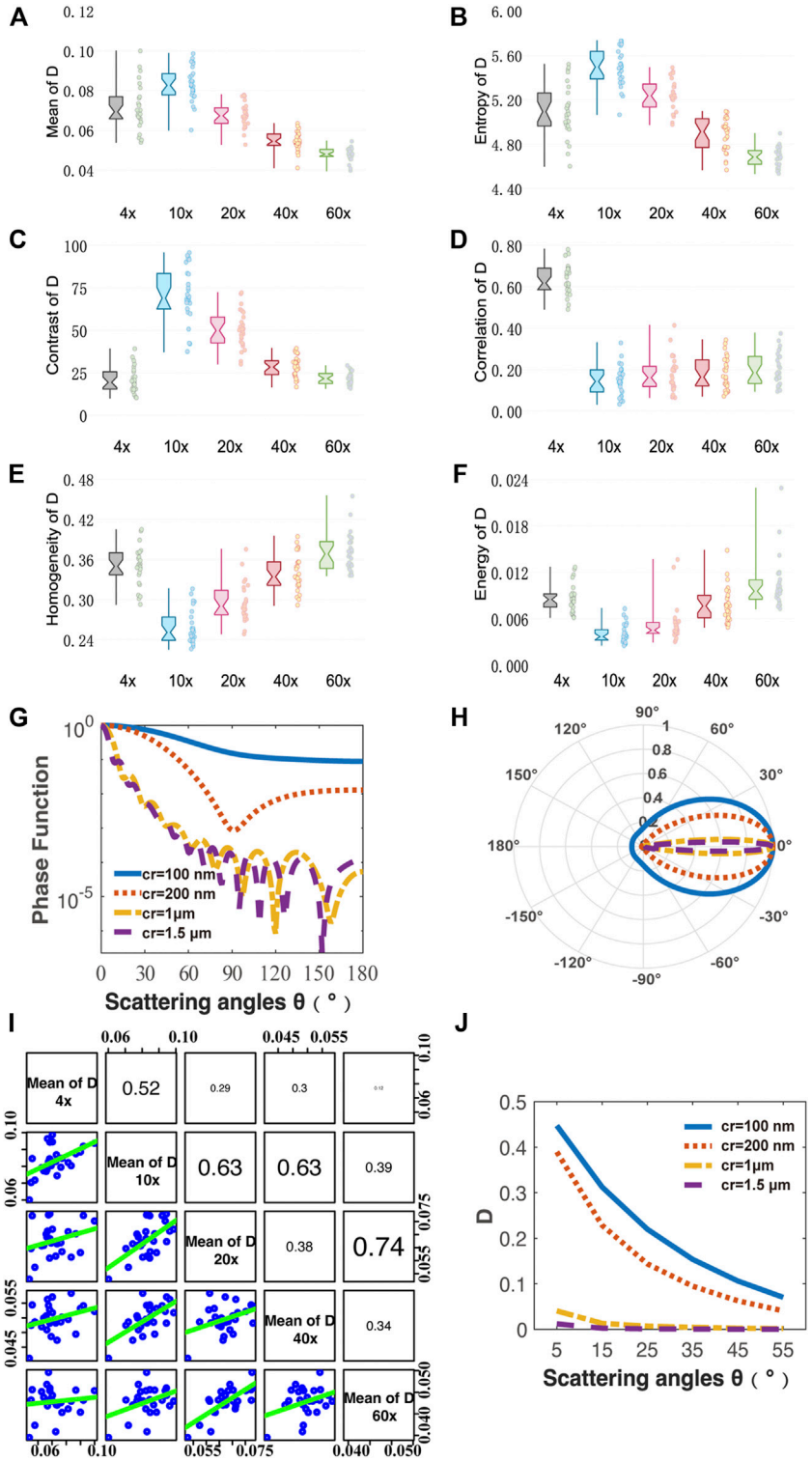

FIGURE 3 | Quantitative analysis of MMPD parameter *D* images under different magnification objectives (4×/NA 0.10, 10×/NA 0.25, 20×/NA 0.40, 40×/NA 0.65, 60×/NA 0.80). **(A–F)** Box plots of Mean, Entropy, Contrast, Correlation, Homogeneity and Energy. **(G,H)** Phase functions for cylinder scatterers with radius of 100, 200, 1, and 1.5 μm. **(I)** The scatter-plot matrix illustrates the general correlation among the Mean value of D under different magnification objectives (4×/NA 0.10, 10×/NA 0.25, 20×/NA 0.40, 40×/NA 0.65, 60×/NA 0.80). The variables are written in a diagonal line from top left to bottom right. On the right of the diagonal are the correlation coefficient *R* between two pairs of mean of *D* at different magnifications, with the larger the font size, the higher the correlation. On the left side of the diagonal is the scatter-plot matrix, with smooth green trend line to illustrate the underlying relationship. **(J)** Monte Carlo simulation results of the parameter *D* using the cylinder scatterer model of different radius: 100, 200, 1, and 1.5 μm. The horizontal axis represents different scattering angle from 5° to 55°.

information induced by the coarse fibers is mainly concentrated in the forward scattering photons. That is to say, as the objective magnification or NA increases, the received scattering angle becomes larger, and more information about the small cylinders produce significant changes. As the objective magnification or NA increases, the received scattering angle becomes larger and the information from the tiny fibers is gradually blurred in the *D* image.

For a better explanation, the CSM-based Monte Carlo simulation was used to further analyze the relationship between scattering angle and parameter *D* value of cylinders with different sizes. Here, the simulation parameters are as follows: the radius of the cylinder scatterer is 100 nm, 200 nm, 1 μm, and 1.5 μm; the scattering coefficient is 200 cm^{-1}; the refractive index is 1.43; the zenith angle is 90°; the cylinders are aligned in the x-y plane, and their orientations fluctuate around both the *x*- and *z-axis* following a Gaussian distribution with a standard deviation of 30° half-width. The refractive index of the medium is 1.35, the wavelength of the incident light is 633 nm, the thickness of the medium is 6 μm, and the number of incident photons is 10^7.

It can be found in the MC simulation results in **Figure 3J** that 1) for the same scattering coefficient the *D* values of the small cylinders (blue and red lines) are larger than that of the coarse fibers (yellow and purple lines); 2) as the scattering angle increases from 5° to 55° the *D* values of the small cylinders decrease prominently, while the variations of the *D* values for large fibers are limited. The high NA objective also collects the photons' information observed by the low NA one. However, the high NA objective receives light from a wider angle, which means that more photons are collected, and the information carried by small-angle photons is diluted by those received at larger angles. Therefore, the overall parameter *D* value becomes smaller. Both the MC simulation results and phase functions are shown in **Figure 3** demonstrate that when a low magnification objective is used, the resolution is insufficient and only the coarse fibrous structures in the tissue can be observed. Since the diattenuation resulting from the coarse cylinder is smaller compared to that by the small fibers, a small mean parameter *D* value was observed at 4×. When the objective was changed from 4× to 10×, the information of small fibrous structures could be gradually detected, therefore the mean value of *D* increased. In the transition from 10× to 60×, the diattenuation brought by the fine fibers decreases as the magnification increases, and therefore the mean value of *D* decreases. The scatter-plot matrix in **Figure 3I** shows the general correlation among the Mean value of *D* under different magnification objectives (4×/NA 0.10, 10×/NA 0.25, 20×/NA 0.40, 40×/NA 0.65, and 60×/NA 0.80). The variables are written in a diagonal line from top left to bottom right. On the right of the diagonal is the correlation coefficient *R* between two pairs of the mean of *D* at different magnifications, with the larger the font size, the higher the correlation. On the left side of the diagonal is the scatter-plot, with smoother green trend lines indicating linear fitting for the data points from two pairs of the mean of *D* at different magnification lines to illustrate the underlying relationship. We can see from **Figure 3I** that the correlation between the mean values of the parameters *D* at different magnifications is not significant, with most of the *R* values ranging from 0.2 to 0.4, implying a moderate correlation. It indicates that the diattenuation information represented by parameter *D* is different at varying magnifications and different reception angles. It suggests that when using features of *D* images to distinguish between different fibrous structures, the relatively low-resolution images may serve as a better choice, such as 10×, which provides more information on fiber structure compared to high magnification together with fast imaging speed and wide FOV. As shown in **Figure 2**, the fibrous structures are clearer in *D* images compared to those in the δ and Δ images at low magnification. In contrast, the images of δ and Δ show clearer fiber structures at high magnification. It indicates that the influence of NA on polarization parameters is different. We can combine *D* images with other polarization parameter images to obtain comprehensive structural information about the sample. Recently, we developed an image fusion method based on color spaces to combine different polarimetric parameters to provide multi-dimensional structural information (Zhai et al., 2022). This method can improve the microstructural characterization at low magnification based on the parameters. Therefore, it may also be helpful to obtain clear *D* images by combining other polarization parameter images at high magnification for biomedical applications.

Analysis of Linear Retardance

Figure 4 shows analysis results of MMPD parameter δ images. From **Figure 4A** we can see that the Mean value of the linear retardance δ gradually increases when the objective magnification increases from 4× to 40×, and then becomes stable when the magnification reaches 60×. The possible reason for such a changing trend is that the greater NA of the objective with a larger magnification means a larger receiving angle of the scattering photons, which have a longer propagation path in tissue compared with the ones of limited scattering numbers. Therefore, the more scattering photons contribute a larger value of linear retardance δ. We can also notice that the changing trend of Entropy shown in **Figure 4B** with the increasing objective magnification is similar to that of the Mean value.

For GLCM parameters, the Contrast value shown in **Figure 4C** gradually increases with the increase of the objective magnification, and the change becomes stable at 40× and 60×. It indicates that the δ image will be clearer when the objective of higher NA is used. Meanwhile, the other three GLCM parameters: Correlation shown in **Figure 4D**, Homogeneity shown in **Figure 4E**, and Energy shown in **Figure 4F** decrease as the magnification increases from 4× to 10×, then become relatively stable as the magnification changes. It indicates that the δ image texture is more uniform, similar, and ordered at a low magnification of 4×. The reason is that the loss of image details can lead to the image becoming smooth. However, when objective lenses of magnification larger than 10× are applied to the tissue sample, the texture feature information contained in δ images is stable. Moreover, as we can see in **Figure 4G**, Mean values of δ images have Pearson correlation coefficients R values > 0.7 for each objective at different magnifications, with a strong

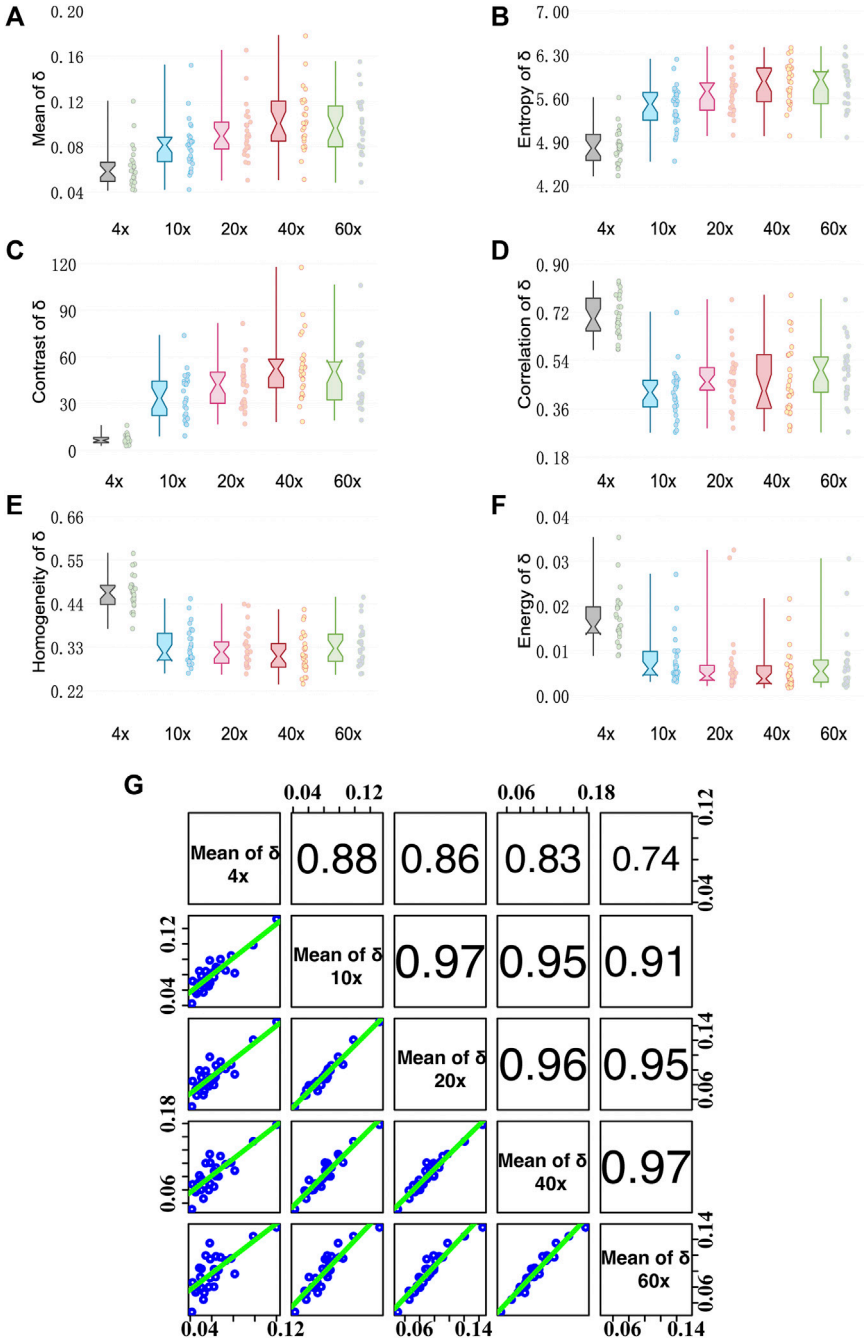

FIGURE 4 | Quantitative analysis results of MMPD parameter δ images under different magnification objectives (4×/NA 0.10, 10×/NA 0.25, 20×/NA 0.40, 40×/NA 0.65, and 60×/NA 0.80). **(A–F)** Box plots of Mean, Entropy, Contrast, Correlation, Homogeneity, and Energy. **(G)** The Correlation coefficient *R* between two pairs of mean of δ at different magnifications. (cf. **Figure 3I**).

correlation with R values > 0.9 for objectives at 10× and higher magnifications. It demonstrates that the information of δ at high magnification can also be well observed at low magnification. The conclusion is in accordance with our previous study (Shen et al., 2020), which is the fibers density information contained in the texture features of the linear retardance δ parameter image is preserved well with the decline of imaging resolution.

Analysis of Depolarization

Figure 5 shows analysis results of MMPD depolarization parameter Δ images. As can be seen in **Figures 5A,B**, the larger magnification of the objective lens, the larger the Mean and Entropy values of Δ obtained. As the magnification of the objective becomes larger, more multiply scattered photons are collected, which contribute more to depolarization (Bicout et al.,

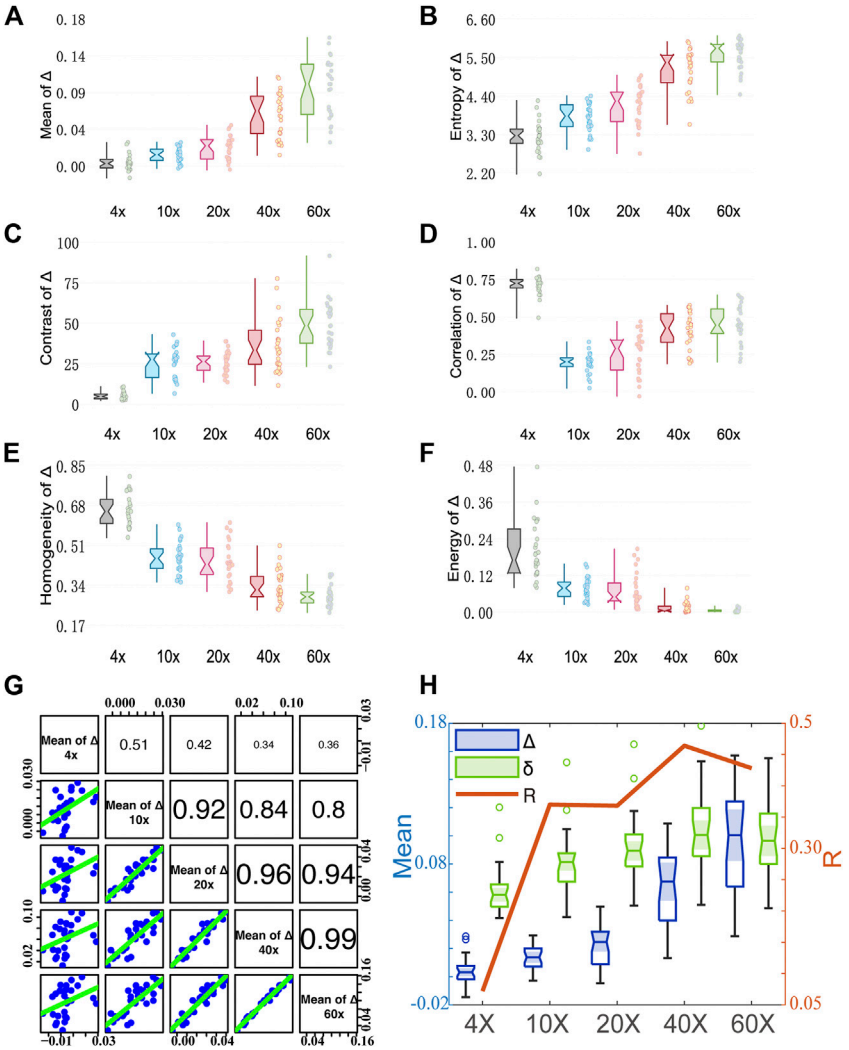

FIGURE 5 | Quantitative analysis results of MMPD parameter *Δ* images under different magnification objectives (4×/NA 0.10, 10×/NA 0.25, 20×/NA 0.40, 40×/NA 0.65, and 60×/NA 0.80). **(A–F)** Box plots of Mean, Entropy, Contrast, Correlation, Homogeneity, and Energy. **(G)** The Correlation coefficient *R* between two pairs of the mean of *Δ* at different magnification objectives. (cf. **Figure 3I**). **(H)** The Correlation coefficient *R* between the mean of *Δ* and *δ*.

1994; Brosseau, 1994; Aiello and Woerdman, 2005), leading to an increase in the observed Mean value of the MMPD *Δ* parameter. Also, the scattered photons contribute to the Entropy value of the *Δ* image. For GLCM parameters, first we can observe in **Figure 5C** that the larger magnification of the objective lens, the larger the Contrast value of *Δ* it shows. The increasing Contrast of the images means that the clarity of the *Δ* image increases significantly at high objective magnification. The values of Homogeneity shown in **Figure 5E** and Energy shown in **Figure 5F** are higher at small magnification. It means that the *Δ* image texture is more similar and ordered when the 4× objective is used. The Correlation shown in **Figure 5D** has a different trend from Homogeneity and Energy, where the value of 4× (0.5–0.8) is significantly higher than the other magnifications (0–0.6) It reflects the correlation of gray scale between pixels and spaced pixels. When the difference in gray values between pixels is small, the calculated correlation value is large. It means that the image texture uniformity is higher at 4×, the less fibrous structure can be observed and the texture looks more blurred, while more information on the fibrous structure can be obtained overall at higher magnification. Combining with **Figure 2**, we can find that under 4×, the image texture information is less, and the fiber structure is not obvious. As the resolution increases from 10× to 60×, the difference in gray value between the pixels of the fiber structure gradually decreases, therefore the Correlation of *Δ* gradually increases. However, the difference between fiber structure and non-fiber structure increases, resulting in the gradual decrease of Contrast-enhance, Homogeneity, and Energy. From **Figure 5G**, we can notice that the correlation of *Δ* images between 10× and higher magnification objectives is larger than 0.8. However, the correlation between 4× and other magnification objectives is relatively small. This also indicates that the information on fibrous structure at higher magnifications is better preserved in *Δ* images at 10×. If we want to obtain the

information on fibrous structure from Δ images, a lower magnification, such as 10×, can be considered. It can be seen in **Figures 4**, **5**, the trends of the first-order statistical moments, GLCM parameters of δ and Δ are similar. Some related literature (Wang and Wang, 2002; Alali, 2012; Ortega-Quijano et al., 2013; Pierangelo et al., 2013; He et al., 2015), indicated that δ can also induce depolarization in the scattering medium. Therefore, we correlate the variation processes of parameters δ and Δ with the magnification. Here, the correlation between Mean values of δ and Δ at different magnifications is plotted in **Figure 5H**. As the objective magnification increases, the receiving scattering angle increases, more multiply scattered photons that have longer propagation paths in tissue are collected, and the correlation between δ and Δ becomes larger, leading to larger Δ values induced by linear retardance.

CONCLUSION

In this study, to analyze the influence of imaging resolution or objective magnification on polarization properties obtained from Mueller matrix microscopy, namely diattenuation, linear retardance, and depolarization, we measured the Mueller matrices of unstained rat dorsal skin tissue slices abundant in collagen fibers. We calculated MMPD parameters D, δ, and Δ images of the sections at a series of different objective magnifications with 4×/NA 0.10, 10×/NA 0.25, 20×/NA 0.40, 40×/NA 0.65, and 60×/NA 0.80. Then, we analyzed the first-order moments and GLCM image texture parameters in conjunction with MMPD parameters D, δ, and Δ images. The results show that 1) when using features of D images to distinguish between different fibrous structures, the relatively low-resolution images may serve as a better choice, such as 10×, which provide more information on fiber structure compared to high magnification together with fast imaging speed and wide FOV. 2) The information of δ at high magnification can also be well observed at low magnification, the fibers density information contained in the texture features of linear retardance δ parameter image is preserved well with the decline of imaging resolution. 3) The information of fibrous structures at higher magnifications is well preserved in Δ images at 10×. If we want to obtain the information on fibrous structures from Δ images, a lower magnification, such as 10×, can be considered. This study provides a criterion to decide which structural information can be accurately and rapidly obtained using a transmission Mueller matrix microscope with low NA objectives to assist pathological diagnosis and other applications.

DATA AVAILABILITY STATEMENT

The raw data supporting the conclusion of this article will be made available by the authors, without undue reservation.

ETHICS STATEMENT

The animal study was reviewed and approved by the Ethics Committee of the Shenzhen International Graduate School, Tsinghua University.

AUTHOR CONTRIBUTIONS

CS and HH conceived the idea of the manuscript. CS, BC, YS, and HZ prepared the samples and performed the experiments. CS wrote the original manuscript and analyzed the results. HH and CH performed the language editing. HH, CH, and HM supervised the study. All authors have given approval to the final version of the manuscript.

FUNDING

This work was supported by the Shenzhen Key Fundamental Research Project (No. JCYJ20210324120012035) and the National Natural Science Foundation of China (NSFC) (No. 61527826).

ACKNOWLEDGMENTS

CH would like to thank the support of the Junior Research Fellowship from St. John's College at the University of Oxford.

REFERENCES

Aiello, A., and Woerdman, J. P. (2005). Physical Bounds to the Entropy-Depolarization Relation in Random Light Scattering. *Phys. Rev. Lett.* 94 (9), 090406. doi:10.1103/PhysRevLett.94.090406

Alali, S. (2012). Quantitative Correlation Between Light Depolarization and Transport Albedo of Various Porcine Tissues. *J. Biomed. Opt.* 17 (4), 045004. doi:10.1117/1.JBO.17.4.045004

Alali, S., and Vitkin, A. (2015). Polarized Light Imaging in Biomedicine: Emerging Mueller Matrix Methodologies for Bulk Tissue Assessment. *J. Biomed. Opt.* 20 (6), 061104. doi:10.1117/1.JBO.20.6.061104

Azzam, R. M. A. (1978). Photopolarimetric Measurement of the Mueller Matrix by Fourier Analysis of a Single Detected Signal. *Opt. Lett.* 2 (6), 148. doi:10.1364/OL.2.000148

Bicout, D., Brosseau, C., Martinez, A. S., and Schmitt, J. M. (1994). Depolarization of Multiply Scattered Waves by Spherical Diffusers: Influence of the Size Parameter. *Phys. Rev. E* 49 (2), 1767–1770. doi:10.1103/PhysRevE.49.1767

Brosseau, C. (1994). "Entropy Production and Depolarization of Multiply Scattered Light by a Random Dense Medium," in *Satellite Remote Sensing*.

Chen, B., Li, W., He, H., He, C., Guo, J., Shen, Y., et al. (2021a). Analysis and Calibration of Linear Birefringence Orientation Parameters Derived from Mueller Matrix for Multi-Layered Tissues. *Opt. Lasers Eng.* 146, 106690. doi:10.1016/j.optlaseng.2021.106690

Chen, C., Chen, X., Wang, C., Sheng, S., Song, L., Gu, H., et al. (2021b). Imaging Mueller Matrix Ellipsometry with Sub-micron Resolution Based on Back Focal Plane Scanning. *Opt. Express* 29 (20), 32712. doi:10.1364/OE.439941

Chen, D., Zeng, N., Xie, Q., He, H., Tuchin, V. V., and Ma, H. (2017). Mueller Matrix Polarimetry for Characterizing Microstructural Variation of Nude

Mouse Skin during Tissue Optical Clearing. *Biomed. Opt. Express* 8 (8), 3559. doi:10.1364/BOE.8.003559

Chen, Y., Chu, J., Tang, W. C., Zhang, R., Zhao, M., and Xin, B. (2022). Study of the Spatial Scale Stability of Mueller Matrix Parameters for Textural Characterization of Biological Tissues. *J. Biophot.* 15 (5), 269. doi:10.1002/jbio.202100269

Chen, Z., Meng, R., Zhu, Y., and Ma, H. (2020). A Collinear Reflection Mueller Matrix Microscope for Backscattering Mueller Matrix Imaging. *Opt. Lasers Eng.* 129, 106055. doi:10.1016/j.optlaseng.2020.106055

Chenault, D. B., Pezzaniti, J. L., and Chipman, R. A. (1992). *Mueller Matrix Algorithms*. Proc Spie, 1746.

Chung, J., Jung, W., Hammer-Wilson, M. J., Wilder-Smith, P., and Chen, Z. (2007). Use of Polar Decomposition for the Diagnosis of Oral Precancer. *Appl. Opt.* 46 (15), 3038. doi:10.1364/AO.46.003038

Dong, Y., He, H., Sheng, W., Wu, J., and Ma, H. (2017). A Quantitative and Non-contact Technique to Characterise Microstructural Variations of Skin Tissues during Photo-Damaging Process Based on Mueller Matrix Polarimetry. *Sci. Rep.* 7 (1), 14702. doi:10.1038/s41598-017-14804-z

Dong, Y., Qi, J., He, H., He, C., Liu, S., Wu, J., et al. (2017). Quantitatively Characterizing the Microstructural Features of Breast Ductal Carcinoma Tissues in Different Progression Stages by Mueller Matrix Microscope. *Biomed. Opt. Express* 8 (8), 3643. doi:10.1364/BOE.8.003643

Dong, Y., Wan, J., Si, L., Meng, Y., Dong, Y., Liu, S., et al. (2021b). Deriving Polarimetry Feature Parameters to Characterize Microstructural Features in Histological Sections of Breast Tissues. *IEEE Trans. Biomed. Eng.* 68 (3), 881–892. doi:10.1109/TBME.2020.3019755

Dong, Y., Wan, J., Wang, X., Xue, J.-H., Zou, J., He, H., et al. (2021a). A Polarization-Imaging-Based Machine Learning Framework for Quantitative Pathological Diagnosis of Cervical Precancerous Lesions. *IEEE Trans. Med. Imaging* 40 (12), 3728–3738. doi:10.1109/TMI.2021.3097200

Dong, Z., Gu, H., Zhu, J., Shi, Y., Nie, L., Lyu, J., et al. (2020). Nonuniform Depolarization Properties of Typical Nanostructures and Potential Applications. *Opt. Lett.* 45 (7), 1910. doi:10.1364/OL.389732

Du, E., He, H., Zeng, N., Sun, M., Guo, Y., Wu, J., et al. (2014). Mueller Matrix Polarimetry for Differentiating Characteristic Features of Cancerous Tissues. *J. Biomed. Opt.* 19 (7), 076013. doi:10.1117/1.JBO.19.7.076013

Fan, C., and Yao, G. (2013). Imaging Myocardial Fiber Orientation Using Polarization Sensitive Optical Coherence Tomography. *Biomed. Opt. Express* 4 (3), 460. doi:10.1364/BOE.4.000460

Fang, M., Gu, H., Song, B., Guo, Z., and Liu, S. (2022). Thickness Scaling Effects on the Complex Optical Conductivity of Few-Layer WSe 2 Investigated by Spectroscopic Ellipsometry. *Adv. Photonics Res.* 3 (4), 2100299. doi:10.1002/adpr.202100299

Ghosh, N., Wood, M. F. G., and Vitkin, I. A. (2008). Mueller Matrix Decomposition for Extraction of Individual Polarization Parameters from Complex Turbid Media Exhibiting Multiple Scattering, Optical Activity, and Linear Birefringence. *J. Biomed. Opt.* 13 (4), 044036. doi:10.1117/1.2960934

Goldstein, D. H. (1992). Mueller Matrix Dual-Rotating Retarder Polarimeter. *Appl. Opt.* 31 (31), 6676. doi:10.1364/AO.31.006676

Guo, Y., Zeng, N., He, H., Yun, T., Du, E., Liao, R., et al. (2013). A Study on Forward Scattering Mueller Matrix Decomposition in Anisotropic Medium. *Opt. Express* 21 (15), 18361. doi:10.1364/OE.21.018361

Haralick, R. M., Shanmugam, K., and Dinstein, I. H. (1973). Textural Features for Image Classification. *IEEE Trans. Syst. Man. Cybern.* SMC-3 (6), 610–621. doi:10.1109/TSMC.1973.4309314

He, C., Chang, J., Salter, P. S., Shen, Y., Dai, B., Li, P., et al. (2022). Revealing Complex Optical Phenomena through Vectorial Metrics. *Adv. Phot.* 4 (02). doi:10.1117/1.AP.4.2.026001

He, C., He, H., Chang, J., Chen, B., Ma, H., and Booth, M. J. (2021). Polarisation Optics for Biomedical and Clinical Applications: a Review. *Light Sci. Appl.* 10 (1), 194. doi:10.1038/s41377-021-00639-x

He, C., He, H., Chang, J., Dong, Y., Liu, S., Zeng, N., et al. (2015). Characterizing Microstructures of Cancerous Tissues Using Multispectral Transformed Mueller Matrix Polarization Parameters. *Biomed. Opt. Express* 6 (8), 2934. doi:10.1364/BOE.6.002934

He, C, C., Chang, J., Hu, Q., Wang, J., Antonello, J., He, H., et al. (2019a). Complex Vectorial Optics through Gradient Index Lens Cascades. *Nat. Commun.* 10 (1), 4264. doi:10.1038/s41467-019-12286-3

He, H, H., Liao, R., Zeng, N., Li, P., Chen, Z., Liu, X., et al. (2019b). Mueller Matrix Polarimetry-An Emerging New Tool for Characterizing the Microstructural Feature of Complex Biological Specimen. *J. Light. Technol.* 37 (11), 2534–2548. doi:10.1109/JLT.2018.2868845

Hu, H., Zhang, Y., Li, X., Lin, Y., Cheng, Z., and Liu, T. (2020). Polarimetric Underwater Image Recovery via Deep Learning. *Opt. Lasers Eng.* 133, 106152. doi:10.1016/j.optlaseng.2020.106152

Jacques, S. L., Ramella-Roman, J. C., and Lee, K. (2002). Imaging Skin Pathology with Polarized Light. *J. Biomed. Opt.* 7 (3), 329. doi:10.1117/1.1484498

Kienle, A., Forster, F. K., Diebolder, R., and Hibst, R. (2003). Light Propagation in Dentin: Influence of Microstructure on Anisotropy. *Phys. Med. Biol.* 48 (2), N7–N14. doi:10.1088/0031-9155/48/2/401

Li, P., Dong, Y., Wan, J., He, H., Aziz, T., and Ma, H. (2022). Polaromics: Deriving Polarization Parameters from a Mueller Matrix for Quantitative Characterization of Biomedical Specimen. *J. Phys. D. Appl. Phys.* 55 (316pp), 034002. doi:10.1088/1361-6463/ac292f

Li, P., Liu, C., Li, X., He, H., and Ma, H. (2016). GPU Acceleration of Monte Carlo Simulations for Polarized Photon Scattering in Anisotropic Turbid Media. *Appl. Opt.* 55 (27), 7468. doi:10.1364/AO.55.007468

Liu, T., Lu, M., Chen, B., Zhong, Q., Li, J., He, H., et al. (2019). Distinguishing Structural Features between Crohn's Disease and Gastrointestinal Luminal Tuberculosis Using Mueller Matrix Derived Parameters. *J. Biophot.* 12 (12), 151. doi:10.1002/jbio.201900151

Liu, Y., Dong, Y., Si, L., Meng, R., Dong, Y., and Ma, H. (2021). Comparison between Image Texture and Polarization Features in Histopathology. *Biomed. Opt. Express* 12 (3), 1593. doi:10.1364/BOE.416382

Lu, S.-Y., and Chipman, R. A. (1996). Interpretation of Mueller Matrices Based on Polar Decomposition. *J. Opt. Soc. Am. A* 13 (5), 1106. doi:10.1364/JOSAA.13.001106

Meng, R., Shao, C., Li, P., Dong, Y., Hou, A., Li, C., et al. (2021). Transmission Mueller Matrix Imaging with Spatial Filtering. *Opt. Lett.* 46 (16), 4009. doi:10.1364/OL.435166

Menzel, M., Axer, M., Amunts, K., De Raedt, H., and Michielsen, K. (2019). Diattenuation Imaging Reveals Different Brain Tissue Properties. *Sci. Rep.* 9 (1), 1939. doi:10.1038/s41598-019-38506-w

Morio, J., and Goudail, F. (2004). Influence of the Order of Diattenuator, Retarder, and Polarizer in Polar Decomposition of Mueller Matrices. *Opt. Lett.* 29 (19), 2234. doi:10.1364/OL.29.002234

Ortega-Quijano, N., et al. (2013). "Polarized Light Monte Carlo Analysis of Birefringence-Induced Depolarization in Biological Tissues," in *Medical Laser Applications & Laser-Tissue Interactions VI*. doi:10.1117/12.2032169

Pierangelo, A., Nazac, A., Benali, A., Validire, P., Cohen, H., Novikova, T., et al. (2013). Polarimetric Imaging of Uterine Cervix: a Case Study. *Opt. Express* 21 (12), 14120. doi:10.1364/OE.21.014120

Qi, J., and Elson, D. S. (2017). Mueller Polarimetric Imaging for Surgical and Diagnostic Applications: a Review. *J. Biophot.* 10 (8), 950–982. doi:10.1002/jbio.201600152

Shen, Y., Huang, R., He, H., Liu, S., Dong, Y., Wu, J., et al. (2020). Comparative Study of the Influence of Imaging Resolution on Linear Retardance Parameters Derived from the Mueller Matrix. *Biomed. Opt. Express* 12 (1), 211–225. doi:10.1364/BOE.410989

Steven, L. J., Jessica, C. R.-R, and Kenneth Lee, M. D. (2002). Imaging Skin Pathology with Polarized Light. *J. Biomed. Opt.* 7 (3), 329. doi:10.1117/1.1484498

Sun, M., He, H., Zeng, N., Du, E., Guo, Y., Liu, S., et al. (2014). Characterizing the Microstructures of Biological Tissues Using Mueller Matrix and Transformed Polarization Parameters. *Biomed. Opt. Express* 5 (12), 4223. doi:10.1364/BOE.5.004223

Sun, T., Liu, T., He, H., Wu, J., and Ma, H. (2018). Distinguishing Anisotropy Orientations Originated from Scattering and Birefringence of Turbid Media Using Mueller Matrix Derived Parameters. *Opt. Lett.* 43 (17), 4092. doi:10.1364/OL.43.004092

Swami, M. K., Manhas, S., Buddhiwant, P., Ghosh, N., Uppal, A., and Gupta, P. K. (2006). Polar Decomposition of 3 X 3 Mueller Matrix: a Tool for Quantitative Tissue Polarimetry. *Opt. Express* 14, 9324. doi:10.1364/OE.14.009324

Wang, C., Chen, X., Chen, C., Sheng, S., Song, L., Gu, H., et al. (2021). Reconstruction of Finite Deep Sub-wavelength Nanostructures by Mueller-

Matrix Scattered-Field Microscopy. *Opt. Express* 29 (20), 32158. doi:10.1364/OE.432611

Wang, X., and Wang, L. V. (2002). Propagation of Polarized Light in Birefringent Turbid Media: A Monte Carlo Study. *J. Biomed. Opt.* 7, 279. doi:10.1117/1.1483315

Wang, Y., He, H., Chang, J., He, C., Liu, S., Li, M., et al. (2016). Mueller Matrix Microscope: a Quantitative Tool to Facilitate Detections and Fibrosis Scorings of Liver Cirrhosis and Cancer Tissues. *J. Biomed. Opt.* 21 (7), 071112. doi:10.1117/1.JBO.21.7.071112

Wood, M. F. G., Ghosh, N., Moriyama, E. H., Wilson, B. C., and Vitkin, I. A. (2009). Proof-of-principle Demonstration of a Mueller Matrix Decomposition Method for Polarized Light Tissue Characterization *In Vivo*. *J. Biomed. Opt.* 14 (1), 014029. doi:10.1117/1.3065545

Yao, Y., Zhang, F., Wang, B., Wan, J., Si, L., Dong, Y., et al. (2022). Polarization Imaging-Based Radiomics Approach for the Staging of Liver Fibrosis. *Biomed. Opt. Express* 13 (3), 1564. doi:10.1364/BOE.450294

Yun, T., Zeng, N., Li, W., Li, D., Jiang, X., and Ma, H. (2009). Monte Carlo Simulation of Polarized Photon Scattering in Anisotropic Media. *Opt. Express* 17 (19), 16590. doi:10.1364/OE.17.016590

Zhai, H., Sun, Y., He, H., Chen, B., He, C., Wang, Y., et al. (2022). Distinguishing Tissue Structures via Polarization Staining Images Based on Different Combinations of Mueller Matrix Polar Decomposition Parameters. *Opt. Lasers Eng.* 152, 106955. doi:10.1016/j.optlaseng.2022.106955

Zhou, J., He, H., Chen, Z., Wang, Y., and Ma, H. (2018). Modulus Design Multiwavelength Polarization Microscope for Transmission Mueller Matrix Imaging. *J. Biomed. Opt.* 23 (01), 1. doi:10.1117/1.JBO.23.1.016007

Conflict of Interest: The authors declare that the research was conducted in the absence of any commercial or financial relationships that could be construed as a potential conflict of interest.

Publisher's Note: All claims expressed in this article are solely those of the authors and do not necessarily represent those of their affiliated organizations, or those of the publisher, the editors, and the reviewers. Any product that may be evaluated in this article, or claim that may be made by its manufacturer, is not guaranteed or endorsed by the publisher.

Copyright © 2022 Shao, Chen, He, He, Shen, Zhai and Ma. This is an open-access article distributed under the terms of the Creative Commons Attribution License (CC BY). The use, distribution or reproduction in other forums is permitted, provided the original author(s) and the copyright owner(s) are credited and that the original publication in this journal is cited, in accordance with accepted academic practice. No use, distribution or reproduction is permitted which does not comply with these terms.

Advantages of publishing in Frontiers

OPEN ACCESS
Articles are free to read for greatest visibility and readership

FAST PUBLICATION
Around 90 days from submission to decision

HIGH QUALITY PEER-REVIEW
Rigorous, collaborative, and constructive peer-review

TRANSPARENT PEER-REVIEW
Editors and reviewers acknowledged by name on published articles

Frontiers
Avenue du Tribunal-Fédéral 34
1005 Lausanne | Switzerland

Visit us: www.frontiersin.org
Contact us: frontiersin.org/about/contact

REPRODUCIBILITY OF RESEARCH
Support open data and methods to enhance research reproducibility

DIGITAL PUBLISHING
Articles designed for optimal readership across devices

FOLLOW US
@frontiersin

IMPACT METRICS
Advanced article metrics track visibility across digital media

EXTENSIVE PROMOTION
Marketing and promotion of impactful research

LOOP RESEARCH NETWORK
Our network increases your article's readership